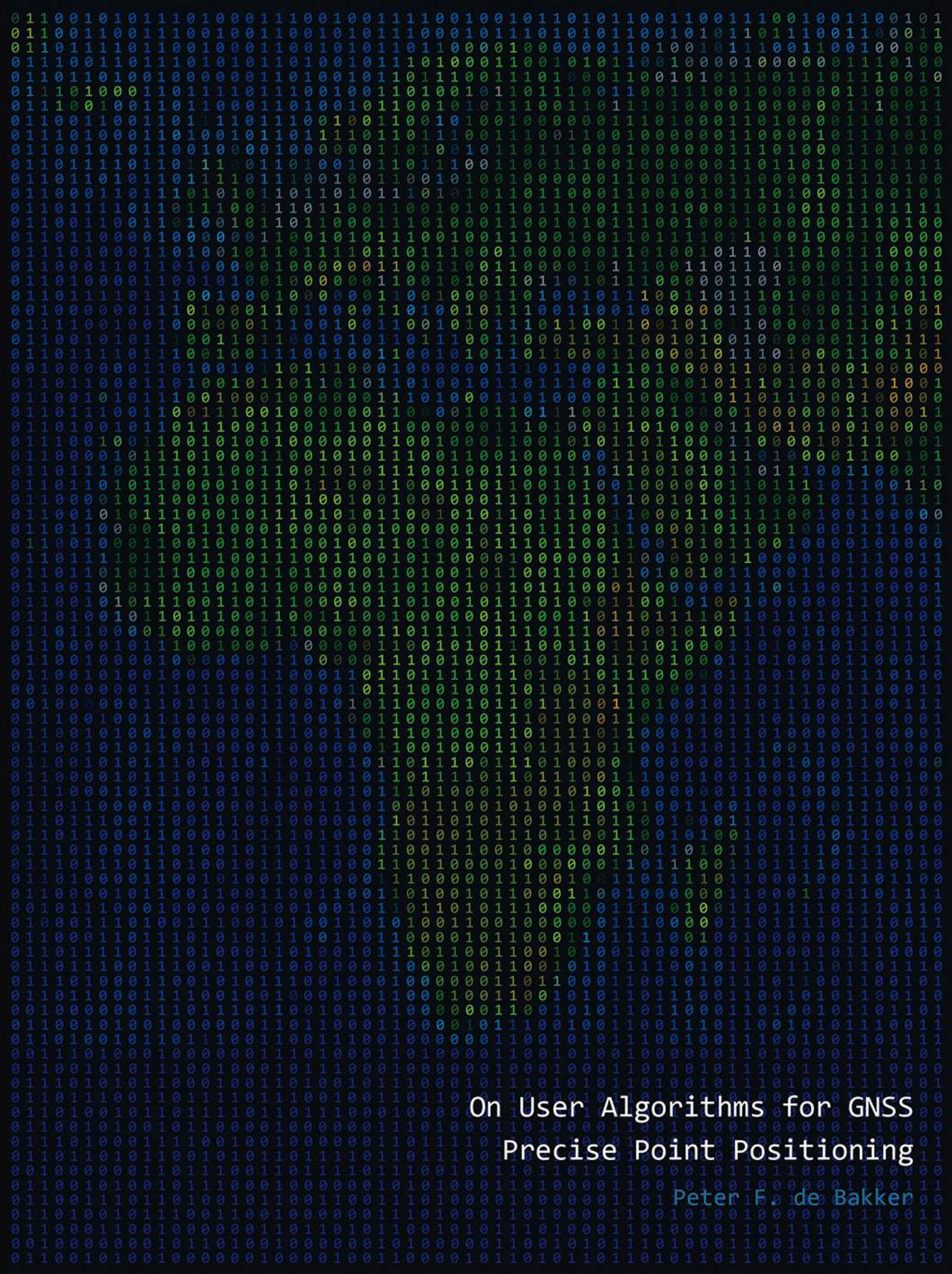

On User Algorithms for GNSS Precise Point Positioning

Peter F. de Bakker

On User Algorithms for GNSS Precise Point Positioning

Proefschrift

ter verkrijging van de graad van doctor
aan de Technische Universiteit Delft,
op gezag van de Rector Magnificus prof.ir. K.Ch.A.M. Luyben;
voorzitter van het College voor Promoties,
in het openbaar te verdedigen op
donderdag 7 januari 2016 om 12:30 uur

door

Peter Foeke DE BAKKER
Ingenieur Luchtvaart- en Ruimtevaarttechniek,
Technische Universiteit Delft, Nederland
geboren te Barendrecht, Nederland

This dissertation has been approved by the

promotor: Prof. dr. ir. P.J.G. Teunissen

copromotor: Dr. ir. H. van der Marel

Composition of the doctoral committee:

Rector Magnificus	chairman
Prof. dr. ir. P.J.G. Teunissen	Delft University of Technology
Dr. ir. H. van der Marel	Delft University of Technology
Independent members:	
Prof. dr. ir. P.N.A.M. Visser	Delft University of Technology
Prof. dr. -ing. habil. R. Klees	Delft University of Technology
Prof. dr. J. Sanz Subirana	Technical University of Catalonia (Spain)
Prof. dr. ir. P.J. Oonincx	Nederlandse Defensie Academie
Dr. ir. F. Kleijer	Septentrio N.V. (Belgium)

This research was partly funded by the European Commission through the Marie Curie action Industry-Academia Partnerships and Pathways (FP7-PEOPLE-IAPP-2008 SIGMA Project)

Cover design: Steven van Asch & Peter de Bakker

Contents

Nomenclature

Acronyms

ACC	International GNSS Service Analysis Center Coordinator, page 89
ADOP	Ambiguity Dilution of Precision, page 48
APC	Antenna Phase Center, page 104
AR	Ambiguity Resolution, page 3
AR(k)	Autoregressive process of order k, page 147
BDS	BeiDou Navigation Satellite System, page 11
C/N_0	Carrier-to-Noise density ratio, page 29
CC	Code-minus-Carrier, page 123
CODE	Center for Orbit Determination in Europe, page 20
COM	Center Of Mass, page 104
CPC	Code-Plus-Carrier, page 34
DCB	Differential Code Bias, page 17
DCPB	Differential Code-Phase Bias, page 56
DD	Double Difference, page 127
DIA	Detection-Identification-Adaptation, page 2
DLR	Deutschen Zentrums fr Luft- und Raumfahrt, page 117
DOP	Dilution of Precision, page 94
DPB	Differential Phase Bias, page 59
ECMWF	European Centre for Medium-range Weather Forecast, page 19
EGNOS	European Geostationary Navigation Overlay Service, page 2
ERP	Earth Rotation Parameters, page 17

ESA	European Space Agency, page 1
GIM	Global Ionosphere Map, page 20
GIOVE	Galileo In-Orbit Validation Element, page 11
GLONASS	GLObal NAvigation Satellite System, page 1
GNSS	Global Satellite Navigation System, page 1
GPS	Global Positioning System, page 1
IAC	GLONASS Information-Analytical Centre, page 1
IF	Ionosphere-Free, page 41
IGDG	Internet-Based Global Differential GPS, page 25
IGS	International GNSS Service, page 25
IGU	International GNSS Service Ultra-rapid products, page 85
IRNSS	Indian Regional Navigation Satellite System, page 11
ISB	Inter-System Bias, page 11
ITRF	International Terrestrial Reference Frame, page 15
JPL	Jet Propulsion Laboratory, page 25
LAMBDA	Least-squares AMBiguity Decorrelation Adjustment, page 3
LNA	Low Noise Amplifier, page 130
LOM	The Local Overall Model, page 204
LOS	Line-Of-Sight, page 25
LSE	Least-Squares Estimator, page 174
MDB	Minimal Detectable Bias, page 2
MP	Multipath linear combination, page 133
MW	Melbourne-Wübbena, page 44
NGA	National Geospacial-intelligence Agency, page 105
NL	Narrow Lane, page 43
NRCan	Natural Resources Canada, page 25
OMC	Observed Minus Computed, page 31

PCO	Phase Center Offset, page 25
PCV	Antenna Phase Center Variation, page 26
PPP	Precise Point Positioning, page 3
PRN	Pseudo-Random Noise sequence (GPS satellite identification), page 95
PVT	Positioning, Velocity and Time, page 1
PWU	Phase Wind-Up or Phase Wrap-Up, page 27
QZSS	Quasi-Zenith Satellite System, page 2
RAIM	Receiver Autonomous Integrity Monitoring, page 2
RETICLE	Real-Time Clock Estimation, page 85
RHCP	Right-Hand Circularly Polarized, page 27
rms	root-mean-square, page 10
RT	Real-Time, page 90
RTK	Real Time Kinematic, page 3
Rx	Receiver, page 125
SB	Short Baseline, page 126
SBAS	Satellite Based Augmentation System, page 2
SD	Single Difference, page 126
SoL	Safety-of-Life, page 1
TEC	Total Electron Content, page 20
UD	Undifferenced, page 125
UMPI	Uniformly Most Powerful Invariant, page 174
URE	User Range Error, page 88
VCE	Variance Component Estimation, page 203
WA-RTK	Wide Area Real Time Kinematic, page 3
WAAS	Wide Area Augmentation System, page 2
WGS84	World Geodetic System 1984, page 15
WL	Wide Lane, page 43

ZB Short Baseline, page 126

Greek symbols

α Probability of false alarm, page 207

β Probability of missed detection, page 207

δt Clock offset, page 13

Δ Difference, page 31

δ Systematic delay on the carrier phase measurement, page 14

ϵ Code measurement error, page 14

$\boldsymbol{\epsilon}$ Measurement errors, page 50

ε Phase measurement error, page 14

γ Ionosphere dispersion factor, page 21

λ Carrier wavelength, page 14

λ_0 Non-centrality parameter, page 176

μ Mean value, page 152

Φ Carrier phase observation, page 14

ψ Power of hypothesis test, page 176

ρ Geometric range, page 14

ϱ Correlation coefficient, page 125

τ Signal travel time, page 14

ξ Slowly changing phase delays, page 123

ζ Slowly changing code delays, page 123

Roman letters

A Carrier phase ambiguity, page 14

$\mathbf{A}$ Design matrix, page 50

c_0 Speed of light in vacuum, page 14

d Systematic delay on the pseudorange measurement, page 14

$\mathbf{e}$ Unit direction vector, page 31

f	Frequency, page 14
g	Combined geometric range, troposphere delay, satellite and receiver clock offset, page 33
$\mathbf{I}_m$	$m \times m$ unit matrix, page 53
$\mathcal{I}$	Ionosphere delay, page 14
k	Time epoch of measurement, page 13
m	Number of satellites, page 53
m	Troposphere mapping function, page 18
N	Integer ambiguity, page 41
P	Pseudorange observation, page 14
$\boldsymbol{Q}$	Covariance matrix, page 32
r	Receiver index, page 14
$\mathbf{r}$	Position, page 14
s	Satellite index, page 14
T	Troposphere delay, page 14
t	System time, page 13
t_r	Time of reception, page 14
t_k	Receiver time tag, page 13
$\mathbf{u}_m$	$m \times 1$ vector with ones, page 53
$\mathbf{x}$	Unknown parameters, page 50
$\mathbf{y}$	Observations, page 50

Mathematical symbols

$\hat{\square}$	Estimated parameter, page 148
$\otimes$	Kronecker product, page 169
$\underline{\square}$	Random variable, page 14
$D\{\square\}$	Dispersion operator, page 123
$E\{\square\}$	Expectation operator, page 123
$\square^*$	Transpose, page 31

Samenvatting

Precieze plaats bepaling (PPP) is een Globaal Navigatie Satelliet System (GNSS) methode van processen met als doel het leveren van hoge positie nauwkeurigheid zonder de noodzaak voor een basis station in de nabijheid van de gebruiker, of een dicht netwerk van referentie stations. Om deze doelstelling te bereiken gebruikt PPP de zeer exacte fasewaarnemingen van de draaggolf naast de grovere pseudoafstandsmetingen. Voordat de fasemetingen bij kunnen dragen aan de positie oplossing, moeten de constante fase meerduidigheden worden geschat uit de metingen. Verder worden, om een accurate positie te berekenen, een aantal methodes gebruikt om de bijdragen van fouten te minimaliseren. Een dun bezaaid wereldwijd netwerk van referentiestations schat GNSS satelliet banen en klok afwijkingen met hoge nauwkeurigheid, en stelt deze data ter beschikking aan de gebruiker. A piori modellen worden gebruikt om te corrigeren voor hydrostatische troposfeer vertragingen, relativistische effecten, draaggolf fase opwinding, fase centrum verschillen en variaties. Wij zullen ons vooral richten op gebruikers dichtbij het aardoppervlak, wat betekent dat verplaatsingseffecten (bijv. door belasting door de oceanen en de vaste aardgetijden) ook moeten worden beschouwd. De natte troposfeer vertraging wordt meestal geschat uit de data, en, in conventionele PPP, worden de ionosfeer vertragingen te niet gedaan door observaties op twee frequenties te combineren in een kleiner aantal ionosfeer-vrije observaties. De nauwkeurigheid die PPP levert op basis van GPS is heel hoog, slechts enkele mm voor 24u statische data.

Echter, PPP heeft een aantal tekortkomingen welke in dit proefschrift worden behandeld:

- De noodzaak om de ionosfeer vertragingen te verwijderen en de fase meerduidigheden te schatten resulteert in een relatief zwak model. Dit leidt tot lange (re)initialisatie tijden voordat een accurate positie berekend kan worden. In dit proefschrift wordt een alternatieve aanpak gentroduceerd, geïmplementeerd en getoetst welke niet een ionosfeer-vrije combinatie vormt, maar de ionosfeer-vertragingen schat uit de observaties. Ten eerst worden (gelinearizeerde) GNSS observatie vergelijkingen geïntroduceerd en het functionele PPP model afgeleid. Hieruit bepalen we de te schatten parameters, en behandelen we de mogelijkheid om de ionosfeer schatting in te perken door externe ionosfeer data te gebruiken. Dit wordt bereikt door observaties met ionosfeer model waardes te corrigeren en alleen de residuele ionosfeer vertraging te schatten. Ten slotte wordt een dynamisch model voor de residuele ionosfeer vertraging bepaald en worden positie resultaten gepresenteerd.

- Een accuraat stochastisch model voor PPP ontbreekt nog, wat leidt tot het suboptimaal wegen van de verschillende observaties-types, een inadequate kwaliteitsbeschrijving van de oplossing, en onbetrouwbare hypothese toetsing. In dit proefschrift wor-

den de stochastische eigenschappen van het PPP model onderzocht, beginnende bij de nauwkeurigheid van de (real-time) satelliet baan en klok afwijkingen, gevolgd door de nauwkeurigheid en correlaties van de GNSS observaties. Wat betreft deze laatste, wordt een nieuw ontwikkelde methode geïntroduceerd gebaseerd op het geometrie-vrije model. Deze analyse bevat ook een schattingsprocedure om vertragingen in pseudoafstandsmetingen veroorzaakt door signaalreflecties (multipath) als een auto-regressief proces te schatten, welke ook gebruikt kan worden om een dynamisch model voor tijd-gecorreleerde parameters op te stellen. Als laatste is een bijna zuiver variantie componenten schattingsalgoritme toegepast op het complete PPP model, met als resultaat een accurate kwaliteitsbeschrijving van de geschatte posities.

- Integriteitscontrole (integrity monitoring) welke hypothese toetsing gebruikt om fouten te detecteren in het model, die niet worden gedekt door de verwachte onzekerheden, is nog niet goed ontwikkeld voor PPP. Dit onderwerp is gerelateerd aan bovenstaande punten, aangezien een accuraat stochastisch model is vereist voor intergriteits-controle, en omdat het schatten en inperken van de ionosfeer vertraging essentieel is voor een hoge mate van integriteit. Het geometrie-vrije model is opnieuw gebruikt in tijdsgedifferentieerde vorm om de integriteitsaspecten van multi-frequentie GNSS modellen en hun kracht om fouten zoals een slip in de fasemetingen te analyseren. De nulhypothese en alternatieve hypothesen worden gepresenteerd en de kleinste nog detecteerbare fouten (Minimal Detectable Biases, MDB) vastgesteld voor verschillende soorten fouten. Analytische uitdrukkingen worden gepresenteerd, ondersteund door numerieke resultaten.

De geometrie-vrije analyse van de ruis op pseudoafstands- en fasemetingen, liet een goede overeenstemming zien met theoretische uitdrukkingen die de ruis op de metingen relateren aan de parameters van de tracking-loops van de ontvanger en signaal-ruis verhouding. Echter, over langere tijds-intervallen zijn ook sterke variaties van the pseudoafstandsmetingen waargenomen, welke het fouten budget domineren als er geen rekening mee wordt gehouden. Het modelleren van tijd series met signaalreflecties (multipath) als een auto-regressief proces AR(k) van orde k, toonde aan dat de geschatte AR(1) parameter bijna altijd zeer significant is, wat een sterke tijdscorrelatie aanduid van de tijd series met signaalreflecties. Het AR(1) model past ook een veel beter met de data dan een AR(0) model met alleen witte ruis, en vermindert de variantie van de residuen aanzienlijk.

Analyse van de real-time precieze producten liet zien dat in vergelijking tot voorspelde satelliet banen, de voorspelde satelliet klokken relatief slecht zijn en daardoor de gecombineerde fout domineren. De kwaliteit van nieuwe producten met kortere vertragingen is veel hoger en benaderd posteriori producten. Er is ook een sterke correlatie tussen de baan en klok producten, een gevolg van het schattings-proces, maar ook door het gebruik van specifieke fase centrum verschillen. Gebruikers kunnen daarom beter de satelliet baan en klok producten van dezelfde leverancier nemen en kunnen producten beter niet door elkaar gebruiken.

Analyse van het tijdsgedifferentieerde geometrie-vrije model liet een sterke impact van het inperken van de ionosfeer variaties over de tijd op intergriteitscontrole zien. Instantane detectie van individuele slips in data gemeten op twee of drie frequenties bleek een hoge kans op succes te hebben onder gematigde ionosfeer condities. Detectie van fase-slips in data gemeten op een enkele frequentie is moeilijker en kan leiden tot een vertraging in detectie. De MDB voor instantane pseudoafstandsfouten is, met uitzondering van data op een enkele frequentie, niet gevoelig voor ionosfeer condities; de precisie van de code metingen is de enige bepalende factor. Toetsing voor een simultane fase-slip op elke frequentie leidt tot een zeer uitgerekte MDB ellips of hyper-ellipsoïde als de ionosfeer niet wordt ingeperkt, wat erop duidt dat specifieke combinaties van slips erg moeilijk te detecteren zijn. Het inperken van de ionosfeer vertraging verkleint de MDB ellips als de precisie van de ionosfeer pseudo-observatie toeneemt.

De positie resultaten laten zien dat zonder correcte modellering, de pseudoafstandsobservaties niet significant bij kunnen dragen aan de oplossing op basis van fasewaarnemingen, zonder de nauwkeurigheid te verslechteren. Hiernaast past de formele kwaliteitsbeschrijving van de oplossing slecht met de empirische positie fouten, als tijdsgecorreleerde effecten worden verwaarloosd. Na deze beide problemen te hebben opgelost, is de kracht van het gecombineerde model getoond door de uitstekende conversie prestaties in zowel de statische als kinematische gevallen. Het inperken van de atmosfeer vertragingen met model waarden verbetert de initiële conversie van de positie schatting verder.

Summary

Precise Point Positioning (PPP) is a Global Navigation Satellite System (GNSS) processing method with the objective of providing high positioning accuracy without the need for a nearby base station or dense network of reference stations operated by the user. To reach this objective, PPP uses the very precise carrier phase measurements in addition to the coarse pseudorange measurements, and precise satellite orbits and clock offsets. Before the carrier phase measurements can contribute to the position solution, the carrier phase biases must be estimated from the measurements. Additionally, to compute an accurate position, a number of approaches are used in PPP to reduce the error contributions. A sparse global network of reference stations estimates very accurate satellite orbits and clock offsets, and provides these to the user. A priori models are used to correct for the hydrostatic troposphere delay, relativistic effects, carrier phase wind-up, phase center offsets and variations. We will mainly consider users on or close to the surface of the Earth, which means that site displacement effects (e.g. ocean loading and solid Earth tides) also should be taken into account. The troposphere wet delay is often estimated from the data, and, in conventional PPP, the ionosphere delays are eliminated by combining dual-frequency observations in a reduced number of ionosphere-free observations. The accuracy provided by PPP based on GPS is very high; just a few mm for 24h of static data.

However, PPP can still be improved in a number of areas which are addressed in this dissertation:

- The need to both eliminate the ionosphere delays and estimate the carrier phase ambiguities results in a relatively weak model. This leads to long (re)initialization times before an accurate position can be computed. In this dissertation a different approach is proposed, implemented and tested that does not form the ionosphere-free combination, but estimates the ionosphere-delays from the observations. First the (linearized) GNSS observation equations are introduced and the functional PPP model is derived. From this we determine the estimable parameters, and treat the possibility of constraining the ionosphere estimation by use of external ionosphere data. This is achieved by correcting the observations with ionosphere model values and estimating only the residual ionosphere delay. Finally, a dynamic model for the residual ionosphere delays is determined and positioning results are presented.

- An accurate stochastic model for PPP is lacking, which leads to a suboptimal weighting of the different observation types, an inadequate quality description of the solution, and unreliable hypothesis testing. In this dissertation the stochastic properties of the PPP model are studied starting with the accuracy of the (real-time) satellite orbit and clock offsets, and continuing with the accuracy and correlation of the GNSS

observations. For the latter a newly developed method is introduced based on the geometry-free model. This analysis also includes an estimation procedure to model pseudorange multipath errors as an auto-regressive process, which can also be used to construct a dynamic model for time-correlated parameters. Finally, an almost unbiased variance component estimation algorithm is applied to the complete PPP model, and an accurate quality description of the positioning results is obtained.

- Integrity monitoring, which uses hypothesis testing to detect errors in the model which are not covered by the expected uncertainties, is not well developed for PPP. This subject is related to the previous points, since an accurate stochastic model is required for integrity monitoring and estimating and constraining the ionosphere delay, is key to high integrity performance. The geometry-free model is used again in time-differenced form to analyze the integrity aspects of (multi-frequency) GNSS models and their power to detect errors such as cycle-slips on the carrier phase measurements. The null hypothesis and alternative hypotheses are presented and the Minimal Detectable Bias (MDB) is derived for different kinds of errors. Analytical expressions are provided supported by numerical results.

The geometry-free analysis of pseudorange and carrier phase measurement noise revealed a good agreement with the theoretical expressions linking the measurement noise to the receiver tracking loop parameters and signal-to-noise ratio. However, strong variations of the pseudorange code measurements over longer time periods were also observed, which dominate the error budget if not accounted for. Modeling of multipath time series as an autoregressive process AR(k) of order k, showed that the estimated AR(1) parameter is almost always significant to a very high level, which indicates strong time correlation of the multipath time series. Indeed the AR(1) model fits the data much better than a white noise or AR(0) model does, significantly reducing the residual variance.

Analysis of the real-time precise products showed that compared to the satellite orbit prediction, satellite clock prediction is relatively poor and thus dominates the combined error. The quality of newer products with shorter delays is much higher and approaches the post-processed products. There also exists strong correlation between the orbit and clock products, resulting from the estimation process, but also due to the use of specific phase center offsets. Users should thus obtain the satellite orbit and clock products from the same provider and not mix products.

Analysis of the time-differenced geometry-free model revealed the strong impact of constraining the ionosphere variations over time on the integrity performance. Instantaneous detection of individual slips in dual- and triple-frequency data was found to have a high probability of success under moderate ionosphere conditions. Detection of phase-slips in single-frequency data is more difficult and may lead to a delay in the detection. The size of the smallest pseudorange outliers which can still be detected is, except for single-frequency data, insensitive to the ionosphere conditions; the precision of the code measurements is the only determining factor. Testing for a simultaneous phase-slip on each frequency leads to a very elongated MDB ellipse or (hyper)ellipsoid if the ionosphere is not constrained, indicating that specific combinations of slips are very difficult to detect. Constraining the ionosphere delay shrinks the MDB ellipse when the precision of the ionospheric pseudo observable increases.

The positioning results show that without proper modeling, the pseudorange observations cannot contribute significantly to the carrier phase solution without degrading the accuracy. Furthermore the formal quality description of the solution poorly fits the empirical position errors if time-correlated effects are neglected. After solving both these issues, the strength of the combined model was demonstrated by the excellent convergence performance in both the static and kinematic case. Constraining the atmosphere delays to model values further improves the initial convergence of the position estimation.

Acknowledgements

There are many people whom I would like to thank for their help in reaching this milestone and/or making the journey that much more enjoyable. Firstly, I would like to thank my promotor Peter Teunissen and copromotor Hans van der Marel. Peter, your analytical thinking and rigorous approach to science have been an inspiration. Hans, your expertise, knowledge and practical approach to research have helped me improve my own research skills. I would like to acknowledge the chairman and the committee members for their role in my defence ceremony.

My research was partly supported by the EU Marie Curie program in the framework of the FP7-PEOPLE-IAPP-2008 (SIGMA) project, which is gratefully acknowledged. I would like to acknowledge the GNSS community and the international research community in general, who so often make data, algorithms, and tools available to all researchers. This includes, but is not limited to the IGS, UNAVCO, the LaTeX community, and a number of Dutch and US government institutes. Having all these resources available at our finger tips really provides a privileged and unprecedented position to researchers in the modern age.

I would like to thank my current and previous colleagues in Delft, including the Mathematical Geodesy and Positioning group, the Remote Sensing group, who have moved with us from Aerospace Engineering, and my new colleagues at Civil Engineering and Geosciences. I would like to thank the permanent staff including Ramon Hanssen, Christian Tiberius and Sandra Verhagen. Christian, thanks for all the collaboration over the years. I have always experienced this as both very pleasant and fruitful. Having a colleague with a personal test vehicle is also a bonus. I would also like to thank my fellow PhD students and all other colleagues, including AliReza Amiri-Simkooei, Anh Quan Le, Roel van Bree, João Oliveira, Gabriele Giorgi, Yan Junlin, Peter Buist, Davide Imparato, Benoît Muth, Hou Yanqing and Barend Lubbers. Yahya Memarzadeh, all the chats, walks and discussions were very enjoyable, and I learned a lot! Lennard Huisman, I have always appreciated your technical support. Prabu Dheenathayalan, I think you will be an excellent committee member one day. You always come up with good, short questions, which really make you think.

During my time as a PhD student I have also had the opportunity to work at a number of different places; these work-living experiences greatly enriched my professional and personal life.

I would like to thank Fernando Nuñez, who made it possible for me to start working on the SIGMA project at Pildo Labs in Barcelona, Spain. I would also like to thank the colleagues and friends I made during my stay there, Santi Soley, Mercedes Reche, Marc Solé, Ivan Fernàndez, Juan Manuel Romero Martin and others. JuanMa, I hope we will meet up again sometime for a late night dinner.

I would like to thank Peter Grognard for making possible my stay at Septentrio N.V. in Leuven, Belgium. I would like to thank the research department at Septentrio, and Frank Boon and Geert van Meerbergen in particular for our collaboration and interesting discussions. Furthermore, I would like to express my gratitude for the opportunity to work in the software development environment of Septentrio. The mountain-biking was also a lot of fun.

I am also very grateful to Peter Teunissen for the opportunity to stay at the GNSS Research Centre at Curtin University, Perth, Australia. So far away from home, it was good to have such great colleagues and friends. All the great coffee breaks, talks over lunch, soccer matches, Go bar moments and dinners made life so much more fun. Thanks for making me, and my family, feel so at home in Perth! André Hauschild, Boris Padovan and Andrea Nardo, we really should meet up for a European reunion. Boris and Andrea, your really useful bath duck is used every day. Yu Xingwang, I really hope we can meet again somewhere. You have such a great outlook on life, I really enjoyed our time together in Perth and the farewell at Little Creatures.

I would like to thank my parents-in-law Rassie & Fienie for their understanding and support. I would also like to thank all my friends for their understanding in missing a lot of social events over the last few years. In particular I would like to thank Steven van Asch for his help with the cover. I would also like to thank my paranimphs and oldest friends, Laurens Ruijs and Jan Willem van Helden for their support and friendship. After all these years it means a lot to have you here with me.

I would like to express my deep gratitude to my parents Hans & Janny de Bakker, who continue to support me in all my endeavors. I would also like to thank my brothers and their extended families for all their support: Arnout, Rute & Olivia. Gerard, Alexandra, Marnix & Fabian. Henk, Iris, Lucas, Pepijn & Lila. I feel really lucky to have such great brothers and friends, and for all the great moments we have shared already. I hope there will be many more.

Finally, and most of all, I would like to thank my wife Vicki Erasmus for her unfailing support throughout the years. Vicki, your optimism, problem solving ability and your confidence in me, have helped me in times when I needed it most. Together we make a pretty decent researcher. More than that, your unconditional love and the love of our children gives purpose to my life. Nathan, thank you for making it so easy for me to realize the truly important things in life, and thank you making me feel all this pride and joy.

Peter Foeke de Bakker
November 21, 2015
Barendrecht

1 Introduction

1.1 Background

The Global Positioning System (GPS) has changed the navigation landscape dramatically. The positioning, velocity and timing (PVT) services offered by GPS receivers are nowadays commonplace and can be found in many appliances and applications. Moreover, society has become very dependent on these services and relies heavily on the continued availability of GPS.

The GPS system was designed in the seventies by the US military and is to date still controlled and operated by the US military, although under agreement with the US department of transportation for the provision of GPS civil services. The very dependency on US controlled satellite navigation systems has prompted the European Union (EU), amongst other reasons, to develop its own Global Satellite Navigation System (GNSS), called Galileo. The first two Galileo test satellites were launched in 2005 and 2008, respectively, the constellation currently consists of 10 satellites (ESA, 2015), and full operational capability is planned for 2020 (ESA, 2012). At the same time the GPS constellation, consisting of 31 satellites, is undergoing a modernization program (gps.gov, 2015); the Russians have revived their own GLObal NAvigation Satellite System (GLONASS), consisting of 24 satellites (IAC, 2015), and the Chinese government is completing their GNSS BeiDou, with a current constellation of 17 satellites (beidou.gov.cn, 2015).

Satellite navigation is based on measurements of the travel time of a coded time signal transmitted by each GNSS satellite. The user receiver calculates its position, velocity and time using travel time measurements to multiple GNSS satellites in view. The receiver uses in its computation the satellite positions, satellite clock errors and some other information which is broadcast by the GNSS satellites themselves (broadcast ephemerides). This is called stand alone positioning, because it does not depend on data sources other than the GNSS system itself.

The accuracy of GPS stand alone positioning based on code observations and broadcast ephemerides is 3-5 meters (standard deviation), and similar for GLONASS and BeiDou. However, for certain applications, e.g. road tolling, geo-information, geodesy and geophysics, the accuracy of standalone GPS is not enough. Also, although GPS is very reliable, the integrity of standalone GPS is not enough for airplane approaches or other 'Safety-of-Life' (SoL) applications.

These issues are addressed to some extend by the introduction of new GNSS systems and new and upgraded GNSS signals. Firstly, the users will benefit from the ability to use multiple GNSS systems simultaneously in order to obtain improved accuracy and integrity. A necessary condition is that the GNSS systems are interoperable and compatible: a system of systems. The main impact will be a sharp increase in the number of available satellites and the reduced dependency on a single provider. Secondly, the new GNSS systems and modernized GPS will feature new frequencies and signals. In particular, the introduction of new frequencies (e.g. L5), increased bandwidths and improved modulation techniques (e.g. BOC, Alt-Boc). Thirdly, also the ground segment and satellite hardware is undergoing an improvement, resulting in improved satellite clocks and more accurate satellite orbits.

In order to address the integrity and accuracy issues with contemporary GPS, Satellite Based Augmentation Systems (SBAS) such as the American Wide Area Augmentation System (WAAS), the European Geostationary Navigation Overlay Service (EGNOS) and Japanese Quasi-Zenith Satellite System (QZSS) have been developed. The European SBAS became operational in 2009. An SBAS monitors the regional GPS performance and relays this information to the users in that region through a (geostationary) satellite using a GPS like L1 signal. An SBAS provides corrections to the GPS orbits and clocks in real-time, gridded ionosphere delays corrections over the region of interest, and information on the accuracy and integrity of the GPS signals. The accuracy of an SBAS enabled receiver is typically better than one meter, thanks to the SBAS corrections and carrier phase smoothing of the code measurements inside the receiver. Integrity of the signal in space is provided by the so-called integrity flag; unless the integrity flag is set the satellite may not be used for SoL applications. Therefore, in general, the SBAS solution will use fewer satellites than standalone GPS. The level of integrity is provided by so-called horizontal and vertical protection levels. Galileo system integrity will be integrated within system by means of the Galileo SoL service.

Integrity at the system level alone is not sufficient to guarantee integrity at the user level. These systems must be complemented by Receiver Autonomous Integrity Monitoring (RAIM). RAIM provides for the integrity at the user level by cross checking the GNSS observations, using statistical methods and hypothesis testing such as the Detection-Identification-Adaptation (DIA) procedure developed at Delft University of Technology. The Minimal Detectable Biases (MDB) and protection levels, the so called External Reliability Levels (ERL), provided by RAIM depend to a large extend on the number of available satellites. RAIM is complementary to system integrity provided by e.g. SBAS and Galileo, and to some extent it could even replace SBAS in the future.

To get the highest possible accuracy from GNSS it is no longer sufficient to use only the code measurements or carrier phase smoothed code measurements in a stand alone or SBAS mode. Key to high accuracy applications, firstly developed in geodesy, has been the use of the very precise, but ambiguous, carrier phase measurements in a relative measurement setup with two or more receivers. Since the ambiguities are unknown they will have to be estimated, which can lead to long initialization times. However, since the ambiguities in a relative measurement setup must be integer, the initialization times can be reduced strongly by integer estimation of the ambiguities, which is called Ambiguity Resolution (AR). One such application is GPS-RTK (Real-Time Kinematic), whereby GPS data is processed in a differential mode together with observations from a nearby base station with precisely known coordinates. This makes it possible to form double differences of the phase observations in which the fractional parts of the ambiguities at the side of both the receiver and satellite are eliminated. The resulting integer ambiguities can then be resolved by using e.g. the Least-squares AMBiguity Decorrelation Adjustment (LAMBDA) method developed at Delft University of Technology (Teunissen, 1994). In addition, many error sources are eliminated in the double difference because they are almost identical for both receivers. The resulting position solution relative to the base station can be as precise as a few mm to cm.

GNSS signals are affected by propagation delays in the Earth's atmosphere; a frequency dependent delay which originates in the ionosphere and a frequency independent delay which originates mainly in the troposphere. The ionospheric delays as function of the baseline length is a determining factor for the success rate of ambiguity resolution. If the baseline is very short (<10km), the ionospheric delay is almost equal for the base station and the user and is removed in the single difference, making successful ambiguity resolution possible. If the base line length increases, the ionospheric delay will start to differ for the base station and the user, and will not be removed in the single difference, thus decreasing the ambiguity resolution success rate. This means that for RTK a dense network of reference receivers is needed in the objective area. Such a network is expensive to set up and maintain. Therefore methods have been developed and are being developed that can still work when the baseline length increases. These methods rely on ionospheric modeling and interpolation of the ionospheric delay. Network RTK is one such method and makes baseline lengths of up to 100km possible. The baseline lengths can be increased even further (to a few hundred km) with Wide Area RTK processing (WA-RTK), which relies on improved ionospheric modeling and additional measurement corrections for e.g. the satellite clocks. However, with increasing baseline lengths the time needed to reach highly accurate positions also increases.

A different, but related, method is Precise Point Positioning (PPP). PPP is a stand alone positioning method with the objective to provide high positioning accuracy (ideally similar to RTK) without the need for a nearby base station or dense network of reference stations. The stand alone approach of PPP, brings with it a number of challenges. Error contributions on the range observations, which in relative positioning are eliminated by taking differences between the observations of two receivers, will now have to be estimated or removed in a different way. Therefore, PPP relies on precise satellite orbits, clocks, differential code biases, and ionospheric models from a service provider to correct these errors. For real-time positioning or navigation these high accuracy products need to be available in (near) real-time as well. Additionally site displacement effects (e.g. ocean loading and solid Earth tides), which are greatly reduced in relative positioning, will now have to be taken into account through proper modeling. And finally, for a stand alone receiver, the carrier phase ambiguities are not integer with conventional precise satellite orbit and clock products (since the fractional part at the side of the satellites cannot be eliminated) which leads to long initialization times. For kinematic applications, the accuracy provided by PPP based on GPS is currently at dm-level and as good as a few mm for static observations over a 24 h period.

One of the advantages of PPP over RTK and WA-RTK is that it is truly global and does not depend on local elements which may or may not be present. Also, PPP will work equally well over land as over the oceans, and can be used on aircraft and (low Earth) orbiting satellites. However, integrity is currently not provided with PPP systems, and it takes considerable time (10-30 minutes) for a PPP solution to converge to decimeter accuracy. Also, because the carrier phase ambiguity needs to be initialized every time after a loss of lock to the satellite signal, it is difficult to use PPP in build up or heavily forested areas, where there are a lot of interruptions and reflections (multipath) on the signals.

1.2 Research objectives

The ultimate goal of Precise Point Positioning is to have a world wide, stand alone positioning system with centimeter accuracy, meter integrity (99%) and short initialization time that is able to work under all operational conditions. Several (related) shortcomings of the conventional PPP algorithms include the treatment of several time correlated errors as white noise or even neglecting them altogether, the lack of a realistic stochastic model of GNSS observables, and not constraining the ionosphere delays either in time or to model values. Also lacking is a robust integrity algorithm to detect errors in the observations and ambiguity resolution for PPP is not not yet fully developed.

The main objectives of this thesis are the following:

Our first objective is to set up the functional PPP model from the observation equations; identify weak points of conventional PPP algorithms and their causes. The conventional ionosphere-free linear combination will be scrutinized and an optimal way of treating the ionosphere delay will be determined.

The second objective is to provide an accurate stochastic model for the GNSS observations and precise satellite products. This is required for the optimal estimation of the position and a realistic quality description of the position solution. But it is also essential for integrity monitoring, based on hypotheses testing, and ambiguity resolution, which among others relies on the variance matrix pertaining to the estimated float ambiguities.

The third objective is to improve integrity monitoring for PPP. Since PPP relies heavily on the carrier phase measurements and the assumption that the carrier phase biases are constant, we aim at detecting cycle slips (and pseudorange outliers) at the earliest possible stages. Cycle slip detection is closely related to ambiguity resolution, as cycle slips can be viewed as time differenced ambiguities.

The fourth objective is to reduce the initialization and re-initialization times without deteriorating the final accuracy. Long initialization times (following from long convergence times of the estimated ambiguities) prevent fast and accurate positioning. In this thesis we would like to provide an approach to mitigate this problem.

1.3 Contributions of this research

The main contributions of this research, to reaching these objectives, are:

1. The PPP observation model is derived and all rank defects are identified and solved. The model is compared to the conventional PPP model and weak points and possible

improvements in the latter are described. The treatment of the ionosphere delays receives special attention.

2. An analysis technique of the quality of the precise satellite orbit and clock offsets is developed and applied to the products of a number of PPP providers. A distinction is made between errors that do and do not impact a user of the precise products.

3. An analysis technique is developed to create an accurate and complete stochastic model for GNSS observations and error sources including (time) correlation. This analysis technique is based on linear combinations of short and zero baseline measurements, which makes it possible to separate the different contributions to the variance of the observations.

4. An integrity monitoring algorithm which uses a time differenced approach to detect errors on the observations is developed. These algorithms can be applied in preprocessing, i.e. before the observations are added to the navigation algorithms.

5. A rigorous PPP algorithm (and implementation thereof) is presented, which makes optimal use of all available data, including external atmosphere models, and provides accurate position estimates.

6. The positioning model is modified to improve the quality description of the solution for both the static and kinematic case and for both the pseudorange, carrier phase and the combined model.

7. An iterative method to fine-tune the elevation dependent weighting of pseudorange and carrier phase measurements is introduced and tested.

8. An iterative approach to estimating unmodeled group delays in the form of antenna patterns and satellite biases is derived and successfully applied to reduce systematic errors in the position estimates.

1.4 Outline of the thesis

Chapter 1 is an introduction to this thesis.

Chapter 2 provides an overview of Precise Point Positioning.

Chapter 3 introduces the (linearized) GNSS observation equations including all the different parameters involved. Several different approaches to using these observations for PPP are treated both with the original observations and ionosphere-free linear combinations of the observations.

In Chapter 4 the approaches described in chapter 3 are extended to complete functional navigation models highlighting the single and dual frequency algorithms (the stochastic model is treated in chapters 6 and 8) and the estimable parameters at the user side are determined.

Chapter 5 describes the precise satellite orbit and clock data provided by PPP service providers to PPP users, their quality and latencies. It also provides results from an analysis of the quality of real-time precise products from several different sources.

In chapter 6 a newly developed method to derive an accurate and realistic model of the stochastic properties of GNSS measurements is presented. This method is based on geometry-free baseline analysis, but the results are generally applicable and here applied to PPP. Measurements from a short and zero baseline are combined using linear combinations of the observations, in order to derive accurate estimates of the stochastic properties of the observables. This analysis is then extended to include a stochastic description of pseudorange multipath errors.

In chapter 7 the integrity of single-receiver, single-channel, multi-frequency GNSS models is studied. The uniformly most powerful invariant test statistics for spikes and slips are derived and their detection capabilities are described by means of minimal detectable biases (MDBs). Analytical closed-form expressions of the phase-slip, code-outlier and ionospheric-disturbance MDBs are given, thus providing insight into the various factors that contribute to the detection capabilities of the various test statistics. This is also done for the phaseless and codeless cases, as well as for the case of a temporary loss-of-lock on all frequencies. The analytical analysis presented is supported by means of numerical results.

In chapter 8 Precise Point Positioning results processed with the derived functional and stochastic models are presented. An iterative method for Variance Component Estimation is introduced and applied, as well as a method to estimate group delays in the form of antenna patterns and satellite biases.

Chapter 9 will summarize the conclusions of this thesis as well as present recommendations for future research.

Overview of Precise Point Positioning 2

2.1 Historical perspective

During the last decade of the 20th century dense networks of continuously operating GPS receivers were established in populated areas of the US, Japan and Europe. To keep the computational burden associated with the data analysis of such networks economically feasible, Zumberge et al. (1997) pioneered a novel technique in 1997. The approach is to first determine precise GPS satellite positions and clock corrections from a globally distributed network of GPS receivers, together with the receiver positions, troposphere delay and other parameters, as is done routinely by analysis centers of the International GNSS Service (IGS). Then, in the second step, called Precise Point Positioning (PPP), the GPS data from the dense networks is analyzed one receiver at a time using the satellite orbits and clock corrections from the previous step. During this second step the receiver position, troposphere delay and phase ambiguity parameters are computed. Beyond a certain number of receivers the quality of satellite orbits and clock corrections do not further improve significantly by including more receivers in the global network. The current number of receivers in the global IGS network is over 300 (Kouba, 2009a), but the number of receivers used for the computation of the precise GPS satellite positions and clock corrections is in the order of 100. The exact number varies per IGS data center and the type of product. Zumberge et al. (1997) showed that the quality of the station parameters determined in the PPP step is equal to the quality of the station parameters in the global network, and also comparable in quality to results from a simultaneous network analysis of all data together.

The new processing technique was called Precise Point Positioning because of the similarity to the more common concept of GPS Point Positioning with pseudo range data and broadcast ephemerides. In PPP the more accurate satellite orbits and clock corrections from the IGS analysis centers are used instead of the broadcast ephemerides. But PPP improves on Point Positioning also through two other important aspects: it uses the much more precise carrier phase measurements, and it conventionally uses dual frequency measurements in order to eliminate the ionospheric delays. Therefore, PPP requires a dual frequency GPS receiver with carrier phase tracking. Because PPP uses the more precise carrier phase data it is necessary to estimate the carrier phase ambiguities along with the station position and receiver clock parameters. To obtain the best possible precision also troposphere delay parameters are estimated (zenith delay and optionally gradient parameters). Zumberge et al. (1997) report a few-millimeter precision for a 24 hour period in horizontal components and centimeter precision in the vertical component.

The best PPP results are obtained if the same models and software are used by the user as for the global network, or at least if the same conventions are used. This is because PPP can be considered a step-wise network adjustment of the global network with one or more additional PPP receivers: the first step consists of the global network adjustment and the second step of a PPP receiver (or a PPP network), using the results from the first step. The third step, back substitution of the results of the second step to improve the first step, is omitted because of its small impact. Also, during the second step the satellite orbits and clock parameters can be fixed because the PPP user will not be able to improve the satellite orbits and clock parameters. This implies that PPP is not truly a point positioning technique, but in essence also a relative or differential technique that does share a number of properties with GPS baseline processing. However, in baseline processing many effects (earth tides, loading, atmosphere) just cancel out by single differencing the observations from two receivers, which in PPP have to be taken into account explicitly. It is therefore essential that the same models and corrections are applied in the PPP step as in the global adjustments, and this is often best guaranteed when the same software is used.

One of the characteristics PPP shares with (long) baseline processing is that it relies primarily on the carrier phase data. To accurately estimate the carrier phase ambiguities it is necessary to collect observations over a long time span. The minimum time span is about half an hour to an hour. This is not a problem for static application which typically processes time spans of one day. If a network of PPP stations is processed, integer ambiguities may be resolved between the PPP stations, resulting in a much improved relative positioning between these PPP stations. Ambiguities between the PPP network and the global network, as well as ambiguities for single PPP stations, were originally not solved, but developments on this point are discussed in section 2.3.2.

Another characteristic of PPP is that it uses satellite orbits and clock corrections from a different source than the GPS ephemerides. Precise satellite ephemeris and satellite clock information have been available from the IGS since 1992 (Beutler et al., 1999). At first this orbit information was only available with a latency of about two weeks, limiting PPP to post-processing applications whereby the PPP solution is computed afterwards (outside the receiver) after downloading orbits and clocks from the Internet. For post-processing the receiver can both be static, resulting in daily (station) coordinates, or kinematic resulting in time-series of receiver coordinates. The processing is usually based on a batch least-squares adjustment or a smoothing filter.

Since then precise IGS products with significantly smaller latencies have become available including predicted orbit and clock information, opening the door for real-time applications of PPP. Nowadays there are several commercial and non-commercial providers of real-time precise orbit and clock data. An overview of the service providers and their products is given in chapter 5.

In order to perform PPP in real-time, a receiver must have an internet connection or some other communication link to such a provider of real-time satellite orbit and clock data. The processing for real-time applications, which is often done inside the receiver, is a kinematic solution based on a Kalman filter type of processing. Because with a real-time Kalman filter only measurements from the past can be processed some time will be needed for the solution to converge to the required level of accuracy. This period depends very much on the available number of satellites and quality of the data, but is typically about

30 minutes to reach decimeter-level under normal conditions (Bisnath and Gao, 2009b). Another difference between static and real-time processing is that, while only carrier phase measurements might be used for static applications with daily position estimates, for real-time processing the carrier phase measurements are used together with the pseudo range measurements. Good quality pseudo range measurements have a beneficial effect on the convergence time for real-time applications.

Although PPP was developed as a dual frequency technique it can also be used with multiple frequencies or even with only a single frequency. Instead of the ionosphere free linear combination single frequency PPP relies on either external ionosphere delay data (Le, 2004; Le and Tiberius, 2006a; de Bakker et al., 2014) or a linear combination of code and carrier phase data to eliminate the ionospheric delay (Yunck, 1996). Global Ionosphere Maps (GIM) computed by IGS analysis centers (IGS, 2015b) are currently the global ionosphere models with the highest accuracy.

2.2 Performance and limitations of PPP

As mentioned, Zumberge et al. (1997) report a few-millimeter daily precision in horizontal components and centimeter precision in the vertical component. This precision has been improved even further since then along with the improvements in IGS orbit and clock corrections obtained by the different IGS analysis centers. This precision is more than sufficient for many applications including most real-time applications. A measurement duration of several hours before this precision is reached is however not acceptable for many applications, especially considering kinematic receivers. Therefore, the challenge for PPP is not so much to improve on the obtained precision but rather to shorten the time to reach a high precision. The convergence period has been studied since the first publications on the PPP technique. Witchayangkoon and Segantine (1999) tested the PPP implementation of the Jet Propulsion Laboratory (JPL), using the precise IGS products and measurements from a static receiver, and found that the repeatability of the PPP solutions ranged from 10 to 20 cm after one hour of observations, and this decreased to a few centimeters after 12 hours, finally reaching 1 cm after 24 hours. Kouba and Héroux (2001) report that cm convergence is reached after processing 2-3 h of observations from an IGS station using precise IGS orbits and clocks products in static mode. They also mention that the convergence time can be decreased to only 30min when high-rate satellite clock products are used.

As precise products with smaller latencies became available, the focus of PPP research has shifted to real-time PPP processing (Kechine et al., 2003; Héroux et al., 2004; Gao and Chen, 2004). Kechine et al. (2003) verified the Internet-based PPP service from the JPL and found 20-30 minutes to achieve dm accuracy for all position coordinates in kinematic processing. Gao and Chen (2004) obtained cm accuracy after 20min using the JPL real-time products in static mode, and report the same accuracy for kinematic processing, but do not mention the convergence period. Landau et al. (2008) report 0.1m accuracy after 90min for real-time static PPP vs a final accuracy of 20mm. For kinematic positioning a final accuracy of 40mm was achieved and a convergence time of 2 hours. Bisnath and Gao (2009a,b) found 10cm accuracy after 20-25min for an airborne platform in kinematic mode.

Table 3.3 on page 23 provides a more complete overview of the reported PPP performance by different authors.

Our main focus will also be on methods and algorithms that can be used for real-time, kinematic applications of single receiver PPP, with the goal of decreasing the time to reach a high positioning accuracy and providing a rigorous quality description of the computed position. Several methods and algorithms to reach this goal are explored in the following sections and chapter 3. For real-time PPP applications the timely availability of satellite orbit and clock products with sufficient accuracy is a prerequisite, which is the subject of chapter 5.

Despite the improvements made in PPP the performance is still far removed from RTK performance which routinely achieves 10mm-20mm accuracy (rms) with average initialization times of 20 s or less (Landau et al., 2008). However, the development of PPP is not finished. A number of research groups work on the use of more than two frequencies and multiple systems for PPP as well as integer ambiguity resolution for PPP.

2.3 PPP developments

2.3.1 GNSS evolution and multi-frequency, multi-constellation PPP

Presently, a significant increase in the available global navigation satellite systems, frequencies and signals is ongoing. **GPS** is in the process of modernization. This is achieved by replacing older satellites by new satellites with expanded and improved capabilities. The civil L2C signal, providing 'true' dual frequency capabilities to civil users thereby making L1 aided tracking of L2 obsolete, is becoming available on more and more satellites (currently about halve of the constellation, gps.gov, 2015). Even more importantly, the newest GPS satellites (currently about one third of the constellation) also transmit an additional (wide-band) signal on the L5 frequency primarily designed for safety-of-life applications. The last Block IIA satellites will soon be decommissioned (currently there are only three left). **GLONASS**, the Russian GNSS, has been fully replenished and at present has 24 active satellites as reported by the GLONASS Information-Analytical Center (IAC, 2015). Planned modernizations of GLONASS include an additional signal transmitted on the L5 frequency, and a switch from Frequency-Division Multiple Access (FDMA) to Code-Division Multiple Access (CDMA) which would increase potential interoperability with other GNSS. **Galileo**, the European GNSS, is still under development. Two GIOVE (Galileo In-Orbit Validation Element) test satellites were launched, GIOVE-A in 2005 and GIOVE-B in 2008, both for testing purposes and to reserve the radio frequencies that Galileo is intended to use. The GIOVE satellites have been followed by four IOV (In-Orbit Validation) Galileo satellites in 2011 and 2012, and six FOC (Full Operational Capability) Galileo satellites in 2014 and 2015 (ESA, 2015). The full Galileo constellation is planned to exist of 30 satellites by the end of 2020 (ESA, 2012). The Galileo system will transmit navigation signals on four different carrier frequencies: L1/E1, L5/E5a, E5b and E6, two of which (E5a and E5b) can also be tracked together as one extra wide-band (Alt-BOC) signal with unprecedented accuracy. The Chinese **BeiDou** Navigation Satellite System (BDS) was designed to provide independent regional navigation in the first stage and global coverage by 2020. Currently the regional system is fully operational, and the first satellite of the second stage has already been launched starting the transition towards a global navigation system (beidou.gov.cn, 2015). The Japanese (**QZSS**) is intended to operate first four, later seven satellites that provide regional time-transfer and positioning services thereby augmenting the GNSS performance in and around Japan (qzss.go.jp, 2015). The Indian Regional Navigation Satellite System (**IRNSS**) is intended to operate with a minimum of seven geosynchronous satellites covering the Indian region. Currently, four satellites are in orbit (Mruthyunjaya, 2014; isro.org, 2015).

Within the IGS a Multi-GNSS Experiment (IGS MGEX) is currently undertaken in parallel to the regular IGS operations, which focuses on the tracking of newly available GNSS signals. Goals include the study and determination of inter-system calibration biases, comparison and testing of equipment and processing software and finally producing multi-GNSS IGS products (Montenbruck et al., 2013). MGEX is now moving towards mainstream IGS and is expected to be part of the operational part of the IGS soon. MGEX stations have become IGS stations already (Maggert, 2015); formats are ready for the new signals and systems.

The realized and expected upgrades of and additions to the available GNSS signals can have a range of improvements on many GNSS applications including PPP. Some of the more important ones are: the higher accuracy of the new signals will improve the convergence time, the availability of many more satellites will drastically improve PPP availability and RAIM performance, and both the availability of more frequencies and satellites will improve the potentials of ambiguity resolution.

The availability of additional satellites and signals can significantly improve PPP performance. The first real-time GPS and GLONASS combined PPP service, providing precise orbit and clock products for both systems, has been developed by Fugro based on their network of 40 ground stations (Melgard et al., 2010) and has since been extended with Galileo and BeiDou (Tegedor et al., 2015).

The German Aerospace Center and the German Federal Agency of Cartography and Geodesy setup the COoperative Network for GIOVE Observation (CONGO) with local support from several international partners, which has produced the first real-time precise orbit and clock products for the Galileo In-Orbit Validation Element (GIOVE) satellites (Montenbruck et al., 2009). Precise Point Positioning with the BeiDou system has also been demonstrated at Wuhan university (Shi et al., 2012; Zhao et al., 2013).

Multi-GNSS positioning also brings new challenges, as so-called Inter-System Biases (ISBs) are introduced in the model. To use multiple systems simultaneously in an optimal manner, these biases must be studied, and if possible corrected or eliminated (Gao, 2008; Odijk and Teunissen, 2013a) (see also section 4.2).

2.3.2 PPP and RTK

In many respects PPP and RTK are similar concepts, a single user is able to obtain a more accurate position by taking advantage of a (regional or global network of) reference station(s). However, there are also a number of differences: The RTK technique relies on estimation or elimination of GNSS errors in the observation space (the most basic approach is to provide all observations from the nearest reference station to the user and form double difference observations), while the PPP technique uses the state space model, in which the GNSS error sources are separated and modeled individually. The success of RTK lies in the fixing of the double differenced ambiguities to their integer values, which enables fast high accurate positioning. Ambiguity resolution is possible due to the strong spatial correlation of several error sources in GNSS processing including the ionosphere delays, which are consequently reduced in the double differences. In its application this means that RTK is limited to relatively short distances to the nearest reference station. PPP, being a global positioning approach, cannot exploit the spatial correlation of error sources to perform ambiguity resolution. Additionally, the initial focus of PPP was on post-processing applications, where ambiguity resolution is of less importance. As a consequence, the global precise products that a PPP user can obtain from service providers were not optimized for ambiguity resolution (e.g. the satellite clock products are aligned with the pseudo range measurements), but this is in the process changing.

Wübbena et al. (2005) proposed the PPP-RTK method which combines the state space approach from PPP but applies it to RTK networks. Advantages with respect to RTK are that the state space model offers a more efficient method to transmit the correction data to users (both the amount of data is reduced, and the same corrections can be used by any number of users), and, due to the advanced error modeling, the inter-station distances can be larger. In this respect the PPP-RTK approach resembles network RTK and the Wide-Area RTK method (Hernandez-Pajares et al., 2008). The advantage of PPP-RTK with respect to PPP is that, due to a redefinition of the precise corrections and the shorter baselines, fast ambiguity resolution becomes possible and with it fast accurate positioning. However, one limitation of PPP-RTK is that the dependency of the performance on the baseline length is reintroduced, as shown in e.g. (Mervart et al., 2008), and is in that sense not truly global. Our focus will be on (global) PPP not PPP-RTK specifically. However, since both PPP and PPP-RTK share the state space approach, the models and methods are closely related.

PPP-RTK has grown in popularity as it has been shown by several authors that it makes fast positioning with cm-level accuracy possible. Many subtly different approaches have been proposed (Weber et al., 2007; Laurichesse and Mercier, 2007; Banville et al., 2008; Collins et al., 2008; Ge et al., 2008; Geng et al., 2009; Laurichesse et al., 2009; Bertiger et al., 2010; Teunissen et al., 2010; Loyer et al., 2012; Lannes and Prieur, 2013), but were shown by Teunissen and Khodabandeh (2015) to be essentially identical *if* an optimal estimation procedure is used. However, the interpretation of the estimated parameters can differ per method as a different S-basis is chosen to solve the rank deficiencies (Baarda, 1973; Teunissen, 1985; de Jonge, 1998). The common approach is to estimate additional PPP products or corrections on the existing PPP (clock) products, from a regional network of reference receivers, but estimation from a global network is also possible (Gabor and Nerem, 1999; Ge et al., 2008). These additional precise products can be used to eliminate the fractional ambiguities at the side of the satellites, thereby making single receiver ambiguity resolution possible. Ambiguity resolution for PPP will be treated in more detail in section 3.5.

GNSS Observation Equations 3

3.1 System time

Before we introduce the observation equations, first we will choose a common time scale to work in. When a single GNSS is used, the choice is trivial. Each GNSS has its own system time and each satellite (and each user receiver) has its offset with respect to this system time. The satellite clock offsets are provided to the user together with the satellite positions. In principal, if multiple GNSS are tracked, the satellite clock offsets provided by each separate system refer to a different system time. However, since a PPP user relies on a (global) network of reference receivers to provide precise clock offsets, the service provider simply needs to choose a time scale and compute offsets for each satellite with respect to this system time (the related but distinct problem of inter-system biases in treated in section 4.2).

The choice of time scale by the service provider is arbitrary, because we can change from one to another by simply applying the time offset between the different time scales. In practice, since GPS was the first fully functional and still is the most ubiquitous GNSS, GPS time is often used also when considering multi-GNSS positioning. GPS time is referenced to Coordinated Universal Time (UTC). However, unlike UTC, which is corrected periodically with an integer number of leap seconds, GPS time is a continuous time scale since midnight on the night of January 5, 1980/morning of January 6, 1980. The GPS Operational Control System (OCS) controls the GPS time scale to be within one microsecond of UTC (modulo one second) (IS-GPS-200D, 2004).

In the following, the chosen system time is simply indicated by t and the satellite and receiver clock offsets by δt^s and δt_r, respectively. The time of reception, which is the time at which the receiver makes the measurements, will be called t_r. Due to the receiver clock offset this will *not* be equal to the 'time tags' which are given to the measurements by the receiver. These receiver time tags will be called t_k and it follows that: $t_r = t_k - \delta t_r$. For GNSS measurements, which are collected at discrete time instants, k then indicates the time epoch of the measurement.

3.2 Observation equations

With these timing conventions in place, the observation equations can now be introduced as follows. The pseudo range code and carrier phase observation equations for receiver r, satellite s and frequency f at time of reception t_r, based on Teunissen and Kleusberg

(1998), are:

$$\begin{aligned} \underline{P}^s_{r,f}\left(t_r\right) &= \left\|\mathbf{r}^s\left(t_r-\tau^s_r\right)-\mathbf{r}_r\left(t_r\right)\right\|+c_0\delta t_r\left(t_r\right)-c_0\delta t^s\left(t_r-\tau^s_r\right)+ \\ & T^s_r\left(t_r\right)+\mathcal{I}^s_{r,f}\left(t_r\right)+c_0 d^s_{r,f}\left(t_r\right)+\underline{\epsilon}^s_{r,f} \end{aligned} \tag{3.1}$$

$$\begin{aligned} \underline{\Phi}^s_{r,f}\left(t_r\right) &= \left\|\mathbf{r}^s\left(t_r-\tau^s_r\right)-\mathbf{r}_r\left(t_r\right)\right\|+c_0\delta t_r\left(t_r\right)-c_0\delta t^s\left(t_r-\tau^s_r\right)+ \\ & T^s_r\left(t_r\right)-\mathcal{I}^s_{r,f}\left(t_r\right)+\lambda_f A^s_{r,f}+c_0\delta^s_{r,f}\left(t_r\right)+\underline{\varepsilon}^s_{r,f} \end{aligned} \tag{3.2}$$

where $\underline{P}$ and $\underline{\Phi}$ are the code and phase observables in meters, $\left\|\mathbf{r}^s\left(t_r-\tau^s_r\right)-\mathbf{r}_r\left(t_r\right)\right\|$ is the geometric range (also expressed as $\rho^s_r(t_r, t_r-\tau^s_r)$) between the satellite position $\mathbf{r}^s$ at time $t_r-\tau^s_r$ and the receiver position $\mathbf{r}_r$ at receiver time t_r with τ^s_r the travel time of the signal, c_0 is the speed of light, T is the tropospheric delay, $\mathcal{I}$ is the ionospheric delay, λ is the carrier wavelength, A is the constant carrier phase ambiguity expressed in cycles, d and δ contain any other systematic delays on the code and phase measurements, respectively, and $\underline{\epsilon}$ and $\underline{\varepsilon}$ are the random code and phase measurement errors, indicated by the underscore in (3.1) and (3.2), and thereby also the code and phase observables become random variables.

Now we will introduce a more convenient notation using index k (time epoch of the measurement) to indicate time dependent parameters. It is important to note that in the actual processing of the data, the time difference between the time of reception and the time of transmission must still be used. Equations (3.1) and (3.2) then simplify to:

$$\underline{P}^s_{r,f,k} = \left\|\mathbf{r}^s_k-\mathbf{r}_{r,k}\right\|+c_0\delta t_{r,k}-c_0\delta t^s_k+T^s_{r,k}+\mathcal{I}^s_{r,f,k}+c_0 d^s_{r,f,k}+\underline{\epsilon}^s_{r,f} \tag{3.3}$$

$$\underline{\Phi}^s_{r,f,k} = \left\|\mathbf{r}^s_k-\mathbf{r}_{r,k}\right\|+c_0\delta t_{r,k}-c_0\delta t^s_k+T^s_{r,k}-\mathcal{I}^s_{r,f,k}+\lambda_f A^s_{r,f}+c_0\delta^s_{r,f,k}+\underline{\varepsilon}^s_{r,f} \tag{3.4}$$

The observation equations are not linear in the receiver (or satellite) position and will have to be linearized before they are combined and used in the positioning algorithms. For this reason the 'so-called' observed-minus-computed measurements will be formed. However, before introducing the linearized equations and positioning algorithms based on these equations, several aspects of the parameters in (3.3) and (3.4) will be discussed.

Position The main goal of GNSS is determine the position of the user receiver in a certain reference frame. In relative positioning, the position solution will be in the same reference frame as the known position of the reference receiver. In PPP the position solution will be in the reference frame of the satellite positions which is the International Terrestrial Reference Frame (ITRF) for IGS products and World Geodetic System 1984 (WGS84, which is aligned with ITRF) for GPS broadcast orbits with or without precise corrections. However, even a stationary receiver will be subject to certain displacements which are not accounted for in the ITRF. These displacements are related to deformations of the solid Earth, the pliability of which can be described by the 'so-called' Love and Shida numbers. The displacement effects are very similar for receivers at relatively short distances, and as a result they are largely eliminated in a relative setup. In PPP the displacements cannot be eliminated and they will have to be modeled and then applied to the position solution to determine the precise position of a stationary receiver in the ITRF:

$$\mathbf{r}_{r,k} = \mathbf{r}_{r,\text{ITRF}} + \Delta\mathbf{r}_{r,k} \tag{3.5}$$

where $\mathbf{r}_{r,k}$ is the solution of the positioning algorithm, $\mathbf{r}_{r,\text{ITRF}}$ is a constant position in the ITRF, and $\Delta\mathbf{r}_r$ are the modeled site displacements of a stationary receiver with respect to the ITRF. Equation (3.5) shows the convention that the site displacement corrections should be subtracted from the position solution. Table 3.1 summarizes the different site displacement effects and their magnitudes. For a comprehensive treatment see Petit and Luzum (2010).

Table 3.1: Site displacement corrections ($\Delta\mathbf{r}_{r,k}$)

Displacement effect	**Magnitude [cm]**
Solid earth tides: The gravitational forces that cause the ocean tides, also act on and deform the solid Earth. This deformation causes a permanent displacement, which can reach up to 12 cm in mid latitudes, and a periodic displacement with predominantly semi diurnal and diurnal periods of changing amplitudes (Kouba, 2009a), just like the ocean tides. The solid Earth tides can be modeled by spherical harmonics (expressions provided in McCarthy and Petit, 2003), of which only the second-degree tides and a height correction term are necessary for 5mm precision (McCarthy, 1989; Kouba, 2009a). The periodic part averages out over 24-hours of static positioning, but due to the permanent part, the solid Earth tide correction cannot be neglected for precise positioning even in this case. Additionally, neglecting the periodic part could significantly affect the other estimated parameters.	radial 30 horiz. 5
Polar tides: The rotational axis of the Earth is not constant in ITRF, which leads to periodical deformation and site displacements. The site displacements are predominately seasonal or have Chandler (∼430 day) periods and as such do not even out over a 24 hour period. The corrections to latitude, longitude and height can be determined from the pole coordinate variations from the mean poles (McCarthy and Petit, 2003; Kouba, 2009a).	height 2.5 horiz. 0.7

Displacement effect	Magnitude [cm]
Ocean loading: The ocean tides exert a load on the under lying and surrounding solid Earth, thereby creating site displacements with diurnal and semi diurnal periods (by convention it does not have a permanent part). This effect depends on the local geography of the ocean and land masses and is strongest in coastal regions. Therefore, it does not have to be taken into account for positioning far from the shore. Also, for long observation times the effect is reduced since it will even out to some extend over 24 hours of data. For highly precise positioning close to the ocean it *does* need to be taken into account. The ocean loading displacement can be determined with a general expression (available from McCarthy and Petit, 2003; Kouba, 2009a) and station specific amplitudes and phases, which can be calculated separately or, for most ITRF stations, can be obtained from tables.	radial <5 horiz. <2
Atmospheric loading: Similar to the oceans, the atmosphere also exerts a load on the solid earth beneath. Thus changes in the pressure distribution of atmosphere, following from temperature changes, lead to deformations of the Earth's crust. Petrov and Boy (2004) report that this effect can be up to 2 cm for the vertical component; Urquhart (2009) mentions that 2 to 3 cm vertical displacements can occasionally occur due to pressure systems moving over the Earth. However, generally these effects are much smaller with magnitudes below 1 cm (Kouba, 2009a). The horizontal components are generally smaller by a factor of 10 (Petit and Luzum, 2010), with values up to 3 mm (Petrov and Boy, 2004). Petit and Luzum (2010) provide models for the systematic effects caused by the diurnal heating of the atmosphere by the Sun. Predicted magnitudes do not exceed 1.5 mm.	max: vert. <3 horiz. $<.3$ typical: vert. $<.15$ horiz. $<.015$

Which effects from table 3.1 are to be taken into account depends on the application at hand, and the target accuracy. For very accurate (static) positioning in ITRF, or relative positioning w.r.t. a known position in ITRF, all of these effects might be relevant and should be modeled. However, if an accuracy of e.g. 10 cm is acceptable, or for dynamic or kinematic applications that might not be able to reach sub decimeter accuracy, only the solid earth tides have to be taken into account. Also, for airborne applications or positioning that is not strictly in ITRF, the displacement effects are not applicable. Finally, the possibility to model ocean loading depends on the availability of the necessary amplitudes and phases for the user location.

Reference frame transformations Although strictly not a site displacement effect, reference frame transformations can lead to errors in the calculated positions of about 3cm in the horizontal plane. For highly accurate transformations between Earth fixed and inertial reference frames, the Earth Rotation Parameters (ERP) are needed. Whether such transformations are necessary depends on the used reference frame for the positioning, and the used precise products with their underlying reference frames. The IGS products are provided in ITRF and so, no ERP are needed if the user works directly in the same reference frame. When computing the range this should be done in a non-rotating frame or quasi inertial frame. If done in an Earth fixed frame additional corrections are necessary to take Earth's rotation into account, but these do not require very accurate knowledge of ERP (rotational speed is sufficient). A second reason for using a quasi inertial frame is when orbit determination is done. However, this is not necessary for PPP. Therefore, for PPP all computations can be done in an earth fixed frame provided we make small corrections for Earth's rotation.

Clocks and differential delays At both satellite and receiver GNSS observations contain frequency and signal dependent hardware delays. One way of representing this is by considering a different clock-offset for each code and phase observable. However, in the above equations a common clock has been introduced and the differential hardware delays are contained in the d and δ terms. However, if we introduce both a common clock and individual hardware delays, we introduce also a rank deficiency in the equations which we will solve in chapter 4 by recombining this common clock with a specific combination of the hardware delays.

The broadcast GPS satellite clock offsets are provided for the ionosphere-free linear combination of dual frequency P-code range observations (this ionosphere-free linear combination will be introduced later), including the satellite code hardware delays for this combination (IS-GPS-200D, 2004). Since the standard approach to PPP, as proposed by JPL, is also to use the ionosphere-free linear combination of dual frequency GPS code and phase measurements, the precise satellite clock products (of both IGS and JPL) are also provided for this combination. Using these clock corrections with the original pseudo range code (and phase) observables introduces a bias in the observations. This bias can be removed by applying the differential hardware delays, also called differential code biases (DCBs), provided with the clock products. For the broadcast clock offsets, the DCBs are also provided in the navigation message. The IGS also provides these satellite DCBs on a regular basis together with their other products. Unlike the clock offsets which change rapidly over time, and as such must be treated kinematically, the DCBs are generally only changing slowly.

This is relevant for single frequency users (who obviously cannot form the dual frequency ionosphere-free combination) but, as will be shown later, also for dual frequency users who are interested in unbiased ionosphere delay estimates (either if the ionosphere delay is the parameter of interest or if the positioning is to be aided by the use of an external *absolute* ionosphere model).

Signal travel time The signal travel time in the observation equations is the distance between the satellite and the receiver (plus any delays) divided by the speed of light:

$$\tau_r^s = \frac{1}{c_0}\left(\left\|\mathbf{r}^s\left(t_r-\tau_r^s\right)-\mathbf{r}_r\left(t_r\right)\right\|+T_r^s\left(t_r\right)+\mathcal{I}_{r,f}^s\left(t_r\right)\right)+d_{r,f}^s\left(t_r\right) \tag{3.6}$$

One complicating factor here is that the travel time appears on both sides of eq. (3.6). To compute the travel time, which depends on the distance, one already needs the satellite position at the time of transmission. Therefore, eq. (3.6) has to be solved iteratively (or by means of a Taylor expansion, Jin, 1996), first using an approximate travel time and then using the solution of eq. (3.6) to improve on the approximation. GPS satellites travel with a velocity of about 4000 m/s and a maximum velocity in the direction of the user of about 1300 m/s for users on the surface of the Earth. This means that, to keep the range error due to the satellite motion below 1 mm (which easily meets the requirements for PPP applications), the travel time should be accurate to .77 μs (or 231 meters at the speed of light). This is larger than the delays that can be expected from the atmosphere (van der Marel, 2009) and the other delay terms in eq. (3.6) see table 3.4. A convenient consequence is that the delays in eq. (3.6) can in fact be ignored for the determination of the satellite positions.

Troposphere Considering the delay of GNSS signals traveling through the atmosphere, the atmosphere can be divided in two main parts. The upper part, called the ionosphere, is a dispersive medium which means that the propagation delay is frequency dependent and acts differently on code and phase measurements (see below). The lower part, called the troposphere, is non-dispersive and acts equally on all signals and frequencies. The troposphere delay itself can also be split in two main contributions namely the hydrostatic delay, caused by dry air and water vapor in hydrostatic equilibrium, and the wet delay only caused by water vapor.

Modern troposphere delay models usually make this distinction and the (slant) tropospheric delays are then modeled as the sum of a hydrostatic delay and a wet delay (Kleijer, 2004). For a GNSS receiver tracking multiple satellites, both parts of the troposphere delay can be approximated by the product of the delay in zenith direction, evaluated at the receiver position, and an elevation dependent mapping function, evaluated separately for each satellite.

This can be expressed with the following equation:

$$T^s_{r,k} = m^s_{h,r,k} T_{zh,r,k} + m^s_{w,r,k} T_{zw,r,k} \tag{3.7}$$

where $T^s_{r,k}$ is the total troposphere slant delay, $m^s_{h,r,k}$ and $T_{zh,r,k}$ are the hydrostatic mapping function and hydrostatic zenith delay and $m^s_{w,r,k}$ and $T_{zw,r,k}$ are the wet mapping function and wet zenith delay. Two models for the troposphere zenith delay widely used in GNSS processing are the Hopfield model (Hopfield, 1969) and the Saastamoinen model (Saastamoinen, 1972). For optimal results, both these models need meteorological data from the receiver position in real-time. For many users this data is not available and instead values derived from the standard atmosphere are used. However, this will degrade the quality of the modeled troposphere zenith delay since it will no longer reflect actual conditions at the user position and time. Another option is to use the EGNOS model which relies on averaged (empirical) parameters and seasonal variations (RTCA, 2001). This model does not use or require meteorological data from the user, which means that this model will not reflect temporal local weather conditions either. However, several papers report that it performs better than the Hopfield or Saastamoinen models if these rely on standard atmosphere values (Qu et al., 2008; Xinlong et al., 2009). The IGS also provides high accurate zenith troposphere delay information but with a latency of 2 to 3 hours which means it is not available for real-time applications (IGS, 2015b), and only for stations in the IGS network.

There are many different mapping functions to translate the modeled zenith delays to (slant) delays from the satellites to the receiver. Most current mapping functions use so-called continued fractions to express the elevation dependence of the troposphere delay (Kleijer, 2004). Differences between the mapping functions consist of the way in which the coefficients of the continued fractions are determined, and whether or not additional meteorological input from the user in needed. Some of the most commonly used mapping functions that take meteorological input are those of Ifadis (1992), with coefficients determined from real weather profiles, and Herring (1992), with coefficients determined from radiosonde data. Mapping functions that do not take meteorological input are those of Niell (1996), with coefficients also determined from radiosonde data, and the EGNOS model, which comes with its own mapping function (RTCA, 2001).

Another approach for troposphere delay modeling is to use (predicted) numerical weather models (Niell, 2001; Boehm et al., 2005; de Haan and van der Marel, 2004), these models can provide more accurate troposphere mapping, reflecting actual weather conditions at the user location, at the cost of more extensive computations and and depending on the availability of such models to the user. The now often used Vienna Mapping Functions (Boehm et al., 2006) and Global Mapping Functions (Boehm et al., 2006) are based on European Centre for Medium-range Weather Forecast (ECMWF) data.

Troposphere models alone are not accurate enough for PPP, and therefore a (residual) troposphere parameter is estimated together with the position solution. Troposphere delay estimation can be performed on an epoch-by-epoch basis or, for filter or batch applications, an assumption can be made about the variability of the troposphere in time to setup a dynamic model and so strengthen the estimation model.

Even when the troposphere is estimated with the position solution, troposphere models can improve the positioning performance for two reasons. Firstly, the model values can be used to initialize the estimation and strengthen the dynamic model for the troposphere delay as will be discussed in chapter 6. For this reason model values for the troposphere delay can be used to correct the observations a-priori in order to form the observed-minus-computed observations, treated in section 3.3:

$$\Delta T^s_{r,k} = T^s_{r,k} - T^s_{r,k|0} = T^s_{r,k} - m^s_{h,r,k} T_{zh,r,k|0} - m^s_{w,r,k} T_{zw,r,k|0} \tag{3.8}$$

Secondly, because the mapping functions for the hydrostatic and wet delays are quite similar it is difficult to estimate both a residual hydrostatic and wet delay separately in the processing. The a priori hydrostatic delay can be modeled with much higher accuracy than the wet delay (Kleijer, 2004). As a result, the residual delays are (mainly) dominated by the residual wet delays. Therefore, only a residual wet delay will be estimated in the processing with the appropriate wet mapping function:

$$\Delta T^s_{r,k} \approx m^s_{w,r,k} \Delta T_{zw,r,k} \tag{3.9}$$

In the discussion above the (residual) troposphere delay was assumed to be horizontally isotropic (e.g. the troposphere delay at any point in time depends on the satellite elevation, but not the azimuth angle). This model can be refined by parameterization of horizontal (azimuth) gradients (Chen and Herring, 1997; Bar-Sever and Kroger, 1998; Kleijer, 2004; Boehm and Schuh, 2007). Troposphere gradients are used in a number of software packages, and can improve the latitude component of the position estimation at mm level (Ghoddousi-Fard, 2009), but are not treated in this thesis.

Ionosphere The ionospheric delay can be split into a propagation effect, which can be approximated with a Taylor-series of the third order, and an effect due to the bending of the signal (Odijk, 2002). For the first-order delay the following inversely proportional relationship between the delay and the squared frequency holds:

$$\mathcal{I}^s_{r,f,k} = \frac{f_i^2}{f_f^2}\mathcal{I}^s_{r,i,k} = \gamma_f \mathcal{I}^s_{r,i,k} \tag{3.10}$$

The first-order delay has opposite effect on code and phase observations (i.e. the phase is actually advanced). The second-and third-order delays, commonly referred to as the ionospheric higher order terms, plus bending terms may be up to 5 cm at mid-latitudes for low elevation angles. For relative GPS applications over distances up to 400 km these terms can safely be neglected (Odijk, 2002). PPP is not a relative positioning technique, which means that neglecting the higher order terms may result in a small error in the positioning solution. However, since the global networks that produce the PPP orbits and clock products only consider the first order term this should also be our approach to be consistent with these products and obtain the best results (this is actually a general 'rule' which will be highlighted in a later section).

The size of the ionosphere delay depends on the number of free electrons on the path that the GNSS signal travels through the atmosphere, quantified by the Total Electron Content (TEC). This depends on the path length, which increases with decreasing satellite elevation, and the electron density of the atmosphere. The electron density displays regular variations with the geomagnetic latitude, time of day, seasonal variation, and an 11 year solar cycle. There are also irregular variations of the electron density, the frequency of occurrence and severity of which may themselves depend on the regular variations, including ionospheric storms and Traveling Ionospheric Disturbances (TID). Finally, ionospheric scintillation may cause sudden changes in phase of the received signal or degrade signal strength (Odijk, 2002; Memarzadeh, 2009).

Several (global) models exist to estimate and correct for the ionosphere delays. These include the often used Klobuchar model (Klobuchar, 1987), which has been integrated in the GPS system for single frequency users. The Klobuchar model can correct for about 50% of the ionosphere delay (IS-GPS-200D, 2004; Memarzadeh, 2009), which suffices for single frequency applications that do not require a very high accuracy. In a similar vein the NeQuick model (Radicella, 2009) is intended for single frequency users of the Galileo system. The NeQuick model has been reported to be able to correct for 60-70% of the ionosphere delay (Galileo OS-SIS-ICD, 2008; Memarzadeh, 2009), thereby outperforming the Klobuchar model. The Global Ionospheric Maps (GIM) from the IGS provide even more accurate ionosphere model values. GIMs are routinely produced based on measurements from the IGS reference network (IGS, 2015b), and contain maps with gridded TEC values. For real-time applications the predicted GIMs from the Center for Orbit Determination in Europe (CODE) can be used (Schaer et al., 1998). GIMs can be used to correct for about 80% of the ionosphere delay (Memarzadeh, 2009).

Alternatively, dual frequency measurements can be used to exploit the dispersive nature of the ionosphere expressed in eq. (3.10) to estimate or eliminate the ionosphere delay. Ionosphere delay estimation can be performed on an epoch-by-epoch basis (mathematically equal to ionosphere elimination) or, for filter or batch applications, an assumption can be

Table 3.2: GNSS frequencies, wavelengths and ionospheric dispersion factors

GNSS band	L1/E1	L2	L5/E5a	E5b	E5	E6
f [MHz]	1575.42	1227.60	1176.45	1207.14	1191.795	1278.75
($f_0 = 10.23$ MHz)	$154 f_0$	$120 f_0$	$115 f_0$	$118 f_0$	$116.5 f_0$	$125 f_0$
$\lambda_f = c_0/f$ [cm]	19.03	24.42	25.48	24.83	25.15	23.44
$\gamma_f = f_1^2/f_f^2$ [-]	1	1.6469	1.7933	1.7032	1.7474	1.5178

made about the variability of the ionosphere in time to setup a dynamic model and so strengthen the estimation model.

Dual frequency estimation of the ionosphere is more accurate than even the best global ionosphere models. Consequently, a dual frequency receiver is generally able to reach a higher position accuracy than a single frequency receiver. However, this does not mean that ionosphere models are not valuable even for dual frequency users, because the model values can be used to initialize the estimation and strengthen the dynamic model for the ionosphere delay as will be discussed in chapter 6. For this reason model values for the (first order) ionosphere delay can be used to correct the observations a-priori in order to form the observed-minus-computed observations, treated in section 3.3:

$$\Delta\mathcal{I}^s_{r,f,k} = \mathcal{I}^s_{r,f,k} - \mathcal{I}^s_{r,f,k|0} = \mathcal{I}^s_{r,f,k} - \gamma_f \mathcal{I}^s_{r,i,k|0} \tag{3.11}$$

Neglecting the higher order terms and only a first order residual ionosphere delay is estimated:

$$\Delta\mathcal{I}^s_{r,f,k} \approx \gamma_f \Delta\mathcal{I}^s_{r,i,k} \tag{3.12}$$

In the following we will also replace the total ionosphere delay, which is different for each observable, in the general observations by the first order term according to (3.10) (the ionosphere delay on a reference frequency, usually L1, with the appropriate ionosphere dispersion factor γ_f). Table 3.2 provides the ionosphere dispersion factors for the code observables on all GPS and Galileo frequencies if L1 is chosen as reference frequency (for the phase observables these are the same but negative).

Carrier phase ambiguities The carrier phase measurements are much more precise than the code measurements, however the carrier phase measurements contain a constant but unknown bias called the carrier phase ambiguity. Only when these biases are known or estimated with enough accuracy can the position solution be estimated from the very precise carrier phase measurement. Otherwise the position solution will rely on the less precise code measurements. Under certain conditions the carrier phase ambiguities can be resolved to an integer number of cycles. In this case methods such as LAMBDA can be used to successfully solve the ambiguities even after a very short measurement duration. This is the basis of Real Time Kinematic. RTK relies on a relative measurement setup to form and solve the integer ambiguities by 'so-called' double differencing. These double differences are formed by taking the single differences between the measurements of two receivers and the difference between the measurements to one reference satellite and all other satellites (Kaplan and Hegarty, 2006; Misra and Enge, 2006). PPP is not a relative setup (we only have one receiver) making this approach impossible. Therefore, in PPP the ambiguities are generally not resolved to integer numbers, but instead estimated as real-valued constant biases. When these real-valued ambiguities have converged, PPP can provide very precise positions for the user receiver, but this does take significantly longer than for RTK. Possibilities of solving the carrier phase ambiguities in PPP as integer numbers are discussed in section 3.5.

Table 3.3 provides an overview of the achieved PPP performance reported by different authors.

Table 3.3: Performance of Precise Point Positioning

Performance		Settings					Comment	Source
Accuracy	**Convergence**	**Signals**	**Products**	**Real-time**	**Dynamics**	**Ambiguities**		
1 cm	24h	GPS L1,L2	IGS	no	static	float	proof of concept	Zumberge et al. (1997)
20 cm	1h	GPS L1,L2	JPL (IGS)	no	static	float		Witchayangkoon and Segantine (1999)
few cm	12h							
1 cm	24h							
40 cm rms	5min	GPS L1,L2	IGS+NRCan	no	-	float	code+phase	Gao and Shen (2001)
1 cm	2-3h	GPS L1,L2	IGS	no	static	float		Kouba and Héroux (2001)
10 cm	20-30 min	GPS L1,L2	JPL	yes	kinematic	float		Kechine et al. (2003)
1 cm	20min	GPS L1,L2	JPL	yes	static	float	IGS station	Gao and Chen (2004)
1 cm	-				kinematic		vehicle and airborne	
40-50 cm rms	10-20 min	GPS L1	JPL	yes	kinematic	float	vehicle	Gao et al. (2006)
20-90 cm rms							marine (height biased)	
50-100 cm 95%	2-3 min	GPS L1	IGS	no	kinematic	float	unfavourable conditions	Le and Tiberius (2006a)
20-50 cm 95%							favourable conditions	
5 cm	3 h	GPS L1,L2	IAC (IGS)	no	static	float	GLONASS improves convergence not accuracy	Cai and Gao (2007b,a)
6 cm		GPS L1,L2 GLO L1,L2						
1 cm	few h	GPS L1,L2	IGU orbit + Real-time clock	yes	kinematic	float	clock estimated via NTRIP	Weber et al. (2007)
1 cm	few min					fixed		
10 cm	1h	GPS L1,L2	NRCan	yes	static	float		Collins et al. (2008)
2 cm 90%						fixed		
5 cm 3d rms	1h	GPS L1,L2	CODE final	no	static	float	IGS station, hourly data	Geng et al. (2008)
3 cm 1d					kinematic		vessel, hourly data	
2 cm 3d rms					static	fixed	IGS station, hourly data	
1 cm 1d					kinematic		vessel, hourly data	
10 cm	90min	GPS L1,L2	IGS	yes	static	float	final accuracy 2cm	Landau et al. (2008)
4 cm	2h				kinematic		reference station	
1 cm	30min	GPS L1,L2	JPL	yes	static	float	IGS station	Bisnath and Gao (2009a,b)
10 cm	20-25min				kinematic		airborne	
17 cm 3d rms	-	GPS L1,L2	CONGO	yes	static	float	GIOVE decreased accuracy but increased availability	Cao et al. (2010)
31 cm 3d rms		GPS L1,L2 GIOVE E1,E5a						
40 cm	27min	GPS L1,L2	Fugro G2	yes	static	float	final accuracy 10cm	Melgard et al. (2010)
40 cm	17min	GPS L1,L2 GLO L1,L2						
15-30 cm	90min	GPS L1	RETICLE	yes	kinematic	float	stationary high-end receiver	van Bree and Tiberius (2012)
2.5 cm	2h	GPS L1,L2	IGS	no	static	float	adding GIOVE improved accuracy GPS L5 did not	Monge et al. (2014)
1 cm	10h							
0.7 cm	24h							
7-18 cm	1h	GPS L1,L2	IGS	no	static	float	clock offsets	Odijk et al. (2015)

Continued on next page

Table 3.3 – continued from previous page

Performance		Settings					Comment	Source
Accuracy	**Convergence**	**Signals**	**Products**	**Real-time**	**Dynamics**	**Ambiguities**		
1-5 cm						fixed	from 110 km baseline	
11-38 cm	2h30min	BDS B1,B2	WUM			float	in Australia	
3-12 cm						fixed		
9-17 cm	30min	GPS L1,L2	IGS			float		
1-5 cm		BDS B1,B2	WUM			fixed		
4-10 cm	2h	GPS L1,L2	MGEX	no	static	fixed		Rabbou (2015)
3-7 cm		GPS L1,L2 GLO L1,L2 GAL, BDS					dual-frequency	

The position accuracy for PPP is a function of the measurement duration, and most authors provide information on both the achieved accuracy and the time it took for the position solution to converge to this accuracy. Unfortunately, almost each author specifies the achieved accuracy for different measurement durations and often uses different metrics to describe the achieved accuracy. Therefore, it is difficult to compare results between authors, but several observations can still be made. The time to reach 1cm accuracy has decreased significantly over the years from 24h to only 30 minutes, which might be a result of the improvements of the precise orbit and clock products. Kinematic processing provides less accurate positions and has longer convergence times than static processing. Single frequency PPP converges much faster than dual frequency PPP but reaches a lower final accuracy. Ambiguity resolution for PPP improves the position accuracy and convergence times. Finally, additional GNSS so far do not improve accuracy but have a positive effect on convergence and availability.

A final, important note about these published results is that, although Bisnath and Gao (2009a) stress the importance of integrity monitoring for PPP few other authors mention integrity for PPP, and even less actually provide integrity results.

Other systematic effects $d_{r,f,k}$, $\delta_{r,f,k}$ All other systematic errors on the code and phase Line-Of-Sight (LOS) observations are summarized in table 3.4.

Table 3.4: Line-Of-Sight effects ($d_{r,f,k}$, $\delta_{r,f,k}$)

Range effect description	**Magnitude [m]**
Satellite Antenna Phase Center Offsets (PCO): GNSS measurements are made between the phase centers of the receiver and satellite antennas. Therefore, the satellite positions used for navigation should also refer to the antenna phase center. For the GPS broadcast navigation message this is indeed the case, and as a result PPP corrections based on the broadcast message such as those available from Internet-Based Global Differential GPS (IGDG) from the Jet Propulsion Laboratory (JPL) (Muellerschoen et al., 2000a) also refer to the antenna phase center. However, the force models used for satellite orbit modeling by the International GNSS Service (IGS) refer to the satellite center of mass, and as a result the IGS GPS precise satellite coordinates and clock products also refer to the satellite center of mass (Kouba, 2009a). In this case the satellite orientation should be determined from its position relative to the position of the Earth and the position Sun and apply the known satellite antenna offsets from the center of mass.	1

Range effect description	Magnitude [m]
Antenna Phase Center Variation (PCV): On top of the constant antenna phase center offsets, the antenna phase center also varies with direction of the signal traveling from the satellite to the receiver. For most GNSS antennas the strongest variations are with the antenna bore-sight angle (for the satellite antenna this is the nadir angle and for an untilted receiver antenna this is the zenith angle or 90° minus the elevation angle), and it is often assumed that the phase center is constant about the bore-sight (i.e. symmetric with azimuth angle). However, the variations with azimuth cannot always be neglected. The PCVs of many receiver antennas with elevation (and azimuth) used on IGS stations were measured in an anechoic chamber or on a short baseline in the field using a robot capable of tilting and rotating one of the antennas, and have in turn been used to determine the PCVs of GPS satellite antennas with nadir angle (not with azimuth) by reprocessing more than 10 years of GPS data (Schmid et al., 2007). Measured PCVs for both receiver antennas and satellites are available online (IGS, 2010).	0.04
Higher order ionosphere delays and bending: As mentioned before, the observation equations only take the first order ionosphere delay into account. Higher order terms, plus bending terms can reach up to 5 cm at mid-latitudes (Odijk, 2002), but are generally significantly smaller. One might consider to also take these higher order terms into account. However, global PPP networks that determine the satellite positions and clocks do not. Which means that if these precise products are used *with* higher order terms, the processing is performed in an inconsistent manner thereby degrading the solution. Therefore, the best approach is to conform to the network processing and account for the higher order terms *only* in the stochastic model.	0.05

Range effect description	Magnitude [m]
Phase wind-up: GNSS signals are Right-Hand Circularly Polarized (RHCP) and as a result a rotation of the satellite or receiver antenna will change the measured carrier phase (this does not impact the code measurements). The size of this effect called phase wind-up or phase wrap-up (PWU) is equal to the carrier wavelength for one complete rotation of the antenna around its bore-sight axis. Consequently for dual frequency receivers PWU is the same on both frequencies, but simply scaled by the wavelength. Rotation of the satellite antennas are related to the antenna being oriented towards the Earth, and the solar panels being oriented towards the Sun. These rotations are relatively slow and can be predicted quite accurately from the relative positions of the receiver, the satellite and the Sun. However, when the Sun, the satellite and the Earth are on a straight line (either when the satellite is in the shadow of the Earth, or vise versa) this rotation can reach one revolution within less than half an hour (Kouba, 2009a), and might be less predictable. For these instances the particular satellite is best not used. Rotation of the receiver antenna depends very much on the platform. A stationary antenna will only be impacted by the slow rotation of the Earth, while an antenna on a moving platform will primarily be impacted by the movement of the platform. If a separate receiver clock is estimated for the code and phase observations, then the carrier phase clock will fully absorb the PWU effect. However, when a common clock is estimated, uncompensated PWU effects will impact the other estimates as well (especially the vertical component). Since GNSS antennas are generally pointed upwards, PWU is closely related to the platform heading. If the platform makes several turns in the same direction the PWU can reach a magnitude of several wavelengths. If platform heading information is available (e.g. with multiple antennas) this effect can be determined and corrected. For a single antenna platform without other means of determining the heading (or attitude) this is not straight forward. However, for highly dynamic platforms (e.g. aircrafts) using the position differences in time can already provide an improvement of the height estimates (Le and Tiberius, 2006b).	0.10

Range effect description	Magnitude [m]
Instrumental delays: As mentioned before, there are frequency and signal dependent hardware delays at both satellite and receiver. These can be taken into account by defining a clock parameter per observable, but in (3.3) and (3.4) we chose to define a common clock parameter and account for the hardware delays in the terms which contain any other systematic effects on the code and phase measurements. However, this 'absolute' common clock is generally *not* estimated, instead the clock with respect to one of (or a combination of) the observables is estimated. Therefore, the absolute values of the hardware delays are not really essential, but rather the *differential* hardware delays are important. The precise satellite clocks from a PPP provider will also already contain the satellite hardware delays pertaining to a certain observable (generally this is the ionosphere-free code observable, see later). When this clock is applied to a different code observable (e.g. for single frequency PPP) it is important to apply the necessary satellite differential code bias. These DCBs are available from the IGS (Kouba, 2009a). Phase measurements also have these differential biases. As will be shown later, for ambiguity resolution these differential phase biases should also be known together with the initial phase at the satellite. Conventional PPP algorithms do not resolve the ambiguities to integers, but rather estimate them as real-valued parameters. In this case the differential phase bias cannot be separated from the ambiguity parameter, nor would this be helpful in any way. Instead they are simply lumped in the positioning algorithm and estimated as a *different* real value. At the side of the receiver we have similar differential biases. However, they are less stable than the satellite hardware delays and are dependent on temperature and change over time. Generally, the necessary receiver hardware delays are estimated (together with a receiver clock parameter), or eliminated in a between satellite difference.	0.60

Range effect description	**Magnitude [m]**
Multipath: Multipath is a physical process where a GNSS antenna receives a signal not only by the direct path (LOS) from the satellite, but also by indirect path(s) after one or more reflections. The impact of these reflected signals can be observed on pseudo range code, carrier phase and carrier-to-noise density ratio (C/N_0) measurements from a receiver. The reflected signals generally arrive at the antenna with a certain delay, which causes a phase difference between the LOS signal and the multipath signal, a different (elevation) angle, which can lead to different attenuation by the antenna, and possibly with changed polarity due to the reflection. The superposition of the direct and multipath waves can lead to a significant increase or decrease in the C/N_0 measurements, but more importantly they can lead to biased code and phase measurements (Braasch and van Dierendonck, 1999). Because multipath is one of the dominant error sources for GNSS, much effort has been spent over the previous decades to combat the averse effects of multipath on receiver performance in different ways. These include, but are not limited to, antenna design to block or attenuate reflected signals, and signal and tracking loop design to reduce the impact of multipath on the pseudo range measurements (Irsigler et al., 2004). For modern receivers multipath can typically lead to range errors in the order of meters for code measurements and in the order of centimeters for phase measurements. An important distinction w.r.t. multipath should be made between static and dynamic platforms. For a static receiver, the same object can reflect certain satellite signals for a long time, leading to slowly changing biases in the range measurements (i.e. the multipath error is highly correlated in time). For a dynamic receiver on the other hand, different reflecting objects will come into and leave view much faster, leading to a much more white noise-like error on the range measurements. Multipath is generally not treated in the functional positioning model, but instead via the stochastic model.	>1 code .01 phase

Range effect description	Magnitude [m]
Relativity: In GPS positioning both general relativity, due to difference in the curvature of space-time close to the surface of the Earth and at the orbital height of the GPS satellites, and special relativity, due to the high relative velocity of the GPS satellites with respect to a GPS user (on Earth), play an important role. For static users on Earth or users (slowly) traveling over the surface of the Earth, these relativistic effects can be corrected in two steps. The first step is already taken care off on board of the GPS satellites by a small intentional offset of the frequency standard of the satellite clocks. This frequency offset correction is valid for circular orbits, but since GPS orbits are actually slightly elliptical a second correction is needed. This second correction, which depends on the actual satellite position and velocity, must be applied by the user (de Jonge, 1998). An expression for this correction is provided in the GPS Interface Control Document (IS-GPS-200D, 2004).	<10

3.3 Linearized observation equations

The observation equations are not linear in the satellite and receiver positions. Therefore, in order to estimate the receiver position with a least squares adjustment, the observation equations will have to be linearized. A first order Taylor expansion of the observation equations eqs. (3.3) and (3.4) around an approximate value x_0 gives:

$$\underline{P}^s_{r,f,k} = P^s_{r,f,k|0} + \sum \left.\frac{\partial P^s_{r,f,k}}{\partial x}\right|_{x_0} \Delta x + \frac{1}{2}\sum \left.\frac{\partial^2 P^s_{r,f,k}}{\partial x^2}\right|_{x_1} \Delta x^2 + \underline{\epsilon}^s_{r,f} \tag{3.13}$$

$$\underline{\Phi}^s_{r,f,k} = \Phi^s_{r,f,k|0} + \sum \left.\frac{\partial \Phi^s_{r,f,k}}{\partial x}\right|_{x_0} \Delta x + \frac{1}{2}\sum \left.\frac{\partial^2 \Phi^s_{r,f,k}}{\partial x^2}\right|_{x_1} \Delta x^2 + \underline{\varepsilon}^s_{r,f} \tag{3.14}$$

The third term on the right-hand side of both equations represent the second order remainder of the Taylor expansion with x_1 between x_0 and $x_0 + \Delta x$. This term cannot be neglected, unless Δx is small enough, which means we already need to have good approximations of the satellite and receiver positions. Teunissen (1989) provides an upper bound for the second order remainder, which is evaluated for GPS in Tiberius (1998), and shows that, if the approximate position is within a hundred meters from the actual position, the second order remainder is below mm level. This can be achieved by iteratively solving the linearized system and use the solution as a new approximation in the following iteration until the solution no longer changes significantly. $P^s_{r,f,k|0}$ and $\Phi^s_{r,f,k|0}$ are the computed observations:

$$P^s_{r,f,k|0} = \left\|\mathbf{r}^s_{k|0} - \mathbf{r}_{r,k|0}\right\| + c_0\delta t_{r,k|0} - c_0\delta t^s_{k|0} + T^s_{r,k|0} + \mathcal{I}^s_{r,f,k|0} + c_0 d^s_{r,f,k|0} \tag{3.15}$$

$$\Phi^s_{r,f,k|0} = \left\|\mathbf{r}^s_{k|0} - \mathbf{r}_{r,k|0}\right\| + c_0\delta t_{r,k|0} - c_0\delta t^s_{k|0} + T^s_{r,k|0} - \mathcal{I}^s_{r,f,k|0} + c_0 \delta^s_{r,f,k|0} \tag{3.16}$$

Model values for the troposphere delay and/or ionosphere delay can also be included in the computed observation, in which case only residual delays are estimated. If the models are unbiased, the residual delays have an expected value of zero, which can be used for the initial estimate of, and the dynamic model for the unknown (state) vector. For practical reasons, one could also opt to include an ambiguity term in the computed observation (e.g. to keep the corresponding state vector element small), but since at first the actual ambiguity is completely unknown, this does not strengthen the positioning model. We can now introduce the linearized observations also called Observed Minus Computed observations (OMC):

$$\Delta \underline{P}^s_{r,f,k} \equiv \underline{P}^s_{r,f,k} - P^s_{r,f,k|0} \tag{3.17}$$

$$\Delta \underline{\Phi}^s_{r,f,k} \equiv \underline{\Phi}^s_{r,f,k} - \Phi^s_{r,f,k|0} \tag{3.18}$$

Evaluating the first order partial derivatives in (3.13) and (3.14) gives the following expression for the linearized observation equations:

$$\begin{aligned} \Delta \underline{P}^s_{r,f,k} \quad = \quad & \mathbf{e}^{s*}_{r,k} \Delta \mathbf{r}^s_k - \mathbf{e}^{s*}_{r,k} \Delta \mathbf{r}_{r,k} + c_0 \Delta \delta t_{r,k} - c_0 \Delta \delta t^s_k + \\ & m^s_{w,r,k} \Delta T_{zw,r,k} + \gamma_f \Delta \mathcal{I}^s_{r,i,k} + c_0 \Delta d^s_{r,f,k} + \underline{\epsilon}^s_{r,f} \end{aligned} \tag{3.19}$$

$$\begin{aligned} \Delta \underline{\Phi}^s_{r,f,k} \quad = \quad & \mathbf{e}^{s*}_{r,k} \Delta \mathbf{r}^s_k - \mathbf{e}^{s*}_{r,k} \Delta \mathbf{r}_{r,k} + c_0 \Delta \delta t_{r,k} - c_0 \Delta \delta t^s_k + \\ & m^s_{w,r,k} \Delta T_{zw,r,k} - \gamma_f \Delta \mathcal{I}^s_{r,i,k} + \lambda_f A^s_{r,f} + c_0 \Delta \delta^s_{r,f,k} + \underline{\varepsilon}^s_{r,f} \end{aligned} \tag{3.20}$$

where $\mathbf{e}^{s*}_{r,k}$ are the unit direction vectors from the receiver to the satellite. In PPP the satellite orbits and clocks are not estimated or adjusted by the user, but kept fixed at the values determined from the estimation by the global network. Therefore, we can remove the satellite positions and clock offsets from the observation equations as we will not estimate these. However, the remaining effects *do* contribute to the stochastic model. As mentioned before, if we take into account the frequency and signal hardware delays, there actually is a different clock for each observable. The impact of the PPP products on the differential hardware delays will be treated later. For now we will only consider the common satellite clock. Removing the satellite clock and orbit results in the following two derived observations:

$$\Delta \overline{\underline{P}}^s_{r,f,k} \equiv \Delta \underline{P}^s_{r,f,k} - \mathbf{e}^{s*}_{r,k} \Delta \underline{\mathbf{r}}^s_k + c_0 \Delta \underline{\delta t}^s_k \tag{3.21}$$

$$\Delta \overline{\underline{\Phi}}^s_{r,f,k} \equiv \Delta \underline{\Phi}^s_{r,f,k} - \mathbf{e}^{s*}_{r,k} \Delta \underline{\mathbf{r}}^s_k + c_0 \Delta \underline{\delta t}^s_k \tag{3.22}$$

Note that, since the orbit and clock values are already used in the linearization, the actual values of $\Delta \underline{\mathbf{r}}^s_k$ and $\Delta \underline{\delta t}^s_k$ in eqs. (3.21) and (3.22) are zero. In the following, Δ is dropped from the notation except for the receiver (and satellite) positions and the OMC observations. Rewriting eqs. (3.19) and (3.20) for these new observations results in:

$$\Delta \overline{\underline{P}}^s_{r,f,k} = -\mathbf{e}^{s*}_{r,k} \Delta \mathbf{r}_{r,k} + c_0 \delta t_{r,k} + m^s_{w,r,k} T_{zw,r,k} + \gamma_f \mathcal{I}^s_{r,i,k} + c_0 d^s_{r,f,k} + \underline{\epsilon}^s_{r,f} \tag{3.23}$$

$$\Delta\underline{\overline{\Phi}}^s_{r,f,k} = -\mathbf{e}^{s*}_{r,k}\Delta\mathbf{r}_{r,k} + c_0\delta t_{r,k} + m^s_{w,r,k}T_{zw,r,k} - \gamma_f\mathcal{I}^s_{r,i,k} + \lambda_f A^s_{r,f} + c_0\delta^s_{r,f,k} + \underline{\varepsilon}^s_{r,f} \quad (3.24)$$

Applying the PPP products changes not only the expectation of the observations, but also the dispersion. If we split (3.21) and (3.22) into the expectation and dispersion we get:

$$\begin{aligned} E\left\{\Delta\underline{\overline{P}}^s_{r,f,k}\right\} &= -\mathbf{e}^{s*}_{r,k}\Delta\mathbf{r}_{r,k} + c_0\delta t_{r,k} + m^s_{w,r,k}T_{zw,r,k} + \gamma_f\mathcal{I}^s_{r,i,k} + c_0 d^s_{r,f,k} \\ D\left\{\Delta\underline{\overline{P}}^s_{r,f,k}\right\} &= \boldsymbol{Q}_{\underline{\epsilon}^s_{r,f}} + \mathbf{e}^{s*}_{r,k}\boldsymbol{Q}_{\Delta\mathbf{r}^s_k}\mathbf{e}^s_{r,k} + c_0^2\boldsymbol{Q}_{\delta t^s_k} \end{aligned} \quad (3.25)$$

$$\begin{aligned} E\left\{\Delta\underline{\overline{\Phi}}^s_{r,f,k}\right\} &= -\mathbf{e}^{s*}_{r,k}\Delta\mathbf{r}_{r,k} + c_0\delta t_{r,k} + m^s_{w,r,k}T_{zw,r,k} - \gamma_f\mathcal{I}^s_{r,i,k} + \lambda_f A^s_{r,f} + c_0\delta^s_{r,f,k} \\ D\left\{\Delta\underline{\overline{\Phi}}^s_{r,f,k}\right\} &= \boldsymbol{Q}_{\underline{\varepsilon}^s_{r,f}} + \mathbf{e}^{s*}_{r,k}\boldsymbol{Q}_{\Delta\mathbf{r}^s_k}\mathbf{e}^s_{r,k} + c_0^2\boldsymbol{Q}_{\delta t^s_k} \end{aligned} \quad (3.26)$$

where $\boldsymbol{Q}_{\underline{\epsilon}^s_{r,f}}$ and $\boldsymbol{Q}_{\underline{\varepsilon}^s_{r,f}}$ are the covariance matrices of the code and phase observables and $\boldsymbol{Q}_{\Delta\mathbf{r}^s_k}$ and $\boldsymbol{Q}_{\delta t^s_k}$ the covariance matrices of the precise satellite position and clock products. Here we made the underlying assumption that the satellite orbit and clock products are unbiased and that any errors can be accounted for in the stochastic model. If this is not the case, a small residual term would remain in the expectation of the derived observations. Using an external troposphere or ionosphere model in the observed-minus-computed observables (as shown above), impacts the variance of the observable similarly. From equations (3.23) and (3.24) it is clear that the applied precise products also generate (strong) correlation between the observables. For the variance of the original observations (including multipath) an elevation dependent weighting is often used and is reported to produce better results than elevation independent weighting, but the quality of the corrections will generally not depend on satellite elevation. As mentioned before, the uncertainty in real-time precise products is generally dominated by uncertainty of the satellite clocks, and unless there is strong multipath or interference, this is often larger then the uncertainty of the measurements. In this case a homogeneous weighting scheme for all observations seems an obvious choice, however, the correlation between the observations should not be neglected.

3.4 PPP algorithms

One aspect of PPP which strongly affects the strength of the model and is closely related to the integrity performance is the treatment of the ionospheric delay. Since the intentional degradation of the accuracy by the US government, known as selective availability, was turned off in 2000, the ionosphere delay is the dominant error source for GNSS users. In relative positioning such as RTK, for short baselines, the ionospheric delay is eliminated in the between-receiver differences. In network RTK and Wide Area RTK, the baseline lengths can be increased through accurate modeling of the ionospheric delays (although the convergence time increases with the baseline length). In PPP an ionosphere-free linear combination of the observations is often used to eliminate the ionospheric delay. Besides eliminating the ionosphere delay, this has the additional advantage of decreasing the CPU load (by halving the design matrix). The widely used ionosphere-free combinations for single frequency users and GPS dual frequency users will be treated in the following paragraphs.

The ionosphere-free combinations also have several disadvantages. The single frequency ionosphere-free observable is ambiguous (like a phase observable), has a noise level comparable to the code observable and is vulnerable to code multipath. In this respect it combines the worst properties of the code and phase observables. The dual frequency ionosphere-free observable has increased measurement noise, makes it impossible to use a priori information of the ionosphere, and is said to destroy the integer nature of the ambiguities. In fact, the dual frequency ionosphere-free linear combination *does* still contain a combination of the integer ambiguities, but has a very short virtual wavelength (for GPS L1, L2 this is 0.63cm, see section 3.5).

If the ionosphere is not eliminated with a linear combination, external information on the ionosphere delay can be used from an ionosphere model or ionosphere maps, which can account for around 80% of the error (Memarzadeh, 2009). However, for PPP the remaining error is still too large.

Therefore, another approach can be considered to account for the remaining ionosphere delay, which is to estimate it each epoch from the measurements, taking into account the differential code and phase biases of the satellite and receiver. For this reason, the ionosphere delay is included in the state vector of the filter. This makes it possible to use a priori information (on the non-white noise stochastic properties) of the ionosphere (i.e. in the form of a dynamical model in the time update equation, like is done with the troposphere delay). Unlike the troposphere delay, the ionosphere delay cannot be accurately described by a single parameter for all satellites. Instead the ionosphere delay needs to estimated separately for each satellite. Therefore, an inherent disadvantage is the increased size of the state vector in the Kalman filter. This approach to the ionosphere delay respects the integer nature of the ambiguities and will improve RAIM performance.

In the following several linear combinations of the observations are considered. These combinations are made from different observations to the same satellite. This means that the geometric range, the troposphere delay and the satellite and receiver clock offsets are the same for each observable. Therefore, the following more concise observation equations can be used instead:

$$\underline{P}^s_{r,f,k} = g^s_{r,k} + \gamma_f \mathcal{I}^s_{r,i,k} + c_0 d^s_{r,f,k} + \underline{\epsilon}^s_{r,f} \tag{3.27}$$

$$\underline{\Phi}^s_{r,f,k} = g^s_{r,k} - \gamma_f \mathcal{I}^s_{r,i,k} + \lambda_f A^s_{r,f} + c_0 \delta^s_{r,f,k} + \underline{\varepsilon}^s_{r,f} \tag{3.28}$$

where g contains the geometric range, the troposphere delay and the satellite and receiver clock offsets, the relation given by (3.10) for the first order ionosphere delay has been substituted. Equations (3.27) and (3.28) form the geometry-free model (Odijk, 2008), so-called because the receiver satellite geometry is no longer present in the equations. The (linear) geometry-free model is often used for GNSS data analysis (see also chapter 6). Here it is used to facilitate a good understanding of the linear combinations involved.

3.4.1 Positioning with ionosphere free linear combinations

As shown above, the first order ionosphere delay (which is by far the largest part) impacts the code and phase observables on different frequencies according to a simple relation depending on the frequencies of the carrier waves. This relation can be used in several different ways to remove the ionosphere delay from the observations.

3.4.1.1 Single frequency algorithms

Since the first order ionosphere delay is equal in size and opposite in sign on the code and phase observable on the same frequency, the ionosphere delay can be eliminated in the code-plus-carrier (CPC) combination (Yunck, 1996). This ionosphere-free combination can be used as the primary observable for single frequency GNSS applications, and is defined as follows:

$$\underline{\mathsf{CPC}}^s_{r,f,k} \equiv \frac{1}{2}\left(\underline{P}^s_{r,f,k} + \underline{\Phi}^s_{r,f,k}\right) \tag{3.29}$$

with eqs. (3.27) and (3.28):

$$\underline{\mathsf{CPC}}^s_{r,f,k} = g^s_{r,k} + \frac{1}{2}A^s_{r,f} + \frac{1}{2}c_0\left(d^s_{r,f,k} + \delta^s_{r,f,k}\right) + \frac{1}{2}\left(\underline{\epsilon}^s_{r,j} + \underline{\varepsilon}^s_{r,j}\right) \tag{3.30}$$

Compared to the original observations the following characteristics of the code-plus-carrier can be noted. The combined geometry term (range, clock and tropospheric delay) are the same as in the original observations; the first order ionosphere delay is removed. The CPC observations contain an ambiguity parameter like the carrier phase observations, but the variance of the noise will be close to half that of the code observations (if we assume that the code noise is much larger than the phase noise and there is no correlation) which is still much larger than the noise on the phase measurements. Finally, the miscellaneous range errors will now be a combination of the code and phase terms. This also means that the CPC combination is vulnerable to code multipath which is generally much stronger than phase multipath. In section 4.5 an observation model with estimable parameters is introduced that corresponds to this linear combination.

3.4.1.2 Dual frequency algorithms

With dual frequency observations, two different ionosphere-free linear combinations can be made; one for the code and one for the phase observables. The first order ionosphere delay is equal on different carrier wave frequencies except for the different dispersion factors γ_f and can thus be eliminated. We define the linear combination of frequencies a and b as:

$$\underline{P}^s_{r,\mathsf{LC},k} \equiv a\underline{P}^s_{r,a,k} + b\underline{P}^s_{r,b,k} \tag{3.31}$$

$$\underline{\Phi}^s_{r,\mathsf{LC},k} \equiv a\underline{\Phi}^s_{r,a,k} + b\underline{\Phi}^s_{r,b,k} \tag{3.32}$$

with eqs. (3.27) and (3.28), expressing the ionosphere delay on frequency $f_0 = 10.23\,\text{MHz}$ as $\mathcal{I}^s_{r,0,k}$ and using $f_i = k_i f_0$ this gives:

$$\begin{aligned} \underline{P}^s_{r,\mathsf{LC},k} = \; & (a+b)g^s_{r,k} + (\tfrac{a}{k_a^2} + \tfrac{b}{k_b^2})\mathcal{I}^s_{r,0,k} + \\ & c_0(ad^s_{r,a,k} + bd^s_{r,b,k}) + (a\underline{\epsilon}^s_{r,a,k} + b\underline{\epsilon}^s_{r,b,k}) \end{aligned} \tag{3.33}$$

$$\begin{aligned} \underline{\Phi}^s_{r,\mathsf{LC},k} = \; & (a+b)g^s_{r,k} - (\tfrac{a}{k_a^2} + \tfrac{b}{k_b^2})\mathcal{I}^s_{r,0,k} + \tfrac{c_0}{f_0}(\tfrac{a}{k_a}A^s_{r,a} + \tfrac{b}{k_b}A^s_{r,b}) + \\ & c_0(a\delta^s_{r,a,k} + b\delta^s_{r,b,k}) + (a\underline{\varepsilon}^s_{r,a,k} + b\underline{\varepsilon}^s_{r,b,k}) \end{aligned} \tag{3.34}$$

The ionosphere can now be eliminated while keeping the original range term by choosing:

$$\begin{cases} a+b & = 1 \\ \frac{a}{k_a^2} + \frac{b}{k_b^2} & = 0 \end{cases} \tag{3.35}$$

which works out as:

$$\begin{cases} a = & \frac{k_a^2}{k_a^2 - k_b^2} = \frac{\gamma_b}{\gamma_b - \gamma_a} \\ b = & \frac{-k_b^2}{k_a^2 - k_b^2} = \frac{-\gamma_a}{\gamma_b - \gamma_a} \end{cases} \tag{3.36}$$

Equations (3.33) and (3.34) then become the following ionosphere-free linear combinations:

$$\underline{P}^s_{r,\mathsf{IF},k} = \; g^s_{r,k} + \tfrac{c_0}{k_a^2 - k_b^2}(k_a^2 d^s_{r,a,k} - k_b^2 d^s_{r,b,k}) + \tfrac{1}{k_a^2 - k_b^2}(k_a^2 \underline{\epsilon}^s_{r,a,k} - k_b^2 \underline{\epsilon}^s_{r,b,k}) \tag{3.37}$$

$$\begin{aligned} \underline{\Phi}^s_{r,\mathsf{IF},k} = \; & g^s_{r,k} + \tfrac{c_0}{(k_a^2 - k_b^2)f_0}(k_a A^s_{r,a} - k_b A^s_{r,b}) + \tfrac{c_0}{k_a^2 - k_b^2}(k_a^2 \delta^s_{r,a,k} - k_b^2 \delta^s_{r,b,k}) + \\ & \tfrac{1}{k_a^2 - k_b^2}(k_a^2 \underline{\varepsilon}^s_{r,a,k} - k_b^2 \underline{\varepsilon}^s_{r,b,k}) \end{aligned} \tag{3.38}$$

or:

$$\underline{P}^s_{r,\mathsf{IF},k} \; = \; g^s_{r,k} + \tfrac{c_0}{\gamma_b - \gamma_a}(\gamma_b d^s_{r,a,k} - \gamma_a d^s_{r,b,k}) + \tfrac{1}{\gamma_b - \gamma_a}(\gamma_b \underline{\epsilon}^s_{r,a,k} - \gamma_a \underline{\epsilon}^s_{r,b,k}) \tag{3.39}$$

$$\begin{aligned} \underline{\Phi}^s_{r,\mathsf{IF},k} \; = \; & g^s_{r,k} + \tfrac{1}{\gamma_b - \gamma_a}(\gamma_b \lambda_a A^s_{r,a} - \gamma_a \lambda_b A^s_{r,b}) + \tfrac{c_0}{\gamma_b - \gamma_a}(\gamma_b \delta^s_{r,a,k} - \gamma_a \delta^s_{r,b,k}) + \\ & \tfrac{1}{\gamma_b - \gamma_a}(\gamma_b \underline{\varepsilon}^s_{r,a,k} - \gamma_a \underline{\varepsilon}^s_{r,b,k}) \end{aligned} \tag{3.40}$$

Besides eliminating the first-order ionosphere delays and keeping the original geometry term (range, clocks and troposphere delay), several remarks can be made about these linear combinations. The miscellaneous range errors on both code ($d^s_{r,f,k}$) and phase ($\delta^s_{r,f,k}$) are now combinations of the two frequencies, as is the ambiguity term in the ionosphere-free phase combination. Furthermore, the noise level of the ionosphere-free combinations is increased. If we assume the same variance of the observables on both frequencies and no cross-correlation, the standard deviation of the noise is increased by a factor of $\sqrt{a^2+b^2}$. Table 3.5 on page 42 shows the values of a, b and the noise multiplication factor for all dual-frequency combinations of the GPS and Galileo frequencies. The table shows that the increase in measurement noise is at least a factor of 2.6, but even much higher for certain other combinations of frequencies.

Finally, note that taking the L1 frequency as reference frequency for the ionosphere delay instead ($\gamma_{\mathrm{L1}} = 1$), and dropping the subscript on the dispersion factor of the L2 frequency ($\gamma_{\mathrm{L2}} = \gamma$), gives the familiar expression for the ionosphere-free combination of the GPS L1 and L2 frequencies (which we will call L3), with a noise multiplication factor of 3.0:

$$\underline{P}^s_{r,\mathrm{L3},k} = \frac{\gamma}{\gamma-1}\underline{P}^s_{r,\mathrm{L1},k} - \frac{1}{\gamma-1}\underline{P}^s_{r,\mathrm{L2},k} \tag{3.41}$$

$$\underline{\Phi}^s_{r,\mathrm{L3},k} = \frac{\gamma}{\gamma-1}\underline{\Phi}^s_{r,\mathrm{L1},k} - \frac{1}{\gamma-1}\underline{\Phi}^s_{r,\mathrm{L2},k} \tag{3.42}$$

In section 4.7 an observation model with estimable parameters is introduced that corresponds to this linear combination.

3.4.1.3 Multi-frequency algorithms

As mentioned previously, recent GPS satellites started to transmit a ranging signal on an additional frequency (the L5 frequency see table 3.2) and other GNSS including Galileo and BeiDou also transmit on multiple frequencies. This section provides some exploratory computations and general considerations for triple-frequency PPP. A third frequency creates new possibilities to combine signals. We could e.g. consider a linear combination that keeps the original range term, eliminates the ionosphere and minimizes the observation noise. It should be noted that from an estimation point of view, this is strictly speaking not allowed since the information content is not preserved; we only present it here to illustrate how an additional frequency impacts the PPP estimation problem. For frequencies a, b and c:

$$\underline{P}^s_{r,\mathrm{LC3},k} \equiv a\underline{P}^s_{r,a,k} + b\underline{P}^s_{r,b,k} + c\underline{P}^s_{r,c,k} \tag{3.43}$$

$$\underline{\Phi}^s_{r,\mathrm{LC3},k} \equiv a\underline{\Phi}^s_{r,a,k} + b\underline{\Phi}^s_{r,b,k} + c\underline{\Phi}^s_{r,c,k} \tag{3.44}$$

If we again assume the same variance of the observables on each frequency and no cross-correlation, we can split these equations in the expectation and dispersion as follows (using eqs. (3.27) and (3.28)):

$$\begin{aligned} E\left\{\underline{P}^s_{r,\mathrm{LC3},k}\right\} &= (a+b+c)g^s_{r,k} + (\tfrac{a}{k_a^2} + \tfrac{b}{k_b^2} + \tfrac{c}{k_c^2})\mathcal{I}^s_{r,0,k} + c_0(ad^s_{r,a,k} + bd^s_{r,b,k} + cd^s_{r,c,k}) \\ D\left\{\underline{P}^s_{r,\mathrm{LC3},k}\right\} &= (a^2+b^2+c^2)\sigma_{\epsilon^s_{r,k}} \end{aligned} \tag{3.45}$$

$$\begin{aligned} E\left\{\underline{\Phi}^s_{r,\mathrm{LC3},k}\right\} &= (a+b+c)g^s_{r,k} - (\tfrac{a}{k_a^2} + \tfrac{b}{k_b^2} + \tfrac{c}{k_c^2})\mathcal{I}^s_{r,0,k} + \\ &\quad \tfrac{c_0}{f_0}(\tfrac{a}{k_a}A^s_{r,a} + \tfrac{b}{k_b}A^s_{r,b} + \tfrac{c}{k_c}A^s_{r,c}) + c_0(a\delta^s_{r,a,k} + b\delta^s_{r,b,k} + c\delta^s_{r,c,k}) \\ D\left\{\underline{\Phi}^s_{r,\mathrm{LC3},k}\right\} &= (a^2+b^2+c^2)\sigma_{\varepsilon^s_{r,k}} \end{aligned} \tag{3.46}$$

An ionosphere-free combination with original range term and minimal measurement noise can now be derived by choosing:

$$\begin{cases} a+b+c & =1 \\ \frac{a}{k_a^2}+\frac{b}{k_b^2}+\frac{c}{k_c^2} & =0 \\ \min(a^2+b^2+c^2) & \end{cases} \tag{3.47}$$

Using these expressions, a can be solved as follows:

$$a=\frac{1}{2}\frac{\left(k_a^2k_b^4+k_a^2k_c^4-k_b^4k_c^2-k_b^2k_c^4\right)k_a^2}{k_a^4k_b^4+k_a^4k_c^4+k_b^4k_c^4-k_a^4k_b^2k_c^2-k_a^2k_b^4k_c^2-k_a^2k_b^2k_c^4} \tag{3.48}$$

Note that in this expression for a, k_b and k_c are interchangeable. Similar expressions can be derived for b and c by exchanging k_a and k_b or k_a and k_c, respectively. Table 3.5 shows the values of a, b, c and the noise multiplication factor for each possible combination of 3 GPS or Galileo frequencies. The table shows that the improvement with respect to the best dual frequency combinations is quite marginal. The best triple-frequency combinations have a noise multiplication factor of 2.55 for GPS and 2.51 for Galileo compared to 2.59 for the best dual-frequency combinations of both systems.

Positioning with this ionosphere-free linear combination, while possible, does not seem to offer significant benefits and as mentioned would not be rigorous due to the reduction in information content. Also the assumption of equal variance for the observables on each frequency is generally not valid, as we will see in chapter 6. However, it *does* illustrate that the simultaneous estimation of position and ionosphere delays does not become a trivial problem in multi-frequency PPP, in fact the performance might resemble dual-frequency PPP if two favorable frequencies can be chosen. A third frequency also opens the possibility to form two independent ionosphere-free combinations for PPP, which holds benefits for the reliability of the system. The redundancy can be used to detect errors in the observations. However, several fundamental problems of these linear combinations remain. Elimination of the ionosphere will still prevent the use of external ionosphere models as well as dynamic models. Also, combining multiple observables will always result in increased noise levels.

3.4.2 Positioning with original observations

The ionosphere-free combinations introduced in the previous section are not the only, and in fact not the optimal way, to perform PPP with single or multi-frequency receivers. The fixed combinations of both single frequency and dual frequency data have disadvantages. For the single frequency combination it was already mentioned that the observable contains an ambiguity parameter like the carrier phase measurements, but the variance of the noise and multipath are close to half that of the code observations, which essentially combines the worst characteristics of the original observables. For the dual frequency combination we can observe that we basically lose half of our observations only to eliminate the ionosphere delay. In the process, the resulting observables become noisier than the original observables due to the propagation of uncertainty (by a factor 3.0 in the case of GPS L1 L2). From these considerations it should become clear that the decision to form the linear combinations should not be taken lightly. In the following sections we will have a closer look at other means to deal with the ionosphere delay.

3.4.2.1 Single frequency algorithms

The single-frequency model using the original observations is introduced in section 4.3 for the code observables only, in section 4.5 for the phase observables, and a combined observation model with estimable parameters is introduced in section 4.7 for the code and phase observables.

As we will see, single frequency PPP is in many ways similar to dual frequency PPP which is treated in more detail in this dissertation. However, there are also some important differences. The first is the treatment of the ionosphere delay. Given the disadvantages of the CPC combination, elimination of the ionosphere as in eq. (3.29) is not preferable for high precision positioning, nor can the ionosphere be estimated each epoch without creating a very weak positioning model. Therefore, single frequency PPP must rely on external ionosphere models or measurements. The Klobuchar ionospheric model, parameters for which are broadcast via the GPS navigation messages, can compensate some 50% of the ionospheric delay leaving residual range errors in the order of meters. This is obviously not acceptable if we are interested in highly precise positions with at least submeter accuracy.

Both IGS and JPL also generate global ionosphere maps (GIM), containing (vertical) Total Electron Content estimates of the atmosphere in a grid over the Earth. A user can determine the ionosphere pierce point for each tracked satellite and determine the local TEC value via interpolation. This TEC value can be converted first to a slant TEC value with a mapping function, and then to the expected ionosphere delay on the tracked signal and carrier. These slant delays can then be applied as corrections to the measurements to remove (most of) the ionosphere from the observations, making submeter accuracy possible (Le, 2004; Le and Teunissen, 2006; Le and Tiberius, 2006a; van Bree and Tiberius, 2012; de Bakker et al., 2014).

Another point of attention was already raised in the discussion of the hardware delays, namely that the satellite clocks provided by PPP services pertain to the ionosphere-free linear code combination. To properly use these clocks for single frequency measurements, the appropriate differential code biases need to be applied (Kouba, 2009a).

Due to the high accuracy of GIMs, single frequency code observations after corrections from a GIM often have a higher precision than the ionosphere-free linear combination of dual frequency code measurements, but this is not true for the phase measurements. It is therefore not unexpected that single frequency PPP typically has shorter convergence time, but lower final accuracy than dual frequency PPP as shown by Keshin et al. (2006). This is an important finding, because it indicates that there is an opportunity for improvement of dual frequency PPP convergence times if GIMs are available. In general if we consider that dual frequency data contains all single frequency data and more besides, there is no reason why dual frequency PPP should perform worse than single frequency PPP, aside maybe from certain practical issues.

An optimal solution for dual frequency PPP with GIMs, should first benefit from the ionosphere model to achieve fast convergence of the estimated ionosphere and the position solution, and then benefit from the dual frequency measurements to improve the ionosphere estimates as well as the position accuracy. The following section describes how this might be achieved.

3.4.2.2 Dual frequency algorithms

The dual frequency model using the original observations is treated in great detail in sections 4.4, 4.6 and 4.8, where the observation model with estimable parameters is derived for code-only, phase-only and the combined code and phase model, and section 4.9 where external ionosphere data is introduced. Chapter 8 also focuses on implementations of these models.

As we will show, with dual frequency data instead of eliminating the ionosphere delays for each satellite, the ionosphere can also be estimated from the measurements. If no additional constraint is put on the estimation this is in fact mathematically equivalent to the elimination of the ionosphere. However, the estimation of the ionosphere offers a number of advantages:

1. While the elimination (as described in section 3.4.1.2) is performed separately for code and phase measurements, the estimation can be combined for the code and phase measurements, since the (first order) ionosphere effect is equal in size on code and phase (and opposite in sign). This effectively decreases the number of unknown parameter, strengthening the model. The combined ionosphere delay estimation for code and phase can be achieved by extending the vector of unknown parameters with one entry for the ionosphere delay per satellite. The corresponding column in the design matrix contains the dispersion factors γ as introduced in eq. (3.10).

2. On a similar note, while the ionosphere elimination is performed on an epoch-by-epoch basis, the estimation can be combined for multiple epochs, again strengthening the model. Either directly, by performing a batch solution, or by using a dynamic model for the ionosphere delay in a Kalman filter. This dynamic model should reflect the variability of the ionosphere in time.

3. The explicit estimation of the ionosphere delay also offers the opportunity of using external model values as additional (pseudo) observations. Or alternatively, the measurements can be corrected a-priori with the model values while estimating a residual ionosphere error, which than has an expectation value of zero which can be used to initialize the unknown parameter and translates into a stronger dynamic model (see chapter 6). Ideally, this should allow the dual frequency PPP algorithm to converge as fast as single frequency PPP.

4. Finally, eliminating the ionosphere has implications for ambiguity resolution, which will be treated in section 3.5. When using the original observations on the other hand and estimating the ionosphere, a unified approach to ambiguity resolution can be taken using the LAMBDA method. In this approach the algorithm itself chooses the optimal combinations for ambiguity fixing from all available ambiguities, while still allowing partial ambiguity fixing.

3.4.2.3 Multi-frequency algorithms

The advantages of using the original observations also hold for the multi-frequency case. The dual frequency model can easily be extended for additional frequencies, and the algorithms will automatically profit from the available observations. The additional frequencies also bring great benefit for integrity monitoring, which uses the redundancy in the model to detect errors in the observations such as outliers in the code observations and slips in the carrier observations. If the ionosphere is constrained, the reliability of the constraint can also be tested. Integrity monitoring will be explored in chapter 7, in which the impact of the available frequencies and observables receives careful attention.

3.5 Ambiguity resolution for PPP

As mentioned before, one of the weak points of conventional dual-frequency PPP is the considerable time for a PPP solution to converge to sub-decimeter accuracy (see table 3.3 for some typical performance figures). It is also difficult to use PPP in build up or heavily forested areas, where there are a lot of interruptions and reflections (multipath) on the signals, because the carrier phase ambiguity needs to be initialized every time after a loss of lock to the satellite signal. The convergence time of the ambiguity estimation in PPP would greatly benefit from fast integer ambiguity resolution. This applies to initialization of the receiver, acquisition of an additional satellite, and after momentary loss-of-lock to one or more satellites. Therefore, considerable effort has been spend over the last years to investigate the possibilities of AR with PPP by several GNSS groups worldwide.

Ambiguity resolution, which lies at the heart of the RTK method, aims to find or eliminate all unknown biases on the carrier phase measurements, because under these conditions, the carrier phase observations can be considered as very accurate pseudo range measurements, needed for precise positioning. In RTK a relative setup with at least two receivers is used to ensure that the ambiguities are of integer nature. In the between-receiver single differences the satellite clocks (including hardware delays) and initial phase terms at the side of the satellite are eliminated and in the between satellite differences the receiver clocks (including hardware delays) and initial phase terms at the side of the receiver are eliminated. The resulting double difference integer ambiguities can then be resolved very efficiently with e.g. the LAMBDA method developed at Delft University of Technology (Teunissen, 1994). The relative setup for RTK has the additional advantage that many error sources including the ionosphere delay, which might otherwise prohibit successful ambiguity resolution, are greatly reduced for short baselines.

In PPP no between receiver difference can be created, since we only have one receiver. This means that the satellite clocks (including hardware delays) and initial phase terms at the side of the satellite cannot be eliminated and that the ionosphere delay (and other error sources) have to be dealt with in another way. In most PPP implementations the latter is achieved by means of the ionosphere-free linear combination. However, this does not solve the problem for AR and, if implemented incorrectly, even exacerbates the problem.

This leads to the identification of three main obstacles for ambiguity resolution in conventional PPP implementations:

1. The conventional ionosphere-free linear combinations of code and phase reduce the number of observables per satellite by two, but only one unknown parameter is eliminated. If this approach is taken, a single-frequency ionosphere-free model is

obtained. However, the virtual wavelength of the ionosphere-free linear combination is very small compared to the L1 or L2 wavelengths and the combined observations are noisier by a factor three.

2. The need to simultaneously estimate (or eliminate) the ionosphere delays and the carrier phase ambiguities, leads to a very weak model, in which ambiguities cannot be solved easily.

3. The satellite clocks, hardware delays and fractional ambiguities cannot be eliminated by single differencing between receivers.

These obstacles are described in the following sections.

Virtual wavelengths The success rate of ambiguity resolution increases with increasing wavelength, which is quite intuitive if one considers that it becomes easier to distinguish between two integer values of the ambiguity if these are spread further apart by a larger wavelength. Therefore we will now consider the wavelength of the Ionosphere-Free (IF) linear combination which is the primary observable for conventional PPP implementations. Equation (3.38) showed that the ionosphere free linear combination contains the following ambiguity terms, which we will call the ionosphere-free ambiguity $\lambda_{\mathsf{IF}} A^s_{r,\mathsf{IF}}$:

$$\lambda_{\mathsf{IF}} A^s_{r,\mathsf{IF}} = \frac{c_0}{(k_a^2 - k_b^2) f_0} [k_a A^s_{r,a} - k_b A^s_{r,b}] \tag{3.49}$$

to show how the ionosphere-free combination impacts ambiguity resolution, we will now only consider the integer part of the ambiguities expressed as $\lambda_f N_f$ with λ the wavelength and N the integer ambiguity. The fractional parts of the ambiguity will be discussed in the following section. Equation (3.49) then becomes (with $\lambda_0 = c_0/f_0$):

$$\lambda_{\mathsf{IF}} N^s_{r,\mathsf{IF}} = \frac{\lambda_0}{k_a^2 - k_b^2} [k_a N^s_{r,a} - k_b N^s_{r,b}] \tag{3.50}$$

Now the term on the right hand side before the square brackets, which acts as the ionosphere-free wavelength, should be made as large as possible while maintaining the integer nature of the term between brackets. Note from table 3.2 that, next to the integer ambiguities $N^s_{r,f}$, the terms k_f are also integer, except for the Galileo E5 frequency. However, in this case we can both divide f_0 by 2 and multiply k_f by 2 to make it an integer. The wavelength can be found with the greatest common divisor (gcd) as follows:

$$\lambda_{\mathsf{IF}} N^s_{r,\mathsf{IF}} = \frac{\mathsf{gcd}(k_a, k_b)\lambda_0}{k_a^2 - k_b^2} \left[\frac{k_a N_a - k_b N_b}{\mathsf{gcd}(k_a, k_b)} \right] \tag{3.51}$$

Proof Given $N^s_{r,f} \in \mathbb{Z}$, $k_f \in \mathbb{N}$, $k_a > k_b$ and $\lambda_0 > 0$; if k_a and k_b have a common divisor $d_1 > 1$, than $\frac{d_1\lambda_0}{k_a^2-k_b^2}\left[\frac{k_a}{d_1}N_a - \frac{k_b}{d_1}N_b\right] = \frac{\lambda_0}{k_a^2-k_b^2}[k_a N^s_{r,a} - k_b N^s_{r,b}]$ with $\left[\frac{k_a}{d_1}N_a - \frac{k_b}{d_1}N_b\right] \in \mathbb{Z}$ and $\frac{d_1\lambda_0}{k_a^2-k_b^2} > \frac{\lambda_0}{k_a^2-k_b^2}$. If k_a and k_b have another common divisor $d_2 > d_1$, than $\frac{d_2\lambda_0}{k_a^2-k_b^2}\left[\frac{k_a}{d_2}N_a - \frac{k_b}{d_2}N_b\right] = \frac{\lambda_0}{k_a^2-k_b^2}[k_a N^s_{r,a} - k_b N^s_{r,b}]$ with $\left[\frac{k_a}{d_2}N_a - \frac{k_b}{d_2}N_b\right] \in \mathbb{Z}$ and $\frac{d_2\lambda_0}{k_a^2-k_b^2} > \frac{d_1\lambda_0}{k_a^2-k_b^2}$. Thus $\lambda_{\mathsf{IF}} = \frac{d_i\lambda_0}{k_a^2-k_b^2}$ is at a maximum when d_i is the greatest common divisor of k_a and k_b. Since $\frac{k_a}{\mathsf{gcd}(k_a,k_b)}$ and $\frac{k_b}{\mathsf{gcd}(k_a,k_b)}$ are coprime by definition, λ_{IF} cannot be increased beyond $\frac{\mathsf{gcd}(k_a,k_b)\lambda_0}{k_a^2-k_b^2}$.

Taking GPS L1/L2 as an example with $k_{\text{L1}} = 154$ and $k_{\text{L2}} = 120$ we find:

$$\lambda_{\text{L3}} N^s_{r,\text{L3}} = \frac{2\lambda_0}{154^2 - 120^2}\left(77N^s_{r,\text{L1}} - 60N^s_{r,\text{L2}}\right) \tag{3.52}$$

which means $\lambda_{\text{L3}} = 2\lambda_0/\left(154^2 - 120^2\right) \approx 0.63cm$. This wavelength is very short and also considering the amplified noise characteristics, it will be very difficult indeed to resolve the IF ambiguities. In fact, this gives rise to the common, but strictly speaking incorrect, assumption that the dual frequency ionosphere-free carrier phase ambiguity is by definition not of integer nature (also noted by Collins, 1999).

To investigate whether this conclusion changes when considering other (newer) GNSS frequencies, table 3.5 shows the virtual wavelength (also compared to L1) and noise multiplication factor for each dual-frequency combination of GPS and Galileo frequencies. The last column shows the wavelength divided by the observation standard deviation, in relation to the L1 frequency. The L1-only case represents a single-frequency short baseline model, in which the ionosphere can be eliminated by between receiver single differencing. The table shows that all combinations score quite poorly in the last column. Even for the most advantageous combinations, GPS L2-L5 and Galileo E5a-E6, the wavelength is more than 25 times smaller w.r.t. the noise standard deviation than for the L1 frequency. Even though several of the newer signals have higher precision than the GPS L1C/A code observations, they cannot make up for this factor of more than 25. Nevertheless, ambiguity resolution for PPP has been one of the most significant advances in the GNSS field achieved over the last years.

f_a-f_b-f_c	a	b	c	$\frac{\sigma_{\text{IF}}}{\sigma_{\text{L1}}}$	λ_{IF}	$\frac{\lambda_{\text{IF}}}{\lambda_{\text{L1}}}$	$\frac{\lambda_{\text{IF}}}{\lambda_{\text{L1}}}\frac{\sigma_{\text{L1}}}{\sigma_{\text{IF}}}$
L1-L2	2.55	1.55		2.98	0.0063	0.0331	0.0111
L1-L5	2.26	1.26		2.59	0.0028	0.0147	0.0057
L2-L5	12.26	11.26		16.64	0.1247	0.6553	0.0394
E1-E5a	2.26	1.26		2.59	0.0028	0.0147	0.0057
E1-E5b	2.42	1.42		2.81	0.0060	0.0315	0.0112
E1-E5	2.34	1.34		2.69	0.0014	0.0076	0.0028
E1-E6	2.93	1.93		3.51	0.0036	0.0190	0.0054
E5a-E5b	-18.92	-19.92		27.47	0.0419	0.2203	0.0080
E5a-E6	-5.51	-6.51		8.53	0.0611	0.3208	0.0376
E5b-E6	-8.19	-9.19		12.30	0.0172	0.0905	0.0074
E5-E6	-6.61	-7.61		10.08	0.0071	0.0375	0.0037
L1-L2-L5	2.33	-0.36	-0.97	2.55	7.56e-13	3.97e-12	1.56e-12
E1-E5-E6	2.38	-1.25	-0.13	2.69	1.81e-15	9.49e-15	3.53e-15
E1-E5a-E5b	2.31	-0.84	-0.48	2.51	7.33e-14	3.85e-13	1.54e-13
E1-E5a-E6	2.27	-1.24	-0.02	2.59	2.64e-13	1.39e-12	5.37e-13
E1-E5b-E6	2.49	-1.24	-0.25	2.79	2.24e-13	1.18e-12	4.21e-13
E5a-E5b-E6	-4.83	-1.01	6.84	8.43	6.31e-12	3.32e-11	3.93e-12

Table 3.5: Ionosphere-free virtual wavelengths and noise scale factors, the triple frequency combinations were optimized for the noise scale factor.

Wide-Lane & Narrow-Lane

Several approaches to ambiguity resolution for PPP, that circumvent these difficult ionosphere-free ambiguities, have been proposed by different authors, which we will introduce below. A number of them rely on the 'so-called' Wide-Lane (WL) and Narrow-Lane

(NL) combinations, which are known to have preferable properties for ambiguity resolution, although as we will show, the second step does not actually involve the narrow lane ambiguity. For frequencies a and b with $f_a > f_b$, the wide-lane combination contains the carrier phase measurement on f_a minus the carrier phase measurement on f_b both expressed in cycles. This is multiplied by a scale factor, chosen such that the WL combination contains the original range term g. As will be shown below, this scale factor is then the (virtual) wavelength of the wide-lane combination. The wide lane combination can be expressed as follows:

$$\underline{\Phi}^s_{r,\mathsf{WL},k} = \frac{\lambda_{\mathsf{WL}}}{\lambda_a}\underline{\Phi}^s_{r,a,k} - \frac{\lambda_{\mathsf{WL}}}{\lambda_b}\underline{\Phi}^s_{r,b,k} \tag{3.53}$$

We will again only consider the integer part of the ambiguities; with eqs. (3.32) and (3.34) this gives:

$$\begin{aligned}\underline{\Phi}^s_{r,\mathsf{WL},k} = \;& (k_a - k_b)\tfrac{\lambda_{\mathsf{WL}}}{\lambda_0}g^s_{r,k} - (\tfrac{1}{k_a} - \tfrac{1}{k_b})\tfrac{\lambda_{\mathsf{WL}}}{\lambda_0}\mathcal{I}^s_{r,0,k} + \lambda_{\mathsf{WL}}(N^s_{r,a} - N^s_{r,b}) + \\ & f_0\lambda_{\mathsf{WL}}(k_a\delta^s_{r,a,k} - k_b\delta^s_{r,b,k}) + \tfrac{\lambda_{\mathsf{WL}}}{\lambda_0}(k_a\underline{\varepsilon}^s_{r,a,k} - k_b\underline{\varepsilon}^s_{r,b,k})\end{aligned} \tag{3.54}$$

as mentioned λ_{WL} is now chosen such that the WL combination contains the original range term g, which means that:

$$\begin{aligned}\lambda_{\mathsf{WL}} &= \tfrac{\lambda_0}{k_a - k_b} \\ a &= \tfrac{k_a}{k_a - k_b} \\ b &= \tfrac{-k_b}{k_a - k_b}\end{aligned} \tag{3.55}$$

The wide-lane observation equation then becomes:

$$\begin{aligned}\underline{\Phi}^s_{r,\mathsf{WL},k} = \;& g^s_{r,k} + \tfrac{1}{k_a k_b}\mathcal{I}^s_{r,0,k} + \lambda_{\mathsf{WL}}(N^s_{r,a} - N^s_{r,b}) + \\ & \tfrac{c_0}{k_a - k_b}(k_a\delta^s_{r,a,k} - k_b\delta^s_{r,b,k}) + \tfrac{1}{k_a - k_b}(k_a\underline{\varepsilon}^s_{r,a,k} - k_b\underline{\varepsilon}^s_{r,b,k})\end{aligned} \tag{3.56}$$

For the GPS L1 and L2 frequencies the wide-lane wavelength can then be computed as $86cm \approx 4.53\lambda_{\mathsf{L1}}$ which is very large, and the very reason that the wide-lane combination is so popular for AR. The ionosphere dispersion factor for the wide-lane combination is k_a/k_b if f_a is taken as ionosphere reference frequency or about 1.28 for GPS L1/L2. This is opposite in sign to the L1 and L2 ionosphere phase delay and in between the L1 and L2 ionosphere phase delay in size. Table 3.6 provides the factors a and b for the wide-lane of all GPS and Galileo frequency combinations, as well as the noise scale factor, assuming equal and uncorrelated noise on each frequency, and the wavelength (also compared to GPS L1). The table shows that for certain combinations the wavelength but also the noise scale factor is very large indeed. To solve the wide-lane ambiguities the narrow-lane code combination can be used, because it has the same ionosphere dispersion factor as the wide-lane phase combination. The narrow-lane combination for frequencies a and b with $f_a > f_b$ is defined as the sum of the measurement on f_a and f_b when both are expressed in cycles. This is again multiplied by a scale factor, the narrow-lane wavelength, chosen such that the NL combination contains the original range term g:

$$\underline{P}^s_{r,\mathsf{NL},k} = \frac{\lambda_{\mathsf{NL}}}{\lambda_a}\underline{P}^s_{r,a,k} + \frac{\lambda_{\mathsf{NL}}}{\lambda_b}\underline{P}^s_{r,b,k} \tag{3.57}$$

	WL					NL					WL/NL
f_a-f_b	a	b	$\frac{\sigma_{\mathsf{WL}}}{\sigma_{\mathsf{L1}}}$	λ_{WL}	$\frac{\lambda_{\mathsf{WL}}}{\lambda_{\mathsf{L1}}}$	a	b	$\frac{\sigma_{\mathsf{NL}}}{\sigma_{\mathsf{L1}}}$	λ_{NL}	$\frac{\lambda_{\mathsf{NL}}}{\lambda_{\mathsf{L1}}}$	$\frac{\lambda_{\mathsf{WL}}}{\lambda_{\mathsf{L1}}}\frac{\sigma_{\mathsf{L1}}}{\sigma_{\mathsf{NL}}}$
L1-L2	4.53	-3.53	5.74	0.86	4.53	0.56	0.44	0.71	0.11	0.56	6.36
L1-L5	3.95	-2.95	4.93	0.75	3.95	0.57	0.43	0.71	0.11	0.57	5.53
L2-L5	24.00	-23.00	33.24	5.86	30.80	0.51	0.49	0.71	0.12	0.66	43.55
E1-E5a	3.95	-2.95	4.93	0.75	3.95	0.57	0.43	0.71	0.11	0.57	5.53
E1-E5b	4.28	-3.28	5.39	0.81	4.28	0.57	0.43	0.71	0.11	0.57	6.00
E1-E5	4.11	-3.11	5.15	0.78	4.11	0.57	0.43	0.71	0.11	0.57	5.75
E1-E6	5.31	-4.31	6.84	1.01	5.31	0.55	0.45	0.71	0.11	0.55	7.47
E5a-E5b	-38.33	39.33	54.92	9.77	51.33	0.49	0.51	0.71	0.13	0.66	72.59
E5a-E6	-11.50	12.50	16.99	2.93	15.40	0.48	0.52	0.71	0.12	0.64	21.76
E5b-E6	-16.86	17.86	24.56	4.19	22.00	0.49	0.51	0.71	0.12	0.63	31.10
E5-E6	-13.71	14.71	20.10	3.45	18.12	0.48	0.52	0.71	0.12	0.64	25.61

Table 3.6: Wide-lane and narrow-lane virtual wavelengths and noise scale factors.

with eqs. (3.31) and (3.33) this gives:

$$\begin{aligned} \underline{P}^s_{r,\mathsf{NL},k} = \; & (k_a + k_b)\tfrac{\lambda_{\mathsf{NL}}}{\lambda_0} g^s_{r,k} + (\tfrac{1}{k_a} + \tfrac{1}{k_b})\tfrac{\lambda_{\mathsf{NL}}}{\lambda_0}\mathcal{I}^s_{r,0,k} + \\ & f_0\lambda_{\mathsf{NL}}(k_a d^s_{r,a,k} + k_b d^s_{r,b,k}) + \tfrac{\lambda_{\mathsf{NL}}}{\lambda_0}(k_a \underline{\epsilon}^s_{r,a,k} + k_b \underline{\epsilon}^s_{r,b,k}) \end{aligned} \tag{3.58}$$

to keep the original range term g in in the NL combination, we take:

$$\begin{aligned} \lambda_{\mathsf{NL}} &= \tfrac{\lambda_0}{k_a + k_b} \\ a &= \tfrac{k_a}{k_a + k_b} \\ b &= \tfrac{k_b}{k_a + k_b} \end{aligned} \tag{3.59}$$

The narrow-lane code observation equation then becomes:

$$\underline{P}^s_{r,\mathsf{NL},k} = g^s_{r,k} + \frac{1}{k_a k_b}\mathcal{I}^s_{r,0,k} + \frac{c_0}{k_a + k_b}(k_a d^s_{r,a,k} + k_b d^s_{r,b,k}) + \frac{1}{k_a + k_b}(k_a \underline{\epsilon}^s_{r,a,k} + k_b \underline{\epsilon}^s_{r,b,k}) \tag{3.60}$$

As mentioned, the ionosphere dispersion factor for the narrow-lane code combination is identical to the wide-lane phase combination. For GPS L1 and L2 the narrow-lane wavelength is 10.7 cm. Table 3.6 shows factors a, b, the noise scale factor (again assuming equal and uncorrelated noise), and the narrow-lane wavelength for all GPS and Galileo dual-frequency combinations. Note that the differences between the narrow-lane combinations of different frequencies is much smaller than the differences between the wide-lane combinations. We can now subtract the narrow-lane code combination from the wide-lane phase combination as follows:

$$\begin{aligned} \underline{\Phi}^s_{r,\mathsf{WL},k} - \underline{P}^s_{r,\mathsf{NL},k} = \; & \lambda_{\mathsf{WL}}(N^s_{r,a} - N^s_{r,b}) + \\ & \tfrac{c_0}{k_a - k_b}(k_a \delta^s_{r,a,k} - k_b \delta^s_{r,b,k}) - \tfrac{c_0}{k_a + k_b}(k_a d^s_{r,a,k} + k_b d^s_{r,b,k}) + \\ & \tfrac{1}{k_a - k_b}(k_a \underline{\varepsilon}^s_{r,a,k} - k_b \underline{\varepsilon}^s_{r,b,k}) - \tfrac{1}{k_a + k_b}(k_a \underline{\epsilon}^s_{r,a,k} + k_b \underline{\epsilon}^s_{r,b,k}) \end{aligned} \tag{3.61}$$

This combination is known as the Melbourne-Wübbena (MW) combination and is often used to fix the wide lane ambiguities in long baseline or network solutions, and has been adopted by the PPP research community. Even with the large multiplication factor for the phase noise, the MW combination is still dominated by the code noise. The rightmost column of table 3.6 shows the wide-lane wavelength divided by the narrow-lane code noise for all GPS and Galileo dual-frequency combinations, both with respect to the GPS L1 single-frequency case. A number larger than one in this column means that the (wide-lane) ambiguity can be solved more easily than the L1 ambiguity on a short baseline. One caveat is that the GPS L1 ambiguities are generally solved with a geometry-based model, while the geometry term is eliminated in the MW combination. The attractiveness of the MW combination for ambiguity resolution is now clear: it has a large wavelength (for GPS L1/L2 $\lambda_{\mathsf{WL}} \approx 4.53\lambda_{\mathsf{L1}}$) relatively low noise $\sigma_{\mathsf{NL}} \approx 0.71\sigma_{L1}$, and is free of the combined range term and ionosphere delay. Table 3.6 also shows that some combinations, sometimes called extra wide-lane combinations, e.g. GPS L2-L5 and Galileo E5a-E5b, are even more easy to fix than most wide-lanes.

When the wide-lane ambiguity for frequencies a and b is fixed it can be added to the phase observations on f_b, thereby eliminating the A_b ambiguity and replacing it with the A_a ambiguity. This changes the effective wavelength of the ionosphere free phase combination, and leads to the following ambiguity term, from eq. (3.50):

$$\lambda_{\mathsf{IF}} N^s_{r,\mathsf{IF}} = \frac{\lambda_0}{k_a + k_b} N^s_{r,a} \tag{3.62}$$

Note that this is the same wavelength as the narrow-lane we found in eq. (3.59) $\lambda_{\mathsf{IF|WL\text{-}fixed}} = \lambda_{\mathsf{NL}}$ and it is also referred to as narrow-lane (Ge et al., 2008), but the ambiguity $N^s_{r,a}$ should *not* be confused with the narrow-lane ambiguity $N^s_{r,\mathsf{NL}} = N^s_{r,a} + N^s_{r,b}$. In fact, solving the wide-lane and narrow-lane ambiguity to integer values would *not* guarantee the original ambiguities to be integer (Teunissen, 1995). Table 3.7 shows the properties of the ionosphere-free combination for each GPS and Galileo dual-frequency case after the wide-lane ambiguity has been fixed. The rightmost column again compares the wavelength divided by the observation noise to the GPS L1 case. If we compare these results to the results in table 3.5, we notice an obvious improvement. For GPS L1/L2 the ionosphere-free wavelength is now increased by a factor 17 and for GPS L1/L5 and Galileo E1/E5a there is even an improvement of a factor 39. However, despite these improvements, ambiguity resolution for these combinations is still significantly more difficult than for the L1 single-frequency ionosphere-free case (i.e. on a short baseline). Also note that the extra wide-lane combinations, such as GPS L2/L5 and Galileo E5a/E5b, for which the wide-lanes can be solved with relative ease, now perform very poorly.

We can extend this analysis to the multi-frequency case as follows. As we saw in table 3.6, the wide-lane combination has favorable properties for ambiguity resolution for each dual-frequency combination. These combinations can obviously still be made when more frequencies are available. Therefore, we will now assume that all wide-lane ambiguities can indeed be fixed. In that case we can derive an optimal ionosphere-free combination to solve the final ambiguity. If the wide-lane ambiguities are solved, eq. (3.46) can be rewritten as:

$$\begin{aligned} E\left\{\underline{\Phi}^s_{r,\mathsf{LC3},k}\right\} &= (a+b+c)g^s_{r,k} - (\tfrac{a}{k_a^2} + \tfrac{b}{k_b^2} + \tfrac{c}{k_c^2})\mathcal{I}^s_{r,0,k} + \\ &\quad \tfrac{c_0}{f_0}(\tfrac{a}{k_a} + \tfrac{b}{k_b} + \tfrac{c}{k_c})A^s_{r,a} + c_0(a\delta^s_{r,a,k} + b\delta^s_{r,b,k} + c\delta^s_{r,c,k}) \\ D\left\{\underline{\Phi}^s_{r,\mathsf{LC3},k}\right\} &= (a^2+b^2+c^2)\sigma_{\varepsilon^s_{r,k}} \end{aligned} \tag{3.63}$$

Rather than minimizing the measurement noise, which leads to very small wavelengths as we saw in table 3.5, instead we maximize the wavelength divided by the measurement noise

f_a-f_b-f_c	a	b	c	$\frac{\sigma_{\mathrm{IF}}}{\sigma_{\mathrm{L1}}}$	$\lambda_{\mathrm{IF\|WL}}$	$\frac{\lambda_{\mathrm{IF\|WL}}}{\lambda_{\mathrm{L1}}}$	$\frac{\lambda_{\mathrm{IF\|WL}}}{\lambda_{\mathrm{L1}}} \frac{\sigma_{\mathrm{L1}}}{\sigma_{\mathrm{IF}}}$
L1-L2	2.55	-1.55		2.98	0.11	0.56	0.19
L1-L5	2.26	-1.26		2.59	0.11	0.57	0.22
L2-L5	12.26	-11.26		16.64	0.12	0.66	0.04
E1-E5a	2.26	-1.26		2.59	0.11	0.57	0.22
E1-E5b	2.42	-1.42		2.81	0.11	0.57	0.20
E1-E5	2.34	-1.34		2.69	0.11	0.57	0.21
E1-E6	2.93	-1.93		3.51	0.11	0.55	0.16
E5a-E5b	-18.92	19.92		27.47	0.13	0.66	0.02
E5a-E6	-5.51	6.51		8.53	0.12	0.64	0.08
E5b-E6	-8.19	9.19		12.30	0.12	0.63	0.05
E5-E6	-6.61	7.61		10.08	0.12	0.64	0.06
L1-L2-L5	2.32	-0.31	-1.00	2.55	0.11	0.57	0.22
E1-E5-E6	2.36	-1.30	-0.06	2.69	0.11	0.57	0.21
E1-E5a-E5b	2.31	-0.86	-0.45	2.51	0.11	0.57	0.23
E1-E5a-E6	2.24	-1.30	0.06	2.59	0.11	0.57	0.22
E1-E5b-E6	2.47	-1.28	-0.19	2.79	0.11	0.56	0.20
E5a-E5b-E6	-4.87	-0.95	6.82	8.44	0.12	0.64	0.08

Table 3.7: Wide-lane and narrow-lane virtual wavelengths and noise scale factors, the triple frequency combinations were optimized for the wave length divided by the noise scale factor (last column).

to optimize for ambiguity resolution:

$$\begin{cases} a+b+c & =1 \\ \frac{a}{k_a^2}+\frac{b}{k_b^2}+\frac{c}{k_c^2} & =0 \\ \max\left(\left(\frac{a}{k_a}+\frac{b}{k_b}+\frac{c}{k_c}\right)/\sqrt{a^2+b^2+c^2}\right) \end{cases} \tag{3.64}$$

This optimization leads to the following expression for a:

$$a = \frac{\left(k_a {k_b}^4 + k_a {k_c}^4 - {k_b}^4 k_c - k_b {k_c}^4\right) {k_a}^2}{{k_a}^4({k_b}^3 - {k_b}^2 k_c - k_b {k_c}^2 + {k_c}^3) + {k_b}^4({k_a}^3 - {k_a}^2 k_c - k_a {k_c}^2 + {k_c}^3) + {k_c}^4({k_a}^3 - {k_a}^2 k_b - k_a {k_b}^2 + {k_b}^3)} \tag{3.65}$$

Note that in this expression for a, k_b and k_c are again interchangeable, and similar expressions can be derived for b and c by exchanging k_a and k_b or k_a and k_c, respectively. Table 3.7 shows the values of a, b, c, the noise multiplication factor, the wavelength, and the wavelength divided by the noise multiplication factor compared to GPS L1, for each possible combination of 3 GPS or Galileo frequencies. Comparison to table 3.5 shows that these new linear combinations are very similar, but have much larger wavelengths. However, if we compare the triple-frequency combinations to the dual-frequency combinations we see that there is no great improvement at all. The performance of each combination is in fact very similar to the performance of the optimal subset of two frequencies out of the available three frequencies. This analysis is by no means exhaustive, or a proposed approach for practical use, but it does illustrate that the problem of ambiguity resolution for PPP is not easily solved by considering multiple frequencies.

The wide-lane, narrow-lane approach improves on the conventional ionosphere-free combination w.r.t. ambiguity resolution for PPP, and undoes the wasteful reduction of observables by two to eliminate a single unknown. Several variations on the wide-lane approach introduced above are used by Laurichesse and Mercier (2007); Collins et al. (2008); Laurichesse et al. (2009); Ge et al. (2008); Geng et al. (2009). A comparison between these models is made by Teunissen and Khodabandeh (2015), which shows that they are all equivalent models and also equivalent to the more generally applicable model introduced by de Jonge (1998). The only differences lie in the manner in which the rank defects in the model are solved (the so-called S-basis, Baarda, 1973; Teunissen, 1985; de Jonge, 1998), different parametrization (where the parameters of one model are linear combinations of the parameters of another model), and the elimination of the ionosphere. This changes the parameters which are estimated and their interpretation, but should not impact the position estimates if rigorously estimated. However, several critical remarks can still be made on the ionosphere-free, wide-lane, narrow-lane approach.

Ambiguity decorrelation

Firstly, the wide-lane combination is only one of many possible integer combinations of the carrier phase observables, each with its own (virtual) wavelength, ionosphere dispersion and noise multiplication factor, and not necessarily the optimal combination. Attractive combinations for ambiguity resolution have a large wavelength (wide-lane), a small ionosphere impact (ideally ionosphere-free) and low observation noise. Collins (1999) identifies, for the GPS L1 L2 observables, 37 independent wide-lane combinations, 73 combinations that reduce the ionosphere impact and an infinite number of (narrow-lane) combinations that reduce the noise level. With the present increase in the number of available GNSS frequencies, these numbers have increased manifold. Identifying the optimal linear combination for each set of frequencies becomes an arduous task, especially considering that it depends on the variance matrix of the observables and potential ionosphere constraints which may change over time.

Choosing the optimal combination, considering all three criteria combined, is directly related to the decorrelation step of the LAMBDA method (Teunissen, 1994, 1997b). The LAMBDA method combines the ambiguities themselves, rather than combining the observations, but with the same goal: to create linear combinations of the ambiguities which are more easily solved than the original ambiguities. Teunissen (1997b) further shows that, while the wide-lane combination does significantly decorrelate the L1-L2 ambiguities, especially for the ionosphere-float model, it is not by definition an optimal decorrelation. Depending on the stochastic properties of the observations and the treatment of the ionosphere, further decorrelation is possible. Note: ambiguity decorrelation does not improve the success rate in the case of an integer least squares approach which employs an ambiguity search; rather it improves the efficiency of the ambiguity search. However, in the case of bootstrapping and/or partial ambiguity resolution, the overall success rate, or number of ambiguities which can be solved with a given success rate, *does* increase (Teunissen, 1998c). The same holds true when using the fixed wide-lane combination, but to a lesser extend. It is with these considerations in mind that, for the work introduced in chapter 7 and continued in Teunissen and de Bakker (2013) where we consider cycle-slips as a type of ambiguity in the time-differenced model, we use the LAMBDA decorrelation rather than a fixed set of linear combinations.

A second potential weak point of the wide-lane, narrow-lane approach is that the wide-lane ambiguities are solved on a satellite-by-satellite basis by some authors, thereby neglecting to exploit the correlation between the ambiguities. While the Ambiguity Dilution of Precision

(ADOP) approximation in Teunissen and Khodabandeh (2015) suggests that the difference is small, it is still not an optimal approach. If all ambiguities are solved together the success rate will be higher.

A third disadvantage of the ionosphere-free, wide-lane, narrow-lane approach was already mentioned in section 3.4. Taking advantage of external ionosphere models, or constraining the dynamics of the ionosphere delays, becomes complicated.

Therefore, the use of the original observables, without forming or depending on certain specific linear combinations, will remain the optimal approach. The dual frequency model can easily be extended for additional frequencies, and the algorithms will automatically profit from the available frequencies and signals. The LAMBDA method for ambiguity resolution will also automatically determine the optimal ambiguities (or ambiguity combinations) to fix.

Finally, as illustrated by table 3.7, ambiguity resolution in an ionosphere-float model (i.e. the ionosphere-delay is not constrained) remains difficult, even if the estimation itself is rigorous. We will again encounter this for the time-differenced model in chapter 7, where we will also see that this problem is not solved by considering additional GNSS frequencies. There always remains one combination of ambiguities which is very difficult to solve, and as long as this is not solved, the carrier phase observations do *not* act as very precise pseudo range observations, in fact the improvement might be marginal (Odijk et al., 2014). The solution to this problem must come from constraining the ionosphere. In the time-differenced model this constraint follows from the smooth behavior of the ionosphere over time, which greatly benefits cycle-slip detection. In the positioning model however, this constraint currently still follows from the spatial correlation of the ionosphere and is thus related to the baseline lengths. Global ionosphere models are not yet as accurate as one might wish for fast ambiguity resolution.

Fractional ambiguities and uncalibrated hardware delays The carrier phase ambiguity as introduced in eq. (3.4) is not integer, because it includes initial phase terms at the receiver and satellite:

$$A^s_{r,f} = \lambda \left(N^s_{r,f} + \varphi^s_{f,0} - \varphi_{r,f,0} \right) \tag{3.66}$$

where $N^s_{r,f}$ is an integer number of cycles, and $\varphi^s_{f,0}$ and $\varphi_{r,f,0}$ are the initial phase at the satellite and receiver in cycles. In RTK, double differencing eliminates the initial phase terms together with the receiver and satellite phase clocks, thereby making ambiguity resolution possible. For a stand alone receiver as is used in PPP, the fractional part at the side of the satellites cannot be eliminated (standard products from IGS and other service providers estimate carrier phase clocks for the ionosphere free linear combination, which are biased by an ionosphere free SD ambiguity, and then line these up with code observations destroying the intrinsic integer properties). Therefore, ambiguity resolution for PPP should take a different approach.

The fractional ambiguities at the side of the user can still be eliminated by a between satellite single difference. In Banville et al. (2008) a different approach to the receiver phase delays is proposed, namely to estimate (or actually calibrate) them a-priori from a test set-up with a GPS signal simulator. However, test result show that separating the receiver clock from the ambiguities is difficult and the differential delays are not constant between reinitialization of the receiver. Banville et al. (2008) state that between-satellite single differencing is still the best approach to eliminate receiver phase biases. This is in line with earlier results that show that the hardware delays of user receivers are generally *not* constant, but will vary with a.o. temperature (Liu et al., 2004).

The fractional ambiguities at the side of the satellite should be treated in a different way. A network of reference stations can be used to generate corrections for the user that can be used to eliminate these single difference satellite fractional ambiguities. Due to the rank defect in the PPP model, the fractional ambiguities cannot be estimated directly, but estimable parameters can be defined, which when used as corrections achieve the same goal (Teunissen and Khodabandeh, 2015). Estimates of these parameters are transmitted to a PPP user together with any other corrections. The PPP user could then use these as corrections on the measurements between satellite single differences to create integer ambiguities. Note that this approach in fact leads to double differenced ambiguities, the second difference being between the PPP user and the reference network (Teunissen and Khodabandeh, 2015).

3.6 Conclusions and outlook

We conclude with a summary of some of the more important findings in this chapter, which guide the further research presented in this thesis. To combine the best characteristics of single frequency and dual frequency PPP, an optimal PPP algorithm should both use external atmosphere models if available *and* estimate, not eliminate, (residual) atmosphere delay parameters on the measurements. For the estimated residual parameters dynamic models can be used to benefit from the limited variability of the atmospheric delays in time (e.g. the generally smooth behavior of the atmospheric delays). For these reasons, the original observables should be used for PPP, instead of any linear combinations. This also provides greater flexibility for including additional frequencies and to benefit from the (expected) GNSS evolutions.

The current lack of integrity information for PPP should be solved by improving the stochastic model for PPP and rigorously applying propagation of uncertainty and hypotheses testing. Finally, the possibilities and opportunities of ambiguity resolution for PPP should be studied.

Single and Dual-Frequency PPP Models

4

4.1 Systems of equations

Not all unknown parameters that appeared in the observation equations of chapter 3 are estimable, due to rank deficiencies in the design matrix. S-system theory can be applied to obtain an estimation model of full rank and a correct interpretation of the estimable parameters (Baarda, 1973; Teunissen, 1985; de Jonge, 1998). For Precise Point Positioning, this problem appears both at the network side and at the user side. In this chapter we will take a closer look into which parameters are estimable and which are not at the user side; any rank deficiencies at the network side are considered solved. However, some remarks are included that explain the consequences of choices made to solve the rank deficiencies at the network side.

For the analysis of the rank deficiencies, we will use subsets of the observation model which include the relevant parameters for the rank deficiency under investigation, but exclude as many other parameters as possible. Also it will be investigated which unknowns can already be estimated from carrier phase measurements only and can thus be expected to have a high accuracy, and which unknowns can only be estimated from the less precise code measurements.

During the following derivations, we will come across the models that represent each of the previously introduced single and dual-frequency approaches to PPP considering the primary observations (i.e. single frequency ionosphere-free, dual frequency ionosphere-free, single frequency original observations, and dual frequency original observations). We will setup linearized models of the form $\Delta\mathbf{y} = \mathbf{A}\Delta\mathbf{x} + \boldsymbol{\epsilon}$, where $\Delta\mathbf{y}$ contains the OMC observations, $\mathbf{A}$ is the design matrix, $\Delta\mathbf{x}$ are the adjustments to the approximate values of the unknowns, and $\boldsymbol{\epsilon}$ contains the measurement noise. In general a matrix is rank defect if the columns and/or rows of the matrix are not linearly independent. If design matrix $\mathbf{A}$ has a rank deficiency in the rows (i.e. the number of rows is larger than the rank of the matrix), the system is over determined, which generally is not undesirable. However, if design matrix $\mathbf{A}$ has a rank deficiency in the columns, the system is under determined and the solution of the unknown parameters will not be unique. Therefore, we will inspect the design matrices for (column)rank deficiencies, which can be found with the following expression:

$$\mathbf{A}\mathbf{v} = \mathbf{0} \;\; \exists \;\; \mathbf{v} \neq \mathbf{0} \tag{4.1}$$

That is if a vector $\mathbf{v} \neq \mathbf{0}$ exists that satisfies $\mathbf{A}\mathbf{v} = \mathbf{0}$, matrix $\mathbf{A}$ is (column)rank defect. Any existing rank deficiencies found in this way can be solved by a reparameterization of the unknown parameters, as is done below, or by regularization of some or all of the unknowns, as will be treated later. In the following we will consider a single epoch of data whenever possible, but some rank deficiencies can only be studied by including multiple epochs. In this case another important aspect with regards to the rank deficiencies is the treatment of the unknown parameters for different epochs. The unknowns can either be estimated each epoch (temporal parameters), held constant over time (global parameters), or given a dynamic model (constrained parameters). Dynamic models will be treated later; for now we will only consider global and temporal parameters.

4.2 Instrumental delays and multi-GNSS Precise Point Positioning

In chapter 3 the PPP observation equations were derived as eqs. (3.23) and (3.24):

$$\Delta\underline{\overline{P}}^{s}_{r,f,k} = -\mathbf{e}^{s*}_{r,k}\Delta\mathbf{r}_{r,k} + c_0\delta t_{r,k} + m^{s}_{w,r,k}T_{zw,r,k} + \gamma_f\mathcal{I}^{s}_{r,i,k} + c_0 d^{s}_{r,f,k} + \underline{\epsilon}^{s}_{r,f} \tag{4.2}$$

$$\Delta\underline{\overline{\Phi}}^{s}_{r,f,k} = -\mathbf{e}^{s*}_{r,k}\Delta\mathbf{r}_{r,k} + c_0\delta t_{r,k} + m^{s}_{w,r,k}T_{zw,r,k} - \gamma_f\mathcal{I}^{s}_{r,i,k} + \lambda_f A^{s}_{r,f} + c_0\delta^{s}_{r,f,k} + \underline{\varepsilon}^{s}_{r,f} \tag{4.3}$$

We will now split the residual LOS delays, $d^{s}_{r,f,k}$ and $\delta^{s}_{r,f,k}$, in four parts:

1. LOS delays which we correct for using accurate models including relativistic effects, carrier phase-wind up, antenna phase center offsets and phase center variations.

2. LOS delays which we do not correct, but account for in the stochastic model including multipath (and higher order ionosphere terms, if we do not correct for these).

3. Instrumental delays at the side of the satellite, d^{s}_{f} and δ^{s}_{f}, which are assumed equal for all receivers, but different for each observable and satellite.

4. Instrumental delays at the side of the receiver, $d_{r,f}$ and $\delta_{r,f}$, which are assumed to be equal for all tracked satellites, but different for each observable and receiver.

The last two groups of instrumental delays form an important subject of this chapter. As we will see, they cannot be determined in an absolute sense, but certain differential terms are estimable. Depending on their context, these delays may have different names. E.g. in the GPS broadcast navigation message the differential term between observables P1 and P2 is called the group delay differential; the differential terms between P1 and L1C/A and between P2 and L2C are called inter-signal corrections. In the context of the precise products from the IGS, instrumental delays on the code measurements are called differential code biases (DCB), while similar hardware delays on the carrier phase observables, of particular interest for ambiguity resolution, are sometimes called differential phase biases (DPB) or uncalibrated (phase) hardware biases. Inter-system biases (ISB), which occur when signals from different GNSS are tracked (on the same frequency), can also be considered as a special case of these instrumental delays. If a receiver tracks satellites s and q from two different GNSS A and B, then $d_{r,f}$ and $\delta_{r,f}$ are not the same for these observables:

$$
\begin{aligned}
\Delta\underline{\overline{P}}^s_{r,f,k} = & -\mathbf{e}^{s*}_{r,k}\Delta\mathbf{r}_{r,k} + c_0\delta t_{r,k} + m^s_{w,r,k}T_{zw,r,k} + \gamma_f\mathcal{I}^s_{r,i,k} + c_0\ d_{r,f,k}|_A + c_0 d^s_{f,k} + \underline{\epsilon}^s_{r,f} \\
\Delta\underline{\overline{P}}^q_{r,f,k} = & -\mathbf{e}^{s*}_{r,k}\Delta\mathbf{r}_{r,k} + c_0\delta t_{r,k} + m^q_{w,r,k}T_{zw,r,k} + \gamma_f\mathcal{I}^q_{r,i,k} + c_0\ d_{r,f,k}|_B + c_0 d^q_{f,k} + \underline{\epsilon}^q_{r,f} \\
\Delta\underline{\overline{\Phi}}^s_{r,f,k} = & -\mathbf{e}^{s*}_{r,k}\Delta\mathbf{r}_{r,k} + c_0\delta t_{r,k} + m^s_{w,r,k}T_{zw,r,k} - \gamma_f\mathcal{I}^s_{r,i,k} + \lambda_f A^s_{r,f} + c_0\ \delta_{r,f,k}|_A + \\
& c_0\delta^s_{f,k} + \underline{\varepsilon}^s_{r,f} \\
\Delta\underline{\overline{\Phi}}^q_{r,f,k} = & -\mathbf{e}^{s*}_{r,k}\Delta\mathbf{r}_{r,k} + c_0\delta t_{r,k} + m^q_{w,r,k}T_{zw,r,k} - \gamma_f\mathcal{I}^q_{r,i,k} + \lambda_f A^q_{r,f} + c_0\ \delta_{r,f,k}|_B + \\
& c_0\delta^q_{f,k} + \underline{\varepsilon}^q_{r,f}
\end{aligned}
\tag{4.4}
$$

Remember that the inter-system time-offset was already treated in section 3.1, and is here considered absent ($\delta t_{r,k}|_A = \delta t_{r,k}|_B = \delta t_{r,k}$). If we rewrite the receiver instrumental delays for GNSS B as $d_{r,f,k}|_B = d_{r,f,k}|_A + d_{r,f,k}|_{AB}$ and $\delta_{r,f,k}|_B = \delta_{r,f,k}|_A + \delta_{r,f,k}|_{AB}$, we have introduced the ISB for code $d_{r,f,k}|_{AB}$ and phase $\delta_{r,f,k}|_{AB}$. Note that a very similar case exists when two different signals are tracked from the same GNSS and on the same frequency, e.g. L2P and L2C. With respect to inter-systems biases there are four different cases to consider (Odijk and Teunissen, 2013a,b; Teunissen, 2014):

1. All satellites are from a single GNSS. This is a trivial case in which no ISB occur.

2. All receivers, both in the network and at the user side, are of the same make and model including the firmware version. In this case ISB are present, but equal for all receivers and can be ignored since they are eliminated in the positioning algorithms, either directly, when observations are differenced for baseline processing, or via the precise clock and bias corrections, in the case of PPP.

3. Inter-system biases are estimated, or separate receiver clock offsets are estimated by the rover receiver. In this case the model will be weaker than if the same number of satellites is tracked from a single GNSS. Also, if for a specific GNSS, only a single satellite is tracked, it will not contribute to the position solution.

4. Inter-system biases are corrected by means of a look-up table of previously estimated values. This option is viable because the ISBs are very stable in time and can indeed be calibrated in this manner.

In the following we will only consider one instrumental code delay and one phase delay on each frequency at the side of the receiver. This covers the case where only a single GNSS is tracked, the case where a single type of receiver is used in both the network and by the user to track any number of GNSS, and the case where different types of receivers are used to track any number of GNSS, but all inter-system biases are known and can be corrected.

4.3 Single frequency code-only

We will start with the simplest positioning model of all, the single frequency code-only positioning model. Equation (4.5) combines eq. (3.23) for m satellites but only one epoch of single frequency data. The satellite positions and clocks have been subtracted from the observations as in eq. (3.21), and for the residual LOS delays it is assumed that the satellite hardware delays are removed together with the satellite clocks (as explained later this is a fair assumption), the receiver hardware delays are still included in eq. (4.5).

$$E\left\{\left[\begin{array}{c} \Delta \boldsymbol{P}^S_{r,f,k} \end{array}\right]\right\} = \left[\begin{array}{ccccc} -\mathbf{e}^{S*}_{r,k} & c\mathbf{u}_m & c\mathbf{u}_m & \mathbf{m}^S_{r,k} & \gamma_f \mathbf{I}_m \end{array}\right] \left[\begin{array}{c} \Delta \mathbf{r}_{r,k} \\ \delta t_{r,k} \\ d_{r,f,k} \\ T_{Z,r,k} \\ \boldsymbol{\mathcal{I}}^S_{r,1,k} \end{array}\right] \tag{4.5}$$

where bold symbols are used for vector or matrix notation, capitol S in superscript indicates a vector with one row per tracked satellite, $\mathbf{u}_m$ is an $m \times 1$ vector with ones, and $\mathbf{I}_m$ is an $m \times m$ unit matrix.

From eq. (4.5) several things can be deduced:

1. From single frequency code-only observations the ionosphere cannot be estimated since there is one unknown ionosphere delay per observation. Therefore, a single frequency user will have to rely on an external ionosphere model to correct the observations for the ionosphere delay.

2. The model contains a rank deficiency between the receiver clock offset and the receiver hardware delay. This is solved by combining these two unknowns into a single observable-specific clock: $dt_{r,f,k} = \delta t_{r,k} + d_{r,f,k}$. In general we can say, that estimated clocks in GNSS positioning never represent the common or 'true' clock offset, but rather clocks that pertain to a specific observable and include the hardware delays corresponding to that observable. Therefore, we will use these observable specific clock offsets in the following analyses rather than the 'true' clock offset.

3. The columns in the design matrix that contain the unit vectors from the receiver to the satellite have different entries for each satellite, and as a result no rank deficiencies exist between these columns and any other columns of the design matrix if enough satellites are tracked. The same goes for the columns pertaining to the troposphere zenith delay, which entries contain the mapping function evaluated for each satellite, and in this regard, the estimation of a zenith troposphere delay can be seen as the estimation of a fourth receiver coordinate. This result does not change when more epochs of data are considered, since the satellite (and possibly receiver) positions change, thereby changing the unit vectors and troposphere mapping parameters. Therefore, we can neglect the columns containing the unit vectors and mapping parameters in the following analyses of the rank deficiencies. So, in order to keep the models as concise as possible, we will assume that the troposphere is corrected a priori (i.e. it no longer appears in the functional model), and, if multiple epochs are considered, that the user position is static.

Equation (4.5) now further simplifies to the well known single point positioning model with the receiver coordinates and receiver clock offset as the only unknowns:

$$E\left\{\left[\begin{array}{c} \Delta \boldsymbol{P}^S_{r,f,k} \end{array}\right]\right\} = \left[\begin{array}{cc} -\mathbf{e}^{S*}_{r,k} & c\mathbf{u}_m \end{array}\right] \left[\begin{array}{c} \Delta \mathbf{r}_{r,k} \\ \delta t_{r,f,k} \end{array}\right] \tag{4.6}$$

The minimal required number of satellites and the redundancy depend on the user dynamics (static or kinematic) and on the choice whether the zenith troposphere delay is estimated. Appendix D contains redundancy tables for each of the models discussed in this chapter.

4.4 Dual frequency code-only

Dual frequency observations *can* be used to estimate (or eliminate) the ionosphere delay, and in fact this is the main reason why GNSS provide ranging signals on multiple frequencies. Therefore, the ionosphere is again included in the functional model. Also, using multiple observables means that there is a separate clock per observable at both the receiver and the satellites. In the following model these separate satellite and receiver clocks are included in the vector of unknown parameters to show their impact on the rank deficiencies.

$$E\left\{\begin{bmatrix} \Delta\mathbf{P}^S_{r,P1,k} \\ \Delta\mathbf{P}^S_{r,P2,k} \end{bmatrix}\right\} = \begin{bmatrix} -\mathbf{e}^{S*}_{r,k} & c\mathbf{u}_m & & \mathbf{I}_m & -c\mathbf{I}_m & \\ -\mathbf{e}^{S*}_{r,k} & & c\mathbf{u}_m & \gamma\mathbf{I}_m & & -c\mathbf{I}_m \end{bmatrix} \begin{bmatrix} \Delta\mathbf{r}_{r,k} \\ dt_{r,P1,k} \\ dt_{r,P2,k} \\ \boldsymbol{\mathcal{I}}^S_{r,k} \\ \boldsymbol{dt}^S_{P1,k} \\ \boldsymbol{dt}^S_{P2,k} \end{bmatrix} \tag{4.7}$$

In eq. (4.7) and following analyses, all entries in the design matrix which have been left empty are actually filled with zeros. From a single receiver with an unknown position and and clock offset (as is generally the case in PPP positioning) the satellite clock offsets cannot be estimated, so they must be provided by a network or reference receiver. In network or baseline processing the satellite clock offsets might indeed be provided per observable, but in classical SPP or PPP this is not the case. In these processing techniques two linear combinations of the clocks are introduced: the ionosphere-free combination and the ionosphere combination:

$$\begin{aligned} \boldsymbol{dt}^S_{P3,k} &= +\tfrac{\gamma}{\gamma-1}\boldsymbol{dt}^S_{P1,k} - \tfrac{1}{\gamma-1}\boldsymbol{dt}^S_{P2,k} \\ \boldsymbol{dt}^S_{PI,k} &= -\tfrac{1}{\gamma-1}\boldsymbol{dt}^S_{P1,k} + \tfrac{1}{\gamma-1}\boldsymbol{dt}^S_{P2,k} \quad = \quad \tfrac{1}{\gamma-1}\boldsymbol{d}^S_{P1P2,k} \end{aligned} \tag{4.8}$$

The 'ionosphere-free clock' $dt^s_{P3,k}$ is then indeed provided to the user via the broadcast messages or the precise products intended for PPP and can be subtracted from the observations following eq. (3.21). The ionosphere linear combination $dt^s_{PI,k}$ reduces to a satellite differential hardware delay $d^s_{P1P2,k}$ also called differential code bias (DCB), as shown. In eq. (4.7) this DCB can now be lumped with the ionosphere delays. If the user is not interested in the absolute ionosphere estimate and no constraint is put on the absolute ionosphere delay in the estimation, the DCB can simply be ignored since it only biases the ionosphere estimate as follows:

$$\bar{\boldsymbol{\mathcal{I}}}^S_{r,k} = \boldsymbol{\mathcal{I}}^S_{r,k} - \tfrac{c}{\gamma-1}\boldsymbol{d}^S_{P1P2,k} \tag{4.9}$$

If the user *is* interested in the absolute ionosphere delay, or if the ionosphere estimation is constrained by e.g. an external ionosphere model, then the observations should be corrected for the satellite DCB. In the case of single frequency code observations described above, a user would also need the DCB to derive the observation specific satellite clock from the ionosphere-free satellite clock. For this reason the DCB is indeed provided together with the satellite clock offset both for the broadcast ephemerides and for the precise ephemerides (satisfying our earlier assumption in section 4.3). An advantage of providing the ionosphere-free clock together with the satellite DCB over providing the satellite clocks for both signals individually, lies in the fact that the DCB is much more stable over time than the satellite clocks themselves, which greatly reduces the necessary update rate for this correction and thereby reduces the amount of data that needs to be provided to the user. In any case, whether the observations are corrected for the DCB or not, the dual frequency code-only positioning model no longer contains unknown satellite clock parameters and simplifies to:

$$E\left\{\begin{bmatrix} \Delta \boldsymbol{P}^S_{r,P1,k} \\ \Delta \boldsymbol{P}^S_{r,P2,k} \end{bmatrix}\right\} = \begin{bmatrix} -\mathbf{e}^{S*}_{r,k} & c\mathbf{u}_m & & \mathbf{I}_m \\ -\mathbf{e}^{S*}_{r,k} & & c\mathbf{u}_m & \gamma\mathbf{I}_m \end{bmatrix} \begin{bmatrix} \Delta\mathbf{r}_{r,k} \\ dt_{r,P1,k} \\ dt_{r,P2,k} \\ \boldsymbol{\mathcal{I}}^S_{r,k} \end{bmatrix} \tag{4.10}$$

This model still contains a rank deficiency between the receiver clock offsets and ionosphere delays. An elegant way to solve this rank deficiency is to introduce the ionosphere-free linear combination and the ionosphere linear combination of the receiver clock offsets as well:

$$\begin{array}{lclcl} dt_{r,P3,k} & = & +\frac{\gamma}{\gamma-1}dt_{r,P1,k} - \frac{1}{\gamma-1}dt_{r,P2,k} & & \\ dt_{r,PI,k} & = & -\frac{1}{\gamma-1}dt_{r,P1,k} + \frac{1}{\gamma-1}dt_{r,P2,k} & = & \frac{1}{\gamma-1}d_{r,P1P2,k} \end{array} \tag{4.11}$$

The ionosphere-free clock is then estimated together with the receiver coordinates, while the ionosphere linear combination again reduces to a differential code bias but now for the receiver. If no additional constraints are put on the ionosphere delay or the DCB estimate, these two unknowns cannot be separated and are simply lumped in the estimation process as follows:

$$\bar{\boldsymbol{\mathcal{I}}}^S_{r,k} = \boldsymbol{\mathcal{I}}^S_{r,k} + \frac{c}{\gamma-1}d_{r,P1P2,k} \tag{4.12}$$

For a GNSS user who is not interested in the absolute ionosphere estimates this approach suffices, since the DCB will only bias the ionosphere estimates. The dual frequency code-only model then simplifies to:

$$E\left\{\begin{bmatrix} \Delta \boldsymbol{P}^S_{r,P1,k} \\ \Delta \boldsymbol{P}^S_{r,P2,k} \end{bmatrix}\right\} = \begin{bmatrix} -\mathbf{e}^{S*}_{r,k} & c\mathbf{u}_m & \mathbf{I}_m \\ -\mathbf{e}^{S*}_{r,k} & c\mathbf{u}_m & \gamma\mathbf{I}_m \end{bmatrix} \begin{bmatrix} \Delta\mathbf{r}_{r,k} \\ dt_{r,P3,k} \\ \bar{\boldsymbol{\mathcal{I}}}^S_{r,k} \end{bmatrix} \tag{4.13}$$

If, on the other hand, a user *is* interested in the absolute ionosphere delay, and wants to constrain the receiver DCB or ionosphere estimates these unknown parameters should not be lumped and the receiver DCB should be estimated as a separate unknown. Estimating one receiver clock and a receiver DCB can still provide some advantage over the estimation of two separate receiver clocks since the DCB is more stable over time than a receiver clock parameter and, consequently, the DCB estimation can be constrained with a more strict dynamic model. In this case the dual frequency code-only model follows as:

$$E\left\{\begin{bmatrix} \Delta \boldsymbol{P}^S_{r,P1,k} \\ \Delta \boldsymbol{P}^S_{r,P2,k} \end{bmatrix}\right\} = \begin{bmatrix} -\mathbf{e}^{S*}_{r,k} & c\mathbf{u}_m & c\mathbf{u}_m & \mathbf{I}_m \\ -\mathbf{e}^{S*}_{r,k} & c\mathbf{u}_m & \gamma c\mathbf{u}_m & \gamma\mathbf{I}_m \end{bmatrix} \begin{bmatrix} \Delta\mathbf{r}_{r,k} \\ dt_{r,P3,k} \\ \frac{1}{\gamma-1}d_{r,P1P2,k} \\ \boldsymbol{\mathcal{I}}^S_{r,k} \end{bmatrix} \tag{4.14}$$

N.B. The model presented in eq. (4.14) is only valid if some additional constraint on the ionosphere delay or DCB is used (since it is rank deficient otherwise). Such a constraint may e.g. come from a dynamic model that also assumes some knowledge on the expectation of the absolute value of the ionospheric delay or DCB. One way to constrain the ionosphere delay that is used in this dissertation is to correct the observations a priori with an external ionosphere model and estimate only a residual ionosphere delay (i.e. the error of the external model is estimated). For this estimate of the residual ionosphere we can assume an expectation of zero with some uncertainty depending on the accuracy of the model. After all, if the expectation of the error in the external ionosphere model would be unequal to zero (without any other knowledge of the specific measurement conditions) the model should be corrected with this expectation. The zero mean expectation for the ionosphere residual solves the rank deficiency in eq. (4.14). It is important to note that constraining the ionosphere in this way, not only impacts the ionosphere estimation itself, but strengthens the entire model thereby also impacting the estimation of the other unknown parameters. The use of an external ionosphere model is expanded on more later in this chapter for the single frequency code & phase models.

4.5 Single frequency phase-only

Phase-only processing is similar to code-only processing in many ways, however there are also some differences. The main difference lies in the fact that the carrier phase measurements are biased by constant but unknown ambiguities. Therefore, these ambiguities need to be estimated together with the other unknown parameters. Equation (4.15) combines eq. (3.24) for m satellites, where the satellite positions have been subtracted from the observations conform eq. (3.22), but not yet the satellite clock offsets to show the impact of the satellite hardware delays on the phase-only model. Similar to the single frequency code-only model, the ionosphere delays cannot be estimated from the single frequency phase-only model either. Therefore, we will assume that the observations are corrected a priori by means of an external ionosphere model. This leads to the following single epoch phase-only positioning model:

$$E\left\{\left[\ \Delta\boldsymbol{\phi}^S_{r,f,k}\ \right]\right\} \;=\; \left[\ -\mathbf{e}^{S*}_{r,1} \quad c\mathbf{u}_m \quad \lambda_f\mathbf{I}_m \quad -c\mathbf{I}_m\ \right]\begin{bmatrix}\Delta\mathbf{r}_{r,1}\\ \delta t_{r,f,k}\\ \mathbf{A}^S_{r,f}\\ \boldsymbol{\delta t}^S_{f,k}\end{bmatrix} \tag{4.15}$$

As mentioned before, the satellite clocks (in this case $\delta t^s_{f,k}$) cannot be estimated from a single receiver with unknown position and clock offset, so they must be provided to the user. In a baseline or network processing setup, these clock products might indeed be provided to the user, but for classical SPP or PPP this clock product is not provided. Only a single clock offset per satellite is provided and, to ensure that the pseudo range code observations are unbiased, they lined up with the code clocks (i.e. they include the satellite code hardware delay). In particular the ionosphere-free code clock $dt^s_{P3,k}$ is provided as shown in section 4.4. The difference between these two clocks reduces to a differential code-phase bias (DCPB) as follows:

$$\boldsymbol{\delta t}^S_{f,k} - \boldsymbol{dt}^S_{P3,k} \;=\; \boldsymbol{\delta}^S_{P3Lf,k} \;=\; \boldsymbol{\delta}^S_{f,k} - \tfrac{\gamma}{\gamma-1}\boldsymbol{d}^S_{P1,k} + \tfrac{1}{\gamma-1}\boldsymbol{d}^S_{P2,k} \tag{4.16}$$

Since this DCPB is generally *not* provided to an SPP or PPP user, it cannot be removed from the functional model. And, because it cannot be estimated separately from the ambiguities, these parameters are lumped as follows:

$$\bar{\mathbf{A}}^S_{r,f} \;=\; \mathbf{A}^S_{r,f} - \tfrac{c}{\lambda_f}\boldsymbol{\delta}^S_{P3Lf,k} \tag{4.17}$$

Equation (4.17) reveals why ambiguity resolution is not possible for this observation model. The estimated ambiguity parameters are biased by the differential hardware delays at the side of the satellite, thereby negating their integer nature. For ambiguity resolution to be possible the DCPB should be made available to the user, or the satellite phase clock should be provided directly. This subject is further expanded upon in section 4.8 when the dual-frequency code & phase model is treated and in section 3.5 where current approaches to PPP ambiguity resolution are discussed.

An additional risk of lumping the ambiguity parameters with the hardware delays as in eq. (4.17) is that it could also negate the constant nature of the estimated ambiguity parameters since the differential hardware delays, although very stable, are not completely constant. To prevent this last problem from occurring a slightly more complex method to compute the precise clock offsets can be performed. By computing both the ionosphere-free code and phase clock offsets, a PPP service provider can provide a user with the satellite clock offsets estimated from the phase measurements but aligned with the code measurements. This is achieved by adding the mean difference over the computation period (e.g. one day) between both clock estimates to the phase clock before providing this combination to the user. The result is that the user ends up with a clock product that is unbiased with respect to the pseudo range observations while having a constant time offset with respect to the phase measurements. A disadvantage of this method is that the differences in the time behavior between the code and phase clocks are then introduced as an additional error term in the OMC code observations. Given the relatively low precision of the code observations this is assumed not to be critical as the code observations are still dominated by the measurement noise and multipath. However, the more important problem of the lost integer nature of the ambiguities is not resolved.

The single frequency phase-only model now simplifies to:

$$E\left\{\left[\ \Delta\boldsymbol{\phi}^S_{r,f,k}\ \right]\right\} \;=\; \left[\ -\mathbf{e}^{S*}_{r,k} \quad c\mathbf{u}_m \quad \lambda_f\mathbf{I}_m\ \right]\left[\begin{array}{c}\Delta\mathbf{r}_{r,k}\\ \delta t_{r,f,k}\\ \bar{\mathbf{A}}^S_{r,f}\end{array}\right] \tag{4.18}$$

Equation (4.18) still contains a rank deficiency between the receiver clock and the ambiguities, see eq. (4.1) with $\mathbf{v}^* = \left[\ \mathbf{0}^*_3 \quad \lambda_f \quad -c\mathbf{u}^*_m\ \right]$. This rank deficiency is solved with another reparameterization of the unknowns. The ambiguity of the first (or a reference) satellite is added to the receiver clock offset and subtracted from all other ambiguities: $\overline{\delta t}_{r,f,k} = \delta t_{r,f,k} + \frac{\lambda_f}{c}A^1_{r,f}$.

$$E\left\{\left[\ \Delta\phi^S_{r,f,k}\ \right]\right\} \;=\; \left[\ -\mathbf{e}^{S*}_{r,k} \quad c\mathbf{u}_m \quad \lambda_f\overset{0\cdots0}{\mathbf{I}_{m-1}}\ \right]\left[\begin{array}{c}\Delta\mathbf{r}_{r,k}\\ \overline{\delta t}_{r,f,k}\\ \bar{\mathbf{A}}^{1S}_{r,f}\end{array}\right] \tag{4.19}$$

where $\overset{0\cdots0}{\mathbf{I}_{m-1}} = [\mathbf{0}_{m-1}, \mathbf{I}_{m-1}]^*$. It is clear that the user coordinates cannot be estimated from a single epoch of phase-only data, because there are as many unknown ambiguity and clock terms as there are observations. Therefore, we will consider at least two epochs of data in the following model. For now we will not consider any dynamic models for the time varying unknown parameters, and in that case the described rank defects are repeated at each epoch. For this reason, the reparameterization is also applied at each epoch leading to the following multi-epoch single-frequency phase-only model:

$$E\left\{\begin{bmatrix} \Delta\boldsymbol{\phi}^S_{r,f,1} \\ \Delta\boldsymbol{\phi}^S_{r,f,2} \\ \vdots \end{bmatrix}\right\} = \begin{bmatrix} -\mathbf{e}^{S*}_{r,1} & c\mathbf{u}_m & & & \lambda_f \overset{0\cdots 0}{\mathbf{I}_{m-1}} \\ -\mathbf{e}^{S*}_{r,2} & & c\mathbf{u}_m & & \lambda_f \overset{0\cdots 0}{\mathbf{I}_{m-1}} \\ \vdots & & & \ddots & \vdots \end{bmatrix} \begin{bmatrix} \Delta\mathbf{r}_r \\ \overline{\delta t}_{r,f,1} \\ \overline{\delta t}_{r,f,2} \\ \vdots \\ \bar{\mathbf{A}}^{1S}_{r,f} \end{bmatrix} \tag{4.20}$$

where vertical and diagonal dots have been used to indicate that similar entries would continue if more epochs of data would have been included. All unknown parameters in eq. (4.20) can now be estimated from the measurements and no additional rank defects are present as long as there are enough satellites and measurement epochs (see table D.3 for the redundancy). Equation (4.20), which was setup for single frequency phase only processing without ionosphere delays, also closely resembles the positioning model based on the code-plus-carrier combination (introduced in section 3.4.1.1) used as primary observable, since the CPC observable eliminates the ionosphere delay and contains an ambiguity just like a carrier phase observable.

4.6 Dual frequency phase-only

Just as in the dual frequency code-only case, a big advantage of the second frequency is that the ionosphere can be estimated from the data. So the ionosphere delays are added to the model as unknown parameters. Also, the clock offsets for both frequencies are included to analyze their impact on the estimated parameters. This gives the following model for a single epoch of data:

$$E\left\{\begin{bmatrix} \Delta\boldsymbol{\phi}^S_{r,L1,k} \\ \Delta\boldsymbol{\phi}^S_{r,L2,k} \end{bmatrix}\right\} = \begin{bmatrix} -\mathbf{e}^{S*}_{r,k} & c\mathbf{u}_m & & -\mathbf{I}_m & \lambda_1\mathbf{I}_m & & -c\mathbf{I}_m & \\ -\mathbf{e}^{S*}_{r,k} & & c\mathbf{u}_m & -\gamma\mathbf{I}_m & & \lambda_2\mathbf{I}_m & & -c\mathbf{I}_m \end{bmatrix} \begin{bmatrix} \Delta\mathbf{r}_r \\ \delta t_{r,L1,k} \\ \delta t_{r,L2,k} \\ \boldsymbol{\mathcal{I}}^S_{r,k} \\ \mathbf{A}^S_{r,L1} \\ \mathbf{A}^S_{r,L2} \\ \boldsymbol{\delta t}^S_{L1,k} \\ \boldsymbol{\delta t}^S_{L2,k} \end{bmatrix} \tag{4.21}$$

For the satellite clock biases a single user receiver is again dependent on a network from a service provider. Ideally these should be both phase clocks, or one phase clock and the differential phase bias. However, for classical SPP and PPP these clocks are not available, instead the ionosphere-free code clock is provided. Therefore, we will again introduce the ionosphere-free and ionosphere satellite clock offsets and, to solve a rank deficiency between the receiver clocks and the ionosphere delay we will also use the same combinations at the receiver side:

$$\begin{array}{rcl} \boldsymbol{\delta t}^S_{L3,k} &=& +\frac{\gamma}{\gamma-1}\boldsymbol{\delta t}^S_{L1,k} - \frac{1}{\gamma-1}\boldsymbol{\delta t}^S_{L2,k} \\ \boldsymbol{\delta t}^S_{LI,k} &=& -\frac{1}{\gamma-1}\boldsymbol{\delta t}^S_{L1,k} + \frac{1}{\gamma-1}\boldsymbol{\delta t}^S_{L2,k} \quad = \quad \frac{1}{\gamma-1}\boldsymbol{\delta}^S_{L1L2,k} \\ \delta t_{r,L3,k} &=& +\frac{\gamma}{\gamma-1}\delta t_{r,L1,k} - \frac{1}{\gamma-1}\delta t_{r,L2,k} \\ \delta t_{r,LI,k} &=& -\frac{1}{\gamma-1}\delta t_{r,L1,k} + \frac{1}{\gamma-1}\delta t_{r,L2,k} \quad = \quad \frac{1}{\gamma-1}\delta_{r,L1L2,k} \end{array} \tag{4.22}$$

The ionosphere clocks again reduce to differential hardware delays (in this case called differential phase biases, DPB) as shown in eq. (4.22). These biases cannot be separated from the ionosphere estimates and are therefore lumped in the parameter estimation:

$$\bar{\boldsymbol{\mathcal{I}}}^S_{r,k} = \boldsymbol{\mathcal{I}}^S_{r,k} - \frac{c}{\gamma-1}\delta_{r,L1L2,k} + \frac{c}{\gamma-1}\boldsymbol{\delta}^S_{L1L2,k} \tag{4.23}$$

As mentioned before the precise clock products are traditionally aligned with the ionosphere-free code observations. We can define the ionosphere-free phase clock with respect to the code clock as follows:

$$\boldsymbol{\delta t}^s_{L3,k} - \boldsymbol{dt}^s_{P3,k} = \boldsymbol{\delta}^s_{P3L3,k} = \frac{\gamma}{\gamma-1}\boldsymbol{\delta}^s_{P1L1,k} - \frac{1}{\gamma-1}\boldsymbol{\delta}^s_{P2L2,k} \tag{4.24}$$

which means that if we correct the observations for the provided satellite clocks we are left with this differential hardware delay in the functional model:

$$E\left\{\begin{bmatrix} \Delta\boldsymbol{\phi}^S_{r,L1,k} \\ \Delta\boldsymbol{\phi}^S_{r,L2,k} \end{bmatrix}\right\} = \begin{bmatrix} -\mathbf{e}^{S*}_{r,k} & c\mathbf{u}_m & -\mathbf{I}_m & \lambda_1\mathbf{I}_m & & -c\mathbf{I}_m \\ -\mathbf{e}^{S*}_{r,k} & c\mathbf{u}_m & -\gamma\mathbf{I}_m & & \lambda_2\mathbf{I}_m & -c\mathbf{I}_m \end{bmatrix} \begin{bmatrix} \Delta\mathbf{r}_r \\ \delta t_{r,L3,k} \\ \bar{\boldsymbol{\mathcal{I}}}^S_{r,k} \\ \mathbf{A}^S_{r,L1} \\ \mathbf{A}^S_{r,L2} \\ \boldsymbol{\delta}^s_{P3L3,k} \end{bmatrix} \tag{4.25}$$

Equation (4.25) still contains several rank deficiencies. First we will solve the rank deficiency between the ionosphere delay and the estimated ambiguity parameters. If we introduce the ionosphere-free and ionosphere linear combinations of the ambiguities, it becomes clear that the ionosphere ambiguity cannot be estimated separately from the ionosphere delays. Therefore, these parameters are lumped as follows:

$$\begin{array}{rcl} \mathbf{A}^S_{r,L3} &=& +\frac{\gamma}{\gamma-1}\lambda_1\mathbf{A}^S_{r,L1} - \frac{1}{\gamma-1}\lambda_2\mathbf{A}^S_{r,L2} \\ \mathbf{A}^S_{r,LI} &=& -\frac{1}{\gamma-1}\lambda_1\mathbf{A}^S_{r,L1} + \frac{1}{\gamma-1}\lambda_2\mathbf{A}^S_{r,L2} \\ \bar{\bar{\boldsymbol{\mathcal{I}}}}^S_{r,k} &=& \bar{\boldsymbol{\mathcal{I}}}^S_{r,k} - \mathbf{A}^S_{r,LI} = \boldsymbol{\mathcal{I}}^S_{r,k} + \frac{1}{\gamma-1}\left(\lambda_1\mathbf{A}^S_{r,L1} - \lambda_2\mathbf{A}^S_{r,L2}\right) \end{array} \tag{4.26}$$

These operations change the dual frequency phase-only model as follows:

$$E\left\{\begin{bmatrix} \Delta\boldsymbol{\phi}^S_{r,L1,k} \\ \Delta\boldsymbol{\phi}^S_{r,L2,k} \end{bmatrix}\right\} = \begin{bmatrix} -\mathbf{e}^{S*}_{r,k} & c\mathbf{u}_m & -\mathbf{I}_m & \mathbf{I}_m & -c\mathbf{I}_m \\ -\mathbf{e}^{S*}_{r,k} & c\mathbf{u}_m & -\gamma\mathbf{I}_m & \mathbf{I}_m & -c\mathbf{I}_m \end{bmatrix} \begin{bmatrix} \Delta\mathbf{r}_r \\ \delta t_{r,L3,k} \\ \bar{\bar{\boldsymbol{\mathcal{I}}}}^S_{r,k} \\ \mathbf{A}^S_{r,L3} \\ \boldsymbol{d}^s_{P3L3,k} \end{bmatrix} \tag{4.27}$$

The next rank deficiency that needs to be solved is between the ionosphere-free ambiguity and the remaining satellite hardware delays. These parameters are lumped as follows:

$$\bar{\mathbf{A}}^S_{r,L3} = \mathbf{A}^S_{r,L3} - \boldsymbol{d}^s_{P3L3,k} \tag{4.28}$$

Just as in the single-frequency model, the ambiguity parameters cannot be estimated separately from the other unknown parameters, which prevents ambiguity resolution. The resulting model becomes:

$$E\left\{\begin{bmatrix} \Delta\boldsymbol{\phi}^S_{r,L1,k} \\ \Delta\boldsymbol{\phi}^S_{r,L2,k} \end{bmatrix}\right\} = \begin{bmatrix} -\mathbf{e}^{S*}_{r,k} & c\mathbf{u}_m & -\mathbf{I}_m & \mathbf{I}_m \\ -\mathbf{e}^{S*}_{r,k} & c\mathbf{u}_m & -\gamma\mathbf{I}_m & \mathbf{I}_m \end{bmatrix} \begin{bmatrix} \Delta\mathbf{r}_r \\ \delta t_{r,L3,k} \\ \bar{\bar{\boldsymbol{\mathcal{I}}}}^S_{r,k} \\ \bar{\mathbf{A}}^S_{r,L3} \end{bmatrix} \tag{4.29}$$

The final rank deficiency in the dual frequency phase-only model exists between the ionosphere-free ambiguities and receiver clock offset. To solve this rank defect, we add the first ambiguity to the clock offset and subtract it from all other ambiguities. The final model for a single epoch then becomes:

$$E\left\{\begin{bmatrix} \Delta\boldsymbol{\phi}^S_{r,L1,k} \\ \Delta\boldsymbol{\phi}^S_{r,L2,k} \end{bmatrix}\right\} = \begin{bmatrix} -\mathbf{e}^{S*}_{r,k} & c\mathbf{u}_m & -\mathbf{I}_m & \overset{0\cdots0}{\mathbf{I}_{m-1}} \\ -\mathbf{e}^{S*}_{r,k} & c\mathbf{u}_m & -\gamma\mathbf{I}_m & \overset{0\cdots0}{\mathbf{I}_{m-1}} \end{bmatrix} \begin{bmatrix} \Delta\mathbf{r}_r \\ \overline{\delta t}_{r,L3,k} \\ \bar{\bar{\boldsymbol{\mathcal{I}}}}^S_{r,k} \\ \bar{\mathbf{A}}^{S-1}_{r,L3} \end{bmatrix} \tag{4.30}$$

with $\overline{\delta t}_{r,L3,k} = \delta t_{r,L3,k} + \frac{1}{c}\bar{A}^1_{r,L3}$. For the single frequency case we already showed that the receiver coordinates cannot be estimated from a single epoch of phase-only data. This result does not change by adding an extra frequency as can be seen from eq. (4.30). Therefore, we must include at least one additional epoch to estimate all unknown parameters. The minimal number of satellites depends on the number of measurement epochs and is tabulated in table D.4. The multi-epoch model becomes:

$$E\left\{\begin{bmatrix} \Delta\boldsymbol{\phi}^S_{r,L1,1} \\ \Delta\boldsymbol{\phi}^S_{r,L2,1} \\ \Delta\boldsymbol{\phi}^S_{r,L1,2} \\ \Delta\boldsymbol{\phi}^S_{r,L2,2} \\ \vdots \end{bmatrix}\right\} = \begin{bmatrix} -\mathbf{e}^{S*}_{r,1} & c\mathbf{u}_m & & -\mathbf{I}_m & & \overset{0\cdots0}{\mathbf{I}_{m-1}} \\ -\mathbf{e}^{S*}_{r,1} & c\mathbf{u}_m & & -\gamma\mathbf{I}_m & & \overset{0\cdots0}{\mathbf{I}_{m-1}} \\ -\mathbf{e}^{S*}_{r,2} & & c\mathbf{u}_m & & -\mathbf{I}_m & \overset{0\cdots0}{\mathbf{I}_{m-1}} \\ -\mathbf{e}^{S*}_{r,2} & & c\mathbf{u}_m & & -\gamma\mathbf{I}_m & \overset{0\cdots0}{\mathbf{I}_{m-1}} \\ \vdots & & \ddots & & \ddots & \vdots \end{bmatrix} \begin{bmatrix} \Delta\mathbf{r}_r \\ \overline{\delta t}_{r,L3,1} \\ \overline{\delta t}_{r,L3,2} \\ \vdots \\ \bar{\bar{\boldsymbol{\mathcal{I}}}}^S_{r,1} \\ \bar{\bar{\boldsymbol{\mathcal{I}}}}^S_{r,2} \\ \vdots \\ \bar{\mathbf{A}}^{S-1}_{r,L3} \end{bmatrix} \tag{4.31}$$

4.7 Single frequency code & phase

Now we will consider a single frequency code and phase measurement model. Since the ionosphere delay has a different sign for the code and phase measurements it can also be estimated from the combination of code and phase observations as follows:

$$E\left\{\begin{bmatrix}\Delta\mathbf{P}^S_{r,f,k}\\ \Delta\boldsymbol{\phi}^S_{r,f,k}\end{bmatrix}\right\} = \begin{bmatrix}-\mathbf{e}^{S*}_{r,k} & c\mathbf{u}_m & & \gamma_f\mathbf{I}_m & & -c\mathbf{I}_m & \\ -\mathbf{e}^{S*}_{r,k} & & c\mathbf{u}_m & -\gamma_f\mathbf{I}_m & \lambda_f\mathbf{I}_m & & -c\mathbf{I}_m\end{bmatrix}\begin{bmatrix}\Delta\mathbf{r}_r\\ dt_{r,f,k}\\ \delta t_{r,f,k}\\ \boldsymbol{\mathcal{I}}^S_{r,k}\\ \mathbf{A}^S_{r,f}\\ \boldsymbol{dt}^S_{f,k}\\ \boldsymbol{\delta t}^S_{f,k}\end{bmatrix} \tag{4.32}$$

We again have a different satellite clock offset for each observable, which we would like to remove from the observations. However, as mentioned earlier from the broadcast message and precise products only the ionosphere code clock and differential code biases are available. From these we can determine any of the pseudo range clocks but not the phase clocks. If we define the satellite phase clock with respect to the code as follows:

$$\boldsymbol{\delta t}^S_{f,k} \;=\; \boldsymbol{dt}^S_{f,k} + \boldsymbol{\delta}^S_{PfLf,k} \tag{4.33}$$

we can remove the satellite code clock from all observables leaving only the differential hardware delays $\boldsymbol{\delta}^S_{PfLf,k} = \boldsymbol{\delta}^S_{f,k} - \boldsymbol{d}^S_{f,k}$. The satellite differential terms (or the phase clock offset directly) could be estimated from a (network of) reference receiver(s), and as we will show later, this is necessary for ambiguity resolution. However, at present this information is not provided to PPP users. Therefore, this term cannot be estimated or corrected. By simply applying the provided satellite clock offset and ignoring the differential term the estimated ambiguities will be biased by the differential term:

$$\bar{\mathbf{A}}^S_{r,f} = \mathbf{A}^S_{r,f} - \frac{c}{\lambda_f}(\delta^S_{PfLf,k}) \tag{4.34}$$

This simplifies the single frequency code and phase model as follows:

$$E\left\{\begin{bmatrix}\Delta\mathbf{P}^S_{r,f,k}\\ \Delta\boldsymbol{\phi}^S_{r,f,k}\end{bmatrix}\right\} = \begin{bmatrix}-\mathbf{e}^{S*}_{r,k} & c\mathbf{u}_m & & \gamma_f\mathbf{I}_m & \\ -\mathbf{e}^{S*}_{r,k} & & c\mathbf{u}_m & -\gamma_f\mathbf{I}_m & \lambda_f\mathbf{I}_m\end{bmatrix}\begin{bmatrix}\Delta\mathbf{r}_r\\ dt_{r,f,k}\\ \delta t_{r,f,k}\\ \boldsymbol{\mathcal{I}}^S_{r,k}\\ \bar{\mathbf{A}}^S_{r,f}\end{bmatrix} \tag{4.35}$$

The next rank defect that we solve is between the ambiguities and the receiver phase clock offset, by adding the first ambiguity to the clock offset and subtracting it from all other ambiguities:

$$\overline{\delta t}_{r,f,k} = \delta t_{r,f,k} + \frac{\lambda_f}{c}\bar{\mathbf{A}}^1_{r,f} \tag{4.36}$$

which gives:

$$E\left\{\begin{bmatrix}\Delta\mathbf{P}^S_{r,f,k}\\ \Delta\boldsymbol{\phi}^S_{r,f,k}\end{bmatrix}\right\} = \begin{bmatrix}-\mathbf{e}^{S*}_{r,k} & c\mathbf{u}_m & & \gamma_f\mathbf{I}_m & \overset{0\cdots0}{} \\ -\mathbf{e}^{S*}_{r,k} & & c\mathbf{u}_m & -\gamma_f\mathbf{I}_m & \lambda_f\mathbf{I}_{m-1}\end{bmatrix}\begin{bmatrix}\Delta\mathbf{r}_r\\ dt_{r,f,k}\\ \overline{\delta t}_{r,f,k}\\ \boldsymbol{\mathcal{I}}^S_{r,k}\\ \bar{\mathbf{A}}^{1S}_{r,f}\end{bmatrix} \tag{4.37}$$

At the side of the receiver there still is a rank deficiency between the clock offsets and the ionosphere estimates. To solve this rank deficiency we reparameterize the receiver clocks with an ionosphere-free and an ionosphere linear combination of the code and phase clocks as follows (note that these linear combinations are not the same as those following from dual frequency observations, but rather follow directly from the opposite sign of the ionosphere in the code and phase observation equations):

$$\begin{array}{rcll} dt_{r,IF,k} & = & \frac{1}{2}dt_{r,f,k} + \frac{1}{2}\overline{\delta t}_{r,f,k} & \\ dt_{r,I,k} & = & \frac{1}{2}dt_{r,f,k} - \frac{1}{2}\overline{\delta t}_{r,f,k} & = \frac{1}{2}(d_{r,f,k} - \bar{\delta}_{r,f,k}) \end{array} \tag{4.38}$$

Note that both these clock parameters are now biased by the reference ambiguity. The ionosphere combination of the clocks reduces to a biased differential hardware delay, which is lumped with the ionosphere delay as it cannot be estimated separately.

$$\bar{\mathcal{I}}^S_{r,k} = \mathcal{I}^S_{r,k} + \frac{c}{2\gamma_f}(d_{r,f,k} - \bar{\delta}_{r,f,k}) \tag{4.39}$$

which gives:

$$E\left\{\begin{bmatrix} \Delta\mathbf{P}^S_{r,f,k} \\ \Delta\boldsymbol{\phi}^S_{r,f,k} \end{bmatrix}\right\} = \begin{bmatrix} -\mathbf{e}^{S*}_{r,k} & c\mathbf{u}_m & \gamma_f\mathbf{I}_m & 0\cdots0 \\ -\mathbf{e}^{S*}_{r,k} & c\mathbf{u}_m & -\gamma_f\mathbf{I}_m & \lambda_f\mathbf{I}_{m-1} \end{bmatrix}\begin{bmatrix} \Delta\mathbf{r}_r \\ dt_{r,IF,k} \\ \bar{\mathcal{I}}^S_{r,k} \\ \bar{\mathbf{A}}^{1S}_{r,f} \end{bmatrix} \tag{4.40}$$

Since an unknown ionosphere delay and ambiguity need to be estimated for each satellite, the position cannot be solved from a single epoch of data. The multi-epoch model can be formed as follows:

$$E\left\{\begin{bmatrix} \Delta\mathbf{P}^S_{r,f,1} \\ \Delta\boldsymbol{\phi}^S_{r,f,1} \\ \Delta\mathbf{P}^S_{r,f,2} \\ \Delta\boldsymbol{\phi}^S_{r,f,2} \\ \vdots \end{bmatrix}\right\} = \begin{bmatrix} -\mathbf{e}^{S*}_{r,k} & c\mathbf{u}_m & & \gamma_f\mathbf{I}_m & & 0\cdots0 \\ -\mathbf{e}^{S*}_{r,k} & c\mathbf{u}_m & & -\gamma_f\mathbf{I}_m & & \lambda_f\mathbf{I}_{m-1} \\ -\mathbf{e}^{S*}_{r,k} & & c\mathbf{u}_m & & \gamma_f\mathbf{I}_m & 0\cdots0 \\ -\mathbf{e}^{S*}_{r,k} & & c\mathbf{u}_m & & -\gamma_f\mathbf{I}_m & \lambda_f\mathbf{I}_{m-1} \\ \vdots & & \ddots & & \ddots & \vdots \end{bmatrix}\begin{bmatrix} \Delta\mathbf{r}_r \\ dt_{r,IF,1} \\ dt_{r,IF,2} \\ \vdots \\ \bar{\mathcal{I}}^S_{r,1} \\ \bar{\mathcal{I}}^S_{r,2} \\ \vdots \\ \bar{\mathbf{A}}^{1S}_{r,f} \end{bmatrix} \tag{4.41}$$

This model is very closely related to positioning with the code-plus-carrier linear combination of the observables introduced by Yunck (1996), where the ionosphere is eliminated rather than estimated (previously discussed in section 3.4.1.1). An advantage of eq. (4.41) is that a dynamic model can be introduced to strengthen the model. However, since this single frequency code & phase model remains relatively weak, a more common approach to single frequency PPP is to use an external ionosphere model to correct the code and phase observations. In this case the number of unknown parameters decreases drastically, thereby strengthening the model. If we determine the estimable parameters for this alternative model, we find that the lack of ionosphere parameters is not the only difference with the model of eq. (4.41). The parameterization of the satellite clocks remains identical to eq. (4.33) and the satellite DCPB is again lumped with the ambiguities as in eq. (4.34).

$$E\left\{\begin{bmatrix}\Delta\mathbf{P}^S_{r,f,k}\\ \Delta\boldsymbol{\phi}^S_{r,f,k}\end{bmatrix}\right\} = \begin{bmatrix}-\mathbf{e}^{S*}_{r,k} & c\mathbf{u}_m & & \\ -\mathbf{e}^{S*}_{r,k} & & c\mathbf{u}_m & \lambda_f\mathbf{I}_m\end{bmatrix}\begin{bmatrix}\Delta\mathbf{r}_r\\ dt_{r,f,k}\\ \delta t_{r,f,k}\\ \bar{\mathbf{A}}^S_{r,f}\end{bmatrix} \tag{4.42}$$

However, the receiver clock offsets must be treated differently. Since no receiver terms can be lumped with the ionosphere delays, the receiver phase clock is instead defined as a differential term with respect to the receiver code clock as follows:

$$\delta t_{r,f,k} \quad = \quad dt_{r,f,k} + \delta_{r,PfLf,k} \tag{4.43}$$

This differential hardware bias at the side of the receiver could also be combined with each of the ambiguity parameters as we did previously for the satellite hardware delays. However, especially for low-end receivers this differential delay might not be as constant over time as the satellite delays. In this case biasing all ambiguity parameters by the receiver differential hardware delay, means that they cannot be kept constant in the estimation process. A better solution is to lump only the first ambiguity with the receiver hardware delays, similar to the lumping of the receiver phase clock and the first ambiguity in the phase-only models. The first ambiguity is also subtracted from all other ambiguities, thereby forming the between satellite single difference ambiguities similar to the phase-only model. These single difference ambiguities are then only biased by the satellite differential hardware delays. This leads to the following single frequency code & phase model without ionosphere estimation:

$$E\left\{\begin{bmatrix}\Delta\mathbf{P}^S_{r,f,k}\\ \Delta\boldsymbol{\phi}^S_{r,f,k}\end{bmatrix}\right\} = \begin{bmatrix}-\mathbf{e}^{S*}_{r,k} & c\mathbf{u}_m & & \\ -\mathbf{e}^{S*}_{r,k} & c\mathbf{u}_m & c\mathbf{u}_m & \lambda_f\overset{0\cdots 0}{\mathbf{I}_{m-1}}\end{bmatrix}\begin{bmatrix}\Delta\mathbf{r}_r\\ dt_{r,f,k}\\ \bar{\delta}_{r,PfLf,k}\\ \bar{\mathbf{A}}^{1S}_{r,f}\end{bmatrix} \tag{4.44}$$

with:

$$\bar{\delta}_{r,PfLf,k} = \delta_{r,PfLf,k} + \frac{\lambda_f}{c}\bar{\mathbf{A}}^1_{r,f} \tag{4.45}$$

Note: Ambiguity terms which are lumped with satellite (differential) hardware delays will be indicated by $\bar{\mathbf{A}}$ while ambiguity parameters that are lumped with receiver (differential) delays will be indicated by $\bar{\delta}$. This difference in notation is used to remind the reader of the fact that the latter might be far less stable over time. Contrary to the model with ionosphere estimation of eq. (4.40), this model *can* be solved from a single observation epoch, and, due to the much smaller number of unknown parameters, has a much shorter convergence time. The minimal number of satellites is tabulated in table D.6. Variations on this model apply 'so-called' carrier phase smoothing of the pseudo range observations, but were shown to be suboptimal (Teunissen, 1991; Le and Teunissen, 2006; Le and Tiberius, 2006a). The model of eq. (4.44) can even compete with traditional dual frequency PPP for short measurement duration and moderate ionosphere activity. An explanation is provided by van der Marel and de Bakker (2012) who compare the precision of the ionosphere-free code observations that are formed in each of the approaches. In the dual frequency model these rely on the ionosphere-free combination of eq. (3.41) which increases the multipath and measurement noise by a factor three, while the single frequency model uses the external ionosphere data to form the ionosphere-free observations. The precision then depends on the quality of the ionosphere data, and especially for mid latitudes this often leads to pseudo range observations of a higher quality then the dual frequency combination. Only when the ambiguity estimates have sufficiently converged in the dual frequency model will the phase observations start to drive the position solution and outperform the single frequency model.

4.8 Dual frequency code & phase

In this section three dual-frequency code & phase models will be derived. For the first model we will follow the same approach as each of the models derived so far, reparameterizing the unknowns only when needed to solve the rank deficiencies in the model. In the second model we will make one additional reparameterization of the ambiguity parameters that is strictly speaking unnecessary but will be shown to be equivalent with the first model. In the third model we will *not* use the knowledge that the ionosphere effect has equal size and opposite sign on the pseudo range and carrier phase observations. Instead we will estimate a separate ionosphere delay for the code and phase observations. This approach is (obviously) suboptimal, but is studied non the less because it is identical to the elimination of the ionosphere by forming the ionosphere-free code and phase observables which is the traditional PPP approach. By deriving this model we will be able to show the differences with the first and second model and comment on the corresponding disadvantages. In eq. (4.46) the dual frequency code and phase model is presented with a different receiver and satellite clock offset for each observable.

$$E\left\{\begin{bmatrix}\Delta\mathbf{P}^S_{r,P1,k}\\ \Delta\mathbf{P}^S_{r,P2,k}\\ \Delta\boldsymbol{\phi}^S_{r,L1,k}\\ \Delta\boldsymbol{\phi}^S_{r,L2,k}\end{bmatrix}\right\} =$$

$$\begin{bmatrix}-\mathbf{e}^{S*}_{r,k} & c\mathbf{u}_m & & & & \mathbf{I}_m & & & -c\mathbf{I}_m & & & \\ -\mathbf{e}^{S*}_{r,k} & & c\mathbf{u}_m & & & \gamma\mathbf{I}_m & & & & -c\mathbf{I}_m & & \\ -\mathbf{e}^{S*}_{r,k} & & & c\mathbf{u}_m & & -\mathbf{I}_m & \lambda_1\mathbf{I}_m & & & & -c\mathbf{I}_m & \\ -\mathbf{e}^{S*}_{r,k} & & & & c\mathbf{u}_m & -\gamma\mathbf{I}_m & & \lambda_2\mathbf{I}_m & & & & -c\mathbf{I}_m\end{bmatrix}\begin{bmatrix}\Delta\mathbf{r}_r\\ dt_{r,P1,k}\\ dt_{r,P2,k}\\ \delta t_{r,L1,k}\\ \delta t_{r,L2,k}\\ \boldsymbol{\mathcal{I}}^S_{r,k}\\ \mathbf{A}^S_{r,L1}\\ \mathbf{A}^S_{r,L2}\\ \boldsymbol{dt}^S_{P1,k}\\ \boldsymbol{dt}^S_{P2,k}\\ \boldsymbol{\delta t}^S_{L1,k}\\ \boldsymbol{\delta t}^S_{L2,k}\end{bmatrix} \tag{4.46}$$

As mentioned previously the ionosphere-free linear combination of the satellite code clocks is generally provided by the broadcast products or the precise products from e.g. the IGS. Therefore, we will reparameterize the satellite clocks as follows:

$$
\begin{aligned}
\boldsymbol{dt}^S_{P3,k} &= +\tfrac{\gamma}{\gamma-1}\boldsymbol{dt}^S_{P1,k} - \tfrac{1}{\gamma-1}\boldsymbol{dt}^S_{P2,k} = \boldsymbol{dt}^S_k + \tfrac{\gamma}{\gamma-1}\boldsymbol{d}^S_{P1,k} - \tfrac{1}{\gamma-1}\boldsymbol{d}^S_{P2,k}\\
\boldsymbol{dt}^S_{PI,k} &= -\tfrac{1}{\gamma-1}\boldsymbol{dt}^S_{P1,k} + \tfrac{1}{\gamma-1}\boldsymbol{dt}^S_{P2,k} = \boldsymbol{d}^S_{PI,k} = \tfrac{1}{\gamma-1}\boldsymbol{d}^S_{P1P2,k}\\
\boldsymbol{\delta t}^S_{L1,k} &= \boldsymbol{dt}^S_{P3,k} + \boldsymbol{\delta}^S_{P3L1,k} = \boldsymbol{dt}^S_{P3,k} - \tfrac{\gamma}{\gamma-1}\boldsymbol{d}^S_{P1,k} + \tfrac{1}{\gamma-1}\boldsymbol{d}^S_{P2,k} + \boldsymbol{\delta}^S_{L1,k}\\
\boldsymbol{\delta t}^S_{L2,k} &= \boldsymbol{dt}^S_{P3,k} + \boldsymbol{\delta}^S_{P3L2,k} = \boldsymbol{dt}^S_{P3,k} - \tfrac{\gamma}{\gamma-1}\boldsymbol{d}^S_{P1,k} + \tfrac{1}{\gamma-1}\boldsymbol{d}^S_{P2,k} + \boldsymbol{\delta}^S_{L2,k}
\end{aligned}
\tag{4.47}
$$

To solve the rank deficiency between the receiver clock offsets and the ionosphere delays, similar combinations are introduced for the receiver clock offsets:

$$
\begin{aligned}
dt_{r,P3,k} &= +\tfrac{\gamma}{\gamma-1}dt_{r,P1,k} - \tfrac{1}{\gamma-1}dt_{r,P2,k} = dt_{r,k} + \tfrac{\gamma}{\gamma-1}d_{r,P1,k} - \tfrac{1}{\gamma-1}d_{r,P2,k}\\
dt_{r,PI,k} &= -\tfrac{1}{\gamma-1}dt_{r,P1,k} + \tfrac{1}{\gamma-1}dt_{r,P2,k} = d_{r,PI,k} = \tfrac{1}{\gamma-1}d_{r,P1P2,k}\\
\delta t_{r,L1,k} &= dt_{r,P3,k} + \delta_{r,P3L1,k} = dt_{r,P3,k} - \tfrac{\gamma}{\gamma-1}d_{r,P1,k} + \tfrac{1}{\gamma-1}d_{r,P2,k} + \delta_{r,L1,k}\\
\delta t_{r,L2,k} &= dt_{r,P3,k} + \delta_{r,P3L2,k} = dt_{r,P3,k} - \tfrac{\gamma}{\gamma-1}d_{r,P1,k} + \tfrac{1}{\gamma-1}d_{r,P2,k} + \delta_{r,L2,k}
\end{aligned}
\tag{4.48}
$$

With these redefined clock offsets the satellite clocks can now be removed from the model by correcting both the code and phase observables. The model then becomes:

$$
E\left\{\begin{bmatrix} \Delta\mathbf{P}^S_{r,P1,k}\\ \Delta\mathbf{P}^S_{r,P2,k}\\ \Delta\boldsymbol{\phi}^S_{r,L1,k}\\ \Delta\boldsymbol{\phi}^S_{r,L2,k}\end{bmatrix}\right\} =
$$

$$
\begin{bmatrix}
-\mathbf{e}^{S*}_{r,k} & c\mathbf{u}_m & c\mathbf{u}_m & & & \mathbf{I}_m & & & -c\mathbf{I}_m & & \\
-\mathbf{e}^{S*}_{r,k} & c\mathbf{u}_m & \gamma c\mathbf{u}_m & & & \gamma\mathbf{I}_m & & & -\gamma c\mathbf{I}_m & & \\
-\mathbf{e}^{S*}_{r,k} & c\mathbf{u}_m & & c\mathbf{u}_m & & -\mathbf{I}_m & \lambda_1\mathbf{I}_m & & & -c\mathbf{I}_m & \\
-\mathbf{e}^{S*}_{r,k} & c\mathbf{u}_m & & & c\mathbf{u}_m & -\gamma\mathbf{I}_m & & \lambda_2\mathbf{I}_m & & & -c\mathbf{I}_m
\end{bmatrix}
\begin{bmatrix}
\Delta\mathbf{r}_r\\ dt_{r,P3,k}\\ d_{r,PI,k}\\ \delta_{r,P3L1,k}\\ \delta_{r,P3L2,k}\\ \boldsymbol{\mathcal{I}}^S_{r,k}\\ \mathbf{A}^S_{r,L1}\\ \mathbf{A}^S_{r,L2}\\ \boldsymbol{d}^S_{PI,k}\\ \boldsymbol{\delta}^S_{P3L1,k}\\ \boldsymbol{\delta}^S_{P3L2,k}
\end{bmatrix}
\tag{4.49}
$$

From eq. (4.49) the rank deficiency between the ionosphere estimates, the ionosphere code clocks, and differential code phase biases become clear. Just like we did in the dual frequency code-only model we solve this rank deficiency by lumping the ionosphere code clocks with the ionosphere delays as follows:

$$
\bar{\boldsymbol{\mathcal{I}}}^S_{r,k} = \boldsymbol{\mathcal{I}}^S_{r,k} + \tfrac{c}{\gamma-1}d_{r,P1P2,k} - \tfrac{c}{\gamma-1}\boldsymbol{d}^S_{P1P2,k} \tag{4.50}
$$

However, by applying this operation to the code and phase model we are also introducing these differential code biases in the observation equations for the carrier phase. To compensate for this effect the same differential code biases are also added to the unknown bias parameters in the phase observations but with opposite sign:

$$\begin{array}{rclcl} \bar{\boldsymbol{\delta}}^S_{L1,k} & = & \boldsymbol{\delta}^S_{P3L1,k} + \frac{1}{\gamma-1}\boldsymbol{d}^S_{P1P2,k} & = & \boldsymbol{\delta}^S_{L1,k} - \frac{\gamma+1}{\gamma-1}\boldsymbol{d}^S_{P1,k} + \frac{2}{\gamma-1}\boldsymbol{d}^S_{P2,k} \\ \bar{\boldsymbol{\delta}}^S_{L2,k} & = & \boldsymbol{\delta}^S_{P3L2,k} + \frac{\gamma}{\gamma-1}\boldsymbol{d}^S_{P1P2,k} & = & \boldsymbol{\delta}^S_{L2,k} - \frac{2\gamma}{\gamma-1}\boldsymbol{d}^S_{P1,k} + \frac{\gamma+1}{\gamma-1}\boldsymbol{d}^S_{P2,k} \\ \bar{\delta}_{r,L1,k} & = & \delta_{r,P3L1,k} + \frac{1}{\gamma-1}d_{r,P1P2,k} & = & \delta_{r,L1,k} - \frac{\gamma+1}{\gamma-1}d_{r,P1,k} + \frac{2}{\gamma-1}d_{r,P2,k} \\ \bar{\delta}_{r,L2,k} & = & \delta_{r,P3L2,k} + \frac{\gamma}{\gamma-1}d_{r,P1P2,k} & = & \delta_{r,L2,k} - \frac{2\gamma}{\gamma-1}d_{r,P1,k} + \frac{\gamma+1}{\gamma-1}d_{r,P2,k} \end{array} \tag{4.51}$$

This changes the model as follows:

$$E\left\{\begin{bmatrix} \Delta\mathbf{P}^S_{r,P1,k} \\ \Delta\mathbf{P}^S_{r,P2,k} \\ \Delta\boldsymbol{\phi}^S_{r,L1,k} \\ \Delta\boldsymbol{\phi}^S_{r,L2,k} \end{bmatrix}\right\} =$$

$$\begin{bmatrix} -\mathbf{e}^{S*}_{r,k} & c\mathbf{u}_m & & & \mathbf{I}_m & & & & \\ -\mathbf{e}^{S*}_{r,k} & c\mathbf{u}_m & & & \gamma\mathbf{I}_m & & & & \\ -\mathbf{e}^{S*}_{r,k} & c\mathbf{u}_m & c\mathbf{u}_m & & -\mathbf{I}_m & \lambda_1\mathbf{I}_m & & -c\mathbf{I}_m & \\ -\mathbf{e}^{S*}_{r,k} & c\mathbf{u}_m & & c\mathbf{u}_m & -\gamma\mathbf{I}_m & & \lambda_2\mathbf{I}_m & & -c\mathbf{I}_m \end{bmatrix} \begin{bmatrix} \Delta\mathbf{r}_r \\ dt_{r,P3,k} \\ \bar{\delta}_{r,L1,k} \\ \bar{\delta}_{r,L2,k} \\ \bar{\boldsymbol{\mathcal{I}}}^S_{r,k} \\ \mathbf{A}^S_{r,L1} \\ \mathbf{A}^S_{r,L2} \\ \bar{\boldsymbol{\delta}}^S_{L1,k} \\ \bar{\boldsymbol{\delta}}^S_{L2,k} \end{bmatrix} \tag{4.52}$$

The remaining rank deficiencies in eq. (4.52) exist between the differential hardware delays and the ambiguity parameters. The satellite hardware delays cannot be estimated separately from the ambiguities and are combined as follows:

$$\begin{array}{rcl} \bar{\mathbf{A}}^S_{r,L1} & = & \mathbf{A}^S_{r,L1} + \frac{c}{\lambda_1}\left(\frac{\gamma+1}{\gamma-1}\boldsymbol{d}^S_{P1,k} - \frac{2}{\gamma-1}\boldsymbol{d}^S_{P2,k} - \boldsymbol{\delta}^S_{L1,k}\right) \\ \bar{\mathbf{A}}^S_{r,L2} & = & \mathbf{A}^S_{r,L2} + \frac{c}{\lambda_2}\left(\frac{2\gamma}{\gamma-1}\boldsymbol{d}^S_{P1,k} - \frac{\gamma+1}{\gamma-1}\boldsymbol{d}^S_{P2,k} - \boldsymbol{\delta}^S_{L2,k}\right) \end{array} \tag{4.53}$$

The differential hardware delays that are lumped with the ambiguities in eq. (4.53) are what prevent ambiguity resolution for dual frequency PPP. By applying the provided DCBs this bias could be reduced to $-\frac{c}{\lambda_f}\boldsymbol{\delta}^S_{P3Lf,k}$ but without any real benefit. Only if these last bias terms are also provided for L1 and L2 is a user able to estimate the ambiguities without additional biases, a prerequisite for ambiguity resolution. The initial phase at the side of the satellite, here not explicitly shown, should then also be included in the phase bias terms δ^S_{Lf}. The differential hardware biases at the side of the receiver are again lumped with the first (or a reference) ambiguity as we did for the single-frequency code & phase model without ionosphere estimation and similar to the lumping of the receiver phase clock and the first ambiguity in the phase-only models.

$$\begin{array}{rcl} \bar{\bar{\delta}}_{r,L1,k} & = & \delta_{r,L1,k} - \frac{\gamma+1}{\gamma-1}d_{r,P1,k} + \frac{2}{\gamma-1}d_{r,P2,k} + \frac{\lambda_1}{c}\bar{\mathbf{A}}^1_{r,L1} \\ \bar{\bar{\delta}}_{r,L2,k} & = & \delta_{r,L2,k} - \frac{2\gamma}{\gamma-1}d_{r,P1,k} + \frac{\gamma+1}{\gamma-1}d_{r,P2,k} + \frac{\lambda_2}{c}\bar{\mathbf{A}}^1_{r,L2} \\ \bar{\mathbf{A}}^{1S}_{r,L1} & = & \bar{\mathbf{A}}^S_{r,L1} - \bar{\mathbf{A}}^1_{r,L1} \\ \bar{\mathbf{A}}^{1S}_{r,L2} & = & \bar{\mathbf{A}}^S_{r,L2} - \bar{\mathbf{A}}^1_{r,L2} \end{array} \tag{4.54}$$

Equation (4.54) reveals that the ambiguities of the reference satellite are biased by an additional receiver dependent term while the single difference ambiguities remain unbiased by this term. This also means that a common bias in all satellite differential code phase delays $\boldsymbol{\delta}^S_{P3Lf,k}$ pertaining to the same frequency f do not impact the estimation by the user other then further biasing the undifferenced reference ambiguities. In practice this common bias might depend on the method of solving the rank defect in the network processing model used to estimates the satellite biases. A comparison of the PPP ambiguity estimation process to that in a baseline or network setup reveals strong similarities and, if the satellite bias terms mentioned previously are provided to the PPP user, can even be considered equivalent. In baseline processing the double differenced ambiguities can be fixed to integer values. This can either by achieved by forming the double differenced observations, or by only parameterizing the ambiguities in double differenced form while keeping the observations in undifferenced form (Odijk, 2002). The later approach is closest to the PPP approach. Here the between satellite single differenced ambiguities are formed in identical manner, and the (pseudo) double differencing is performed by applying the differential phase hardware delays (including the initial phase) provided by a (network of) reference receiver(s). The final model without ambiguity resolution becomes:

$$
E\left\{\begin{bmatrix}\Delta\mathbf{P}^S_{r,P1,k}\\ \Delta\mathbf{P}^S_{r,P2,k}\\ \Delta\boldsymbol{\phi}^S_{r,L1,k}\\ \Delta\boldsymbol{\phi}^S_{r,L2,k}\end{bmatrix}\right\}=\begin{bmatrix}-\mathbf{e}^{S*}_{r,k} & c\mathbf{u}_m & & & \mathbf{I}_m & & \\ -\mathbf{e}^{S*}_{r,k} & c\mathbf{u}_m & & & \gamma\mathbf{I}_m & & \\ -\mathbf{e}^{S*}_{r,k} & c\mathbf{u}_m & c\mathbf{u}_m & & -\mathbf{I}_m & \lambda_1\overset{0\cdots0}{\mathbf{I}_{m-1}} & \\ -\mathbf{e}^{S*}_{r,k} & c\mathbf{u}_m & & c\mathbf{u}_m & -\gamma\mathbf{I}_m & & \lambda_2\overset{0\cdots0}{\mathbf{I}_{m-1}}\end{bmatrix}\begin{bmatrix}\Delta\mathbf{r}_r\\ dt_{r,P3,k}\\ \bar{\bar{\delta}}_{r,L1,k}\\ \bar{\bar{\delta}}_{r,L2,k}\\ \bar{\boldsymbol{\mathcal{I}}}^S_{r,k}\\ \bar{\mathbf{A}}^{1S}_{r,L1}\\ \bar{\mathbf{A}}^{1S}_{r,L2}\end{bmatrix} \tag{4.55}
$$

In this model there are no rank deficiencies and all parameters can be estimated from a single epoch of data if enough satellites are tracked (see table D.7). However, remember from the phase-only model that not all parameters can be estimated from one epoch of phase measurements. It is then important to realize that the estimates from the first epoch are only based on the code measurements and only later will the phase measurements start to contribute to the estimation of the user position and other parameters.

Another approach to derive the dual frequency code and phase model, is to apply the ionosphere-free and ionosphere combinations not only to the code biases, but to apply the same combinations to the phase biases and the ambiguities as we did in the phase-only model. Equation (4.46) can then by written as:

$$
E\left\{\begin{bmatrix}\Delta\mathbf{P}^S_{r,P1,k}\\ \Delta\mathbf{P}^S_{r,P2,k}\\ \Delta\boldsymbol{\phi}^S_{r,L1,k}\\ \Delta\boldsymbol{\phi}^S_{r,L2,k}\end{bmatrix}\right\} =
$$

$$
\begin{bmatrix}
-\mathbf{e}^{S*}_{r,k} & c\mathbf{u}_m & c\mathbf{u}_m & & & \mathbf{I}_m & & & -c\mathbf{I}_m & -c\mathbf{I}_m & & \\
-\mathbf{e}^{S*}_{r,k} & c\mathbf{u}_m & \gamma c\mathbf{u}_m & & & \gamma\mathbf{I}_m & & & -c\mathbf{I}_m & -\gamma c\mathbf{I}_m & & \\
-\mathbf{e}^{S*}_{r,k} & & & c\mathbf{u}_m & c\mathbf{u}_m & -\mathbf{I}_m & \mathbf{I}_m & \mathbf{I}_m & & & -c\mathbf{I}_m & -c\mathbf{I}_m \\
-\mathbf{e}^{S*}_{r,k} & & & c\mathbf{u}_m & \gamma c\mathbf{u}_m & -\gamma\mathbf{I}_m & \mathbf{I}_m & \gamma\mathbf{I}_m & & & -c\mathbf{I}_m & -\gamma c\mathbf{I}_m
\end{bmatrix}
\begin{bmatrix}\Delta\mathbf{r}_r\\ dt_{r,P3,k}\\ dt_{r,PI,k}\\ \delta t_{r,L3,k}\\ \delta t_{r,LI,k}\\ \boldsymbol{\mathcal{I}}^S_{r,k}\\ \mathbf{A}^S_{r,L3}\\ \mathbf{A}^S_{r,LI}\\ \boldsymbol{dt}^S_{P3,k}\\ \boldsymbol{dt}^S_{PI,k}\\ \boldsymbol{\delta t}^S_{L3,k}\\ \boldsymbol{\delta t}^S_{LI,k}\end{bmatrix}
\tag{4.56}
$$

with the following ionosphere and ionosphere-free combinations of the satellite and receiver clocks as well as ambiguities:

$$
\begin{array}{lllll}
\boldsymbol{dt}^S_{P3,k} & = & +\frac{\gamma}{\gamma-1}\boldsymbol{dt}^S_{P1,k} - \frac{1}{\gamma-1}\boldsymbol{dt}^S_{P2,k} & & \\
\boldsymbol{dt}^S_{PI,k} & = & -\frac{1}{\gamma-1}\boldsymbol{dt}^S_{P1,k} + \frac{1}{\gamma-1}\boldsymbol{dt}^S_{P2,k} & = \boldsymbol{d}^S_{PI,k} & = \frac{1}{\gamma-1}\boldsymbol{d}^S_{P1P2,k} \\
\boldsymbol{\delta t}^S_{L3,k} & = & +\frac{\gamma}{\gamma-1}\boldsymbol{\delta t}^S_{L1,k} - \frac{1}{\gamma-1}\boldsymbol{\delta t}^S_{L2,k} & & \\
\boldsymbol{\delta t}^S_{LI,k} & = & -\frac{1}{\gamma-1}\boldsymbol{\delta t}^S_{L1,k} + \frac{1}{\gamma-1}\boldsymbol{\delta t}^S_{L2,k} & = \boldsymbol{\delta}^S_{LI,k} & = \frac{1}{\gamma-1}\boldsymbol{\delta}^S_{L1L2,k}
\end{array}
\tag{4.57}
$$

$$
\begin{array}{lllll}
dt_{r,P3,k} & = & +\frac{\gamma}{\gamma-1}dt_{r,P1,k} - \frac{1}{\gamma-1}dt_{r,P2,k} & & \\
dt_{r,PI,k} & = & -\frac{1}{\gamma-1}dt_{r,P1,k} + \frac{1}{\gamma-1}dt_{r,P2,k} & = d_{r,PI,k} & = \frac{1}{\gamma-1}d_{r,P1P2,k} \\
\delta t_{r,L3,k} & = & +\frac{\gamma}{\gamma-1}\delta t_{r,L1,k} - \frac{1}{\gamma-1}\delta t_{r,L2,k} & & \\
\delta t_{r,LI,k} & = & -\frac{1}{\gamma-1}\delta t_{r,L1,k} + \frac{1}{\gamma-1}\delta t_{r,L2,k} & = \delta_{r,LI,k} & = \frac{1}{\gamma-1}\delta_{r,L1L2,k}
\end{array}
\tag{4.58}
$$

$$
\begin{array}{lll}
\mathbf{A}^S_{r,L3} & = & +\frac{\gamma}{\gamma-1}\lambda_1\mathbf{A}^S_{r,L1} - \frac{1}{\gamma-1}\lambda_2\mathbf{A}^S_{r,L2} \\
\mathbf{A}^S_{r,LI} & = & -\frac{1}{\gamma-1}\lambda_1\mathbf{A}^S_{r,L1} + \frac{1}{\gamma-1}\lambda_2\mathbf{A}^S_{r,L2}
\end{array}
\tag{4.59}
$$

To solve the rank deficiencies between the ionosphere and the hardware delays, we can then rearrange the code and phase biases as follows:

$$
E\left\{\begin{bmatrix} \Delta\mathbf{P}^S_{r,P1,k} \\ \Delta\mathbf{P}^S_{r,P2,k} \\ \Delta\boldsymbol{\phi}^S_{r,L1,k} \\ \Delta\boldsymbol{\phi}^S_{r,L2,k} \end{bmatrix}\right\} =
$$

$$
\begin{bmatrix}
-\mathbf{e}^{S*}_{r,k} & c\mathbf{u}_m & c\mathbf{u}_m & & & \mathbf{I}_m & & & -c\mathbf{I}_m & -c\mathbf{I}_m & & \\
-\mathbf{e}^{S*}_{r,k} & c\mathbf{u}_m & \gamma c\mathbf{u}_m & & & \gamma\mathbf{I}_m & & & -c\mathbf{I}_m & -\gamma c\mathbf{I}_m & & \\
-\mathbf{e}^{S*}_{r,k} & c\mathbf{u}_m & -c\mathbf{u}_m & c\mathbf{u}_m & c\mathbf{u}_m & -\mathbf{I}_m & \mathbf{I}_m & \mathbf{I}_m & -c\mathbf{I}_m & c\mathbf{I}_m & -c\mathbf{I}_m & -c\mathbf{I}_m \\
-\mathbf{e}^{S*}_{r,k} & c\mathbf{u}_m & -\gamma c\mathbf{u}_m & c\mathbf{u}_m & \gamma c\mathbf{u}_m & -\gamma\mathbf{I}_m & \mathbf{I}_m & \gamma\mathbf{I}_m & -c\mathbf{I}_m & \gamma c\mathbf{I}_m & -c\mathbf{I}_m & -\gamma c\mathbf{I}_m
\end{bmatrix}
\begin{bmatrix} \Delta\mathbf{r}_r \\ dt_{r,P3,k} \\ d_{r,PI,k} \\ \delta_{r,P3L3,k} \\ \delta_{r,PI+LI,k} \\ \boldsymbol{\mathcal{I}}^S_{r,k} \\ \mathbf{A}^S_{r,L3} \\ \mathbf{A}^S_{r,LI} \\ \boldsymbol{dt}^S_{P3,k} \\ \boldsymbol{d}^S_{PI,k} \\ \boldsymbol{\delta}^S_{P3L3,k} \\ \boldsymbol{\delta}^S_{PI+LI,k} \end{bmatrix} \tag{4.60}
$$

From eq. (4.60) the provided satellite clock parameter can be eliminated and the differential code biases can be lumped with the ionosphere delays:

$$
\bar{\boldsymbol{\mathcal{I}}}^S_{r,k} = \boldsymbol{\mathcal{I}}^S_{r,k} + \tfrac{c}{\gamma-1} d_{r,P1P2,k} - \tfrac{c}{\gamma-1}\boldsymbol{d}^S_{P1P2,k} \tag{4.61}
$$

which leads to the following model:

$$
E\left\{\begin{bmatrix} \Delta\mathbf{P}^S_{r,P1,k} \\ \Delta\mathbf{P}^S_{r,P2,k} \\ \Delta\boldsymbol{\phi}^S_{r,L1,k} \\ \Delta\boldsymbol{\phi}^S_{r,L2,k} \end{bmatrix}\right\} =
$$

$$
\begin{bmatrix}
-\mathbf{e}^{S*}_{r,k} & c\mathbf{u}_m & & & \mathbf{I}_m & & & & \\
-\mathbf{e}^{S*}_{r,k} & c\mathbf{u}_m & & & \gamma\mathbf{I}_m & & & & \\
-\mathbf{e}^{S*}_{r,k} & c\mathbf{u}_m & c\mathbf{u}_m & c\mathbf{u}_m & -\mathbf{I}_m & \mathbf{I}_m & \mathbf{I}_m & -c\mathbf{I}_m & -c\mathbf{I}_m \\
-\mathbf{e}^{S*}_{r,k} & c\mathbf{u}_m & c\mathbf{u}_m & \gamma c\mathbf{u}_m & -\gamma\mathbf{I}_m & \mathbf{I}_m & \gamma\mathbf{I}_m & -c\mathbf{I}_m & -\gamma c\mathbf{I}_m
\end{bmatrix}
\begin{bmatrix} \Delta\mathbf{r}_r \\ dt_{r,P3,k} \\ \delta_{r,P3L3,k} \\ \delta_{r,PI+LI,k} \\ \bar{\boldsymbol{\mathcal{I}}}^S_{r,k} \\ \mathbf{A}^S_{r,L3} \\ \mathbf{A}^S_{r,LI} \\ \boldsymbol{\delta}^S_{P3L3,k} \\ \boldsymbol{\delta}^S_{PI+LI,k} \end{bmatrix} \tag{4.62}
$$

There remains a rank deficiency between the ambiguities and the satellite hardware delays which we solve as follows:

$$
\begin{aligned}
\bar{\mathbf{A}}^S_{r,L3} &= \mathbf{A}^S_{r,L3} - c\boldsymbol{\delta}^S_{P3L3,k} \\
\bar{\mathbf{A}}^S_{r,LI} &= \mathbf{A}^S_{r,LI} - c\boldsymbol{\delta}^S_{PI+LI,k}
\end{aligned} \tag{4.63}
$$

Here one might observe that since the ionosphere combination of the satellite code hardware delays $\boldsymbol{d}^S_{PI,k}$ are generally available the bias of the ionosphere ambiguity $\bar{\mathbf{A}}^S_{r,LI}$ could be reduced to only include differential phase delays. However, as long as the ionosphere combination of the satellite phase hardware delays $\boldsymbol{\delta}^S_{LI,k}$ are not available this holds no great advantage. The model now becomes:

$$E\left\{\begin{bmatrix}\Delta\mathbf{P}^S_{r,P1,k}\\ \Delta\mathbf{P}^S_{r,P2,k}\\ \Delta\boldsymbol{\phi}^S_{r,L1,k}\\ \Delta\boldsymbol{\phi}^S_{r,L2,k}\end{bmatrix}\right\} = \begin{bmatrix}-\mathbf{e}^{S*}_{r,k} & c\mathbf{u}_m & & & \mathbf{I}_m & & \\ -\mathbf{e}^{S*}_{r,k} & c\mathbf{u}_m & & & \gamma\mathbf{I}_m & & \\ -\mathbf{e}^{S*}_{r,k} & c\mathbf{u}_m & c\mathbf{u}_m & c\mathbf{u}_m & -\mathbf{I}_m & \mathbf{I}_m & \mathbf{I}_m \\ -\mathbf{e}^{S*}_{r,k} & c\mathbf{u}_m & c\mathbf{u}_m & \gamma c\mathbf{u}_m & -\gamma\mathbf{I}_m & \mathbf{I}_m & \gamma\mathbf{I}_m\end{bmatrix}\begin{bmatrix}\Delta\mathbf{r}_r\\ dt_{r,P3,k}\\ \delta_{r,P3L3,k}\\ \delta_{r,PI+LI,k}\\ \bar{\boldsymbol{\mathcal{I}}}^S_{r,k}\\ \bar{\mathbf{A}}^S_{r,L3}\\ \bar{\mathbf{A}}^S_{r,LI}\end{bmatrix} \quad (4.64)$$

And finally we combine the receiver hardware delays with the first ambiguity and form the between satellite single difference ambiguity parameters as before:

$$\begin{aligned}\bar{\bar{\delta}}_{r,L3,k} &= \delta_{r,P3L3,k} &+\tfrac{1}{c}\bar{\mathbf{A}}^1_{r,L3}\\ \bar{\bar{\delta}}_{r,LI,k} &= \delta_{r,PI+LI,k} &+\tfrac{1}{c}\bar{\mathbf{A}}^1_{r,LI}\end{aligned} \quad (4.65)$$

$$E\left\{\begin{bmatrix}\Delta\mathbf{P}^S_{r,P1,k}\\ \Delta\mathbf{P}^S_{r,P2,k}\\ \Delta\boldsymbol{\phi}^S_{r,L1,k}\\ \Delta\boldsymbol{\phi}^S_{r,L2,k}\end{bmatrix}\right\} = \begin{bmatrix}-\mathbf{e}^{S*}_{r,k} & c\mathbf{u}_m & \mathbf{I}_m & & & & \\ -\mathbf{e}^{S*}_{r,k} & c\mathbf{u}_m & \gamma\mathbf{I}_m & & & & \\ -\mathbf{e}^{S*}_{r,k} & c\mathbf{u}_m & -\mathbf{I}_m & c\mathbf{u}_m & \overset{0\cdots0}{\mathbf{I}_{m-1}} & c\mathbf{u}_m & \overset{0\cdots0}{\mathbf{I}_{m-1}} \\ -\mathbf{e}^{S*}_{r,k} & c\mathbf{u}_m & -\gamma\mathbf{I}_m & c\mathbf{u}_m & \overset{0\cdots0}{\mathbf{I}_{m-1}} & \gamma c\mathbf{u}_m & \gamma\overset{0\cdots0}{\mathbf{I}_{m-1}}\end{bmatrix}\begin{bmatrix}\Delta\mathbf{r}_r\\ dt_{r,P3,k}\\ \bar{\boldsymbol{\mathcal{I}}}^S_{r,k}\\ \bar{\bar{\delta}}_{r,L3,k}\\ \bar{\mathbf{A}}^{1S}_{r,L3}\\ \bar{\bar{\delta}}_{r,LI,k}\\ \bar{\mathbf{A}}^{1S}_{r,LI}\end{bmatrix} \quad (4.66)$$

The model we end up with in eq. (4.66) is equivalent with the model of eq. (4.55). The only difference in the parameterization is that of the ambiguity parameters, but these can be transformed from one to the other before or after the estimation process.

4.8.1 Two ionosphere parameters

In this section we present one more alternative for the dual frequency code and phase model. The common approach to PPP is to form the ionosphere-free combinations of both code and phase observations. In this approach the ionosphere is eliminated twice, which is equivalent to estimating two ionosphere parameters per satellite. Namely one for the code observations and one for the phase observations. This can be expressed in a (rank deficient) positioning model as follows:

$$E\left\{\begin{bmatrix}\Delta\mathbf{P}^S_{r,P1,k}\\ \Delta\mathbf{P}^S_{r,P2,k}\\ \Delta\boldsymbol{\phi}^S_{r,L1,k}\\ \Delta\boldsymbol{\phi}^S_{r,L2,k}\end{bmatrix}\right\}=$$

$$\begin{bmatrix}-\mathbf{e}^{S*}_{r,k} & c\mathbf{u}_m & & & & \mathbf{I}_m & & & & -c\mathbf{I}_m & & & \\ -\mathbf{e}^{S*}_{r,k} & & c\mathbf{u}_m & & & \gamma\mathbf{I}_m & & & & & -c\mathbf{I}_m & & \\ -\mathbf{e}^{S*}_{r,k} & & & c\mathbf{u}_m & & & -\mathbf{I}_m & \lambda_1\mathbf{I}_m & & & & -c\mathbf{I}_m & \\ -\mathbf{e}^{S*}_{r,k} & & & & c\mathbf{u}_m & & -\gamma\mathbf{I}_m & & \lambda_2\mathbf{I}_m & & & & -c\mathbf{I}_m\end{bmatrix}\begin{bmatrix}\Delta\mathbf{r}_r\\ dt_{r,P1,k}\\ dt_{r,P2,k}\\ \delta t_{r,L1,k}\\ \delta t_{r,L2,k}\\ \boldsymbol{\mathcal{I}}^S_{r,P,k}\\ \boldsymbol{\mathcal{I}}^S_{r,L,k}\\ \mathbf{A}^S_{r,L1}\\ \mathbf{A}^S_{r,L2}\\ \boldsymbol{dt}^S_{P1,k}\\ \boldsymbol{dt}^S_{P2,k}\\ \boldsymbol{\delta t}^S_{L1,k}\\ \boldsymbol{\delta t}^S_{L2,k}\end{bmatrix} \tag{4.67}$$

Equation (4.67) has significantly more unknown parameters than the previously treated models, and more parameter lumping will be needed to obtain a design matrix of full rank. We start with the ionosphere parameters and the differential receiver and satellite hardware delays. Since the ionosphere parameters for the code and phase observables are not linked we can lump the differential hardware delays as we did in the code-only and the phase-only models:

$$\begin{aligned}\bar{\boldsymbol{\mathcal{I}}}^S_{r,P,k} &= \boldsymbol{\mathcal{I}}^S_{r,P,k}+\tfrac{c}{\gamma-1}d_{r,P1P2,k}-\tfrac{c}{\gamma-1}\boldsymbol{d}^S_{P1P2,k}\\ \bar{\boldsymbol{\mathcal{I}}}^S_{r,L,k} &= \boldsymbol{\mathcal{I}}^S_{r,L,k}-\tfrac{c}{\gamma-1}\delta_{r,L1L2,k}+\tfrac{c}{\gamma-1}\boldsymbol{\delta}^S_{L1L2,k}\end{aligned} \tag{4.68}$$

In stead of a receiver and satellite clock offset per observable we are now only left with the ionosphere-free clock offsets for both code and phase at both the receiver and satellite:

$$E\left\{\begin{bmatrix}\Delta\mathbf{P}^S_{r,P1,k}\\ \Delta\mathbf{P}^S_{r,P2,k}\\ \Delta\boldsymbol{\phi}^S_{r,L1,k}\\ \Delta\boldsymbol{\phi}^S_{r,L2,k}\end{bmatrix}\right\}=$$

$$\begin{bmatrix}-\mathbf{e}^{S*}_{r,k} & c\mathbf{u}_m & & \mathbf{I}_m & & & & -c\mathbf{I}_m & \\ -\mathbf{e}^{S*}_{r,k} & c\mathbf{u}_m & & \gamma\mathbf{I}_m & & & & -c\mathbf{I}_m & \\ -\mathbf{e}^{S*}_{r,k} & & c\mathbf{u}_m & & -\mathbf{I}_m & \lambda_1\mathbf{I}_m & & & -c\mathbf{I}_m\\ -\mathbf{e}^{S*}_{r,k} & & c\mathbf{u}_m & & -\gamma\mathbf{I}_m & & \lambda_2\mathbf{I}_m & & -c\mathbf{I}_m\end{bmatrix}\begin{bmatrix}\Delta\mathbf{r}_r\\ dt_{r,P3,k}\\ \delta t_{r,L3,k}\\ \bar{\boldsymbol{\mathcal{I}}}^S_{r,P,k}\\ \bar{\boldsymbol{\mathcal{I}}}^S_{r,L,k}\\ \mathbf{A}^S_{r,L1}\\ \mathbf{A}^S_{r,L2}\\ \boldsymbol{dt}^S_{P3,k}\\ \boldsymbol{\delta t}^S_{L3,k}\end{bmatrix} \tag{4.69}$$

Next we express the ionosphere-free phase clock at receiver and satellite with respect to the ionosphere-free code clock. These reduce to differential code phase biases for the receiver $\delta_{r,P3L3,k}$ and satellites $\boldsymbol{\delta}^S_{P3L3,k}$ as before. The provided ionosphere-free code satellite clock offset can then be eliminated from the observations as follows:

$$E\left\{\begin{bmatrix}\Delta\mathbf{P}^S_{r,P1,k}\\ \Delta\mathbf{P}^S_{r,P2,k}\\ \Delta\boldsymbol{\phi}^S_{r,L1,k}\\ \Delta\boldsymbol{\phi}^S_{r,L2,k}\end{bmatrix}\right\}=\begin{bmatrix}-\mathbf{e}^{S*}_{r,k} & c\mathbf{u}_m & & \mathbf{I}_m & & & & \\ -\mathbf{e}^{S*}_{r,k} & c\mathbf{u}_m & & \gamma\mathbf{I}_m & & & & \\ -\mathbf{e}^{S*}_{r,k} & c\mathbf{u}_m & c\mathbf{u}_m & & -\mathbf{I}_m & \lambda_1\mathbf{I}_m & & -c\mathbf{I}_m\\ -\mathbf{e}^{S*}_{r,k} & c\mathbf{u}_m & c\mathbf{u}_m & & -\gamma\mathbf{I}_m & & \lambda_2\mathbf{I}_m & -c\mathbf{I}_m\end{bmatrix}\begin{bmatrix}\Delta\mathbf{r}_r\\ dt_{r,P3,k}\\ \delta_{r,P3L3,k}\\ \bar{\boldsymbol{\mathcal{I}}}^S_{r,P,k}\\ \bar{\boldsymbol{\mathcal{I}}}^S_{r,L,k}\\ \mathbf{A}^S_{r,L1}\\ \mathbf{A}^S_{r,L2}\\ \boldsymbol{\delta}^S_{P3L3,k}\end{bmatrix} \tag{4.70}$$

To solve the rank deficiencies between the ionosphere and the ambiguities we introduce the ionosphere and ionosphere-free combinations of the ambiguities as we did in the previous model and in the phase-only model:

$$\begin{array}{lcl}\mathbf{A}^S_{r,L3} & = & +\frac{\gamma}{\gamma-1}\lambda_1\mathbf{A}^S_{r,L1}-\frac{1}{\gamma-1}\lambda_2\mathbf{A}^S_{r,L2}\\ \mathbf{A}^S_{r,LI} & = & -\frac{1}{\gamma-1}\lambda_1\mathbf{A}^S_{r,L1}+\frac{1}{\gamma-1}\lambda_2\mathbf{A}^S_{r,L2}\end{array} \tag{4.71}$$

This changes the model as follows:

$$E\left\{\begin{bmatrix}\Delta\mathbf{P}^S_{r,P1,k}\\ \Delta\mathbf{P}^S_{r,P2,k}\\ \Delta\boldsymbol{\phi}^S_{r,L1,k}\\ \Delta\boldsymbol{\phi}^S_{r,L2,k}\end{bmatrix}\right\}=\begin{bmatrix}-\mathbf{e}^{S*}_{r,k} & c\mathbf{u}_m & & \mathbf{I}_m & & & & \\ -\mathbf{e}^{S*}_{r,k} & c\mathbf{u}_m & & \gamma\mathbf{I}_m & & & & \\ -\mathbf{e}^{S*}_{r,k} & c\mathbf{u}_m & c\mathbf{u}_m & & -\mathbf{I}_m & \mathbf{I}_m & \mathbf{I}_m & -c\mathbf{I}_m\\ -\mathbf{e}^{S*}_{r,k} & c\mathbf{u}_m & c\mathbf{u}_m & & -\gamma\mathbf{I}_m & \mathbf{I}_m & \gamma\mathbf{I}_m & -c\mathbf{I}_m\end{bmatrix}\begin{bmatrix}\Delta\mathbf{r}_r\\ dt_{r,P3,k}\\ \delta_{r,P3L3,k}\\ \bar{\boldsymbol{\mathcal{I}}}^S_{r,P,k}\\ \bar{\boldsymbol{\mathcal{I}}}^S_{r,L,k}\\ \mathbf{A}^S_{r,L3}\\ \mathbf{A}^S_{r,LI}\\ \boldsymbol{\delta}^S_{P3L3,k}\end{bmatrix} \tag{4.72}$$

A further lumping of the observations is needed to solve the rank deficiencies between the ambiguities and the satellite hardware delays and between the ionosphere and the ambiguities:

$$\begin{array}{lcl}\bar{\mathbf{A}}^S_{r,L3} & = & \mathbf{A}^S_{r,L3}-\boldsymbol{\delta}^S_{P3L3,k}\\ \bar{\bar{\boldsymbol{\mathcal{I}}}}^S_{r,L,k} & = & \bar{\boldsymbol{\mathcal{I}}}^S_{r,L,k}-\mathbf{A}^S_{r,LI}\end{array} \tag{4.73}$$

$$E\left\{\begin{bmatrix}\Delta\mathbf{P}^S_{r,P1,k}\\ \Delta\mathbf{P}^S_{r,P2,k}\\ \Delta\boldsymbol{\phi}^S_{r,L1,k}\\ \Delta\boldsymbol{\phi}^S_{r,L2,k}\end{bmatrix}\right\}=\begin{bmatrix}-\mathbf{e}^{S*}_{r,k} & c\mathbf{u}_m & & \mathbf{I}_m & & \\ -\mathbf{e}^{S*}_{r,k} & c\mathbf{u}_m & & \gamma\mathbf{I}_m & & \\ -\mathbf{e}^{S*}_{r,k} & c\mathbf{u}_m & c\mathbf{u}_m & & -\mathbf{I}_m & \mathbf{I}_m\\ -\mathbf{e}^{S*}_{r,k} & c\mathbf{u}_m & c\mathbf{u}_m & & -\gamma\mathbf{I}_m & \mathbf{I}_m\end{bmatrix}\begin{bmatrix}\Delta\mathbf{r}_r\\ dt_{r,P3,k}\\ \delta_{r,P3L3,k}\\ \bar{\boldsymbol{\mathcal{I}}}^S_{r,P,k}\\ \bar{\bar{\boldsymbol{\mathcal{I}}}}^S_{r,L,k}\\ \bar{\mathbf{A}}^S_{r,L3}\end{bmatrix} \tag{4.74}$$

The final rank deficiency in eq. (4.74) exists between the receiver differential hardware delay and the ambiguities. Therefore, we again add the first ambiguity to the hardware delay and subtract it from all other ambiguities:

$$\bar{\delta}_{r,P3L3,k} = \delta_{r,P3L3,k} + \tfrac{1}{c}\bar{\mathbf{A}}^{1}_{r,L3} \tag{4.75}$$

The final model then becomes:

$$E\left\{\begin{bmatrix} \Delta\mathbf{P}^{S}_{r,P1,k} \\ \Delta\mathbf{P}^{S}_{r,P2,k} \\ \Delta\boldsymbol{\phi}^{S}_{r,L1,k} \\ \Delta\boldsymbol{\phi}^{S}_{r,L2,k} \end{bmatrix}\right\} = \begin{bmatrix} -\mathbf{e}^{S*}_{r,k} & c\mathbf{u}_m & & \mathbf{I}_m & & \\ -\mathbf{e}^{S*}_{r,k} & c\mathbf{u}_m & & \gamma\mathbf{I}_m & & \\ -\mathbf{e}^{S*}_{r,k} & c\mathbf{u}_m & c\mathbf{u}_m & & -\mathbf{I}_m & \overset{0\cdots0}{\mathbf{I}_{m-1}} \\ -\mathbf{e}^{S*}_{r,k} & c\mathbf{u}_m & c\mathbf{u}_m & & -\gamma\mathbf{I}_m & \overset{0\cdots0}{\mathbf{I}_{m-1}} \end{bmatrix} \begin{bmatrix} \Delta\mathbf{r}_r \\ dt_{r,P3,k} \\ \bar{\delta}_{r,P3L3,k} \\ \bar{\boldsymbol{\mathcal{I}}}^{S}_{r,P,k} \\ \bar{\bar{\boldsymbol{\mathcal{I}}}}^{S}_{r,L,k} \\ \bar{\mathbf{A}}^{1S}_{r,L3} \end{bmatrix} \tag{4.76}$$

Close comparison of the vector of unknown parameters in eq. (4.66) and eq. (4.76) reveals that 1 differential code phase bias and $m-1$ (constant) ambiguity parameters have been replaced by m additional ionosphere parameters, while all other parameters are identical. This clearly makes the model of eq. (4.66) a stronger model if multiple epochs are considered, which will also improve the precision of the estimated parameters they have in common including the user position. From this we can conclude that the often used PPP model based on the ionosphere-free combinations of the code and phase observables is not optimal.

4.9 Dual frequency code, phase & ionosphere

As mentioned before, the single-frequency PPP model can outperform the dual-frequency model for short measurement duration if the former uses additional ionosphere information from an external ionosphere model such as a Globel Ionosphere Map (van der Marel and de Bakker, 2012). Since estimation should always improve or at least remain equal if more information is added to the model, it is clear that dual-frequency PPP can also benefit from using the additional ionosphere information. For this reason we will introduce the dual-frequency code and phase model with external ionosphere data. As will become clear the unknown ionosphere delay parameters can no longer be lumped with other unknown parameters in this model. Therefore, we will now start with the model of eq. (4.49), i.e. before the ionosphere is reparameterized, and add an ionosphere (pseudo) observable for each satellite that comes from the ionosphere map. Additionally, since we can no longer lump the satellite DCBs with the ionosphere parameters, they will need to be estimated or corrected. Thus we will also include the DCBs, that can be seen as part of our external ionosphere data, as pseudo observables to our model:

$$
E\left\{\begin{bmatrix} \Delta\mathbf{P}^S_{r,P1,k} \\ \Delta\mathbf{P}^S_{r,P2,k} \\ \Delta\boldsymbol{\phi}^S_{r,L1,k} \\ \Delta\boldsymbol{\phi}^S_{r,L2,k} \\ \tilde{\boldsymbol{\mathcal{I}}}^S_{r,k} \\ \tilde{\boldsymbol{d}}^S_{PI,k} \end{bmatrix}\right\} =
$$

$$
\begin{bmatrix}
-\mathbf{e}^{S*}_{r,k} & c\mathbf{u}_m & c\mathbf{u}_m & & & \mathbf{I}_m & & & -c\mathbf{I}_m & & \\
-\mathbf{e}^{S*}_{r,k} & c\mathbf{u}_m & \gamma c\mathbf{u}_m & & & \gamma\mathbf{I}_m & & & -\gamma c\mathbf{I}_m & & \\
-\mathbf{e}^{S*}_{r,k} & c\mathbf{u}_m & & c\mathbf{u}_m & & -\mathbf{I}_m & \lambda_1\mathbf{I}_m & & & -c\mathbf{I}_m & \\
-\mathbf{e}^{S*}_{r,k} & c\mathbf{u}_m & & & c\mathbf{u}_m & -\gamma\mathbf{I}_m & & \lambda_2\mathbf{I}_m & & & -c\mathbf{I}_m \\
 & & & & & \mathbf{I}_m & & & & & \\
 & & & & & & & & \mathbf{I}_m & &
\end{bmatrix}
\begin{bmatrix} \Delta\mathbf{r}_r \\ dt_{r,P3,k} \\ d_{r,PI,k} \\ \delta_{r,P3L1,k} \\ \delta_{r,P3L2,k} \\ \boldsymbol{\mathcal{I}}^S_{r,k} \\ \mathbf{A}^S_{r,L1} \\ \mathbf{A}^S_{r,L2} \\ \boldsymbol{d}^S_{PI,k} \\ \boldsymbol{\delta}^S_{P3L1,k} \\ \boldsymbol{\delta}^S_{P3L2,k} \end{bmatrix}
\tag{4.77}
$$

The precision of the pseudo observations depends on the quality of the GIM. To show the equivalence of the presented model with pseudo observables to a model where the receiver observables are corrected with the ionosphere and DCB information we consider the following transformation matrix:

$$
\boldsymbol{D}_{\mathcal{I}} = \begin{bmatrix} 1 & & & & -1 & c \\ & 1 & & & -\gamma & \gamma c \\ & & 1 & & 1 & \\ & & & 1 & \gamma & \\ & & & & 1 & \\ & & & & & 1 \end{bmatrix} \otimes \mathbf{I}_m \tag{4.78}
$$

When the observation vector is premultiplied with $\boldsymbol{D}_{\mathcal{I}}$, we obtain corrected receiver observables (code and phase) and also keep the additional (pseudo) observables for the GIM. Note that the transformation also impacts the covariance matrix of the observables introducing additional variance and correlation on the corrected receiver observables. Since the transformation matrix is of full rank and invertible, we do not loose any information content in the transformation:

$$
\begin{bmatrix} \overline{\Delta\mathbf{P}}^S_{r,P1,k} \\ \overline{\Delta\mathbf{P}}^S_{r,P2,k} \\ \overline{\Delta\boldsymbol{\phi}}^S_{r,L1,k} \\ \overline{\Delta\boldsymbol{\phi}}^S_{r,L2,k} \\ \tilde{\boldsymbol{\mathcal{I}}}^S_{r,k} \\ \tilde{\boldsymbol{d}}^S_{PI,k} \end{bmatrix} = \boldsymbol{D}_{\mathcal{I}} \begin{bmatrix} \Delta\mathbf{P}^S_{r,P1,k} \\ \Delta\mathbf{P}^S_{r,P2,k} \\ \Delta\boldsymbol{\phi}^S_{r,L1,k} \\ \Delta\boldsymbol{\phi}^S_{r,L2,k} \\ \tilde{\boldsymbol{\mathcal{I}}}^S_{r,k} \\ \tilde{\boldsymbol{d}}^S_{PI,k} \end{bmatrix} = \begin{bmatrix} \Delta\mathbf{P}^S_{r,P1,k} & - & \tilde{\boldsymbol{\mathcal{I}}}^S_{r,k} & + & c\tilde{\boldsymbol{d}}^S_{PI,k} \\ \Delta\mathbf{P}^S_{r,P2,k} & - & \gamma\tilde{\boldsymbol{\mathcal{I}}}^S_{r,k} & + & \gamma c\tilde{\boldsymbol{d}}^S_{PI,k} \\ \Delta\boldsymbol{\phi}^S_{r,L1,k} & + & \tilde{\boldsymbol{\mathcal{I}}}^S_{r,k} & & \\ \Delta\boldsymbol{\phi}^S_{r,L2,k} & + & \gamma\tilde{\boldsymbol{\mathcal{I}}}^S_{r,k} & & \\ \tilde{\boldsymbol{\mathcal{I}}}^S_{r,k} & & & & \\ \tilde{\boldsymbol{d}}^S_{PI,k} & & & & \end{bmatrix} \tag{4.79}
$$

To form the positioning model for the corrected observations of eq. (4.79) we premultiply the design matrix with the same transformation matrix. Since the transformation is invertible the resulting model is equivalent to the model of eq. (4.77) where the receiver observables were not corrected. The unknown parameters are kept identical and neither the redundancy nor the rank of the design matrix are impacted:

$$E\left\{\begin{bmatrix} \overline{\Delta\mathbf{P}}^S_{r,P1,k} \\ \overline{\Delta\mathbf{P}}^S_{r,P2,k} \\ \overline{\Delta\boldsymbol{\phi}}^S_{r,L1,k} \\ \overline{\Delta\boldsymbol{\phi}}^S_{r,L2,k} \\ \tilde{\boldsymbol{\mathcal{I}}}^S_{r,k} \\ \tilde{\boldsymbol{d}}^S_{PI,k} \end{bmatrix}\right\} = \begin{bmatrix} -\mathbf{e}^{S*}_{r,k} & c\mathbf{u}_m & c\mathbf{u}_m & & & & & & & & \\ -\mathbf{e}^{S*}_{r,k} & c\mathbf{u}_m & \gamma c\mathbf{u}_m & & & & & & & & \\ -\mathbf{e}^{S*}_{r,k} & c\mathbf{u}_m & & c\mathbf{u}_m & & & \lambda_1\mathbf{I}_m & & & -c\mathbf{I}_m & \\ -\mathbf{e}^{S*}_{r,k} & c\mathbf{u}_m & & & c\mathbf{u}_m & & & \lambda_2\mathbf{I}_m & & & -c\mathbf{I}_m \\ & & & & & \mathbf{I}_m & & & & & \\ & & & & & & & & \mathbf{I}_m & & \end{bmatrix} \begin{bmatrix} \Delta\mathbf{r}_r \\ dt_{r,P3,k} \\ dt_{r,PI,k} \\ \delta_{r,P3L1,k} \\ \delta_{r,P3L2,k} \\ \boldsymbol{\mathcal{I}}^S_{r,k} \\ \mathbf{A}^S_{r,L1} \\ \mathbf{A}^S_{r,L2} \\ \boldsymbol{dt}^S_{PI,k} \\ \boldsymbol{\delta}^S_{P3L1,k} \\ \boldsymbol{\delta}^S_{P3L2,k} \end{bmatrix} \tag{4.80}$$

After this transformation the m unknown ionosphere delays only appear in the m observation equations of the ionosphere (pseudo) observations. Similarly the m unknown DCB parameters only appear in the m observation equations for the DCB (pseudo) observations. Therefore, the ionosphere and DCB (pseudo) observables are free variates in the transformed model. Free variates do not contribute to the solution of the remaining parameters in the adjustment and may therefore be omitted from the model (Teunissen, 2000a):

$$E\left\{\begin{bmatrix} \overline{\Delta\mathbf{P}}^S_{r,P1,k} \\ \overline{\Delta\mathbf{P}}^S_{r,P2,k} \\ \overline{\Delta\boldsymbol{\phi}}^S_{r,L1,k} \\ \overline{\Delta\boldsymbol{\phi}}^S_{r,L2,k} \end{bmatrix}\right\} = \begin{bmatrix} -\mathbf{e}^{S*}_{r,k} & c\mathbf{u}_m & c\mathbf{u}_m & & & & & & \\ -\mathbf{e}^{S*}_{r,k} & c\mathbf{u}_m & \gamma c\mathbf{u}_m & & & & & & \\ -\mathbf{e}^{S*}_{r,k} & c\mathbf{u}_m & & c\mathbf{u}_m & & \lambda_1\mathbf{I}_m & & -c\mathbf{I}_m & \\ -\mathbf{e}^{S*}_{r,k} & c\mathbf{u}_m & & & c\mathbf{u}_m & & \lambda_2\mathbf{I}_m & & -c\mathbf{I}_m \end{bmatrix} \begin{bmatrix} \Delta\mathbf{r}_r \\ dt_{r,P3,k} \\ dt_{r,PI,k} \\ \delta_{r,P3L1,k} \\ \delta_{r,P3L2,k} \\ \mathbf{A}^S_{r,L1} \\ \mathbf{A}^S_{r,L2} \\ \boldsymbol{\delta}^S_{P3L1,k} \\ \boldsymbol{\delta}^S_{P3L2,k} \end{bmatrix} \tag{4.81}$$

If no dynamic model is available for the ionosphere delays, using the reduced model of eq. (4.81) has the advantage that since it is not explicitly present in the state vector, we can simply ignore it in the time update of a Kalman filter. If we *do* want to use a dynamic model for the ionosphere delay we should use the complete model of eq. (4.77) instead. Remaining rank deficiencies in eq. (4.81) exist between the ambiguities and the hardware delays. These are solved similar to the previous models: the satellite hardware delays are lumped with the ambiguity terms and the ambiguity of the first (or reference) satellite is lumped with the receiver differential hardware delay and subtracted from all other ambiguities:

$$E\left\{\begin{bmatrix}\overline{\Delta\mathbf{P}}^{S}_{r,P1,k}\\ \overline{\Delta\mathbf{P}}^{S}_{r,P2,k}\\ \overline{\Delta\boldsymbol{\phi}}^{S}_{r,L1,k}\\ \overline{\Delta\boldsymbol{\phi}}^{S}_{r,L2,k}\end{bmatrix}\right\}=\begin{bmatrix}-\mathbf{e}^{S*}_{r,k} & c\mathbf{u}_m & c\mathbf{u}_m & & & & \\ -\mathbf{e}^{S*}_{r,k} & c\mathbf{u}_m & \gamma c\mathbf{u}_m & & & & \\ -\mathbf{e}^{S*}_{r,k} & c\mathbf{u}_m & & c\mathbf{u}_m & & \lambda_1\mathbf{I}^{0\cdots0}_{m-1} & \\ -\mathbf{e}^{S*}_{r,k} & c\mathbf{u}_m & & & c\mathbf{u}_m & & \lambda_2\mathbf{I}^{0\cdots0}_{m-1}\end{bmatrix}\begin{bmatrix}\Delta\mathbf{r}_r\\ dt_{r,P3,k}\\ d_{r,PI,k}\\ \bar{\delta}_{r,P3L1,k}\\ \bar{\delta}_{r,P3L2,k}\\ \bar{\mathbf{A}}^{1S}_{r,L1}\\ \bar{\mathbf{A}}^{1S}_{r,L2}\end{bmatrix} \tag{4.82}$$

The model of eq. (4.82) is of full rank, and all unknown parameters can be estimated from a single epoch of data. The redundancy and the minimal number of satellites are presented in table D.8 for different numbers of epochs. An inspection of the table shows a high redundancy of this model compared to the previously presented models.

One should note that the ionosphere (pseudo) observables from a GIM are generally strongly correlated in time. Consequently the corrected observables are polluted by these time correlated errors. This type of time correlated error can be dealt with via state vector augmentation if it can be modeled as a Gauss-Markov process, similarly to the approach suggested in section 6.3 for the pseudo range multipath errors. In this case we reintroduce a (residual) ionosphere parameter per satellite to the model of eq. (4.81). Or we can directly take the time correlation into account when introducing the ionosphere pseudo observables as we will do in the next section.

4.9.1 Residual ionosphere estimation

As mentioned, errors in a Global Ionosphere Map, are often strongly correlated in time. To see how we can deal with this time correlation we go back to the model of eq. (4.49) one more time. We will again introduce ionosphere pseudo observations to the model but now taking into account their time correlation. However, to keep the number of parameters to a managable number we first combine the satellite DCBs with the ionosphere parameters and make the necessary adaptions to the satellite differential phase delays:

$$\begin{aligned}\bar{\boldsymbol{\mathcal{I}}}^{S}_{r,k} &= \boldsymbol{\mathcal{I}}^{S}_{r,k}-c\boldsymbol{d}^{S}_{PI,k} & & \\ \bar{\boldsymbol{\delta}}^{S}_{L1,k} &= \boldsymbol{\delta}^{S}_{P3L1,k}+\boldsymbol{d}^{S}_{PI,k} &=& \boldsymbol{\delta}^{S}_{L1,k}-\tfrac{\gamma+1}{\gamma-1}\boldsymbol{d}^{S}_{P1,k}+\tfrac{2}{\gamma-1}\boldsymbol{d}^{S}_{P2,k}\\ \bar{\boldsymbol{\delta}}^{S}_{L2,k} &= \boldsymbol{\delta}^{S}_{P3L2,k}+\boldsymbol{d}^{S}_{PI,k} &=& \boldsymbol{\delta}^{S}_{L2,k}-\tfrac{2\gamma}{\gamma-1}\boldsymbol{d}^{S}_{P1,k}+\tfrac{\gamma+1}{\gamma-1}\boldsymbol{d}^{S}_{P2,k}\end{aligned} \tag{4.83}$$

This reduces the model to:

$$E\left\{\begin{bmatrix} \Delta\mathbf{P}^{S}_{r,P1,k} \\ \Delta\mathbf{P}^{S}_{r,P2,k} \\ \Delta\boldsymbol{\phi}^{S}_{r,L1,k} \\ \Delta\boldsymbol{\phi}^{S}_{r,L2,k} \end{bmatrix}\right\} =$$

$$\begin{bmatrix} -\mathbf{e}^{S*}_{r,k} & c\mathbf{u}_m & c\mathbf{u}_m & & & \mathbf{I}_m & & & & \\ -\mathbf{e}^{S*}_{r,k} & c\mathbf{u}_m & \gamma c\mathbf{u}_m & & & \gamma\mathbf{I}_m & & & & \\ -\mathbf{e}^{S*}_{r,k} & c\mathbf{u}_m & & c\mathbf{u}_m & & -\mathbf{I}_m & \lambda_1\mathbf{I}_m & & -c\mathbf{I}_m & \\ -\mathbf{e}^{S*}_{r,k} & c\mathbf{u}_m & & & c\mathbf{u}_m & -\gamma\mathbf{I}_m & & \lambda_2\mathbf{I}_m & & -c\mathbf{I}_m \end{bmatrix} \begin{bmatrix} \Delta\mathbf{r}_r \\ dt_{r,P3,k} \\ d_{r,PI,k} \\ \delta_{r,P3L1,k} \\ \delta_{r,P3L2,k} \\ \bar{\boldsymbol{\mathcal{I}}}^{S}_{r,k} \\ \mathbf{A}^{S}_{r,L1} \\ \mathbf{A}^{S}_{r,L2} \\ \bar{\boldsymbol{\delta}}^{S}_{L1,k} \\ \bar{\boldsymbol{\delta}}^{S}_{L2,k} \end{bmatrix} \tag{4.84}$$

Similarly we combine the ionosphere pseudo observables from the GIM with the satellite DCBs from the same:

$$\tilde{\tilde{\boldsymbol{\mathcal{I}}}}^{S}_{r,k} = \tilde{\boldsymbol{\mathcal{I}}}^{S}_{r,k} - c\tilde{\boldsymbol{d}}^{S}_{PI,k} \tag{4.85}$$

For this combined pseudo observable we assume the following AR(1) process:

$$\tilde{\tilde{\boldsymbol{\mathcal{I}}}}^{S}_{r,k} = -a_1\tilde{\tilde{\boldsymbol{\mathcal{I}}}}^{S}_{r,k-1} + \varepsilon_{\mathcal{I}k} \tag{4.86}$$

If we now add the additional observable to the model we need to extend the state vector with an additional term per satellite which represents the time correlated error in the ionosphere model:

$$E\left\{\begin{bmatrix} \Delta\mathbf{P}^{S}_{r,P1,k} \\ \Delta\mathbf{P}^{S}_{r,P2,k} \\ \Delta\boldsymbol{\phi}^{S}_{r,L1,k} \\ \Delta\boldsymbol{\phi}^{S}_{r,L2,k} \\ \tilde{\tilde{\boldsymbol{\mathcal{I}}}}^{S}_{r,k} \end{bmatrix}\right\} =$$

$$\begin{bmatrix} -\mathbf{e}^{S*}_{r,k} & c\mathbf{u}_m & c\mathbf{u}_m & & & \mathbf{I}_m & & & & & \\ -\mathbf{e}^{S*}_{r,k} & c\mathbf{u}_m & \gamma c\mathbf{u}_m & & & \gamma\mathbf{I}_m & & & & & \\ -\mathbf{e}^{S*}_{r,k} & c\mathbf{u}_m & & c\mathbf{u}_m & & -\mathbf{I}_m & & \lambda_1\mathbf{I}_m & & -c\mathbf{I}_m & \\ -\mathbf{e}^{S*}_{r,k} & c\mathbf{u}_m & & & c\mathbf{u}_m & -\gamma\mathbf{I}_m & & & \lambda_2\mathbf{I}_m & & -c\mathbf{I}_m \\ & & & & & \mathbf{I}_m & -\mathbf{I}_m & & & & \end{bmatrix} \begin{bmatrix} \Delta\mathbf{r}_r \\ dt_{r,P3,k} \\ d_{r,PI,k} \\ \delta_{r,P3L1,k} \\ \delta_{r,P3L2,k} \\ \bar{\boldsymbol{\mathcal{I}}}^{S}_{r,k} \\ \boldsymbol{\delta\mathcal{I}}^{S}_{r,k} \\ \mathbf{A}^{S}_{r,L1} \\ \mathbf{A}^{S}_{r,L2} \\ \bar{\boldsymbol{\delta}}^{S}_{L1,k} \\ \bar{\boldsymbol{\delta}}^{S}_{L2,k} \end{bmatrix}$$

(4.87)

In this model the ionosphere pseudo observable does not have any observation noise (the stochastic properties are completely captured by the time correlated error). Like before we can pre-multiply the observations and design matrix with an invertible transformation matrix to reach the following model with corrected pseudo range and carrier phase observables. Note that now the variance matrix of the receiver observations does *not* change since the pseudo observables have no observation noise:

$$E\left\{\begin{bmatrix} \overline{\Delta\mathbf{P}}^{S}_{r,P1,k} \\ \overline{\Delta\mathbf{P}}^{S}_{r,P2,k} \\ \overline{\Delta\boldsymbol{\phi}}^{S}_{r,L1,k} \\ \overline{\Delta\boldsymbol{\phi}}^{S}_{r,L2,k} \\ \tilde{\bar{\boldsymbol{\mathcal{I}}}}^{S}_{r,k} \end{bmatrix}\right\} =$$
$$\begin{bmatrix} -\mathbf{e}^{S*}_{r,k} & c\mathbf{u}_m & c\mathbf{u}_m & & & & \mathbf{I}_m & & & & \\ -\mathbf{e}^{S*}_{r,k} & c\mathbf{u}_m & \gamma c\mathbf{u}_m & & & & \gamma\mathbf{I}_m & & & & \\ -\mathbf{e}^{S*}_{r,k} & c\mathbf{u}_m & & c\mathbf{u}_m & & & -\mathbf{I}_m & \lambda_1\mathbf{I}_m & & -c\mathbf{I}_m & \\ -\mathbf{e}^{S*}_{r,k} & c\mathbf{u}_m & & & c\mathbf{u}_m & & -\gamma\mathbf{I}_m & & \lambda_2\mathbf{I}_m & & -c\mathbf{I}_m \\ & & & & & \mathbf{I}_m & -\mathbf{I}_m & & & & \end{bmatrix} \begin{bmatrix} \Delta\mathbf{r}_r \\ dt_{r,P3,k} \\ d_{r,PI,k} \\ \delta_{r,P3L1,k} \\ \delta_{r,P3L2,k} \\ \bar{\boldsymbol{\mathcal{I}}}^{S}_{r,k} \\ \boldsymbol{\delta\mathcal{I}}^{S}_{r,k} \\ \mathbf{A}^{S}_{r,L1} \\ \mathbf{A}^{S}_{r,L2} \\ \bar{\boldsymbol{\delta}}^{S}_{L1,k} \\ \bar{\boldsymbol{\delta}}^{S}_{L2,k} \end{bmatrix} \tag{4.88}$$

In this model the ionosphere pseudo observable has again become a free variate which we can leave out of the model:

$$E\left\{\begin{bmatrix} \overline{\Delta\mathbf{P}}^{S}_{r,P1,k} \\ \overline{\Delta\mathbf{P}}^{S}_{r,P2,k} \\ \overline{\Delta\boldsymbol{\phi}}^{S}_{r,L1,k} \\ \overline{\Delta\boldsymbol{\phi}}^{S}_{r,L2,k} \end{bmatrix}\right\} =$$
$$\begin{bmatrix} -\mathbf{e}^{S*}_{r,k} & c\mathbf{u}_m & c\mathbf{u}_m & & & \mathbf{I}_m & & & & \\ -\mathbf{e}^{S*}_{r,k} & c\mathbf{u}_m & \gamma c\mathbf{u}_m & & & \gamma\mathbf{I}_m & & & & \\ -\mathbf{e}^{S*}_{r,k} & c\mathbf{u}_m & & c\mathbf{u}_m & & -\mathbf{I}_m & \lambda_1\mathbf{I}_m & & -c\mathbf{I}_m & \\ -\mathbf{e}^{S*}_{r,k} & c\mathbf{u}_m & & & c\mathbf{u}_m & -\gamma\mathbf{I}_m & & \lambda_2\mathbf{I}_m & & -c\mathbf{I}_m \end{bmatrix} \begin{bmatrix} \Delta\mathbf{r}_r \\ dt_{r,P3,k} \\ d_{r,PI,k} \\ \delta_{r,P3L1,k} \\ \delta_{r,P3L2,k} \\ \boldsymbol{\delta\mathcal{I}}^{S}_{r,k} \\ \mathbf{A}^{S}_{r,L1} \\ \mathbf{A}^{S}_{r,L2} \\ \bar{\boldsymbol{\delta}}^{S}_{L1,k} \\ \bar{\boldsymbol{\delta}}^{S}_{L2,k} \end{bmatrix} \tag{4.89}$$

The remaining rank deficiencies between the ambiguities and the hardware delays are solved as before (the satellite hardware delays are lumped with the ambiguity terms and the ambiguity of the reference satellite is lumped with the receiver differential hardware delay and subtracted from all other ambiguities):

$$E\left\{\begin{bmatrix}\overline{\Delta\mathbf{P}}^{S}_{r,P1,k}\\ \overline{\Delta\mathbf{P}}^{S}_{r,P2,k}\\ \overline{\Delta\boldsymbol{\phi}}^{S}_{r,L1,k}\\ \overline{\Delta\boldsymbol{\phi}}^{S}_{r,L2,k}\end{bmatrix}\right\}=\begin{bmatrix}-\mathbf{e}^{S*}_{r,k} & c\mathbf{u}_m & c\mathbf{u}_m & & & \mathbf{I}_m & & \\ -\mathbf{e}^{S*}_{r,k} & c\mathbf{u}_m & \gamma c\mathbf{u}_m & & & \gamma\mathbf{I}_m & & \\ -\mathbf{e}^{S*}_{r,k} & c\mathbf{u}_m & & c\mathbf{u}_m & & -\mathbf{I}_m & \lambda_1\overset{0\cdots0}{\mathbf{I}_{m-1}} & \\ -\mathbf{e}^{S*}_{r,k} & c\mathbf{u}_m & & & c\mathbf{u}_m & -\gamma\mathbf{I}_m & & \lambda_2\overset{0\cdots0}{\mathbf{I}_{m-1}}\end{bmatrix}\begin{bmatrix}\Delta\mathbf{r}_r\\ dt_{r,P3,k}\\ d_{r,PI,k}\\ \bar{\delta}_{r,P3L1,k}\\ \bar{\delta}_{r,P3L2,k}\\ \boldsymbol{\delta\mathcal{I}}^{S}_{r,k}\\ \bar{\mathbf{A}}^{1S}_{r,L1}\\ \bar{\mathbf{A}}^{1S}_{r,L2}\end{bmatrix} \tag{4.90}$$

The final model for the ionosphere corrected observations at first glance seems quite similar to the model we found in eq. (4.55) where we did not use an external ionosphere model. However, there are some important differences. Firstly, we now have to estimate the receiver DCB, as we cannot lump it with the ionosphere parameters. Secondly, the estimated differential code phase biases are subtly different as they are not biased by the ionosphere-free combination of the receiver code clock offsets. And finally, in eq. (4.90) rather than estimating the entire ionosphere delay we only estimate a residual ionosphere term. This can be seen as the estimation of the error in the GIM model. The advantage of estimating a residual term rather than the complete ionosphere delay is that we have an expectation of zero for these parameters and we could add a pseudo observation for each additional unknown, thereby not impacting the redundancy of eq. (4.81), and they can be constrained with a much stronger dynamic model.

4.10 Summary and conclusions

When enough satellites and measurement epochs are available, the estimated receiver coordinates are not affected by any rank efficiencies in the SPP and PPP models because the unit direction vectors from the receiver to the satellites are different for each satellite. This means that if no unmodeled errors occur, the position can be estimated without biases. If a zenith troposphere delay parameter is included in the estimation it will also remain unbiased, and in this respect the zenith troposphere parameter can be viewed as a fourth coordinate for the estimation process.

The GNSS measurement model contains a rank deficiency between the clock offsets and the hardware delays. As a result the estimated clocks are always biased by the hardware delays. The specific combination of hardware delay terms depends on the used observations and positioning model. It is therefore often more appropriate to consider the clock offset that pertains to a certain observable rather than the unbiased clock offset of a satellite or receiver.

From single frequency code-only or phase-only observations the ionosphere cannot be estimated, which means that single frequency users will have to rely on an external ionosphere model to correct the observations for the ionosphere delay. The ionosphere can be estimated from dual frequency observations or single frequency code and phase observations. However, the estimates will be biased by differential hardware delays.

More generally, the analysis in this chapter revealed that, if the satellite clock offsets are not provided for each observable some of the estimated parameters will become biased by the satellite differential hardware delays. This does not always negatively impact the user positioning, e.g. when no differential hardware delays are available and the ionosphere delays are estimated without any additional constraints, the ionosphere estimates will be biased and the estimated receiver clock offset will pertain to the ionosphere-free linear combination, but without impacting the receiver position estimate.

However, if unbiased estimates are needed e.g. when we intend to strengthen the positioning model by means of external ionosphere information, the differential hardware delays (in this case the DCBs) are required. Additionally the receiver DCB needs to be estimated as it can no longer be lumped with the ionosphere delay parameters. To strengthen the model in this way the ionosphere information can be added to the model in the form of pseudo observables, or the receiver observables can be corrected with the ionosphere information, both approaches leading to the same model. If the ionosphere model is not considered accurate enough a differential term can be estimated without impacting the redundancy, if the differential term has an expectation of zero.

Another case where unbiased estimates are needed is for ambiguity resolution. Thus for ambiguity resolution to be possible for PPP, it is required that the satellite clock offsets are provided for each observable and more specific the phase observations. These observable specific satellite clock offsets do not all have to be provided in full, if at least one clock offset is provided the other clock parameters can be expressed in the form of differential delays. An advantage of providing some of the clock offsets as differential delays is that these delays change much slower over time, which means that they can be provided to the user with a lower update rate. The observable specific receiver offsets can also be expressed as one full clock and a number of differential delays as shown in this chapter. The advantage in this case is that due to their slower changes over time, a more strict dynamic model can be used to strengthen the positioning model.

From the phase-only models, only between satellite single differenced ambiguities can be estimated without being biased by receiver dependent terms, since a rank deficiency exists between the ambiguities and the receiver clock offsets. In the dual frequency code and phase model these rank deficiencies instead exist between the ambiguities and the differential hardware delays, which means that also in this model only single differenced ambiguities can be estimated without being biased by receiver dependent terms.

The phase-only models showed that the presence of the unknown phase ambiguities prevent the estimation of the receiver position from a single epoch of data. For code and phase (Kalman) filter implementation, this means that, if the ambiguities cannot be resolved from a single epoch, the position coordinates and other unknown parameters are first estimated from the code observations with the corresponding uncertainty. Only after the ambiguities have been estimated with enough precision will the phase measurements start to contribute to the estimation of the other parameters.

Satellite Orbit and Clock Data for PPP 5

GNSS single point positioning techniques rely on satellite positions and clock offsets which are estimated by a global network of GNSS receivers. Therefore, the positioning accuracy that can be achieved by single point positioning is directly dependent on the accuracy of the estimated satellite positions and clock offsets. This chapter will give an overview of currently available satellite products in section 5.1 and develpoments in section 5.2, before providing a quality analysis of several PPP products that are available in real-time in section 5.3. In section 5.4, the results are compared to those of other authors, and finally section 5.5 draws conclusions on the findings.

5.1 Sources of satellite orbit and clock products

5.1.1 Broadcast ephemerides

Basic GPS positioning relies on the satellite orbits and clock offsets determined by the GPS Control Segment which currently includes 16 monitoring stations worldwide (gps.gov, 2015). The accuracy of the broadcast ephemeris is routinely monitored by the IGS analysis centers and shows a clear improvement over the years. Currently the broadcast orbits have a root-mean-square (rms) error of 1m and the satellite clock offsets have an rms error of 1.5m and a standard deviation of 0.75m, computed by removing a constant bias per satellite (IGS, 2015b,a). This is an accuracy improvement of a factor larger than 10 w.r.t. the accuracy when selective availability was still in place and another improvement of a factor of 2-3 since selective availability was switched off at 04:00 UTC on May 2, 2000. However, the current accuracy is still not high enough for the purpose of PPP, which means that we need another source of satellite orbit and clock products. Several initiatives have been launched over the last decades to provide GNSS users with satellite orbits and clocks of higher accuracy.

It should be noted that the GPS broadcast products are provided in a recent version of the World Geodetic System 1984 reference frame (currently WGS84 G1150) while the other products are provided in a recent version of the International Terrestrial Reference Frame (currently ITRF2008). Differences between WGS84 and ITRF are at centimeter level worldwide (NIMA, 2004) and no official (Helmert) transformation parameters are available. In the following we will assume that the WGS84 coordinates are expressed in ITRF with an accuracy of a few centimeters. However, since the errors in the broadcast products are much larger, this should not impact the results provided in section 5.3, where we assess the accuracy of the broadcast products by comparing them to the precise IGS products (in

ITRF2008).

The GPS broadcast satellite orbit and clock information is transmitted to the user by the GPS satellites as a set of parameters in the navigation message. These parameters enable a user to determine the satellite positions and clock offsets via the closed form formulae defined in the user algorithm for ephemeris determination in the GPS interface specification (IS-GPS-200D, 2004). Several PPP products (introduced below) are provided as corrections to the broadcast ephemeris solely to decrease the amount of data that needs to be transmitted to the user. A user can simply evaluate the closed form formulae and apply the corrections to the outcome. This is a simple deterministic procedure and does not impact the stochastic properties of the PPP products. The Issue Of Data of the Ephemeris (IODE) identifies the ephemeris that should be used for each of the corrections.

The accuracy of the GLONASS broadcast products has traditionally been worse than the GPS broadcast products by a factor of 7-8 (Gibbons, 2006). This difference was due to several factors including less stable clocks and orbits of the GLONASS satellites, and a ground monitoring segment limited to Russian territory (Gibbons, 2008). Since then a number of Antarctic research stations have been added to the GLONASS control and monitoring segment (Cameron, 2010). In 2008 Wanninger (2008) reported that the 3-D errors in GLONASS broadcast orbits were about three times larger than the GPS errors. Heng et al. (2011b) report that this gap has been closed as the GLONASS broadcast products have achieved sub-meter orbital accuracy over the years 2009 to 2011. However, the less stable clocks of the GLONASS satellites further decrease the accuracy for single point positioning (for differential positioning this is less of a problem as the satellite clocks can be eliminated).

Unlike GPS, GLONASS positioning does not use closed form formulae to determine the satellite positions from the ephemeris. Instead, GLONASS satellites broadcast their coordinates and velocity for a reference time, which is updated every 30 minutes. To determine the position at another time instant, within a 15 minute interval from the reference time, the provided position has to be integrated numerically. This leads to a degradation in the orbit accuracy of some 13cm (Heng et al., 2011b). The GLONASS Interface Control Document (GLONASS, 2008) suggests the use of 4th order Runge-Kutta integration but the integration step size is not prescribed, and can be chosen by the user. Consequently, the determined satellite positions and clock offsets depend to some extend on the chosen step size for the numerical integration. This last point is also important for GLONASS precise products, if they are provided w.r.t. the broadcast products. The user should then apply the same integration step size as the service provider.

Chen et al. (2013) investigated the accuracy of the BeiDou broadcast ephemerides and found sub-meter accuracy for the satellites in an Inclined Geosynchronous Orbit (IGSO) or Medium Earth Orbit (MEO) but a 2 m accuracy for the Geostationary (GEO) satellites. Montenbruck et al. (2015) performed a simultaneous analysis of the broadcast products of all available system and found 0.7 m accuracy for GPS, about 1.5 m for Galileo and BeiDou and 1.9 m for GLONASS. QZSS was also included (one satellite only) and found to be accurate to 0.6 m, all over a 12-month period in 2013/2014.

5.1.2 Satellite Based Augmentation System corrections

In 1994 the Federal Aviation Administration (FAA) and the Department of Transportation (DOT) of the United States started the development of WAAS to provide improved accuracy, integrity, availability, and continuity for the use of GPS during all phases of flight in civil aviation. WAAS is a Satellite Based Augmentation Systems (SBAS) that provides additional messages transmitted by geostationary satellites to GPS users in a specific target region (in this case North America). These messages contain corrections on main error sources of GPS, and are computed from a network of monitoring stations located in and around the target region.

In 2003 the WAAS signal became available for aviation across large parts of continental North America, and in 2009 the first precision approaches were performed relying on WAAS augmented GPS positioning. Following in the footsteps of WAAS, the Japanese Multi-functional Satellite Augmentation System (MSAS) and the EGNOS have also become operational, and plans are in place for an Indian GPS Aided Geo Augmented Navigation system (GAGAN) and a Chinese Satellite Navigation Augmentation System (SNAS).

Since December 2001, Delft University of Technology is operating an EGNOS monitor station, which is part of the EGNOS Data Collection Network (EDCN). The EDCN was established by Eurocontrol to continuously monitor and independently assess the performance of the EGNOS system. Just like WAAS, the EGNOS system provides corrections on the satellite positions and clock offsets as well as corrections for the atmosphere for user in a specific service area, in this case the European Civil Aviation Conference (ECAC) Area. While the EGNOS network does track GLONASS satellites, corrections are currently provided without any commitment (GSA, 2014). However, future plans are for EGNOS to support multiple GNSS.

Current SBAS systems primarily focus on position integrity rather than position precision, but SBAS corrections can be used in a PPP-like processing strategy, see e.g. (u-blox, 2015). An advantage of this approach is that the corrections can be retrieved free of charge and without the need for an additional (internet) communication link. However, the correction precision does not match that of dedicated PPP products.

5.1.3 Precise satellite and clock products from the IGS

Precise satellite ephemeris and satellite clock information, needed for PPP, have been available from the International GNSS Service (then called International GPS Service) since 1992 even 2 years before its official start (Beutler et al., 1999). This orbit information is determined in post-processing and at first was only available around two weeks after GPS data acquisition. As a result, PPP was mainly of interest to the scientific and research community for applications in which latency was not important. Since then much effort has been put into decreasing the latency of precise IGS orbit and clock information, first leading to the rapid orbits with about one day of latency and later to the ultra-rapid orbits with 3-9 hours of latency including a predicted part which can be used in real-time. Recently high-accuracy ephemeris data have also become available in real-time from several commercial services (introduced below), so that now PPP methods can be used for a wide range of real-time applications such as offshore positioning, aircraft navigation, high-precision farming.

Table 5.1 displays the currently available IGS satellite orbit and clock products, their accuracy and latency compared to the GPS broadcast ephemeris (IGS, 2015b). This table was downloaded from the IGS website in 2011 and has remained unchanged to 2015, but it is likely to change as a result of the Multi-GNSS Experiment and IGS Real-time Service. For post processing applications, where latency is not an issue, the rapid or even final products can be used. These have accuracy at centimeter level for both satellite positions and clocks, and, using proper PPP software, this results in mm position accuracy for static receivers. This makes PPP a viable and user friendly alternative to network processing. A number of web-based processing services are available including the Automatic Precise Positioning Service from JPL (Muellerschoen et al., 2000b), CSRS-PPP from Natural Resources Canada (Mireault et al., 2008), GPS Analysis and Positioning Software from University of New Brunswick (Leandro et al., 2007), magicGNSS from GMV (Píriz et al., 2008) and Trimble RTX-PP (Doucet et al., 2012). However, for (near) real-time applications (where our main interests lie), only the predicted half of the ultra-rapid products qualify. The ultra-rapid products, released four times per day, contain 48 hours worth of satellite orbits and clock offsets: the first half computed from observations and the second half containing predicted orbits and clock offsets. When the products first become available the measured half is already 3 hours old and the satellite positions at the current epoch can only be computed from the predicted half.

An inspection of the IGS ultra-rapid products (IGU) in table 5.1 reveals that even the predicted half of the orbits has a high accuracy of about 5 centimeters. However, the predicted half of the IGU satellite clocks have a root mean square (rms) of about 90 centimeters. The satellite clock products only reach a comparable high accuracy when based on post-processing of the measurements (i.e. for the observed half of the ultra-rapid products). It is obvious that the accuracy of the satellite clocks are the weak point of the predicted part of the ultra-rapid products. The reason for this difference in accuracy between the predicted clocks and orbits is that the physical process of the satellite oscillators is less well behaved than the very steady movement of the satellites in their orbits. For real-time PPP applications this remains a weak point of the presented IGS products.

One solution to this problem is to use the predicted IGS orbits and compute the satellite clock separately from one or more reference stations. This clock solution then needs to be provided to the PPP user together with the satellite orbits. This solution is the underlying principle of the RETICLE system (Hauschild and Montenbruck, 2008). Corrections from the RETICLE system are also included in the accuracy analysis in section 5.3. A more general solution is to instead rely on corrections from a global network with smaller latencies, which are available from several commercial services and is currently developed as IGS Real-time Service.

The very high accuracy of the final products, which has been the subject of intensive studies performed by the IGS based on independent laser ranging, and repeatability of the products over long time intervals, makes it possible to assess the accuracy of all (near) real-time products by comparison to the final products. This will be the approach in section 5.3.

(IGS, 2015b) also lists precise orbit and clock data for the GLONASS satellites, with a

Table 5.1: IGS Products, downloaded in 2011 and unchanged to 2015 (IGS, 2015b)

IGS Product Table					
GPS Satellite Ephemerides & Satellite Clocks		Accuracy (rms) Precision (σ)	Latency	Updates	Sample Interval
Broadcast	orbits	$\sim$100 cm	real time	-	daily
	clocks	rms $\sim$150 cm σ $\sim$75 cm			
Ultra-Rapid (predicted half)	orbits	$\sim$5 cm	real time	at 03, 09, 15, 21 UTC	15 min
	clocks	rms $\sim$90 cm σ $\sim$45 cm			
Ultra-Rapid (observed half)	orbits	$\sim$3 cm	3 - 9 hours	at 03, 09, 15, 21 UTC	15 min
	clocks	rms $\sim$4.5 cm σ $\sim$1.5 cm			
Rapid	orbits	$\sim$2.5 cm	17 - 41 hours	at 17 UTC daily	15 min
	clocks	rms $\sim$2.3 cm σ $\sim$0.75 cm			5 min
Final	orbits	$\sim$2.5 cm	12 - 18 days	every Thursday	15 min
	clocks	rms $\sim$2.3 cm σ $\sim$0.60 cm			30s

Note 1: Orbit accuracies are 1D mean rms values over the three XYZ geocentric components. IGS accuracy limits, except for predicted orbits, are based on comparisons with independent laser ranging results and discontinuities between consecutive days. The precision is better.
Note 2: The accuracy (neglecting any contributions from internal instrumental delays, which must be calibrated separately) of all clocks is expressed relative to the IGS timescale, which is linearly aligned to GPS time in one-day segments. The standard deviation (σ) values are computed by removing a separate bias for each satellite and station clock, whereas this is not done for the rms values.

reported accuracy of 3 cm. However, there are several limitations:

1. For GLONASS, only IGS final products are available with a latency of 12 to 18 days and a sample interval is 15min. At present only two IGS analysis centers compute (ultra)rapid products CODE and ESA/ESOC, which is not enough for an IGS combined product (Springer and Dach, 2010). Furthermore, only the latter contains satellite clock data.

2. There are only separate GPS and GLONASS products from the IGS, no GPS + GLONASS combined products are available. This means that these products might not be fully consistent. CODE and ESA/ESOC *do* provide combined products (Springer and Dach, 2010).

3. Torre and Caporali (2015) compared precise products from different analysis centers for the available GNSS and report that, while results are very consistent for GPS, precise products for other GNSS still show significant inconsistencies between analysis centers.

5.1.4 Commercial services

5.1.4.1 Precise satellite and clock products from the JPL

Another source of PPP corrections is the Global Differential GPS (GDGPS) System from the Jet Propulsion Laboratory (JPL). JPL estimates precise real-time orbit and clock solutions from a global network of about 100 stations with their Real Time GIPSY software. Their approach is to then subtract the GPS broadcast ephemeris from these precise products to generate orbit and clock corrections for the user. In this way the amount of data that has to be transferred to the user is minimized. The GDGPS system provides corrections to the three coordinates of the GPS satellite positions and to the clocks, with accuracies and latencies as reported in table 5.2, downloaded from the JPL website in 2011 and unchanged to 2015 (JPL, 2015). The user can then add the corrections to the broadcast ephemerides to recover the precise orbit and clock of the satellites. The correction messages also include velocities of the orbital corrections, enabling the user to propagate the corrections into the future, and be resilient to short data outages.

The JPL products are available to paying customers from several service providers (e.g. Veripos, Navcom and Fugro), either as a main or backup service, via different media including internet connection and geostationary satellite broadcast. These service providers generally also offer PPP software to the user (either JPL licenced or in the case of Veripos developed inhouse) next to a range of other GNSS related services.

The Veripos Ultra correction stream, which is based on the JPL network, recorded with a Septentrio receiver L-band antenna are included in the accuracy analysis in section 5.3.

Comparison of the IGS products (table 5.1) to the JPL products (table 5.2) reveals some differences in the conventions but more importantly some important differences in the quality and latencies. The comparison is slightly complicated by the differences in the

Table 5.2: JPL precise products, downloaded in 2011 and unchanged to 2015 (JPL, 2015)

Attribute		Performance
Accuracy	Orbits	$<$ 20 cm 3D rms
	Clocks	$<$ 20 cm rms (after de-biasing and de-trending)
	URE	$<$ 10 cm rms
Latency		4-6 seconds
Time span		Complete information in 32 seconds
Frequency	Orbits	30 seconds
	Clocks	1 second

reported accuracy measures (e.g. for the satellite orbits, the IGS reports 1D root-mean-square (rms) values while JPL reports 3D rms values). If the correlation between the directions and products would be available, one could be translated into the other, but unfortunately it is not. Also the exact procedures are not reported here. That strong correlation *does* exist between the products is revealed by accuracy of the User Range Error (URE) in table 5.2 (which is a measure for the error that a user can expect on the range if the precise satellite orbits and clocks are used) which is better than the accuracy of precise satellite clocks. Despite the difficulties in the comparison of the IGS and JPL products, the following can be observed:

The JPL products, even though based on observations, have a very low latency ($\sim$5 s) and can consequently be used for real-time applications, while the observation-based IGS products have a latency of at least 3 hours, and cannot be used for real-time applications. Therefore, a comparison of the accuracies for real-time PPP should primary focus on the IGS predicted products vs the JPL corrections. Then it becomes clear that the IGS orbits are somewhat better, but the predicted IGS clocks are worse than the JPL products. Even if we compare the standard deviation of the IGS clocks to the rms of the JPL clocks (since the latter have biases and trends removed) there remains a factor two difference. Since the predicted IGS satellite clocks have the lowest accuracy of all real-time products under consideration, it can be expected that real-time PPP will perform better with JPL corrections than with IGS predicted products. This comparison will be extended with the quality analysis in section 5.3.

5.2 Developments

As mentioned in section 2.3, two important developments in PPP are towards the use of multiple constellations and ambiguity resolution. Much effort has been spent by the providers of precise satellite orbit and clock products to support these developments.

As mentioned GPS + GLONASS products have been available from CODE and ESA/ESOC for some time. Real-time precise orbit and clock products for the Galileo test satellites were first made available based on the CONGO network (Montenbruck et al., 2009). Precise products for the BeiDou system were developed at Wuhan university (Shi et al., 2012; Zhao et al., 2013). The RETICLE system has also already been extended to provide multi-constellation products in near real-time via the N-trip protocol. And the IGS started the

Multi-GNSS Experiment (IGS M-GEX) with the provision of multi-GNSS IGS products as one of its goals (Montenbruck et al., 2013), and has come close to being operational.

Commercial parties have also started to support multi-constellation PPP. Fugro first started to provide combined GPS and GLONASS products (Melgard et al., 2010) and have since extended this with Galileo and BeiDou (Tegedor et al., 2015). And Veripos has also developed their own correction service.

Precise satellite orbit and clock products that allow the resolution of integer ambiguities in PPP were made available by the Centre National d'Études Spatiales (CNES) as part of their PPP-WIZARD project (Precise Point Positioning With Integer and Zero-difference Ambiguity Resolution Demonstrator CNES, 2012; Laurichesse and Mercier, 2007). JPL has added ambiguity resolution to their post-processing GIPSY-OASIS software, and several other research institutes have also been working towards PPP products for ambiguity resolution.

5.3 Quality analysis of real-time satellite orbit and clock products

This section contains an analysis and comparison of the quality of several real-time satellite orbit and clock products, by comparison to the very accurate (non real-time) IGS final products. Several authors have previously made similar analyses for the GPS broadcast ephemerides, either considering the orbits only (Warren and Raquet, 2003) or both orbits and clocks (Langley et al., 2000; Cohenour, 2009; Heng et al., 2011c,a). The IGS Analysis Center Coordinator (ACC) also routinely monitors the accuracy of the broadcast and IGU products by comparison to the IGS rapid or final products (IGS, 2015a). In Springer and Hugentobler (2001) the IGS ultra-rapid orbits were shown to have an accuracy of 30cm. Heng et al. (2011b) characterized nominal GLONASS ephemeris errors in a similar manner, but did not consider clock errors. The BeiDou broadcast ephemerides were studied in a similar manner by Chen et al. (2013), and Montenbruck et al. (2015) performed a comparison of all available GNSS.

Our main goal for this analysis is to obtain an accurate description of the quality of the products, which can be used to setup the stochastic and/or dynamic model for the positioning filter and integrity monitoring. Therefore, our approach will be from the point of view of the user and we will focus on the errors that impact the measured pseudo ranges. First the methodology is described, then results are presented, and finally the results and findings are compared to those found by the ACC and Heng et al. (2011c,a).

5.3.1 Methodology

In order to asses real-time PPP product accuracy, three different methods can be considered:

1. Direct comparison of satellite coordinates and clocks. This method simply evaluates

the differences in the coordinates and clock offsets as follows:

$$\begin{array}{lllll} \Delta x^s & = & x^s_{RT} - x^s_{IGS}, & \Delta y^s & = & y^s_{RT} - y^s_{IGS}, \\ \Delta z^s & = & z^s_{RT} - z^s_{IGS}, & \Delta \delta t^s & = & \delta t^s_{RT} - \delta t^s_{IGS} \end{array} \quad (5.1)$$

where x^s, y^s and z^s are the satellite coordinates, δt^s is the satellite clock offset, and the subscripts RT and IGS indicate, respectively, the Real-Time and IGS final products. If we neglect the errors in the IGS final products (since they are much smaller than the errors in the RT products), then the distribution of the differences in eq. (5.1) correspond to the distribution of the errors in the RT products which can thus be evaluated.

Instead of looking at the satellite position errors in x, y and z direction, we can also consider the radial position error:

$$\Delta r^s = \|\mathbf{r}^s_{RT}\| - \|\mathbf{r}^s_{IGS}\| = \sqrt{(x^s_{RT})^2 + (y^s_{RT})^2 + (z^s_{RT})^2} - \sqrt{(x^s_{IGS})^2 + (y^s_{IGS})^2 + (z^s_{IGS})^2} \quad (5.2)$$

For GNSS users on the surface of the Earth the radial position error of the satellite is related to the ranging error by the angle between the satellite position vector and the vector from the user to the satellite, called the (off) nadir angle η. The nadir angle is related to the elevation angle θ as:

$$\eta = sin^{-1}(cos(\theta)\frac{R_E}{r_{GPS}}) \quad (5.3)$$

Figure 5.1 shows the geometrical relation between the radial and tangential position error of the satellite (S) and the error in the range from the satellite to the user (U) on the surface of the Earth for a satellite at the horizon all with respect to the center of the Earth (O). The figure shows that the fraction of the radial position error that impacts the range is $cos\,(\eta)$. The size of this fraction is provided in the top pane of fig. 5.2 as a function of the nadir angle η (top axis) and, for a user on the surface of the Earth, as a function of the elevation angle θ (bottom axis).

For satellites at lower elevation angles the tangential satellite position error (perpendicular to the radial direction) also impacts the geometric range from the satellite to the user. Figure 5.1 shows that the fraction of the tangential position error that impacts the pseudo range error is $sin\,(\eta)$ for an error in the plane containing the center of the Earth, the user and the satellite (errors perpendicular to this plane have a projection of zero on the range). The size of this fraction is shown in the bottom pane of fig. 5.2. The worst geometry is for large nadir angles corresponding to low elevation angles and, for a user on the surface of the Earth, reaches a maximum of about 0.24 (R_E/r_{GPS}) for satellites at the horizon. In other words, the tangential position errors are decreased by a factor of at least 4 for satellites with 0 degrees of elevation, and even much more for satellites with higher elevation. Several authors have averaged the impact of the tangential errors on the range over the footprint of the satellite, which gives a reduction of about a factor 7 for GPS

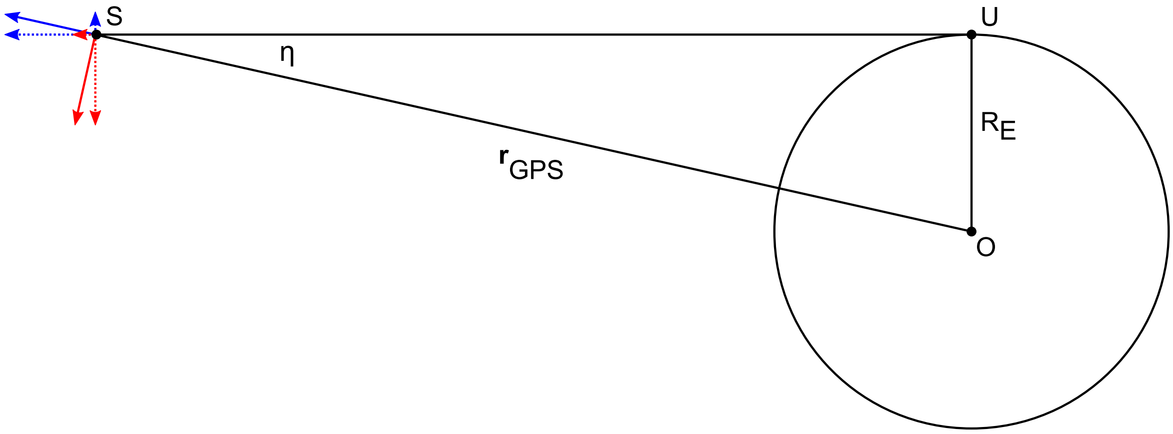

Figure 5.1: Maximum nadir angle for satellite at horizon

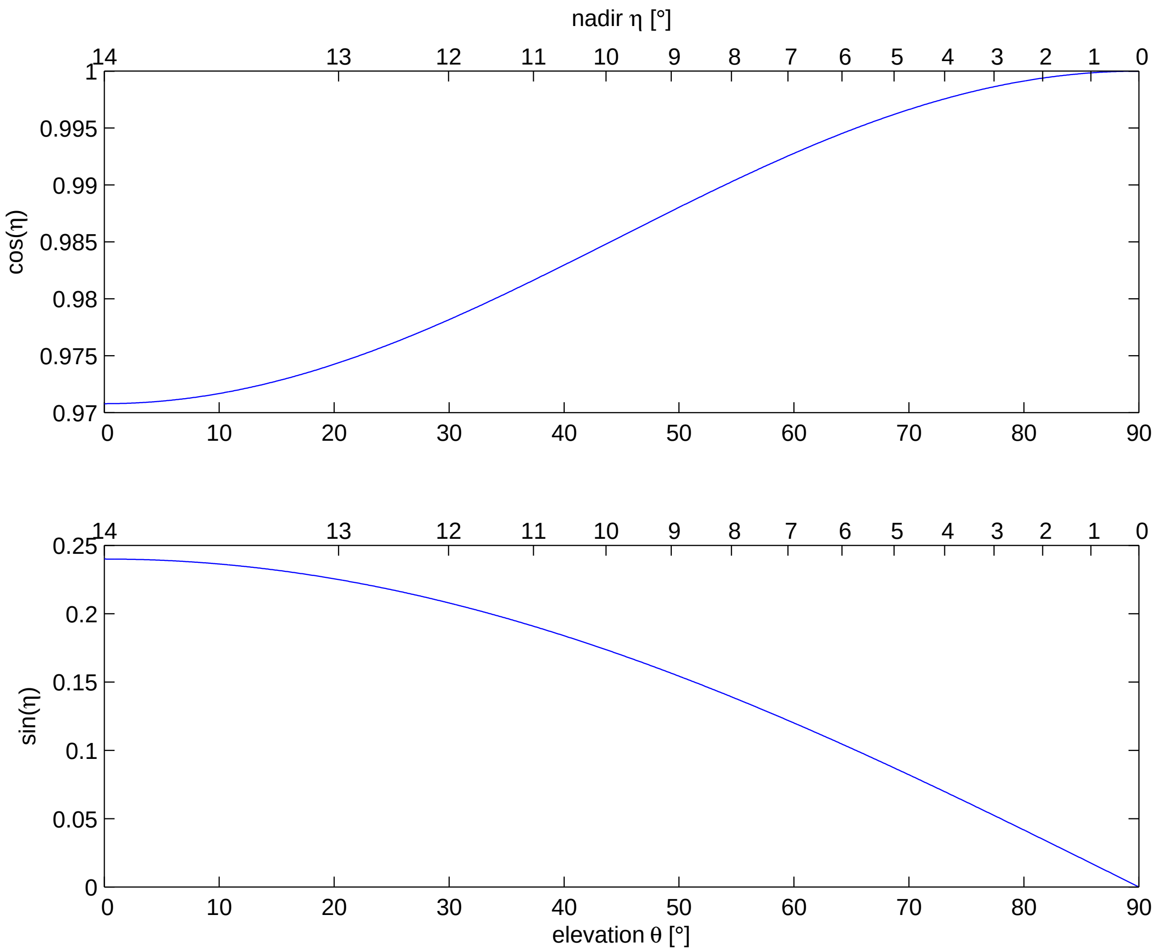

Figure 5.2: Fractional parts of radial and tangential error that impact the range as a function of elevation

satellites (Malys et al., 1997; Warren and Raquet, 2003; Heng et al., 2011c; Chen et al., 2013; Montenbruck et al., 2015).

The radial errors can be used as a first indication of the range errors that can be expected for high elevation satellites and is a more meaningful quality parameter than the position error in e.g. the x direction. However, because the tangential errors are generally *not* smaller than the radial errors (this is be confirmed by the results below), they can not be neglected completely. A more general approach is to project the satellite position error on the range from the satellite to the user. As a consequence, the accuracy analysis becomes dependent on the user position. However, for PPP products this should not have a large influence on the results since PPP is intended for global positioning.

A more important shortcoming of the direct comparison of satellite positions and clock offsets, is that it does not take into account that the errors in the satellite positions can be correlated with the satellite clock errors (which is also confirmed by the results). Therefore we will use the following combined comparison method.

2. Comparison in pseudo range domain. This method aims to determine the remaining User Range Error (URE) due to the satellite orbits and clocks in the pseudo range and carrier phase measurements if RT PPP products are used for positioning. For this purpose, the RT satellite positions and clock offsets are combined with a (virtual) user position to form a pseudo range. The same is done with the IGS final products and the two are again compared to assess the accuracy of the RT products:

$$URE^s_{r,RT} = \Delta\rho^s_r = \underbrace{\|\mathbf{r}^s_{RT} - \mathbf{r}_r\| - c\delta t^s_{RT}}_{\textit{RT pseudorange}} - \left(\underbrace{\|\mathbf{r}^s_{IGS} - \mathbf{r}_r\| - c\delta t^s_{IGS}}_{\textit{IGS pseudorange}}\right) \tag{5.4}$$

where, ρ^s_r is the pseudo range between the user and the satellite, $\mathbf{r}^s_{RT}$ and $\mathbf{r}_r$ are, respectively, the satellite and user position vectors and c is the speed of light. As before, the results of this method will to some extend depend on the chosen user position. For our global quality analysis, the center of the Earth was chosen as user position, but the influence of the user position is also shown when relevant.

Unobservable biases Some biases in the PPP products will not influence the position solution of the user since they cannot be observed by a user (they are absorbed by other parameters in the solution). Therefore such biases should also not be considered in the quality assessment of the PPP products from a user perspective. In this analysis two such biases have been identified.

(a) Common clock or common mode bias. If all pseudo ranges measured at one epoch have a common bias, this bias will be absorbed by the receiver clock bias in the user algorithms. This does not influence the position. Therefore, in this quality assessment, one common bias is removed from all UREs for each epoch (this is simply the mean URE value per epoch) to determine the effective UREs:

$$URE^s_{r,RT,\text{eff}}(t) = \Delta\rho^s_r(t) - \frac{1}{m}\sum_{s=1}^{m}\Delta\rho^s_r(t) \tag{5.5}$$

where m is the total number of satellites. In the results presented in this section a common clock bias has been estimated and removed, except when explicitly stated otherwise.

(b) Constant satellite bias. When relying only on phase measurements in PPP (and without ambiguity fixing), the user is also insensitive to constant biases in the PPP products since these biases will be absorbed by the estimated real-valued phase ambiguities. PPP products which are computed by a network using only phase measurements might include such biases. Also, PPP products for GLONASS might contain this type of bias if the receiver front-end delays are not estimated by the network. Even if the PPP corrections do not contain these biases (which is generally the case for GPS), the floating phase ambiguity will still absorb the mean value of all errors on the corrections for one satellite. In order to assess the effective PPP product accuracy, when processing only carrier phase measurements, these biases (which are simply the mean URE value per satellite) should be removed from the URE.

$$URE^{s}_{r,RT,\mathrm{eff}}\left(t\right) = \Delta\rho^{s}_{r}\left(t\right) - \frac{1}{T}\sum_{t=1}^{T}\Delta\rho^{s}_{r}\left(t\right) \tag{5.6}$$

where T is the total number of epochs considered. However, when processing pseudo range *and* carrier phase measurements together, a user *is* sensitive to this type of biases (they might in turn bias the estimated parameters or result in biased residuals). Therefore, in the results presented in this section the constant satellite biases have *not* been removed, except when explicitly stated.

If both types of biases 2a and 2b are to be removed, an unweighted least squares approach can be used to estimate both simultaneously. A big advantage of method 2 is that it evaluates the errors that are introduced in the measurements of a PPP user. Therefore, the results of this comparison can directly be used to setup the stochastic model for positioning and integrity monitoring.

3. Comparison in user position domain. The final step in the accuracy analysis is to translate the accuracy of the PPP products from the measurement domain to the user position domain. There are several ways to perform this operation:

(a) Propagate the pseudo range errors to the position domain and then determine the distribution. This can e.g. be achieved by a Best Linear Unbiased Estimation (BLUE) where the pseudo range errors are used as observations. The errors in the user position can then be determined as follows:

$$\Delta\mathbf{r}_{r,RT} = \left(A^{*}Q^{-1}_{RT}A\right)^{-1}A^{*}Q^{-1}_{RT}\Delta\rho^{s}_{r,RT} \tag{5.7}$$

where $\Delta\mathbf{r}_{r}$ are the errors in the user position, Q_{RT} is the variance matrix of the RT PPP products determined with method 2 and A is the design matrix. This approach depends on a weighting scheme for the pseudo range errors (in case of the BLUE the inverse of the variance matrix) and on the local satellite geometry through A which should contain only satellites in view.

(b) Propagate the variance matrix of the pseudo range errors to the position domain. This is a more direct approach to translate the errors in the pseudo range to the position domain. For the BLUE this can be performed as follows:

$$Q_{\mathbf{r}_{r,RT}} = \left(A^* Q_{RT}^{-1} A\right)^{-1} \tag{5.8}$$

where $Q_{\mathbf{r}_{r,RT}}$ is the variance in the user position due to the variance of the PPP products.

Equation (5.8) is related to the Dilution of Precision (DOP) which is an often used measure for the expected accuracy of GNSS positioning. The DOP relies on three further assumptions:

i. the satellite products can be described by a scaled identity matrix ($Q_{RT} = \sigma_{RT}^2 \mathbf{I}$), simplifying eq. (5.8) to $Q_{\mathbf{r}_{r,RT}} = \sigma_{RT}^2 \left(A^* A\right)^{-1}$, where σ_{RT}^2 is the variance of the pseudo range errors for the RT PPP products, and $\left(A^* A\right)^{-1}$ is the correlation matrix.

ii. the user position and clock offset are the only unknown parameters, which means $\left(A^* A\right)^{-1}$ is a 4×4 matrix.

iii. there is no correlation between the unknown parameters and the square root of the trace of $\left(A^* A\right)^{-1}$ captures the complete uncertainty in the solution.

Neither of these three assumption is particularly well suited for PPP, where the goal is to reach a very high accuracy (using a realistic variance matrix) and additional unknown parameters (e.g. the troposphere zenith delay) are often also estimated. The relation between eq. (5.8) and the DOP is here only presented for reference. DOP can be expressed for all unknown parameters combined, then called Geometric Dilution of Precision GDOP, or DOP can be expressed for a combination of some components of the unknown parameters including the Position (PDOP), Horizontal component (HDOP), Vertical component (VDOP), and Time (TDOP) each computed with a combination of the elements from $\left(A^* A\right)^{-1}$ (Langley, 1999). The uncertainty in each of these unknown parameters can now be expressed as the uncertainty of the satellite products times the corresponding DOP value ($\sigma_X^2 = XDOP\sigma_{RT}^2$), where X can be the geometry or any of the DOP components (Wells, 1989).

The main advantage of method 3 is that it directly assesses the final effect of using the PPP products on the estimated user position, and is a straight forward and general manner to get a very first impression of the position accuracy that can be achieved with the PPP products.

5.3.2 Results

5.3.2.1 IGS Ultra-rapid products (predicted part)

In this section IGS Ultra-rapid products are analyzed for a one year period from Jun 27, 2010 to Jun 25, 2011. Results from the periodic analysis of the IGS ACC shows an improving accuracy over time (IGS, 2015a). For the predicted orbits the curve has flattened out around 2009, which means that results presented in this section are still representative of the current performance in 2015. The satellite clock predictions on the other hand still show improvement over the last few years. This is in no small part due to the gradual replacement of older GPS satellites by new satellites of a different type with more stable clocks. Results in this section distinguish between these different satellite types, so a reader might focus on the newer satellites that better represent the current performance. More importantly the methods and relations presented in this chapter are general and still apply.

As mentioned, only the predicted IGS products are available for real-time applications. During real-time processing the prediction time will vary from 3 hours, when the ultra-rapid products first become available, to 9 hours, just before the next ultra-rapid products become available. Therefore, the following analysis first focuses on these 6 hours of the IGS Ultra-rapid products, by comparison to the IGS final products. Then the impact of the prediction time is studied by considering the entire 24 hours of predicted data in the Ultra-rapid products. For convenience the acronym IGU will be used for the (predicted) Ultra-rapid products and IGS for the final products in the tables and figures below (following the IGS convention).

First the accuracy of the clock and orbit products are shown individually, then the impact of the errors in the real-time orbit and clock products on the measured ranges is evaluated by means of eq. (5.4). Figure 5.3 shows the distribution of the differences of the satellite clock offsets between IGU and IGS separately for each GPS satellite by means of a boxplot. Satellites are identified by their Pseudo-Random Noise (PRN) sequence. On each box, the central mark is the median clock differences for that satellite, the edges of the box are the 25th and 75th percentiles, the whiskers extend to the most extreme data points not considered outliers, and outliers are plotted individually (McGill et al., 1978).

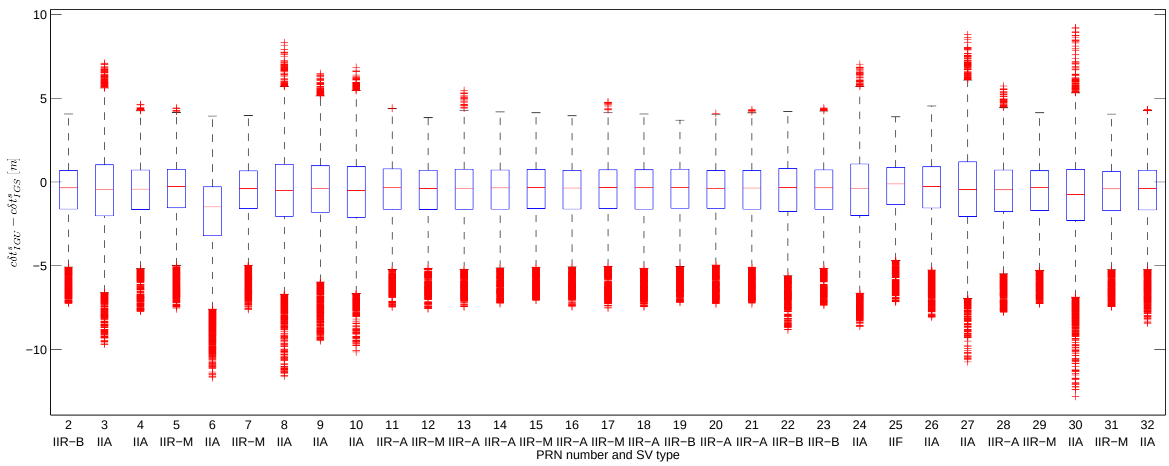

Figure 5.3: Boxplot of IGU (predicted) satellite clock offset w.r.t. IGS final for period Jun 27, 2010 - Jun 25, 2011

Figure 5.3 reveals that the predicted clock offsets have a negative bias of 0.6m over this period. Most boxes, which contain 50% of the data, are between -2m and 1m, only PRN6 has a larger negative bias than all other satellites. It can also be seen that the predicted clock offsets have larger errors for the older GPS block IIA satellites (rms = 2.3m) than the newer block IIR and block IIF satellites (rms = 1.9m). However, the differences are not very large and the errors on both old and new satellites seem much larger than the claimed accuracy of 0.9m (see table 5.1). This apparent discrepancy will be resolved when the common clock bias is removed below, and the difference between the GPS satellite types will also become much more pronounced.

Besides this nominal distribution, clock outliers of over 50m were found for PRN30 on May 13 and 14, 2011 shortly before it was decommissioned (not included in fig. 5.3 for clarity). Notice Advisory to Navstar Users (NANU) 2011042 issued by the United States Coast Guard and the GPS Operations Center, warned not to use PRN30 from 20:55 on May 13, but the IGU files kept including orbit and clock predictions of this satellite for some time after. Figure 5.4 shows how the predicted IGU clock differs from the IGS final clock before and during the occurrence of these outliers. The figure also shows the most recent IGU file available at each epoch and the moment at which PRN30 was no longer supposed to be used according to the NANU. The figure shows that the clock prediction starts to degrade from 15:00 hours (during the validity of igu16355_12.sp3) and reaches an error of almost 9m just before the NANU message kicks in. After that the clock error quickly grows to about 55m and remains at that level during the validity of igu16355_18.sp3. The standard deviation of the satellite clock prediction (provided in the same file) reaches a maximum value of 4.34m during this period. Although this standard deviation is higher than the standard deviation of the other satellites, it does not account for the very large errors in the clock predictions. At the start of igu16356_00.sp3 PRN30 is no longer included in the IGU products.

To prevent these large clock errors from degrading the position solution, the GNSS user should monitor the quality of the clock products and exclude misbehaving satellites from the positioning algorithm. In this particular case, monitoring the advisory messages from the GPS operator would suffice (even though the errors manifest themselves in the clock products from the IGS), but in general this is the domain of integrity monitoring (see chapter 7). The IGU products do *not* give warning of this type of error.

Figure 5.5 shows the error distribution of the satellite position in the radial direction (conform eq. (5.2)) again using a boxplot with one box for each GPS satellite. The errors in the range generally stay well below 0.5m except for some large outliers on PRN21 and PRN25. An inspection of the outliers on these satellites, reveals that in both instances the outliers all occur within a relatively short period of 1-3 days.

Figure 5.6 shows the outliers for PRN21. It can be seen that the orbit accuracy starts degrading at September 11, 2010, and that the large outliers of up to 3.5m occur between 12:00 on the 11th and 12:00 the next day. Figure 5.6 also shows missing data samples during this period. Two IGU files do not contain any data for PRN21, which was apparently excluded from the orbit estimation and prediction. In the IGU files where PRN21 *is* present, no indication is given that the values may be wrong (such as a warning or unusually large reported standard deviation).

Figure 5.7 shows the outliers for PRN25. For this satellite the degraded orbit prediction occurs over the days December 22-25, 2010. During this period 7 IGU files do not contain data for PRN25, but for those IGU files that do include PRN25, again no indication is given that these predictions might be erroneous.

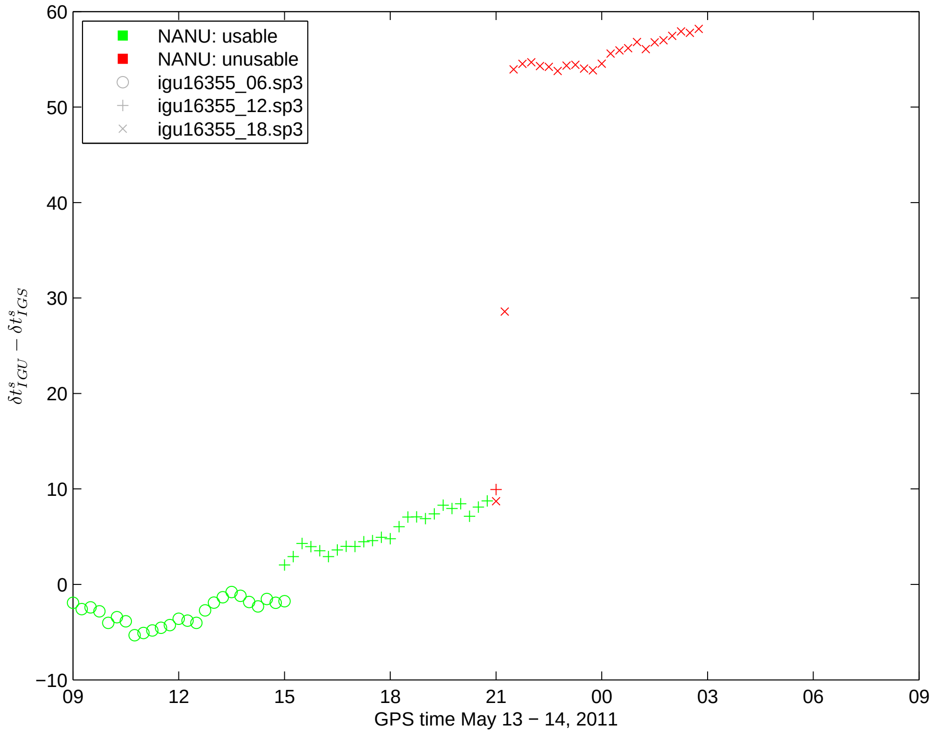

Figure 5.4: IGU (predicted) satellite clock offset w.r.t. IGS final for PRN30

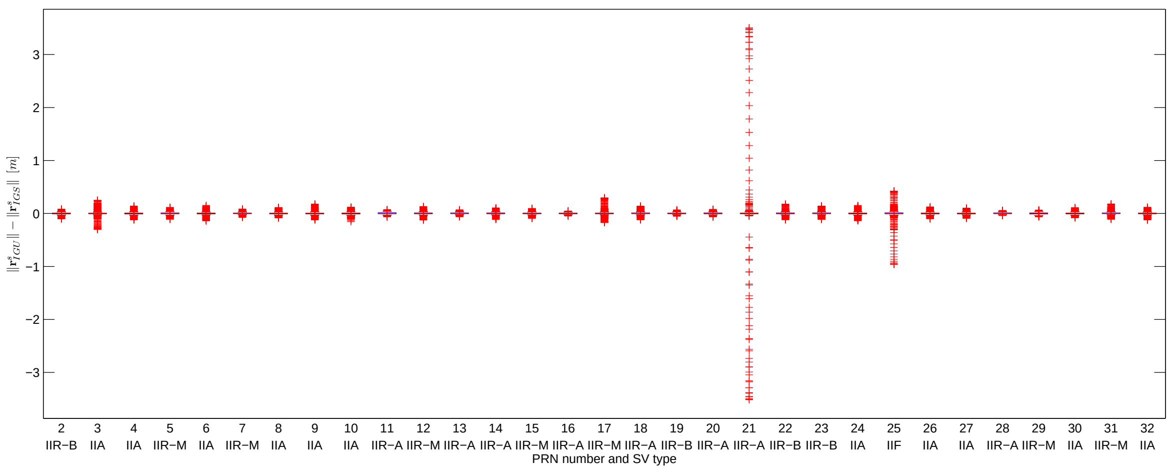

Figure 5.5: Boxplot of IGU (predicted) satellite range w.r.t. IGS final for period Jun 27, 2010 - Jun 25, 2011

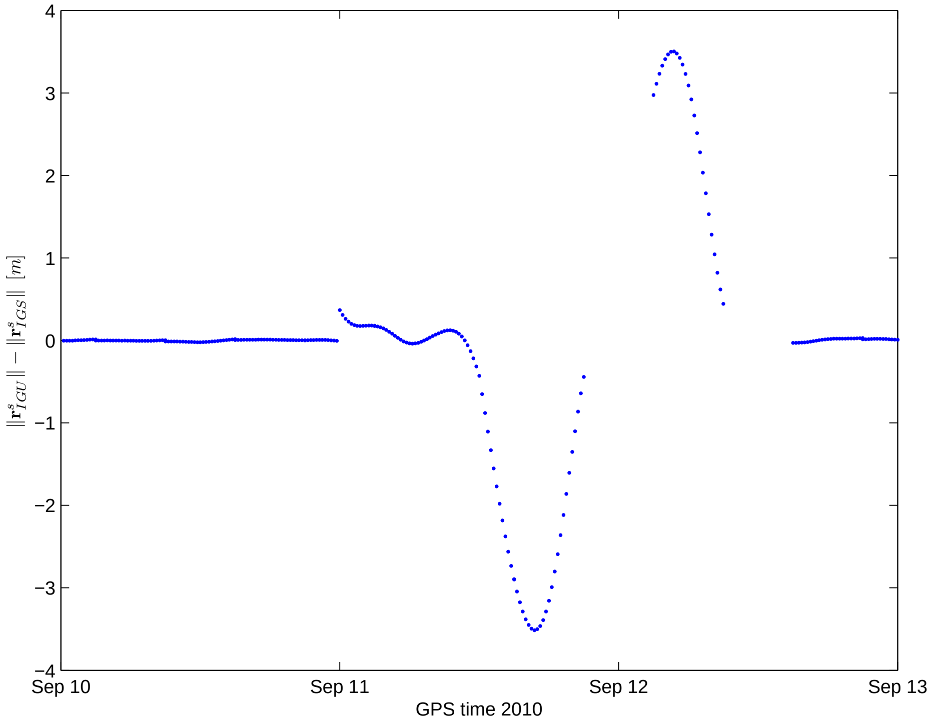

Figure 5.6: IGU (predicted) satellite range w.r.t. IGS final for PRN21

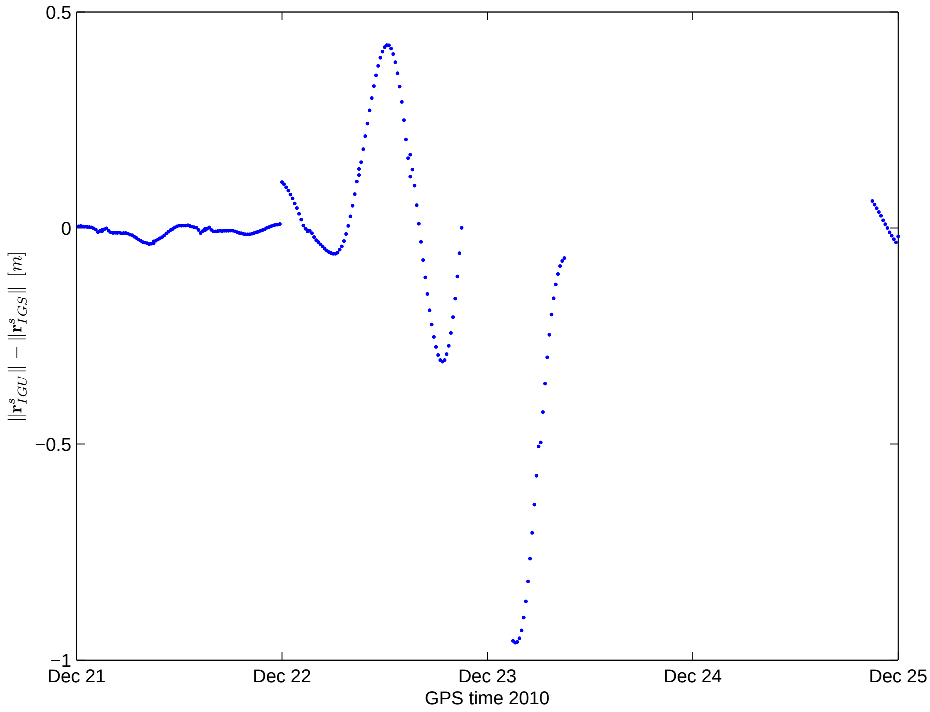

Figure 5.7: IGU (predicted) satellite range w.r.t. IGS final for PRN25

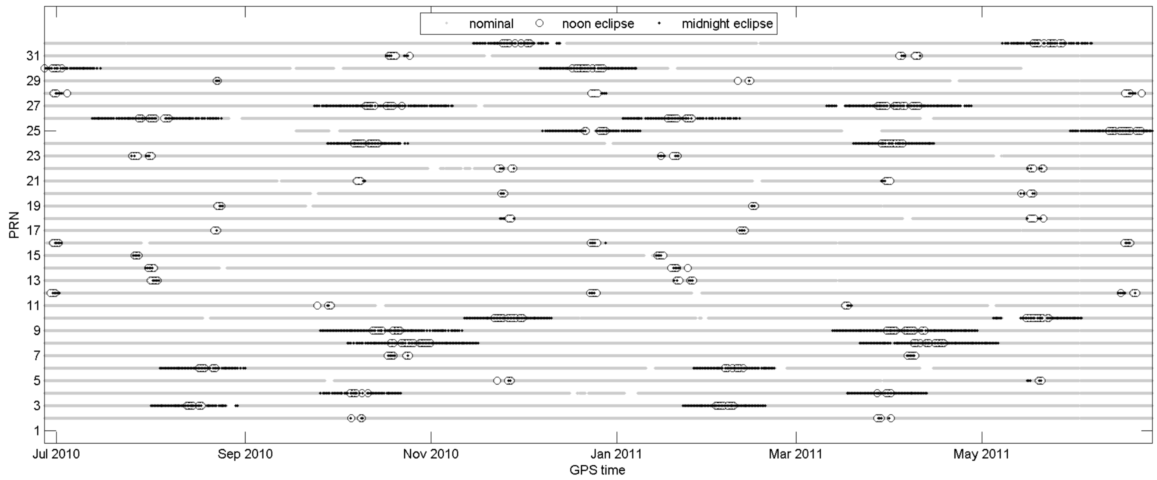

Figure 5.8: Eclipsing GPS satellites

For the period with degraded prediction for PRN21, the IGS final products also do not provide clock estimates for PRN21 for a significant number of epochs. The same is true for the outliers found for PRN25, but to a lesser extend. This indicates that not only the orbit prediction, but also the final orbit and clock estimation was difficult. This fact also reveals a limitation of the presented method for the accuracy analysis, since missing data in the IGS final products prevents the quantification of the errors in the real-time products and might hide temporarily degraded accuracy. This does not prevent the quantification of the accuracy under nominal conditions, but it does influence the determination of the frequency of occurrence of outliers. To make sure we err on the side of caution, it will be assumed that when a certain satellite is not present in the IGS final products (e.g. it has been rejected from the estimation process), the real-time product will have a degraded accuracy. This seems to be a reasonable assumption since generally there is no reason to assume that real-time estimation or prediction would perform better than estimation in post-processing.

One source of degraded estimation and prediction might be maneuvers performed by the GPS satellites but too insignificant to warrant a NANU. GPS satellites perform such maneuvers during eclipses in order to keep the solar panels oriented towards the Sun. These maneuvers can involve antenna rotations of up to one revolution within less than half an hour (Kouba, 2009a). To investigate whether the found outliers coincide with noon or midnight eclipses, the eclipsing seasons for GPS satellites were determined with a routine based on the work by Kouba (2009b). Figure 5.8 shows noon and midnight eclipses for the GPS satellites during the period Jun 27, 2010 - Jun 25, 2011. Careful investigation of fig. 5.8 shows that PRN25 was indeed in eclipsing season during December 22-25, 2010. A routine to identify satellites in eclipsing season might thus help prevent the inclusion of misbehaving satellites in the positioning. However, this does not offer full protection since PRN21 was in fact *not* in eclipse when the outliers for that satellite occurred on September 11, 2010.

As mentioned before, the IGU errors on the pseudo range are dominated by the clock errors, which means that these outliers in the satellite positions do not cause exceptionally large errors in the pseudo range and from that respect are not critical. However, since other PPP services (e.g. RETICLE) combine IGU orbits with more accurate clock products, it is important to know that errors of several meters can be present in the orbit data. Since neither the IGU files nor the NANU messages provide warning for the temporarily degraded performance, and since satellite eclipsing only explains part of the outliers, we must rely on integrity monitoring to detect large orbit and/or clock errors and remove the corresponding observations from the positioning filter.

Figure 5.9 again shows the error distribution of the satellite positions (in radial direction) after removal of the large outliers identified above. The figure reveals a very narrow distribution for the orbit errors (e.g. a high accuracy) but with more, smaller outliers. The strength of the positioning model and the chosen probability of false alarm will determine which size of outlier can still be detected with a certain probability by the integrity algorithms. It will also be important to determine what size of error can still be accepted, see chapter 7. For now we will assume that these smaller outliers are part of the distribution under nominal conditions. The radial accuracy is very high and similar for all satellites (rms = 1.4cm). These radial errors are much smaller than the mean errors over all direction both from our analysis (rms = 4.1cm), and the values provided by the IGS (rms = 5cm see table 5.1). This difference in accuracy is directly related to the fact that GPS receivers on the surface of the Earth, used to determine the satellite positions, are much more sensitive to errors in the radial direction. Additionally, the (large) satellite velocities are almost perpendicular to the radial direction.

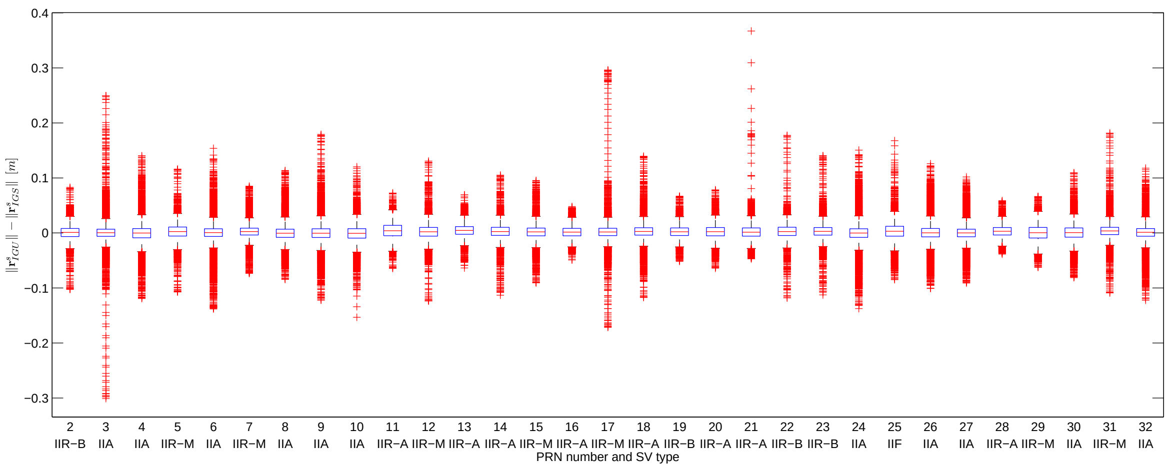

Figure 5.9: Boxplot of IGU (predicted) satellite range w.r.t. IGS final, after removal of largest outliers, for period Jun 27, 2010 - Jun 25, 2011

A comparison of figs. 5.3 and 5.9 confirms that the errors in the predicted clock are much larger than the errors in the satellite positions, and will thus dominate the errors in the combined pseudo range according to eq. (5.4).

Figure 5.10 shows the comparison of the real-time IGU products against the IGS final products in the pseudo range domain. This figure shows almost identical results as fig. 5.3 (except with opposite sign), which confirm that the clock errors drown out the (radial) position errors, and consequently dominate the pseudo range errors. Changing the user position to any location on the surface of the Earth does not change this fact and results for different user positions are not presented here.

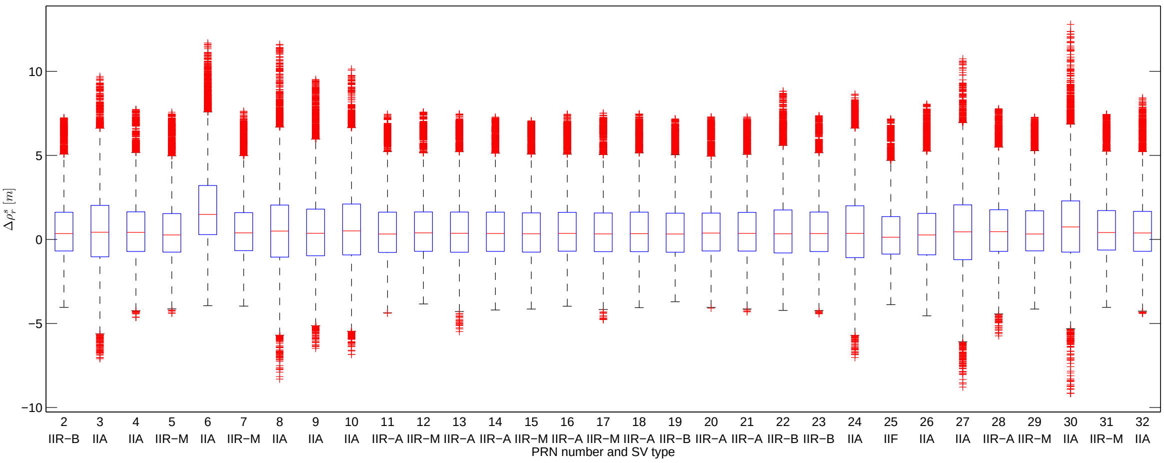

Figure 5.10: Boxplot of IGU (predicted) pseudo range (i.e. range minus clock) w.r.t. IGS final (eq. (5.4)), for period Jun 27, 2010 - Jun 25, 2011

Three factors that *do* play an important role are the common clock bias introduced in eq. (5.5), the satellite type, and the prediction interval, which are here discussed in turn.

Figure 5.11 shows the same results as fig. 5.10, but now after removal of the common clock bias. Several observations can be made from a comparison of the two figures. In general the residual errors are much smaller after the removal of the common clock bias, which has absorbed the constant 0.6m bias as well as a time varying offset between the IGU and IGS solutions. The overall rms value for all satellites is 0.9m, and only PRN6 is significantly biased (1.3m). Further, differences between the satellites now are much more pronounced, with much larger errors for the older block IIA satellites (rms 1.4m) compared to the newer block IIR and IIF satellites (rms 0.35m). Although it should be noted that some block IIA satellites (i.e. PRN4, PRN26 and PRN32) are performing better than the other block IIA satellites. The residuals shown in fig. 5.11 lead to errors in the pseudo ranges when using the IGU products for positioning. Therefore, for optimal results, the stochastic model should account for these residuals and differentiate between the GPS satellite types (or directly between the satellite vehicles).

The quality of the predictions degrades with increasing prediction interval. To show this degradation we will now look at the complete prediction time of 0 to 24 hours for the IGU products from the period Mar 27 - Apr 3, 2011. Figure 5.12 shows the error distribution as a function of the prediction interval for block IIA satellites (top pane) and block IIR and IIF satellites (bottom pane). The quality of the predicted orbit and clock products reduces significantly with the prediction interval for both types of satellites. Although, the degradation remains quite limited within the 3 to 9 hour window used for real-time positioning, it should be taken into account in the stochastic model for positioning to obtain realistic description of the accuracy of the position solution.

The degraded quality of the predicted satellite clocks in particular is also the incentive for the estimation of the satellite clocks with much less lag between the measurements and

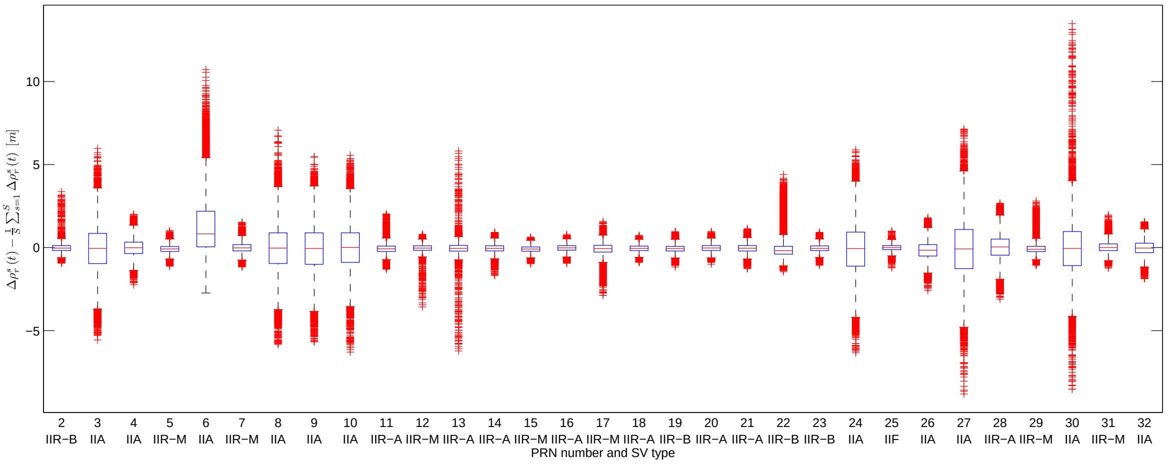

Figure 5.11: Boxplot of IGU (predicted) pseudo range (i.e. range minus clock) w.r.t. IGS final after removing a common clock bias eq. (5.5), for period Jun 27, 2010 - Jun 25, 2011

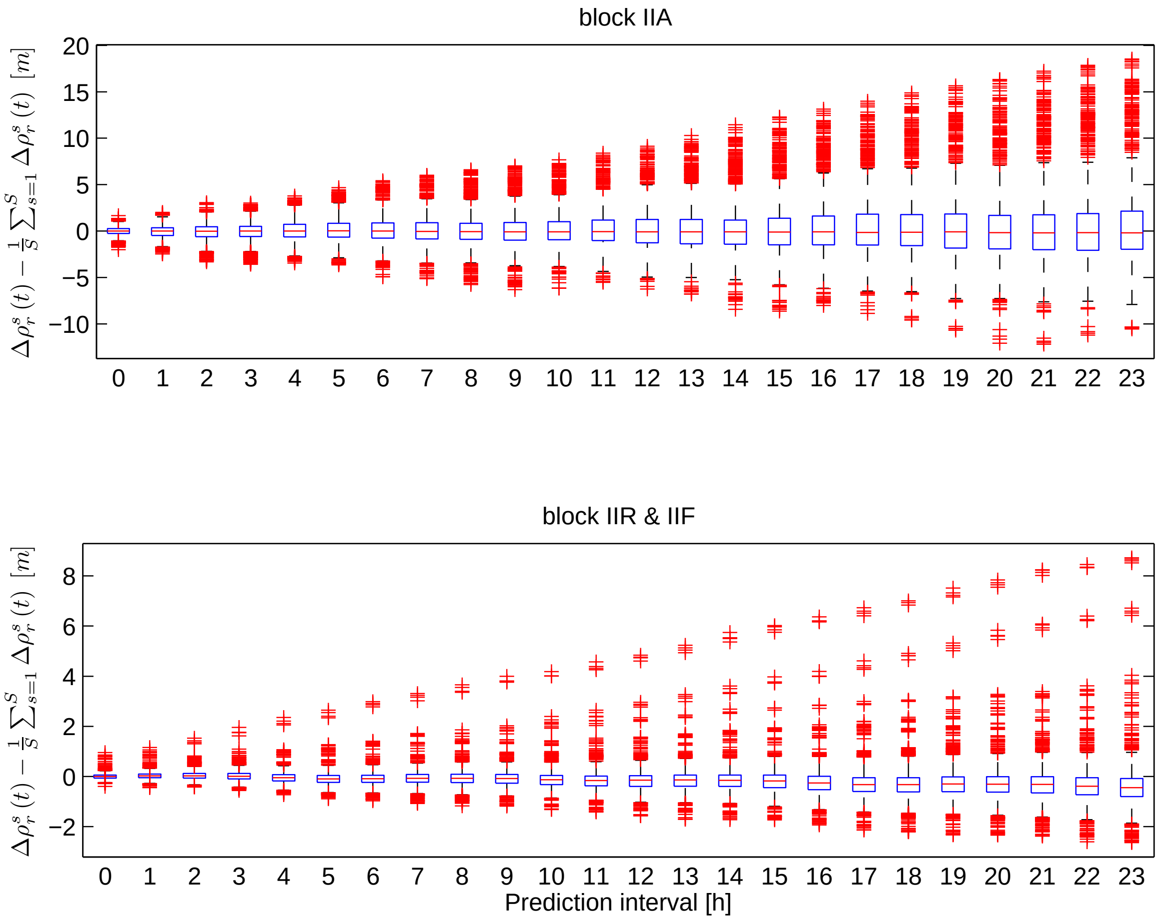

Figure 5.12: Boxplot of IGU (predicted) pseudo range (i.e. range minus clock) w.r.t. IGS final after removing a common clock bias versus prediction interval, for period Mar 27 - Apr 3, 2011

the availability of the products (such as clock estimations of the RETICLE system).

5.3.2.2 RETICLE clock products

To assess the quality of the RETICLE products 24h of satellite clock estimates have been collected on Mar 31, 2011 (combined with the corresponding IGU products). During this period RETICLE products were available for 26 satellites for a total of 224,640 clock offsets. This section first focuses on the quality of the satellite clock products and then looks at the combined product. Figure 5.13 shows the distribution of the RETICLE clock offsets w.r.t. the IGS final products separately for each GPS satellite. The figure shows that all RETICLE clocks offsets for this period have a bias of about -2.4m with respect to the IGS final products. The distribution about this mean has a standard deviation of 22cm, which is much smaller than the IGU predicted clock offsets but still much larger than the IGU orbit errors. Therefore, the errors in the pseudo range domain are still dominated by the clock errors. In fact a boxplot of these errors would again be almost identical to fig. 5.13 with opposite sign and is not presented here.

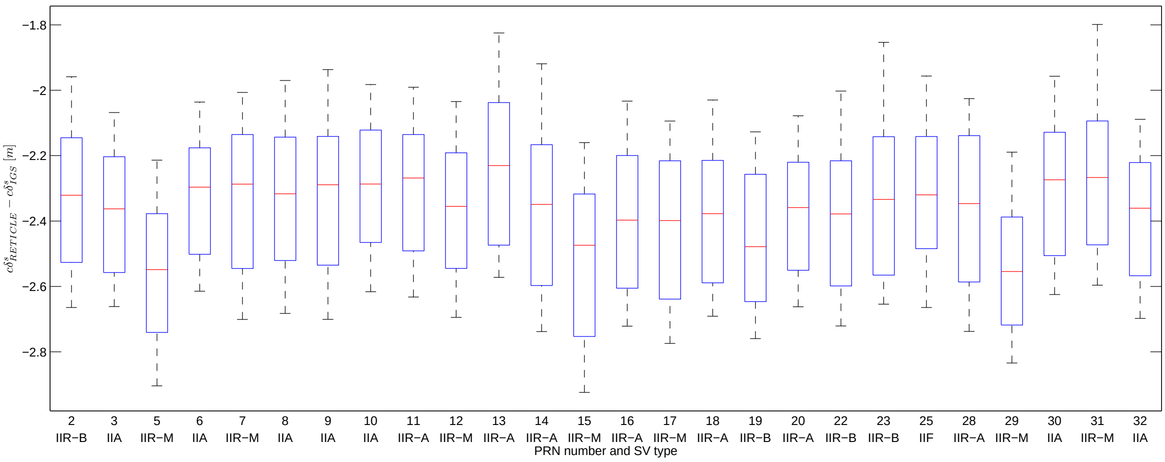

Figure 5.13: Boxplot of RETICLE satellite clock offset w.r.t. IGS final for 24 hours on Mar 31, 2011

The improvement of the RETICLE clocks on the predicted IGU clocks becomes even more apparent if we remove the common mode error, as presented in fig. 5.14. The results have an overall rms of 9cm consisting of individual satellite biases of up to 20cm and standard deviations of about 4cm. No large differences are apparent between the GPS satellite types. If we compare these results to the IGU products (fig. 5.11) the improvement is very clear indeed. For this comparison we should of course keep in mind that there is a large difference in the length of the observed period (24h vs 1 year). The number of outliers is indeed expected to grow with the observation period and this is visible by an increased number of plus-signs in the IGU figures. The rms values on the other hand are not expected to change significantly with an increasing observation period especially after subtraction of the mean value per epoch and if enough samples are considered (here more than 200,000).

The errors in the pseudo range domain are still dominated by the clock errors, since the orbit errors are significantly smaller, and thus almost invariant for the user position. The

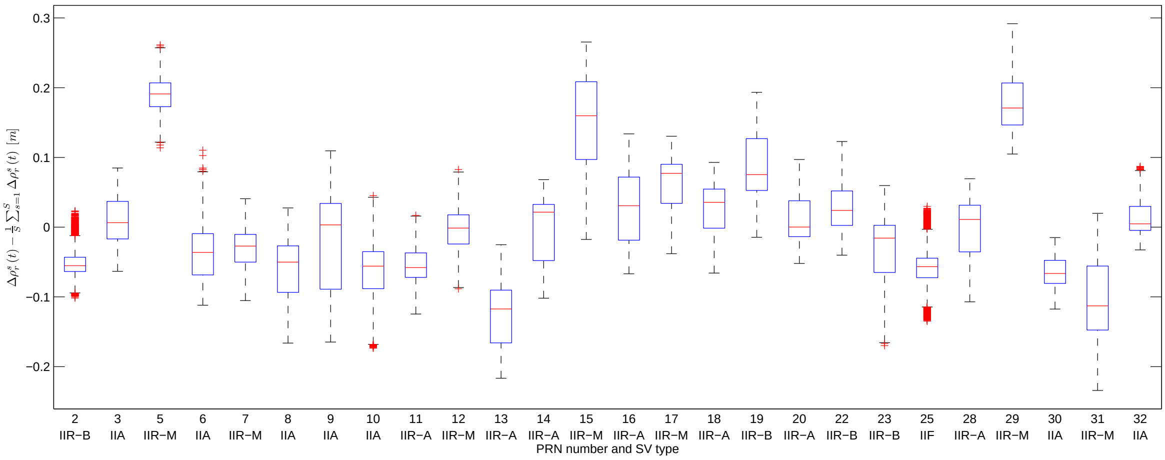

Figure 5.14: Boxplot of RETICLE pseudo range (i.e. range minus clock) w.r.t. IGS final after removing a common clock bias (eq. (5.5)) for 24 hours on Mar 31, 2011

errors in the pseudo range that occur at a certain time and place *does* depend on the subset of satellites in view and the quality of the clock estimates for those satellites at that time.

5.3.2.3 JPL real-time products (collected from Veripos with L-band antenna)

To assess the quality of the JPL products from the Veripos Ultra service, 24h of satellite orbit and clock corrections have been collected from 10:00 on Mar 31 until 10:00 on Apr 01, 2011. During this period JPL corrections were available for 24 satellites for a total of 50,644 corrections.

The JPL products refer to the satellite Antenna Phase Center (APC) to which the measurements are made as described in table 3.4. The IGS products on the other hand refer to the satellite Center Of Mass (COM) generally used for orbit modeling and estimation. To obtain the APC from the COM the Phase Center Offsets (PCO) need to be applied. For the IGS products this is left to the user, who must apply the PCOs published online by the IGS. In the JPL corrections, the PCO have already been taken into account. However, the PCOs used by different providers of satellite orbit data are not necessarily equal to or even consistent with each other, which leads to considerable differences in the computed APCs.

Schmid et al. (2007) made a comparison of i.a. the absolute PCOs used for the IGS antenna model igs05.atx (since then replaced by igs08.atx) and the PCOs of the National Geospacial-intelligence Agency (NGA) which are consistent with the broadcast ephemeris results below. The IGS and NGA models agree that the Block IIR satellites actually consist of 2 subgroups (called IIR-A and IIR-B) of which the Block IIR-B satellites have the smallest radial PCO. However, large differences are found when comparing the mean values for each of the blocks. The most extreme differences are the Block II/IIA satellites with the IGS values being *larger* than the NGA values by 144 cm and the Block IIR-A satellites with the IGS values being *smaller* than the NGA values by 44 cm. The JPL uses a set of radial PCOs which differs even more from the IGS model in absolute sense and does not distinguish between different subgroups of the Block IIR satellites (Bar-Sever, 2012). The exact differences between the IGS and JPL depend on block number, but are on average 1.5 m with the IGS radial PCOs being larger than the JPL values.

A comparison of the APCs between the JPL corrections, broadcast ephemerides, and the IGS products will be dominated by these large differences in the PCOs. This is confirmed by fig. 5.15 which shows the distribution of the radial orbit errors of the APC per satellite. The figure shows that the satellite positions from the JPL products have a bias in the radial direction of about 1.5m as well as (much smaller) individual satellite biases. These biases are due to the different PCOs as discussed above.

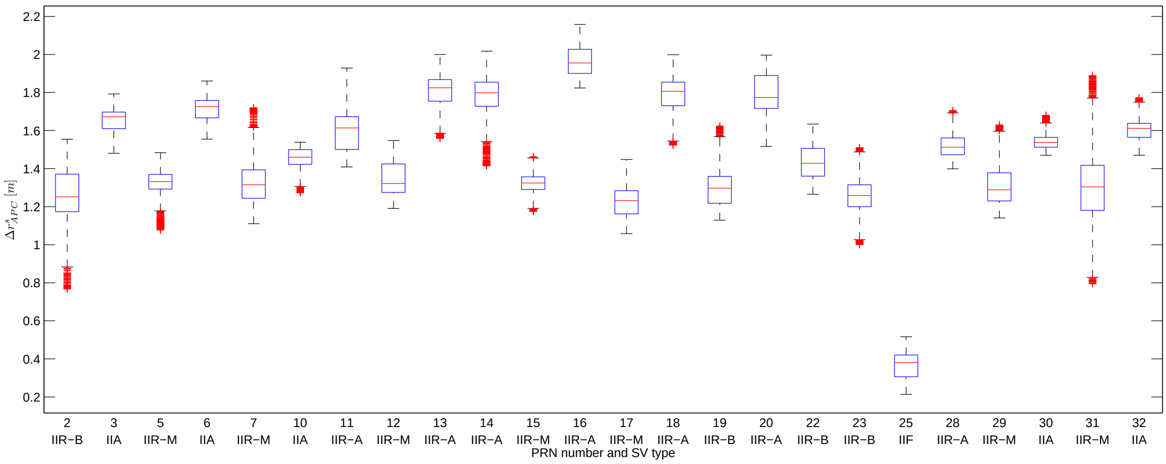

Figure 5.15: Boxplot of JPL radial satellite APC positions w.r.t. IGS final product for 24 hours on Mar 31 and Apr 01, 2011

Figure 5.16 shows the distribution of the satellite clock errors. The figure shows that satellite clocks from the JPL products have a bias of about -2m (i.e. -6.7ns) with respect to the IGS final products and again (smaller) individual satellite biases. Close inspection of figs. 5.15 and 5.16 reveals that these individual satellite biases are very similar for the satellite clocks offsets and radial position errors. Since the satellite clock difference in eq. (5.4) has a minus sign, this means that the radial biases in the satellite APCs are (largely) compensated by similar differences in the satellite clock offsets. Despite this compensation, the large differences in APC will still lead to range differences for satellites at lower elevation angles as discussed in section 5.3.1. In fact, the user range is only indifferent to a (radial) PCOs and equal clock offsets if the satellite is directly over head of a user.

To assess the accuracy of the real-time orbit products, the COM can be used instead of the APC, since this should really describe the same physical point for all orbit products. Therefore, the COM has been determined for the JPL orbit corrections by subtracting the JPL PCOs. In order to keep a consistent set of PPP products and in order to assess the quality of the real-time clock products, a similar operation is performed on the satellite clocks. The radial part of the PCO is added to the clock offset $(c\Delta\delta t^s + PCO \cdot \frac{\mathbf{r}^s}{\|\mathbf{r}^s\|})$.

Figure 5.17 shows the distribution of the radial orbit errors of the COM per satellite and reveals that these are *not* biased and have an overall rms of 11 cm. Just like for the IGU products this is significantly lower than the reported 3D accuracy of 20 cm (table 5.2).

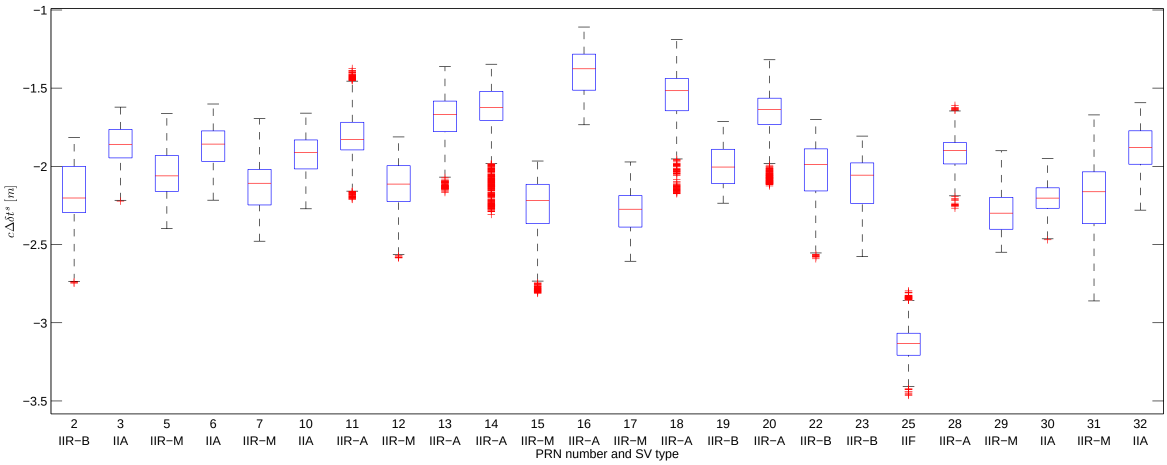

Figure 5.16: Boxplot of JPL satellite clock offsets w.r.t. IGS final satellite clock offsets for 24 hours on Mar 31 and Apr 01, 2011

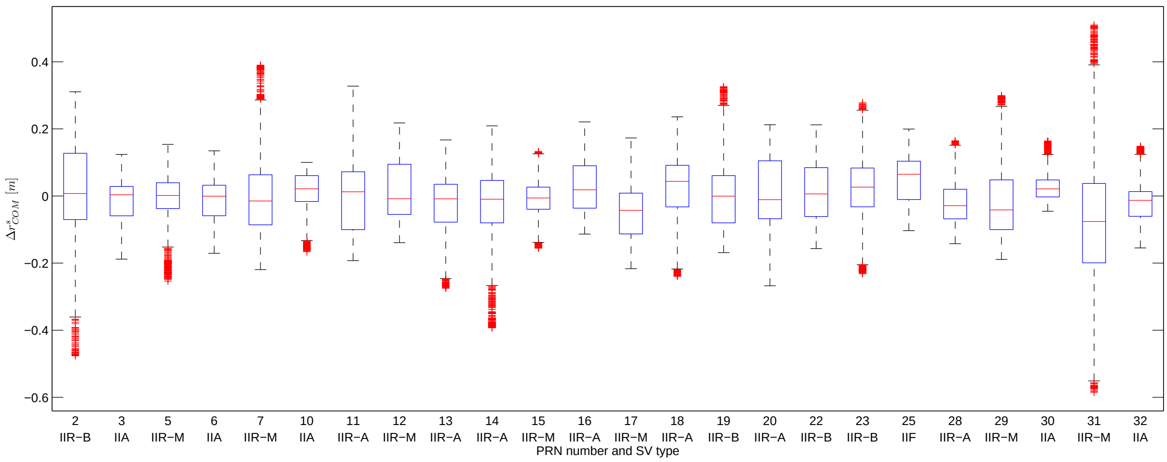

Figure 5.17: Boxplot of JPL radial satellite COM positions w.r.t. IGS final product for 24 hours on Mar 31 and Apr 01, 2011

The corresponding clock is shown in fig. 5.18. The figure shows that the overall bias in the satellite clocks has actually increased in absolute sense to -3.5m (i.e. -12ns), but the distribution around this mean value is much smaller with a standard deviation of 19cm.

Combining the orbit and clock products to assess the errors in the pseudo range domain, eq. (5.4), leads to the results presented in fig. 5.19. The figure clearly shows an offset of about 3.5m on all pseudo ranges computed with the JPL products with respect to those computed from the IGS products. This bias is a combination of the biases in the satellite clocks and the different PCOs of the satellites as already found in fig. 5.18. The common mode error from eq. (5.5) will absorb some of the differences between the JPL and IGS solution, which is treated below.

The JPL correction stream received from Veripos through the L-band antenna does not provide corrections for all satellites simultaneously. Instead corrections are provided for up to 8 satellites at a time, completing a full set of corrections in about 30s. The relatively stable reference clock of the JPL network ensures that these corrections, received shortly

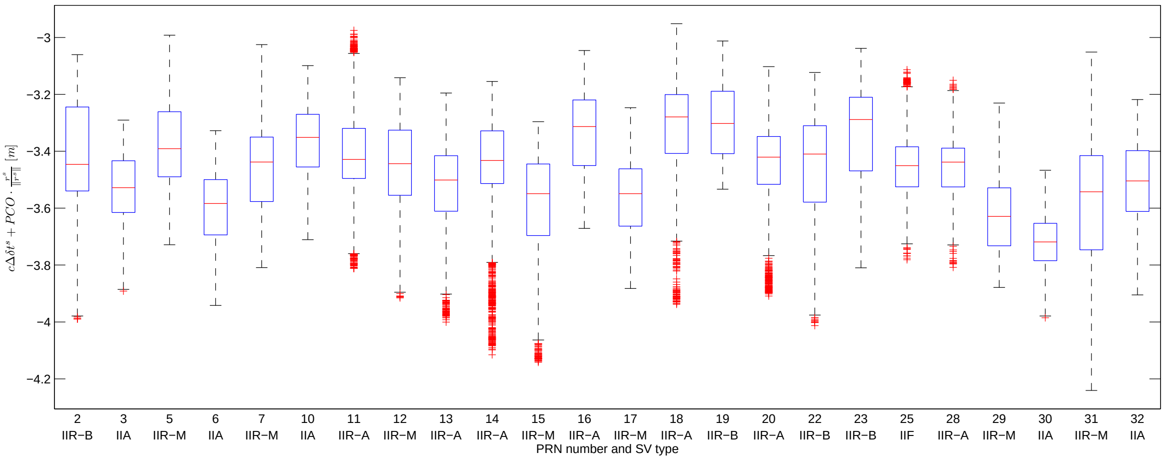

Figure 5.18: Boxplot of JPL derived satellite clock offsets w.r.t. IGS final satellite clock offsets for 24 hours on Mar 31 and Apr 01, 2011

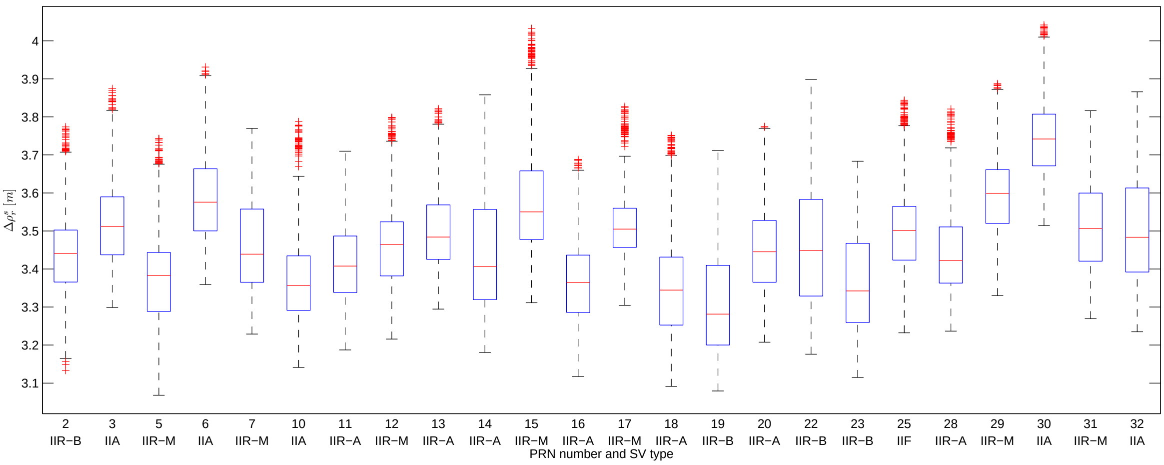

Figure 5.19: Boxplot of computed pseudo range (i.e. range minus clock) from JPL products w.r.t. IGS final products for 24 hours on Mar 31 and Apr 01, 2011

after each other and with slightly different times of applicability, can be used together. So to determine the mean value of the differences between the JPL corrections and the IGS final products for all satellites at a certain epoch, conform eq. (5.5), the time of applicability cannot be used directly. Instead a staircase function of time is introduced with steps of 30s, and the mean value is determined for each step of this function.

$$t_{30} = t - mod(t, 30) \tag{5.9}$$

$$URE^s_{r,RT,\mathsf{eff}}(t) = \Delta\rho^s_r(t) - \frac{1}{m}\sum_{s=1}^{m}\Delta\rho^s_r(t_{30}) \tag{5.10}$$

The common mode error is treated in fig. 5.20. The top pane shows the results of the comparison in computed pseudo range for all satellites before any biases are removed conform eq. (5.4) (the data was down-sampled by a factor of 5 for the figures only).

Several observations can be made from the figure. On top of the 3.5m bias between the JPL and IGS solutions, a noisy, time varying, signal is very clearly visible in the time series of each satellite. Also, there are smaller slowly changing biases between the satellites. The middle pane of fig. 5.20 shows the estimated common mode (clock) error introduced in eq. (5.10) (i.e. the mean value over all satellites per 30 second time step). The estimated common mode error nicely follows the signal already seen in the top pane, and also absorbs the 3.5m bias between the JPL and IGS products as expected. The bottom pane shows the residuals after estimation of the common mode error. These represent the (residual) errors in the JPL products which directly impact the position solution of a PPP user. The figure shows that these residuals are characterized by slowly changing biases of up to 30cm and noise at cm level.

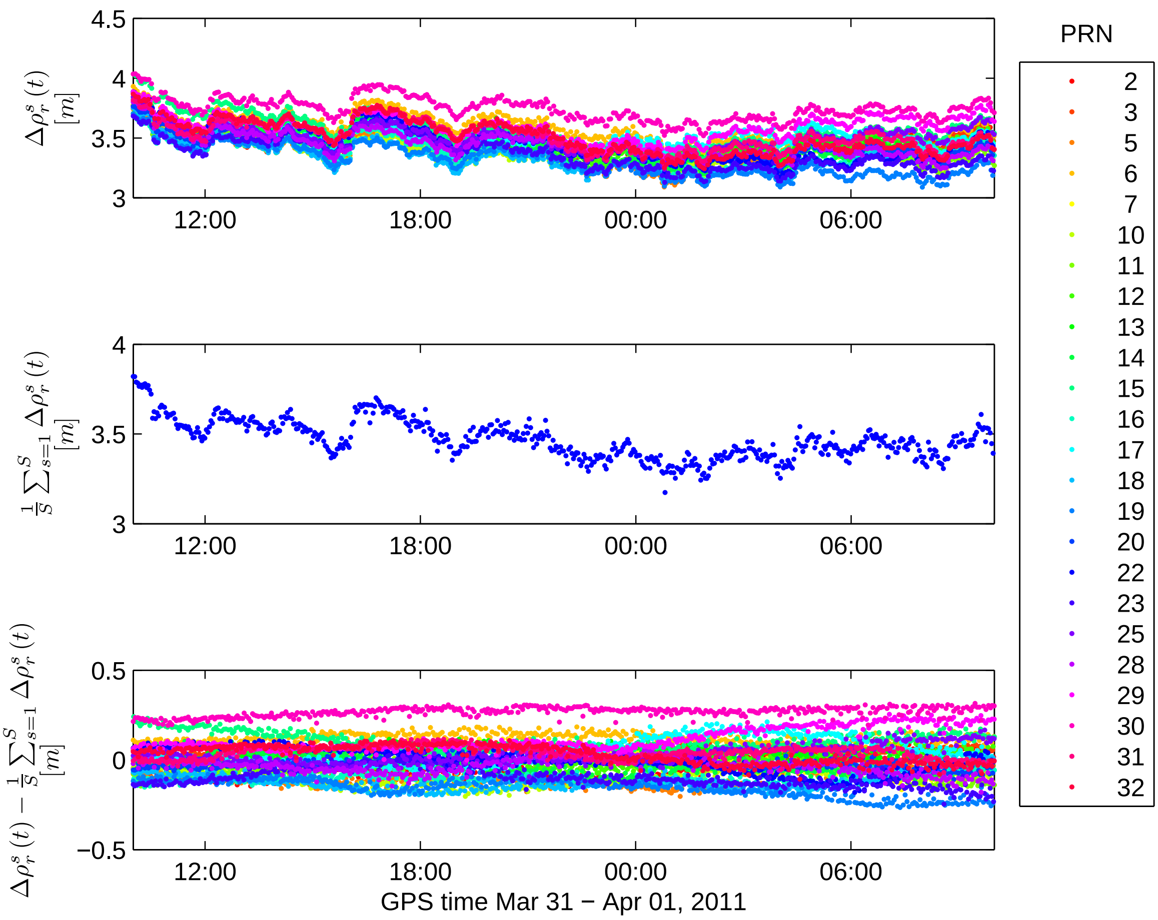

Figure 5.20: Pseudo range (i.e. range minus clock) computed from JPL corrections w.r.t. IGS final. top - 'raw' computed pseudo range difference; middle - mean value per 30s; bottom - computed pseudo range difference minus mean value per 30s

The errors in the JPL products for this period can thus be separated in the following components: a constant bias of about 3.5m, a time varying (common mode) error with rms of 11cm and slowly changing residuals with rms of 10cm. A user of the products is only impacted by the last part and the stochastic model should be set up accordingly. These residuals are also shown with a boxplot with one box for each GPS satellite in fig. 5.21.

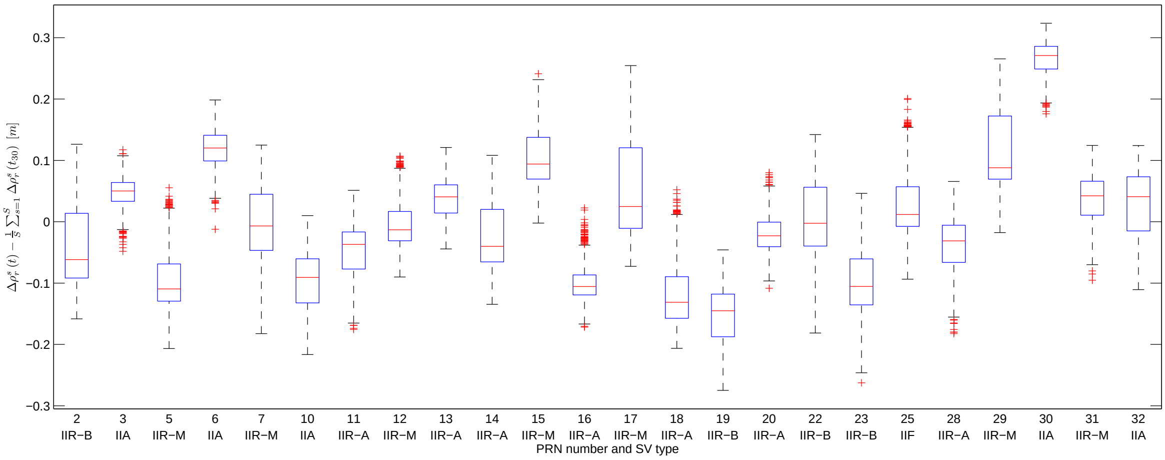

Figure 5.21: Boxplot of computed pseudo range (i.e. range minus clock) from JPL products w.r.t. IGS final products after removing a common clock bias (eq. (5.10)) for 24 hours on Mar 31 and Apr 01, 2011

Given the comparable precision of the JPL clocks and orbits, the correlation between the clocks and orbit is of special interest. The correlation between the satellite orbit and clock products is visualized in fig. 5.22. The left pane shows a scatter plot of each combination of a radial APC position error (vertical axis) and a clock error (horizontal axis) and a 95% confidence ellipse. Uncorrelated errors would appear in this plot as an elliptical point cloud with principal axis in horizontal and vertical directions. What the figure shows are individual point clouds for each of the different satellite types (the block IIF satellite PRN25 is even biased by 1m with respect to the other satellites). The 95% ellipse is strongly elongated with major axis in the direction of the line $\Delta r^s = c\Delta\delta t^s$ which corresponds to strong positive correlation. This is confirmed by the computed correlation coefficient of 0.91. The correlation is largely due to the PCOs as described above.

To investigate the correlation of orbits and clocks (after correcting for the different PCOs), the middle panel of fig. 5.22 shows the COM radial position errors and the corresponding satellite clocks instead. All satellite point clouds are now centered at the same point. However, to see the relevant correlation more clearly the common mode error should also be compensated. In the right pane of fig. 5.22 the mean clock error per 30s (similar to eq. (5.10) but applied to the clock offsets only, so as not to introduce any correlation ourselves) has been removed. The results show that the orbits errors (rms 11cm) and satellite clock errors (rms 16cm) are of comparable size and strongly correlated (correlation coefficient of .75) leading to smaller combined errors (rms 10cm).

A conclusion from this analysis is that, to benefit from the precision of the JPL products, the orbit corrections should only be used with corresponding clock corrections. First, because this ensures consistency between the PCOs and clock offsets; otherwise errors in the order of meters might be introduced. Secondly, even if the orbit or clock products are corrected for differences in PCO, a mixing of products from different providers will degrade their quality because the errors in the clock and orbits are correlated and only eliminated when combined in the pseudo range combination. The only exception is when the combined products have a similar correlation to the JPL products themselves, such as might be the case if new clock products are computed using the JPL satellite positions.

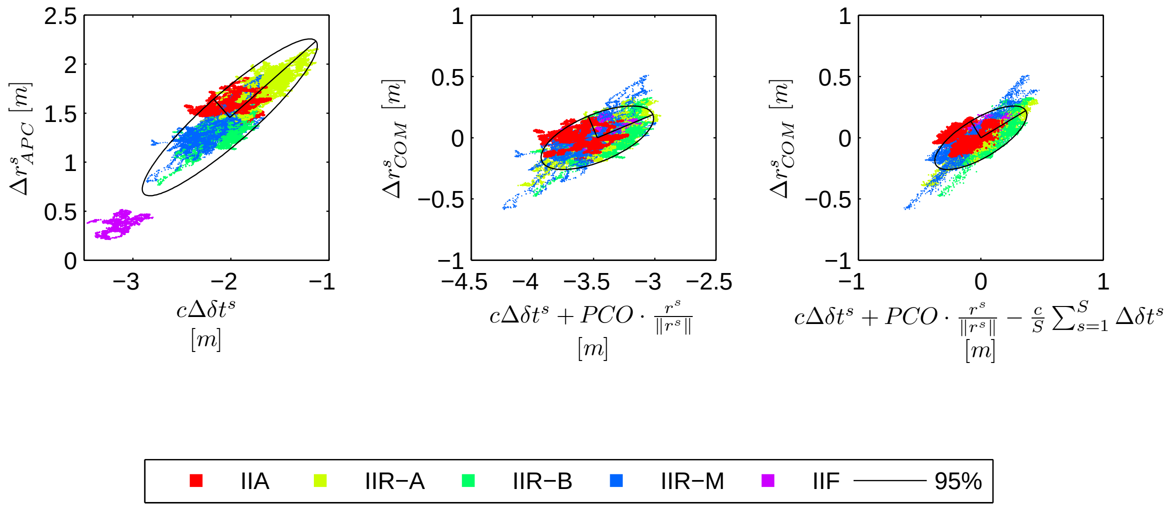

Figure 5.22: left pane: Correlation of the satellite APC radial position errors and clock errors of JPL products; middle pane: Correlation of the satellite COM radial position errors and corresponding clock errors of JPL products; right pane: Correlation after removal of mean clock error per 30s (similar to eq. (5.10) but applied to the clock offsets only) for 24 hours on Mar 31 and Apr 01, 2011

Given the strong correlation and rather large errors in the satellite APC positions, it becomes especially interesting how the pseudo range errors depend on the user position. For this reason fig. 5.23 shows the rms of all satellites combined for different positions on the Earth.

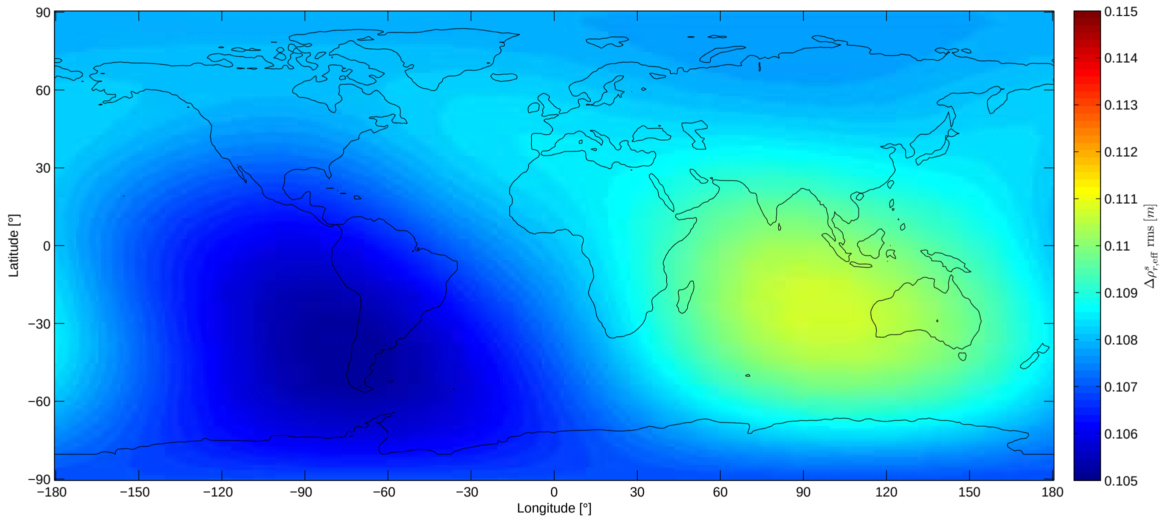

Figure 5.23: Accuracy of the JPL products for all GPS satellites combined for different positions on Earth, for 24 hours on Mar 31 and Apr 01, 2011

Figure 5.23 shows that the variation over the Earth is quite limited, as it should be for a (global) PPP product. The rms over all satellites combined varies between 10.5 and 11.1 cm. However, another effect that influences the accuracy for a given point on Earth is the subset of satellites visible from that position at a certain time. To visualize this effect, fig. 5.24 shows the rms of the errors in the pseudo range domain from the JPL products for all satellites in view from that point on Earth over the 24h period. Note that during these 24h the subset of satellites changes continuously and that the common mode error has been estimated from the visible satellites only.

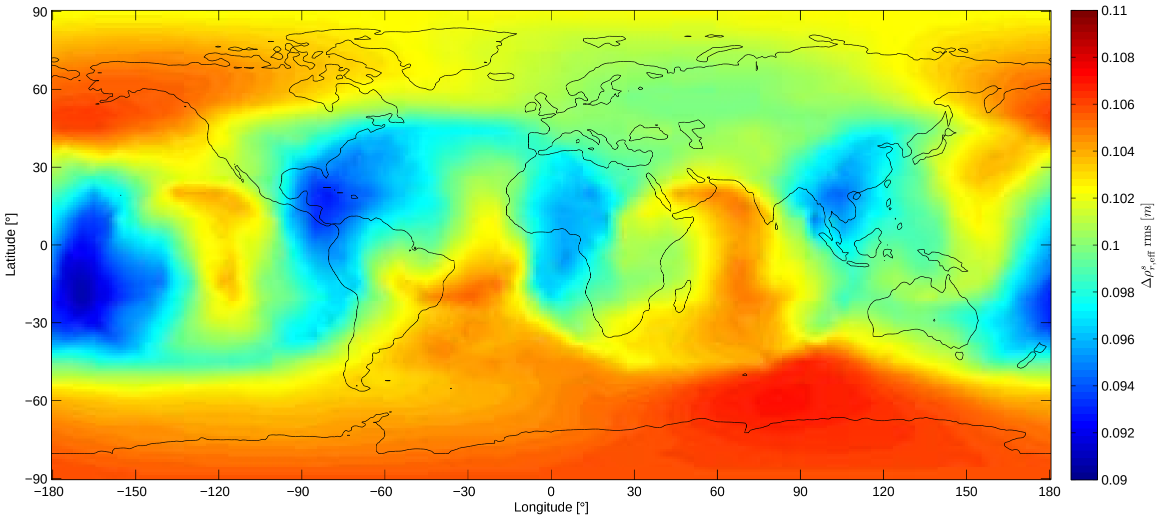

Figure 5.24: Accuracy of the JPL products for all GPS satellites in view for different positions on Earth, for 24 hours on Mar 31 and Apr 01, 2011

Comparison of figs. 5.23 and 5.24 reveals that the rms values decrease on average when only the visible satellites are considered, and that the variation of the rms values with the user position increases. An overall decrease of about 2% is related to the fact that the common mode error is now estimated from a smaller number of satellites, the increase in variation on the other hand is related to specific subsets of visible satellites, and whether satellites with larger errors (e.g. PRN30) have long passes over a specific position on Earth.

5.3.2.4 GPS broadcast products

In section 5.1.1 it was already mentioned that the accuracy of the broadcast ephemerides is not high enough for PPP. Therefore, results of the analysis of the broadcast products are presented here mainly for reference and to show the analogy as well as the differences between the Broadcast and JPL products. To do this the exact same period has been processed again but now looking at the broadcast products. Like the JPL products, the broadcast products refer to the antenna phase center. Figure 5.25 shows the APC of the broadcast ephemerides compared to the IGS final products. Large biases are present in the results, the size of which clearly depends on the satellite type. Figure 5.26 shows the clock offsets of the broadcast ephemerides compared to the IGS final products, with similar satellite type dependent biases as well as an overall bias of about -2.3m.

These satellite type dependent biases are again largely due to differences in the PCOs. To make a fair comparison between the satellite orbits, the COM for the broadcast products has been computed by subtracting the PCOs provided by the NGA (NGA, 2012). Figure 5.27 shows that the biases are now strongly reduced.

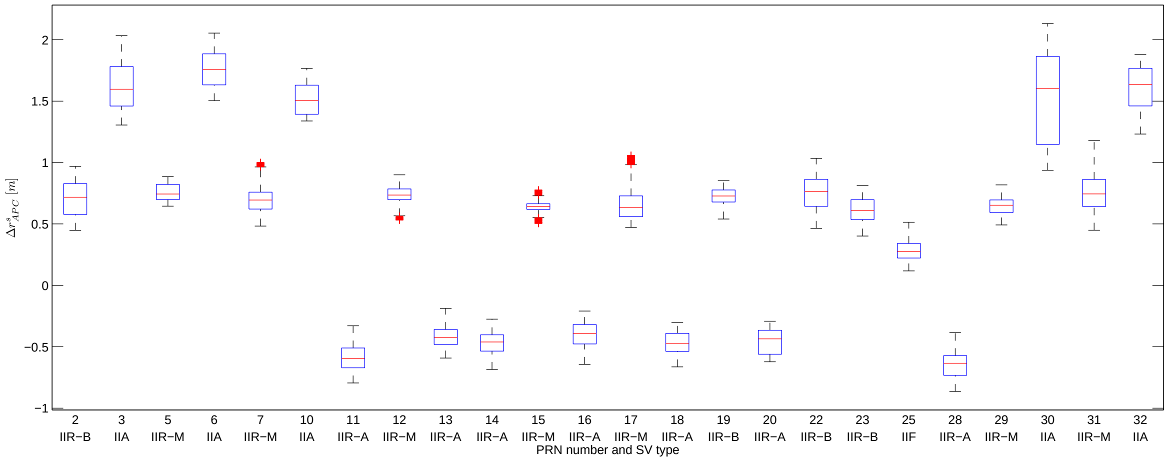

Figure 5.25: Boxplot of broadcast radial satellite APC positions w.r.t. IGS final product for 24 hours on Mar 31 and Apr 01, 2011

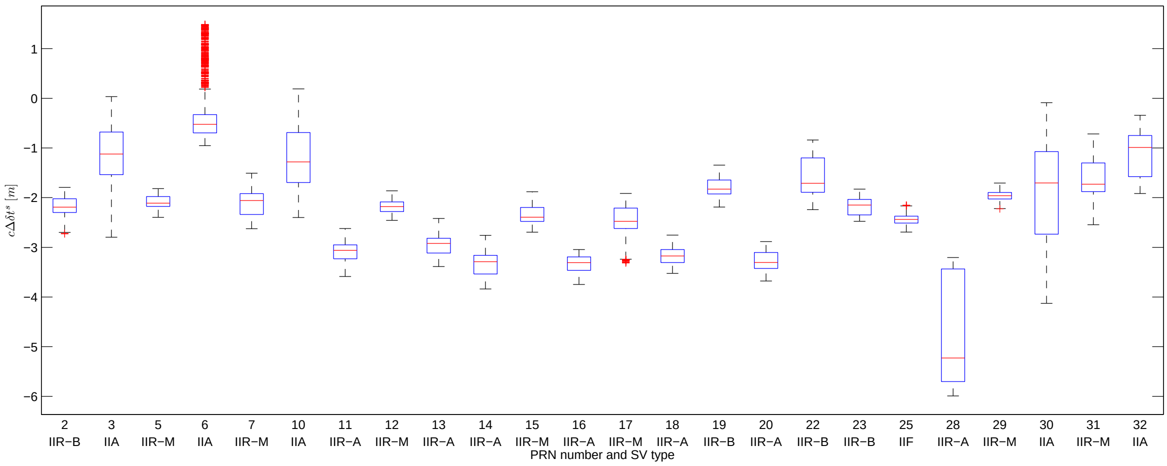

Figure 5.26: Boxplot of broadcast satellite clock offsets w.r.t. IGS final satellite clock offsets for 24 hours on Mar 31 and Apr 01, 2011

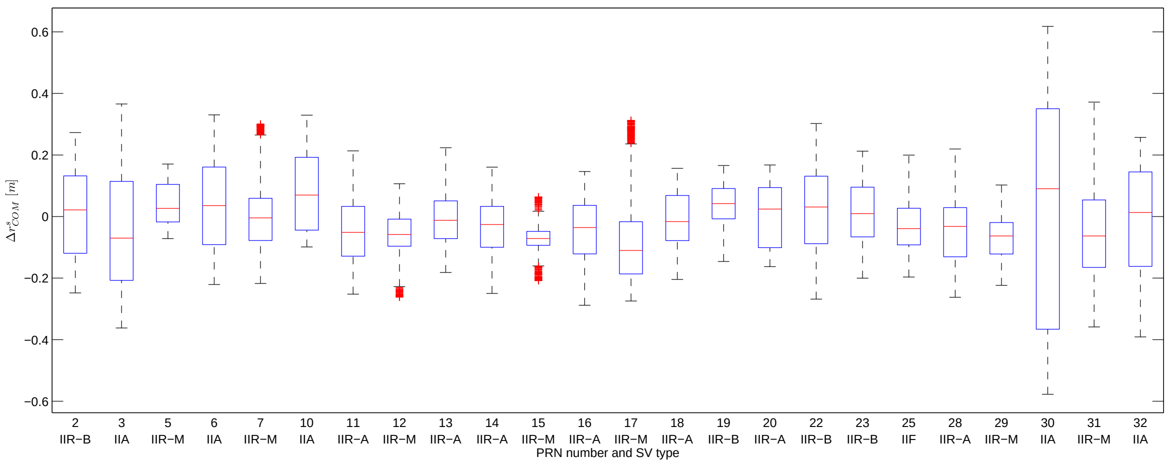

Figure 5.27: Boxplot of broadcast radial satellite COM positions w.r.t. IGS final product for 24 hours on Mar 31 and Apr 01, 2011

The top pane of fig. 5.28 shows the results of the comparison in computed pseudo range for all satellites before any biases are removed (the data was down-sampled by a factor of 5 for the figures only). Several observations can be made from the figure. Firstly, there is the overall bias mentioned before. Additionally several satellites have deteriorating clock estimates over time. This is not surprising as the broadcast clocks are in fact predicted values. The middle pane of fig. 5.28 contains the estimated common mode (clock) error (i.e. the mean value over all satellites) and reveals that the bias slowly changes over time from 3m to 2.5m. The bottom pane shows the residuals after estimation of the common mode error. These represent the (residual) errors in the broadcast products which impact the user. The figure shows that these residuals are now dominated by the deteriorated clocks of some satellites. These residuals are also shown with a boxplot with one box for each GPS satellite in fig. 5.29 in which it is easier to identify the worst satellites. Just as for the IGU products, these are a number of Block IIA satellites (PRN 6, 10, 30, 32) and one Block IIR-A satellite (PRN 28).

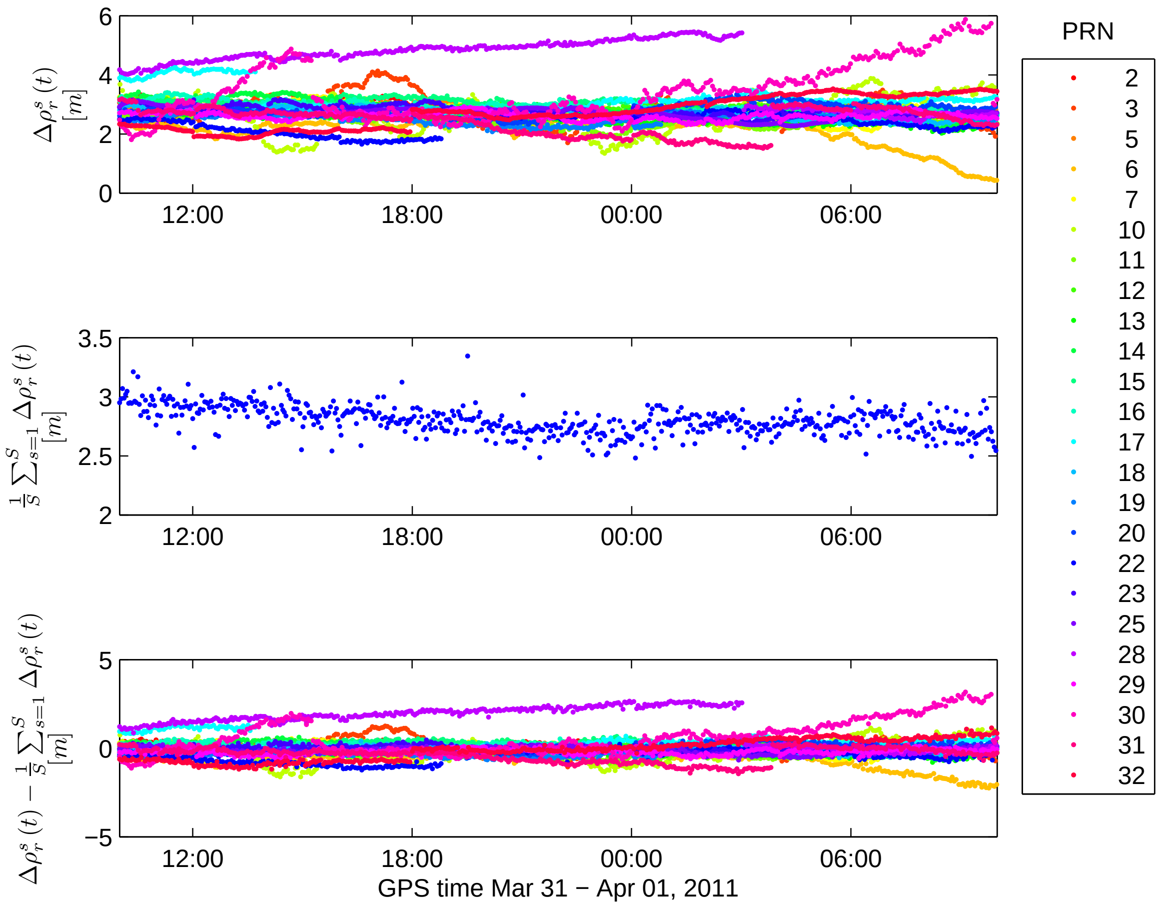

Figure 5.28: Pseudo range computed from broadcast corrections (i.e. range minus clock) w.r.t. IGS final. top - 'raw' computed pseudo range difference; middle - mean value per 30s; bottom - computed pseudo range difference minus mean value per 30s

Figure 5.30 shows the correlation of the radial position errors and clock offsets from the broadcast ephemeris. The left most pane, containing the satellite APCs and the broadcast clocks, shows strong correlation of the broadcast products (correlation coefficient 0.83).

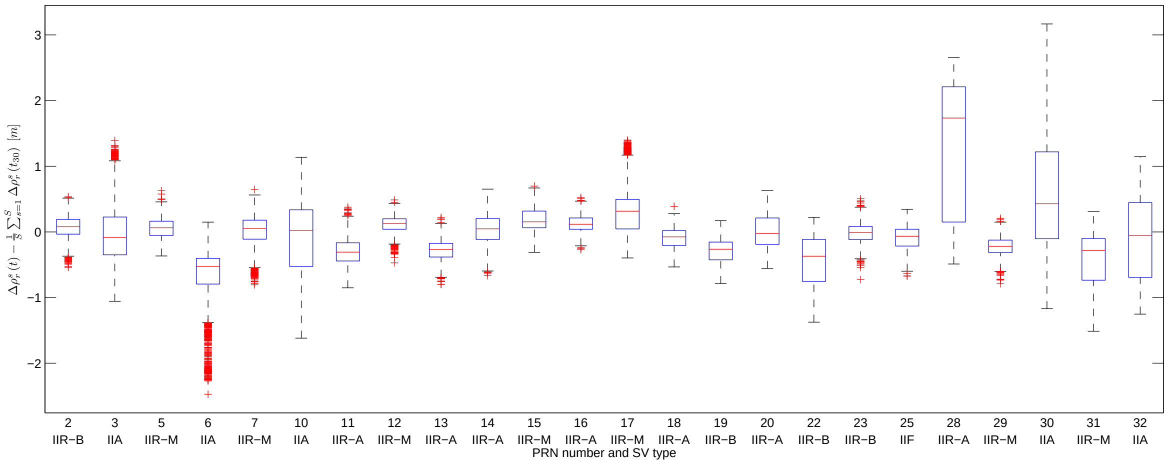

Figure 5.29: Boxplot of computed pseudo range from broadcast products (i.e. range minus clock) w.r.t. IGS final products after removing a common clock bias (eq. (5.10)) for 24 hours on Mar 31 and Apr 01, 2011

However, just like for the JPL products this correlation is mainly due to the PCOs which again explains the distinct cloud points for the different satellite types. If we correct for the PCOs and look at the COM and corresponding clock instead (middle pane) all point clouds converge, the correlation drops considerably, and the clock errors are clearly larger than the radial position errors. The effect of removing the common clock bias (right pane) is rather small, the clock errors (rms 58cm) are still much larger than the radial position errors (rms 14cm) and the correlation remains relatively small (correlation coefficient 0.22).

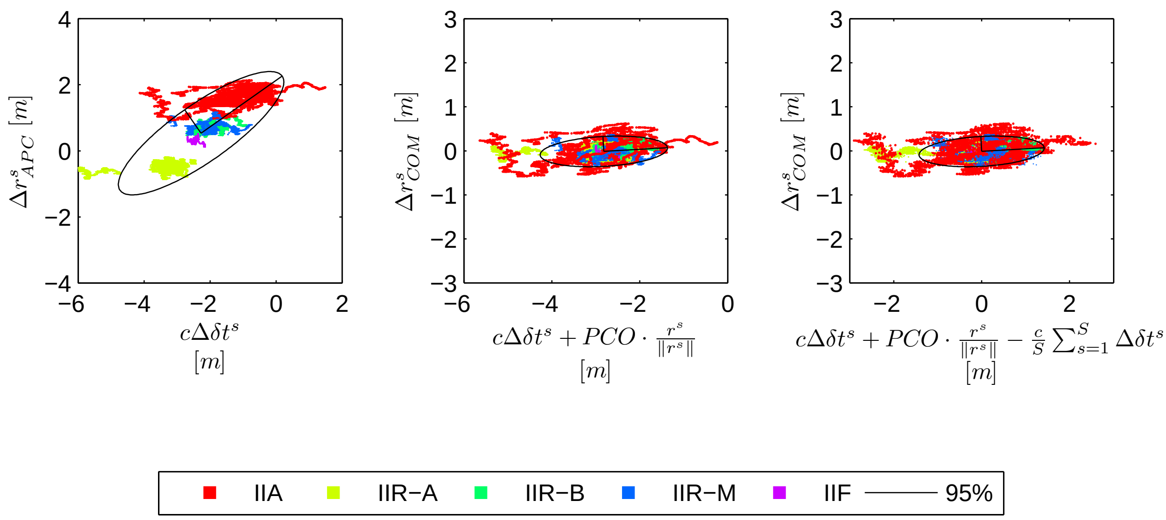

Figure 5.30: left pane: Correlation of the satellite APC radial position errors and clock errors of broadcast products; middle pane: Correlation of the satellite COM radial position errors and corresponding clock errors of broadcast products; right pane: Correlation after removal of mean clock error per 30s (similar to eq. (5.10) but applied to the clock offsets only) for 24 hours on Mar 31 and Apr 01, 2011

5.4 Comparison to other analyses

As mentioned, the IGS ACC routinely monitors the accuracy of the broadcast and IGU products as well as the IGS rapid and final products (IGS, 2015a). The IGS ACC provides results from daily comparisons between the broadcast products and the IGS rapid products by means of the weighted rms orbit errors, the rms clock errors and the standard deviations of the clock errors. Similar to our analysis, the IGS rapid products are expected to be much more accurate than the broadcast products, and as such these results might be considered as describing the accuracy of the broadcast products. Additionally, weekly averages of the 7 Helmert transformation parameters (3 translation, 3 rotation, and 1 scale parameters) of the Broadcast orbits with respect to the IGS Rapid products are provided. No results are provided in the pseudo range domain.

If we consider GPS week number 1629, as a typical example, and focus first on the orbit comparison, the IGS ACC finds a scale factor between -20 and -25 parts per billion (ppb) and a weighted rms between 0.90m and 1.05m. These results are in line with our results from section 5.3.2.4 for the APC. For the APCs we found an overall radial bias of 0.53m which corresponds to a scale factor of 20.1 ppb, and a radial rms error of 0.93cm. It should be noted that the IGS ACC results do not specify their weighting or whether the results are 3 dimensional or in a specific direction. For the satellite clocks the IGS ACC finds an rms error between 3.5ns and 5ns and a standard deviation between 3ns and 4ns (after removing a separate bias for each satellite clock). These results are also in line with our results if we assume that the common clock offset between the IGS rapid products and the broadcast products has been removed first (we found an rms error of 3.8ns after removing this bias). Since we have not removed a separate bias for each satellite clock we cannot compare the AC standard deviation results.

Despite the fact that our results for the APC and the satellite clock offsets provided by the broadcast ephemeris are consistent with the results from the IGS ACC, they do not, in our opinion, give a good representation of the quality of the broadcast products. As shown in the left hand pane of fig. 5.30, the radial orbit errors are strongly correlated with the clock errors mainly due to the use of a different set of phase center offsets. Taking the PCOs into account (middle and right pane) removes most of the correlation and significantly reduces the errors on both the clocks (rms 0.58m or 1.94ns) and radial positions (rms 0.14m). The errors in the pseudo range domain are now dominated by the clock errors with an rms of 0.57m.

Heng et al. (2011a) have investigated the GPS signal in space integrity by analyzing all broadcast ephemerides information since selective availability (SA) was switched off in 2000. They compared satellite APCs from the broadcast products to the IGS precise products after applying the PCOs. Trying PCOs from both the IGS and the NGA, they found that the IGS PCOs led to biases in the radial direction and opted to use the NGA PCOs. This is in line with our findings that the PCOs from the NGA are consistent with the broadcast products. Unlike our approach in section 5.3.2.4, Heng et al. (2011a) do not mention a similar consideration for the satellite clock offsets. Results show that, during the first year after SA was switched off, many anomalies occurred on all satellites. Afterwards, and specifically after 2004, anomalies were much less frequent. Heng et al. (2011c) show that the clock performance dominates the performance in the pseudo range domain; the radial orbit errors are reported to have a standard deviation of 13 cm to 24 cm between the blocks and the clocks of 38cm to 107cm. These results are conform our finding for the broadcast products with an rms error of 14cm for the radial direction and 58cm for the satellite clocks.

The IGS ACC also provides results from comparisons of IGU predicted results to IGS rapid products as well as a log file of any events that may have impacted the IGU performance or delivery. For the period under investigation the IGS ACC reports weighted rms errors of about 2 cm for the orbits and 2 ns (i.e. 60cm) for the clock offsets. These results are based on the first 6 hours of the predicted orbits and clocks. However, as mentioned the IGU products have a latency of 3 hours which means that the prediction interval relevant for real-time positioning is actually 3-9 hours, which is also the interval considered in section 5.3.2.1. Therefore, the IGS ACC results should show a better accuracy than our results. This is indeed the case since we found an orbit rms error of 4.1 cm on average over all directions and a clock rms error of 90 cm. For the full 24 hours of prediction the IGS ACC reports an orbit accuracy of about 5cm weighted rms. The IGS ACC does not provide any results for the degradation of the clock predictions, even though this turns out to be a dominant and growing error source in our analysis (fig. 5.12). Another reason that might explain some of the differences between our results and the IGS ACC is the weighting scheme which is not provided. This is quite crucial as we found an rms of 140 cm for the block IIA satellites and only 35cm for the block IIR satellites. Results in the pseudo range domain are again not provided by the IGS ACC.

The outliers we found in the IGU orbit products of satellites PRN21 and PRN25 are also listed in the event log file of the IGS ACC. The eclipsing season of PRN25 was identified as a possible cause of its misbehavior. No cause was found for the misbehavior of PRN21. The absence of satellite PRN30 starting from igu16356_00.sp3 is also listed, the large clock prediction errors in the preceding files is not mentioned.

5.5 Conclusions

In this chapter the orbit and clock offsets were both studied separately and combined. The results showed that the errors in the orbit and clock products individually are actually larger than the errors in the combined product as they impact the user. This is in part due to correlation resulting from the estimation process, but also due to the use of different phase center offsets. These different PCOs lead to differences in the computed satellite phase center positions (mainly in the radial direction), which are for a large part absorbed by the satellite clock offsets. It can thus be concluded that a PPP user should obtain the satellite orbit and clock products from the same provider and not mix products.

This result also illustrates that the quality of a given PPP product can only be assessed by analyzing the orbit and clock information together. Since neglecting the correlation will not give a correct representation of the accuracy of the product. Performing the quality assessment in the (pseudo) range domain also prevents possibly different PCOs from clouding the comparison between products. Furthermore the significance of both the common clock and constant bias per satellite were demonstrated. Whether these impact the accuracy of the estimated parameters of interest, depends on the user algorithms and they should be treated accordingly.

Another finding was that compared to the IGS satellite orbit prediction the clock prediction is relatively poor, and dominates the combined error. Additionally the clock prediction for older GPS satellites is worse than for the newer satellites. If these products are used for PPP, the stochastic model should reflect both these effects. It should be noted that a number of older GPS Block IIA satellites has been decommissioned after the period which was analyzed in this chapter. The Block IIR and newer satellites thus give a better representation of the current performance.

In recent years the international GNSS community, including the IGS itself, has started to focus on (near) real-time provision of precise satellite orbit and clock products. The RETICLE clock products from DLR/GSOC are one such near real-time product. These satellite clock offsets are estimated while keeping the satellite orbits fixed to the values predicted by the IGS. In this case the products can be mixed since the same PCOs are used by definition and errors in the orbit will (partially) be compensated by the computed satellite clocks. Thanks to the near real-time aspect of these clock offsets the poor predictability of the satellite clocks (and in particular the older GPS satellite clocks) plays a much less significant role. The quality of these products is much higher and approaches the post-processed products. In addition a separate treatment of the older GPS satellites in the stochastic model is not needed (similar to the post-processed products).

6 Geometry-free Analysis of GNSS Signal Stochastics

In general, when fitting a model to a physical process, a choice needs to be made whether to treat certain parameters in a functional or in a stochastic manner. The parameters that are included in the functional model are generally those we wish to estimate or for which we have accurate models. For other parameters we often do not have enough knowledge of the underlying process, and we have to suffice with a stochastic treatment of the parameters.

For Precise Point Positioning, the main error sources that have to be accounted for in the stochastic model are pseudo range and carrier phase measurement noise and satellite orbit and clock errors. Other error sources (e.g. atmospheric delays) can be modeled and/or estimated in the positioning filter (see chapter 3 for a complete overview), although errors in the model values must still be taken into account.

Multipath on GNSS pseudo range measurements can be approached from both angles. With precise knowledge of the geometric and physical properties of reflecting objects, the multipath detour and impact on the receiver can be determined from a functional multipath model, with an approach known as ray tracing. In Tiberius et al. (2009) it was shown that for specific cases a simple multipath model based on specular reflection can already predict the observed multipath to some extend. Also from inspection of the receiver behavior itself, either of the tracking loops directly or of the resulting measured range and carrier-to-noise ratio (C/N_0), certain multipath parameters can be determined via functional modeling. For static receivers, another approach is to map the multipath delays a priori versus elevation and azimuth (together with possible antenna delays), which we will explore in chapter 8. However, since the multipath environment of an antenna is generally not known with enough detail and can change rapidly for a moving receiver or due to reflecting objects or temperature and humidity changes, a stochastic modeling approach is often preferred.

Since chapter 5 already treated satellite orbit and clock errors, this chapter will focus on measurement noise and multipath errors. For this purpose, a geometry-free GNSS measurement analysis approach is presented that separates the different contributions to the measurement errors of pseudo range code and carrier phase observations at the receiver. The analysis relies on linear combinations of the available observables and can be applied to a single receiver setup, a short baseline setup, and/or a zero baseline setup. Quantitative results are presented for the thermal code and phase measurement noise and for the correlation between the observations. The influence of multipath on the different combinations of observations is also determined. Comparison of the results with theoretical approximations confirms the validity of the used approach.

The goal of this chapter is to provide insight into the stochastic properties of GNSS range measurements which can be used to setup the stochastic model of the observations essential for positioning algorithms (chapter 8) and to the RAIM model (chapter 7).

Section 6.1 is an adaptation of de Bakker et al. (2009) and introduces the analysis method for single frequency linear combinations and presents results of GPS, EGNOS and GIOVE short and zero baseline measurements on the L1/E1 frequency. In section 6.2, which is adaptated from de Bakker et al. (2012), the analysis method is extended to dual and multi frequency data, and results are presented for short and zero baseline measurements of the GPS L1C/A and L5Q signals as well as the GIOVE E1B and E5aQ signals. Section 6.3 focuses on multipath and other time correlated errors present in the pseudo range measurements, and was previously published as de Bakker (2011) in an adapted form. Here results are presented for several single receiver setups and for the GPS L1, L2 and L5 frequencies as well as the GIOVE E1, E5, E5a and E5b frequencies. The data sets used in sections 6.1 and 6.2 were opportunity driven as they represent some of the earliest measurements made to the Galileo In Orbit Validation Element (GIOVE) satellites. GIOVE A and B have since been decommissioned and were followed by a number of IOV (In-Orbit Validation) and FOC (Full Operational Capability) satellites, with similar if not identical characteristics (ESA, 2015). The methods presented in this chapter are generally applicable (see e.g. Cai et al., 2015).

6.1 Single frequency analysis

Several useful single frequency linear combinations will be introduced and demonstrated using some of the earliest datasets collected in the field with both GIOVE A and B; simultaneously collected GPS and EGNOS signals are also included. At the time of the measurement campaign there was no publicly available GIOVE orbit data with sufficient accuracy. This makes the geometry-free model ideal for this analysis, since it does not rely on satellite orbit data.

6.1.1 Single frequency measurement campaign

On the 6^{th} and 10^{th} of July 2008 a short and zero baseline were measured respectively with two identical Septentrio AsteRx1 single frequency receivers with Galileo enabled firmware. The short baseline was measured, in a fairly benign radio environment, in a field near Delft with virtually no obstacles within a radius of a few kilometers. The receivers were connected to two identical Septentrio PolaNt survey antennas that were placed equally oriented on tripods at 4 meters distance from each other. More details can be found in Tiberius et al. (2008). The zero baseline was measured on a flat roof in Delft on top of a six story building with both receivers connected through a signal splitter to a single Septentrio PolaNt antenna. Sky visibility on the roof was unobstructed down to the horizon, but due to the roof significant multipath effects occurred. The multipath mitigation technique of the receivers was *not* applied during this measurement campaign. Table 6.1 summarizes the relevant properties of the antennas and receivers. During the measurement campaign GPS, EGNOS (European Geostationary Navigation Overlay Service) and Galileo satellites were tracked by the receivers with a measurement rate of 1 Hz. A minimum of eight GPS satellites were visible during the entire measurement period. Galileo, the European

GNSS, at the time of these measurements had two test satellites in orbit: GIOVE A and B (indicated in the graphs by E32 and E31 respectively). Both GIOVE satellites were visible simultaneously for over 1.5 hours during the short baseline measurements and for over 2.5 hours during the zero baseline measurements. The E1BC signal from the GIOVE satellites was tracked with a pure Binary Offset Carrier BOC(1,1) replica, not multiplexed BOC (for GIOVE-B), but the corresponding loss is less than 1 dB (Hein et al., 2006). The GIOVE satellites did not transmit usable navigation messages during the measurement campaign. EGNOS, the European space based augmentation system, uses three geostationary satellites of which two were tracked during the measurement campaign (S120 and S126). Figures 6.1 and 6.2 show the sky plots for the short and zero baseline measurements respectively.

Table 6.1: Receiver and antenna parameters and settings

Receiver	AsteRx1
Manufacturer	Septentrio NV
Frontend bandwidth	>20MHz
Channel configuration	12 GPS channels
	4 SBAS channels (2 used)
	2 Galileo channels
Delay lock loop bandwidth	0.25 Hz (single sided)
Phase lock loop bandwidth	10 Hz (single sided)
Antenna	PolaNt
Manufacturer	Septentrio NV
Gain role off	10 dB

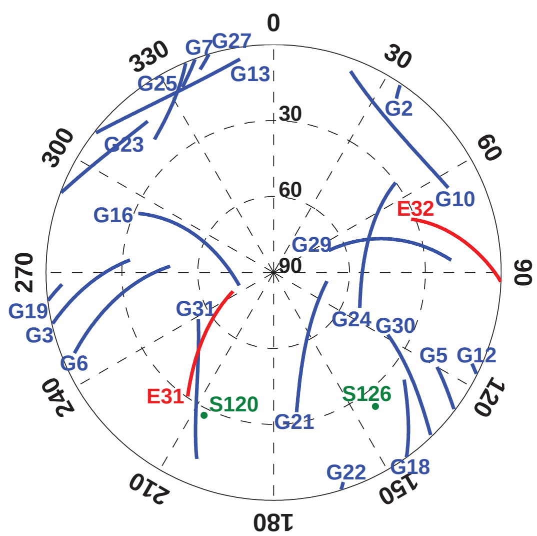

Figure 6.1: Skyplot for the short baseline measurements (20:10-22:05 UTC 6^{th} July 2008)

Table 6.2 summarizes important properties of the tracked signals. It is important to note that the geostationary EGNOS satellites by definition move very little with respect to a stationary receiver on Earth, so the multipath delay also changes very little. The received signal strength is different for the three systems. However, as all results in this section are presented with respect to a carrier-to-noise density ratio (C/N_0) of 45 dB-Hz, this does not influence the conclusions.

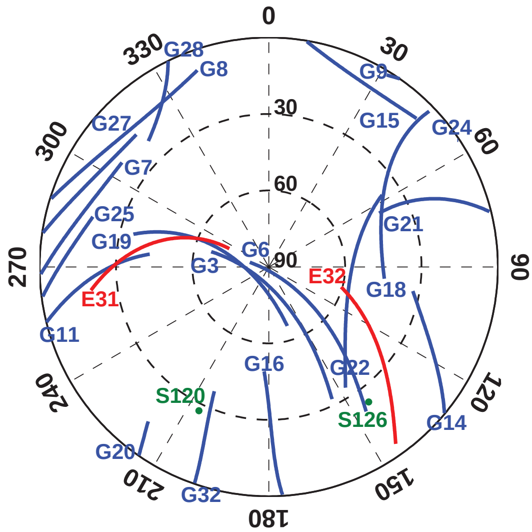

Figure 6.2: Skyplot for the zero baseline measurements (23:05-01:50 UTC $10^{th}/11^{th}$ July 2008)

Table 6.2: GNSS signal specifics

	Transmit BW [MHz]	Code rate [Mchip/s]	Sub carrier [MHz]	Symbol duration [ms]
GPS L1C/A	20.46	1.023	-	20
Galileo E1BC	>20	1.023	1.023	4
EGNOS L1C/A	2.2	1.023	-	2

To visualize the influence of different conditions, receiver performance is often shown versus the satellite elevation. In this section the measured C/N_0 is used instead, because the received signal strength is different for each GNSS. For comparison, the C/N_0 versus satellite elevation is presented in figs. 6.3 and 6.4 for the short and zero baseline respectively. The elevation of the GIOVE satellites was computed from NASA two line elements. For GPS the C/N_0, presented in the figures for both receivers at the baseline, is averaged over all satellites. The variation of the C/N_0 with elevation is mainly due to the receiver antenna gain pattern and multipath. Other influences are the distance to the satellite, the satellite antenna gain pattern and the atmospheric losses. The transmitted power of individual GPS satellites can also differ slightly. The differences between the short and zero baseline results are due to the different multipath environments. The zero baseline measurements show multipath that slowly changes with satellite elevation. This could be a result of a reflective surface, in this case the roof, very close to the antenna. The antenna was mounted only 0.1 m above the roof. The short baseline measurements show multipath that changes more rapidly with satellite elevation. This could be a result of a reflective surface, in this case the ground, further away from the antenna. The figures clearly show that, for the same elevation, the measured C/N_0 for one component of the GIOVE E1BC signal is 3-4 dB-Hz lower than for the GPS C/A signal. This effect is mainly due to the specified received power, which is lower for the GIOVE signal component than for the GPS C/A signal and the actual transmitted power of the GPS satellites that tends to be above specifications.

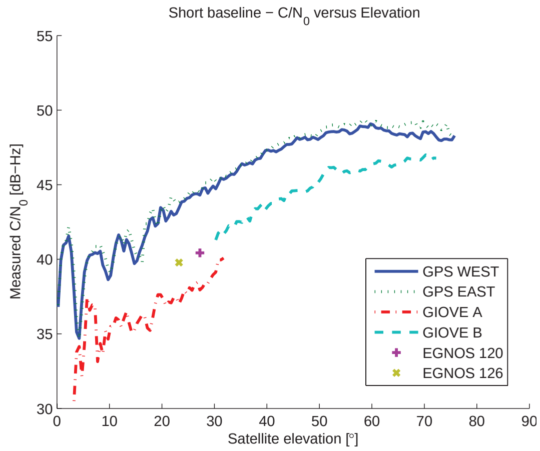

Figure 6.3: Measured C/N_0 versus satellite elevation for the short baseline showing both receivers WEST and EAST averaged for all GPS satellites and only receiver WEST for GIOVE and EGNOS satellites separately

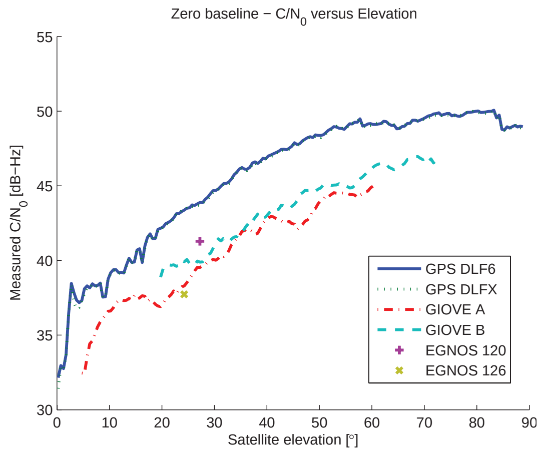

Figure 6.4: Measured C/N_0 versus satellite elevation for the zero baseline showing both receivers DLF6 and DLFX averaged for all GPS satellites and only receiver DLF6 for GIOVE and EGNOS satellites separately

6.1.2 Linear combinations of single frequency observations

The single frequency observation equations for one satellite (expressed in units of range) can be obtained by simplifying eqs. (3.3) and (3.4) as follows:

$$P = \|\mathbf{r}^s - \mathbf{r}_r\| + c\delta t_r - c\delta t^s + T + \mathcal{I} + m + \zeta + \epsilon \tag{6.1}$$

$$\Phi = \|\mathbf{r}^s - \mathbf{r}_r\| + c\delta t_r - c\delta t^s + T - \mathcal{I} + \mu + A + \xi + \varepsilon \tag{6.2}$$

with P the pseudo range code observation, Φ the carrier phase observation, $\|\mathbf{r}^s - \mathbf{r}_r\|$ the geometric range, c the speed of light, δt_r the receiver clock error, δt^s the satellite clock error, T the tropospheric delay, $\mathcal{I}$ the ionospheric delay, A the phase ambiguity, ϵ and ε random code and phase measurement errors respectively with expectation equal to zero ($E\{\epsilon\} \equiv 0$; $E\{\varepsilon\} \equiv 0$).

Other systematic delays on the code and phase measurements have been separated based on their variability over time, m contains the quickly varying code delays and is dominated by the code multipath, μ contains the quickly varying phase delays and is dominated by the phase multipath, ζ contains the slowly changing code delays including the instrumental code delays, and ξ contains the slowly changing phase delays including the instrumental phase delays, the phase windup and the phase center variations.

Geometry-free model In the geometry-free model (see e.g. Odijk, 2008) the first 4 terms ($\|\mathbf{r}^s - \mathbf{r}_r\| + c\delta t_r - c\delta t^s + T$) at the right-hand side of eqs. (6.1) and (6.2), as well as other non-dispersive delays, are equal for all observables and can be denoted by g:

$$P = g + \mathcal{I} + m + \zeta + \epsilon \tag{6.3}$$

$$\Phi = g - \mathcal{I} + \mu + A + \xi + \varepsilon \tag{6.4}$$

Code-minus-Carrier A linear combination that can be used to determine the code noise is the so-called Code-minus-Carrier (CC):

$$CC \equiv P - \Phi \approx 2\mathcal{I} - A + m + \zeta - \xi + \epsilon \tag{6.5}$$

In this combination the lumped parameter g (geometric range, receiver and satellite clock and tropospheric delay) is eliminated from the observation equation. The phase noise and phase multipath are assumed to be an order of magnitude smaller than the code noise and code multipath respectively and they are consequently neglected.

Stand alone receiver This section presents two methods to determine the code noise from the Code-minus-Carrier measurements of a single receiver. The first is by fitting a low order polynomial to the data and then subtracting this polynomial from the data. The second, called time differencing, is by taking the differences between measurements from consecutive epochs.

Low order polynomial fitting By fitting a low order polynomial to the code-minus-carrier data, the slowly changing components can be removed from the data. This includes the instrumental delays (Liu et al., 2004), the constant ambiguities, the low frequency multipath and the low frequency ionospheric delay. This leaves twice the high frequency ionospheric delay, the high frequency code multipath and the code noise. The expectation E and dispersion D of the code-minus-carrier observations are:

$$\begin{aligned} E\{CC - p(t)\} &\approx 2d\mathcal{I} + dm \\ D\{CC - p(t)\} &\approx \sigma_P^2 \end{aligned} \tag{6.6}$$

where $p(t)$ is the low order polynomial, σ_P is the standard deviation of the code measurement noise, $d\mathcal{I}$ and dm are the residual ionospheric and multipath delay respectively. The top pane of fig. 6.5 shows the code-minus-carrier combination (solid line) and the fitted polynomial (dashed line) for GPS PRN18 and the bottom pane shows the measured C/N_0. The periodic effect that is clearly visible in both panes is most likely caused by multipath. PRN18 was selected for its distinct multipath pattern, but other satellites show similar results. Figure 6.5 confirms that the polynomial does not follow the multipath variations and consequently the multipath is not removed when the polynomial is subtracted from the code-minus-carrier observations.

The order of the polynomial should be chosen such that it removes most of the ionosphere delays while not significantly reducing the measurement noise that we want to quantify. Additionally, the polynomial should be estimated from enough data points that its uncertainty can be neglected in the dispersion of eq. (6.6). In the following we will use a second order polynomial for data segments of 120 epochs. In this case the polynomial reduces the random white noise by less than 1% while eliminating most ionosphere delays.

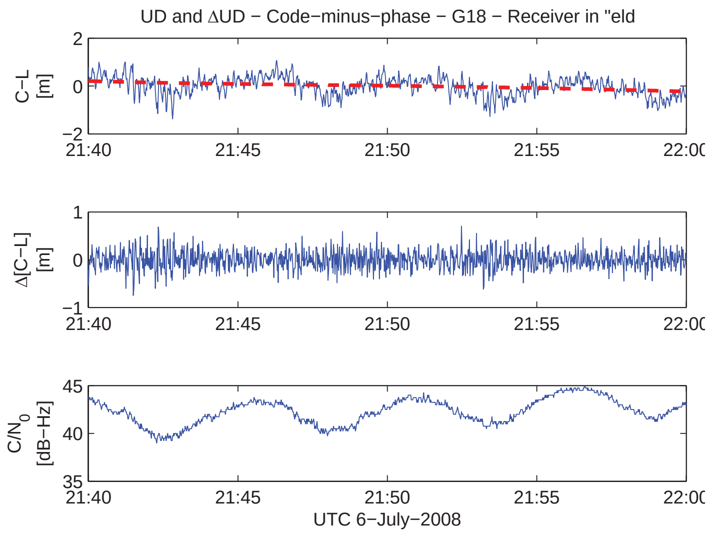

Figure 6.5: Stand alone receiver code-minus-carrier observations for GPS PRN18 on short baseline (top: undifferenced; middle: time differenced; bottom: measured C/N_0). Both the undifferenced observations and the measured C/N_0 show a periodic effect, most likely caused by multipath. The time differenced observations do not show these delays, but the variance of the noise changes with the C/N_0.

The standard deviation of the code-minus-carrier observations after subtraction of the polynomial is presented in fig. 6.6 versus the measured C/N_0 for each GNSS. Each data point represents 120 epochs. For each GNSS the mean standard deviation of the observations for a C/N_0 of 45 dB-Hz is estimated by fitting a line to the data that describes the standard deviation as a function of the measured C/N_0. The slope of these lines follows from the inversely proportional relation between the C/N_0 (as ratio-Hz) and the variance of the noise (see e.g. Braasch and van Dierendonck, 1999) and fits well with the data. These results together with results from other analysis techniques are also provided in table 6.3 (there called 1Rx-UD short for single Receiver Undifferenced). It is clear that the GIOVE satellites perform better than the GPS satellites for the same measured C/N_0, because of the different signal modulation. The EGNOS satellites show a larger standard deviation than both the GPS and GIOVE satellites, mainly due to the smaller transmit bandwidth.

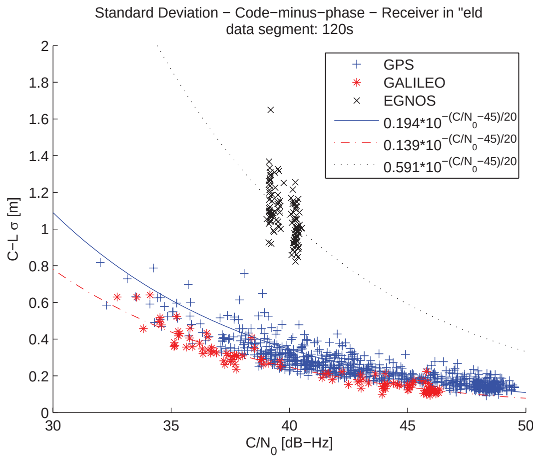

Figure 6.6: Stand alone receiver code-minus-carrier standard deviation versus the measured C/N_0 on short baseline for data segments of 120s with fitted line based on theoretical relation for GPS, EGNOS and Galileo

Time difference In the difference between two epochs, the phase ambiguity is eliminated and the ionospheric delay, multipath and instrumental delays are reduced. The expectation and dispersion of the time differenced code-minus-carrier observations are:

$$\begin{aligned} E\{\Delta CC\} &\approx 2\Delta\mathcal{I} + \Delta m \\ D\{\Delta CC\} &\approx 2\left(1-\varrho_\Delta\right)\sigma_P^2 \end{aligned} \tag{6.7}$$

where Δ indicates the time difference and ϱ_Δ is the time correlation coefficient ($|\varrho_\Delta| < 1$) between two consecutive code observations. The standard deviation of the code measurements is assumed to be constant from one epoch to the next. The middle pane in fig. 6.5 shows the time differenced code-minus-carrier observations for GPS PRN18. The multipath delays, present in the undifferenced code-minus-carrier observations (top pane), are removed in the time differenced observations (Δm is small). The variations in the measured C/N_0 due to multipath (bottom pane) do still influence the variance of the time differenced code-minus-carrier observations; careful inspection of fig. 6.5 shows that the variation in the middle pane is larger when the C/N_0 is smaller. For the time differenced observations the standard deviation for a C/N_0 of 45 dB-Hz has again been estimated by fitting a line to the 120s data segments. This fitting of the data is very similar for each combination of observations and therefore no more figures like fig. 6.6 are presented. Results are provided in table 6.3 (1Rx-ΔUD) after normalization to the undifferenced levels by division of the standard deviation by $\sqrt{2}$. This is the factor by which the standard deviation increases by differencing if there is no correlation.

Between receiver difference Measurements from two receivers tracking the same satellites can be combined to remove common errors from the measurements. Traditionally, the main purpose of taking the between receiver single difference (SD) is to eliminate the satellite clocks from the observation equations, but these are already removed in the geometry-free code-minus-carrier combination. Now the fractional part of the phase ambiguity and the instrumental delay at the satellite are removed. For a short baseline (SB) the ionospheric delay is also removed, because the differential ionospheric delay can be neglected for a short baseline (here only 4 m). The antenna hardware delays are reduced in the single difference if the same antenna type is used at both ends of a short baseline, which is true for this measurement campaign. For a zero baseline (ZB) the ionospheric delay, the multipath errors and the antenna hardware delays are removed, because they are the same for both receivers. The resulting observations contain the SD phase ambiguity, the remaining SD hardware delay, the SD code noise and, for the short baseline, the SD multipath error. The expectation and dispersion of the SD code-minus-carrier observations are:

$$\begin{aligned} E\{CC_{\mathsf{SD}}\} &\approx -A_{\mathsf{SD}} + (\zeta - \xi)_{\mathsf{SD}} + [m_{\mathsf{SD}}]_{\mathsf{SB}} \\ D\{CC_{\mathsf{SD}}\} &\approx 2\,(1 - [\varrho_{\mathsf{SD}}]_{\mathsf{ZB}})\,\sigma_P^2 \end{aligned} \tag{6.8}$$

where ϱ_{SD} is the correlation coefficient between the code observations of the two receivers. For the short baseline it is assumed that there is very little correlation between measurement noise of the two receivers ($[\varrho_{\mathsf{SD}}]_{\mathsf{SB}} \approx 0$), but for the zero baseline a large part of the noise is the same for both receivers (Gourevitch, 1996) giving a high correlation ($[\varrho_{\mathsf{SD}}]_{\mathsf{ZB}} \neq 0$). Therefore, an increase of the variance of the noise by a factor 2 is only a good assumption for the SD short baseline observations. For multipath it is the other way round, multipath is absent for the zero baseline ($[m_{\mathsf{SD}}]_{\mathsf{ZB}} \equiv 0$), but not for the short baseline ($[m_{\mathsf{SD}}]_{\mathsf{SB}} \neq 0$). Subtraction of the mean value from the observations removes the phase ambiguity, which is constant if there are no cycle slips, and reduces the remaining hardware delay. Figure 6.7 again shows the undifferenced code-minus-carrier observations for GPS PRN18 in the top pane and the measured C/N_0 in the bottom pane, but now for both receivers in the short baseline setup. The multipath effects for the two receivers are similar but not the same. The middle pane shows the SD code-minus-carrier observations. These observations still contain multipath in the same order of magnitude as the undifferenced code-minus-carrier observations. For the SD observations the estimated standard deviation for a C/N_0 of 45 dB-Hz is again provided in table 6.3 (SB-SD and ZB-SD) after normalization to the undifferenced levels.

Time difference By taking the difference between the SD observations of two epochs, the phase ambiguity is eliminated and the remaining hardware delay and multipath are reduced. This gives the following expectation and dispersion for the time differenced SD code-minus-carrier observations:

$$\begin{aligned} E\{\Delta CC_{\mathsf{SD}}\} &\approx [\Delta m_{\mathsf{SD}}]_{\mathsf{SB}} \\ D\{\Delta CC_{\mathsf{SD}}\} &\approx 4\,(1 - \varrho_{\Delta})\,(1 - [\varrho_{\mathsf{SD}}]_{\mathsf{ZB}})\,\sigma_P^2 \end{aligned} \tag{6.9}$$

The variance of the time differenced SD measurements is dependent on both the time correlation between two epochs and the correlation between the observations from the

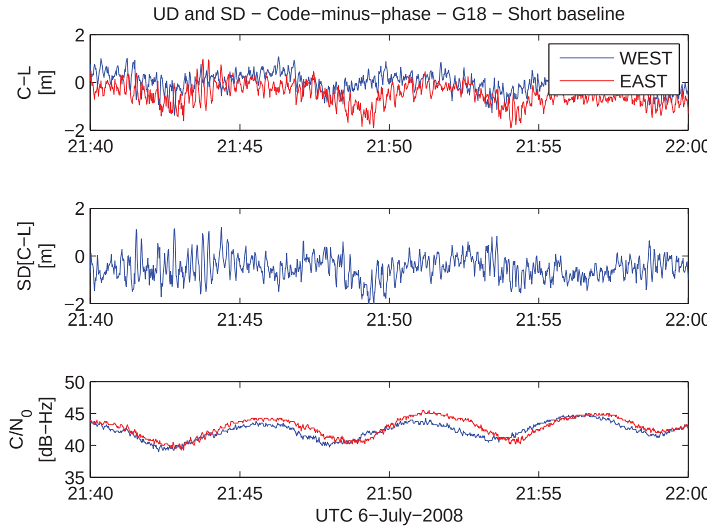

Figure 6.7: Single difference short baseline code-minus-carrier observations for GPS PRN18 (top: undifferenced; middle: single difference; bottom: measured C/N_0). The periodic effect visible in the undifferenced observations and the measured C/N_0 that is most likely caused by multipath, is not removed in the single difference.

two receivers. Results for the estimated standard deviation of the time differenced SD observations for a C/N_0 of 45 dB-Hz are provided in table 6.3 (SB-ΔSD and ZB-ΔSD) after normalization to the undifferenced levels.

Double difference Subtracting the measurements to one reference satellite from the measurements to all other satellites, removes all common terms from the measurements. Traditionally, the main purpose of taking the between satellite difference is to eliminate the receiver clocks from the observation equations, but these are already removed in the geometry-free code-minus-carrier combination. Now the fractional part of the phase ambiguity and the instrumental delay at the receiver are removed. By taking the between satellite difference and the between receiver difference the so called double differences (DD) are formed. All terms that are removed in the SD are also removed in the DD. This leaves the DD phase ambiguity, the DD code noise and, for the short baseline only, the DD multipath error. The variance of the code noise increases by a factor 4 if there is no correlation between the observations. The noise on the observations made to different satellites is assumed to be uncorrelated. As pointed out with the SD, for the short baseline the observations of the two receivers to the same satellite are also assumed to be uncorrelated, but this is not true for the zero baseline. The expectation and dispersion of the DD code-minus-carrier observations is:

$$\begin{aligned} E\{CC_{\mathsf{DD}}\} &\approx -\lambda N + [m_{\mathsf{DD}}]_{\mathsf{SB}} \\ D\{CC_{\mathsf{DD}}\} &\approx 4\,(1 - [\varrho_{\mathsf{SD}}]_{\mathsf{ZB}})\,\sigma_P^2 \end{aligned} \tag{6.10}$$

Because all fractional parts of the phase ambiguities are removed the resulting DD ambiguities have an integer value (indicated by N) times the wavelength λ.

Between satellite difference C/N_0 As we have to combine two satellites for the between satellite differences, a pseudo C/N_0 is computed with the following equation:

$$(C/N_0)_{12} = -10\log\left\{\frac{1}{2}\left(10^{-\frac{(C/N_0)_1}{10}} + 10^{-\frac{(C/N_0)_2}{10}}\right)\right\} \tag{6.11}$$

where $(C/N_0)_{12}$ is the between satellite difference carrier-to-noise density ratio; $(C/N_0)_1$ and $(C/N_0)_2$ are respectively the carrier-to-noise density ratios of the reference satellite and the second satellite forming the satellite pair. This equation follows from the inverse relation between the variance and the carrier-to-noise density ratio when expressed in ratio-Hertz. A factor $\frac{1}{2}$ is added to normalize the C/N_0 to the undifferenced levels. A certain value of the pseudo C/N_0 can be interpreted as following from the difference between 2 observations with this same value of the C/N_0. Table 6.3 shows the results for the standard deviation of the DD code-minus-carrier observations for a C/N_0 of 45 dB-Hz, for both the short and zero baseline (SB-DD and ZB-DD).

Time difference In the time difference between the DD observations of two epochs (also called triple difference), the phase ambiguity is eliminated and the multipath is reduced. This gives the following expectation and dispersion for the time differenced DD code-minus-carrier observations:

$$\begin{aligned} E\left\{\Delta CC_{\mathsf{DD}}\right\} &\approx [\Delta m_{\mathsf{DD}}]_{\mathsf{SB}} \\ D\left\{\Delta CC_{\mathsf{DD}}\right\} &\approx 8\left(1-\varrho_{\Delta}\right)\left(1-[\varrho_{\mathsf{SD}}]_{\mathsf{ZB}}\right)\sigma_P^2 \end{aligned} \tag{6.12}$$

The expectation value is very close to zero especially for the zero baseline setup. Results for the estimated standard deviation of the measurement noise are again provided in table 6.3 (SB-ΔDD and ZB-ΔDD).

Table 6.3: Normalized standard deviations of the code noise in meters for $C/N_0 = 45$ dB-Hz for all analysis techniques and each GNSS

	Observation combination	Comparison with thermal noise	GPS Field	GPS Roof	Galileo Field	Galileo Roof	EGNOS Field	EGNOS Roof
1	1Rx-UD	+multipath	0.20	0.38	0.14	0.39	0.59	0.90
	SB-SD		0.20		0.14		0.60	
	SB-DD		0.20		0.14		0.60	
2	1Rx-ΔUD	−time correlation	0.10	0.12	0.07	0.09	0.39	0.47
	SB-ΔSD		0.10		0.07		0.37	
	SB-ΔDD		0.10		0.06		0.39	
3	ZB-SD	−common LNA noise		0.11		0.06		0.21
	ZB-DD			0.11		0.05		0.23
4	ZB-ΔSD	−time correlation		0.07		0.04		0.16
	ZB-ΔDD	−common LNA noise		0.07		0.04		0.16

Carrier phase analysis In all analyses so far the carrier phase acted as an accurate reference in the code-minus-carrier combination. The noise of the carrier phase itself can be analyzed along similar lines using the DD carrier phase observations. A low order polynomial must be fitted to the DD carrier phase segments in between cycle slips and receiver clock jumps in order to remove carrier phase ambiguities, DD geometric range and clock synchronization effects. For the short baseline this leaves the carrier phase measurement noise and the carrier phase multipath. For the zero baseline multipath is removed in the between receiver difference so this leaves mainly the phase noise. For the zero baseline the measurement noise of the phase observations of the two receivers is correlated (Gourevitch, 1996), giving the following expectation value and dispersion:

$$\begin{aligned} E\{\Phi_{\mathsf{DD}} - p(t)\} &\approx [\mu_{\mathsf{DD}}]_{\mathsf{SB}} \\ D\{\Phi_{\mathsf{DD}} - p(t)\} &\approx 4\,(1 - [\varrho_{\mathsf{SD}}]_{\mathsf{ZB}})\,\sigma_\Phi^2 \end{aligned} \tag{6.13}$$

The polynomial p(t) is again based on enough data points to safely neglect its uncertainty in the dispersion of eq. (6.13). Results for the standard deviation of the DD phase observations for a C/N_0 of 45 dB-Hz are presented in table 6.4 for both the short and zero baseline (SB-DD and ZB-DD). Because the results are very similar for each GNSS, no distinction is made in table 6.4 between the different systems. This is in line with expectations since the standard deviation of the carrier phase depends only on the C/N_0 and not on the signal modulation. Because the geometric effect of the receiver clock offset is not completely removed by the polynomial fitting, there remains a small effect on the DD phase observations proportional to the Doppler offset. As a result the stationary EGNOS satellites perform slightly better than the other satellites.

Table 6.4: Normalized standard deviations of the phase noise in cycles for $C/N_0 = 45$ dB-Hz for all analysis techniques

	Observation combination	Comparison with thermal noise	Normalized noise standard deviation
1	SB-DD	+multipath	0.0043
2	SB-ΔDD	−time correlation	0.0040
3	ZB-DD	−common LNA noise	0.0014
4	ZB-ΔDD	−time correlation −common LNA noise	0.0015

Time difference In the triple difference phase observations the DD geometric range and the geometric effects of the clock offsets are reduced and the carrier phase ambiguities are eliminated. In addition most of the phase multipath is removed leaving mainly the phase noise. This gives the following expectation value and dispersion:

$$\begin{aligned} E\{\Delta\Phi_{\mathsf{DD}}\} &\approx [(\Delta\mu)_{\mathsf{DD}}]_{\mathsf{SB}} \\ D\{\Delta\Phi_{\mathsf{DD}}\} &\approx 8\,(1 - \varrho_\Delta)\,(1 - [\varrho_{\mathsf{SD}}]_{\mathsf{ZB}})\,\sigma_\Phi^2 \end{aligned} \tag{6.14}$$

Figure 6.8 shows the ΔDD phase observations for 120s data segments for each GNSS for the short baseline observations. From this figure it can be concluded that the standard deviation of the phase observations as a function of the C/N_0 is the same for each GNSS. Therefore, the standard deviation for a C/N_0 of 45 dB-Hz has been estimated from all observations simultaneously (see table 6.4 SB-ΔDD and ZB-ΔDD).

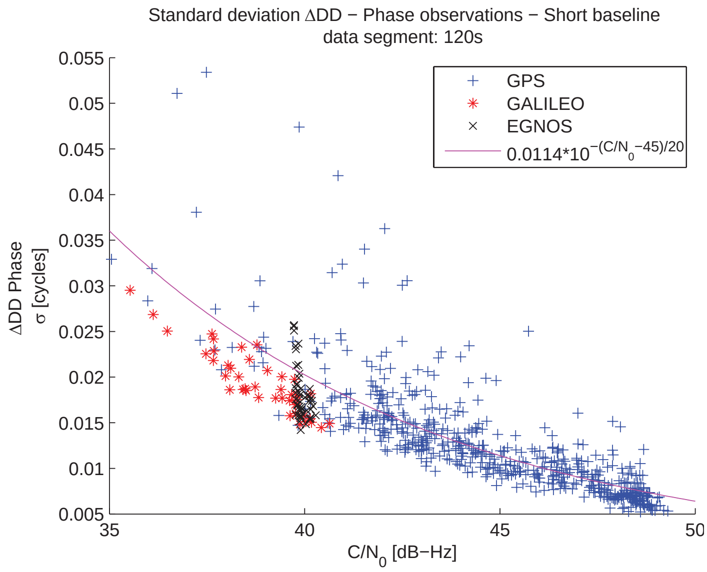

Figure 6.8: Short baseline ΔDD phase observations versus measured C/N_0 for data segments of 120s. The three navigation systems perform very similar, so one line has been fitted to all the data points

Comparison with theory Table 6.3 shows the standard deviation of the observations for each of the discussed combinations for a C/N_0 of 45 dB-Hz. These standard deviations have been normalized to the undifferenced levels. To clarify the similarities and differences in the normalized standard deviations of the code noise for the different combinations of the observables, an analysis is presented here, with special attention for three effects that influence the computed standard deviations. These are: multipath, time correlation of the observations (resulting from the tracking loops) and correlation resulting from both receivers tracking the same signal traveling through the atmosphere, antenna and Low Noise Amplifier (LNA) in the zero baseline setup (Gourevitch, 1996). In table 6.3 the different observation combinations are grouped based on how they deal with these three effects. The first group (single receiver, short baseline SD and short baseline DD) does not remove the multipath from the observations. Therefore, it is expected that the computed noise for this group is larger than the theoretical thermal noise. The second group (single receiver time difference, short baseline time difference SD, and short baseline time difference DD) removes most of the multipath from the measurements. In addition the standard deviation of the noise is further reduced if the measurements are positively correlated in time. Therefore, it is expected that the computed noise is smaller than the theoretical thermal noise if the correlation is positive. The third group (zero baseline SD and zero baseline DD) also removes the multipath from the measurements. In addition the standard deviation of the noise is further reduced because the measurements of the two receivers are correlated as a result of being connected to the same antenna and LNA ($[\varrho_{\mathrm{SD}}]_{\mathrm{ZB}} = \varrho_{\mathrm{LNA}} \neq 0$). Therefore, it is expected that the computed noise is smaller than the theoretical thermal noise. The noise levels of group two and three cannot easily be compared. The fourth group (zero baseline time difference SD and zero baseline time difference DD) also removes the multipath from the measurements. In addition the computed standard deviation of the code noise is further reduced by both the time correlation and the correlation resulting from the antenna and LNA and so it is expected that this group has the smallest standard deviation of the noise. The values in table 6.3 are very close to each other within each group, with the exception of group one. This is an expected result, because the multipath is very different for the field and roof environment. Using results of group three and four, the time correlation of the observations can be determined by solving the following relation for the time correlation coefficient ϱ_Δ:

$$\sigma_\Delta^2 = 2\,(1 - \varrho_\Delta)\,\sigma^2 \tag{6.15}$$

where σ and σ_Δ are the (not normalized) standard deviations of the code noise of group three and the corresponding time differenced code noise of group four respectively. Appendix A shows that this approach is equivalent to the determination of the autocorrelation coefficient at a time delay equal to the measurement interval. When the correlation has been determined, the undifferenced thermal code noise (σ) can be estimated by applying eq. (6.15) to the standard deviation of group two (σ_Δ). Here it is assumed that the tracking loop time correlation is the same for the short and zero baselines. Amiri-Simkooei and Tiberius (2007) showed that this is a good assumption for the baseline components. The resulting estimated code noise represents thermal noise (without multipath and without underestimation due to time correlation or correlation due to the LNA in the zero baseline measurements). In a similar way using results of group two and four the correlation between the zero baseline measurements mostly due to the LNA can be determined ($[\varrho_{\mathsf{SD}}]_{\mathsf{ZB}} = \varrho_{\mathsf{LNA}}$). Table 6.5 shows the results of these computations for each GNSS. The results show significant correlation between the code observations made by two receivers in the zero baseline setup as well as significant time correlation between code observations of consecutive epochs. Neglecting this correlation may lead to an over optimistic stochastic model. Table 6.5 also shows the theoretical thermal noise values for $C/N_0 = 45$ dB-Hz that have been determined with the formulas presented in (Sleewaegen et al., 2004) and the receiver and signal properties given in tables 6.1 and 6.2. For the integration time the symbol duration has been used and a common narrow correlator spacing has been assumed for GPS and Galileo. For EGNOS a correlator spacing of $\frac{1}{2}$ chip has been assumed. The measured results are very close to the theoretical values for GPS and Galileo. For EGNOS the measured values are somewhat higher than the theoretical values, which might be due to the fixed geometry of the geostationary EGNOS satellites.

Table 6.5: Time correlation coefficient and zero baseline LNA correlation coefficient, thermal noise estimate and theoretical value of the standard deviation of the code noise in meters for $C/N_0 = 45$ dB-Hz

	ϱ_Δ [-]	ϱ_{LNA} [-]	$\sigma_{measured}$ [m]	$\sigma_{theoretical}$ [m]
GPS	0.63	0.49 - 0.64	0.16 - 0.19	0.18
Galileo	0.55 - 0.57	0.69 - 0.84	0.10 - 0.14	0.11
EGNOS	0.41 - 0.51	0.82 - 0.88	0.48 - 0.67	0.42

The same technique has been used to compute the time correlation, the correlation due to the LNA and the thermal noise of the phase observations. The results of these calculations are presented in tables 6.4 and 6.6. The results are very similar for each GNSS and no distinction is made in the tables between the different systems. Just like the code observations, the phase observations made by two receivers in the zero baseline setup are highly correlated. Unlike the code observations, the phase observations show very little time correlation at a sampling rate of 1Hz. The measured values are relatively close to, though somewhat higher than, the theoretical value determined with the formula presented in (Sleewaegen et al., 2004) and the receiver and signal properties given in tables 6.1 and 6.2.

Table 6.6: Time correlation coefficient and zero baseline LNA correlation coefficient, thermal noise estimate and theoretical value of the standard deviation of the phase noise in cycles for $C/N_0 = 45\,\text{dB-Hz}$

ϱ_Δ [-]	ϱ_{LNA} [-]	$\sigma_{measured}$ [cycles]	$\sigma_{theoretical}$ [cycles]
-0.045	0.87	0.0039	0.0028

6.2 Dual and multi frequency analysis

In this section the geometry-free analysis is extended to dual and multi frequency observations. The well-known multipath linear combination, which relies on dual-frequency carrier phase data, is introduced and again illustrated by means of a new measurement campaign with GPS and both GIOVE-A and B. We analyze and address in particular the measurements on the wideband signals at the L5/E5a frequency. We not only study random errors in the data, but also systematic errors which dominate the data behavior over longer time scales.

6.2.1 Dual frequency measurement campaign

This measurement campaign consists of two measurement setups. A zero baseline was measured on May 29, 2009 with two Septentrio PolaRx3G receivers connected to a single Leica AR25 3D choke ring antenna on top of a 14-floor building. A short baseline was measured on June 1, 2009 with the same two Septentrio PolaRx3G receivers each connected to its own Leica AR25 3D choke ring antenna installed on tripods in the open field about 6 meters separated.

GIOVE E1B and E5aQ signals were tracked from GIOVE-A and B and the GPS L1 C/A and L5Q signals were tracked from GPS SVN49 (PRN01). Additionally, the GPS L1 C/A signal was tracked from all other visible GPS satellites. Measurements were collected at a 1 second interval and stored in RINEX-format version 3 (Gurtner and Estey, 2007). For further details on the measurement campaign the reader is referred to Tiberius et al. (2009).

In order to compare and to provide an independent check of the findings from this measurement campaign, measurements from UNAVCO, contributors to the International GNSS Service (Dow et al., 2009), of the L1 C/A, L2C and L5Q signals transmitted on June 1, 2009 by GPS SVN49 were also processed. These GPS-only data were collected with a 76-channel Trimble NetR8 receiver able to track modernized GPS L2C and L5 signals (Trimble

Navigation Limited, 2008b), and a Trimble GNSS choke ring antenna that supports all GPS frequency bands (Trimble Navigation Limited, 2008a). The receiver was located on the roof of the UNAVCO headquarters in Boulder, Colorado, USA.

6.2.2 Linear combinations for multi-frequency observations

For this multi-frequency analysis, we start with the geometry-free measurement eqs. (6.3) and (6.4) and generalize them for frequency j:

$$\begin{aligned} P_j &= g + \tfrac{f_i^2}{f_j^2}\mathcal{I}_i + m_j + \zeta_j + \epsilon_j \\ \Phi_j &= g - \tfrac{f_i^2}{f_j^2}\mathcal{I}_i + \mu_j + A_j + \xi_j + \varepsilon_j \end{aligned} \tag{6.16}$$

where P and Φ are the code and phase measurements, g is a geometric term which includes the geometric range between the receiver and satellite, the troposphere delay, the receiver clock error, and the satellite clock error. The symbol f denotes the carrier frequency, $\mathcal{I}_i$ is the ionosphere delay on reference frequency i, m and μ are the code and phase multipath, A is the phase ambiguity, ζ and ξ are the instrumental code and phase delays, and ϵ and ε are random code and phase measurement errors respectively. All quantities are expressed in meters except frequency f is in Hertz.

Multipath linear combination

Using dual-frequency phase measurements and a single-frequency code measurement of one receiver, we can eliminate the first-order ionospheric effect as well as the geometric term g from eq. (6.16) with the multipath combination (see e.g. Estey and Meertens, 1999):

$$MP_{ji} = P_j - \tfrac{f_j^2+f_i^2}{f_j^2-f_i^2}\Phi_j + \tfrac{2f_i^2}{f_j^2-f_i^2}\Phi_i \tag{6.17}$$

with $i \neq j$. If the phase noise and phase multipath are neglected, this leads to the following expectation and dispersion values of the multipath combination:

$$\begin{aligned} E\left\{MP_{ji}\right\} &\approx m_j + \zeta_j - \tfrac{f_j^2+f_i^2}{f_j^2-f_i^2}\left(A_j + \xi_j\right) + \tfrac{2f_i^2}{f_j^2-f_i^2}\left(A_i + \xi_i\right) \\ D\left\{MP_{ji}\right\} &\approx \sigma_{P,j}^2 \end{aligned} \tag{6.18}$$

The MP combination eq. (6.18) contains code multipath, a constant ambiguity term which is a combination of the ambiguities of the two phase measurements, a combined hardware delay and thermal noise. Subtraction of the mean value from the measurements removes the phase ambiguities, which are constant if there are no cycle slips. The behavior of receiver hardware delays was studied in Liu et al. (2004), with reported values for the hardware delay change rates under normal conditions below 0.1 mm/s. Satellite hardware delay change rates are assumed to be constrained to even smaller values. Therefore, the remaining differential hardware delays in eq. (6.18) will have little impact on short time scales. The resulting time series is dominated by code multipath and thermal noise.

With the measured dual-frequency data two MP-combinations can be formed: one for the code on L1/E1 and one for the code on L5/E5a. For the triple frequency UNAVCO data many more MP-combinations can be formed with different, some very large, multiplication factors. We have used MP_{15}, MP_{21} and MP_{51} which have relatively small multiplication factors and therefore are less impacted by phase errors.

When differencing consecutive epochs, the constant ambiguity terms are eliminated and the slowly changing hardware delays are greatly reduced. This leads to the following expectation and dispersion for the time-differences:

$$\begin{aligned} &E\left\{\Delta MP_{ji}\right\} \approx \Delta m_j \\ &D\left\{\Delta MP_{ji}\right\} \approx 2\left(1-\varrho_{\Delta}\right)\sigma_{P,j}^2 \end{aligned} \tag{6.19}$$

For the measured 1Hz data, the time-differenced multipath is very small and the residual time series mainly shows the random effects captured in the dispersion. This dispersion depends on the thermal noise and the time correlation.

Overview of linear combinations

Table 6.7 summarizes the single and multi-frequency linear combinations for the code and carrier measurements introduced in this chapter. The linear combinations (l.c.) considered are the Code-minus-Carrier (CC) and the multipath (MP) combination in undifferenced (UD), between-receiver single differenced (SD), double differenced (DD), and time-differenced (Δ) form. Table 6.7 also shows the expectation and dispersion values of each combination for three different measurements setups: single receiver (1Rx), short baseline (SB), and zero baseline (ZB).

Table 6.7: Expectation and dispersion values of different linear combinations

#	Setup	Diff.	l.c.	Expectation	Correction	Dispersion
1	1Rx	UD	CC	$2\mathcal{I} - A + m + \xi_{CC}$	Polynomial	σ_P^2
	1Rx	UD	MP	$m + A_{MP} + \xi_{MP}$	Mean	σ_P^2
	SB	SD	CC	$m_{SD} - A_{SD} + \xi_{SD}$	Mean	$2\sigma_P^2$
	SB	DD	CC	$-\lambda N_{DD} + m_{DD}$	Mean	$4\sigma_P^2$
2	1Rx	Δ	CC	$2\Delta\mathcal{I} + \Delta m$	None	$2\left(1-\varrho_\Delta\right)\sigma_P^2$
	1Rx	Δ	MP	Δm	None	$2\left(1-\varrho_\Delta\right)\sigma_P^2$
	SB	ΔSD	CC	Δm_{SD}	None	$4\left(1-\varrho_\Delta\right)\sigma_P^2$
	SB	ΔDD	CC	Δm_{DD}	None	$8\left(1-\varrho_\Delta\right)\sigma_P^2$
3	ZB	SD	CC	$-A_{SD} + \xi_{SD}$	Mean	$2\left(1-\varrho_{SD}\right)\sigma_P^2$
	ZB	DD	CC	$-\lambda N_{DD}$	Mean	$4\left(1-\varrho_{SD}\right)\sigma_P^2$
4	ZB	ΔSD	CC	0	None	$4\left(1-\varrho_\Delta\right)\left(1-\varrho_{SD}\right)\sigma_P^2$
	ZB	ΔDD	CC	0	None	$8\left(1-\varrho_\Delta\right)\left(1-\varrho_{SD}\right)\sigma_P^2$

Column five (expectation) shows the systematic effects that are present in each of the linear combinations. These include ionospheric delay $\mathcal{I}$, hardware delays ξ, code multipath m, and carrier phase ambiguity A if real-valued or λN if integer-valued where N is the integer number and λ the wavelength. Even though multipath is a very complex phenomenon that is difficult to predict, it is considered a systematic effect in this approach. The undifferenced CC combination contains the ionospheric delay; a second order polynomial is fitted typically over a 120 seconds time span and subtracted to remove this effect. The ambiguity terms which are present in some of the linear combinations are removed by subtracting the mean value, as indicated in column six (correction) of table 6.7, using again a 120 seconds time span.

Column seven (dispersion) contains the random effects that are present in each of the linear combinations. This is the random measurement noise with variance σ_P^2 for the pseudorange code impacted by correlation of the measurements. Similar to the single frequency case, two important types of correlation are considered for the code measurements. These are time correlation ϱ_Δ, and correlation between the code measurements of the two receivers in the zero baseline setup ϱ_{SD}. To determine these stochastic parameters, the linear combinations in table 6.7 are again divided into four groups based on their dispersion and remaining systematic effects.

From table 6.7 it may seem straightforward to determine the variance of the random thermal measurement noise σ_P^2 directly from one of the linear combinations in group 1 of table 6.7. However, this is not trivial because systematic multipath effects cannot easily be removed from the measurements. Therefore, the indirect method introduced in the previous section is used to determine σ_P^2 and both correlation parameters from groups 2, 3 and 4. This method can be summarized as follows:

Multipath is strongly correlated over time spans of seconds, and therefore it is greatly reduced in time-differenced measurements such as those in group 2. Remaining ionospheric delay and hardware delays can be neglected. Consequently, the variance of the random errors in group 2 can be estimated accurately from the measurements. For zero baselines in groups 3 and 4, the multipath is eliminated by single differencing. This means that the variance of the random errors in groups 3 and 4 can also be estimated from the measurements. In fact, the variance of the measurements will closely represent the dispersion given in table 6.7. The estimated values will contain thermal noise as well as correlation between the measurements. Since there are only three unknown parameters ϱ_Δ, ϱ_{SD} and σ_P, they can all be determined from the variance estimates of groups 2, 3 and 4. All computations are performed with respect to a reference C/N_0 of 45 dB-Hz.

6.2.3 Dual frequency results

First the random measurement noise on the new wideband signals is analyzed, then the remaining systematic measurement errors in the linear combinations are highlighted.

6.2.3.1 Random measurement noise

Table 6.8 shows the standard deviations of the measurement residuals on the signals tracked during the short baseline measurements in the field and the zero baseline measurements on the roof for each of the discussed linear combinations. The measured time series were split into data segments of 120 seconds and the standard deviation for each of these segments was determined. Based on these standard deviations, which were measured at different C/N_0, the standard deviation for a C/N_0 of 45dB-Hz was estimated from all data. The well known inversely proportional relation between the C/N_0, expressed in ratio-Hz, and the variance of the noise, reduces this estimation to a linear regression on a logarithmic scale with only one unknown parameter (as was shown in fig. 6.6). Finally, for easy comparison and for this table only, the increase in variance due to differencing has been compensated, assuming zero correlation.

Table 6.8: Standard deviations of different measurement combinations and signals expressed in meters. The standard deviations are estimated for C/N_0 = 45dB-Hz based on data segments of 120s and are normalized to undifferenced level.

Linear	GPS L1 C/A		GPS L5Q		Galileo E1B		Galileo E5aQ	
Combination	SB	ZB	SB	ZB	SB	ZB	SB	ZB
	Field	Roof	Field	Roof	Field	Roof	Field	Roof
UD CC	0.27	0.43	0.10	0.14	0.20	0.27	0.07	0.07
UD MP	0.38	0.49	0.10	0.14	0.20	0.27	0.07	0.07
SD CC	0.28		0.11		0.21		0.07	
DD CC	0.28				0.18		0.07	
ΔCC	0.15	0.18	0.05	0.05	0.11	0.12	0.04	0.04
ΔMP	0.20	0.20	0.05	0.05	0.11	0.12	0.04	0.04
ΔSD CC	0.15		0.05		0.11		0.04	
ΔDD CC	0.15				0.10		0.04	
SD CC		0.20		0.05		0.16		0.04
DD CC		0.19				0.14		0.04
ΔSD CC		0.13		0.04		0.10		0.03
ΔDD CC		0.12				0.09		0.03

As expected, table 6.8 displays a high precision of the GPS L5Q and Galileo E5aQ signals compared to the signals on the L1/E1 frequency. For the GPS L5Q and Galileo E1B and E5aQ signals, the standard deviation of the CC combination is equal to the standard deviation of the MP combination, showing that the ionospheric delay has been removed successfully from the CC by fitting a second order polynomial without influencing the noise characterization.

For the GPS L1 C/A signal the results for the CC combination represent the mean value of all tracked GPS satellites, while the MP combination is only formed for SVN49. This explains that we have different results for these combinations in table 6.8: 0.38 vs. 0.27, and 0.49 vs. 0.43. For GPS SVN49 the code and carrier phase on L5 could only be measured continuously for relatively high satellite elevation due to the sharp decrease of C/N_0 with elevation for the L5 signal. As a result, the multipath combination for the L1 C/A signal transmitted by SVN49 could also only be determined for high satellite elevation and thus for relatively high C/N_0 values of about 50dB-Hz for this signal. Note, the sharp decrease of C/N_0 with elevation with the demo payload on SVN49 (Marquis et al., 2009) is only present on the L5 frequency. The standard deviation of the MP_{15} combination for C/N_0 = 45dB-Hz, could therefore only be extrapolated from the measured values at higher C/N_0, resulting in an inaccurate estimate.

Comparison of GPS L5Q and Galileo E5aQ results reveals that, for undifferenced observations the GPS L5Q signal has a larger standard deviation by a factor of 1.5-2. This is explicable because the majority of L5Q measurements were collected with high C/N_0. It should be noted that DD GPS L5Q results are not available because at the time of measurements only one GPS satellite transmitted the L5Q signal.

The results in table 6.8 allow the estimation of the standard deviation, the time correlation, and the ZB SD correlation as discussed in the previous section. The ZB SD correlation expresses the relation between two different noise contributions, namely amplifier noise, which includes sky and ground noise and which is equal for both receivers in the zero baseline set-up, and internal receiver noise (Tiberius et al., 2009). The results from these noise and correlation computations are presented in table 6.9, and compare well to the single frequency results in table 6.5. In order to assess the sensitivity of our approach to the length of the data segments, the entire processing has been repeated for data segments of 1,800 seconds. For this data segment length, the UD CC and MP results are significantly larger than those presented in table 6.8, especially for the L5Q and E5aQ signals. However, such an increase is no longer present in the time-differenced and ZB SD measurements due to the absence of multipath in these combinations. The final estimate of the pseudorange measurement noise is only slightly larger for the longer data segments as shown in table 6.9. The correlation values vary little.

Table 6.9: Time correlation, zero baseline correlation, measured and theoretical thermal noise on code measurements

			GPS		Galileo	
		segments	L1 C/A	L5Q	E1B	E5aQ
ϱ_Δ[-]			0.59	0.35	0.60	0.43
ϱ_{ZB-SD} [-]			0.51	0.28	0.30	0.43
σ_P [m]	measured	120s	0.23	0.06	0.17	0.05
σ_P [m]	measured	1,800s	0.24	0.07	0.18	0.06
σ_P [m]	theoretical		0.18	0.06	0.11	0.06

Table 6.9 also shows the expected standard deviation using the theoretical expressions by Braasch and van Dierendonck (1999) and Sleewaegen et al. (2004), and the receiver and signal properties from Tiberius et al. (2009).

Both the GPS L5Q and the Galileo E5aQ wide band signals have thermal measurement noise on the order of about 6 cm, which is much lower than seen for the E1B and especially the L1 C/A signal.

The carrier phase measurement noise was also analyzed by forming the double difference carrier phase (DDΦ) combination. Figure 6.9 shows part of the DDΦ time series in panes 1 and 3 and corresponding C/N_0 values in panes 2 and 4 for both frequencies of GIOVE-A and B. A 2^{nd} order polynomial $p\,(2)$ has been fitted, between receiver clock jumps to remove the geometric effect and carrier phase ambiguity in the short-baseline (SB) set-up. The E5a carrier phase measurements are noisier than the E1 carrier phase measurements. This is in small part due to the larger wavelength, but the main reason is the lower received signal power which can be seen in the C/N_0 measurements. An interesting detail is that the C/N_0 measurements themselves are also noisier on E5a than on E1.

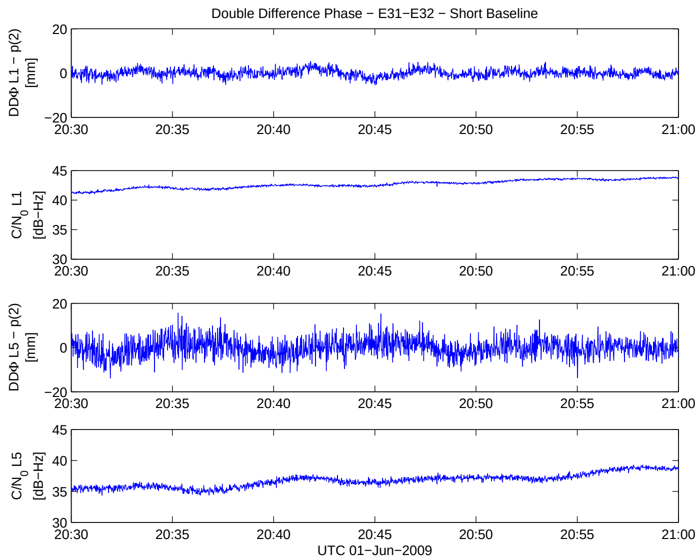

Figure 6.9: Double difference phase measurements of GIOVE-A and B for E1 and E5a for the short baseline. E5a is tracked here with lower signal power and consequently has more measurement noise.

Analogously to the pseudorange code noise, the thermal carrier phase noise has been estimated for GPS L1, Galileo E1, and Galileo E5a with respect to a C/N_0 of 45dB-Hz. Since only one GPS satellite was transmitting the L5Q signal, the GPS L5 carrier phase noise could not be evaluated in this manner. Table 6.10 shows the results for the DDΦ and time-differenced DDΦ for the short and zero baselines. Table 6.11 shows that the measured values are very close to the theoretical expectations, and are comparable to the single frequency results in table 6.6. There is little time correlation on these 1Hz phase measurements, but the ZB SD correlation is significant.

Table 6.10: Standard deviation of DD and ΔDD carrier phase measurements in millimeters for both measurement set-ups, estimated for $C/N_0 = 45$dB-Hz based on data segments of 120s and normalized to undifferenced level.

Linear Combination	GPS L1 C/A	Galileo E1B	E5aQ
SB DDΦ	0.58	0.53	0.68
SB ΔDDΦ	0.52	0.53	0.69
ZB DDΦ	0.34	0.39	0.47
ZB ΔDDΦ	0.34	0.40	0.48

6.2.3.2 Systematic measurement errors

The expectations in table 6.7 show that the residuals of the linear combinations still contain some systematic effects. Most of these effects can either be removed by detrending the data, e.g. the ionospheric delay can be removed by fitting a second order polynomial to the undifferenced CC measurements, or be neglected for the purposes of this study, e.g. the slowly changing hardware delays. However, not all systematic effects fall into these

Table 6.11: Time correlation, zero baseline correlation, measured and theoretical thermal noise on carrier phase measurements

		GPS	Galileo	
		L1 C/A	E1B	E5aQ
$\varrho_{\Delta,\Phi}$ [-]		-0.03	-0.02	-0.05
$\varrho_{ZB-SD,\Phi}$ [-]		0.57	0.44	0.53
σ_Φ [mm]	measured	0.51	0.53	0.68
σ_Φ [mm]	theoretical	0.54	0.54	0.72

categories. The most important remaining systematic effect, i.e. multipath, is not removed from the undifferenced residuals or from the short baseline single differences.

Long term variations in the time series such as those that could result from multipath from a nearby reflector eventually have little impact on the noise characterization through tables 6.8 and 6.9, based on 120s data segments. However, multipath dominates the residual time series on longer time scales as can be seen in fig. 6.10. Panels a), b) and c) show for the short baseline measurements the MP_{51} combination, the measured C/N_0, and the satellite elevation for GIOVE-A, GIOVE-B and GPS SVN49. The mean value over the full time span has been subtracted to present the variations more clearly. The MP combination shows strong variations in the order of meters over long periods of time. This type of variation was not encountered on the L1/E1 frequency.

These measurements have been carried out with the manufacturer proprietary multipath mitigation intentionally disabled to show the 'raw' multipath effects. For comparison fig. 6.11 shows the MP_{51} results for GIOVE-B from the roof measurements (ZB). These results are very similar for both receivers, since multipath effects are largely the same for both receivers for a zero baseline. The MP combination again shows strong variations in the order of one meter. The pattern is typical of multipath with the strongest effects at low satellite elevation.

Figure 6.12 shows the MP_{15} results for GPS SVN49 and GIOVE-B from the field measurements. The very large variations found in the L5/E5a (MP_{51}) results are not observed with L1/E1 (MP_{15}); note that the vertical axis ranges only from – 2m to +2m. There is a slowly changing elevation dependent bias on the GPS SVN49 measurements on L1, which was previously reported by Erker et al. (2009). This effect, caused by a signal reflection inside the satellite (Langley, 2009), will not significantly influence our noise assessment due to its slow nature, but does show up on the complete L1 C/A time series.

As mentioned above, the UNAVCO measurements of June 1, 2009 were also processed and are presented for comparison. The top and middle panes of fig. 6.13 show the multipath combinations in, respectively, undifferenced and time-differenced form of the L1 C/A (MP_{15}) , L2C (MP_{21}) and L5Q (MP_{51}) signals for GPS SVN49 for this day. The time series of the different frequencies are offset by 2 meters for visual purposes. The bottom pane shows the C/N_0 of the same signals. The MP combinations of each signal show typical code multipath effects at the start and end of the time series, i.e. at low elevation, with amplitudes of a few meters. Multipath effects on the L5Q signal are in the same order of magnitude as those on the other two signals, which means that the higher signal bandwidth does not reduce these effects. In addition, fig. 6.13 shows the previously mentioned

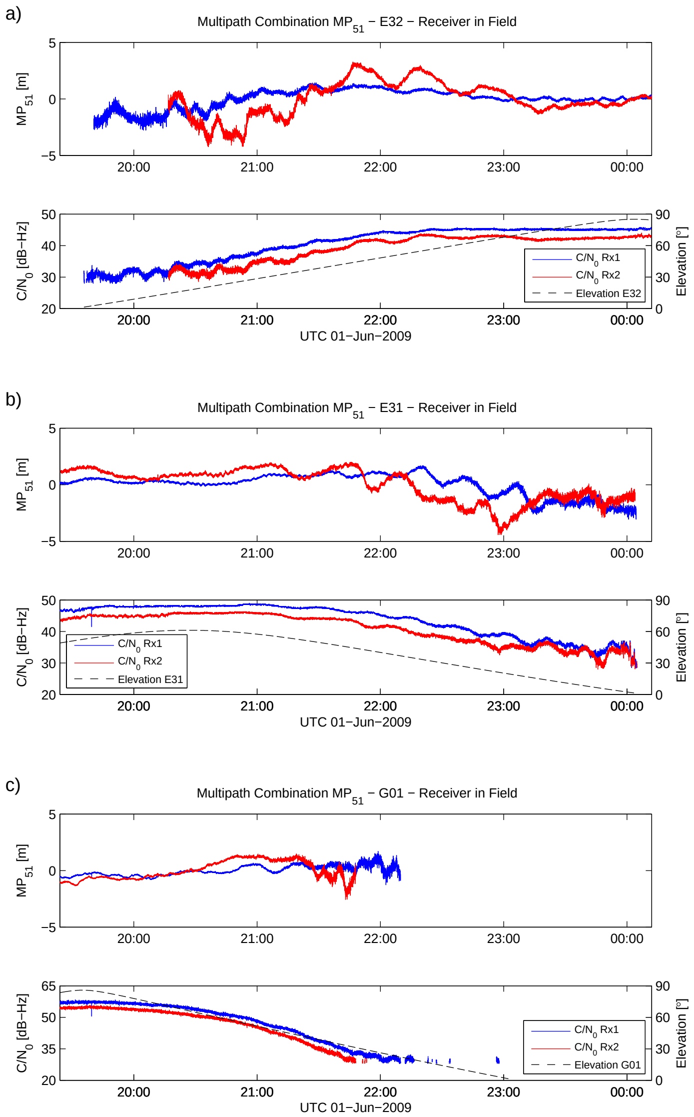

Figure 6.10: Multipath combination, C/N_0 and satellite elevation for field observations of a) GIOVE-A, b) GIOVE-B and c) GPS SVN49.

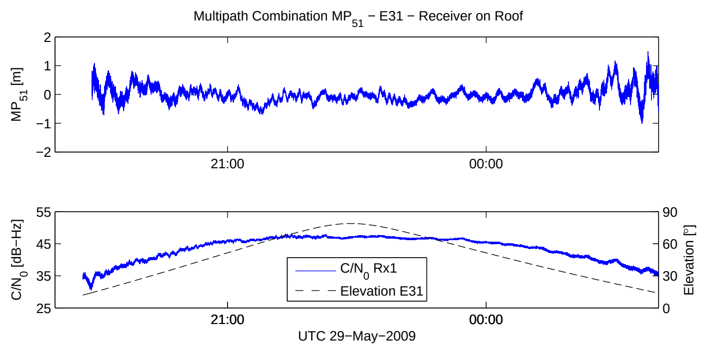

Figure 6.11: Multipath combination, C/N_0 and satellite elevation for GIOVE-B for receiver Rx1 located on the roof.

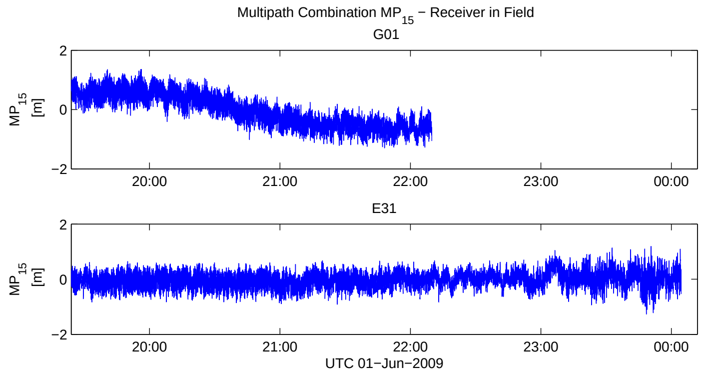

Figure 6.12: MP_{15} combination for GPS SVN49 and GIOVE-B for the field measurements.

elevation dependent bias on L1 C/A (MP_{15}), but also a clear long term systematic effect on L5Q (MP_{51}). This could be caused by elevation dependent differential hardware delays, or other systematic effects, which are amplified differently in the multipath combinations. The systematic effects are largely eliminated in the time-differences, resulting in a white noise-like signal. Due to the 15 second measurement interval, the residual time-differences are significantly larger than those for the PolaRx3G data which was measured at 1 Hz. The measured C/N_0 values for L5Q show the strong elevation dependence reported by Erker et al. (2009).

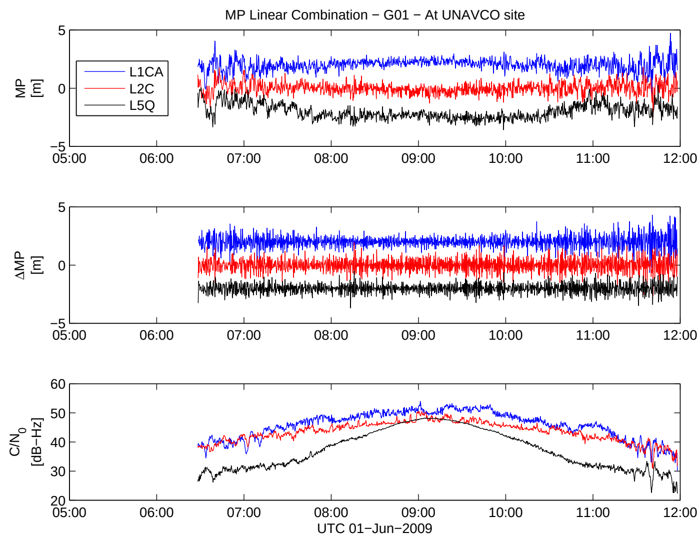

Figure 6.13: Multipath combinations, time-differences and C/N_0 values of L1 C/A (MP_{15}), L2C (MP_{21}) and L5Q (MP_{51}) from UNAVCO measurements to GPS SVN49 on June 1, 2009. The time series within both the top and middle panes are offset by 2 meters for visual purposes.

Figure 6.14 shows the standard deviation of the multipath linear combination as a function of the mean satellite elevation for data segments of 600s (40 epochs with 15s measurement interval) for a 7-day period of the UNAVCO measurements of GPS SVN49. The figure shows that the L1 C/A code has the largest range in standard deviation with high precision at high C/N_0, noting that such large values are not reached for the other signals, and low precision for lower C/N_0. The L2C signal shows a similar precision for midrange C/N_0, but the precision remains better for lower C/N_0. The precision of the L5Q signal is also comparable to the other signals, but this is reached for much smaller values of the C/N_0, which seems to indicate a better performance of this signal.

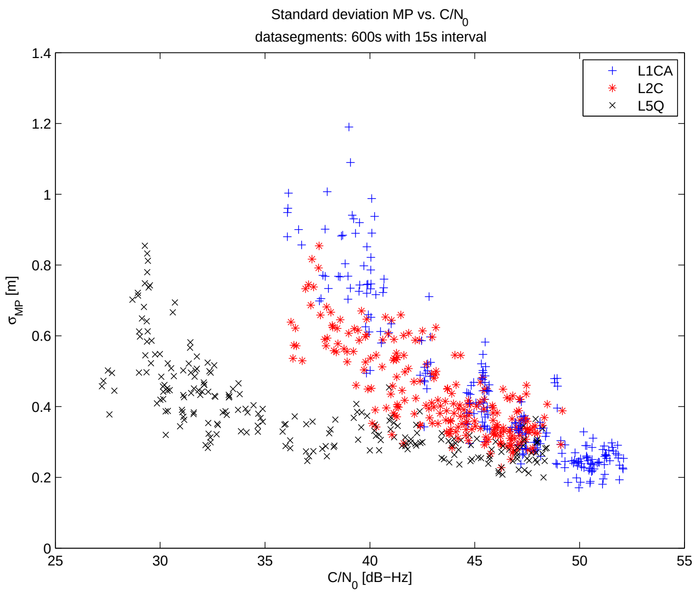

Figure 6.14: Multipath combination standard deviation vs. C/N_0 of the L1 C/A (MP_{15}), L2C (MP_{21}) and L5Q (MP_{51}) signals for GPS SVN49 for June 1-7, 2009 from the UNAVCO measurements. Each marker represents the standard deviation of a data segment of 600s (at 1/15 Hz) at the mean C/N_0 during the segment.

Figure 6.15 shows the same data but now as a function of satellite elevation. It does not show this strong improvement of the L5Q signal with respect to the other signals, although the L1 C/A signal still shows the widest range in precision. The connection between figs. 6.14 and 6.15 is formed by the measured C/N_0 as a function of elevation, which mainly depends on the antennas of the receiver and, especially for L5, the satellite. As can be seen, the standard deviation as a function of elevation is very similar for the three signals despite the large differences in C/N_0. This can be explained as follows: the standard deviation for 600s data segments with 15s measurement interval is not just a function of the C/N_0, but it is also greatly impacted by multipath. Since multipath strongly depends on elevation this becomes clearly visible in fig. 6.15.

Although these results are greatly affected by the strong elevation dependence of the C/N_0 for L5Q and limited by the 15s measurement interval, this analysis shows that the expected high performance of the wide band L5Q signal might not present itself in the presence of multipath. The performance of future applications using the wide band signals on E5a and L5 might be severely compromised by the variations on the multipath and code-minus-carrier combinations which were measured in the field. Therefore, a better understanding of their source is desirable. Multipath from a reflector close to the antenna is one effect that could cause long term variations like those encountered on the CC and MP combinations of the L5/E5a measurements seen in fig. 6.10. In Tiberius et al. (2009) this was explored in more detail and, although no definite conclusion was reached, the most likely cause

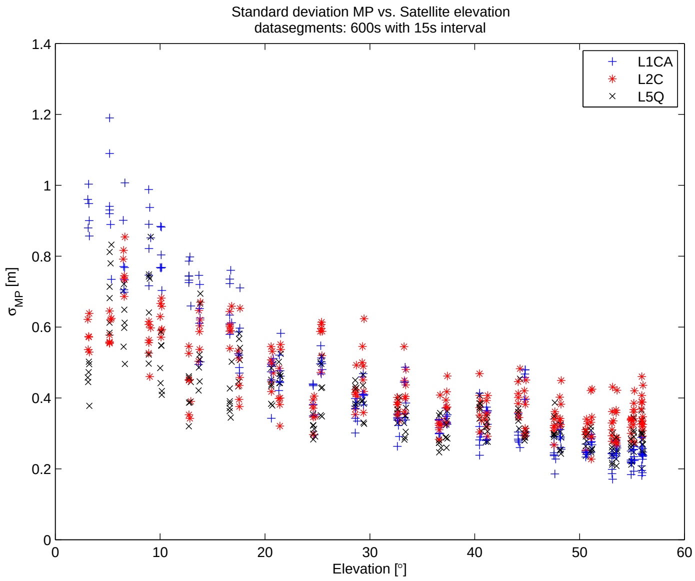

Figure 6.15: Multipath combination standard deviation vs. satellite elevation of the L1 C/A (MP_{15}), L2C (MP_{21}) and L5Q (MP_{51}) signals for GPS SVN49 for June 1-7, 2009 from the UNAVCO measurements. Each marker represents the standard deviation of a data segment of 600s (at 1/15 Hz) at the mean elevation during the segment.

is indeed severe multipath in combination with weak multipath rejection of the antenna. Bedford et al. (2009) indicate that in the low frequency band (L5, E5a, E5b) the Leica AR25 3D choke ring antenna has a front-back ratio which is 10dB lower than a traditional 2D choke ring antenna. This results from the design trade-off between multipath rejection and low elevation tracking of satellites, the latter of which has significantly improved for the 3D antenna. The front-back ratio indicates the antenna's directivity and resistance to multipath, driven by the antenna's shielding and sensitivity to left-hand circularly polarized signals with respect to the right-hand circularly polarized line-of-sight signals. Slowly changing differential hardware delays can also result in variations in the multipath combinations on very long timescales. Such variations were found in the UNAVCO data (fig. 6.13) and might also be present on our own measurements, but there they would not be noticeable due to the very strong variations which are probably caused by multipath.

Figures 6.16 and 6.17 show the SD and DD data for the GIOVE-A and B satellites for the short and zero baselines. The top pane of each figure shows the SD for each of the satellites, while the middle panes show the DD between the satellites. The bottom panes show the DD C/N_0 which is a combination of the C/N_0 for the two satellites, as introduced in eq. (6.11), and gives a measure for the noise that can be expected in the DD measurements.

Table 6.7 shows that the DD CC combination mainly contains the integer DD ambiguity, code multipath and code noise. In the mean value of a time series of DD CC, the noise term averages out leaving just the ambiguity and the multipath contributions. In addition, for the zero baseline, the multipath is eliminated in the single and double differences. This means that the expectation value of the mean of a time series of DD CC measurements, divided by the wavelength, is equal to the integer ambiguity which thus can be determined.

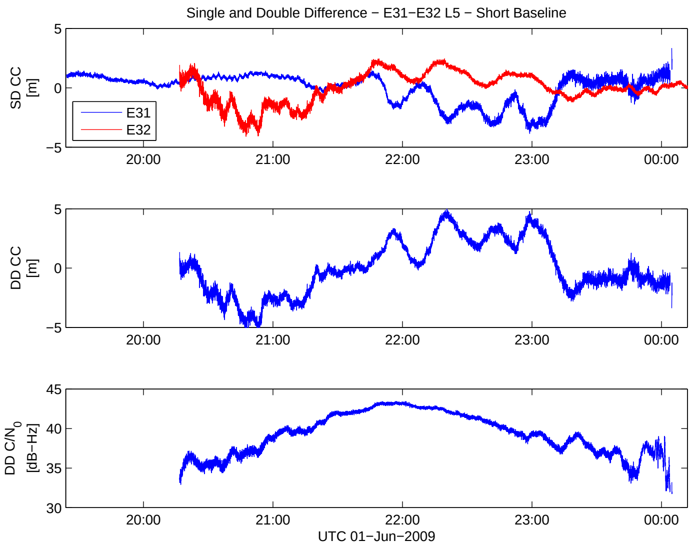

Figure 6.16: Single and Double Difference Code-minus-Carrier measurements and DD C/N_0 for GIOVE-A and B for the short baseline.

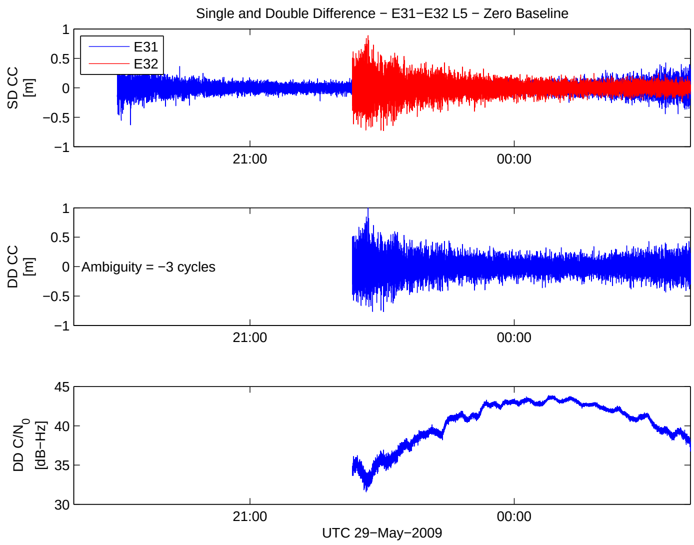

Figure 6.17: Single and Double Difference Code-minus-Carrier measurements and DD C/N_0 for GIOVE-A and B on the zero baseline.

From figs. 6.16 and 6.17 it is clear that the strong multipath-like variations are indeed not eliminated in the SD or DD for the short baseline, but they are eliminated for the zero baseline (table 6.7). These multipath effects prevent successful geometry-free ambiguity resolution on the short baseline, while successful geometry-free ambiguity resolution is possible on the zero baseline (de Bakker et al., 2012).

In conclusion we can state that short and zero baseline measurements have revealed low thermal noise of about 6 cm on both the GPS L5Q and the Galileo/GIOVE E5aQ signals which is in line with theoretical expectations for these wide band signals. However, the results also showed strong variations of the pseudorange code measurements over longer time periods, the magnitude of the variations easily reaching up to 20 times the thermal noise standard deviation. Despite being observed in what would generally be considered a benign multipath environment, the most likely cause of these variations is severe short-range multipath combined with low multipath rejection by the antenna.

Many applications might not be able to take full benefit of the high precision of the new L5Q and E5aQ signals due to the presence of the strong multipath variations encountered on the measurements.

6.3 Multipath analysis, variance and correlation estimation

The previous sections revealed that multipath is the dominant (unmodeled) error source on the pseudo range observations over longer time spans. The most basic stochastic treatment of multipath is to simply use a higher value for the expected variance of the (white) noise of the pseudo range measurements (for which multipath is expected) which translates into a decrease of the weighting in the positioning algorithms. An improved and often used method is to use an elevation dependent or C/N_0 dependent weighting scheme, since multipath is often most severe for satellites with low elevation and C/N_0.

For a kinematic receiver this approach might suffice, since the geometry of the reflecting objects changes rapidly with respect to the user, resulting in a white noise-like multipath environment. However, static receivers are often impacted by the same reflecting objects for long time spans, since the GNSS satellite geometry only changes slowly. This leads to high time correlation in the multipath delays, which should be taken into account. Also, considering the new GPS L5 and Galileo E5 wide band signals, the white noise stochastic approaches do not suffice if one wants to make optimal use of the increased precision of these new signals. Section 6.2 confirmed the higher precision of these new signals based on short and zero baseline measurements, but also revealed multipath delays on the L5/E5 measurements similar to those on the GPS L1C/A measurements. Simsky et al. (2008) showed the improved multipath rejection of wide-band Galileo modulations, but also found that this advantage does not hold for short-range multipath. Accounting for this multipath in the white noise of the measurements, means that the L5/E5 signals get equal weight as the GPS L1C/A signals in the positioning solution, thus taking no advantage of the increased precision. Elevation dependent weighting might perform somewhat better, since it can at least use the higher precision for satellites with high elevation. Although it should be noted that significant multipath was also encountered at higher elevations in section 6.3.

In this section we will investigate multipath together with (time correlated) measurement errors on GNSS pseudo range measurements as a stochastic process in the measurement domain. Multi-frequency data collected by static receivers will again be used to form the multipath linear combination. From investigation of measured multipath time series in the previous section and Tiberius et al. (2009), we found that multipath has strong time correlation at 1 Hz and in this section it will be shown that it can be modeled by a low order AR process.

The estimated multipath models can have a number of uses. Firstly, they can be used to characterize the multipath environment as well as the multipath properties of the GNSS receiver and antenna, and the quality of the resulting pseudo range measurements. Secondly, the estimated models provide a simple method to generate realistic artificial multipath time series, which can e.g. be used in a GNSS (software) simulator. Thirdly, the detection of multipath errors on the GNSS measurements with integrity algorithms will improve from having a more realistic model for multipath time series.

Finally, GNSS positioning algorithms based on filtering techniques can greatly benefit from the more realistic approach to multipath compared to a white-noise treatment of multipath. This is done by extending the state vector with additional entries (see e.g. Salzmann and Teunissen, 1990, appendix B.2).

Multipath linear combination

The following analyses are again based on the multipath linear combination, introduced in eq. (6.17), for frequency j (all expressed in meters except frequency f in Hertz):

$$MP_{ji} = P_j - \frac{f_j^2+f_i^2}{f_j^2-f_i^2}\Phi_j + \frac{2f_i^2}{f_j^2-f_i^2}\Phi_i \tag{6.20}$$

with $i \neq j$. For the multi-frequency data considered in this section several different MP-combinations can be formed with different, sometimes very large, multiplication factors. We have used MP_{12} for the GPS L1 signal, MP_{15} for the GIOVE E1 signal, and for all other signals the L1 frequency was used as the reference frequency i. These combinations all have relatively small multiplication factors and are therefore impacted less by phase errors. Filling in eq. (6.16) in eq. (6.20) and recombining the different terms leads to:

$$MP_{ji} = A_{MP} + \xi_{MP} + m_j + \mu_{MP} + \epsilon_j + \varepsilon_{MP} \tag{6.21}$$

The MP combination contains a constant ambiguity term A_{MP} which is a combination of the ambiguities of the two carrier phase measurements, a combined hardware delay ξ_{MP} pseudo range multipath m_j and carrier phase multipath μ_{MP}, pseudo range measurement noise ϵ_j and carrier phase measurement noise ε_{MP}. As mentioned before, subtraction of the mean value from the measurements removes the carrier phase ambiguities, which are constant if there are no cycle slips. The behavior of receiver hardware delays was studied in Liu et al. (2004), with reported values under normal conditions below 10^{-4} m/s. Satellite hardware delay change rates are assumed to be constrained to even smaller values. Therefore, the remaining differential hardware delays in eq. (6.21) will have little impact on short time scales. Furthermore, the carrier phase measurement noise and carrier phase multipath are negligible compared to the pseudo range measurement noise, which is an order of magnitude larger. Therefore, the resulting time series is dominated by pseudo range multipath and measurement noise (which may also be correlated in time). And it is these two effects that we wish to describe with an autoregressive process.

6.3.1 Autoregressive process

For an autoregressive process of order k, notation: AR(k), we have:

$$\sum_{i=0}^{k} a_i \underline{X}_{t-i} = \underline{\varepsilon}_t \tag{6.22}$$

Where $\underline{X}_t$ is the time series sample at time t, $\underline{\epsilon}$ is a white noise process, and a_i are the AR parameters with $a_0 = 1$ by definition. If we rewrite this, we can express the sample $\underline{X}_t$ as a function of previous sample values and a noise term:

$$\underline{X}_t = -a_1 \underline{X}_{t-1} - \ldots - a_k \underline{X}_{t-k} + \underline{\varepsilon}_t \tag{6.23}$$

From this expression it becomes clear that the AR parameters define the autocorrelation of the time series. From eqs. (6.22) and (6.23) we can also observe that an AR(k) process with the last AR parameter a_k zero, is an AR(k-1) process. According to eq. (6.23), an AR(0) process is in fact a white noise process, with:

$$\underline{X}_t = \underline{\varepsilon}_t \tag{6.24}$$

We can also write our white-noise process as an AR(1) process with $a_1 = 0$, i.e.

$$\underline{X}_t = -a_1 \underline{X}_{t-1} + \underline{\varepsilon}_t, \text{ with } a_1 = 0 \tag{6.25}$$

In this contribution we will look at time AR series $\underline{X}_t$ that are wide-sense stationary. For an AR(k) process to be stationary, all roots of the following polynomial should lie within a unit circle (Priestley, 1981):

$$g(z) = z^k + a_1 z^{k-1} + \ldots + a_k \tag{6.26}$$

For $k = 1$ this simply means $|a_1| < 1$. Also the white-noise process $\underline{\epsilon}_t$ should have constant variance σ_ϵ^2. Furthermore we will only consider time series around their mean value, so:

$$E\{\underline{X}_t\} = 0 \ \forall \ t \tag{6.27}$$

6.3.1.1 Estimation of AR parameters

Different methods exist to estimate the parameters of an autoregressive process from an AR time series. The approach we use is a least squares adjustment. To perform a least-squares adjustment we will write the AR time series in the form of a model of observation equations:

$$\underline{y} = Ax + \underline{\varepsilon} \tag{6.28}$$

The unknown AR parameters are contained in vector x. For the observation vector $\underline{y}$ we use the samples of the time-series. But also the A matrix is built up of samples of the time-series, with corresponding uncertainty. For an optimal estimation of the 'true' autoregressive parameters, an errors-in-variables models such as total least squares could be used. However, we will not treat the entries of matrix A as stochastic variables. As a result our estimated parameters will to some extend differ from the 'true' values of the underlying process; for the AR(1) model, the time correlation will be underestimated (Greene, 2002). However, the estimated values will provide consistent prediction with similarly noisy input parameters. The error vector $\underline{\epsilon}$ contains the white noise process that drives the AR process. For an AR time series with N samples, we can now fill in eq. (6.28) as follows:

$$\begin{bmatrix} \underline{X}_{k+1} \\ \underline{X}_{k+2} \\ \vdots \\ \underline{X}_{N} \end{bmatrix} = \begin{bmatrix} X_k & X_{k-1} & \cdots & X_1 \\ X_{k+1} & X_k & \cdots & X_2 \\ \vdots & \vdots & \ddots & \vdots \\ X_{N-1} & X_{N-2} & \cdots & X_{N-k} \end{bmatrix} \begin{bmatrix} a_1 \\ a_2 \\ \vdots \\ a_k \end{bmatrix} + \begin{bmatrix} \underline{\varepsilon}_{k+1} \\ \underline{\varepsilon}_{k+2} \\ \vdots \\ \underline{\varepsilon}_{N} \end{bmatrix} \tag{6.29}$$

Note that vector $\underline{y}$ now has $N - k$ entries. The best linear unbiased estimator and its variance for this system are (using the inverse of the covariance matrix to weight the observations):

$$\underline{\hat{x}} = \left(A^* Q_y^{-1} A\right)^{-1} A^* Q_y^{-1} \underline{y} \tag{6.30}$$

$$Q_{\hat{x}} = \left(A^* Q_y^{-1} A\right)^{-1} \tag{6.31}$$

For the variance of the $\underline{y}$ vector we can use a unit matrix scaled by the (constant) variance of the white noise process, conform our assumption that the time series is wide sense stationary.

$$Q_y = \sigma_\varepsilon^2 I \tag{6.32}$$

This is not the variance of the AR process itself, but only the part that is not accounted for by Ax in the model. This further simplifies the estimated parameters and their variance to:

$$\underline{\hat{x}} = \left(A^* A\right)^{-1} A^* \underline{y} \tag{6.33}$$

$$Q_{\hat{x}} = \sigma_\varepsilon^2 \left(A^* A\right)^{-1} \tag{6.34}$$

The entries of the product of A^*A, which is a $k \times k$ matrix, contains inner products of the columns of A, which themselves contain the AR time-series with different time offsets.

$$A^*A = \begin{bmatrix} \sum_{t=k}^{N-1} X_t^2 & \sum_{t=k-1}^{N-2} X_t X_{t+1} & \cdots & \sum_{t=1}^{N-k} X_t X_{t+(k-1)} \\ \sum_{t=k-1}^{N-2} X_t X_{t+1} & \sum_{t=k-1}^{N-2} X_t^2 & \cdots & \sum_{t=1}^{N-k} X_t X_{t+(k-2)} \\ \vdots & \vdots & \ddots & \vdots \\ \sum_{t=1}^{N-k} X_t X_{t+(k-1)} & \sum_{t=1}^{N-k} X_t X_{t+(k-2)} & \cdots & \sum_{t=1}^{N-k} X_t^2 \end{bmatrix} \tag{6.35}$$

These entries are closely related to the auto-covariance of the AR time-series. If we look at the unbiased estimate of the auto-covariance for a zero mean time series at delay τ:

$$\hat{R}(\tau) = \frac{1}{N - |\tau|} \sum_{t=1}^{N-|\tau|} X_t X_{t+|\tau|} \tag{6.36}$$

We can recognize the elements of A^*A as the first $k-1$ auto-covariance samples evaluated over different intervals of the AR time-series. Now we can rewrite A^*A as:

$$A^*A = \\ (N-k)\begin{bmatrix} \hat{R}(0)_{\{k,N-1\}} & \hat{R}(1)_{\{k-1,N-1\}} & \cdots & \hat{R}(k-1)_{\{1,N-1\}} \\ \hat{R}(1)_{\{k-1,N-1\}} & \hat{R}(0)_{\{k-1,N-2\}} & \cdots & \hat{R}(k-2)_{\{1,N-2\}} \\ \vdots & \vdots & \ddots & \vdots \\ \hat{R}(k-1)_{\{1,N-1\}} & \hat{R}(k-2)_{\{1,N-2\}} & \cdots & \hat{R}(0)_{\{1,N-k\}} \end{bmatrix} \tag{6.37}$$

where braces are used to indicate the interval of the AR time series. For our wide sense stationary AR process, the expectation of the auto covariance estimates is equal for these slightly different intervals. For $N \to \infty$ the estimates of the auto covariance $\hat{R}(\tau)$ will go to the actual auto covariance $R(\tau)$, and if $N >> k$ which generally is the case (and also in our approach), we can write:

$$A^*A \approx N \begin{bmatrix} R(0) & R(1) & \cdots & R(k-1) \\ R(1) & R(0) & \cdots & R(k-2) \\ \vdots & \vdots & \ddots & \vdots \\ R(k-1) & R(k-2) & \cdots & R(0) \end{bmatrix} \tag{6.38}$$

If we call the matrix with auto covariances R_k, we find the following asymptotic expression for the variance of the AR parameter estimates:

$$Q_{\hat{x}} = \frac{\sigma_\varepsilon^2}{N} R_k^{-1} \tag{6.39}$$

This result is conform Mann and Wald (1943). However, for the problem at hand we do not know the variance of the white noise process and we will estimate it from the least squares residuals $\underline{\hat{\varepsilon}}$.

$$\underline{\hat{\varepsilon}} = \underline{y} - A\underline{\hat{x}} \tag{6.40}$$

The unbiased estimate of the variance is:

$$\underline{\hat{\sigma}}_\varepsilon^2 = \frac{\underline{\hat{\varepsilon}}^* \underline{\hat{\varepsilon}}}{N-2k} \tag{6.41}$$

where $N-2k$ is the redundancy.

6.3.1.2 Testing significance of AR parameters

After estimation of the AR parameters we want to be able to determine whether the parameters are significant at a certain level of significance α. Since we do not know beforehand how many AR parameters we need to estimate, in order to describe the AR time series, we will use a step by step approach.

This step by step approach can be described as follows. We start off by estimating an AR(1) process from the data, and then test the significance of the $\hat{a}_1$ estimate. If this is significant we now estimate an AR(2) process and test the significance of the $\hat{a}_2$ estimate.

We repeat this increasing the AR order by one each time until the significance test fails. So if we estimate an AR process of order k, we test $\hat{a}_k$ for significance. Because we expect that, if the time series behaves as an AR(k-1) process, the $\hat{a}_k$ estimate will not significantly differ from zero.

This step by step approach is attractive because it is straight forward and intuitive. However, it does have some limitations. Firstly, the stop criterion is rather greedy. The fact that $\hat{a}_k$ is not significant for an AR process of a certain order does not guarantee that the $\hat{a}_k$ parameter for an AR process of order one higher is not significant. Secondly, the tests we perform are all one dimensional since we only test $\hat{a}_k$ where we could also perform more-dimensional tests to see if all combinations of two or more of the estimated AR parameters are also significant.

To test the significance of the AR parameters, we have the following null hypothesis H_0 and alternative hypothesis H_a:

$$H_{0,k} : E\left\{\underline{y}\right\} = Ax, \;\; c_k^* x = 0 \tag{6.42}$$

$$H_{a,k} : E\left\{\underline{y}\right\} = Ax, \;\; c_k^* x = \nabla, \text{ with } \nabla \neq 0 \tag{6.43}$$

where c is a k-vector with zeros except for the k^{th} entry which is a one. Under H_0 a_k is zero, while under H_a a_k is unequal to zero. The test statistic $\underline{v}$ for this test with unknown σ_ϵ is (Teunissen et al., 2007):

$$\underline{v} = \frac{c_k^* \hat{\underline{x}}}{\hat{\underline{\sigma}}_\varepsilon \sqrt{c_k^* \left(A^* A\right)^{-1} c_k}} = \frac{\hat{\underline{a}}_k}{\hat{\underline{\sigma}}_{\hat{a}_k}} \tag{6.44}$$

with the following decision rule:

$$\text{reject } H_{0,k} \text{ if } |v| > t_{\alpha/2}\left(N - 2k\right) \tag{6.45}$$

where $t_{\alpha/2}(N-2k)$ is the critical value for $\alpha/2$ from the t-distribution with $N-2k$ degrees of freedom. We have chosen a 2-sided test, because we do not make any assumptions on the sign of a_k under the alternative hypothesis.

6.3.2 Multipath measurement campaign

In this subsection the methods described above to model multipath time series as an AR process is applied to measurements collected with different receivers and antennas. Table 6.12 shows the receiver and antenna combinations that have been used, as well as the measurement period and tracked signals.

Each of the hardware configurations in table 6.12 was measured at TU Delft GNSS observatory platform and combines a high-end receiver with a high-end antenna. This should limit, but not eliminate, the multipath impact and provides insight into the (time correlated) pseudo range errors that are still experienced with such a high-end hardware setup. The antenna used for DLF5 was replaced in Feb 2011 and this provides the opportunity to compare the measurements from one receiver (PolaRx2) when used with two different antennas (at different locations). Currently, DLF5 and DLF1 are connected to the same antenna, which makes it possible to make a comparison between the two receivers. The DLF1 setup also provides the opportunity to compare many of the currently available GPS and GIOVE signals.

DLF5 GPS L1C/A signal

The first dataset is 24 hours of measurements from the permanent receiver DLF5 collected on January 1, 2011. DLF5, part of the EGNOS Data Collection Network, is a Septentrio PolaRx2 receiver connected to a Leica AT504 antenna, located on top of a 6 story building in Delft, the Netherlands. The data has been split into 1476 data segments of 600-s each, for which the multipath linear combinations of eq. (6.21) have been formed. For each of these data segments, we have estimated the parameters for AR processes of increasing order (here up to order 4). The estimated AR parameters for the L1 C/A signal are presented in figs. 6.18 to 6.21, and the empirical mean and standard deviation of the estimated values are displayed in table 6.13.

Table 6.12: Hardware setups considered in this section, the measurement period and tracked signals

Stat	Receiver	Antenna	Date	Time	Signals	Remark
DLF5	Septentrio PolaRx2[1]	Leica AT504	Jan 1, 2011	24h	GPS L1C/A, L1P, L2P	Part of EGNOS monitoring network
		Leica AR25 3D chokering	Sep 7, 2011			
DLF1	Trimble NETR9[1]	Leica AR25 3D chokering	Sep 7-13, 2011	7·24h	GPS L1C/A, L2(Z-tr.), L2C, L5I+Q GIOVE E1B+C, E5aI+Q, E5bI+Q, E5I+Q	Part of IGS MGEX network

1 Receivers were used with default tracking loop bandwidths and without applying pseudo range smoothing

Table 6.13: Estimated AR parameters order 1-4 for the GPS L1 C/A signal measured with DLF5 based on 600-s data segments, and the estimated σ_ϵ at 90[°] of elevation and at C/N_0=50dB-Hz

	$\hat{a}_1$		$\hat{a}_2$		$\hat{a}_3$		$\hat{a}_4$		$\hat{\sigma}_\varepsilon$[m]	
	μ	σ	μ	σ	μ	σ	μ	σ	at $90°$	50dB-Hz
AR(0)									0.18	0.20
AR(1)	-0.90	0.034							0.07	0.08
AR(2)	-1.2	0.16	0.31	0.14					0.07	0.08
AR(3)	-1.2	0.14	0.22	0.16	0.073	0.10			0.07	0.08
AR(4)	-1.2	0.14	0.21	0.14	0.071	0.078	0.004	0.084	0.07	0.08

Figure 6.18 shows a histogram of the AR(1) parameter estimated for each of the data segments. The AR(1) parameter has empirical mean $\mu = -0.90$ and standard deviation $\sigma = 0.03$ for this dataset. From these results it is clear that the data indeed behaves like an autoregressive process with a relatively high a_1 parameter, which suggests strong time correlation of the multipath time series (an a_1 parameter of –0.90 at 1 Hz corresponds to a correlation time of 9.5s). Multipath is not the only possible source of this time correlation,

since the receiver tracking loops may also result in correlated measurements. Because the estimates are distributed closely around the mean, the time correlation apparently does not vary widely between the 600-s intervals. For this dataset the estimated AR parameter is always smaller than 1 in absolute sense ($|\underline{\hat{a}}_1| < 1$), which is one of the conditions for an AR(1) time series to be wide sense stationary, conform our earlier assumption.

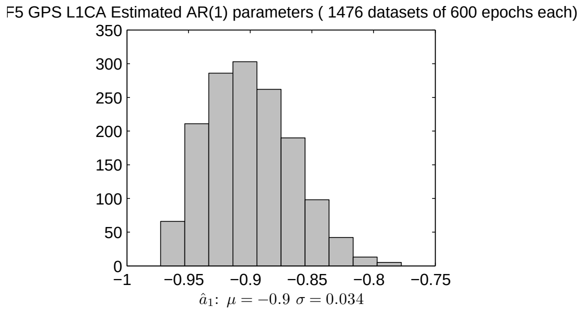

Figure 6.18: AR(1) parameter estimated for the GPS L1 C/A signal measured with DLF5.

Figure 6.19 shows histograms of the estimated AR(2) parameters and again reveals a strong signal, as will be confirmed by our parameter significance tests below. Estimation of an a_2 parameter also significantly changes the estimate of the a_1 parameter, since now the time correlation is captured by the combination of the two parameters. The estimated parameter pairs still satisfy condition of eq. (6.26), which means that all estimated AR processes are stable.

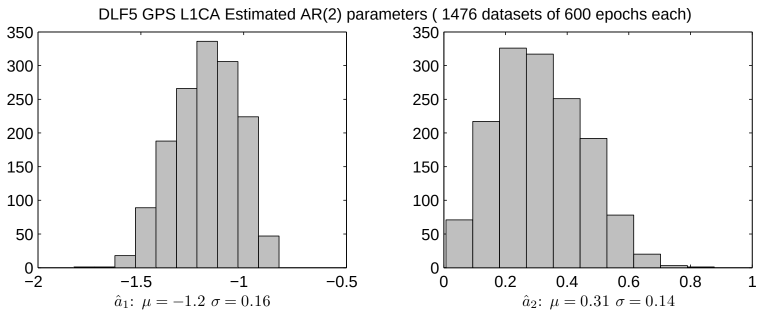

Figure 6.19: AR(2) parameters estimated for the GPS L1 C/A signal measured with DLF5.

Figures 6.20 and 6.21 show the parameters for an AR(3) and an AR(4) model, respectively, estimated from the same DLF5 dataset. The higher order AR parameters get smaller with increasing AR order; in fact the mean values of the estimates of a_3 and a_4 are smaller than their empirical standard deviations. The method described in the previous section is used to test the significance of the parameters and to determine the appropriate order of the AR process.

We test the k^{th} parameter for an AR(k) process starting with $k = 1$. Instead of evaluating the hypothesis at a fixed level of significance, with an accept or reject, we choose a slightly different approach. We compute the probability $\alpha_{\underline{\hat{a}}_k}$ that the test statistic will take a value that is at least as extreme as the observed value of the statistic when the null hypothesis

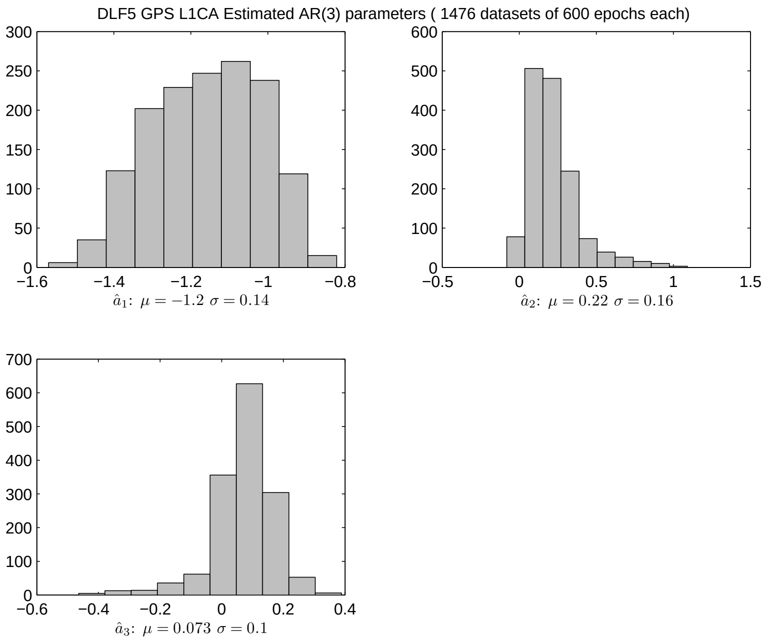

Figure 6.20: AR(3) parameters estimated for the GPS L1 C/A signal measured with DLF5.

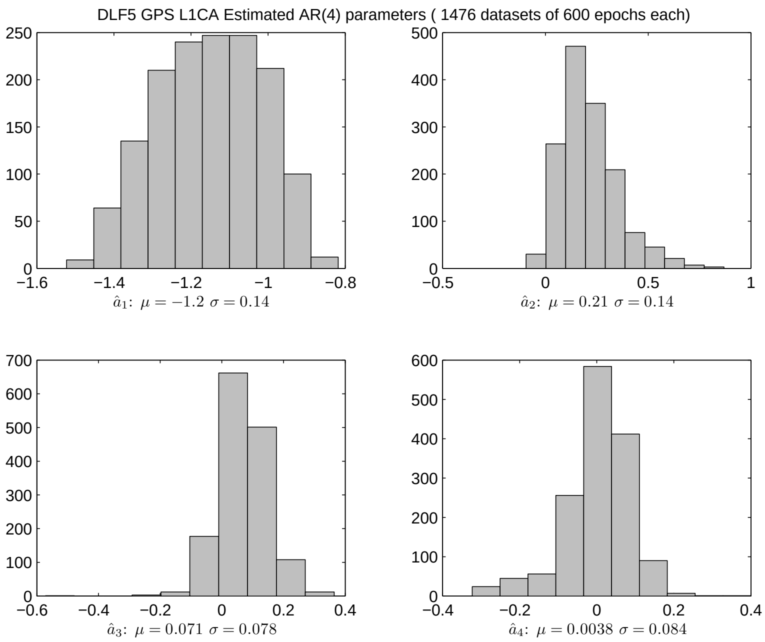

Figure 6.21: AR(4) parameters estimated for the GPS L1 C/A signal measured with DLF5.

is true: this is called the observed level of significance. If the observed level of significance is smaller than the critical level of significance the null hypothesis is rejected; we can then say that the parameter is statistically significant and we increase the AR order by one. The main advantage of this approach is that we can count the number of times the null hypothesis is rejected for different levels of significance. Figure 6.22 shows a cumulative histogram of the observed (2-sided) level of significance of the estimated AR parameters. The figure can be interpreted as follows: if we look at a significance of e.g. 0.1 we find that 100% of the data segments have a significant AR(1) parameter. So we estimated an AR(2) process and found the estimated a_2 parameter to be significant for 98% of the data segments for this level of significance. For these 98% an AR(3) process is estimated and for 65% of the total number of data segments the a_3 parameter is found to be significant. Finally we estimated an AR(4) process for these 65% and found a significant a_4 parameter for 24% of the total number of data segments.

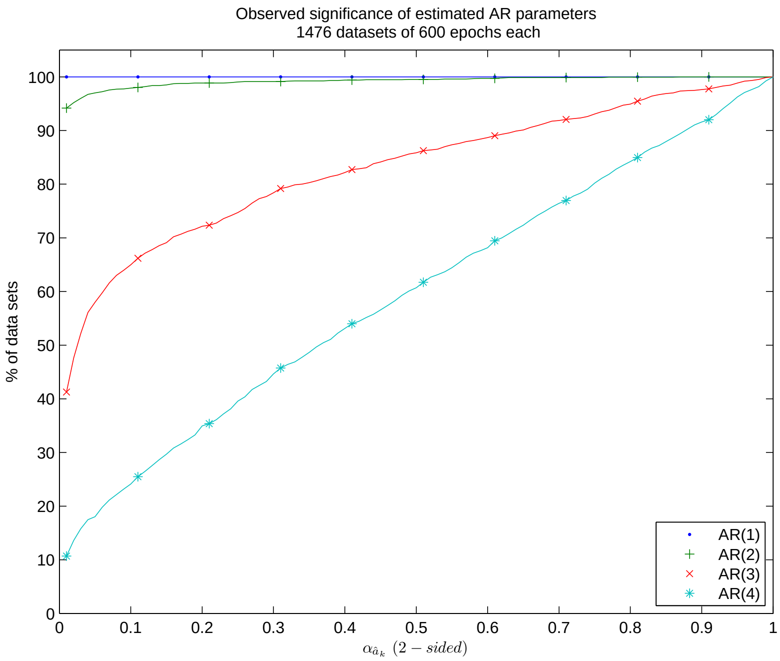

Figure 6.22: Percentage of datasets with significant AR parameters as function of the level of significance α for the GPS L1 C/A signal measured with DLF5.

A level of significance of 0.1 is still very large: it means we have 10% probability of wrongly rejecting the null hypothesis (false alarm rate), and wrongly assume that the parameter is significant. Therefore, fig. 6.23 provides the same data on a logarithmic x-axis in order to show more details for smaller levels of significance. Figure 6.23 reveals that for these smaller levels of significance the estimated a_4 parameter is only significant for a small percentage of the data segments. For this small percentage of the data segments we could of course continue to estimate AR processes of increasing order, but the following practical considerations may lead us to a different approach.

If we look at filtering techniques for positioning, it is not feasible to work with AR processes of such high orders. For each order we need to extend the state-vector with an additional element, both increasing the computational burden and weakening the positioning model

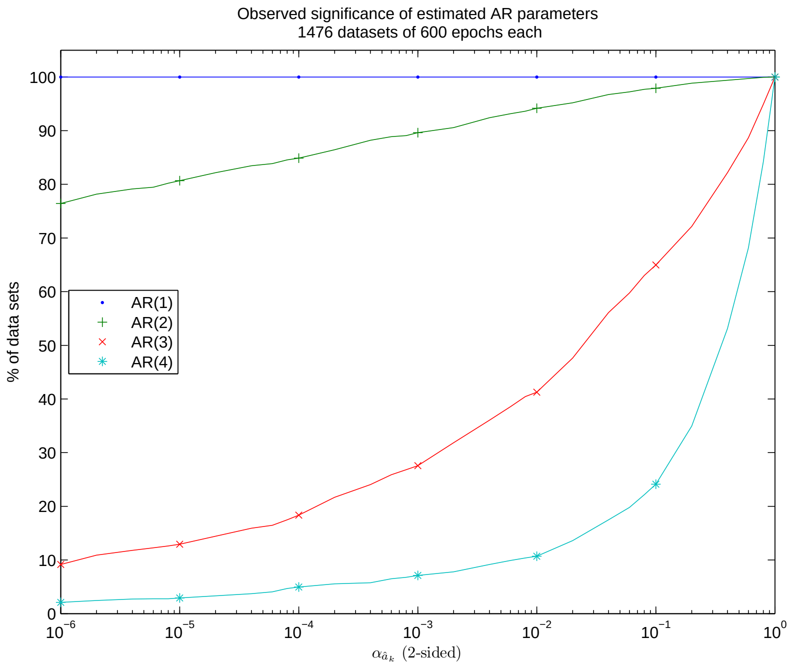

Figure 6.23: Percentage of datasets with significant AR parameters as function of the level of significance α, plotted on a logarithmic scale for the GPS L1 C/A signal measured with DLF5.

by increasing the number of unknown parameters. Also, for integrity monitoring similar reservations hold, as the number of (multi-dimensional) tests we would need to perform increases dramatically. For multipath simulations, on the other hand, higher order models do not pose any real problem. However, it is questionable what the gain would be of using AR models of orders much higher than those considered in the positioning filter. For these reasons, and given the weak signal for the AR(4) parameter ($\underline{\hat{a}}_4 : \mu = 0.004$) and the fact that it is only significant for a small percentage of the data segments, we will not consider higher order models here.

As described in the previous sections, the multipath linear combination is dominated by pseudo range multipath and measurement noise. Multipath depends amongst other things on elevation with the strongest multipath effects generally occurring at low satellite elevation. Measurement noise mainly depends on the carrier-to-noise ratio and certain receiver properties. The C/N_0 in turn depends strongly on the antenna gain pattern, which means that the measurement noise also strongly depends on elevation. Due to strong dependency of the C/N_0 on the elevation, the two mechanisms described above cannot really be separated from each other. Therefore, the impact of the elevation and C/N_0 on the estimated AR processes is here studied together.

Figure 6.24 shows the estimated AR(1) parameter versus the measured C/N_0. These DLF5 results only reveal a small dependency of the estimated AR parameters on the C/N_0 (or the elevation angle). However, the estimated σ_ϵ of eq. (6.41) *does* show a strong dependency on elevation and C/N_0.

Figure 6.25 shows the estimated σ_ϵ as a function of the C/N_0 for different orders of the AR process including AR(0), the white noise process. Each marker in the figure represents

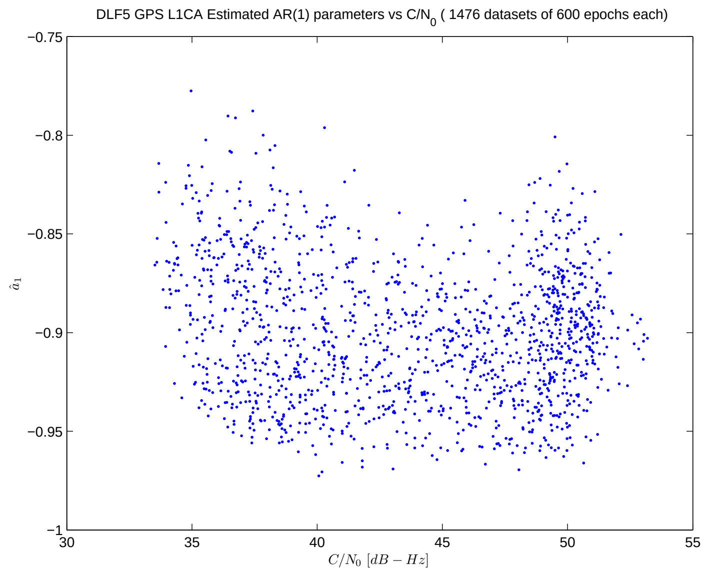

Figure 6.24: AR(1) parameter vs. C/N_0 estimated for the GPS L1 C/A signal measured with DLF5.

the estimated σ_ϵ for one multipath time series of 600 epochs (at 1 Hz). The figure shows a sharp decrease in the estimated σ_ϵ from an AR(0) to an AR(1) model, which indicates that an AR(1) model fits the data much better than a white-noise process does. The figure also reveals a very clear decrease of the estimated σ_ϵ with increasing C/N_0. It turns out that this decrease can accurately be described by an inversely proportional relation between the C/N_0, expressed in ratio-Hz, and the variance of the noise. This relation is known to describe the thermal measurement noise of a GPS receiver as mentioned in the previous sections (Braasch and van Dierendonck, 1999). This indicates that the tracking loops of the receiver play an important role in the formation of the time correlated errors captured in the multipath time series. This could also explain why the AR parameters, and thus the time correlation, does not vary strongly with elevation.

The relation found between the standard deviation of the noise and the C/N_0 only has one unknown parameter, which is the standard deviation of the noise at a reference C/N_0. This parameter has been estimated from the data points for each of the AR processes at the (arbitrary) reference C/N_0 of 50 dB-Hz. The resulting relations are presented in the legend of fig. 6.25 and are also represented by the black lines drawn through the data points (results are also displayed in table 6.13). The estimated standard deviation of the noise decreases by a factor of more than 2 from an AR(0) to an AR(1) process.

Extending the AR model beyond the first order further decreases the estimated σ_ϵ. This is not surprising, as a more complex model (with more parameters) will always fit the data better, which leads to smaller residuals. And smaller residuals directly decrease the estimated σ_ϵ as is clear from eq. (6.41). However, fig. 6.25 and table 6.13 reveal that the effect of adding more AR parameters is much less pronounced. In fact, the lines for AR(2) to AR(4) lie almost on top of each other and computed values are well below cm level. This shows that the added benefit from this increase of complexity of the model, and the related increase in computational burden, may not be beneficial.

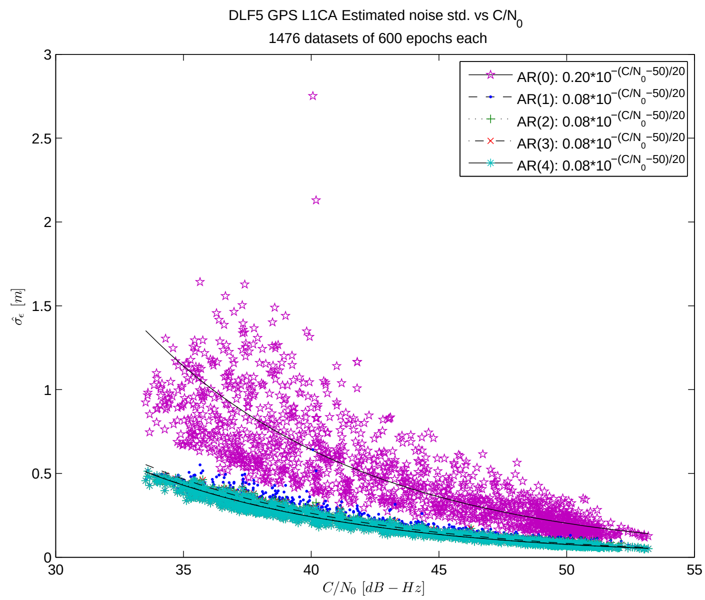

Figure 6.25: Estimated σ_ϵ vs. C/N_0 for the GPS L1 C/A signal measured with DLF5.

Figure 6.26 shows the same data as fig. 6.25 but now with the satellite elevation on the horizontal axis. The estimated noise standard deviation decreases significantly with increasing elevation angle. The lines drawn through the data points for each AR order show a cosecant function $(1/sin(e))$ of the elevation with the standard deviation at 90 degrees of elevation estimated from the data. The formula for each of these lines is again presented in the figure legend (results are also displayed in table 6.13). The results again show a sharp decrease in the noise standard deviation from AR(0) to AR(1) and a much smaller decrease from AR(1) to higher order AR processes. The cosecant function can be used for elevation dependent weighting of the satellite measurements (Vermeer, 1997).

The connection between figs. 6.25 and 6.26 is formed by the measured C/N_0 as a function of elevation, which strongly depends on among others the antenna gain pattern. Therefore, the weighting scheme that best fits the data will depend on the used antenna. Also, it is clear that for this particular receiver and antenna combination the C/N_0 model of fig. 6.25 provides a much better fit than the cosecant function of fig. 6.26: therefore, in this case, it is more appropriate to base the pseudo-range weights on C/N_0 instead of elevation.

The variations of σ_ϵ with elevation and C/N_0 between the 600-s data segments, suggests that σ_ϵ may also vary within the data segments. This might lead us to question our assumption of wide sense stationarity for these 600-s time series, and it might be more appropriate to shorten the data segment in order to limit the variation of σ_ϵ within each data segment. To investigate this further we have also estimated AR processes for shorter data segments of 120-s and compared these to the 600-s results. Results of the 120-s data segments are presented in table 6.14 and fig. 6.27. Table 6.14 shows the mean and empirical standard deviation of estimated AR parameters for an AR process of order 1 to 4, and the estimated σ_ϵ at 90 degrees of elevation and at C/N_0=50dB-Hz determined via curve fitting as described above. Figure 6.27 shows the observed significance of the a_k estimates for AR order 1 to 4. Comparing the 120-s results in table 6.14 to the 600-s results

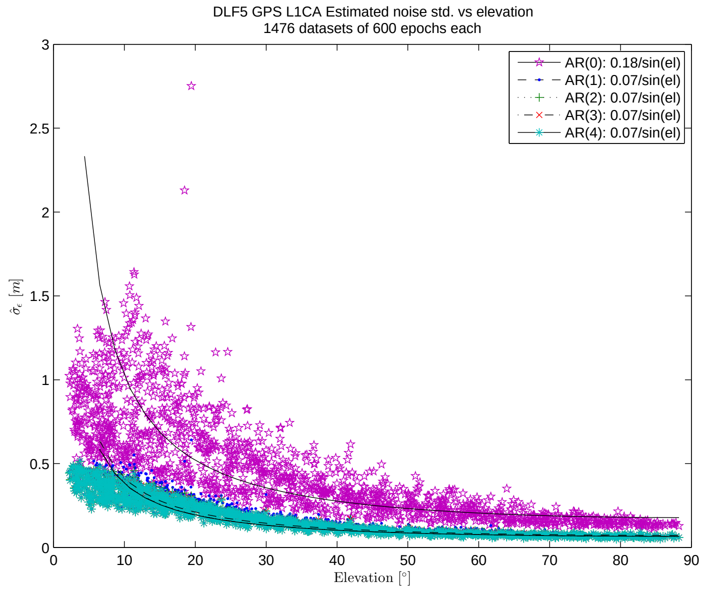

Figure 6.26: Estimated σ_ϵ vs. elevation for the GPS L1 C/A signal measured with DLF5.

obtained previously in table 6.13, reveals that there are some differences. Especially the mean value of the estimated a_4 parameter is larger for the 120-s interval, but also all of the empirical standard deviations are larger. If we look at the significance of the a_4 estimate for 120-s data segments in fig. 6.27, and compare this to the 600-s results in fig. 6.23, we see that it is even less significant for 120-s data segments than for the 600-s data segments. This is directly related to the variance of the estimates as was shown in eq. (6.44). There obviously is a trade-off for the length of the data segments. Shorter data segments limit the variations of σ_ϵ within the data segments thereby satisfying the conditions for wide sense stationarity better, while longer data segments enable us to estimate the AR parameters with much higher precision. Finally, table 6.14 shows that the estimated σ_ϵ is lower for the 120-s second data segments, especially for the AR(0) process. This is directly related to the time correlation which is partially removed by splitting the data in short segments.

Table 6.14: Estimated AR parameters order 1-4 for the GPS L1 C/A signal measured with DLF5 based on 120-s datasegments, and the estimated σ_ϵ at 90° of elevation and at C/N_0=50dB-Hz

	$\hat{a}_1$		$\hat{a}_2$		$\hat{a}_3$		$\hat{a}_4$		$\hat{\sigma}_\varepsilon$[m]	
	μ	σ	μ	σ	μ	σ	μ	σ	at 90°	50dB-Hz
AR(0)									0.16	0.19
AR(1)	-0.88	0.053							0.07	0.08
AR(2)	-1.2	0.18	0.32	0.16					0.07	0.08
AR(3)	-1.1	0.17	0.21	0.20	0.085	0.13			0.06	0.08
AR(4)	-1.1	0.16	0.21	0.19	0.057	0.15	0.026	0.12	0.06	0.08

So far we have looked at results from DLF5 with the PolaRx2 receiver and Leica AT504 antenna. Now we will look at some other hardware setups and investigate the impact on the estimated AR models. For this purpose a more recent dataset from DLF5 (Sep 7, 2011)

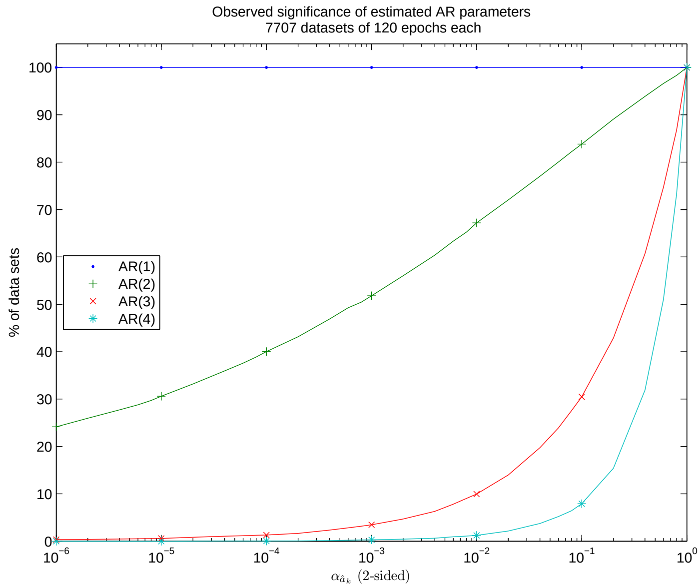

Figure 6.27: Percentage of datasets with significant AR parameters as function of the level of significance α for for the GPS L1 C/A signal measured with DLF5 for 120-s data segments.

is processed. In the meantime the antenna has been replaced with a multi GNSS Leica AR25.R3 3D choke-ring antenna and placed at a different position at a few meters distance from the old position. The receiver is still the Septentrio PolaRx2, and as it turns out the differences between the results with the two antennas are not very large. The estimated AR parameters only differ slightly and the estimated σ_ϵ as a function of the elevation angle is also very similar, except at low elevations angles, as can be seen from fig. 6.28, where the new antenna setup performs slightly better and measurements are available at smaller elevation angles.

A possible explanation for the similarities between the results with the two antennas is that both antennas and sites are very similar regarding multipath, however, a more likely explanation is that the multipath time series for DLF5 depend mainly on the receiver, i.e. is dominated by measurement noise due to the tracking loops.

DLF1 GPS L1C/A signal

To investigate this further, a third dataset has been processed from the permanent receiver DLF1. DLF1 is a Trimble NETR9 receiver and is connected to the same Leica AR25.R3 3D choke-ring antenna as DLF5. The results for DLF1 are very different from those for DLF5. Figure 6.29 shows the estimated AR(1) parameter, and comparison with fig. 6.18 for DLF5 immediately shows that the estimated value for DLF1 is much smaller in absolute sense. This indicates that the time correlation of the pseudo range measurements is smaller for DLF1. Figure 6.30 again shows the estimated σ_ϵ as a function of satellite elevation angle. The large reduction in the residuals for higher order AR processes that was found for DLF5 now only occurs for low elevation angles. It seems that the time correlation now depends on the elevation angle. And indeed, the estimated AR parameters now show an elevation dependence. Figure 6.30 also shows that an AR(2) process only gives a minor decrease in the estimated noise parameter. Therefore, we will now focus on the AR(0) and AR(1)

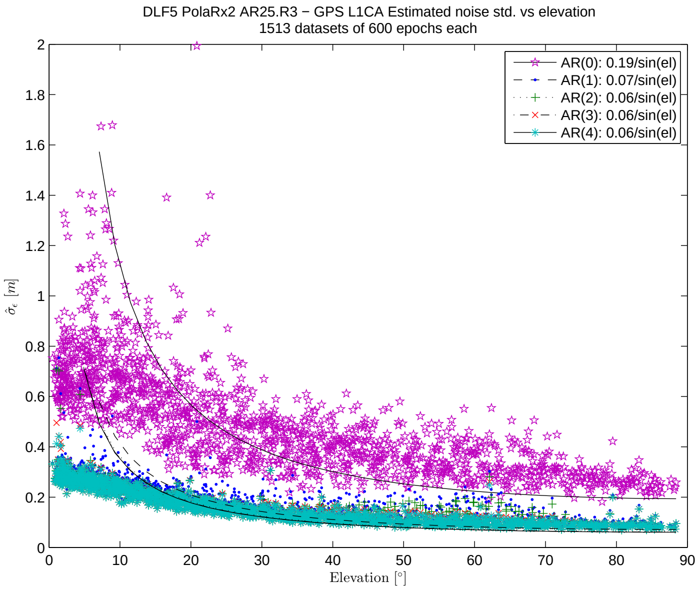

Figure 6.28: Estimated σ_ϵ vs. elevation for the GPS L1 C/A signal measured with DLF5 on Sep 7, 2011 PolaRx2 receiver and AR25.R3 antenna.

processes.

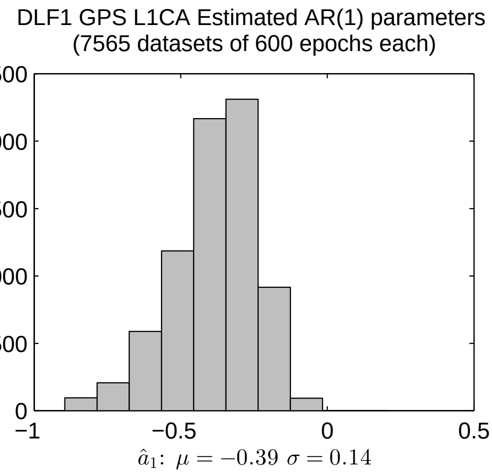

Figure 6.29: AR(1) parameter estimated for the GPS L1 C/A signal measured with DLF1.

Figure 6.31 shows the estimated AR(1) parameter as a function of the elevation angle and azimuth angle in a skyplot. The color shows the value of the AR parameter. The white gaps represent combinations of elevation and azimuth angles (mostly to the North of the receiver) where no satellites have been measured. A general effect that can be seen is that the AR value in absolute sense is larger for low elevation angles (at the outer circle of the figure) and smaller for high elevation angles (in the center of the figure). Figure 6.31 also shows variations with the azimuth angle. Figure 6.32 shows skyplots of the estimated noise parameter for an AR(0) and AR(1) process. These plots again show an increase of this noise parameter with decreasing elevation angle. There is also a clear relation between

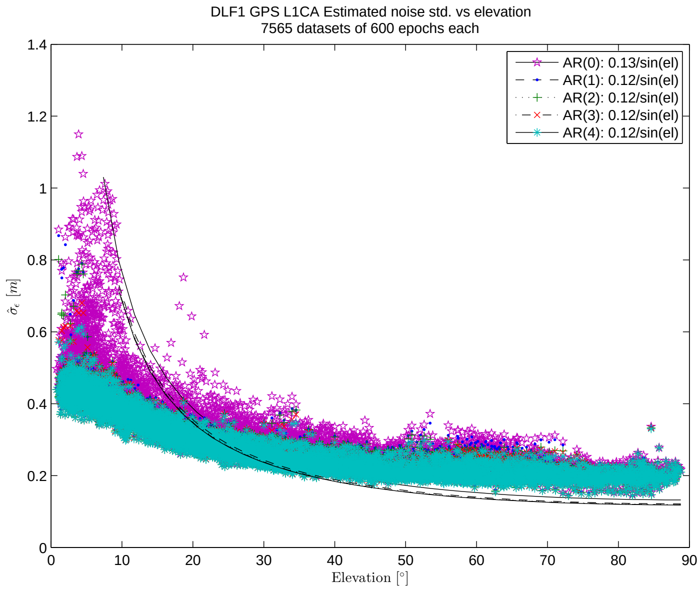

Figure 6.30: Estimated σ_ϵ vs. elevation for the GPS L1 C/A signal measured with DLF1.

the largest values of the AR(1) parameter (in absolute sense) in fig. 6.31 and the largest estimates for the noise parameter for the AR(0) process in fig. 6.32. Apparently, the higher noise values for the AR(0) and higher estimates of the AR(1) parameter are related, which could point in the direction of multipath. The large values for the noise parameter in the AR(0) process are significantly reduced in the AR(1) process, as can be seen in the skyplot in the bottom pane of fig. 6.32.

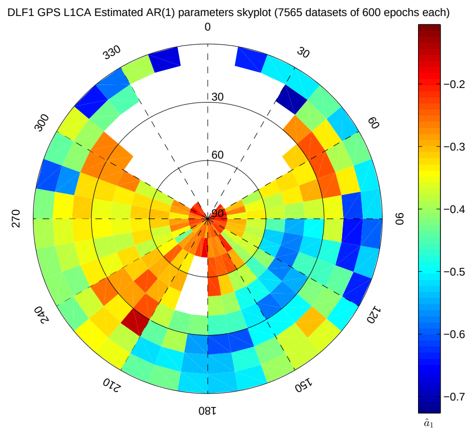

Figure 6.31: Skyplot of AR(1) parameter estimated for the GPS L1 C/A signal measured with DLF1.

Comparison of the DLF1 and DLF5 results, when both are connected to the same antenna, shows that at low elevation angles, where we expect most multipath, both the DLF5 and DLF1 measurements have a high time correlation. However, at high elevation angles, the DLF1 results have much less time correlation than the DLF5 results. This is an indication that the time correlation of the DLF5 (at high elevation) is related to the tracking loops

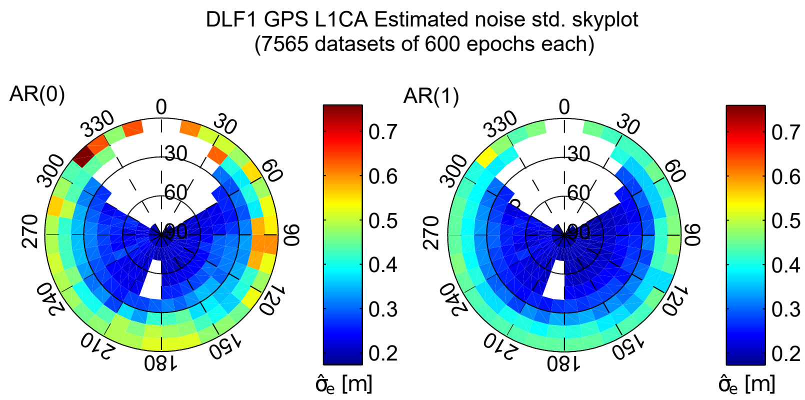

Figure 6.32: Skyplot of estimated σ_ϵ for AR(0) (left pane) and AR(1) (right pane) for the GPS L1 C/A signal measured with DLF1.

of the receiver rather than the physical process of multipath.

DLF1 Different GNSS signals

The DLF1 hardware setup (Trimble NETR9 receiver and Leica AR25.R3 3D choke-ring antenna) is able to track multiple GNSS including GPS, Galileo, GLONASS and EGNOS. In this contribution, the following signals have been considered: GPS L1C/A, L2(Z-track.), L2C, L5I+Q and GIOVE E1B+C, E5aI+Q, E5bI+Q, E5I+Q. Because several of these signals are only transmitted by one or a few satellites, a complete week of data (Sep 7-13, 2011) has been processed in order for the results to have some statistical significance. To keep the amount of results manageable, we focus on the AR(0) and AR(1) process, and make use of boxplots (McGill et al., 1978) to present the results. Figure 6.33 shows the estimated σ_ϵ for an AR(0) process for each of the GPS and GIOVE signals tracked by DLF1. Each box shows the distribution for one of the signals: the central mark is the median, the edges of the box are the 25th and 75th percentiles, the whiskers extend to the most extreme data points not considered outliers, and outliers are plotted individually. The boxplot shows different distributions for each of the signals but all 25 to 75 percentile boxes are below 0.5m with whiskers and outliers extending upwards. Investigation of the elevation dependence shows that the median and 25 and 75 percentiles are mainly determined by the measurements at medium to high satellite elevations, while the top whiskers and outliers describe the behavior for low satellite elevation. The elevation pattern in fig. 6.30 for the residuals of the AR(0) process is quite typical for all signals except for the E5I+Q (AltBOC) signal which clearly has less noise than all other signals. The high precision of the L5I+Q, E5aI+Q and E5bI+Q signals, compared to the L1C/A signal, is not apparent from this figure. All signals, except for the E5I+Q signal (and to a lesser extend the E1B+C signal) show comparable maximum values for the noise parameter.

Figure 6.34 shows the estimated AR(1) parameter for each of the signals. The median values differ quite a bit between the signals, with the E5I+Q (AltBoc) signal having the smallest value and the E5bI+Q signal having the largest value. These values indicate

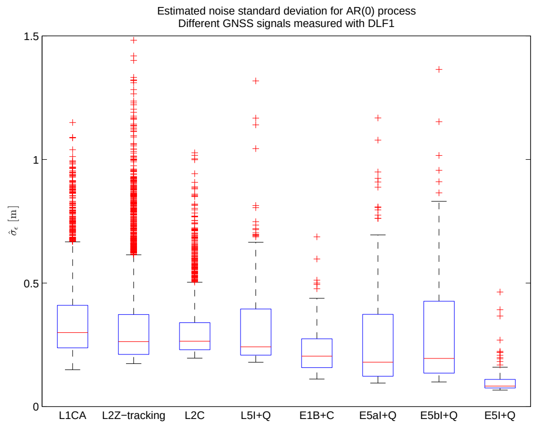

Figure 6.33: Estimated σ_ϵ for the AR(0) process for each of the GNSS signals measured with DLF1.

different time correlation for these signals, but all signals have whiskers extending close to -1. These data segments with the strongest time correlation again correspond to low satellite elevation.

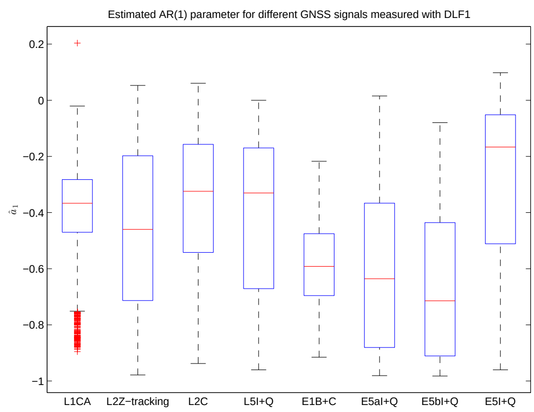

Figure 6.34: AR(1) parameter estimated for each of the GNSS signals measured with DLF1.

Figure 6.35 shows the estimated σ_ϵ values for the AR(1) process. In this figure the differences between the L1C/A signal and the newer (wide-band) signals *is* very clear, especially when looking at the top whiskers for each signal. While the top whisker of the L1C/A signal still exceeds 0.6 meter, the other signals are constrained to significantly smaller values. The median values are not impacted so much, because the strong time correlation is limited to lower elevation angles. If these AR(1) processes would be used in a positioning algorithm, the smaller residuals for the wide-band signals make proper weighting of the measurements possible (e.g. the wide-band measurements can be given more weight than the L1C/A measurements).

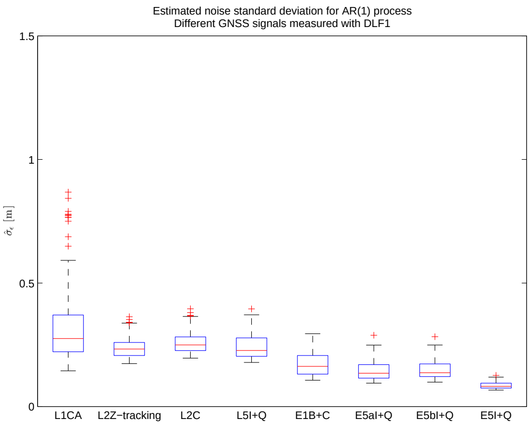

Figure 6.35: Estimated σ_ϵ for the AR(1) process for each of the GNSS signals measured with DLF1.

6.4 Conclusions

In sections 6.1 and 6.2 the different contributions of the code and phase measurement noise have been investigated with a geometry-free model using measurements from short and zero baselines as well as stand-alone receivers. Using the single, double and time differences of the code-minus-carrier and multipath combinations, the code noise, code multipath delays, and time correlation of the code observations have been quantified. From these investigations the undifferenced code noise without multipath could be estimated. The estimated values were in good agreement with the theoretical formulae linking the measurement noise to tracking loop parameters and the C/N_0. Therefore, these theoretical expressions can be used in the stochastic model to account for the pseudo range measurement noise.

The phase noise and phase multipath have also been studied from the double difference phase observations. The results show that the estimated phase noise is close to the theoretical thermal noise and almost equal for each GNSS as expected. Unlike the code observations the phase observations show very little time correlation at a sampling rate of 1Hz. This means that the theoretical relations again suffice for the part of the stochastic model that accounts for the carrier phase measurement noise.

The observations made to different satellites turned out to be almost uncorrelated as expected and consequently this correlation can be neglected in the stochastic model.

However, the results also showed strong variations of the pseudorange code measurements over longer time periods, the magnitude of the variations easily reaching up to 20 times the thermal noise standard deviation. These time correlated (multipath) errors were further studied in sections 6.2.3.2 and 6.3. The multipath linear combination of GNSS measurements, which is dominated by pseudo range multipath and (time correlated) measurement noise was modeled as an autoregressive process. The estimated AR parameters, the standard deviation of the residuals and their dependence on e.g. satellite elevation differ for each of the GNSS signals and are also different for the two receivers considered in this chapter. However, the following general conclusion can be reached.

The AR(0), or white noise, model shows a clear dependency of the standard deviation of the residuals on satellite elevation where larger residuals are encountered for smaller elevation angles. This can be translated to a white noise stochastic model with elevation dependent weighting which can be used for positioning. However, the estimated AR(1) parameter is almost always significant to a very high level, which indicates time correlation of the multipath time series. Estimation of an AR(1) model reduces the estimate of σ_ϵ by a significant amount (especially for satellites with low elevation angles), which shows that an AR(1) model fits the data much better than does a white noise or AR(0) model in those cases. The AR(1) parameter itself does not show a strong dependency on satellite elevation, but the standard deviation of the residuals *does* show this dependency. This AR(1) model can be used for the stochastic model by extending the Kalman state vector with an additional entry per signal with multipath. The transition matrix for these entries then take the (constant) values of the estimated AR(1) parameters and the process noise is taken as a satellite elevation dependent value. With increasing order the estimated AR parameters decrease in magnitude and become less significant. Also the reduction in σ_ϵ, an indication of the improvement in the model fit, becomes negligible. Each increase in the AR order leads to an additional filter state, thereby increasing the computational burden and decreasing the strength of the model. Therefore, higher order AR models seem unattractive for the stochastic model used for positioning based on this analysis.

This means that for the positioning algorithms the AR(0), or white noise process, and AR(1) models are best suited. A user or application designer can then make a trade-off between using a simple (elevation dependent) white noise model or a more accurate AR(1) model at the cost of additional computational burden.

The correlation time of the multipath time series found in this chapter is in the order of 10 s, which means that another approach to avoid this problem is to use a larger measurement interval, e.g. 30 s. However, other time correlated errors, e.g. the ionosphere delays, with longer correlation times cannot be dismissed in this way. Then autoregressive models provide a much better alternative as we will show in chapter 8.

7 Geometry-free Integrity Monitoring

7.1 Introduction

For GNSS users the level of integrity (or reliability) quantifies the trust that the user can place in the position solution. This goes beyond the concept of variance (or precision) which can account for the uncertainty in the measurements, but does not provide protection against (unexpected) systematic errors such as outliers or biases. Integrity operates at two levels: reliable position estimates and reliable accuracy information. Statistical tests can be applied to provide reliability to a user. These tests use the redundancy of the (positioning) model to detect errors in the observations or external information, or more formally errors in the functional and stochastic model assumptions. The null-hypothesis, under which there are no model errors present, is tested against different alternative hypotheses that define different types of model errors which might be encountered (Baarda, 1968; Teunissen, 2000b).

Bisnath and Gao (2009a) stresses the importance of integrity monitoring for any positioning system, and especially for PPP processing where some parameters are estimated, while others are obtained from a separate process. However, they also report that quantitative quality measures of PPP results are often limited. Integrity monitoring for PPP has only quite recently received more attention (Juan et al., 2012; Seepersad and Bisnath, 2013; Feng et al., 2014; Jokinen, 2014). There are different ways to provide integrity to a GNSS user. At system level, the GNSS provider (or in this case the PPP service provider) can monitor the integrity of the system, and provide this information to the user (e.g. if there is a satellite which produces large ranging errors) much like this is currently done for SBAS systems. This will provide the user with more confidence in the position solution. However, system level integrity *cannot* protect against errors caused by local events such as multipath, interference or unexpected receiver behavior. In this chapter we will focus on integrity aspects at user level, that *can* protect against local events.

The contents of this chapter is based on Teunissen and de Bakker (2012) and de Bakker et al. (2009), and to a lesser extend Teunissen and de Bakker (2013). The remainder of this introduction and sections 7.2 and 7.7 follow the analytical derivations and corresponding numerical results of Teunissen and de Bakker (2012) with the exception of sections 7.4.3 and 7.7.3, which provide additional numerical results based on de Bakker et al. (2009). In section 7.3 an insert with the main causes of cycle slips was added. Section 7.8 contains the conclusions which are synthesized from Teunissen and de Bakker (2012) and de Bakker et al. (2009); (cross)references have been adjusted to follow the conventions of this dissertation.

As mentioned, integrity monitoring and quality control can be exercised at different stages of the GNSS data processing chain (Teunissen, 1998a; Leick, 2004). These stages range from the single-receiver, single-channel case to the multi-receiver/antenna case, sometimes even with additional constraints included. An example of the latter is the quality control of baseline-constrained GNSS attitude models (Giorgi et al., 2012), while geometry dependent RAIM is an example of the single-receiver, multi-channel case (Teunissen, 1997a; Wieser et al., 2004; Feng et al., 2006; Hewitson and Wang, 2006).

In this chapter, we study the single-receiver, single-channel model. It is the weakest model of all, due to the absence of the relative receiver-satellite geometry. Despite its potential weakness, there are several advantages to single-receiver, single-channel data validation. First, since it is the simplest model of all, it can be executed in real-time inside the (stationary or moving) receiver, thus enabling early quality control on the raw data. Second, the geometry-free single-channel approach has the advantage that no satellite positions need to be known per se and thus no complete navigation messages need to be read and used. Additionally, such an approach also makes the method flexible for processing data from any other (future) GNSS or for parallel processing, which could prove relevant when considering large numbers of receivers.

We study the carrier phase-slip and code-outlier detection capabilities of the single-receiver, single-channel model. For the integrity monitoring of carrier-phase data, various studies can already be found in the literature. For dual frequency GPS data, for instance, methods of carrier phase-slip detection are discussed and tested in (Lipp and Gu, 1994; Mertikas and Rizos, 1997; Blewitt, 1998; Teunissen, 1998a; Gao and Li, 1999; Jonkman and de Jong, 2000; Bisnath and Langley, 2000; Bisnath et al., 2001; Liu, 2010; Miao et al., 2011; Cai et al., 2013). More recent studies on triple-frequency carrier phase-slip detection can be found in (Fan et al., 2006; Dai et al., 2009; Wu et al., 2010; Xu and Kou, 2011; Fan et al., 2011; Lacy et al., 2012; Zhao et al., 2015). Our contribution differs from these previous studies, because of its focus on the detectability of single-receiver, single-channel modeling errors. Next to the phase-slip detection, the detectability of code-outliers is studied as well. Our analysis is analytical, while supported by numerical results. Analytical expressions are derived for the Minimal Detectable Biases (MDBs) of the uniformly most powerful invariant tests (Baarda, 1967, 1968; Teunissen, 1990b). The MDB is an important diagnostic tool for inferring the strength of model validation. Examples of such studies for geometry-dependent and integrated GNSS models can be found in (Salzmann, 1991; Teunissen, 1998b; de Jong, 2000; de Jong and Teunissen, 2000; Hewitson and Wang, 2010).

This chapter is organized as follows. In section 7.2 we formulate the multi-frequency, single-receiver, geometry-free GNSS model. This is done for an arbitrary number of frequencies. An overview of the model's redundancy for different measurement scenarios gives a first indication of the model's testability. In section 7.3 the uniformly most powerful invariant test-statistics for spikes and slips are developed. It is shown how they can be applied to test for code-outliers, phase-slips and ionosphere disturbances. The strength of these test-statistics is described by their corresponding MDBs, for which lower bounds and upper bounds are also given. Due to the relatively simple structure of the geometry-free model, the expression for the MDB can be decomposed into a time-dependent and a time-invariant component. The effect of the time-dependent component is shown in section 7.3, while the characteristics of the time-independent part are studied in the sections following. The detectability of phase-slips is treated in section 7.4. An analytical expression for the phase-slip MDB is derived and it is used to assess the single-, dual- and multi-frequency phase-slip detectability for GPS and Galileo. To evaluate the influence of the code data, the analysis is performed for both the case with code data present and without code data present. The latter case is also of interest, for instance, when one wants to avoid the use of multipath corrupted code data. In section 7.5, an analytical expression for the code-outlier MDB is derived. It is used to study the code-outlier detectability for the single-, dual- and multi-frequency GPS and Galileo case, including the case that phase data are absent. In section 7.6, the MDB for an ionospheric disturbance is presented and analysed. The detectability of temporary loss-of-lock on all phase observables is treated in section 7.7. Finally, section 7.8 contains the summary and conclusions.

7.2 The multi-frequency, single-receiver geometry-free model

7.2.1 Functional model

The carrier phase and pseudorange (code) observation equations of a single receiver that tracks a single satellite on frequency $f_j = c_0/\lambda_j$ (c_0 is speed of light, λ_j is jth wavelength and $j = 1, \ldots, n$) at time instant t ($t = 1, \ldots, k$), are given as (Teunissen and Kleusberg, 1998; Misra and Enge, 2001; Hofmann-Wellenhoff and Lichtenegger, 2001; Leick, 2004),

$$\begin{array}{rcl} \phi_j(t) & = & \rho'(t) - \gamma_j \mathcal{I}(t) + b_{\phi_j} + n_{\phi_j}(t) \\ p_j(t) & = & \rho'(t) + \gamma_j \mathcal{I}(t) + b_{p_j} + n_{p_j}(t) \end{array} \tag{7.1}$$

where $\phi_j(t)$ and $p_j(t)$ denote the single receiver observed carrier phase and pseudorange, respectively, with corresponding zero mean noise terms $n_{\phi_j}(t)$ and $n_{p_j}(t)$. The unknown parameters are $\rho'(t)$, $\mathcal{I}(t)$, b_{ϕ_j} and b_{p_j}. The lumped parameter $\rho'(t) = \rho(t) + c_0\delta t_r(t) - c_0\delta t^s(t) + T(t)$ is formed from the receiver-satellite range $\rho(t)$, the receiver and satellite clock errors, $c_0\delta t_r(t)$ and $c_0\delta t^s(t)$, respectively, and the tropospheric delay $T(t)$. The parameter $\mathcal{I}(t)$ denotes the ionospheric delay expressed in units of range with respect to the *first* frequency. Thus for the f_j-frequency pseudorange observable, its coefficient is given as $\gamma_j = f_1^2/f_j^2$. The GPS and Galileo frequencies and wavelengths are given in table 7.1. The parameters b_{ϕ_j} and b_{p_j} are the phase bias and the instrumental code delay, respectively. The phase bias is the sum of the initial phase, the phase ambiguity and the instrumental phase delay.

Table 7.1: GPS and Galileo frequencies (f) and wavelengths (λ).

	L1/E1	L2	L5/E5a	E5b	E5	E6
f (MHz)	1575.42	1227.60	1176.45	1207.14	1191.795	1278.75
λ (cm)	19.0	24.4	25.5	24.8	25.2	23.4

Both b_{ϕ_j} and b_{p_j} are assumed to be time-invariant. This is allowed for relatively short time spans, in which the instrumental delays remain sufficiently constant (Liu et al., 2004). The time-invariance of b_{ϕ_j} and b_{p_j} implies that only time-differences of $\rho'(t)$ and $\mathcal{I}(t)$ are estimable. We may therefore just as well formulate the observation equations in time-differenced form. Then the parameters b_{ϕ_j} and b_{p_j} get eliminated and we obtain

$$\begin{array}{rcl} \phi_j(t,s) & = & \rho'(t,s) - \gamma_j \mathcal{I}(t,s) + n_{\phi_j}(t,s) \\ p_j(t,s) & = & \rho'(t,s) + \gamma_j \mathcal{I}(t,s) + n_{p_j}(t,s) \end{array} \tag{7.2}$$

where $\phi_j(t,s) = \phi_j(t) - \phi_j(s)$, with a similar notation for the time-difference of the other variates.

Would we have a priori information available about the ionospheric delays, we could model this through the use of additional observation equations. In our case, we do not assume information about the *absolute* ionospheric delays, but rather on the *relative*, time-differenced, ionospheric delays. We therefore have the additional (pseudo) observation equation

$$\mathcal{I}_o(t,s) = \mathcal{I}(t,s) + n_{\mathcal{I}}(t,s) \tag{7.3}$$

with the (pseudo) ionospheric observable $\mathcal{I}_o(t,s)$. The sample value of $\mathcal{I}_o(t,s)$ is usually taken to be zero, and $n_{\mathcal{I}}$ is then related to the power spectral density of the ionospheric variations.

If we define:

$$\begin{array}{rcl} \phi(t) & = & (\phi_1(t), \ldots, \phi_n(t))^* \\ p(t) & = & (p_1(t), \ldots, p_n(t))^* \\ y(t) & = & (\phi(t)^*, p(t)^*, \mathcal{I}_o(t))^* \\ g(t) & = & (\rho'(t), \mathcal{I}(t))^* \\ \gamma & = & (\gamma_1, \ldots, \gamma_n)^* \\ y(t,s) & = & y(t) - y(s) \\ g(t,s) & = & g(t) - g(s) \end{array} \tag{7.4}$$

then the expectation E of the $2n+1$ observation eqs. (7.2) and (7.3) can be written in the compact vector-matrix form

$$E\{(y(t,s)\} = Gg(t,s) \tag{7.5}$$

where

$$G = \begin{bmatrix} e_n & -\gamma \\ e_n & +\gamma \\ 0 & 1 \end{bmatrix} \tag{7.6}$$

with e_n the n-vector of ones and $\gamma = (\gamma_1, \ldots, \gamma_n)^*$. This two-epoch model can be extended to an arbitrary number of epochs. Let $y = (y(1)^*, \ldots, y(k)^*)^*$ and $g = (g(1)^*, \ldots, g(k)^*)^*$, and let D_k be a full rank $k \times (k-1)$ matrix of which the columns span the orthogonal complement of $e_k = (1, \ldots, 1)^*$, $D_k^* e_k = 0$. Then $dy = (D_k^* \otimes I_{2n+1})y$ and $dg = (D_k^* \otimes I_2)g$ are the time-differenced vectors of the observables and parameters, respectively, and the k-epoch version of eq. (7.5) can be written as

$$E\{dy\} = (I_{k-1} \otimes G)dg \tag{7.7}$$

where $\otimes$ denotes the Kronecker product. The Kronecker product of an $a \times b$ matrix $M = (m_{ij})$ and a $c \times d$ matrix $N = (n_{ij})$ is an $ac \times bd$ matrix defined as $M \otimes N = (m_{ij}N)$. For properties of the Kronecker product, see e.g., Rao (1973). The model of eq. (7.7), or its two-epoch variant eq. (7.5), is called the time-differenced, single receiver geometry-free model. It will be referred to as our null hypothesis $\mathcal{H}_0$.

7.2.2 Stochastic model

The $n \times n$ variance matrices of the undifferenced carrier phase and (code) pseudo range observables $\phi(t)$ and $p(t)$ are denoted as $Q_{\phi\phi}$ and Q_{pp}, respectively. We assume these variance matrices to be time-invariant and we also assume cross-correlation between phase and code to be absent. Thus for the dispersion of the two-epoch model eq. (7.5) we have

$$D\{y(t,s)\} = \text{blockdiag}(2Q_{\phi\phi}, 2Q_{pp}, \sigma^2_{d\mathcal{I}}) \tag{7.8}$$

where the scalar $\sigma^2_{d\mathcal{I}}$ denotes the variance of the time-differenced ionospheric delay.

To determine the variance matrix of the time-differenced ionospheric delays, let $D\{\mathcal{I}\} = Q_{\mathcal{I}\mathcal{I}}$ be the variance matrix of the *absolute* ionospheric delay vector $\mathcal{I} = (\mathcal{I}(1), \ldots, \mathcal{I}(k))^*$. The variance matrix of the time-differenced ionospheric delay vector $dI = (D_k^* \otimes 1)\mathcal{I}$ is then given as $D\{d\mathcal{I}\} = D_k^* Q_{\mathcal{I}\mathcal{I}} D_k$.

It is through the choice of $Q_{\mathcal{I}\mathcal{I}}$ that we can model the time-smoothness of the ionospheric delays. If we assume that the time series of ionospheric delays can be modeled as a *first-order autoregressive* stochastic process, then the covariance between $\mathcal{I}(t)$ and $\mathcal{I}(s)$ is given as $\sigma^2_{\mathcal{I}}\varrho^{|t-s|}$, with $0 \leq \varrho \leq 1$. The two extreme cases are $\varrho = 0$ and $\varrho = 1$. In the first case, $Q_{\mathcal{I}\mathcal{I}}$ is a scaled unit matrix and $\mathcal{I}(t)$ is considered a *white noise* process. In the second case, the variance matrix equals the rank-one matrix $Q_{\mathcal{I}\mathcal{I}} = \sigma^2_{\mathcal{I}} e_k e_k^*$ and $\mathcal{I}(t)$ is considered a *random constant*. In the first case we have $D\{d\mathcal{I}\} = \sigma^2_{\mathcal{I}} D_k^* D_k$, while in the second case we have $D\{d\mathcal{I}\} = 0$.

For the two-epoch case of eq. (7.8), the variance of the time-differenced first-order autoregressive ionospheric delay works out as

$$\sigma^2_{d\mathcal{I}} = 2\sigma^2_{\mathcal{I}}(1 - \varrho^{|t-s|}) \tag{7.9}$$

For two successive epochs we have $\sigma^2_{d\mathcal{I}} = 2\sigma^2_{\mathcal{I}}(1-\varrho)$, while for larger time-differences the variance will tend to the white-noise value $\sigma^2_{d\mathcal{I}} = 2\sigma^2_{\mathcal{I}}$ if $\varrho < 1$. Thus $\sigma^2_{\mathcal{I}}$ and ϱ can be used to model the level and smoothness of the noise in the ionospheric delays. We used the above stochastic model for both our analytical and numerical analyses. The proper value of $\sigma_{d\mathcal{I}}$ that can be used to constrain the model depends on the measurement interval, which can be selected by the user, and the ionosphere variability, which itself depends on i.a. the user latitude, (local) time of day, satellite elevation, and ionosphere activity. The values for the expected conditions can be determined a priori from dual frequency carrier phase observations, but the actual time-differenced ionosphere delay should be tested just like the pseudorange and carrier phase measurements themselves. The detectability of ionospheric disturbances is treated in section 7.6. For moderate ionospheric conditions at mid-latitude (Delft, the Netherlands), an approximate range of $\sigma_{d\mathcal{I}}$-values is given in table 7.2, for measurements intervals of 1, 10 and 30 seconds with a cut-off elevation angle of 10 degrees (Teunissen and de Bakker, 2013).

For the stochastic model of the measurement precision of the multi-frequency GNSS signals we have used values reported by Simsky et al. (2008) and sections 6.1 and 6.2 (de Bakker et al., 2009, 2012) which are based on real measurements. The precision of the Galileo E1 signal reported by these publications are in close agreement, for the E5a signal the more conservative value of (Simsky et al., 2008) has been adopted. For the GPS L2 signal we will

	min. $\sigma_{d\mathcal{I}}$	max. $\sigma_{d\mathcal{I}}$
1 sec	1.5×10^{-3}	3.0×10^{-3}
10 sec	2.0×10^{-3}	1.0×10^{-2}
30 sec	4.5×10^{-3}	2.5×10^{-2}

Table 7.2: Approximate range of values for $\sigma_{d\mathcal{I}}$ (m) when sampling with intervals of 1, 10 and 30 seconds, respectively, using a 10 degree cut-off elevation angle. These values were obtained for a static receiver at mid-latitude (Delft) under moderate ionospheric conditions.

use the same value as for the GPS L1 signal. All zenith-referenced values are summarized in table 7.3. To obtain the standard deviations for an arbitrary elevation, these values still need to be multiplied with an elevation dependent function. Several authors studied this dependence, either as function of signal-to-noise (SNR) ratios (e.g., carrier-to-noise density ratio C/N_0) or as function of elevation itself, e.g., (Euler and Goad, 1991; Ward, 1996; Langley, 1997; Hartinger and Brunner, 1999; Collins and Langley, 1999; Wieser et al., 2005). Such weighting will also help suppressing the effect of multipath (de Bakker, 2011). For our purposes of studying and evaluating the MDBs, the differences between these functions are negligible. The simplest function, being the cosecant as function of elevation, has a value of about 4 at 15 degrees elevation and reaches its minimum of 1 at 90 degrees elevation.

	L1	L2	L5	E1	E5a	E5b	E5	E6
p (cm)	25	25	15	20	15	15	7	15
ϕ (mm)	1.0	1.3	1.3	1.0	1.3	1.3	1.3	1.2

Table 7.3: Zenith-referenced standard deviations of undifferenced GPS and Galileo code (p) and phase (ϕ) observables (sections 6.1 and 6.2; Simsky et al., 2008; de Bakker et al., 2009, 2012).

7.2.3 Redundancy

A prerequisite for being able to perform statistical tests is the existence of redundancy. For a full rank model, redundancy is defined as the number of observations minus the number of unknown parameters. We have summarized the redundancy of the k-epoch model eq. (7.7) in table 7.4.

We discriminate between the ionosphere-weighted case and the ionosphere-float case. Note that ionosphere-weighted here refers to constraining the ionosphere variations over time, this is related to but distinct from constraining the ionosphere variations over distance, i.e. over a baseline. In the ionosphere-float case, no a priori information is assumed about the ionospheric delays. Hence, in this case, all ionospheric delays are treated as completely unknown. This results therefore in a redundancy reduction of $k-1$, being the number of unknown time-differenced ionospheric delays.

We also discriminate between the phase *and* code case, and the code-only (phaseless) and phase-only (codeless) cases. When both phase and code data are used, the ionosphere-weighted redundancy equals $(k-1)(2n-1)$. Thus in this case, redundancy exists for any number of frequencies, provided $k \geq 2$. That at least two epochs of data are needed is of course due to the fact that we are working with time-differenced data. That already single-frequency ($n = 1$) processing provides redundancy is due to the ionospheric information. Without this information, there would be no redundancy in the single-frequency case, but only in the dual- and multi-frequency cases, provided both phase and code data are used.

The phase-only and code-only redundancies are the same. In the phase-only and code-only cases we have $(k-1)n$ observations fewer than in the phase and code case. Hence, this is the number by which the redundancy drops when either the code data or the phase data are left out. Thus in the phase-only or code-only cases, single-frequency testing is impossible even if ionospheric information is provided.

	Phase and Code	Phase-only	Code-only
I-weighted	$(k-1)(2n-1)$	$(k-1)(n-1)$	$(k-1)(n-1)$
I-float	$2(k-1)(n-1)$	$(k-1)(n-2)$	$(k-1)(n-2)$

Table 7.4: Redundancy for k-epoch, n-frequency, iono-weighted and iono-float, single-receiver geometry-free model eq. (7.7).

7.3 Testing and reliability

In this section we formulate our alternative hypotheses and present the corresponding test statistics.

7.3.1 Outliers, cycle slips and loss-of-lock

We now formulate our alternative hypotheses for the single-receiver, geometry-free GNSS model. They accommodate model biases such as outliers in the pseudo range data, slips in the carrier phase data and loss-of-lock.

Recall that the undifferenced observational vector of epoch t is given as $y(t) = (\phi(t)^*, p(t)^*, \mathcal{I}(t))^*$. Now assume that a model error has occurred in the data of epoch l and that this $(2n+1)$-bias vector can be parametrized as Hb, where H is a given matrix of order $(2n+1) \times q$ and b is an unknown vector having q entries. Then Hb is the difference between the expectation of $y(l)$ under the null hypothesis $\mathcal{H}_0$ and the expectation of $y(l)$ under the alternative hypothesis $\mathcal{H}_a$. Thus $E\{y(l)|\mathcal{H}_a\} = E\{y(l)|\mathcal{H}_0\} + Hb$. Through the choice of matrix H, we can describe the type of model error. For instance, if all the phase data are assumed erroneous, as would be the case after a temporary loss-of-lock on all phase observables, then $H = (I_n, 0, 0)^*$ and $q = n$. But if only the pseudo range data on frequency j is corrupted with an outlier, then $H = (0, \delta_j^*, 0)^*$ and $q = 1$, where δ_j is an n-vector having a 1 as its jth entry and zeros elsewhere.

Apart from describing the model error through matrix H, we also need to specify the time behavior of the model error. Here we consider *spikes* and *slips*. A model error behaves as a spike if it occurs at one and only one epoch. A model error is said to behave as a slip if it persists after occurrence. Examples of spikes are outliers in the pseudo range data or in the ionospheric delays. Examples of slips are cycle slips in the phase data or momentary loss-of-lock (see insert for causes of cycle slips).

Causes of cycle slips are given by Hofmann-Wellenhof et al. (1997) as:

1. Obstruction of the satellite signal. When the satellite signals are obstructed and a receiver (temporarily) loses lock, all integer ambiguities are reset causing a cycle slip on all frequencies. If the occurrence of this event is registered by the receiver the loss-of-lock indicator is set and, when the interruption is longer then the measurement interval, is accompanied by missing data.

2. Failure of the receiver tracking loop. When a receiver fails to track a carrier wave correctly this can lead to a cycle slip. A receiver tracks each carrier wave on a separate channel. Therefore, the occurrence of cycle slips on different frequencies can be considered as independent events. Given the relatively small probability of a cycle slip occurring at a certain epoch under normal conditions, the probability of multiple cycle slips occurring simultaneously is quite small.

3. Low carrier-to-noise density ratio (C/N_0). When a receiver is tracking a satellite with a low C/N_0, e.g. a satellite with low elevation, the receiver may not be able to track the carrier waves correctly, which can lead to a lot of cycle slips. The probability of cycle slips occurring on multiple frequencies simultaneously also increases.

If we assume the model error Hb to behave as a spike at epoch l, then $E\{y|\mathcal{H}_a\} = E\{y|\mathcal{H}_0\} + (s_l \otimes H)b$, where s_l is a k-vector having a 1 as its lth entry and zeros elsewhere. Would we assume the error to be persistent, however, as would be the case after a loss-of-lock or after a slip, then s_l is a k-vector having zeros in its first $l-1$ entries, but 1s in all its remaining entries.

Thus with suitable choices for the vector s_l and the matrix H, one can model outliers in the code data, cycle slips in the phase data, disturbances in the ionosphere and even a complete loss-of-lock. The formulation of the alternative hypotheses in terms of the time-differenced data follows then from pre-multiplying $E\{y|\mathcal{H}_a\} = E\{y|\mathcal{H}_0\} + (s_l \otimes H)b$ with $D_k^* \otimes I_{2n+1}$. The null- and alternative hypotheses treated in this chapter are therefore given as

$$\begin{aligned} \mathcal{H}_0 :\ & E\{dy\} = (I_{k-1} \otimes G)dg \\ \mathcal{H}_a :\ & E\{dy\} = (I_{k-1} \otimes G)dg + (D_k^* s_l \otimes H)b \end{aligned} \tag{7.10}$$

where

$$\underset{(2n+1)\times q}{H} = \begin{cases} (\delta_j^*, 0, 0)^* & \text{(single carrier phase)} \\ (0, \delta_j^*, 0)^* & \text{(single pseudorange)} \\ (0, 0, 1)^* & \text{(ionosphere disturbance)} \\ (I_n, 0, 0)^* & \text{(phase loss-of-lock on all frequencies)} \end{cases} \tag{7.11}$$

and

$$\underset{k\times 1}{s_l} = \begin{cases} (\overset{1}{0}, \ldots, 0, \overset{l}{1}, 0, \ldots, \overset{k}{0})^* & \text{(spike)} \\ (0, \ldots, 0, 1, 1, \ldots, 1)^* & \text{(slip)} \end{cases} \tag{7.12}$$

In order to test $\mathcal{H}_0$ against $\mathcal{H}_a$, the *Uniformly Most Powerful Invariant* (UMPI) test is used, see e.g., (Arnold, 1981; Koch, 1999; Teunissen, 2000b). It rejects the null hypothesis in favor of the alternative hypothesis, if

$$T_q = \hat{b}^* Q_{\hat{b}\hat{b}}^{-1} \hat{b} > \chi^2_\alpha(q, 0) \tag{7.13}$$

where $\hat{b}$, with variance matrix $Q_{\hat{b}\hat{b}}$, is the Least-Squares Estimator (LSE) of b under $\mathcal{H}_a$. The UMPI-test statistic T_q has a central χ^2-distribution under $\mathcal{H}_0$ with q degrees of freedom, $T_q \overset{\mathcal{H}_0}{\sim} \chi^2(q, 0)$. Hence, with α being the probability of wrongful rejection, the critical value $\chi^2_\alpha(q, 0)$ of eq. (7.13) is computed from the relation $\alpha = \mathsf{P}[T_q > \chi^2_\alpha(q, 0)|\mathcal{H}_0]$.

7.3.2 Test statistics for spikes and slips

In order to derive the appropriate test statistics, we first determine the least-squares estimator of b in eq. (7.10). Here and in the following we assume $D\{d\mathcal{I}\} = \sigma^2_{\mathcal{I}} D_k^* D_k$ and therefore $D\{y(i)\} =$ blockdiag$(Q_\phi, Q_p, \sigma^2_{\mathcal{I}}) \overset{call}{=} Q$. The least-squares estimator of b and its variance matrix is given in the following theorem.

Theorem 1 (UMPI test statistic) With the dispersion given as $D\{dy\} = D_k^* D_k \otimes Q$, $Q =$ blockdiag$(Q_\phi, Q_p, \sigma^2_{\mathcal{I}})$, the least-squares estimator of b under $\mathcal{H}_a$ (cf. eq. (7.10)) and its variance matrix are given as

$$\begin{array}{rcl} \hat{b}(l,k) & = & (\bar{s}_l^* \bar{s}_l \otimes \bar{H}^* Q^{-1} \bar{H})^{-1} (\bar{s}_l^* \otimes \bar{H}^* Q^{-1}) y \\ Q_{\hat{b}\hat{b}}(l,k) & = & (\bar{s}_l^* \bar{s}_l)^{-1} \otimes (\bar{H}^* Q^{-1} \bar{H})^{-1} \end{array} \tag{7.14}$$

and the uniformly most powerful invariant test statistic for testing $\mathcal{H}_0$ against $\mathcal{H}_a$ is given as

$$T_q(l,k) = \hat{b}(l,k)^* Q_{\hat{b}\hat{b}}(l,k)^{-1} \hat{b}(l,k) = y^* \left(P_{\bar{s}_l} \otimes Q^{-1} P_{\bar{H}} \right) y \tag{7.15}$$

where $\bar{s}_l = P_{D_k} s_l$ and $\bar{H} = P_G^\perp H$, with the projectors $P_{D_k} = D_k (D_k^* D_k)^{-1} D_k^*$, $P_G^\perp = I_{2n+1} - G(G^* Q^{-1} G)^{-1} G^* Q^{-1}$, $P_{\bar{s}_l} = \bar{s}_l (\bar{s}_l^* \bar{s}_l)^{-1} \bar{s}_l^*$ and $P_{\bar{H}} = \bar{H}(\bar{H}^* Q^{-1} \bar{H})^{-1} \bar{H}^* Q^{-1}$.

Proof: See appendix C.

The bias estimator and its variance matrix are given the arguments l and k (with $l \leq k$) to emphasize that it is an estimator of an error occurring at epoch l, based on k epochs of data.

From the Kronecker product structure of eq. (7.14) it follows that $\hat{b}(l,k)$ and its variance matrix can be computed directly from its single-epoch counterparts. We therefore have the following result.

Corollary 1 Let the single-epoch bias estimator and its variance matrix be given as

$$\begin{array}{rcl} \hat{\beta}(i) & = & (\bar{H}^* Q^{-1} \bar{H})^{-1} \bar{H}^* Q^{-1} y(i) \\ Q_{\hat{\beta}\hat{\beta}} & = & (\bar{H}^* Q^{-1} \bar{H})^{-1} \end{array} \tag{7.16}$$

and define the $(2n+1) \times k$ matrix $\hat{B}_k = [\hat{\beta}(1), \ldots, \hat{\beta}(k)]$. Then

$$\begin{aligned} \hat{b}(l,k) &= \hat{B}_k \bar{s}_l (\bar{s}_l^* \bar{s}_l)^{-1} \\ Q_{\hat{b}\hat{b}}(l,k) &= (\bar{s}_l^* \bar{s}_l)^{-1} Q_{\hat{\beta}\hat{\beta}} \end{aligned} \tag{7.17}$$

and

$$T_q(l,k) = \frac{\bar{s}_l^* \hat{B}_k^* Q_{\hat{\beta}\hat{\beta}}^{-1} \hat{B}_k \bar{s}_l}{\bar{s}_l^* \bar{s}_l} \tag{7.18}$$

Note that the time dependency in the coefficients of eq. (7.18) is captured by $\bar{s}_l$, which will be different for spikes and slips.

Spikes For spike-like biases the k-vector s_l is a unit vector having a 1 as its lth entry. If we make use of $P_{D_k} = I_k - e_k(e_k^* e_k)^{-1} e_k^*$, it follows that $\bar{s}_l = \delta_l - \frac{1}{k} e_k$ and $\bar{s}_l^* \bar{s}_l = 1 - \frac{1}{k}$. For spikes, the bias expression eq. (7.17) therefore simplifies to

$$\begin{aligned} \hat{b}(l,k) &= \frac{k}{k-1} \left(\hat{\beta}(l) - \frac{1}{k} \sum_{i=1}^{k} \hat{\beta}(i) \right) \\ &= \hat{\beta}(l) - \frac{1}{k-1} \sum_{i=1, i \neq l}^{k} \hat{\beta}(i) \end{aligned} \tag{7.19}$$

This last expression clearly shows that $\hat{b}(l,k)$ is the difference of the local estimator $\hat{\beta}(l)$ and the time-average of the $\hat{\beta}(i)$ over the error-free time instances $i = 1, \ldots, k; i \neq l$. Under $\mathcal{H}_a$ the mean of the local estimator is b and that of the time-average is zero. Although one can use the local estimator $\hat{\beta}(l)$ as the bias-estimator, the local estimator does not make use of the information that all other epochs are assumed to be bias-free. Hence, the local estimator can be improved by including this information through subtraction of the zero-mean time-average of the bias-free time instances.

For computational purposes it is easier to use the first expression of eq. (7.19), because of the presence of the running average (which can also be computed recursively). We therefore use this expression to formulate the corresponding test statistic for spikes. It reads

$$T_q(l,k) = \frac{k}{k-1} ||\hat{\beta}(l) - \bar{\beta}(k)||^2_{Q^{-1}_{\hat{\beta}\hat{\beta}}} \tag{7.20}$$

with the running average $\bar{\beta}(k) = \frac{1}{k} \sum_{i=1}^{k} \hat{\beta}(i)$.

The test statistic of eq. (7.20) can be used for any $l \leq k$. However, when $l < k$, there is a delay in testing of $k - l$. For some applications this may not be acceptable or necessary. For those cases one will use eq. (7.20) with $l = k$, which gives

$$T_q(k,k) = \frac{k-1}{k} ||\hat{\beta}(k) - \bar{\beta}(k-1)||^2_{Q^{-1}_{\hat{\beta}\hat{\beta}}} \tag{7.21}$$

Thus in this case, the test statistic is formed from the difference of the local bias estimator $\hat{\beta}(i)$ for $i = k$ and its time-average over the previous $k - 1$ epochs, $\bar{\beta}(k-1)$.

Slips For slip-like biases the k-vector s_l is a vector having 1s as its last $k-l+1$ entries and zeros elsewhere. If we make use of $P_{D_k} = I_k - e_k(e_k^* e_k)^{-1} e_k^*$, it follows that $\bar{s}_l = s_l - \frac{k-l+1}{k} e_k$ and $\bar{s}_l^* \bar{s}_l = \frac{(k-l+1)(l-1)}{k}$. We therefore have

$$\begin{aligned} \hat{b}(l,k) &= \frac{k}{k-l+1}\left(\frac{1}{k}\sum_{i=1}^{k}\hat{\beta}(i) - \frac{1}{l-1}\sum_{i=1}^{l-1}\hat{\beta}(i)\right) \\ &= \frac{1}{k-l+1}\sum_{i=l}^{k}\hat{\beta}(i) - \frac{1}{l-1}\sum_{i=1}^{l-1}\hat{\beta}(i) \end{aligned} \tag{7.22}$$

This last expression clearly shows that in case of a slip, $\hat{b}(l,k)$ is the difference of two time-averages of the $\hat{\beta}(i)$. The first time-average averages over all epochs that supposedly contains the bias, while the second is the time-average over all bias-free epochs. Under $\mathcal{H}_a$, the mean of the first time-average is b, while that of the second time-average is zero.

Note that eq. (7.22) reduces to eq. (7.19) when $l = k$. This shows that one can not discriminate between spikes and slips on the basis of one single epoch. That is, one needs to have a delay ($k > l$) to be able to separate spikes from slips.

For computational purposes it is easier to use the first expression of eq. (7.22), because of the presence of the running averages. We therefore use this expression to formulate the corresponding test statistic for slips. It reads

$$T_q(l,k) = \frac{k(l-1)}{k-l+1}||\bar{\beta}(k) - \bar{\beta}(l-1)||^2_{Q^{-1}_{\hat{\beta}\hat{\beta}}} \tag{7.23}$$

It is thus formed from the difference of two time-averages of the $\hat{\beta}(i)$, namely the time-average over the epochs up to and including the time of testing k and the time-average over the epochs up to time l at which the slip is assumed to have started. For $l = k$ this test statistic becomes identical to eq. (7.21).

7.3.3 Minimal Detectable Biases

Under the alternative hypothesis $\mathcal{H}_a$, the test statistic T_q is distributed as a noncentral χ^2-distribution with q degrees of freedom, $T_q \overset{\mathcal{H}_a}{\sim} \chi^2(q, \lambda_0)$, where $\lambda_0 = b^* Q_{\hat{b}\hat{b}}(l,k)^{-1} b$ is the *noncentrality parameter*. The test of eq. (7.13) is an UMPI-test, meaning that for all b, it maximizes the power within the class of invariant tests. Here power, denoted as ψ, is defined as the probability of correctly rejecting $\mathcal{H}_0$, thus $\psi = \mathsf{P}[T_q > \chi^2_\alpha(q,0)|\mathcal{H}_a]$.

The power of test eq. (7.13) depends on the degrees of freedom q (i.e., the dimension of b), the level of significance α, and through the noncentrality parameter λ_0, on the bias vector b. Once q, α and b are given, the power can be computed. One can however also follow the inverse route. That is, given the power ψ, the level of significance α and the dimension q, the noncentrality parameter can be computed, symbolically denoted as $\lambda_0 = \lambda(\alpha, q, \psi)$. Figure 7.1 shows the relation between λ_0 and ψ for different values of q and α. With λ_0 given, one can formulate the following *quadratic* equation in b,

$$b^* Q_{\hat{b}\hat{b}}(l,k)^{-1} b = \lambda_0 \tag{7.24}$$

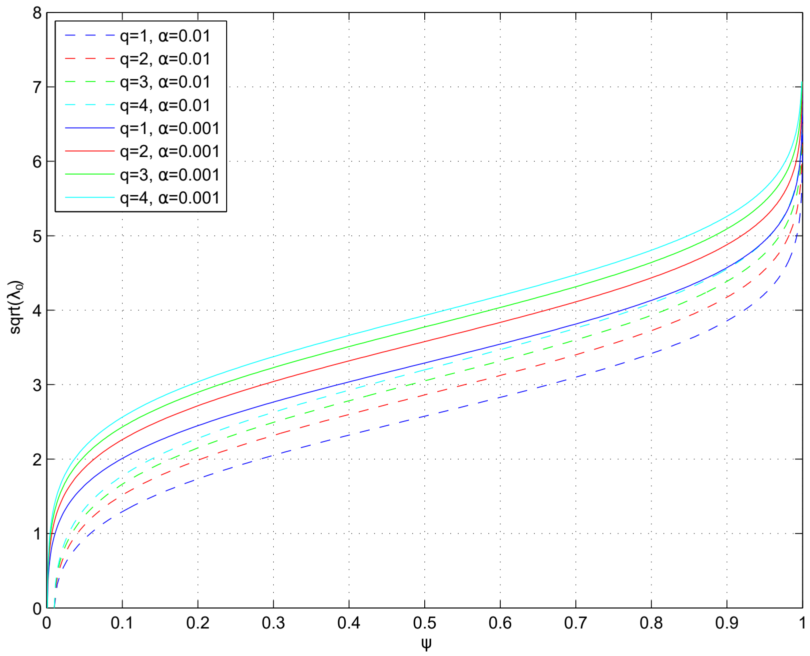

Figure 7.1: Square-root of noncentrality parameter λ_0 as function of power ψ for different degrees of freedom q and different levels of significance α.

This equation is said to describe, for the test of eq. (7.13), the *reliability* of the null hypothesis $\mathcal{H}_0$ with respect to the alternative hypothesis $\mathcal{H}_a$. For $q = 1$, eq. (7.24) describes an interval, for $q = 2$ it describes an ellipse and for $q > 2$ it describes an (hyper)ellipsoid. Bias vectors $b \in R^q$ that lie on or outside the ellipsoid of eq. (7.24) can be found with at least probability ψ.

To determine the bias vectors that satisfy eq. (7.24), we use the factorization $b = ||b||d$, where d is a unit vector $(d^*d = 1)$. Substitution into eq. (7.24) and inversion gives

$$\text{MDB}(l,k) = \sqrt{\left(\frac{\lambda_0}{d^* Q_{\hat{b}\hat{b}}(l,k)^{-1} d}\right)} d \qquad (d = \text{ unit vector}) \tag{7.25}$$

This is the celebrated *Minimal Detectable Bias* (MDB) vector of Baarda's reliability theory (Baarda, 1967, 1968). Its length is the smallest size of bias vector that can be found with probability ψ in the direction d with test eq. (7.13). By letting d vary over the unit sphere in R^q one obtains the whole range of MDBs that can be detected with probability ψ with test eq. (7.13). For the one-dimensional case $(q = 1)$, we have $d = \pm 1$ and therefore $\text{MDB}(l,k) = \sigma_{\hat{b}}(l,k)\sqrt{\lambda_0}$.

Baarda, in his work on the strength analysis of general purpose networks, applied his general MDB-form to data snooping thus obtaining the scalar boundary values (in Dutch: 'grenswaarden'). Applications of the vectorial form can be found, for example, in (Mierlo, 1980, 1981; Kok, 1982b) for deformation analysis, in (Förstner, 1983) for photogrammetric linear trend testing and in (Teunissen, 1986) for testing digitized maps. For recursive testing, with application of testing time and types of error, the first innovation-based vectorial MDB was given in (Teunissen, 1990a). Application of the generalized eigenvalue problem to the vectorial form to obtain MDB-bounds can be found in e.g. (Teunissen, 2000b; Knight et al., 2010).

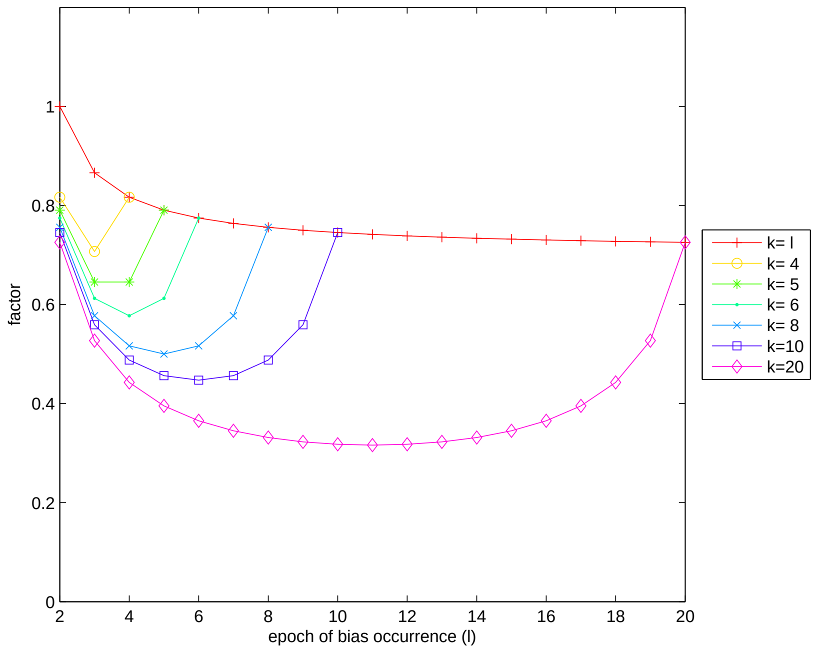

Figure 7.2: The function $f(l,k) = \sqrt{\frac{1}{2}\left(\frac{1}{k-l+1} + \frac{1}{l-1}\right)}$ for variable $k = l$ and for variable $l \leq k$, with k fixed ($k = 4, 5, 6, 8, 10, 20$).

Above it was assumed that the variance matrix $Q_{\hat{b}\hat{b}}$ in the test statistic T_q is known, cf. eq. (7.13). In case, however, the variance factor σ^2 in $Q_{\hat{b}\hat{b}} = \sigma^2 G_{\hat{b}\hat{b}}$ is unknown, then the Chi-square distributed test statistic needs to be replaced by the F-distributed test statistic $T'_{q,df} = \hat{b}^* G^{-1}_{\hat{b}\hat{b}} \hat{b}/(\hat{\sigma}^2 q)$, in which $\hat{\sigma}^2$ is the unbiased estimator of the variance factor under the alternative hypothesis and df is its degrees of freedom. This test statistic is distributed under $\mathcal{H}_a$ as $T'_{q,df} \sim F(q, df, \lambda_0)$, with the same noncentrality parameter as that of T_q (Kok, 1982a; Koch, 1999). Therefore also in case σ^2 is estimated, will the same MDB expression be found as given in eq. (7.25). Hence, similarly as with the other statistical parameters, the effect on the MDB, for the two cases σ^2 known versus σ^2 estimated, is only felt through the scaling factor λ_0. In this chapter we work with λ_0 computed from the Chi-square distribution.

If we substitute eq. (7.17) into eq. (7.25), the MDBs for spikes and slips work out as

$$\text{MDB}(l,k) = f(l,k)\ \text{MDB}(2,2) \tag{7.26}$$

with

$$\text{MDB}(2,2) = \sqrt{\left(\frac{2\lambda_0}{d^* Q^{-1}_{\hat{\beta}\hat{\beta}} d}\right)} d \tag{7.27}$$

and

$$f(l,k) = \sqrt{\frac{1}{2}\left(\frac{1}{k-l+1} + \frac{1}{l-1}\right)} \begin{cases} \text{for spikes} & l = k \\ \text{for slips} & l \leq k \end{cases} \tag{7.28}$$

The MDBs get smaller if more epochs of data are used (k gets larger) and/or a more precise bias-estimator $\hat{\beta}$ is used ($Q_{\hat{\beta}\hat{\beta}}$ gets 'smaller'). Note that the spike-MDB depends on k, whereas the slip-MDB depends on both l and k. Hence, the detectability of spikes does not depend on the time instance of their occurrence, whereas the detectability of slips does depend on these time instances; both depend on the amount of data. For k fixed, the slip-MDB reaches its minimum at $\lfloor k/2 \rfloor + 1$. Hence, for a given observational time span, slips are best detectable if they occur 'half way' in the time span. The graph of the function $f(l,k)$ is given in fig. 7.2. It shows by how much the MDB$(2,2)$ improves when l and k are larger than 2.

In the following, we present the MDBs for the two-epoch case ($k = 2, l = 2$). The corresponding MDB-values for arbitrary epochs can then be obtained by using the multiplication factor $f(l,k)$ of eq. (7.26).

7.4 Detectability of carrier phase slips

In this section we present and analyze the phase-slip MDBs. This is done for the single-, dual- and multi-frequency case. We also analyze the phase-slip MDBs in case code data are absent.

7.4.1 Minimal detectable carrier phase slips

In the following, MDB values have been computed numerically using the complete set of code and phase variances according to table 7.3, and analytical MDB expressions have been derived for which the phase and code variance matrices have been simplified to scaled unit-matrices, i.e., $Q_{\phi\phi} = \sigma_\phi^2 I_n$ and $Q_{pp} = \sigma_p^2 I_n$. For the standard deviation of the scaled unit-matrices we have used the mean value of the standard deviations of the available signals (except when explicitly stated otherwise). The MDB values from both the numerical computations and the analytical expressions are presented graphically in figs. 7.3 to 7.6 and 7.8 to 7.13 (the dashed curves correspond to the analytical expressions, while the full curves correspond to the MDBs computed from the actual variance matrices). The differences between the two are shown to be small, especially when the used signals have comparable precision, which indicates that the analytical expressions indeed give a proper representation of the single-receiver, single-channel detectability. In some cases the analytical approximations are so close to the numerical solution, that the curves lie on top of each other. For all MDBs which pertain to an error on a single frequency, we have chosen to compute the MDB for an error on the first frequency of the available frequencies. For GPS this is the L1 frequency and for Galileo the E1 frequency when available.

The analytical expression for the multi-frequency phase-slip MDB is given in the following theorem.

Theorem 2 (Phase-slip MDB): Let $H = (\delta_j^*, 0, 0)^*$, $Q_{\phi\phi} = \sigma_\phi^2 I_n$ and $Q_{pp} = \sigma_p^2 I_n$. Then for $k = 2$, the MDB for a slip in the jth frequency carrier phase observable is given as

$$\text{MDB}_{\phi_j} = \sigma_\phi \sqrt{\left(\frac{2\lambda_0}{1 - \frac{1}{n'}} \right)} \tag{7.29}$$

with scalar

$$\frac{1}{n'} = \frac{1}{n}\frac{1}{1+\epsilon}\left(1 + \frac{(\gamma_j - \frac{1-\epsilon}{1+\epsilon}\bar{\gamma})^2}{\frac{1}{n}\sum_{i=1}^n \gamma_i^2 - \left(\frac{1-\epsilon}{1+\epsilon}\right)^2 \bar{\gamma}^2 + \frac{2\sigma_\phi^2/\sigma_{d\mathcal{I}}^2}{n(1+\epsilon)}}\right) \tag{7.30}$$

where $\epsilon = \sigma_\phi^2/\sigma_p^2$ is the phase-code variance ratio and $\bar{\gamma} = \frac{1}{n}\sum_{i=1}^n \gamma_i$ is the average of the squared frequency ratios $\gamma_i = f_1^2/f_i^2$, $i = 1, \ldots, n$.

Proof see appendix C.

Note that the slip MDB is scaled with σ_ϕ, the small standard deviation of the carrier phase observable. Thus if the bracketed ratio of eq. (7.29) is not too large, small carrier phase slips will be detectable. The bracketed term depends on λ_0 and on n'. The scalar n' is dependent on ϵ, γ_i $(i = 1, \ldots, n)$ and $\sigma_\phi^2/\sigma_{d\mathcal{I}}^2$. Hence, it depends on the measurement precision, on the number of frequencies and their spacings, and on the smoothness of the ionosphere. The MDB gets smaller if ϵ gets larger, i.e., if more precise code data are used. The MDB also gets smaller if n gets larger, i.e., if more frequencies are used. Finally note that the MDB-dependence on the frequency diversity (i.e., on $\gamma_i, i = 1, \ldots, n$) is driven to a large part by the smoothness of the ionosphere. This dependence is absent for $\sigma_{d\mathcal{I}} = 0$ and it gets more pronounced the larger $\sigma_{d\mathcal{I}}$ gets.

We now analyze the slip MDB for the GPS and Galileo single-, dual- and triple-frequency cases.

7.4.1.1 Single-frequency case

For the single-frequency case $(n = 1)$, the carrier phase slip MDB eq. (7.29) can be worked out to give

$$\text{MDB}_{\phi_j} = \sigma_p \sqrt{2\left(1 + \frac{\sigma_\phi^2}{\sigma_p^2} + 2\gamma_j^2 \frac{\sigma_{d\mathcal{I}}^2}{\sigma_p^2}\right)\lambda_0} \tag{7.31}$$

This result shows that single-frequency phase slip detection is possible in principle, but that its performance depends very much on the smoothness of the ionosphere and on the measurement precision of code. If $\sigma_{d\mathcal{I}}^2 = \infty$, then $\text{MDB}_{\phi_j} = \infty$, meaning that single-frequency slip detection has become impossible. If the ionospheric delay is so smooth that the ratio $\sigma_{d\mathcal{I}}^2/\sigma_p^2$ may be neglected, we get with $\epsilon \approx 0$, $\text{MDB}_{\phi_1} = \sigma_p\sqrt{2\lambda_0}$. Hence, for a sufficiently smooth ionospheric delay, we may detect slips of about six times the code standard deviation (here and in the following the reference value of the noncentrality parameter is taken as $\lambda_0 = 17.02$; it corresponds to $q = 1$, $\alpha = 0.001$ and $\psi = 0.80$, see fig. 7.1.

The numerical values of the GPS and Galileo single-frequency phase-slip MDBs are graphically displayed in fig. 7.3 as function of $\sigma_{d\mathcal{I}}$. It shows that the MDBs are approximately constant for $\sigma_{d\mathcal{I}} \leq 10^{-2}$ m, but then rapidly increase for larger values of $\sigma_{d\mathcal{I}}$. The constant values are about 146 cm for L1 and L2, 117 cm for E1, 88 cm for L5, E5a, E5b and E6 and 41 cm for E5. These three levels reflect the difference in the code measurement precision of the signals. Since these single-frequency MDBs are all larger than their corresponding

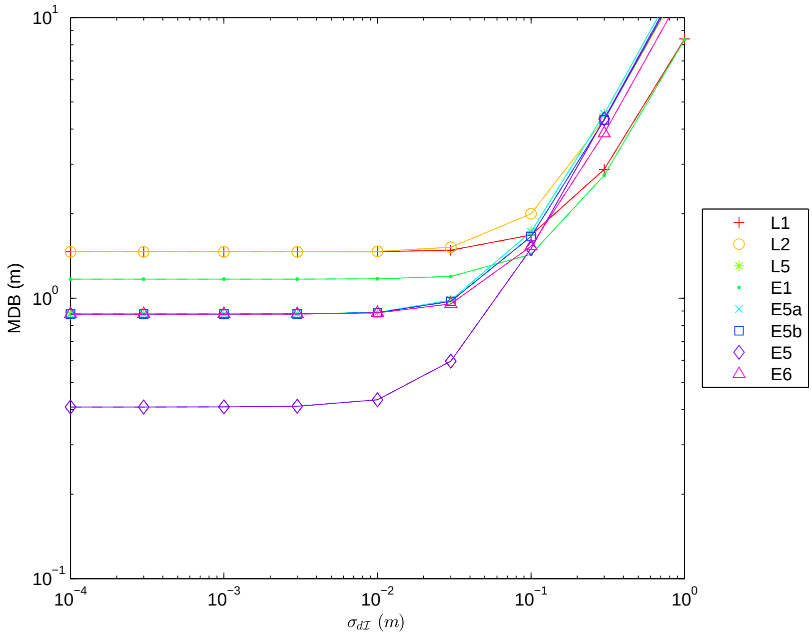

Figure 7.3: Single-frequency GPS and Galileo phase-slip MDBs for $k = 2$; dashed curves are based on eq. (7.31).

wavelengths, time-windowing ($N = k - l + 1 > 1$ c.f. eq. (7.26)) will be needed to bring the MDBs down to smaller values. Accepting a delay in testing is then the price one has to pay for the increase in detectability.

7.4.1.2 Dual and multi-frequency case

It follows from eq. (7.29) that the dual- and multi-frequency phase-slip MDB is bounded from below as

$$\text{MDB}_{\phi_j} \geq \sigma_\phi \sqrt{2\left(\frac{n(1+\epsilon)}{n(1+\epsilon)-1}\right)\lambda_0} \tag{7.32}$$

This lower bound is obtained for $\sigma_{d\mathcal{I}} = 0$. Very small slips on a single frequency can be detected (in order of a few cm), if the ionospheric delays are sufficiently smooth ($\sigma_{d\mathcal{I}} \leq 10^{-2}$ m), even for the two-epoch case. This is confirmed by the S-shaped MDB graphs of fig. 7.4. Note that the case of simultaneous slips on multiple frequencies are treated later. In the case of a slip on a single frequency with smooth ionosphere delays, there is also no significant difference between the dual-frequency and multi-frequency performance. This difference is present though, for larger values of $\sigma_{d\mathcal{I}}$. In particular the dual-frequency GPS phase-slip MDBs, and the Galileo E1 E5a, increase steeply when $\sigma_{d\mathcal{I}} \geq 10^{-2}$ m gets larger. For the multi-frequency phase-slip MDBs the increase is much more moderate. All the multi-frequency phase-slip MDBs remain less than 7 cm, whereas the dual-frequency MDBs are all smaller than 22 cm. Those of Galileo are smaller than their GPS counterparts, due to their improved code precision, except that L1-L2-L5 outperforms E1-E5a-E5b due to a better distribution of the frequencies. We can also see that the analytical expression is further removed from the numerical results for the E1-E5 combination, which is a result of

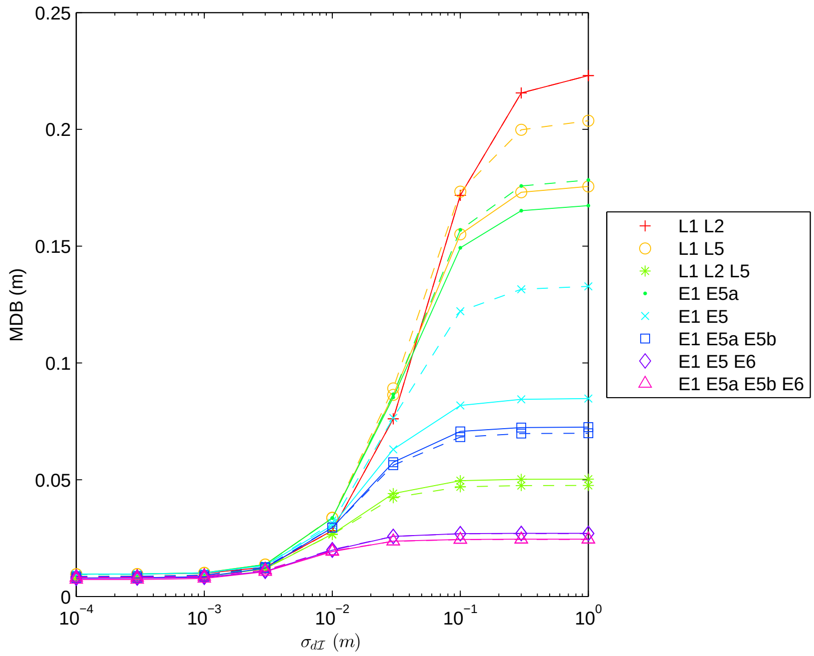

Figure 7.4: Dual- and multi-frequency GPS and Galileo phase-slip MDBs on L1/E1 for k=2; dashed curves are based on eqs. (7.29) and (7.30).

the large difference in precision between these two signals. The scaled unit matrix used for the code variance approximates the actual variance matrix less well.

7.4.2 Cycle slip detection without code data

Since code data are generally much less precise than carrier phase data, one may wonder whether code data are really needed for carrier phase slip detection. This is also of interest for those applications where the code data are corrupted by multipath. In this section we therefore investigate what happens when $\sigma_p \to \infty$. The corresponding MDBs can be obtained from Theorem 1 by taking the limit $\lim_{\sigma_p \to \infty}$ MDB_{ϕ_j}. We have the following result.

Lemma 1 (Codeless phase-slip MDB): The codeless phase-slip MDB $\lim_{\sigma_p \to \infty}$ MDB_{ϕ_j} follows from eq. (7.29) using

$$\lim_{\sigma_p \to \infty} \left(1 - \frac{1}{n'}\right) = \left(1 - \frac{1}{n}\right) - \frac{(\gamma_j - \bar{\gamma})^2}{\sum_{i=1}^{n}(\gamma_i - \bar{\gamma})^2 + 2\sigma_\phi^2/\sigma_{d\mathcal{I}}^2} \tag{7.33}$$

or using the limit of the inverse

$$\lim_{\sigma_p \to \infty} \left(1 - \frac{1}{n'}\right)^{-1} = \left(1 - \frac{1}{n}\right)^{-1} + \frac{(\gamma_j - \bar{\gamma}_{(j)})^2}{\sum_{i \neq j}^{n}(\gamma_i - \bar{\gamma}_{(j)})^2 + 2\sigma_\phi^2/\sigma_{d\mathcal{I}}^2} \tag{7.34}$$

where $\bar{\gamma}_{(j)} = \frac{1}{n-1}\sum_{i \neq j}^{n} \gamma_i$ is the average of the squared frequency ratios that excludes γ_j.

Proof The expression of eq. (7.33) follows from taking the limit of eq. (7.30). The expression of eq. (7.34) follows from inverting eq. (7.33) and rearranging terms.

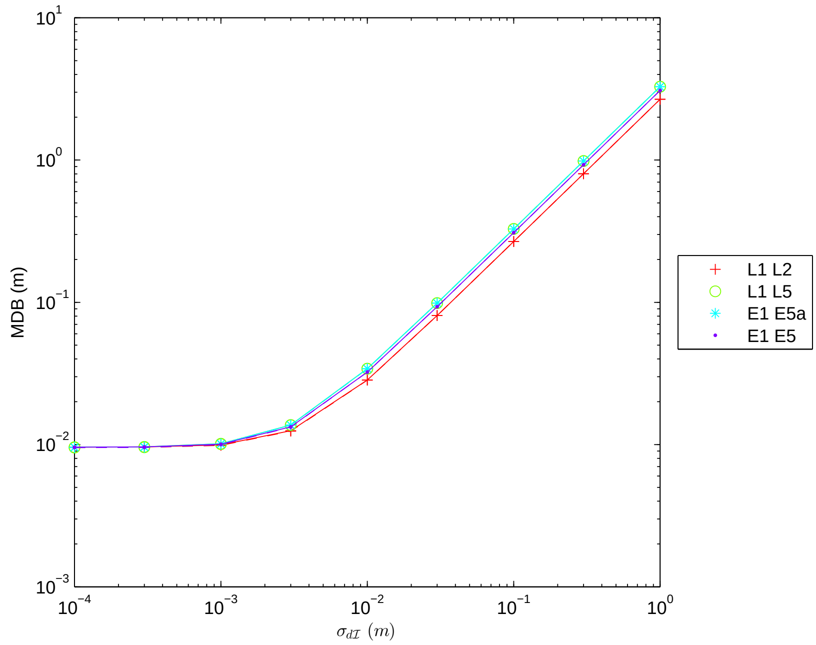

Figure 7.5: Dual-frequency GPS and Galileo phase slip MDB on L1/E1 without code data for $k = 2$; dashed curves are based on eq. (7.35).

The above two expressions clearly show that within a set of $n > 1$ MDBs, the smallest MDB$_{\phi_j}$ is the one for which γ_j is closest to the average $\bar{\gamma}$.

7.4.2.1 Single-frequency case

In the single-frequency case we have $n = 1$ and thus no frequency diversity, i.e., $\sum_{i=1}^{n}(\gamma_i - \bar{\gamma})^2 = 0$. This shows that $n' = 1$ for $n = 1$, c.f. eq. (7.33), and that therefore MDB$_{\phi_j} = \infty$. Hence, phase-slip detection without code data is impossible for the single-frequency case (see also the redundancy table 7.4).

7.4.2.2 Dual-frequency case

In the dual-frequency case $(n = 2)$ we have $(\gamma_j - \bar{\gamma})^2 = \frac{1}{2}(\sum_{i=1}^{n}(\gamma_i - \bar{\gamma})^2)$. Hence, $n' = 1$ c.f. eq. (7.33), if $n = 2$ and $\sigma_{d\mathcal{I}} = \infty$. In that case dual-frequency phase-slip detection without code data becomes impossible. In all other cases, however, we have

$$\lim_{\sigma_p \to \infty} \text{MDB}_{\phi_j} = \sigma_\phi \sqrt{\left(4 + (\gamma_1 - \gamma_2)^2 \frac{\sigma_{d\mathcal{I}}^2}{\sigma_\phi^2}\right) \lambda_0} \tag{7.35}$$

This shows that very small phase-slips can be detected when the ionospheric delays are sufficiently smooth. Figure 7.5 shows them to be less than 3 cm for $\sigma_{d\mathcal{I}} \leq 10^{-2}$ m. For larger values, the MDBs increase linearly, with the gradient driven by the frequency diversity; the closer the frequencies, the less steep the increase is.

When we compare fig. 7.5 with fig. 7.4, we note that the phase-slip MDB values are not too different for sufficiently small $\sigma_{d\mathcal{I}}$, but that their differences increase for larger $\sigma_{d\mathcal{I}}$. Thus the presence of the code data are particularly needed when the ionospheric delays are

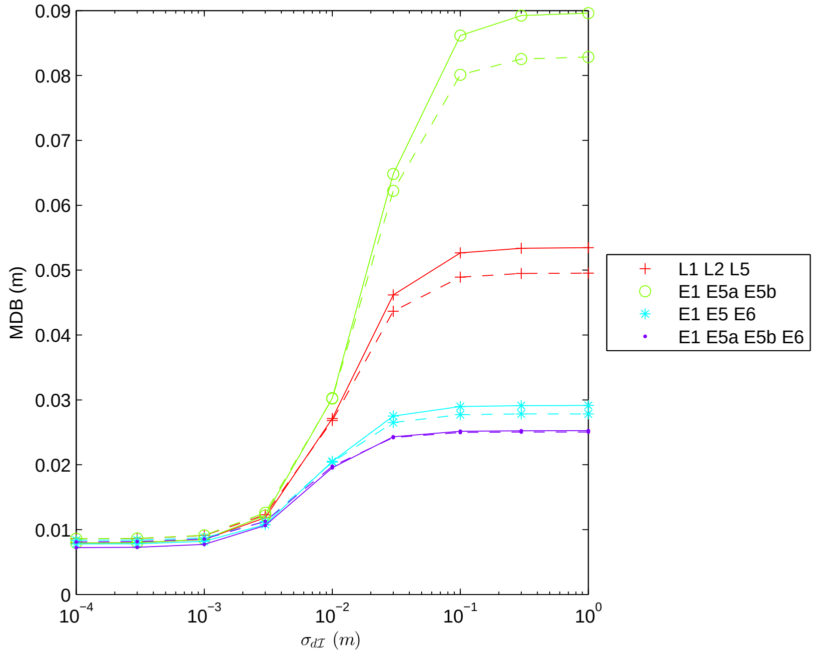

Figure 7.6: Multi-frequency GPS and Galileo phase slip MDB on L1/E1 without code data for $k = 2$; dashed curves are based on eq. (7.36).

not smooth enough. Codeless dual-frequency phase-data is sufficient to detect phase-slips otherwise.

7.4.2.3 Multi-frequency case

In the multi-frequency case the general form of the codeless phase-slip MDB follows from eqs. (7.29) and (7.34) as

$$\lim_{\sigma_p \to \infty} \text{MDB}_{\phi_j} = \sigma_\phi \sqrt{2 \left(\frac{n}{n-1} + \frac{(\gamma_j - \bar{\gamma}_{(j)})^2}{\sum_{i \neq j}^{n} (\gamma_i - \bar{\gamma}_{(j)})^2 + 2\sigma_\phi^2/\sigma_{d\mathcal{I}}^2} \right) \lambda_0} \tag{7.36}$$

To discuss its dependence on the ionospheric variance and on the frequency distribution, we start from the most optimal scenario. The MDB is smallest when $\sigma_{d\mathcal{I}}^2 = 0$, in which case the frequency dependence only includes the number of frequencies but not their diversity,

$$\lim_{\sigma_p \to \infty, \sigma_{d\mathcal{I}} \to 0} \text{MDB}_{\phi_j} = \sigma_\phi \sqrt{2 \left(\frac{n}{n-1} \right) \lambda_0} \tag{7.37}$$

For $\sigma_{d\mathcal{I}}^2 \neq 0$, the MDB is smallest if all frequencies are the same ($\gamma_i = 1, i = 1, \ldots, n$), i.e., if the vector $\gamma = (\gamma_1, \ldots, \gamma_n)^*$ is parallel to the vector $e_n = (1, \ldots, 1)^*$. One would then get the same MDB as eq. (7.37), i.e., the one that corresponds with $\sigma_{d\mathcal{I}}^2 = 0$. This can be explained as follows. If γ and e_n are parallel vectors, then the ionospheric delay $\mathcal{I}(i)$ gets lumped with $\rho'(i)$, c.f. eqs. (7.5) and (7.6), reducing the model in essence to an ionosphere-fixed one. Thus in the absence of code data, the absence of frequency diversity is best for phase-slip detection.

Now assume that not all components of vector γ are the same, but that instead all but one of them are the same. Thus $\gamma_i = \tilde{\gamma}, \forall i \neq j$. Then the codeless phase-slip MDB eq. (7.36) works out as

$$\lim_{\sigma_p \to \infty} \text{MDB}_{\phi_j} = \sigma_\phi \sqrt{2\left(\frac{n}{n-1} + (\gamma_j - \tilde{\gamma})^2 \frac{\sigma_{d\mathcal{I}}^2}{2\sigma_\phi^2}\right) \lambda_0} \tag{7.38}$$

This expression generalizes eq. (7.35) for $n > 2$. Its value goes to infinity for $\sigma_{d\mathcal{I}}^2 \to \infty$. In this case, it is the lack of frequency diversity in the $n-1$ phase data, $\phi_i, i \neq j$, that makes it impossible to solve for the ionospheric delay and therefore also for detecting a slip in the jth frequency phase observable.

For the triple-frequency case $(n = 3)$, the following bounds can be formulated,

$$\sigma_\phi \sqrt{3\lambda_0} \leq \lim_{\sigma_p \to \infty} \text{MDB}_{\phi_j} \leq \sigma_\phi \sqrt{2\left(1 + \frac{(\gamma_{j_1} - \gamma_{j_3})^2 + (\gamma_{j_1} - \gamma_{j_2})^2}{(\gamma_{j_2} - \gamma_{j_3})^2}\right) \lambda_0} \tag{7.39}$$

with the cyclic indices $(j_1, j_2, j_3) = (1,2,3), (2,3,1), (3,1,2)$ depending on whether $j = 1$, 2 or 3. The lower bound corresponds with $\sigma_{d\mathcal{I}}^2 = 0$, while the upper bound corresponds with $\sigma_{d\mathcal{I}}^2 = \infty$.

These bounds show that very small phase-slips can be detected, even when the code data are absent. This is confirmed by the graphs of fig. 7.6. All codeless phase-slip MDBs are less than 10 cm and even as small as about 1 cm when $\sigma_{d\mathcal{I}} \leq 3 \times 10^{-3}$ m. For larger values of $\sigma_{d\mathcal{I}}$ the differences in the triple-frequency MDBs become clearly visible. This is due to their frequency dependence.

When we compare the codeless results of fig. 7.6 with the triple- and quadruple-frequency results of fig. 7.4, no big differences can be seen. Hence, the impact of the code data on the phase-slip MDBs becomes less pronounced if more than two frequencies are used. The only noteworthy difference between the results of the two figures is the performance of E1-E5a-E5b. This difference in performance, compared to the other triple-frequency results, is due to the small frequency separation of E5a and E5b.

7.4.3 Carrier phase slips at other frequencies

So far only carrier phase slips on the first available frequency were considered. For a carrier phase slip on a different frequency the results are very similar. However, the actual values will depend on the carrier frequency combination and the carrier frequency on which the slip occurs. Figure 7.7 shows the MDB for a slip on one of the phase observables of dual frequency data as a function of the carrier frequencies. To highlight the impact of the frequencies on the MDB a simplified stochastic model was again used with code and phase variance matrices as scaled unit-matrices. For the standard deviation of the code observables we have used 15 cm and for the carrier phase observables we used 1 mm.

The solid lines show the MDB for a slip on the first carrier phase observable which is displayed in the legend. The horizontal axis shows the frequency of the second carrier phase observable. The line corresponding to the L2 phase observable shows that the MDB has a minimum value when the second phase observable has the same frequency. This would correspond to a receiver tracking two identical, but independent signals from the same satellite. The MDB increases with increasing distance between the two frequencies, which results in the largest MDBs in the figure for a carrier frequency combination including L1 and E5a. The dotted lines show the MDB for the same carrier frequency combinations, but now for a slip on the second phase observable. Careful inspection of the figure reveals that for a given frequency combination the MDB is largest for a slip on the lowest frequency (largest dispersion factor γ).

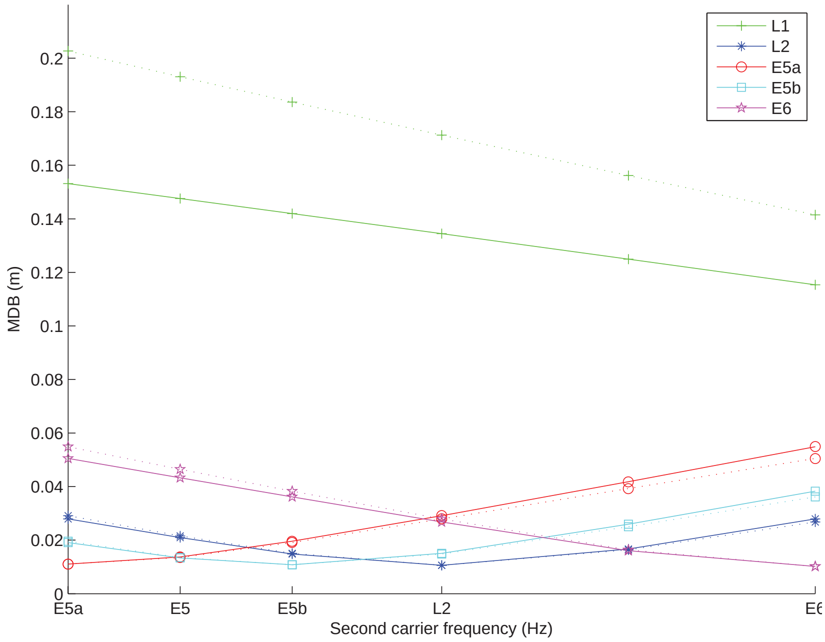

Figure 7.7: MDB for a slip on the first (solid) or second (dotted) phase observable of dual frequency data as a function of the carrier frequency of the second phase observable. The carrier frequency of the first phase observable is given in the legend.

7.5 Detectability of code outliers

In this section we present and analyze the code-outlier MDBs. This is done for the single-, dual- and multi-frequency case. We also analyze the code-outlier MDBs in case phase data is absent.

7.5.1 Minimal detectable code outliers

The analytical expression for the multi-frequency code-outlier MDB is given in the following theorem.

Theorem 3 (Code-outlier MDB): Let $H = (0, \delta_j^*, 0)^*$, $Q_{\phi\phi} = \sigma_\phi^2 I_n$ and $Q_{pp} = \sigma_p^2 I_n$. Then for $k = 2$, the MDB for an outlier in the jth frequency code observable is given as

$$\text{MDB}_{p_j} = \sigma_p \sqrt{\left(\frac{2\lambda_0}{1 - \frac{1}{m'}}\right)} \tag{7.40}$$

with

$$\frac{1}{m'} = \frac{1}{n}\frac{\epsilon}{1+\epsilon}\left(1 + \frac{(\gamma_j + \frac{1-\epsilon}{1+\epsilon}\bar{\gamma})^2}{\frac{1}{n}\sum_{i=1}^{n}\gamma_i^2 - \left(\frac{1-\epsilon}{1+\epsilon}\right)^2\bar{\gamma}^2 + \frac{\sigma_\phi^2/\sigma_{\mathcal{I}}^2}{n(1+\epsilon)}}\right) \tag{7.41}$$

where $\epsilon = \sigma_\phi^2/\sigma_p^2$ is the phase-code variance ratio and $\bar{\gamma} = \frac{1}{n}\sum_{i=1}^{n}\gamma_i$ is the average of the squared frequency ratios $\gamma_i = f_1^2/f_i^2$, $i = 1, \ldots, n$.

Proof As the phase observables and code observables play a dual role in the two-epoch model eq. (7.5), the code-outlier MDB can be found from the expression of the phase-slip MDB eq. (7.29) through an interchange of the phase and code variance.

Although eqs. (7.40) and (7.41) have the same structure as eqs. (7.29) and (7.30), respectively, there are marked differences between these expressions. First note that eq. (7.40) is scaled by the standard deviation of code and not by that of phase as in eq. (7.29). Second, the frequency-dependent term between brackets in eq. (7.41) is multiplied with the very small phase-code variance ratio ϵ, while this is not the case with the bracketed term of eq. (7.30). The consequences of these differences are that the dual- and multi-frequency code-outlier MDBs are generally larger than those of the phase-slip MDBs and that they are less sensitive to the number of frequencies and their spacing. The exception occurs in the single-frequency case.

7.5.1.1 Single-frequency case

In the single-frequency case, for $k = 2$, the code-outlier MDB is identical to that of the phase-slip MDB. This follows if we interchange the role of σ_p^2 and σ_ϕ^2 in eq. (7.31). For $k > 2$, however, the MDBs differ of course. In case of a slip the multiplication factor is $\frac{1}{\sqrt{2}}\sqrt{\frac{1}{k-l+1} + \frac{1}{l-1}}$, while for a code-outlier it is $\frac{1}{\sqrt{2}}\sqrt{1 + \frac{1}{k-1}}$.

7.5.1.2 Dual and multi-frequency case

We already remarked that in case of a sufficiently smooth ionosphere, the dual- and multi-frequency phase-slip MDBs become relatively insensitive to the number of frequencies and their spacings. This can be seen in fig. 7.4, but it also follows from the lower bound eq. (7.32). The reason for this insensitivity lies in the fact that the frequency-dependent bracketed term of eq. (7.30) reduces to 1 for $\sigma_{d\mathcal{I}} \to 0$. This effect is also present in the code-outlier MDB bracketed term of eq. (7.41). However, with eq. (7.41) there is the additional effect that the bracketed term is multiplied with the very small phase-code variance ratio. Hence, the MDB is now also less sensitive to the number of frequencies and their spacings for larger values of $\sigma_{d\mathcal{I}}$. This means that one can expect the lower bound

$$\text{MDB}_{p_j} \geq \sigma_p\sqrt{2\lambda_0} \tag{7.42}$$

to be a good approximation to the code-outlier MDB. After all, this lower bound follows from neglecting $\frac{1}{m'}$ in eq. (7.41). Thus, for $\alpha = 0.001$ and $\psi = 0.80$, giving $\lambda_0 = 17.02$, one can expect the code-outlier MDB to be about six times the code standard deviation.

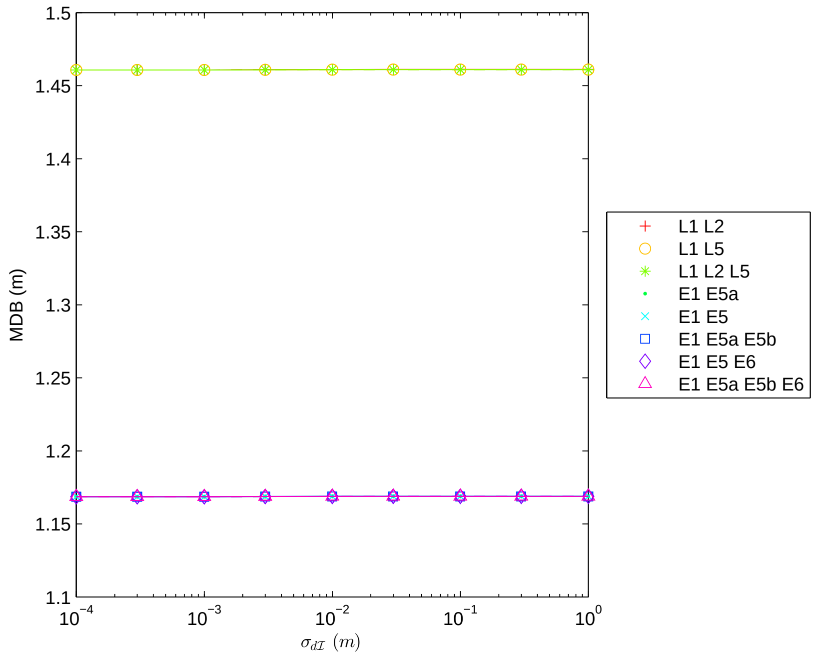

Figure 7.8: Dual- and multi-frequency GPS and Galileo code outlier MDBs on L1/E1 for $k = 2$; dashed curves are based on eq. (7.40) and eq. (7.41).

This is confirmed by the graphs of fig. 7.8. The figure shows that the code-outlier MDBs are not very sensitive to the available signals and frequencies. Additionally, the MDBs are nearly constant with the variance of the time-differenced ionospheric delay (no MDB variations are visible at the scale of this figure). Compare with phase-slip MDB fig. 7.4. The two levels shown in fig. 7.8 correspond with the different code measurement precision levels of the GPS L1 and Galileo E1 signals (cf. table 7.3). Figure 7.8 is the only figure for which we have directly used the standard deviation of the L1 and E1 signals in the analytical expressions (instead of the mean value of the available signals), since only the precision of these signals has any impact on the size of the MDBs.

7.5.2 Code outlier detection without phase data

The lower bound of eq. (7.42) follows from taking the limit $\sigma_\phi^2 \to 0$ in eq. (7.40). We now consider the other extreme, $\sigma_\phi^2 \to \infty$. It corresponds to code outlier detection without the use of carrier phase data. The corresponding MDB will be larger than eq. (7.42). Furthermore, the absence of carrier phase data will now make the MDB dependent on the frequencies and the ionospheric variance. This follows, since the phase-variance limit of eq. (7.41) reads

$$\lim_{\sigma_\phi^2 \to \infty} \frac{1}{m'} = \frac{1}{n} + \frac{(\gamma_j - \bar{\gamma})^2}{\sum_{i=1}^{n} (\gamma_i - \bar{\gamma})^2 + \sigma_p^2/\sigma_{\mathcal{I}}^2} \tag{7.43}$$

We now again discriminate between the three cases $n = 1$, $n = 2$ and $n > 2$.

7.5.2.1 Single-frequency case

Just like single-frequency codeless phase-slip detection is impossible, so is single-frequency code-outlier detection without phase data. This follows directly from table 7.4, which shows that redundancy is absent, when phase data is absent in case $n = 1$. It also follows from eq. (7.43), which shows that $m' = 1$ if $n = 1$.

7.5.2.2 Dual-frequency case

In the dual-frequency case, the phaseless code-outlier MDB is given as

$$\text{MDB}_{p_{j=1}} = \sigma_p \sqrt{\left(4 + \frac{(\gamma_1 - \gamma_2)^2 \sigma_{d\mathcal{I}}^2}{\sigma_p^2}\right) \lambda_0} \tag{7.44}$$

It follows from interchanging the role of the phase- and code variance in eq. (7.35). The expression in eq. (7.44) shows that the MDB gets larger (poorer detectability) if the frequency separation gets larger (larger $|\gamma_2 - \gamma_1|$). This is perhaps contrary to what one would expect. However, one should not confuse the estimability of the ionosphere in the absence of biases, i.e., under the null hypothesis $\mathcal{H}_0$, with the detectability of biases in the presence of the ionosphere. Since the variance of the ionospheric delay can be shown to be inversely proportional to $|\gamma_2 - \gamma_1|$, the ionospheric delay estimator gets indeed more precise when the frequencies are further separated. The contrary happens however, with the outlier detectability. The detectability of the outliers becomes poorer for larger frequency separation and this effect becomes more pronounced for larger $\sigma_{d\mathcal{I}}^2$. This frequency dependence is absent in case $\sigma_{d\mathcal{I}}^2 = 0$.

The graphs for the dual-frequency phaseless code-outlier MDBs are given in fig. 7.9. Compare this figure with fig. 7.5. The graphs in both figures show a similar shape. In the case of the code-outlier MDBs, however, the graphs do not coincide because of the different levels of code measurement precision of the signals. When we compare fig. 7.9 with fig. 7.8, we also clearly show the impact of the phase data. With the phase data included, the code-outlier MDB not only becomes smaller, but also the steep increase experienced in the phaseless case for $\sigma_{d\mathcal{I}} \geq 10^{-1}$ m is eliminated. Without the phase data, the code-outlier MDB is more dependent on the smoothness of the ionospheric delay.

7.5.2.3 Multi-frequency case

The multi-frequency phaseless code-outlier MDB follows from interchanging the phase and code variance in eq. (7.36). Their graphs are shown in fig. 7.10. When compared to fig. 7.9, they seem to show the same behavior as in the dual-frequency case. This is not true however. In the dual-frequency case the code-outlier MDB keeps growing with increasing $\sigma_{d\mathcal{I}}$, whereas in the multi-frequency case the MDB levels off for large enough $\sigma_{d\mathcal{I}}$. Hence, for larger values than $\sigma_{d\mathcal{I}} = 10^0$ m, the graphs of fig. 7.10 would become S-shaped, just like those of fig. 7.6.

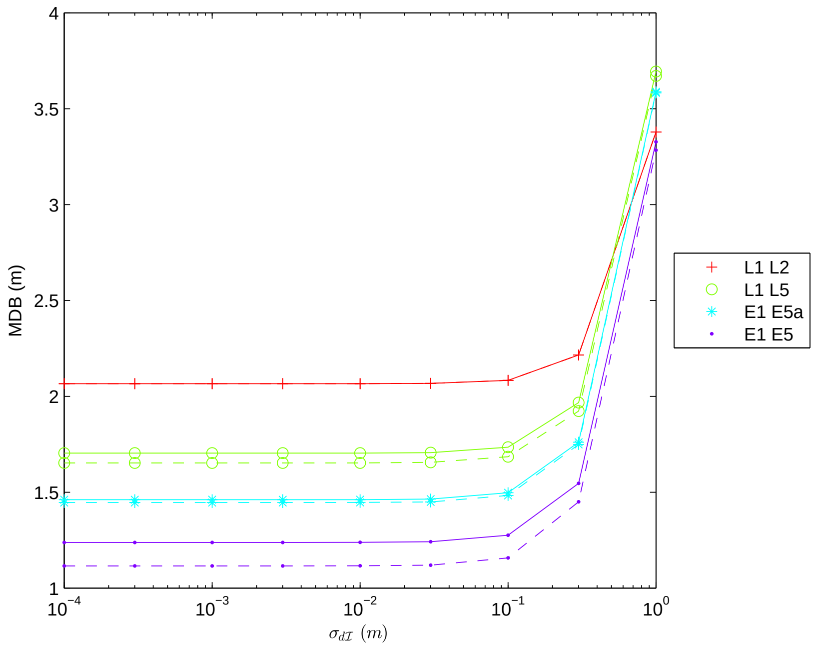

Figure 7.9: Dual-frequency GPS and Galileo code-outlier MDBs on L1/E1 for $k = 2$ without phase data; dashed curves are based on eq. (7.44).

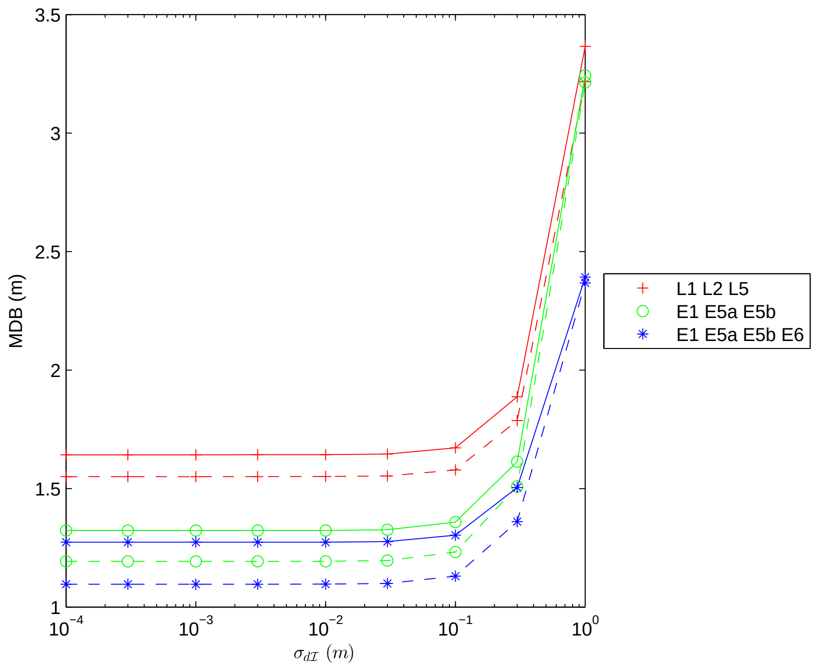

Figure 7.10: Multi-frequency GPS and Galileo code-outlier MDBs on L1/E1 for $k = 2$ without phase data; dashed curves are based on eqs. (7.40) and (7.43).

7.6 Detectability of ionospheric disturbances

The analytical expression for the multi-frequency ionospheric disturbance MDB is given in the following theorem.

Theorem 4 (Ionospheric MDB): Let $H = (0,0,1)^*$, $Q_{\phi\phi} = \sigma_\phi^2 I_n$ and $Q_{pp} = \sigma_p^2 I_n$. Then for $k = 2$, the MDB for an ionospheric disturbance is given as

$$\text{MDB}_{d\mathcal{I}} = \sigma_{d\mathcal{I}} \sqrt{\left(1 + \frac{\sigma_{\hat{d\mathcal{I}}}^2}{\sigma_{d\mathcal{I}}^2}\right) \lambda_0} \tag{7.45}$$

with

$$\sigma_{\hat{d\mathcal{I}}}^2 = \frac{2\sigma_\phi^2}{n\sigma_\gamma^2}\left[1 + \epsilon\left(1 + \frac{4}{1+\epsilon}\frac{\bar{\gamma}^2}{\sigma_\gamma^2}\right)\right]^{-1} \tag{7.46}$$

where $\epsilon = \sigma_\phi^2/\sigma_p^2$ is the phase-code variance ratio, $\bar{\gamma} = \frac{1}{n}\sum_{i=1}^n \gamma_i$ is the average and $\sigma_\gamma^2 = \frac{1}{n}\sum_{i=1}^n (\gamma_i - \bar{\gamma})^2$ is the 'variance' of the squared frequency ratios $\gamma_i = f_1^2/f_i^2$, $i = 1, \ldots, n$.

Proof Let $\hat{d\mathcal{I}}$, with variance defined by eq. (7.46), be the LS estimator of $d\mathcal{I}$ based on the two-epoch model under $\mathcal{H}_0$, cf. eq. (7.10), using phase and code data only. Then it follows from the structure of the model under $\mathcal{H}_a$, that the LS bias estimator of the ionospheric disturbance is given as the difference $\hat{b}_{d\mathcal{I}} = d\mathcal{I} - \hat{d\mathcal{I}}$. Therefore, its variance is given by the sum $\sigma_{d\mathcal{I}}^2 + \sigma_{\hat{d\mathcal{I}}}^2$, from which the result follows.

The above result clearly shows what role is played by the a-priori ionospheric standard deviation, $\sigma_{d\mathcal{I}}$, the measurement precision, σ_ϕ and σ_p, and the distribution of the frequencies, f_i, $i = 1, \ldots, n$. In case all n frequencies are equal, then $\sigma_\gamma^2 = 0$, and the MDB reduces to

$$\text{MDB}_{d\mathcal{I}} = \sigma_{d\mathcal{I}} \sqrt{\left(1 + \frac{\sigma_p^2}{\sigma_{d\mathcal{I}}^2}\frac{1+\epsilon}{2n\bar{\gamma}^2}\right) \lambda_0} \tag{7.47}$$

Although ionospheric disturbance testing is then still possible in principle, its performance will then primarily be driven by the code variance. Figure 7.11 shows the MDB for the single-frequency case $(n = 1)$.

When there is a nonzero 'variance' in the frequencies, $\sigma_\gamma^2 \neq 0$, then codeless or phaseless testing is possible as well. The codeless MDB follows from eq. (7.45) as

$$\lim_{\sigma_p \to \infty} \text{MDB}_{d\mathcal{I}} = \sigma_{d\mathcal{I}} \sqrt{\left(1 + \frac{\sigma_\phi^2}{\sigma_{d\mathcal{I}}^2}\frac{2}{n\sigma_\gamma^2}\right) \lambda_0} \tag{7.48}$$

If we replace σ_ϕ^2 in this expression by σ_p^2, we obtain the corresponding phaseless MDB. Figures 7.12 and 7.13 show the codeless and phaseless MDBs for the different cases.

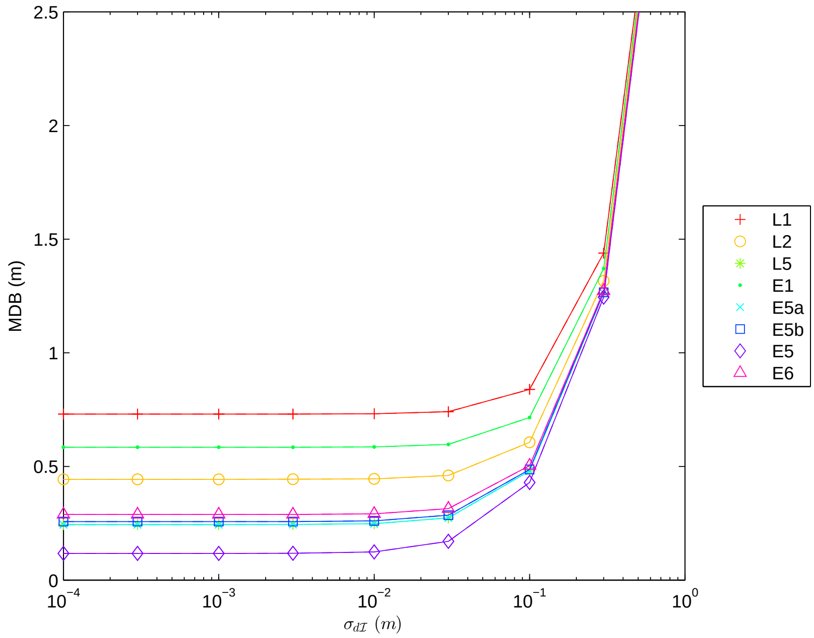

Figure 7.11: Single-frequency ionospheric MDBs for $k = 2$; dashed curves are based on eq. (7.47).

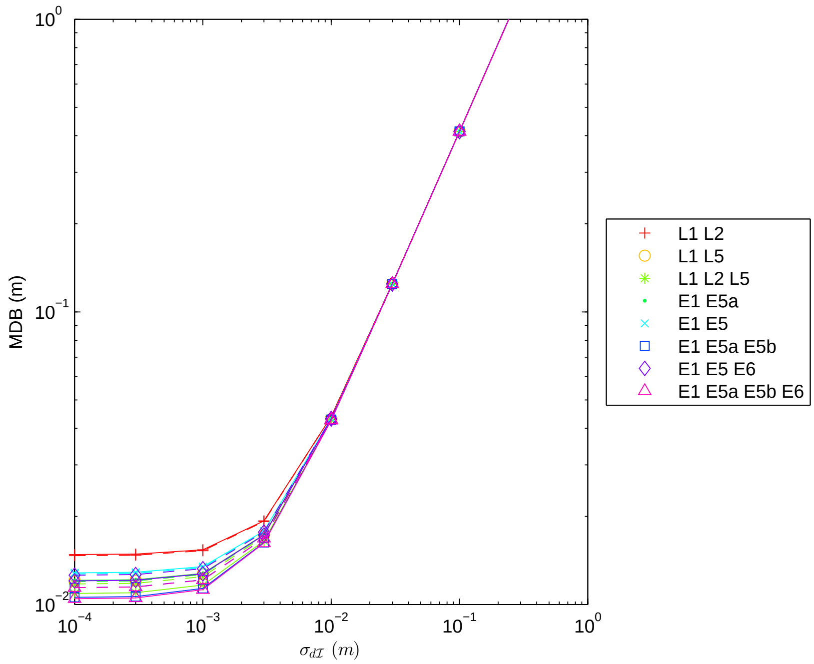

Figure 7.12: Dual- and multi-frequency codeless ionospheric MDBs for $k = 2$; dashed curves are based on eq. (7.48).

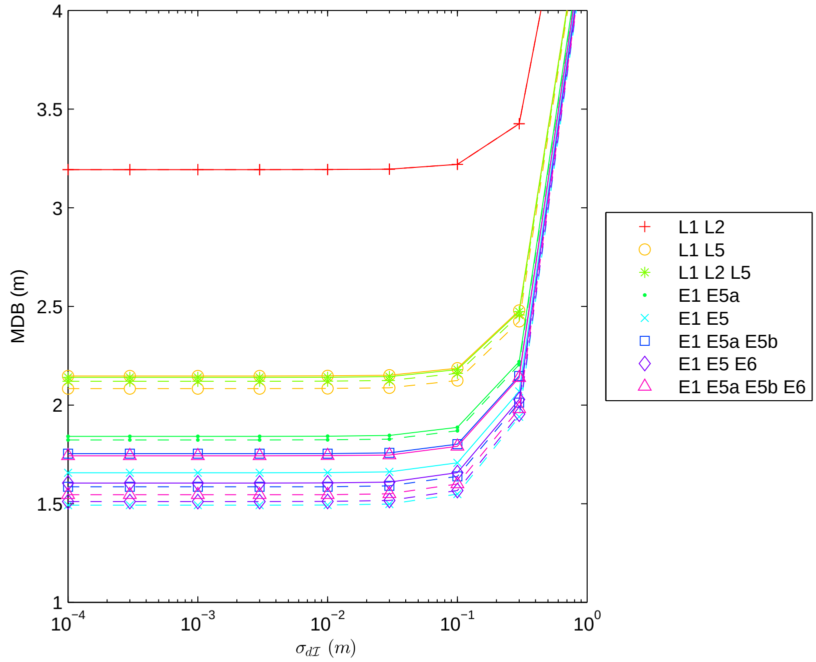

Figure 7.13: Dual- and multi-frequency phaseless ionospheric MDBs for $k = 2$; dashed curves are based on eq. (7.48), with code variance replaced by phase variance.

7.7 Detectability of phase loss-of-lock

Phase loss-of-lock is defined as the simultaneous occurrence of an unknown multivariate slip in all n carrier phase observables. To study its detectability, we first determine the variance matrix of the multivariate slip under $\mathcal{H}_a$ and then provide bounds on the norm of the phase loss-of-lock MDB-vector.

7.7.1 The variance matrix of the multivariate slip

In the presence of a phase loss-of-lock, the design matrix of the alternative hypothesis defined by eq. (7.10) takes for $k = l = 2$ the form $[G, H]$, with $H = [I_n, 0, 0]^*$. From the structure of $[G, H]$, it follows that the carrier phase vector $\phi(t, s)$ will not contribute to the estimation of the parameters $\rho'(t, s)$ and $\mathcal{I}(t, s)$ under $\mathcal{H}_a$. These parameters are therefore solely determined by the code observables and a priori ionospheric information. As a consequence, the two-epoch bias estimator is given as the difference $\hat{b} = \phi(t, s) - \hat{\phi}(t, s)$, where $\hat{\phi}(t, s) = e_n\hat{\rho}'(t, s) - \gamma\hat{\mathcal{I}}(t, s)$ is the least-squares phase estimator based solely on the code observables and a priori ionospheric information. Solving for $\hat{\rho}'(t, s)$ and $\hat{\mathcal{I}}(t, s)$, followed by applying the variance propagation law to $\hat{b} = \phi(t, s) - e_n\hat{\rho}'(t, s) + \gamma\hat{\mathcal{I}}(t, s)$ gives then the variance matrix of the multivariate slip. The result is given in the following Lemma.

Lemma 2 (Variance matrix of multivariate slip) For $k = l = 2$ and $H = (I_n, 0, 0)^*$, the variance matrix of the least-squares estimator of b in eq. (7.10) is given as

$$Q_{\hat{b}\hat{b}} = 2Q_{\phi\phi} + 2P_{e_n}Q_{pp}P_{e_n}^* + \sigma_{d\hat{\mathcal{I}}}^2 R_{e_n}\gamma\gamma^T R_{e_n}^* \tag{7.49}$$

with $\sigma^2_{d\hat{\mathcal{I}}} = (\frac{1}{2}\gamma^* Q_{pp}^{-1} P_{e_n}^{\perp}\gamma + \sigma_{d\mathcal{I}}^{-2})^{-1}$, $P_{e_n}^{\perp} = I_n - P_{e_n}$, $P_{e_n} = e_n(e_n^* Q_{pp}^{-1} e_n)^{-1} e_n^* Q_{pp}^{-1}$ and $R_{e_n} = I_n + P_{e_n}$.

Note that the variance matrix is a sum of three matrices, the entries of which may differ substantially in size. The first matrix is governed by the precision of the phase observables and will therefore have small entries. The second matrix is governed by the precision of the code observables and will therefore have generally much larger entries than the first matrix in the sum. The third matrix depends, next to the precision of the code observables, also on γ and $\sigma^2_{d\mathcal{I}}$. Its entries will become smaller, if $\sigma^2_{d\hat{\mathcal{I}}}$ gets smaller. This happens for smaller $\sigma^2_{d\mathcal{I}}$ (smoother ionospheric delays) and/or larger $\gamma^* Q_{pp}^{-1} P_{e_n}^{\perp}\gamma$ (better code precision and/or larger frequency diversity). Thus if $\sigma^2_{d\mathcal{I}} = \infty$, frequency diversity is needed (i.e., $\gamma^* Q_{pp}^{-1} P_{e_n}^{\perp}\gamma \neq 0$) so as to avoid the entries of the third matrix in eq. (7.49) to become infinite.

We now discuss the detectability of the phase loss-of-lock for $n \geq 2$. The single-frequency case $n = 1$ is already treated, cf. eq. (7.31), since phase loss-of-lock is then equivalent to having a phase-slip.

7.7.2 Bounding the MDB vector

The variance matrix of eq. (7.49) can be used together with eq. (7.26) to determine the phase loss-of-lock MDB-vector. Its length depends on the direction d in which the multivariate slip occurred,

$$|| \text{MDB}|| = \sqrt{\frac{\lambda_0}{d^* Q_{\hat{b}\hat{b}}^{-1} d}} \tag{7.50}$$

For certain directions, this may result in a short vector, while for other directions, it may be a long vector.

For its length, the following upper bound can be used,

$$|| \text{MDB}|| \leq \sigma_{d^*\hat{b}}\sqrt{\lambda_0} \tag{7.51}$$

where $\sigma^2_{d^*\hat{b}} = d^* Q_{\hat{b}\hat{b}} d$ is the variance of $d^*\hat{b}$, with d being the unit vector that points in the direction of the slip. The upper bound is easier to obtain as it avoids the inversion of the variance matrix of eq. (7.49).

Considering eq. (7.49), it is not difficult to see in which directions the MDB-vector will be short. If $d \perp e_n$, then $P_{e_n}^* d = 0$, meaning that the second term of eq. (7.49) will not contribute. And if $d \perp \text{ span}\{e_n, \gamma\}$, then $R_{e_n}^* d = 0$ and $P_{e_n}^* d = 0$, meaning that now also the third term will not contribute. Thus

$$|| \text{MDB}|| \leq \sqrt{2\lambda_0 d^* Q_{\phi\phi} d} \quad \text{if } d \perp \text{ span}\{e_n, \gamma\} \tag{7.52}$$

This shows that the length of the MDB vector is very small indeed if d lies in the $(n-2)$-dimensional space $\text{span}\{e_n, \gamma\}^{\perp}$. In this case, the phase loss-of-lock has very good detectability, since the MDB is then solely driven by the very precise carrier phase data.

The situation changes drastically, however, if d is taken to lie in span$\{e_n, \gamma\}$. In that case the large code variance dependent second and third term of eq. (7.49) will contribute as well. The largest possible value that the length of the MDB vector can take corresponds with d being the eigenvector of $Q_{\hat{b}\hat{b}}$ with largest eigenvalue. The corresponding bounds for the ionosphere-fixed and ionosphere-float case, are given in the following Lemma.

Lemma 3 (Phase loss-of-lock MDB upper bounds) Let $Q_{\phi\phi} = \sigma_\phi^2 I_n$, $Q_{pp} = \sigma_p^2 I_n$. Then

$$|| \text{ MDB}|| \leq \begin{cases} \sigma_p \sqrt{2(1+\epsilon)\lambda_0} & \text{if } \sigma_{d\mathcal{I}}^2 = 0 \\ \sigma_p \sqrt{2\left(1+\epsilon+\frac{2}{\sqrt{f-1}}\right)\lambda_0} & \text{if } \sigma_{d\mathcal{I}}^2 = \infty \end{cases} \tag{7.53}$$

with $f = 1 + \left(\frac{\sigma_\gamma}{\bar{\gamma}}\right)^2$, where $\sigma_\gamma^2 = \frac{1}{n}\sum_{i=1}^n (\gamma_i - \bar{\gamma})^2$ and $\bar{\gamma} = \frac{1}{n}\sum_{i=1}^n \gamma_i$.

Proof: see Appendix C.

The ionosphere-fixed upper bound corresponds with a slip in the e_n-direction, while the ionosphere-float upper bound corresponds with a slip in the direction $e_n + \frac{\sqrt{n}}{||\gamma||}\gamma$. Thus phase loss-of-lock is most difficult to detect if it results in a slip with such direction. For example, for the ionosphere-fixed, dual- and triple-frequency ($q = 2, 3$) cases, the length of the MDB-vector will then be about six to seven times the code standard deviation.

To conclude, we note that we can apply the duality of phase and code to the above lemma and so obtain directly also the length of the MDB vector $||\text{MDB}||_p$ that corresponds to the case that the complete n-dimensional code vector is outlying. By interchanging the phase- and code variance in eq. (7.53), we obtain

$$||\text{MDB}||_p \leq \begin{cases} \sigma_p \sqrt{2(1+\epsilon)\lambda_0} & \text{if } \sigma_{d\mathcal{I}}^2 = 0 \\ \sigma_p \sqrt{2\left(1+\epsilon(1+\frac{2}{\sqrt{f-1}})\right)\lambda_0} & \text{if } \sigma_{d\mathcal{I}}^2 = \infty \end{cases} \tag{7.54}$$

The ionosphere-fixed upper bound is the same as in eq. (7.53), but the ionosphere-float upper bound differs. In this second bound we note that the effect of frequency diversity (i.e., the effect of f) gets reduced due to its multiplication with the small phase-code variance ratio ϵ. This corresponds to our earlier findings in section 7.5.1.2, where it was stated that over the considered range of $\sigma_{d\mathcal{I}}^2$, the code-outlier MDB is much more insensitive to frequency diversity than the phase-slip MDB is.

7.7.3 Numerical results MDB vector

Figure 7.14 and table 7.5 show results for the MDB ellipse for a simultaneous slip on both frequencies of dual frequency GPS data. Figure 7.14 shows that the MDB ellipse is very elongated, which confirms that certain combinations of simultaneous biases on L1 and L2 are more difficult to detect than others. The first column in table 7.5 gives the standard deviation of the time differenced ionospheric pseudo-observation and its two limiting cases: ionosphere float and ionosphere fixed. The elongation of the ellipse is displayed in the right most column showing the semimajor axis of the ellipse divided by the semiminor axis. The MDB along the major axis and the direction of the major axis are displayed in column two and three, respectively. For the ionosphere-float model considered here, the weakest direction for error detection is given by the unit vector $(0.62, 0.79)^*$. In this direction a bias of 7.27 m can just be detected with the chosen power and probability of false alarm. This result reveals an important weak point of cycleslip detection with an ionosphere-float model. After a momentary loss-of-lock to a satellite, specific combinations of simultaneous slips can be present in the receiver data which are very difficult to detect.

The weakest direction for cycleslip detection depends on the ionospheric dispersion factors γ. A combination of slips of unknown size on both phase observables of dual frequency data with a time differenced model, is comparable to an undifferenced model with unknown phase ambiguities. The directions of the principal axis of the ellipses presented in table 7.5 are therefore closely related to those pertaining to the well-known linear combinations used for ambiguity float estimation.

For the ionosphere-weighted approach, the MDB ellipse shrinks and becomes less elongated when the precision of the ionospheric pseudo observable increases. The weakest direction also changes slowly, until it becomes equal to the line MDB$_{L1}$ = MDB$_{L2}$ for the ionosphere-fixed model. At this point the uncertainty in the lumped parameter $\rho'(t, s)$ becomes the dominant factor instead of the uncertainty in the ionospheric delay $\mathcal{I}(t, s)$. This uncertainty, which again results in a very elongated ellipse, impacts each of the phase observables identically, resulting in the weakest direction for cycleslip detection given by MDB$_{L1}$ = MDB$_{L2}$ for this situation.

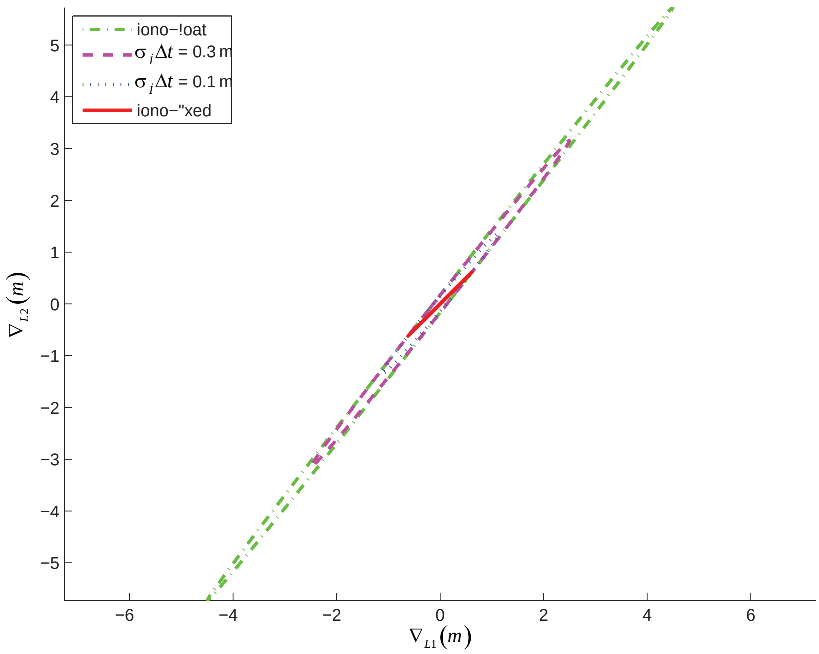

Figure 7.14: MDB ellipse of a simultaneous slip on both frequencies of GPS L1 L2 data for different ionospheric models.

Tables 7.6 and 7.7 display similar results as table 7.5 but now for, respectively, three and four frequency data. Only the major axis is presented here because in this direction the largest undetected slips can occur and the improvement in this direction resulting from the ionospheric pseudo observable is most important. Analogous to the two dimensional case the weakest direction for the ionosphere-fixed model is along the line $\text{MDB}_{Li} = \text{MDB}_{L1}$ for $i = 2, \ldots, n$. When the precision of the ionospheric pseudo observable increases the elongation of the ellipsoid first decreases significantly and finally increases slightly again when the model starts to behave as the ionosphere-fixed model.

Table 7.5: Two dimensional MDB ellipses

$\sigma_{d\mathcal{I}}$ (m)	$\max(\|\text{MDB}\|)$ (m)	direction major axis $(L1, L2)^*$	$\frac{\max(\|\text{MDB}\|)}{\min(\|\text{MDB}\|)}$
float	7.2697	$(0.62, 0.79)^*$	69
1	6.6122	$(0.62, 0.79)^*$	63
0.3	4.0199	$(0.62, 0.78)^*$	39
0.1	1.7548	$(0.64, 0.77)^*$	19
0.03	0.9916	$(0.69, 0.73)^*$	20
0.01	0.8900	$(0.70, 0.71)^*$	45
0.003	0.8777	$(0.71, 0.71)^*$	99
0.001	0.8766	$(0.71, 0.71)^*$	125
fixed	0.8765	$(0.71, 0.71)^*$	129

Table 7.6: Three dimensional MDB ellipsoids

$\sigma_{d\mathcal{I}}$ (m)	$\max(\|\text{MDB}\|)$ (m)	direction major axis $(L1, L2, L5)^*$	$\frac{\max(\|\text{MDB}\|)}{\min(\|\text{MDB}\|)}$
float	6.3597	$(0.49, 0.60, 0.63)^*$	841
1	6.1363	$(0.49, 0.60, 0.63)^*$	811
0.3	4.7020	$(0.49, 0.60, 0.63)^*$	622
0.1	2.2065	$(0.49, 0.60, 0.63)^*$	292
0.03	0.7829	$(0.51, 0.60, 0.62)^*$	103
0.01	0.4363	$(0.55, 0.59, 0.59)^*$	58
0.003	0.3769	$(0.57, 0.58, 0.58)^*$	50
0.001	0.3712	$(0.58, 0.58, 0.58)^*$	54
fixed	0.3705	$(0.58, 0.58, 0.58)^*$	57

7.8 Summary and conclusions

In this chapter we presented an analytical and numerical study of the integrity of the multi-frequency single-receiver, single-channel GNSS model. The UMPI test statistics for spikes and slips are derived and their detection capabilities are described by means of the concept of minimal detectable biases (MDBs). Analytical closed-form expressions of the phase-slip and code outlier MDBs have been given, thus providing insight into the various factors that contribute to the detection capabilities of the various test statistics. This was also done for the phaseless and codeless cases, as well as for the case of loss-of-lock.

Table 7.7: Four dimensional MDB hyper-ellipsoids

$\sigma_{d\mathcal{I}}$ (m)	$\max(\lVert\text{MDB}\rVert)$ (m)	direction major axis $(E1, E5a, E5b, E6)^*$	$\frac{\max(\lVert\text{MDB}\rVert)}{\min(\lVert\text{MDB}\rVert)}$
float	3.1742	$(0.42, 0.54, 0.53, 0.50)^*$	451
1	3.1509	$(0.42, 0.54, 0.53, 0.50)^*$	448
0.3	2.9393	$(0.42, 0.54, 0.53, 0.50)^*$	418
0.1	2.0136	$(0.42, 0.54, 0.53, 0.50)^*$	286
0.03	0.7913	$(0.43, 0.54, 0.53, 0.50)^*$	112
0.01	0.3585	$(0.46, 0.52, 0.52, 0.50)^*$	51
0.003	0.2623	$(0.49, 0.50, 0.50, 0.50)^*$	37
0.001	0.2521	$(0.50, 0.50, 0.50, 0.50)^*$	38
fixed	0.2508	$(0.50, 0.50, 0.50, 0.50)^*$	40

The MDBs were evaluated numerically for the several GPS and Galileo frequencies. From these analyses it can be concluded that detectability of a single phase-slip in dual- and triple-frequency data works well for two epochs ($k = l = 2$). Single-frequency phase-slip detectability, however, is problematic, thus requiring more epochs of data.

From the codeless phase-slip MDBs it follows that detectability is not possible in the single-frequency case, but that it is possible for the dual- and triple-frequency cases. In the dual-frequency case the codeless phase-slip MDBs are less than 10 cm if $\sigma_{d\mathcal{I}} \leq 3$ cm, while for the triple-frequency case this is already true for $\sigma_{d\mathcal{I}} \leq 1$ m. In the triple-frequency case, the phase-slip MDBs get even as small as a few centimeters if $\sigma_{d\mathcal{I}} \leq 3$ cm. These codeless results are important as it shows that in the presence of code multipath, one can do away with the code data and then still have integrity for single phase slips.

The code outlier MDBs are, except for the single-frequency case, all relative insensitive to the smoothness of the ionosphere. The effect of the frequencies is also hardly present in the multi-frequency code-outlier MDBs. Their value is predominantly determined by the precision of the code measurements. From the phaseless code-outlier MDBs it follows that, except for the single-frequency case, code outlier detection is still possible. The multi-frequency phaseless code-outlier MDBs all lie around 1 m for $\sigma_{d\mathcal{I}} \leq 10$ cm. They increase rapidly, however, for larger values of $\sigma_{d\mathcal{I}}$.

The hypothesis of a simultaneous slip on each phase observable of multi-frequency GNSS data was shown to give a very elongated MDB ellipse or (hyper)ellipsoid with the ionosphere-float model. These very elongated ellipses reveal a weak point of cycleslip detection with an ionosphere-float model because specific combinations of slips, which can be present in the receiver data after a momentary loss-of-lock to a satellite, are very difficult to detect. One way to remedy this shortcoming, which is related to the uncertainty in the ionospheric delay, is to use an ionosphere-weighted model. For an ionosphere-weighted approach, the MDB ellipse shrinks when the precision of the ionospheric pseudo observable increases. For optimal performance of a cycleslip detection algorithm, including slip combinations that are difficult to detect, it is advisable to use an ionosphere-weighted model in combination with a short time interval between the measurements.

The case where a combination of slips occurs on a subset of the available frequencies was not treated separately in this chapter. However, it stands to reason that the single-slip and the complete loss-of-lock on all frequencies are the two extremes which bound this case. Furthermore, it can be reasoned that if at least one frequency does not contain a phase slip, a combination of slips in the weakest direction, as shown in tables 7.5 to 7.7, cannot occur. Therefore, detection performance in this case will perform much better.

8 Results of Precise Point Positioning

In this chapter the models and theory presented in the previous chapters are applied to collected dual-frequency GNSS data with the aim of both bringing the analysis of the functional and stochastic models to a conclusion and to present the corresponding positioning results. Staying true to our approach of separating the precise positioning problem into smaller sub-problems the different user dynamics are first discussed in section 8.1, before the phase-only processing model is treated in section 8.2, followed by the code-only processing model in section 8.3. These two models are then combined in the code+phase processing model in section 8.4, and the addition of atmosphere constraints is treated in section 8.5. In section 8.6 the results are compared and discussed further.

8.1 User dynamics

(Precise) Point Positioning can be performed for different user dynamics summarized in table 8.1.

Table 8.1: User dynamics in positioning algorithms and their application

Processing method	Receiver movement Stationary	 Moving
Fixed position	Error analysis and atmosphere monitoring	Error analysis (needs reference track)
Static processing	Positioning and performance analysis	N/A
Kinematic processing	Performance analysis	Positioning for unknown receiver dynamics
Dynamic processing	Performance analysis	Positioning for known receiver dynamics

1. Fixed position. In this method no actual positioning is performed, instead the receiver coordinates are kept fixed to the known reference position (or reference track) and are not allowed to change, which strengthens the model considerably. Since the other unknown parameters including the receiver clock offset, troposphere and ionosphere delays can still be estimated using this stronger model, this method is very well suited for e.g. time transfer and atmosphere estimation. Additionally, the much stronger

model makes it possible to analyze the errors on the pseudo range and carrier phase measurements by studying the residuals of the Kalman filter.

However, the error analysis is sensitive to errors in the fixed position, which could bias the results. This is particularly true for the temporal station displacements (see table 3.1). The fixed station position can be obtained to a sufficient degree of accuracy from a static processing using several weeks of data, using the same or different software.

2. Static processing stationary receiver. In this method the receiver coordinates are kept constant over time, but they are not fixed to any (known) position, and the estimated coordinates are updated at each epoch. The accuracy of the estimated position solution will increase as more epochs of data and more measurements are processed; the last processed epoch is the final static solution. This processing technique can be used to accurately determine an unknown position of a stationary receiver. Additionally, if the receiver position is known (e.g. from a different measurement campaign), the static position performance can be analyzed including the convergence behavior.

3. Kinematic processing. In this method the receiver position coordinates are not kept constant, but instead are estimated anew at each epoch. Since the carrier phase ambiguities *are* kept constant the accuracy will still improve over time, but this convergence will be less pronounced than in the static case. This processing method corresponds to the use of PPP for a moving receiver in a real world scenario, without constraining the changes of the position over time. Additionally, if the receiver position is known (from a different source), the kinematic processing performance can be analyzed.

4. Dynamic processing. In this method the user position is not kept constant, but the changes in position over time *are* constrained. This method can be used if a dynamic model for the receiver position is available. This model should describe how the position coordinates change over time, which can be anywhere from very smooth predictable behavior to strong erratic behavior. In the first case the performance might approach that of static processing, while the performance in the second case will be close to that of kinematic processing. The dynamic model that can be used depends strongly on the PPP application and user platform. The dynamic model itself can be very simple where the previous position estimate is simply used as a prediction of the current position with a certain precision, or more complex using velocity, acceleration, and forces acting on the user.

In this dissertation the focus will be on the first three processing methods. First the position coordinates are kept fixed to analyze the measurement errors and tune the stochastic model. Then the performance of both static and kinematic positioning are determined. We will now consider a data set from DLF1, a permanent receiver setup at the TU Delft GNSS observatory platform already introduced in section 6.3. The setup consists of a Trimble NETR9 receiver connected to a Leica AR25 3D choke-ring antenna; the IGS final products were used to obtain precise satellite positions and clock offsets. Another permanent receiver at the TU Delft GNSS observatory, named DELF, is part of the EUREF Permanent GNSS Network (EPN). From the EPN solution of DELF, and the accurately known local geometry at the observatory, the reference position for DLF1 was computed.

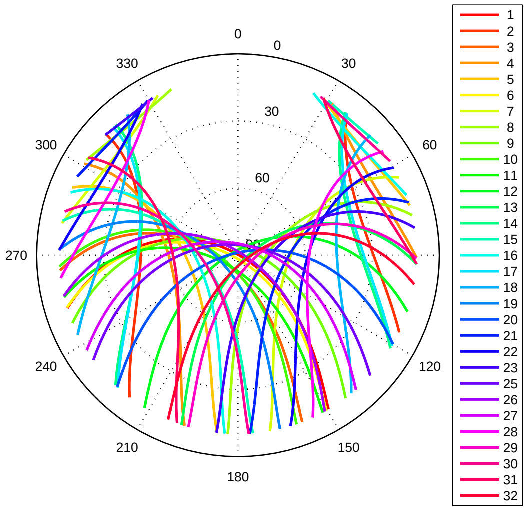

(a) Skyplot

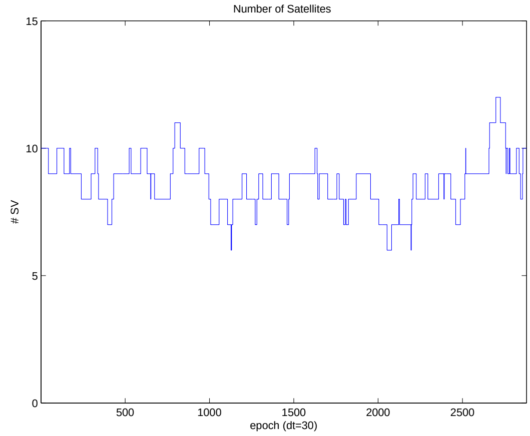

(b) Number of visible satellites

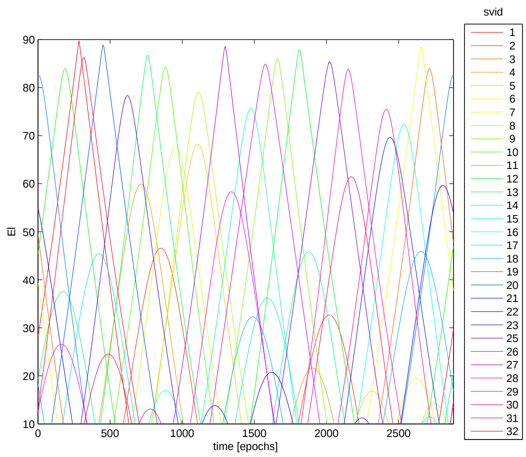

(c) Satellite elevation

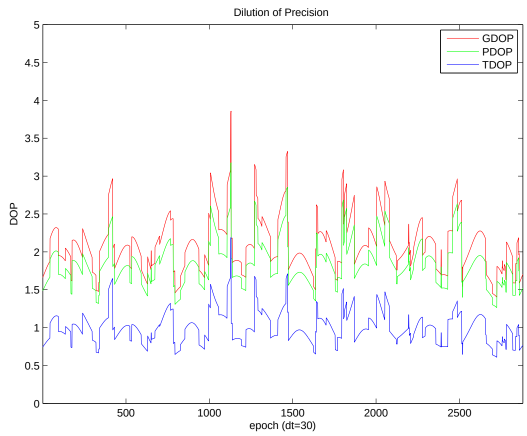

(d) Dilution Of Precision of the Geometry, Position and Time

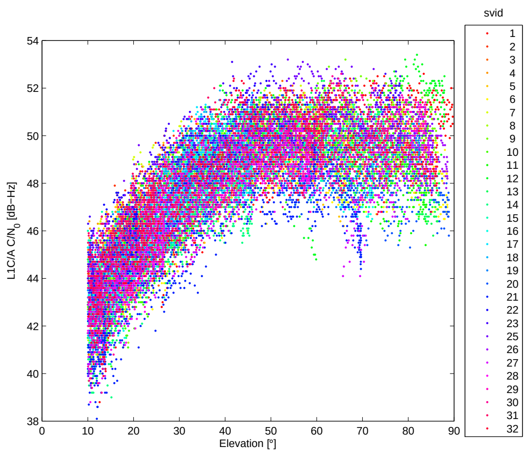

(e) C/N$_0$ of the L1C/A signal vs elevation

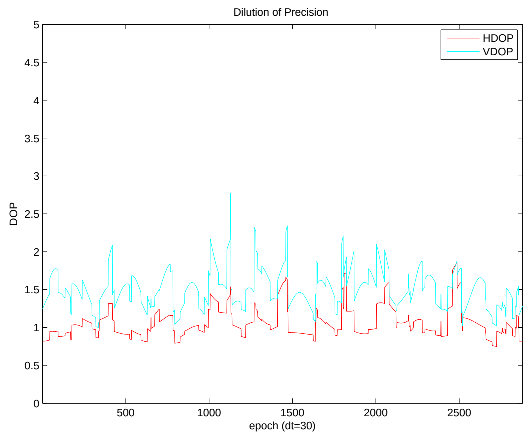

(f) Horizontal and Vertical Dilution Of Precision

Figure 8.1: GPS availability measures for June 1, 2012 measured at Delft

A representative dataset for a period of 30 days, from June 1 to to June 30, 2012, has been processed. The day to day results are very similar. Figure 8.1 provides a first glace at the first day of data. The skyplot in fig. 8.1(a) shows the look angles, i.e. the elevation angle with respect to the horizon and the azimuth angle with respect to the North direction, for all tracked GPS satellites. Since the GPS ground track repeats within 24 hours, no begin or end point appear in the skyplot, except at 10° elevation at the outer edges of the figure, which correspond to the elevation mask angle. Since the antenna has a free view of the sky above 10° elevation, there are also no visible interruptions in the satellite tracks. The large empty circle at the top of the plot, typical for locations at mid-latitude on the Northern hemisphere, is due to the inclination of 55° of GPS satellite orbits which means no satellites can be observed above the polar region.

Figure 8.1(b) shows the number of available satellites above the cutoff elevation angle of 10° versus the epoch number (the measurement interval is 30 s). The number of satellites varies between 6 and 12, and is 8 or 9 on most epochs. Figures 8.1(d) and 8.1(f) show the Dilution Of Precision (DOP, already introduced in section 5.3.1) for different (combinations of the) unknown coordinates and clock offset. The DOP gives a first impression of how the measurement uncertainty propagates to the estimated parameters; lower values of the DOP correspond to better precision. By definition a combination of certain parameters will have a higher DOP value than the individual components, e.g. the Geometry DOP (GDOP), which combines the position and clock offset, is higher than both the Position DOP (PDOP) and Time DOP (TDOP) individually. The variation of the DOP over time depends on the number of available satellites, as can be seen from the correlation between figs. 8.1(d) and 8.1(f) on the one hand and fig. 8.1(b) on the other hand (e.g. the highest peak in the DOP lines, corresponds to one of the epochs with only 6 satellites in view), but also on the relative geometry of the satellites and the receiver. This last point explains the variations of the DOP values while the number of satellites remains constant. The DOP values do not show any extreme excursions, which means that the positioning performance is not expected to be poor at any time.

Figure 8.1(c) shows the satellite elevation angle versus time, and fig. 8.1(e) shows the measured C/N_0 at each elevation. The latter shows the typical curve with higher C/N_0 values for higher satellite elevation (in this case the C/N_0 increases from about 43 dB-Hz at 10° elevation to 49 dB-Hz at 90° elevation). This curve is mainly due to the receiver antenna gain pattern, and in smaller part due to the free-space loss which is higher at lower elevation angles, the satellite antenna gain which is designed to cancel the free-space loss variation and the slightly higher atmosphere attenuation at lower elevation angles. The observed C/N_0 values above 10° elevation are all reasonably high which indicates that the measurements are expected to be of good quality.

This chapter will now continue with the first type of processing, i.e. with known user position. The main goal is to evaluate the validity of the stochastic model and improve it using Variance Component Estimation (VCE) (Förstner, 1979). Several parts of the stochastic model can be isolated by only considering part of the available observables. For that reason we start with phase-only processing.

8.2 Phase-only processing

8.2.1 Fixed coordinates - Variance Component Estimation

In this section VCE is performed for the phase-only model with the following settings:

- The receiver coordinates are kept fixed at accurate reference values.
- The receiver clock offset and troposphere zenith delay are estimated kinematically.
- The slant ionosphere delay is estimated kinematically for each satellite.
- The ambiguities are estimated as real-valued constants.
- The observations from different satellites and different epochs are assumed to be uncorrelated.

As explained in appendix G, the observation model then becomes equivalent to:

$$E\left\{\left[\underline{\Delta\boldsymbol{\phi}}^{S}_{r,L3,k}\right]\right\} = \left[\begin{array}{ccc} c\mathbf{u}_m & \mathbf{m}^{S}_{r,k} & \mathbf{I}^{0\cdots 0}_{m-1} \end{array}\right]\left[\begin{array}{c} \overline{\delta t}_{r,L3,k} \\ T_{Z,r,k} \\ \bar{\mathbf{A}}^{S-1}_{r,L3} \end{array}\right]; \quad D\left\{\left[\underline{\Delta\boldsymbol{\phi}}^{S}_{r,L3,k}\right]\right\} = \boldsymbol{Q}_{\boldsymbol{\phi}^{S}_{r,L3,k}} \tag{8.1}$$

In the software implementation the ionosphere is still estimated even though this does not contribute to the parameter estimation or VCE. In order to illustrate the process of Variance Component Estimation, a scaled identity matrix is used as the initial stochastic model:

$$\boldsymbol{Q}_{\phi_{L3}} = \sigma^2_{\phi_{L3}}\boldsymbol{I} \text{ with } \sigma_{\phi_{L3}} = 15\,\mathrm{mm}. \tag{8.2}$$

The Local Overall Model (LOM) test and the measurement residuals are first considered to analyze the validity of the stochastic model. The LOM test has an expectation value equal to the redundancy if the stochastic model fits with the data (Teunissen, 2006, 2000a). If the LOM test is divided by the redundancy (we will call this the normalized LOM), it has an expectation of 1. If the empirical value is larger than 1 on average, the stochastic model is too optimistic, and if it is smaller the stochastic model is too pessimistic. This is closely related to the estimation of the variance of unit weight. In fact, if we consider a stochastic model with a single variance component, and we multiply the normalized LOM test with the variance used in the stochastic model, we end up with an unbiased estimator of the actual measurement variance. However, in this case a single variance component does not suffice. Figure 8.2(a) shows the normalized LOM test statistic. From the figure it is clear that the mean value of the normalized LOM test is much smaller than 1, which indicates that the stochastic model is too pessimistic. Additionally, fig. 8.2(a) shows the critical value for the normalized LOM test and the test decision. The critical value varies with the redundancy, and in this figure is never exceeded by the LOM test value. Therefore, the test decision is accept (=1) at all epochs.

More details can be derived from fig. 8.2(b) which shows the measurement residuals (dots) versus the satellite elevation, as well as twice their formal standard deviation (dashed lines). Based on the residual plot in fig. 8.2(b) several observations can be made:

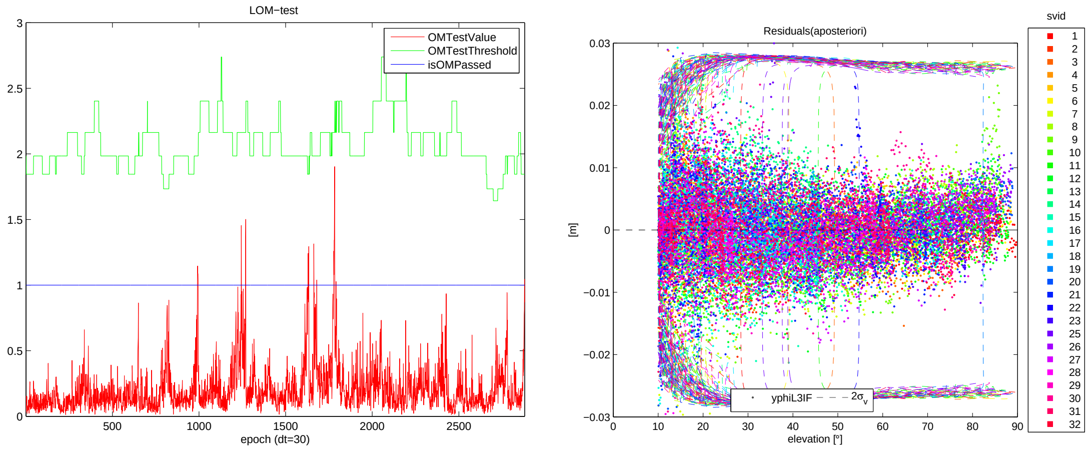

(a) Normalized Local Overall Model (LOM) test; mean LOM value is much smaller than 1, indicating a pessimistic stochastic model

(b) L3IF carrier phase residuals versus elevation; elevation dependance of the residuals is not represented well by the formal 2-sigma values

Figure 8.2: Phase-only results with fixed position and scaled identity matrix as stochastic model for June 1, 2012 measured at Delft

1. The formal 2-sigma values are for the most part close to 30 mm, but never above this value, which can be explained as follows. By definition the formal residual standard deviation is smaller than or equal to the measurement standard deviation. The standard deviation of the observations on L1 and L2 was set to 5 mm in this run, therefore the standard deviation of the ionosphere-free combination is 15 mm (table 3.5), and hence the 2-sigma is 30 mm.

2. Whenever a satellite is first included in the positioning filter the residuals and the corresponding 2-sigma values are zero. This happens when the filter is first started and when a satellite first becomes available, at 10 ° elevation. The explanation for this is that, when this happens, both the ionosphere delay and the ionosphere-free combination of the ambiguities for that satellite are still completely unknown (the same holds for the original ambiguities). Therefore, there is no redundancy for the new observations and consequently their residuals are zero (see appendices F.3 and F.4). As more observations of these satellites are used, the ambiguity estimates improve and the residuals grow closer to the measurement standard deviation.

3. On top of the effect mentioned in the previous point, the 2-sigma values also decrease at low elevation angles in general, both for ascending and descending satellites. The reason for this effect is that the troposphere mapping function has larger values for lower elevation. Therefore, the low-elevation satellites contribute more to the troposphere estimation and have smaller residuals.

4. The residuals are clearly larger for lower elevation angles, which is as expected as the observation errors are generally larger at lower elevation, but this is not reflected in the formal 2-sigma values. In fact this is one of the main motivations for this section, as the goal is to tune the stochastic model to reflect the actual observation precision including the elevation dependence.

To obtain an accurate stochastic model of the elevation dependent measurement errors, the iterative procedure described in appendix G is applied, in which the almost unbiased variance component estimation is applied to groups of observations (in this case 1 ° elevation bins). Figure 8.3(a) shows the VCE results after the first processing run (i.e. using the

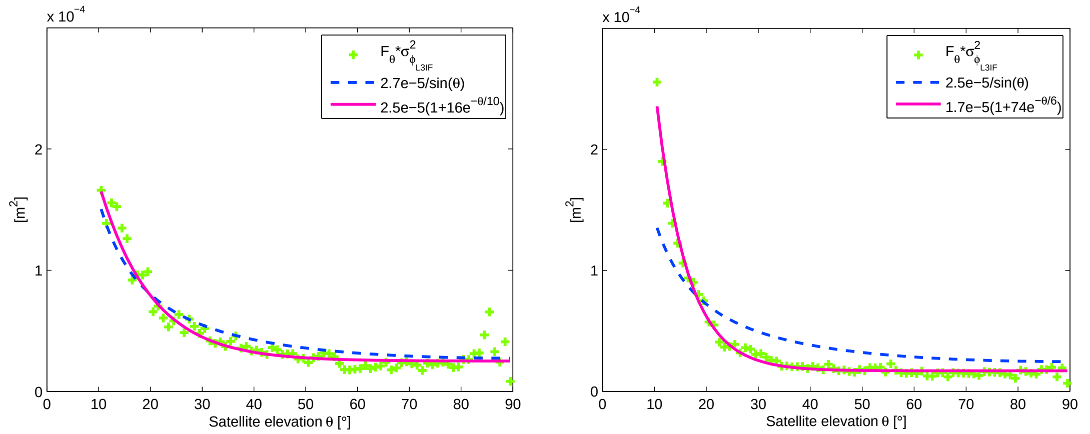

(a) VCE results first iteration; Both models fit well to estimated variance components per elevation bin

(b) VCE results after final iteration; only exponential model fits variance components per elevation bin

Figure 8.3: Phase-only VCE results with fixed position for June 1, 2012 measured at Delft; the ionosphere-free combination is shown

scaled identity matrix as a stochastic model). The 'plus'-signs represent the results per elevation bin and show a clear elevation dependence. This elevation dependence can be modeled quite accurately by a number of common weighting functions; here shown are the cosecant (=1/sin) and an exponential function of the form introduced by Euler and Goad (1991). Only at high elevation angles do some larger deviations from the fitted curves occur. Since these elevation bins contain far fewer observations than the bins at lower elevation angles, these estimates are consequently less precise. As the VCE is iterated the estimated variance for low elevation angles keeps increasing, and for the higher elevation angles it keeps decreasing (see fig. 8.4). The VCE converges after 13 iterations to the results shown in fig. 8.3(b). From these figures it is clear that the cosecant function can no longer closely follow the binned values, while the exponential function can still be used to model the elevation dependence accurately. Therefore, this is the model that is chosen and used in all further processing. Also note that the deviations from the curve at higher elevation angles are much reduced.

Figure 8.5(a) again shows the normalized LOM test statistic now for the converged variance model. From the figure it is clear that the mean value of the normalized LOM test is now much closer to 1 , which indicates that the stochastic model fits much better. Also, the LOM test is now rejected (=0) for 3% of the epochs. In our testing approach we follow Baarda (1968) in that we chose the probability of missed detection ($\beta = 0.001$) and false alarm ($\alpha_1 = 0.001$) for the 1-dimensional test and compute the corresponding non-centrality parameter. The same non-centrality parameter and probability of missed detection are then used for the LOM test. One should note that the probability of false alarm for the LOM test will in this case be much higher than the probability of false alarm for

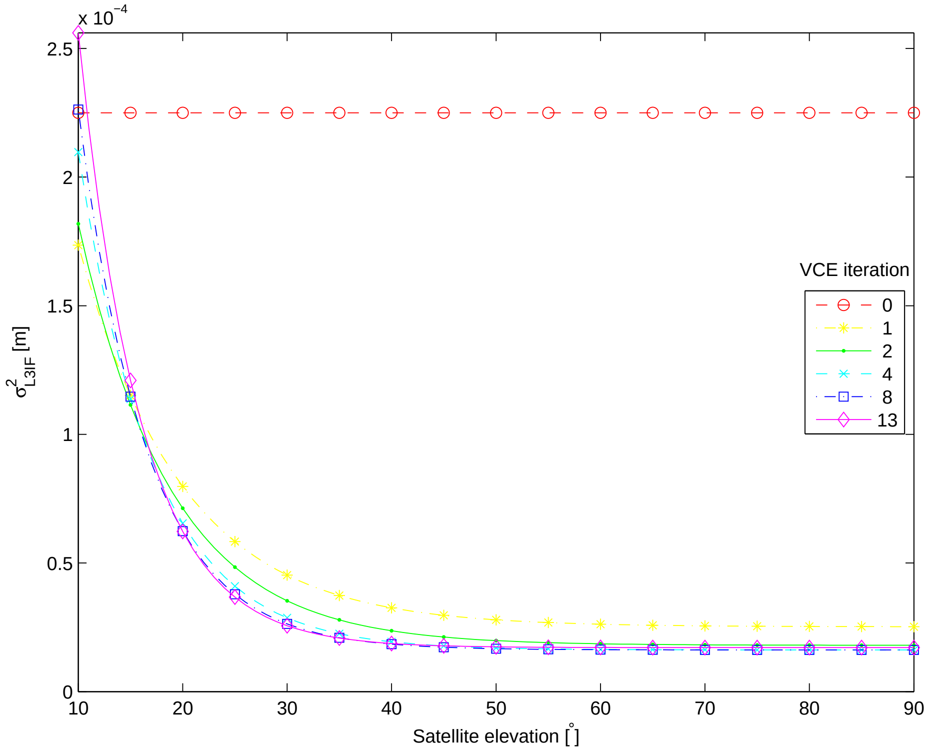

Figure 8.4: VCE iterations for phase-only model; the elevation dependence becomes more pronounced after each iteration. The process converges after 13 iterations.

the 1-dimensional tests. For the data at hand the probability of false alarm for the LOM test (α_0) is 0.04 on average, and the LOM test rejection rate of 3% closely matches this number. Figure 8.5(b) repeats the measurement residuals (dots) versus the satellite elevation for the converged stochastic model, as well as twice their formal standard deviation (dashed lines). The elevation dependence of the residuals, which was already present in fig. 8.2(a) is now mirrored in the formal standard deviations, which give a close fit over the whole elevation range. Based on these figures, the VCE can be considered a success. Figure 8.6 shows the unknown parameters that were estimated while keeping the receiver position fixed. No reference values are available for these parameters, but the computed values do not show any strange behavior. The receiver clock offset, expressed in meters, is small and quite stable as could be expected from the hardware setup. The carrier phase ambiguities, estimated as real-valued constants, converge quickly to their final values. The troposphere estimate shows typical magnitude and variation in time. Since the ionosphere estimates are biased (see eqs. (4.23) and (4.26)) only the variation over time can be assessed and is also typical. The ionosphere delays are highest for low-elevation satellites and around local noon.

8.2.2 Static positioning

With the stochastic model in place the positioning itself can now be performed, starting with static positioning for the month of June, 2012. Differences between the day-to-day results are quite small. Therefore, results for June 1 are here presented to illustrate the daily

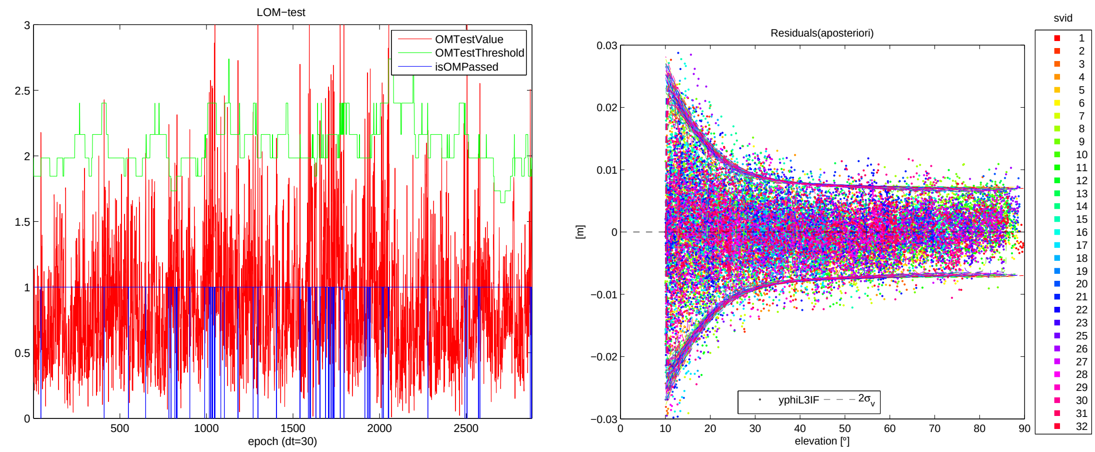

(a) Normalized Local Overall Model (LOM) test; mean value is close to expectation of 1

(b) L3IF carrier phase residuals versus elevation; formal 2-sigma values fit well to residuals

Figure 8.5: Phase-only results with fixed position and converged stochastic model for June 1, 2012 measured at Delft

performance, before the aggregated results for the whole month of June are presented for a general more detailed performance analysis. Figure 8.7 shows the estimated positioning solution w.r.t. the accurate reference position in the East, North and Up directions, with their formal standard deviations in lighter shaded patches, versus the observation time. The left pane only shows the first hour of the processing run to highlight the initial performance and convergence behavior, while the right pane shows all 24 hours and, by changing scaling of the y-axis, highlights the performance after the initial convergence.

Several different periods can be distinguished in these time series of estimated positions. The left pane shows that during the first 5 minutes or so, the solution varies erratically and the errors change sign several times. After 5 minutes the errors start to vary more slowly and begin to converge to the reference position. The position errors drop below 10 cm after some 20 minutes and below 5 cm after 30 minutes, and the errors remain at this level for some time. However, the right pane shows that the solution keeps improving in the long run. The different convergence performance of the Up component w.r.t the horizontal components also becomes apparent. Not only does it take longer for the error to drop below 2 cm (1h45m vs. 1h20m) and 1 cm (7h30m vs. 2h20m for the horizontal components), but the Up component also shows an excursion of about 6 mm over the second half of the day. The final position errors are 1.5 mm in the Up direction and below 1 mm for each of the horizontal directions. The poorer performance of the position estimation in the Up direction is due to the geometry of the positioning problem, which is disadvantageous for height estimation as evidenced by the VDOP results in fig. 8.1(f).

Comparison of the position errors to the formal standard deviations of the position reveals that during the first 30 minutes the position errors are at times larger than the standard deviation but always in the same order of magnitude; after the first 30 minutes the standard deviation becomes much smaller while the position errors decrease less drastically, leading to position errors of up to 10 times the size of the formal standard deviations. This effect will now be analyzed in more detail by considering the results of a number of positioning

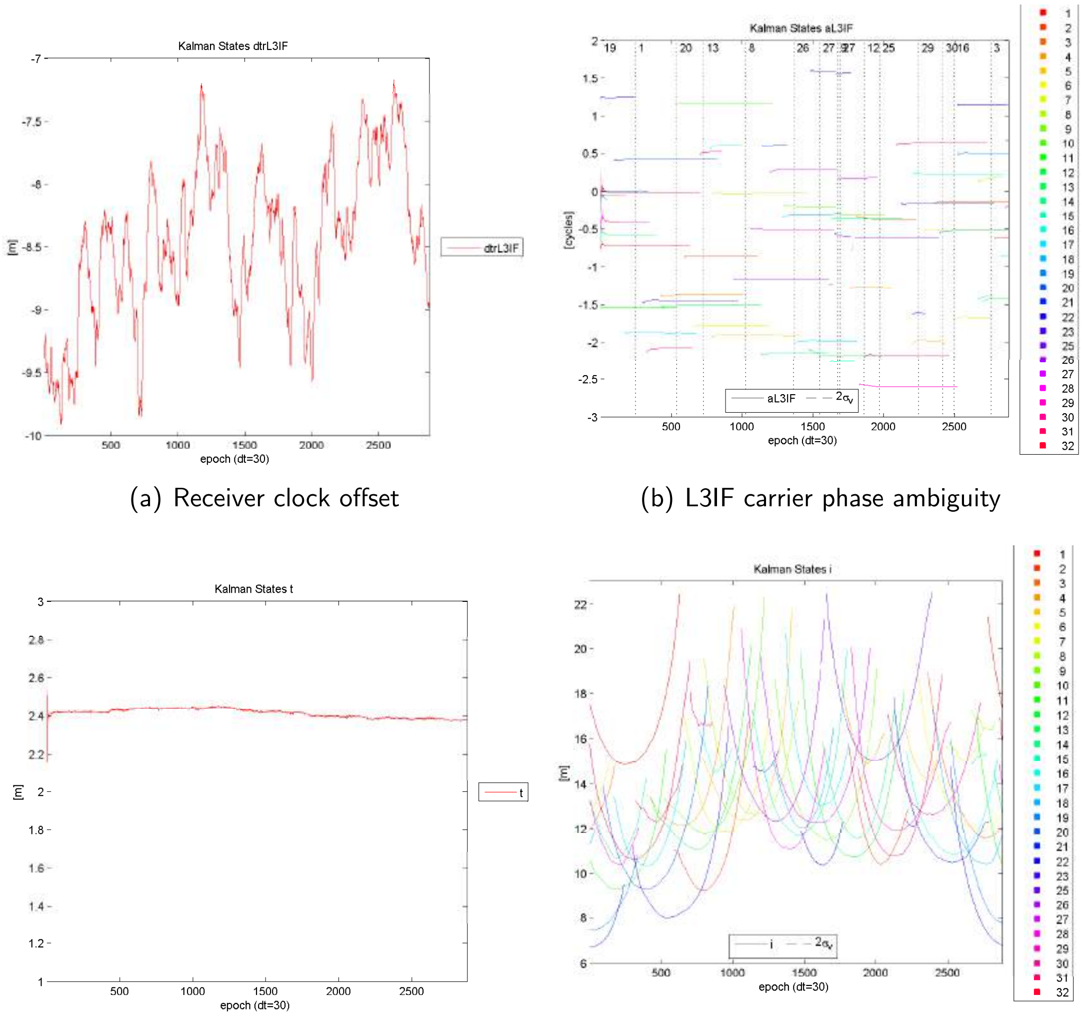

(a) Receiver clock offset

(b) L3IF carrier phase ambiguity

(c) Troposphere delay

(d) Ionosphere delay; values are biased by ambiguities

Figure 8.6: Estimated parameters fixed coordinates June 1, 2012 measured at Delft

filter runs together.

Figure 8.8 shows the positioning error time series for all 30 daily solutions for the month of June 2012, in East, North and Up directions (solid lines, days are differentiated by color hue). Each of the solutions behaves similar to the results previously seen in fig. 8.7; the position errors are quite large when the positioning filter just starts and the estimated position converges to the reference position as the observation period increases.

The position errors, different for each day and random to a large extend, still show some systematism. This is especially clear between the 2nd and 8th hour into each run. E.g. the Up component shows a positive error of on average 2 cm after 2 hours of processing, which is mostly gone after 8 hours of processing. The size of the error as well as the exact location in time varies for each day but seems correlated over different days evidenced by the fact that the lines corresponding to consecutive days (displayed by neighboring color hues) lie close to each other. Possible reasons for these position errors and their behavior

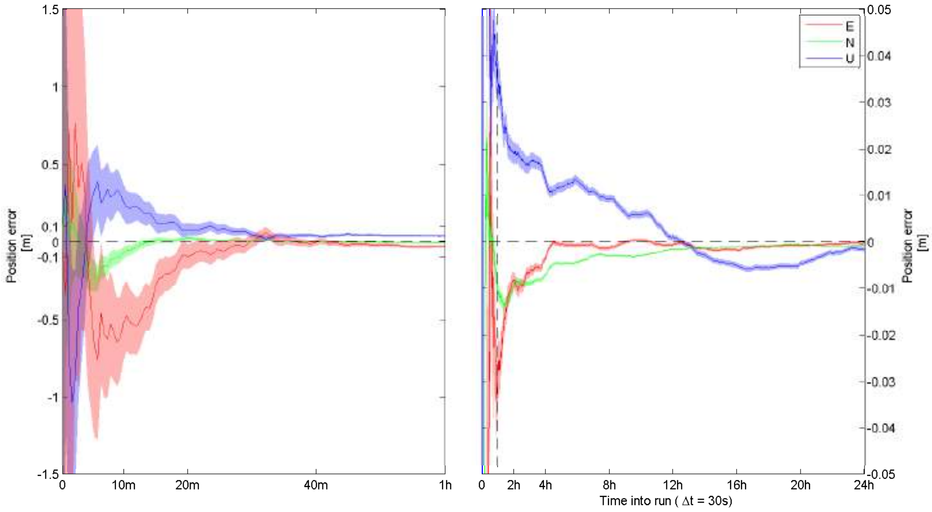

Figure 8.7: ENU position errors (solid lines) and formal standard deviation (shaded patches) for static positioning of data for June 1, 2012 in Delft

are (carrier phase) multipath, satellite hardware delays and receiver antenna delays, which repeat every sidereal day along with the GPS constellation. Since the processing starts at the beginning of each GPS day, the error signal is translated by about 4 minutes each day. The size of the resulting position error, which dependents on the observation period, thus also changes each day. These time-varying errors are also observed and further analyzed in the kinematic position computations. The final position errors are at centimeter level, and slightly higher in the Up direction. A slight bias in each of the directions can also be observed; the reference position *does* lie within the spread of the individual solutions.

The formal standard deviations are also presented in fig. 8.8 (dashed lines), while different for each run, the behavior as well as the numerical values are quite similar for each of the runs. As we saw before the standard deviations are in the same order of magnitude as the position errors as the filter starts, but become much smaller than the position errors as more observations are accumulated. To further compare the formal precision of the position solution to the empirical distribution of the estimated positions, the root-mean-square (rms) position error of the 30 daily solutions is computed at each epoch into the run. The rms is used instead of the standard deviation because we are interested in the distribution of the solution about the reference position, not the distribution about the mean estimate. The computed empirical rms is now compared to the mean formal standard deviation in fig. 8.9. The North direction quickly asserts itself as the best determined direction, initially followed by the Up direction and the East direction being most poorly determined. The empirical rms in North, Up and East direction drops below 5 cm after 10, 20 and 30 minutes respectively. After about 35 minutes the lines corresponding to the East and Up directions cross each other, after which the East direction catches up to the North direction after about 1h45m and both decrease further to some 3-4 mm, while the Up directions decreases more slowly to about 5 mm. As shown in chapter 4 the receiver position cannot be computed with the phase-only model from a single measurement epoch. A rigorous method to solve this problem is to initialize the (Kalman) filter using two measurement epochs. However, in the

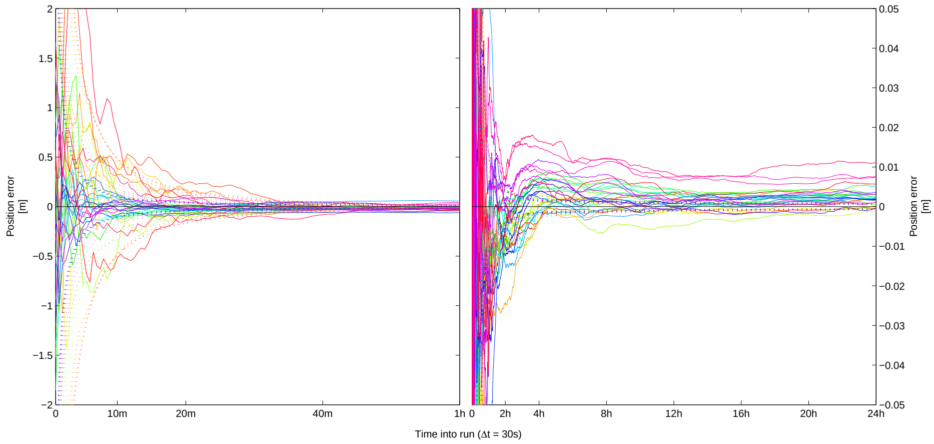

(a) East

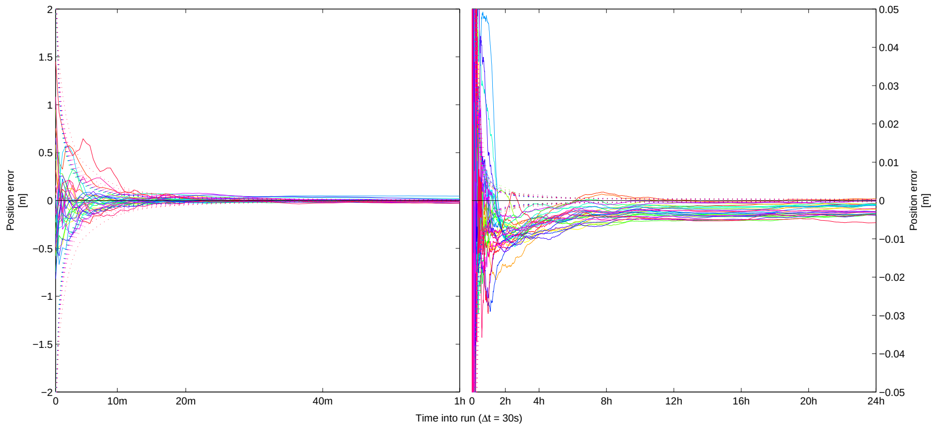

(b) North

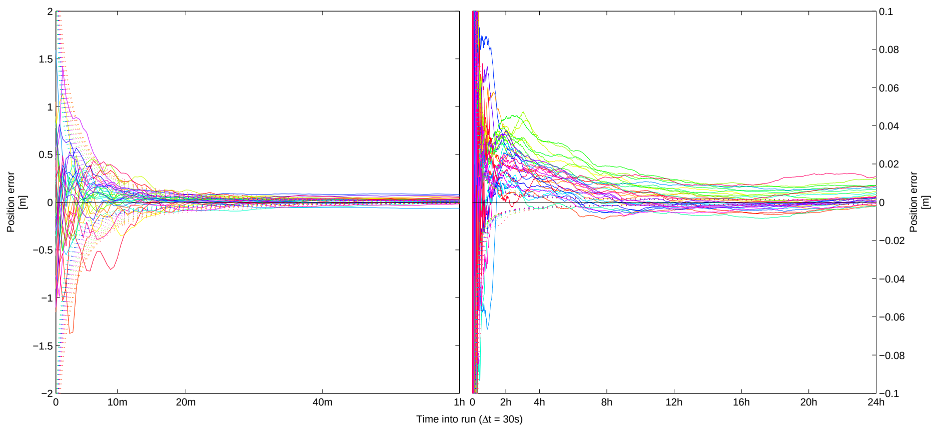

(c) Up

Figure 8.8: Phase-only static positioning errors (solid lines) and formal standard deviations (dashed lines) for 30 daily runs for DLF1 station during June, 2012; results show both systematic and random effects.

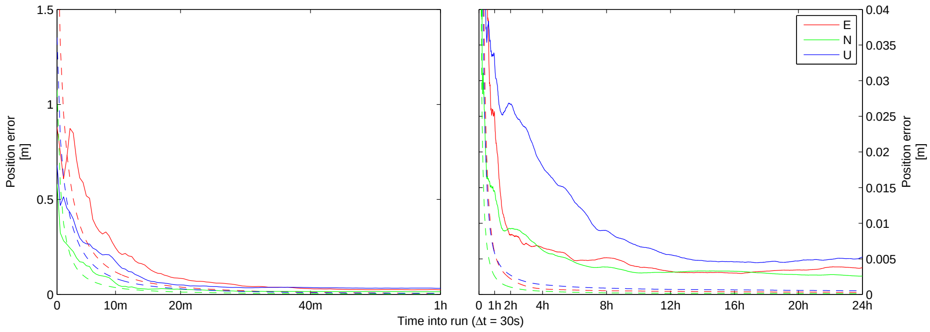

Figure 8.9: East, North and Up empirical rms error (solid lines) and formal standard deviation (dashed lines) for static phase-only processing of June, 2012; formal standard deviations decrease to much smaller values than empirical errors

software implementation a more practical approach is used that initializes the filter using the code observations of a single epoch. The weight given to the code solution is very low to minimize its impact on the eventual phase-only positioning, but it can still be observed in fig. 8.9 where the empirical rms error (rmse) is initially smaller than the formal standard deviation (std). After a few epochs this effect is no longer visible, and it obviously does not appear in the code-only or code+phase models later in this chapter.

The figure shows that the empirical rms fits the formal standard deviation reasonably well during the first 30 minutes or so, although the formal std. is somewhat smaller than the empirical rms. However, as the observation period increases this discrepancy increases as well, and after a few hours the formal standard deviation clearly does not represent the empirical distribution any longer. This discrepancy in the results could be caused by two related and in practice often difficult to distinguish problems. First, remaining unmodeled systematic effects, e.g. limitations of the Earth tide models, can cause biased results, and depending on the time behavior of the effect, these biases can be of a temporary or permanent nature. Secondly, time correlated (random) errors such as those resulting from the tracking loops of the receiver cannot properly be accounted for in the stochastic model of the recursive least squares algorithm. In fact the recursive least squares method (and also the Kalman filter) is based on the assumption that the measurements are not correlated in time. This problem will be treated further in section 8.2.4.

8.2.3 Kinematic positioning

If the position of a moving receiver needs to be determined without knowledge of its dynamic behavior, a kinematic processing strategy should be adopted. Figure 8.10 shows the results for the kinematic positioning model for June 1, 2012. Compared to the static results shown in fig. 8.7 the kinematic results are noisier, the accuracy improves more slowly over time, and the position errors remain larger after the solution has converged. Additionally, fig. 8.10 shows that after about 15 hours, the position solution degrades significantly for a period of little over an hour. This degradation can be found in each of the daily positioning results to some extend as will be shown in fig. 8.13. However, first a much more severe degradation will be treated that occurred on 2 days during the month

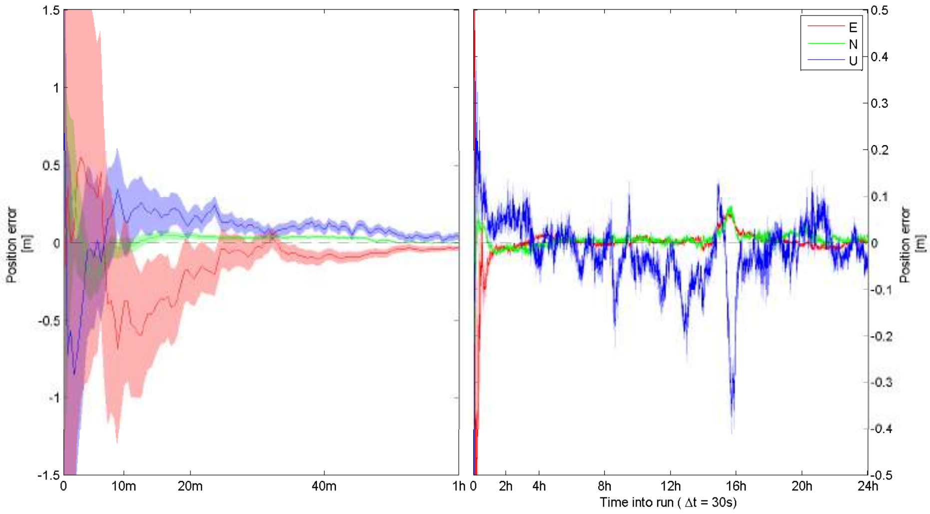

Figure 8.10: ENU position errors (solid lines) and formal standard deviation (shaded patches) for kinematic positioning of data from June 1, 2012 in Delft

of June, see fig. 8.11.

On June 21 and June 27, an event caused significantly degraded carrier-to-noise ratios (C/N_0) for all satellites and signals tracked by the DLF1 receiver, and a complete loss of observations for almost all satellites during a short period of time. This type of performance degradation could be caused by a source of radio frequency interference in the GPS frequency bands (or close to these bands if it can overcome the frequency filtering) that is strong enough to cause saturation of the receiver front-end and disrupt the receiver tracking loops (de Bakker, 2007), but other sources such as a disturbance of the antenna cabling or signal blockage cannot be excluded. Figures 8.12(a) and 8.12(b) show the observed C/N_0 for the L1CA and L2P signals during these events, and reveals that the C/N_0 on both frequencies is impacted so severely that it drops below the tracking threshold for the majority of satellites. Figures 8.12(c) and 8.12(d) and figs. 8.12(e) and 8.12(f) show the satellite signal availability and lock-of-loss indicators during these events for, respectively, the original 1 Hz and decimated 30 second data which was later processed. For each of the GPS satellites, indicated by their PRN numbers on the y-axis, all available pseudo ranges are presented as circles, with a center dot if phase observation are also present. Red crosses are presented if the receiver indicated a loss-of-lock on that frequency. The figures show that, on June 21, the receiver either misses observations and/or experiences loss-of-lock for all satellites during the possible interference event. On June 27, PRN12 and PRN17 are the exceptions, while the receiver again misses observations or indicates a loss-of-lock for all other satellites. It is interesting to note that the L5 signal, only available on PRN01 and PRN25 at the time of observation, is similarly impacted as the traditional L1 and L2 signals. Generally, when a receiver loses lock of a carrier phase signal, the corresponding ambiguity needs to be estimated anew when the receiver starts to track the carrier phase again. Therefore, if an event causes a loss-of-lock for all satellite signals, while processing all unknown parameters except the carrier phase ambiguities kinematically, the positioning filter is effectively restarted, since all parameters are estimated again without

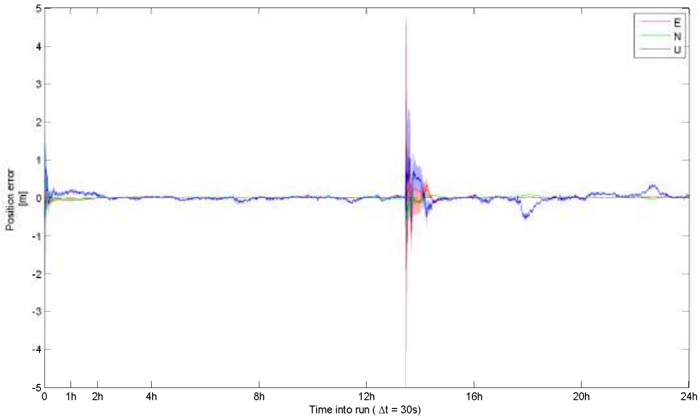

(a) June 21, 2012

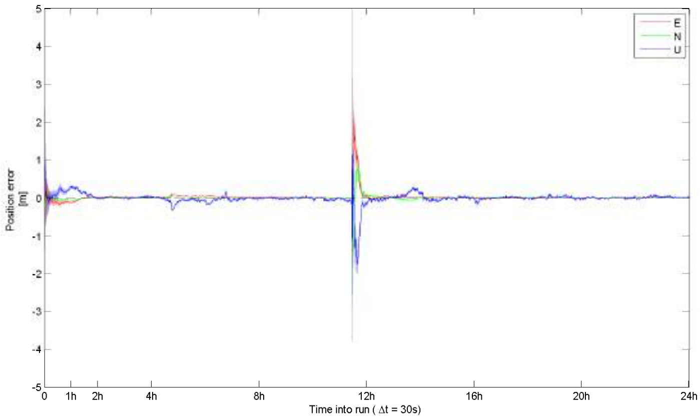

(b) June 27, 2012

Figure 8.11: Phase-only kinematic positioning errors (solid lines) and formal standard deviation (shaded patches) during probable interference event

prior knowledge. This is exactly what happens on June 21 around 13:25. On June 27, a slightly better performance might be expected since 2 satellites (PRN12 and PRN17) are still being tracked during the probable interference event. However, closer inspection of the processing result with a fixed receiver position reveals that in fact cycle-slips occur on the carrier phase observations for these two satellites. For this reason June 21 and June 27 are excluded from the following convergence analysis, as a restart of the positioning for two runs at different times would only complicate matters. For the static positioning results this problem did not present itself since the position solution does not degrade if no observations are present, additionally the newly estimated ambiguities converge relatively fast when a good position estimate is already present. For the kinematic case presented here the given situation illustrates the importance of the work started in chapter 7 and continued in Teunissen and de Bakker (2013) of (integer) cycle-slip detection and ambiguity resolution in the time-differenced model.

Figure 8.13 shows the positioning errors for the remaining 28 daily solutions. The daily solutions are quite comparable to each other, the position errors in the Up direction drops

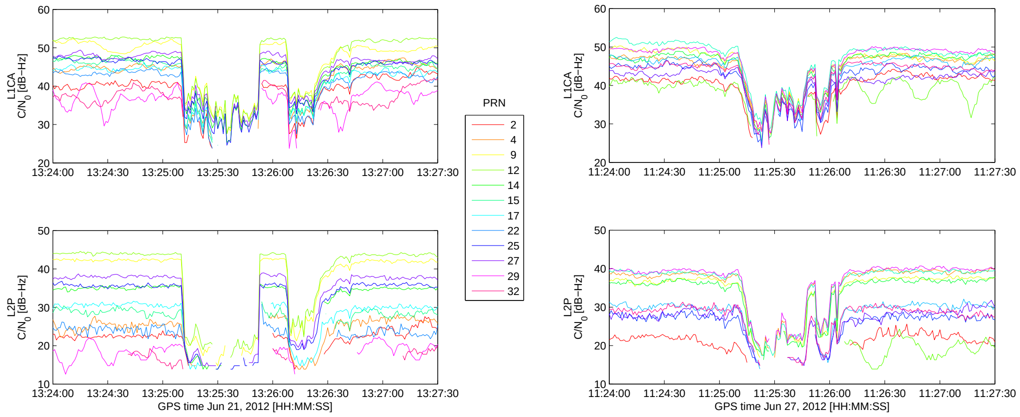

(a) Carrier-to-noise ratio (b) Carrier-to-noise ratio

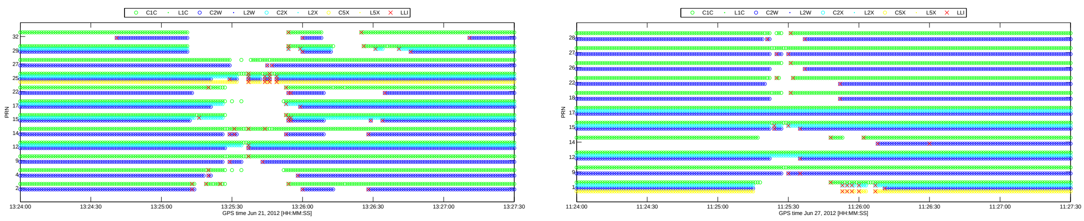

(c) Satellite signal availability and loss-of-lock indicators at 1Hz (d) Satellite signal availability and loss-of-lock indicators at 1Hz

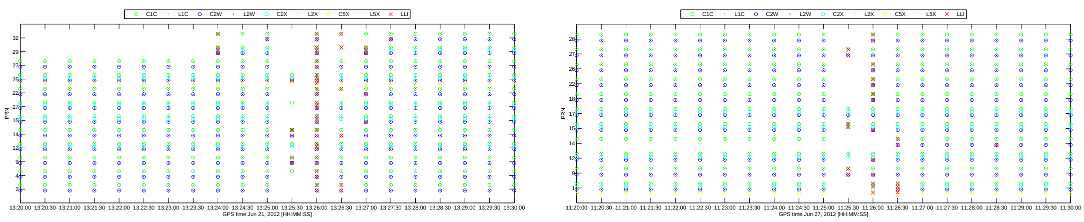

(e) Satellite signal availability and loss-of-lock indicators at 30s (f) Satellite signal availability and loss-of-lock indicators at 30s

Figure 8.12: Carrier-to-noise ratios and signal availability for DLF1 receiver during probable interference event on June 21 and June 27, 2012. The C/N_0 values drop on all three frequency bands (only two are shown) and the receiver loses track of almost all satellite signals.

below 50 cm within 30 minutes for all runs, and faster for the horizontal directions. Each of the directions show some systematic behavior best visible after about the 1 hour into each run, where all daily solutions are biased in a similar manner, just like we observed in the static positioning results, but the more random behavior here takes over much sooner than in the static case, and after about 3-4 hours the biases can no longer be distinguished. As previously noted in fig. 8.10 the position solution degrades between 15 and 16 hours of processing, visible in each of the daily results, most notably in the Up direction, but to a lesser extend also in the North direction. The exact time at which the maximum position error occurs differs slightly for each run, which is directly related to the GPS constellation which repeats every siderial day, i.e. about 23 hours 56 minutes and 4.1 seconds. Figure 8.14 shows the same daily results, but now versus the time of siderial day in which the degradation of each daily run is indeed closely aligned. (Note that the repetition is only a close approximation, since length of sidereal day is not divisible by the measurement interval of 30 seconds, and moreover the exact orbital period differs slightly for each GPS satellite.) This systematic degradation of the position solution was not observed in the static positioning results for two reasons. First, the static solution has by this time converged to such a high precision, that new observations only have a small impact on the solution, protecting it from temporally degraded observations. Secondly, the stronger static model helps the integrity monitoring algorithm to identify the corrupted observation(s) for which the model can than be adapted. In this case PRN25 and 27 have larger measurement residuals during this period, given the daily repeating pattern most likely caused by multipath, and are rejected from the static positioning solution. The weaker kinematic model is not able to identify these satellites before they cause the position to degrade, but they are identified at some point, after which the position solution starts to improve again.

Figure 8.15 shows the empirical rms position error (solid lines) and the mean formal standard deviation (dashed lines) for the phase-only kinematic processing in the East, North and Up directions. As previously observed, the empirical rms and formal standard deviation fit reasonably well when the processing is just started, but the formal standard deviations improve faster and to a higher precision than the empirical results. In the horizontal directions the standard deviation decreases to 5-6 mm, while the rms does not improve beyond 1-2 cm. In the Up direction the standard deviation decreases to 2-3 cm while the rms stays in the 4-6 cm range. Additionaly, we see a peak up to 15 cm related to the probable multipath problem discussed above. Although the discrepancy between the formal and empirical quality measures is less pronounced for the kinematic case than for the static case, it still needs to be addressed in a similar way. This is the subject of the following section.

A final observation about fig. 8.15 is that the performance degrades somewhat at the end of the day. This is due to the use of daily orbit and clock products from the IGS which lead to degraded interpolation performance at the date change.

8.2.4 Carrier phase bias estimation

In both the static and kinematic positioning results presented so far, a common problem was found that the formal standard deviation decreases to much smaller values that the

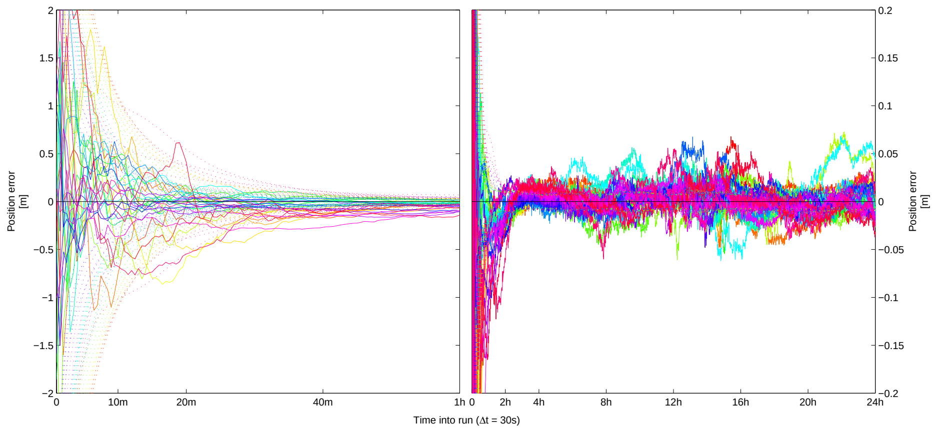

(a) East

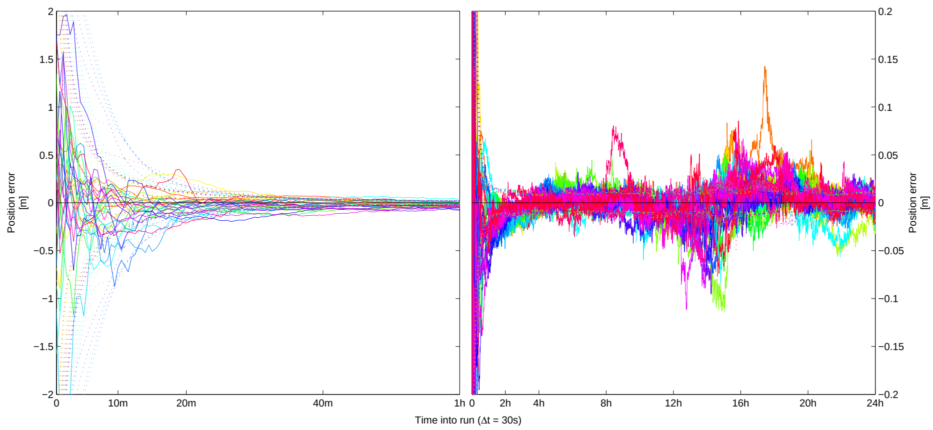

(b) North

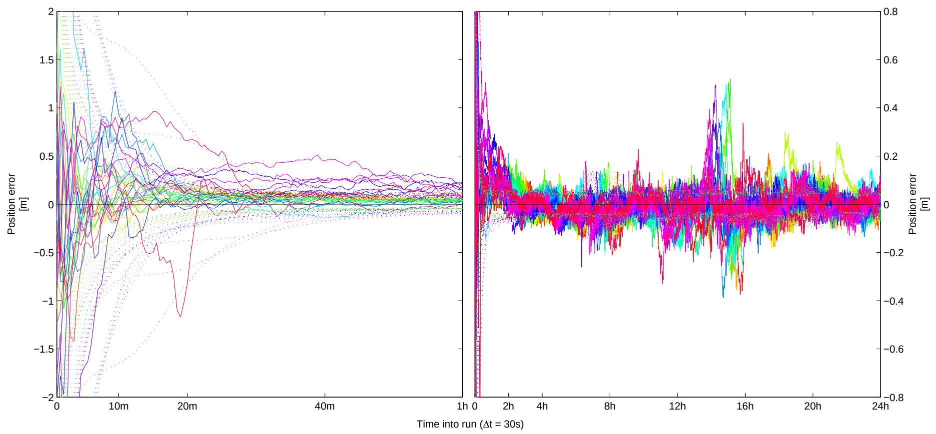

(c) Up

Figure 8.13: Phase-only kinematic positioning errors (solid lines) and formal standard deviations (dashed lines) for 28 daily runs for DLF1 station during June, 2012

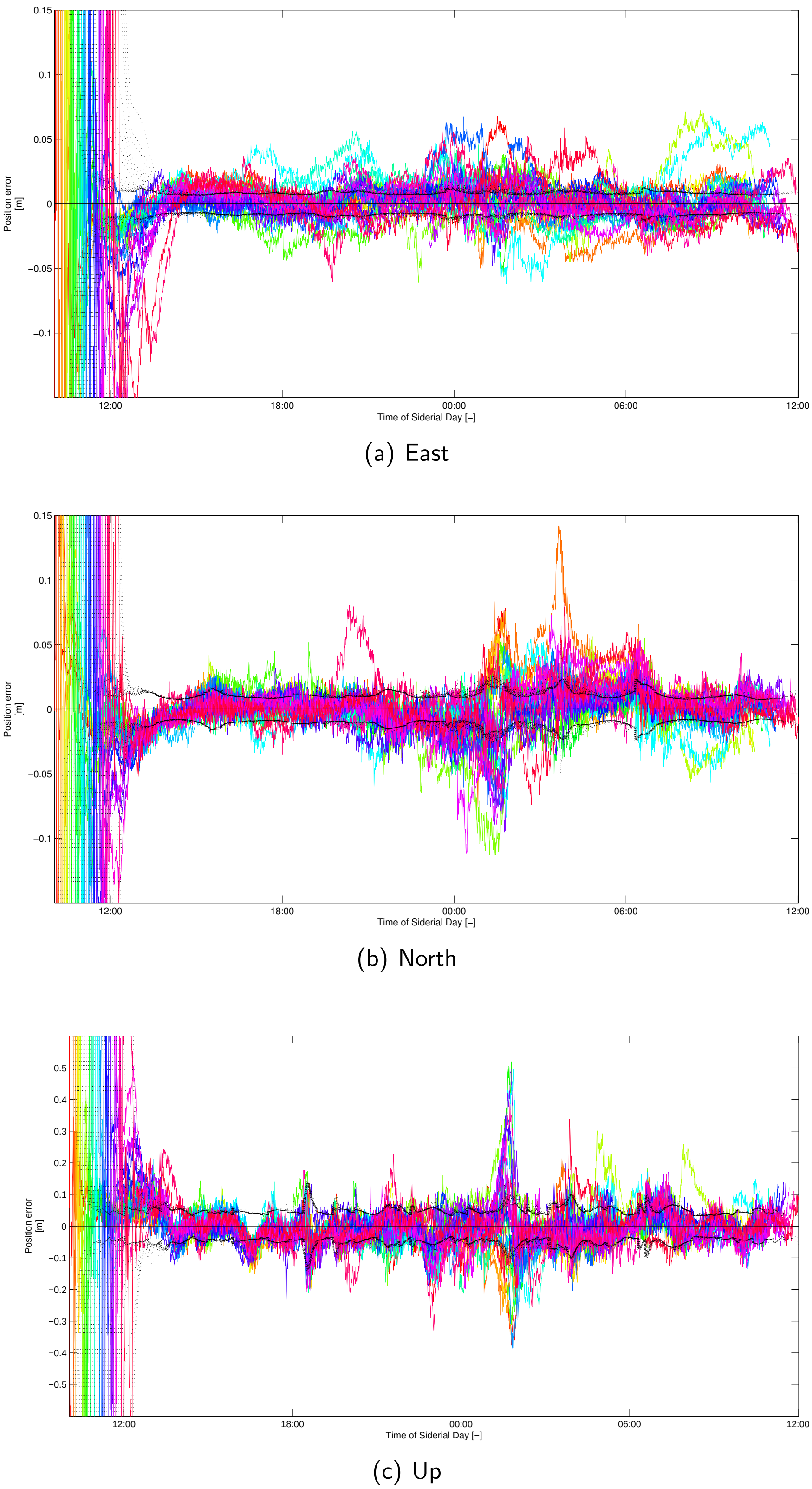

Figure 8.14: Phase-only kinematic positioning errors (solid lines) and formal standard deviations (dashed lines) as a function of the siderial time of day for 28 daily runs for DLF1 station during June, 2012; a daily repeating pattern can be distinguished.

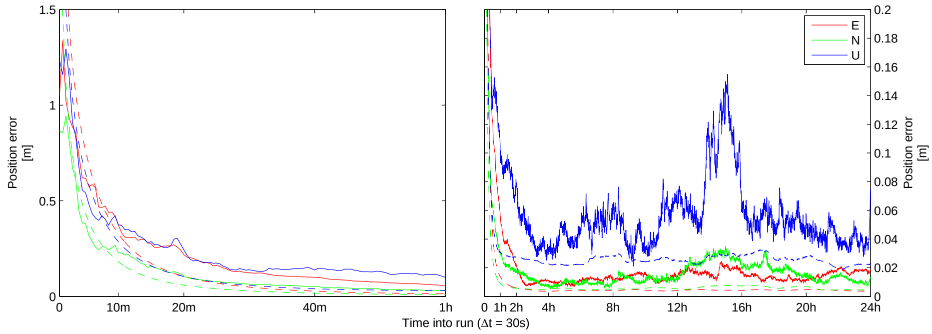

Figure 8.15: East, North and Up empirical rmse (solid lines) and formal standard deviation (dashed lines) for kinematic phase-only processing of June, 2012; the position errors in the up component are larger than the formal standard deviation.

rms of the empirical position errors as the filter converges. This problem is due to the fact that the recursive least squares algorithm (and the Kalman filter) is based on the assumption that the observation errors have no time correlation, while the actual errors are not completely uncorrelated in time.

The solution then is to adjust the functional model in such a way that it captures the time correlated errors to a large extend and leaves only uncorrelated measurement errors for the stochastic model. To address this problem, we will now shortly revisit the phase-only estimation models treated in chapter 4, starting with the complete, rank defect phase-only model for a single epoch:

$$E\left\{\begin{bmatrix}\Delta\boldsymbol{\phi}^S_{r,L1,k}\\ \Delta\boldsymbol{\phi}^S_{r,L2,k}\end{bmatrix}\right\}=\begin{bmatrix}-\mathbf{e}^{S*}_{r,k} & \mathbf{m}_m & \mathbf{u}_m & \mathbf{u}_m & & -\mathbf{I}_m & \mathbf{I}_m & & -\mathbf{I}_m & \\ -\mathbf{e}^{S*}_{r,k} & \mathbf{m}_m & \mathbf{u}_m & & \mathbf{u}_m & -\gamma\mathbf{I}_m & & \mathbf{I}_m & & -\mathbf{I}_m\end{bmatrix}\begin{bmatrix}\Delta\mathbf{r}_r\\ T_{Z,r,k}\\ dt_{r,k}\\ \delta_{r,L1,k}\\ \delta_{r,L2,k}\\ \boldsymbol{\mathcal{I}}^S_{r,k}\\ \mathbf{A}^S_{r,L1}\\ \mathbf{A}^S_{r,L2}\\ \boldsymbol{\delta}^S_{L1,k}\\ \boldsymbol{\delta}^S_{L2,k}\end{bmatrix} \tag{8.3}$$

The term $\boldsymbol{\delta}^S_{L1,k}$ and $\boldsymbol{\delta}^S_{L2,k}$ accounts for delays that can differ for each frequency, each epoch and each satellite. In chapter 4 we took into account a constant part, which then becomes lumped with the constant ambiguity term, a satellite clock offset which can be corrected by external data, and a white noise component that is accounted for in the stochastic model. Now we consider an additional component that changes over time but cannot be corrected with external data, such as multipath, or residual time-correlated clock errors.

The L1 and L2 delays are transformed to ionosphere and ionosphere-free ($\boldsymbol{\delta}^S_{L3IF,k}$ and $\boldsymbol{\delta}^S_{LI,k}$) combinations in eq. (4.22), and the ionosphere combination was lumped with the ionosphere parameter in eq. (4.23). Since the ionosphere parameter is allowed to change freely over time, so are the other errors in the ionosphere combination. The ionosphere-free combination of these errors is lumped with the ionosphere-free ambiguities in eq. (4.28). Since the ambiguities are estimated as constants, any variations in $\boldsymbol{\delta}^S_{L3IF,k}$ create (time-correlated) errors in the model.

Therefore, the model can be improved by allowing the carrier phase bias parameters to change over time. However, if we leave these errors to change over time freely, i.e. if we estimate them as kinematic parameters, we end up with a model without any redundancy which cannot be used to estimate the position or other parameters of interest. For this reason we introduce a dynamic model for the carrier phase bias parameters that constrains the time variation. Appendix B treats the convergence behavior of several dynamic models, and presents the relation between the measurement noise, the process noise and the variance of the estimated parameters in a fully converged filter. Since the lumped carrier phase bias parameters do *not* have a zero-mean property we will use the random walk model.

To determine an appropriate value for the process noise, the equations in appendix B are used to get a first rough estimate. The approach is then to adjust this value and reprocess the data until the formal standard deviation of the position estimates matches the empirical distribution of the positioning results. This approach turns out to work quite well, because even though the estimated (position) parameters do change slightly due to the model changes, the empirical (converged) distribution over the 30 days does not change much. The formal distribution does change significantly as expected and, with a process noise standard deviation of 1 mm, fits the empirical results much better as is evident from figs. 8.16 and 8.17 for both static and kinematic positioning.

The kinematic positioning performance degradation at the end of the day, earlier observed in fig. 8.15, is now more pronounced. This is not surprising since the time-varying phase-biases also lead to a position solution that can change more easily with new observations.

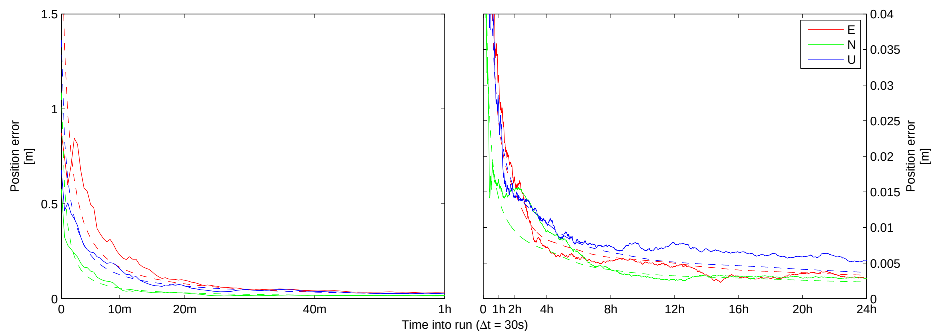

Figure 8.16: East, North and Up empirical rmse (solid lines) and formal standard deviation (dashed lines) for static phase-only processing with time-varying phase-biases for June, 2012; agreement between formal and empirical measures is now much better.

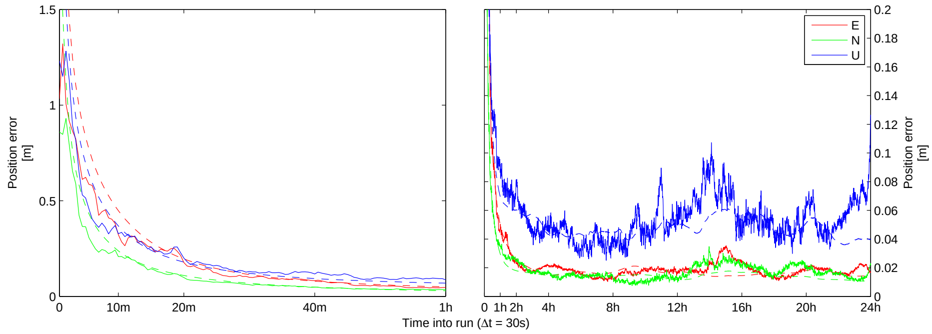

Figure 8.17: East, North and Up empirical rmse (solid lines) and formal standard deviation (dashed lines) for kinematic phase-only processing with time-varying phase-biases for June, 2012; formal and empirical measures agree very well.

8.3 Code-only processing

8.3.1 Fixed coordinates - Variance Component Estimation

In this section VCE is performed for the code-only model with the following settings:

- The receiver coordinates are kept fixed at accurate reference values.
- The receiver clock offset and troposphere zenith delay are estimated kinematically.
- The slant ionosphere delay is estimated kinematically for each satellite.
- The observations from different satellites and different epochs are assumed to be uncorrelated.

The observation model then becomes equivalent to (note that this has become an epoch-by-epoch processing model, since all remaining parameters are estimated kinematically):

$$E\left\{\left[\underline{\Delta \boldsymbol{P}}^{S}_{r,L3,k}\right]\right\} = \begin{bmatrix} c\mathbf{u}_m & \mathbf{m}^{S}_{r,k} \end{bmatrix} \begin{bmatrix} \overline{\delta t}_{r,L3,k} \\ T_{Z,r,k} \end{bmatrix}; \quad D\left\{\left[\underline{\Delta \boldsymbol{P}}^{S}_{r,L3,k}\right]\right\} = \boldsymbol{Q}_{\boldsymbol{P}^{S}_{r,L3,k}} \tag{8.4}$$

As before, first the observations are grouped in elevation bins, then the almost unbiased estimator is applied to each bin and finally an elevation dependent function is fitted to the bin values. For the elevation dependent function an exponential function is selected for its good fit to the data at hand. The VCE is iterated until convergence. The Variance Component Estimation process is initialized with the following scaled identity matrix:

$$\boldsymbol{Q}_{\boldsymbol{P}_{L3}} = \sigma^2_{\boldsymbol{P}_{L3}} \boldsymbol{I} \text{ with } \sigma_{\boldsymbol{P}_{L3}} = 1.5\,\mathrm{m}. \tag{8.5}$$

Figure 8.18(a) shows the results of different iterations of the VCE. The whole process has already converged after just three iterations. Figure 8.18(b) shows the results of the elevation dependent function fit for the final iteration of the VCE. A cosecant function has been included to illustrate both the superior fit of the exponential function, but also that the cosecant function provides a reasonable alternative. Figures 8.18(c) and 8.18(d) show, respectively, the normalized LOM test and the measurement residuals of the ionosphere-free combination of the code observations. The mean value of the LOM test is 1.00 and the percentage of failed LOM tests, where the w-tests are not rejected, of 4.1 % is also very close to the mean probability of false alarm. The measurement residuals also fit very nicely to the 2-sigma formal precision, at all elevation angles. Figure 8.19 shows the estimated

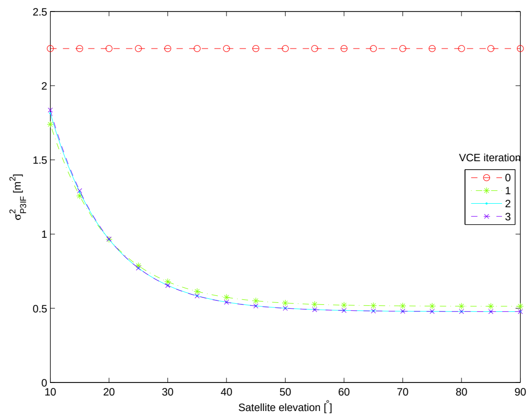

(a) VCE iterations; the process converges in 3 iterations

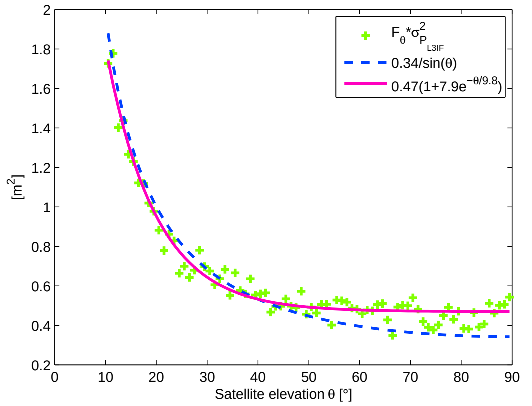

(b) VCE results after final iteration; both the exponential and cosecant function give a reasonable fit

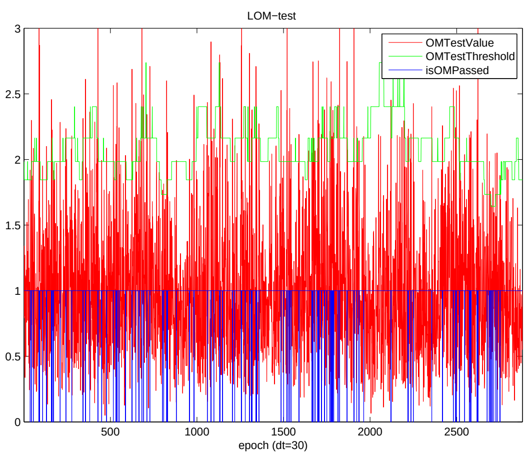

(c) Normalized Local Overall Model test

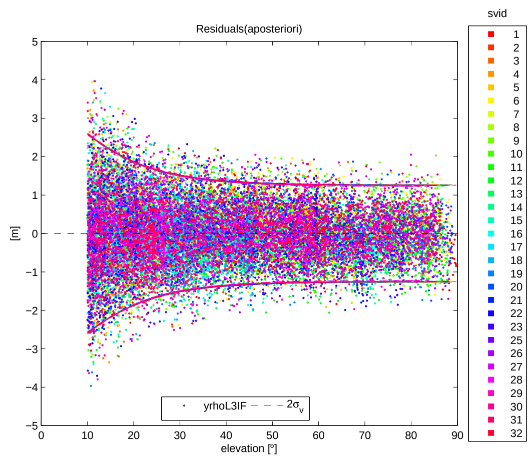

(d) L3IF pseudorange residuals versus elevation; the formal 2-sigma values correspond well to the empirical values

Figure 8.18: Estimated parameters fixed coordinates June 1, 2012 measured at Delft

filter states with their formal standard deviations in lighter shaded patches. If we compare these figures with the phase-only results in fig. 8.6, we find similarities in the shape of the curves, but there are 3 noticeable differences. First, the estimated parameters are much noisier, especially visible in the estimated troposphere and ionosphere delays (the receiver clock is already quite noisy in the phase-only solution). Secondly, the formal standard deviations are larger for the code-only processing. Both these differences follow directly from the lower precision of the code observables. And thirdly, the absolute values of the estimated ionosphere delays differ between the code-only and phase-only results. This last difference is in agreement with the findings in chapter 4, where to solve the rank defects in the phase-only model, the ionosphere delays where lumped with the ionosphere combination of the carrier phase ambiguities.

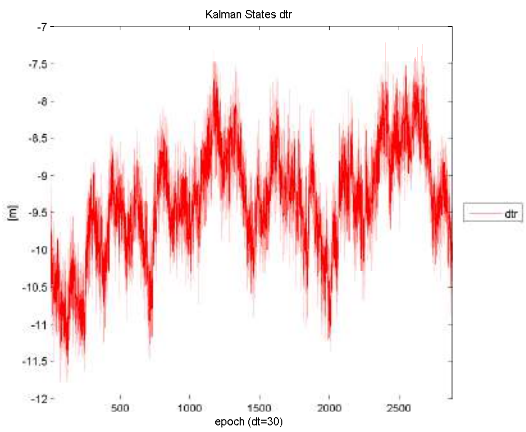

(a) Receiver clock offset

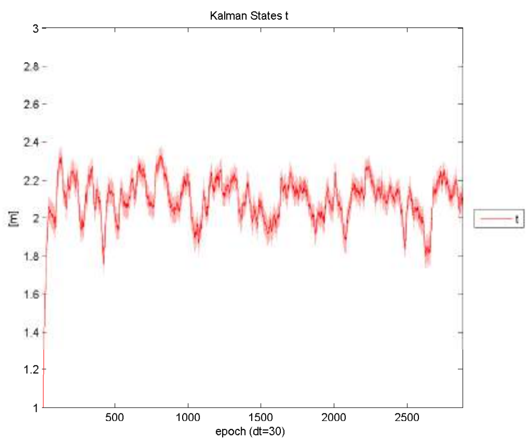

(b) Troposphere zenith delay

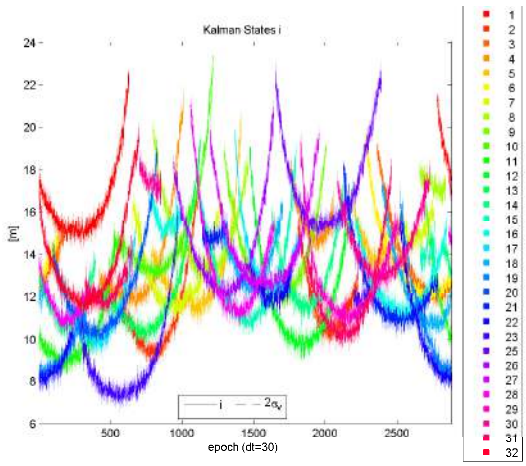

(c) Ionosphere slant delay on L1

Figure 8.19: Estimated code-only state parameters (solid lines) and formal standard deviations (shaded patches) for June 1, 2012 measured at Delft; the precision is poorer than for the phase-only model, but the estimated ionosphere is not biased by ambiguities

8.3.2 Static positioning

With the code-only stochastic model in place, the code-only positioning can now also be performed, starting with static positioning in this section. Figure 8.20 shows the positioning errors in the East, North and Up directions again, with their formal standard deviations in lighter shaded patches, versus the observation time. The initial errors in each direction are in the order of 1 meter. The error in North direction decreases to 10 cm in about 10 minutes and eventually improves to below centimeter level. In the Eastern direction it takes a full hour for the error to decrease to about 10 cm and it does not further improve. The Up direction again shows the poorest performance, the error stays at about 1 m during the first 3 hours, after which it starts decreasing to the final value of about 50 cm. The formal standard deviations again decrease faster than the empirical errors leading to position errors of close to 10 times the size of the formal standard deviation in especially the Up direction. Figure 8.21 shows the code-only static positioning error time series for all 30

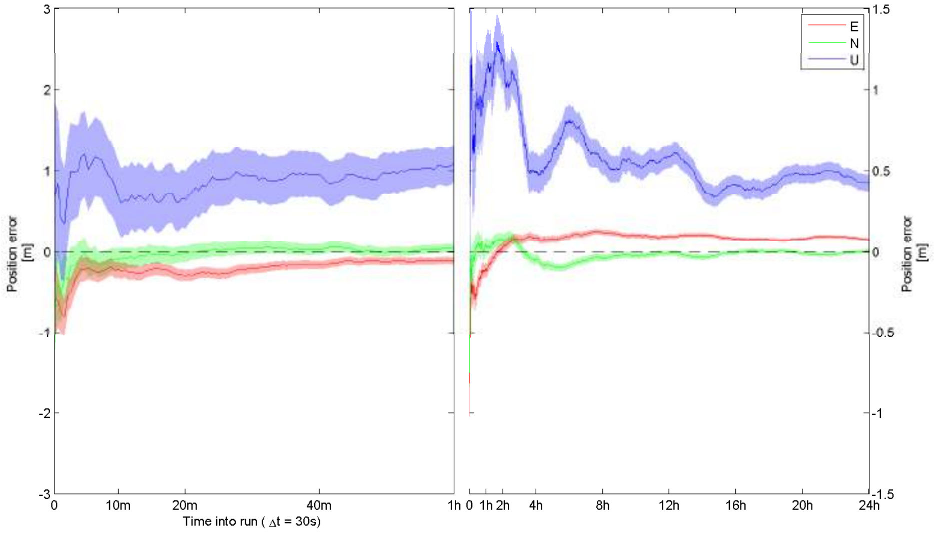

Figure 8.20: ENU position errors (solid lines) and formal standard deviations (shaded patches) for code-only static positioning of data from June 1, 2012 in Delft

daily solutions for the month of June 2012, in East, North and Up directions (solid lines, days are differentiated by color hue). The position errors show strong wave-like patterns that diminish over the day but do not disappear entirely, and additionally a significant position bias is present, especially in the Up component of about 50 cm. The amplitude and phase of the periodic errors changes slightly with each consecutive day, displayed by neighboring color hues. These patterns are caused by pseudorange delays that repeat each sidereal day with the GPS constellation, each processing run starting at a slightly different time of sidereal day (remember that the solar day is longer by 3 minutes and 55.9 seconds). There are several pseudorange delays that repeat with the GPS constellation including the satellite hardware delays (which change with the visible satellites), and the multipath and receiver antenna delays which change with the geometry of the satellites w.r.t. the user. The instantaneous impact of these pseudorange delays on the positioning solution will become clear from the code-only kinematic position computations in section 8.3.3. The formal standard deviations of the daily results, also presented in fig. 8.21 by the dashed lines, are very similar for each run. The formal standard deviation fits closely to the initial position errors in East and North direction as well as the initial spread in the Up direction, but it does not represent the systematic wave-like patterns over time, nor does it fit the 50 cm bias in Up direction. This is not surprising, because the standard deviation holds information about the random errors in the estimation, and cannot account for such strong systematic biases. These findings are confirmed by fig. 8.22 which shows both empirical rms position errors and the mean formal standard deviation as a function of the processing time based on the results from all 30 daily runs. The formal standard deviations initially fit the empirical rms errors in the horizontal directions, but quickly decrease to much smaller

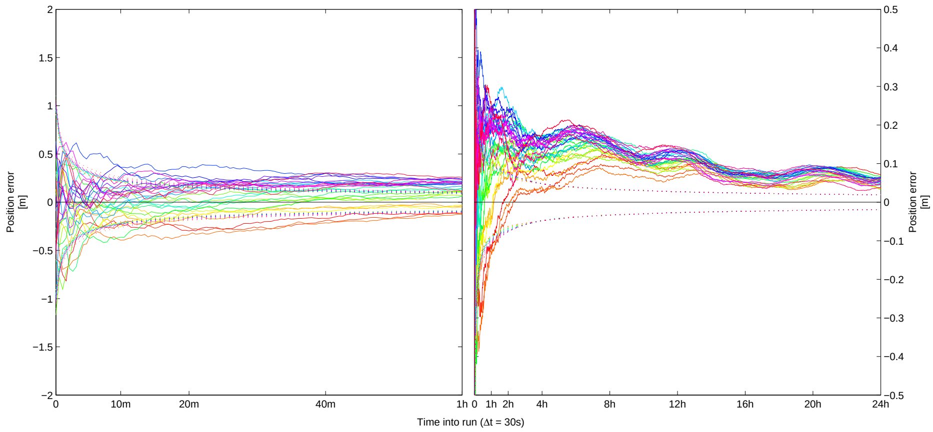

(a) East

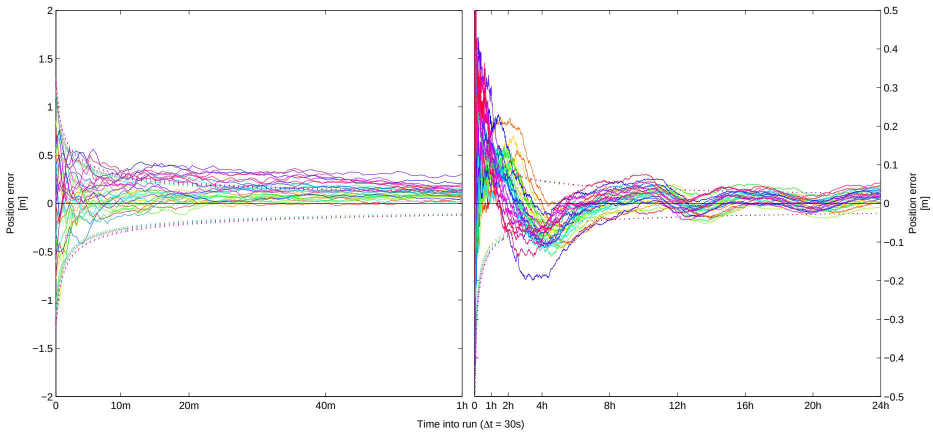

(b) North

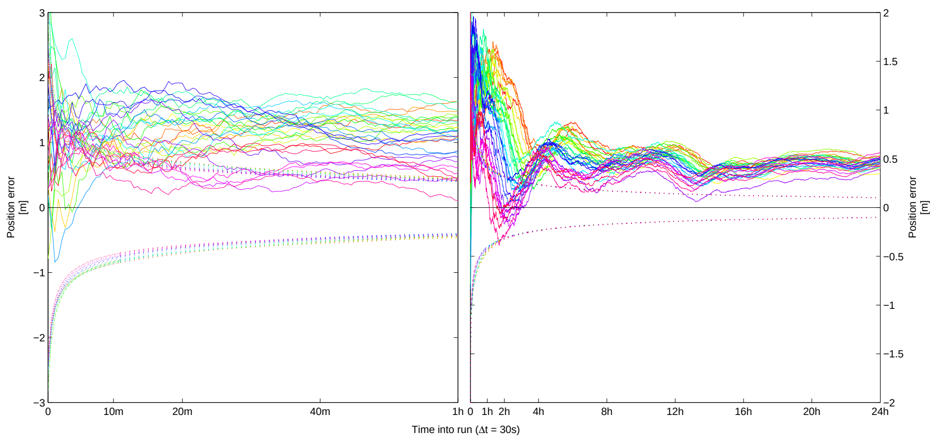

(c) Up

Figure 8.21: Code-only static positioning errors (solid lines) and formal standard deviations (dashed lines) for 30 daily runs for DLF1 station during June, 2012; strong systematic effects are visible.

values than the empirical rms errors; in the Up direction the mean standard deviation is already smaller than the empirical rms from the start. An approach to deal with the found

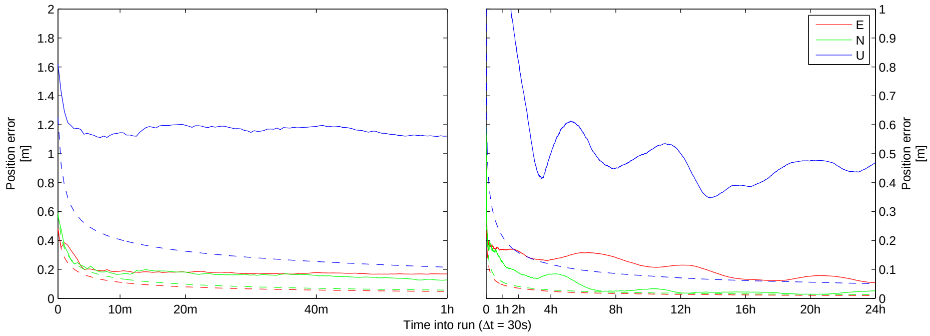

Figure 8.22: East, North and Up empirical rmse (solid lines) and formal standard deviation (dashed lines) for static code-only processing of June, 2012; the up component shows a large error not covered by the formal standard deviation.

systematic pseudorange delays that cause the biased results is detailed in section 8.3.4.

8.3.3 Kinematic positioning

If the position is estimated kinematically the code-only model again becomes an epoch-by-epoch processing model, similar to the fixed position code-only processing. In such a model time correlated (zero-mean) measurement errors should not pose any problem, and this is confirmed by the results. Figure 8.23 shows the positioning results for June 1, 2012, which are quite noisy as expected from single epoch code-only solution. The errors in the horizontal directions are in the meter range, while the errors in the Up direction are larger by about a factor 2. The results of each day are again very similar but shifted in time by about 4 minutes per day, and since the time into the processing run does not play a role in these epoch-by-epoch results, fig. 8.24 combines the position errors for all 30 days of June as a function of the time of sidereal day (each dot represents a single position solution). The formal 2-sigma values, which are nearly identical for each day, are shown by a single set of thin black lines. Figure 8.24 also shows a central moving average of the position solutions with a window of 999 samples (i.e. 16.7 minutes with 30 time series of 30-second data) with a wider black line. Table 8.2 holds the statistics of the empirical results. Comparison of the figure and the table reveals that the observed 0.5 m bias in the Up direction is in fact not constant in time, but rather the mean value of a time-varying signal that at times goes up to 2 meters. In the horizontal directions the moving average only shows much smaller excursions (also relative to the size of the random, noise-like errors). Overall, the formal 2-sigma values fit the empirical results quite well. This is confirmed by the results in fig. 8.25 which, as for the previous processing schemes shows the empirical rms (colored dots) and the formal standard deviation (black lines) of the 30 daily runs. The horizontal directions show a very good agreement between the empirical rms and the formal standard deviation in fig. 8.25, not only in magnitude but also behavior over time. The only problems with these single epoch code-only results are thus the strong variations and the bias in the Up component, which at times lead to larger empirical errors than the formal standard deviation predicts.

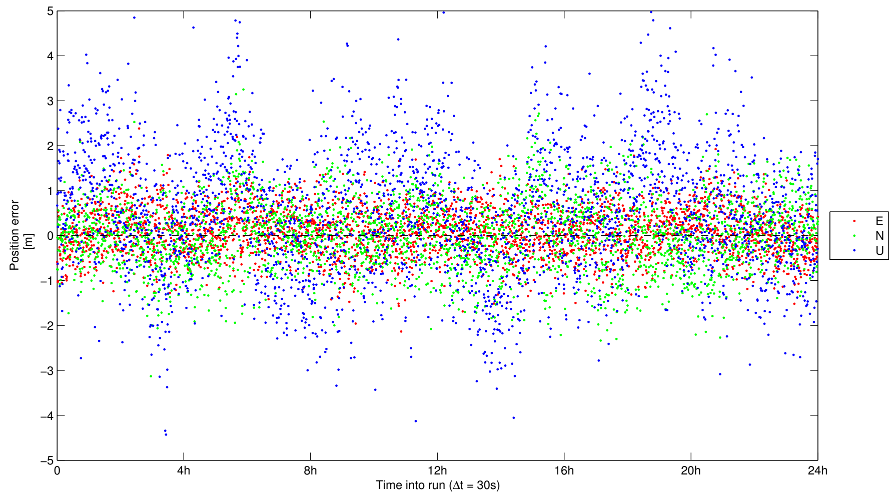

Figure 8.23: ENU position errors for kinematic code-only positioning of data from June 1, 2012 in Delft

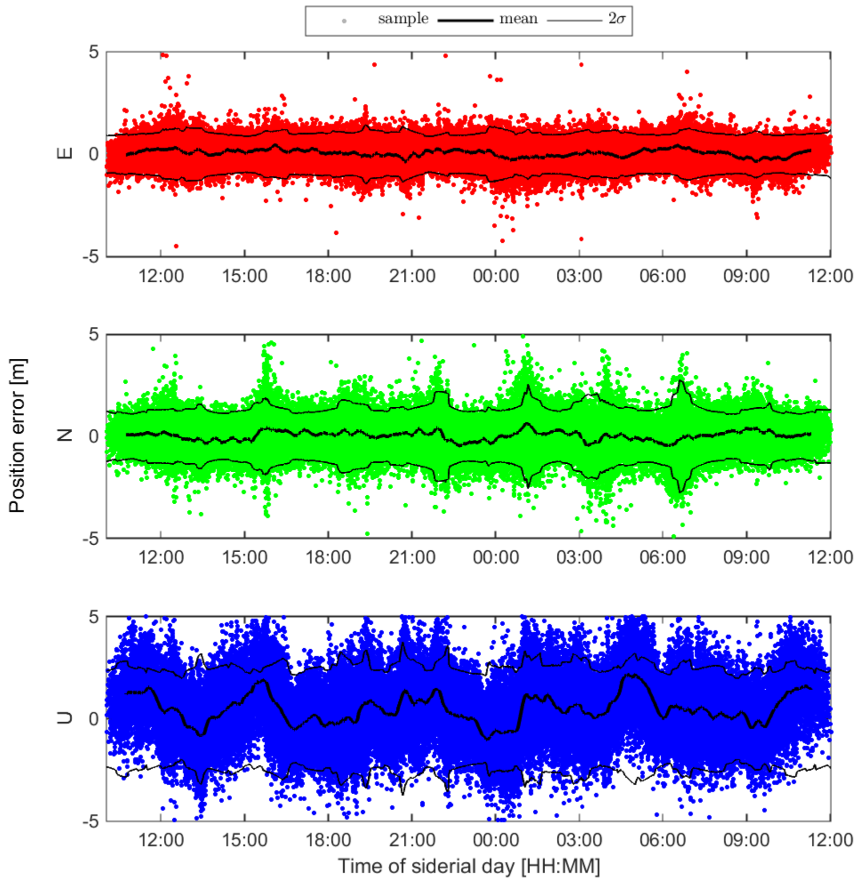

Figure 8.24: Code-only kinematic positioning errors as a function of the siderial time of day for 30 daily runs for DLF1 station during June, 2012

(m)	mean	sigma	rms
East	0.05	0.55	0.55
North	0.03	0.79	0.79
Up	0.47	1.41	1.49

Table 8.2: Empirical kinematic code-only positioning results

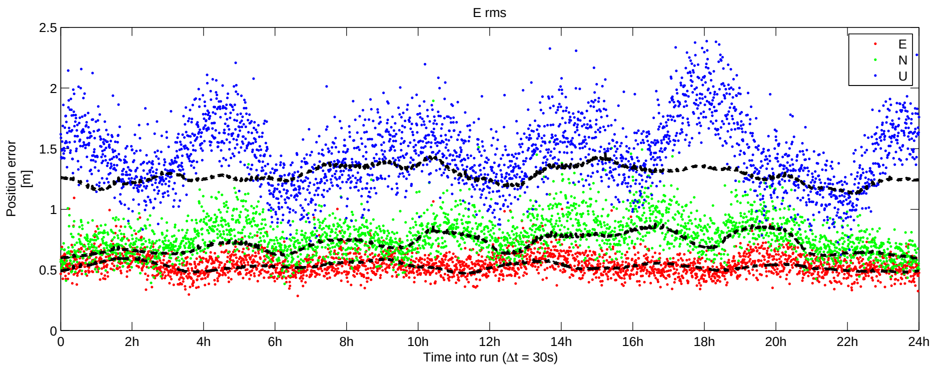

Figure 8.25: East, North and Up empirical rmse (dots) and formal standard deviation (dashed lines) for kinematic code-only processing of June, 2012; the formal and empirical measures fit very well for the horizontal components, but errors in the up component are at times too large.

8.3.4 Differential group delay estimation

The previous sections showed two systematic effects in the code-only solution, which cannot be solved by adjusting the stochastic model. The first is a bias in the up direction of 0.5 m, and the second are large variations that repeat daily. The source of these effects can be found by studying the pseudorange residuals of the processing with fixed position. Figure 8.26 shows these residuals by means of a boxplot with a box per satellite (top left pane). The figure clearly shows that the residuals contain a different bias for each satellite,

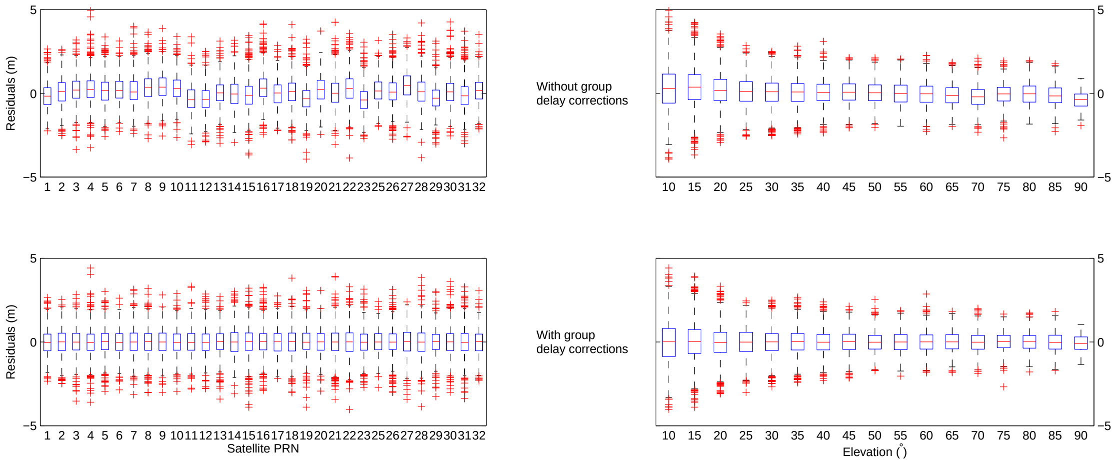

Figure 8.26: Boxplot of ionosphere-free residuals from fixed position processing. Without group delay corrections (top row), the residuals show a bias per satellite and an elevation dependency. After applying group delay corrections (bottom row), these biases are no longer present.

even though their expectation is zero (and as we found earlier the residuals of all satellites combined are unbiased). The top right pane in fig. 8.26 again shows a boxplot of the residuals but now each box represents a 5° elevation bin. This figure shows a bias in the residuals that varies with elevation; the bias is positive at low elevation and negative at high elevation angles. Smaller variations were also found with azimuth angle, as will be shown in the following. These biases will in turn bias the estimated position (when this is not fixed) and other estimated parameters.

The best way to deal with these errors depends on their properties, and especially their variation in time and space. If the errors would change from day to day and from place to place, the only solution would be to estimate them together with the unknown parameters. Appendix E shows that the pseudorange biases in the ionosphere-free observations can be estimated together with the other unknown parameters (including the position), but at the cost of much lower redundancy thereby significantly weakening the pseudorange processing model. However, if we assume that the biases are constant over a number of days (an assumption that we will investigate later), they can be estimated from one dataset, preferably while keeping the position fixed, and be used to correct the observations while processing a different dataset. We will estimate a constant bias per satellite and, following van der Marel and Gündlich (2003), an antenna group delay pattern to capture the elevation and azimuth dependent variations. Note: a constant bias per satellite or a constant antenna delay pattern will still cause a time varying bias in the position estimation because the available satellites, their observed observation, and the weight they obtain in the estimation changes over time. This time varying signal will repeat when the constellation repeats after one sidereal day. We will first consider a constant bias per satellite and then extend it with an antenna delay pattern.

The precise satellite clock offsets from the IGS, which were used in these computations, are referenced to the ionosphere free combination of the L1P and L2P signals. However, the Trimble NetR9 receiver tracks the L1C/A and L2P codes. To account for the offset between the L1P and L1C/A signals, the P1C1 bias (estimated by several IGS analysis centers) is applied to the L1C/A signal. Equation (3.41) shows that they act on the ionosphere-free linear combination via the scale factor $\frac{\gamma}{\gamma-1} = \frac{f_1^2}{f_1^2-f_2^2}$. That means that one interpretation of our estimates is a correction to the P1C1 DCB if we divide them by this scale factor. The advantage of this approach is that we can compare our results to those of the IGS analysis centers. The P1C1 DCB also impacts the ionosphere estimates, but since we have no truth data for these estimates we will not consider this effect here. This interpretation of the biases is equivalent to the P1C1 estimation procedure proposed in Leandro (2009), and results are in good agreement.

Figure 8.27 shows the estimated P1C1 biases for DLF1 and compares them to the values of the Center for Orbit Determination in Europe (CODE). Values range from -80 cm and +65 cm (top pane) and show a very similar pattern, while differences (lower pane) are between -15 cm and +15 cm. Leandro (2009) reports discrepancies with results from CODE in the exact same range of -15 cm and +15 cm for a 10 days dataset from a single station. This discrepancy is about halved when the mean value for 8 stations is considered. CODE routinely compares several methods to estimate the P1C1 biases, including direct estimation from receivers tracking both the L1C/A and L1P signals, and estimation with their network processing algorithms (CODE, 2015, on which their PPP products are based). Differences between these methods can already reach up to 15 cm and significant differences between receivers are also reported. (The CODE values presented here are 30-day averages computed from a global network with about 80 stations.)

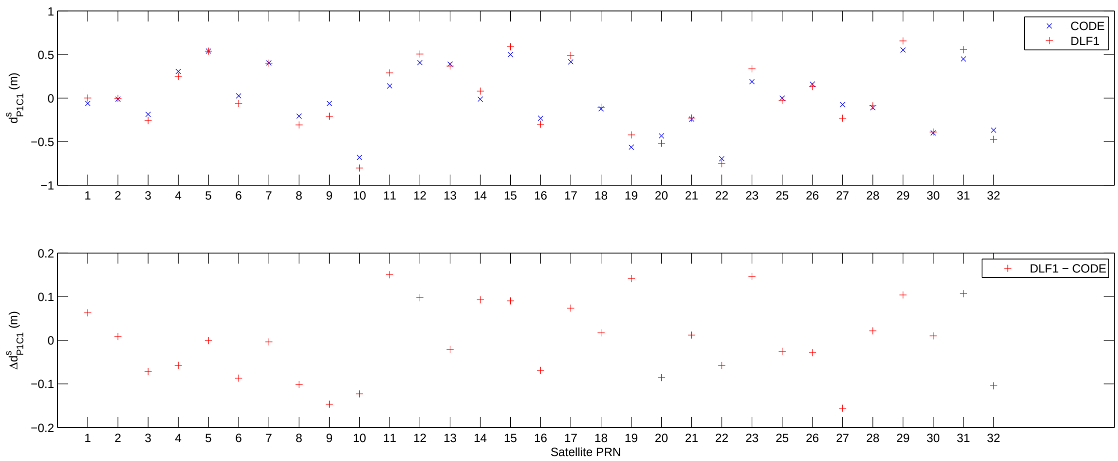

Figure 8.27: Estimated DCBs from ionosphere-free residuals of fixed position processing; the estimates values largely correspond to the CODE values, but show differences of up to 15 cm.

The differences between our results, specific for DLF1, and the estimates from CODE can be caused by either receiver or antenna specific hardware delays (that also differ between satellites) or the time-average of unmodeled effects such as multipath. Therefore, adding more stations with different receivers and antennas to our estimation process is expected to average these individual estimates out to the values estimated by CODE. However, in the remainder of this section we will show the advantage of using DLF1-specific estimates.

Figures 8.28 and 8.29 show, respectively the code-only kinematic positioning results for June 16, 2012 using the P1C1 DCBs from CODE and using the P1C1 DCBs computed from DLF1 data for June 1, 2012.

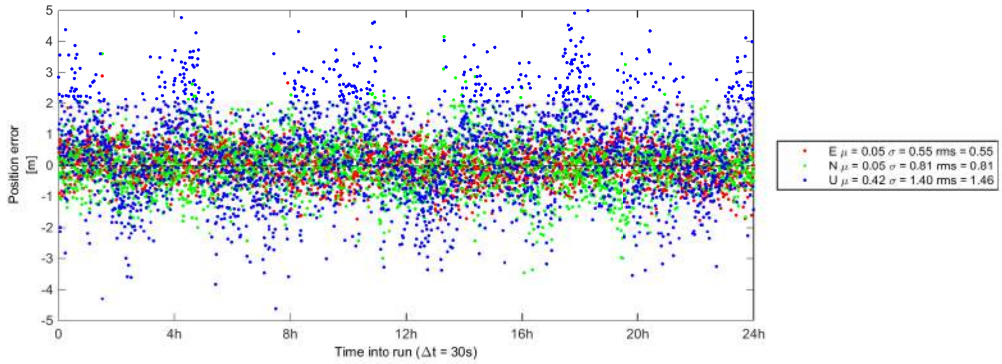

Figure 8.28: Code-only kinematic position errors for DLF1 on June 16, 2012 using P1C1 DCBs computed by CODE for June, 2012; strong variations in the up component as well as a significant bias are visible.

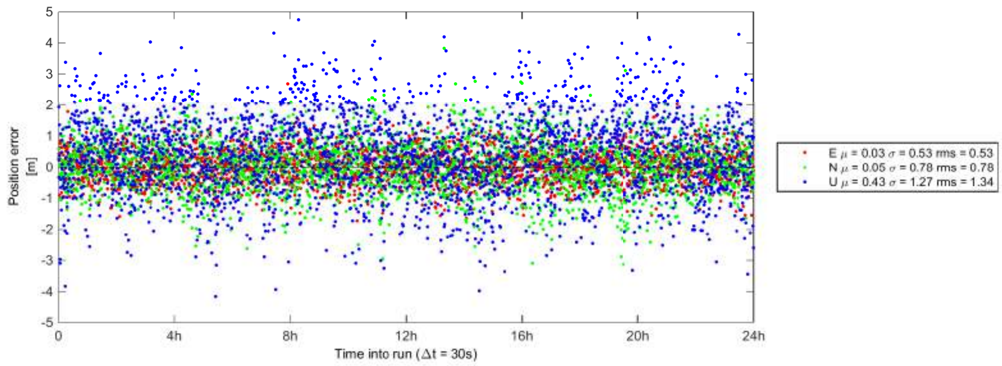

Figure 8.29: Code-only kinematic position errors for DLF1 on June 16, 2012 using P1C1 DCBs computed from DLF1 data for June 1, 2012; the bias in the up component remains, but the strong variations are much reduced.

Comparing these two figures, shows that the slow variations in the estimated positions and especially the Up component are largely reduced. The reduction in the standard deviation and root-mean-squared errors of the Up component, presented in the figure legends, are quite significant, although the random variations remain dominant. However, more importantly, the bias in the up component has not been removed at all. Therefore, we will now take one more step in modeling the group delays by means of an antenna delay pattern. While it is possible to extend our positioning model to include these antenna parameters, we take a different approach based on the Gauss-Seidel method as explained in appendix F.5. In this approach the group delay parameters (both satellite biases and antenna pattern) are estimated in a second step from the residuals of the normal processing model. The whole estimation then needs to be iterated while correcting the observations for these estimated group delays. These iterations needed to obtain the final results are an obvious disadvantage of this method. However, this disadvantage is offset by the fact that it offers the possibility to try several models for the group delays without the need to reprocess the complete (time dependent) GNSS model, and without adapting the positioning software each time.

The antenna pattern is estimated from the residuals and the corresponding elevation and azimuth angles by means of a least squares ridge estimator (Matlab implementation by D'Errico, 2005). The delay is computed over a grid of points, while also constraining the partial derivatives at the grid-points (much like a 2 dimensional spline). The relative weight of the extra constraint with respect to the residuals and the distance between the grid-points together determine the smoothness of the estimated antenna pattern. However, if a grid of elevation and azimuth angles with constant interval is used, this actually leads to a very uneven two-dimensional distribution of the grid-points (i.e. because all lines of constant azimuth intersect at the zenith). Therefore, the elevation and azimuth angles are first transformed with the Lambert azimuthal equal-area projection (Snyder, 1987), and the grid fitting is performed in these transformed coordinates. This leads to a more uniform point distribution and consequently to a more uniform smoothness. An additional advantage of the Lambert projection is that no discontinuity occurs at 90° elevation or between 360° and 0° azimuth. The estimated antenna delay pattern is subsequently back transformed to the elevation and azimuth angles and stored in the ANTEX file format (Rothacher and Schmid, 2010). The ANTEX file is then used during positioning in a similar manner as the antenna phase delay patterns. Figure 8.30 shows the estimated antenna delay pattern and the elevation curves at different azimuth angles. At all azimuth angles the curves show the same general trend of decreasing delays with increasing elevation to a common value at zenith. Note that we cannot estimate the absolute value of the antenna pattern, instead we keep the mean value at zero. The pattern and magnitude of the estimated delays is in reasonable agreement with other authors, although a direct comparison is not possible (Wübbena et al., 2008; Kersten and Schön, 2013).

After adopting the estimated group delay parameters, the variance component estimation also needs to be iterated since the stochastic model should now reflect the errors of the corrected observations. The new stochastic model in turn influences the estimated group delay parameters to some extend, which leads to a multilevel iteration procedure. Fortunately the iteration converges to cm level after only 2 iterations, and fig. 8.30 already shows the end result of this iteration procedure.

Figure 8.31 shows the converged results of the new stochastic model, again after three sub-iterations. Comparison to our earlier results in fig. 8.18(b) show that the measurement variance has decreased. This is as expected since part of the errors that were previously captured in the stochastic model, are now corrected. Figure 8.31 also shows a much better fit of the fitted curves to the elevation bins, both the exponential function as well as the cosecant function. The fit is still slightly poorer at high elevation, related to the smaller

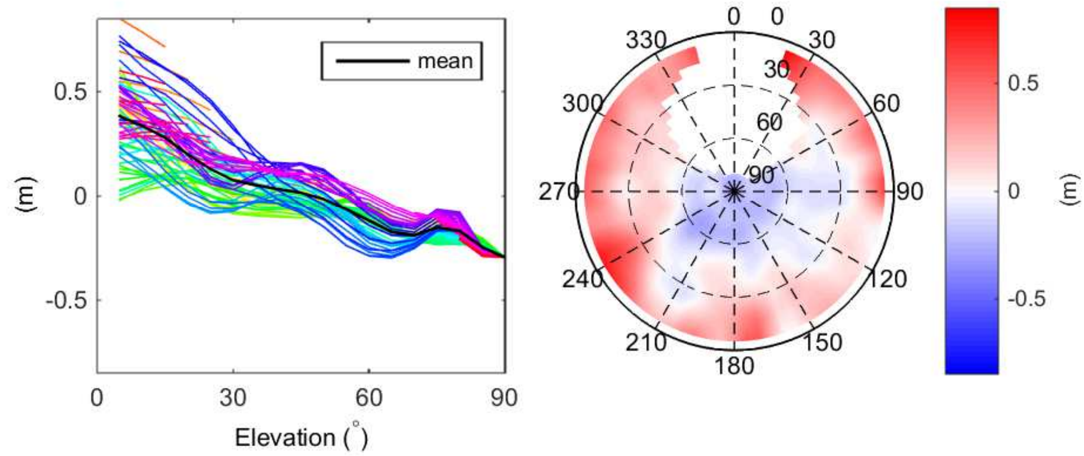

Figure 8.30: Estimated group delays as a function of elevation and azimuth (in the left pane the different colored lines are for different azimuth angles); a strong dependency on elevation is apparent while variations over azimuth are smaller.

number of samples in these bins.

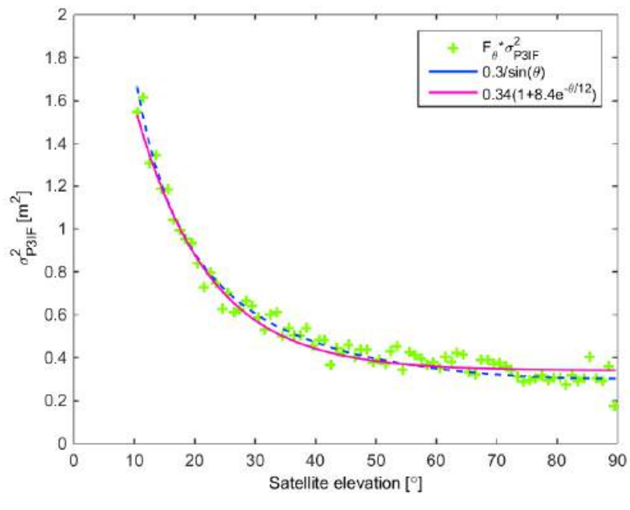

Figure 8.31: VCE after group delay corrections; the variance level has decreased as part of the errors have been removed.

8.3.4.1 Static positioning

With updated stochastic model and using the group delay estimates from June 1, 2012 (P1C1 DCBs and antenna delay pattern), the month of June 2012 has been reprocessed.

Figure 8.32 again shows the rms of the empirical errors and the formal standard deviation using identical processing options as those used in section 8.3.2. Comparison of this figure to fig. 8.22 reveals a vast improvement in the empirical position errors in the Up component. A moderate improvement in the East component can also be observed, while the North shows a slight degradation after about 7 hours into the run (note that the scale in the left-hand pane of fig. 8.32 is different from that in fig. 8.22). The rms errors in each direction now converge to 5 cm or better. The empirical results also fit formal standard deviations much better with the same exception that the empirical errors in the North component do not decrease at the same rate as the formal standard deviation.

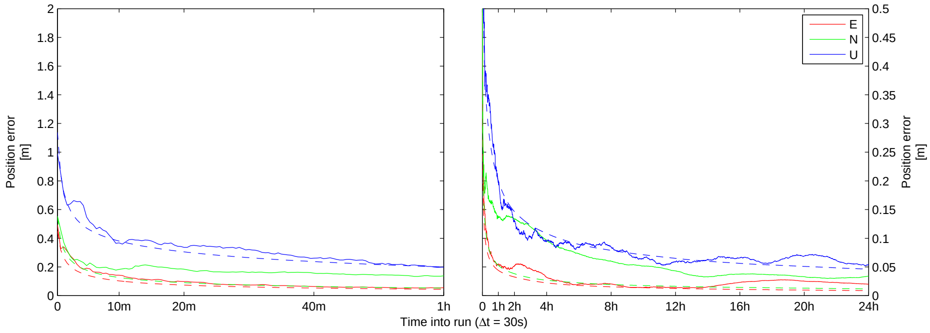

Figure 8.32: East, North and Up empirical rmse (solid lines) and formal standard deviation (dashed lines) for static code-only processing after group-delay corrections for June, 2012

8.3.4.2 Kinematic positioning

As previously mentioned the code-only positioning model with kinematic position and atmospheric parameters is in essence an epoch-by-epoch model. The positioning performance is therefore mainly governed by the current satellite geometry, repeating each sidereal day. Figure 8.33 presents the performance as a function of the time of sidereal day. Each dot represents a single position solution, the thin black lines represent the formal 2-sigma values, and the wider black line shows a central moving average of the position solutions with a window of 16.7 minutes (i.e. 999 samples). Table 8.3 shows the mean, standard deviation and rms errors of these results. Comparing this figure and table to fig. 8.24 and table 8.2, respectively, reveals that the group delay corrections have indeed solved both problems found in section 8.3.3: the strong variations in time are strongly reduced and the bias in the Up component is almost completely removed. In fact all statistics provided in the table are improved w.r.t. the original model. Figure 8.34 shows the empirical rms

(m)	mean	sigma	rms
East	-0.02	0.53	0.53
North	0.02	0.77	0.77
Up	-0.05	1.26	1.26

Table 8.3: Empirical kinematic code-only positioning results after group delay corrections

(colored dots) and the mean formal standard deviation (black lines) of the 30 daily runs.

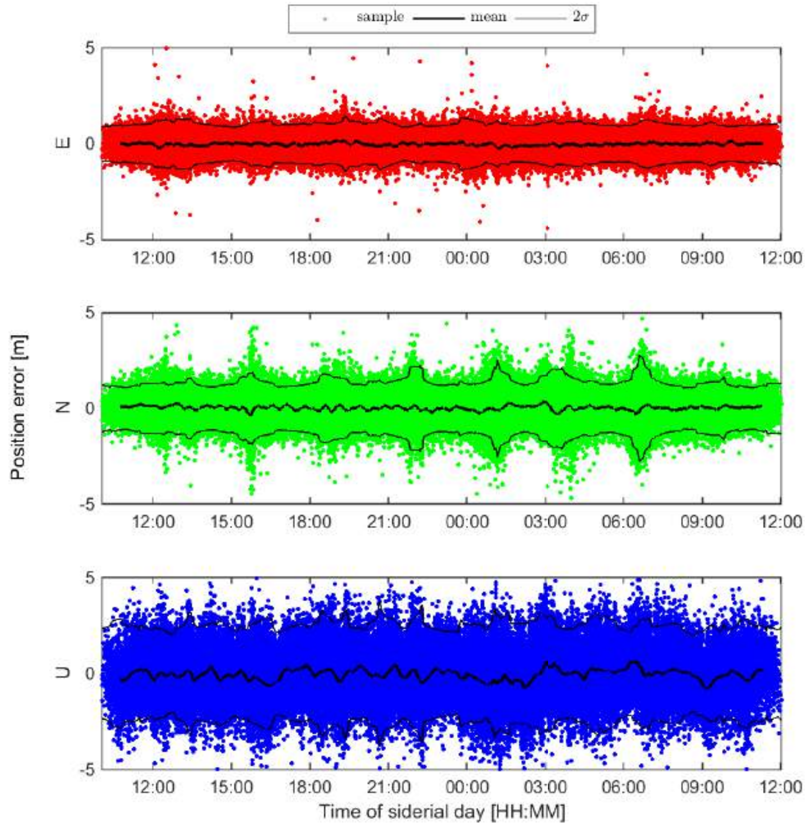

Figure 8.33: Code-only kinematic positioning errors as a function of the siderial time of day for 30 daily runs for DLF1 station during June, 2012

The empirical rms and the formal standard deviation show an almost perfect agreement in both magnitude and behavior over time. This shows that our model now corresponds to the actual observations very well, and that our assumption that the group delay parameters are constant over a number of days (in this case up to a month) is valid.

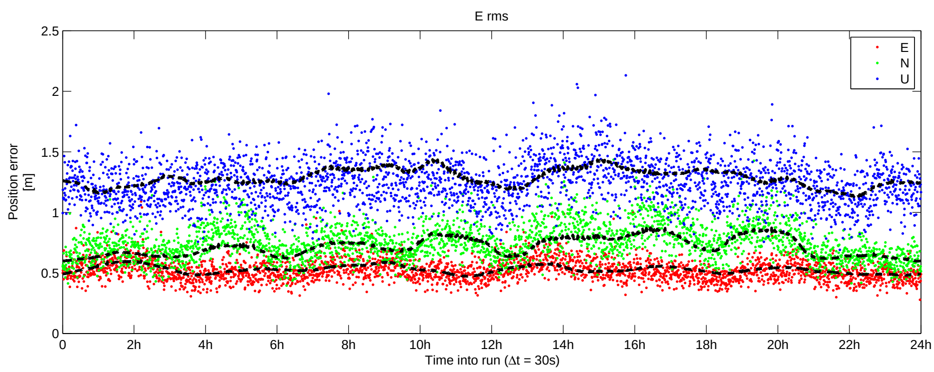

Figure 8.34: East, North and Up empirical rmse (dots) and formal standard deviation (dashed lines) for kinematic code-only processing after group-delay corrections for June, 2012; the formal and empirical values are in close agreement.

8.4 Code+phase processing

With the code and phase models now performing satisfactorily, this section combines both types of observations in the code+phase model introduced in section 4.8. The code and phase model improvements proposed in the previous sections are both applied (i.e. the group delays are corrected with the a priori estimates for DLF1, and the ionosphere-free phase biases are allowed to change slowly over time). The increased redundancy of the code+phase model means that the stochastic model parameters can theoretically be estimated more precisely (e.g. in a multilevel iterative process). However, the differences turn out to be very small and we will keep using the previous results to obtain a more straight forward comparison between the different processing models.

Figure 8.35 shows the empirical position rms errors and the mean formal standard deviation versus the processing time for the daily runs for June, 2012 for the static case. As expected, the position errors on the first epoch are at the level of the code-only solution (fig. 8.32), but they improve much faster already reaching 30 cm after just 3 epochs (i.e. 90 s). The accuracy keeps improving to 2 cm in 1 h and 1 cm in 4 h, all while the formal standard deviation gives a good representation of the empirical results. The accuracy keeps improving to about 5 mm in the Up component, and even smaller in the horizontal components. Compared to the phase-only solution (fig. 8.16) the code+phase solution performs significantly better during the first 30 min; the phase-only solution only catches up completely after about 6 h. During the second half of the day, the phase-only solution even performs slightly better than the code+phase solution in the Up component. This might be due to the fact that the group delay modeling performed in section 8.3.4 is ultimately not accurate enough to perform positioning with mm accuracy. Improvements that could be considered include: estimation using multiple days of data, smaller elevation and azimuth bins, or accounting for (small) variations over time.

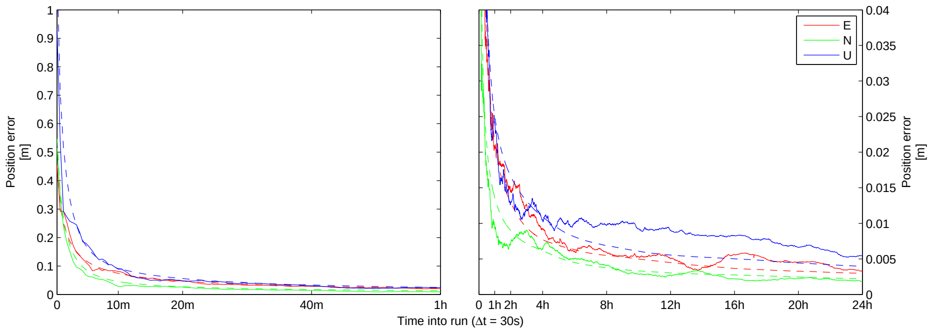

Figure 8.35: East, North and Up empirical rmse (solid lines) and formal standard deviation (dashed lines) for static code+phase processing of June, 2012; this model outperforms both the phase-only and code-only models.

Figure 8.36 shows the kinematic results for the code+phase model. The size of the errors again start at the code-only level, but decrease very fast to about 10 cm in 10 min. After 1 h the rms in the Up component has decreased to about 5 cm and about 2 cm in the horizontal directions. This level of accuracy is the same as we observed for the phase-only model (fig. 8.17), but there it was only reached after about 3 h. The performance degradation at the end of the day (related to the date change), is now again smaller than for the phase-only model with time-varying phase biases. The addition of the code observations increases the strength of the model, and the position solution becomes less sensitive to temporarily degraded observations or corrections.

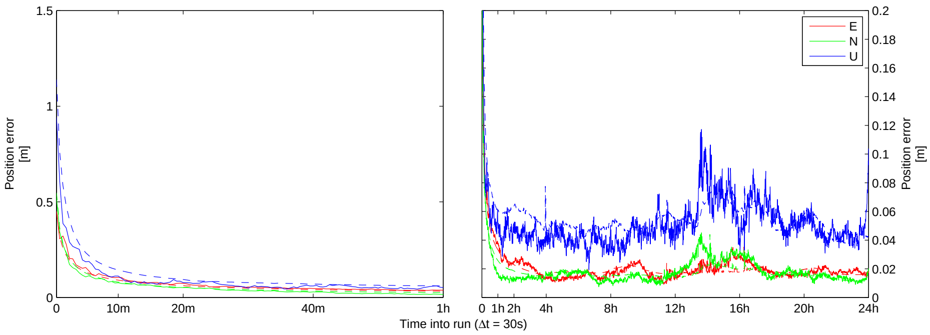

Figure 8.36: East, North and Up empirical rmse (solid lines) and formal standard deviation (dashed lines) for kinematic code+phase processing of June, 2012; this model outperforms both the phase-only and code-only models.

8.5 Code+phase processing with atmosphere constraints

In this section the code+phase model is further strengthened by adding both ionosphere pseudo-observables from a Global Ionosphere Map (GIM) from the Center for Orbit Determination in Europe (CODE) and troposphere pseudo-observable from the EGNOS troposphere model (RTCA, 2001) to the positioning algorithms. As detailed in section 4.9 this is equivalent to correcting the observables with the ionosphere and troposphere model values and constraining the estimated residual atmosphere parameters. The stochastic model of the code and phase observables are in this case not adjusted, but we do need to derive appropriate dynamic models for the residual atmosphere parameters. To do this we first estimate the residual atmosphere delays without any constraints and then apply the auto-regressive parameter estimation method introduced in section 6.3.

Figure 8.37 shows the estimated ionosphere delays after correcting the observables with the GIM values (see fig. 8.6(d) as reference for the full ionosphere delays). From the magnitudes of the residual ionosphere delays, in the order of several decimeters, it is apparent that we *cannot* ignore these effects if we want to obtain sub decimeter accurate positions (NB: In single frequency PPP the ionosphere residuals *are* generally ignored and contribute to the position errors). Even though the residual ionosphere delays for individual satellites are not zero mean, the overall residual ionosphere delay can be approximated by a zero-mean effect with very strong time correlation. Applying the first-order auto-regressive parameter estimation method introduced in section 6.3 gives an AR(1) parameter of $.9973$ for these 30 s data (equivalent to a correlation time of about 3:08 [h:mm]). The standard deviation of the white-noise process is estimated at 2 cm (also used for the process noise in the Kalman filter), which gives a steady-state standard deviation of 27 cm (which is used to initialize the estimated parameters).

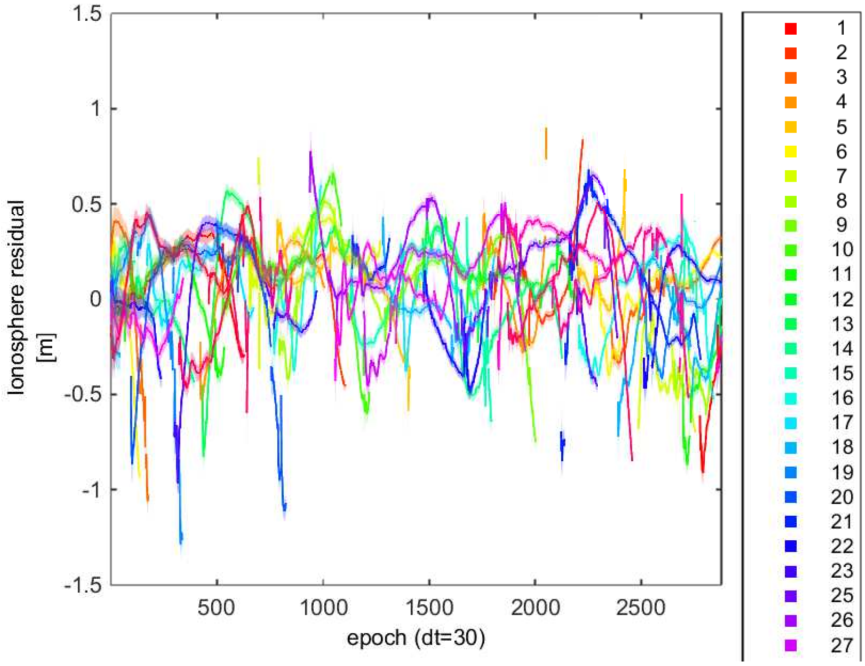

Figure 8.37: Residual ionosphere delay (solid lines) and formal standard deviation (shaded patches) after applying GIM corrections for June 1, 2012

Figure 8.38 shows the estimated troposphere delay after correcting the observables with the EGNOS troposphere model values (see fig. 8.6(c) as reference for the full troposphere delay). The magnitude of the residual troposphere delay is in the order of several centimeters; much smaller than the ionosphere residuals. The residual troposphere delay is also approximated by a zero-mean effect with very strong time correlation. Applying the first-order auto-regressive parameter estimation method again gives an AR(1) parameter of $.9972$ for these 30 s data (equivalent to a correlation time of about 2:58 [h:mm]). The standard deviation of the white-noise process is estimated at 2 mm (also used for the process noise in the Kalman filter), which gives a steady-state standard deviation of 3 cm (which is used to initialize the estimated parameters). Since these values were estimated from the phase measurements, which have mm-level precision themselves, the actual troposphere effect might be even more smooth.

The 30 daily runs for June, 2012 were reprocessed now correcting the observations with the atmosphere model values and applying the derived dynamic models to the estimated residual atmosphere delays. Figure 8.39 shows the empirical and formal position results for the static case. The atmosphere models already contribute to the solution on the first epoch, and the initial position errors are indeed smaller than for the code-only solution. The initial position rmse in both horizontal directions is already below 30 cm and the vertical position rmse is at about 60 cm, compared to about 60cm and 90 cm without atmosphere corrections. As both the atmosphere-free code+phase model and the atmosphere-constrained code+phase model converge the performance differences are reduced, and after about 5 minutes the atmosphere-free model catches up to the atmosphere-constrained model. The performance of both models remains almost identical for the remainder of the 24 h period.

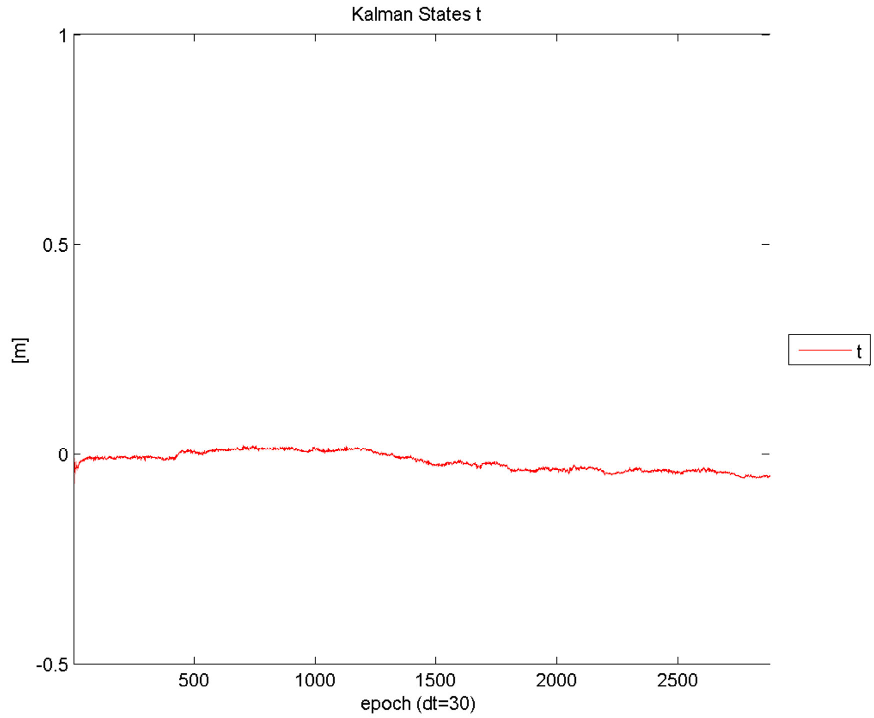

Figure 8.38: Residual troposphere delay after applying EGNOS troposphere model corrections for June 1, 2012

The kinematic results are presented in fig. 8.40 and show similar behavior. The initial errors of the ionosphere-constrained model are smaller than for the ionosphere-free model (in fact they are the same as the static results), but the ionosphere-free model catches up after some time (in this case 2.5 minutes) and both models perform equivalently for the remainder of the 24 h period. Banville (2014) found a similar performance improvement by initializing the slant ionosphere delay estimates with GIM model values. Although our integrated model is strictly speaking stronger, the high time-correlation of the ionosphere model values explains that using only the initial value already gives most of the benefit.

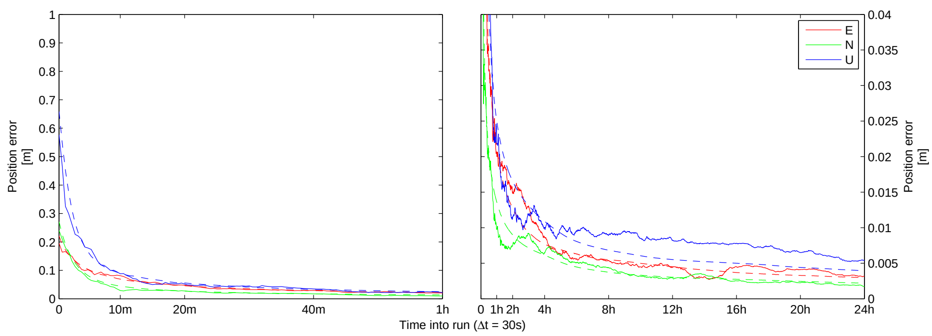

Figure 8.39: East, North and Up empirical rmse (solid lines) and formal standard deviation (dashed lines) for static code+phase processing and atmosphere constraints for June, 2012; the errors during the initial convergence are reduced.

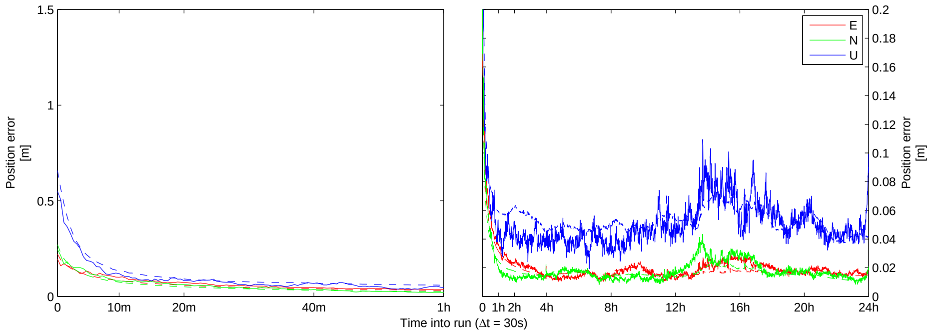

Figure 8.40: East, North and Up empirical rmse (solid lines) and formal standard deviation (dashed lines) for kinematic code+phase processing and atmosphere constraints for June, 2012; the errors during the initial convergence are reduced.

8.6 Comparison and conclusions

The performance of the different static positioning models presented in this chapter are compared in fig. 8.41 by means of the empirical root-mean-square 3D position errors (i.e. the Euclidean distance). The code-only solution before the group delays are corrected is not included in fig. 8.41 because of its large position bias. The PPP service of Natural Resources Canada (NRCan) was also used to process the same dataset and results are included in the figure for comparison. In the left pane we can see the phase-only models, both with constant and time-varying phase biases, start with large position errors but a final accuracy below cm-level. (The first few minutes of the convergence curves are distorted due to the fact that the phase-only model is initialized with a single epoch code-only solution, as mentioned previously). The code-only solution with group delay corrections has a smaller initial error, but does not reach cm-level accuracy within 24 h. The code+phase model starts as the code-only model and improves to below cm-level faster than the phase-only models, thereby combining the strong points of both observation types. The best performing model is the code+phase model with atmosphere constraints, which outperforms the regular code+phase model during the first 5 minutes. The NRCan code+phase solution has larger initial position errors and converges more slowly than our code+phase model. This can be explained from the lack of station specific group delays and stochastic model, which means that the code observations cannot be used to their full effect. After about 12 minutes the NRCan solution catches up to our code+phase solution. However, the NRCan solution converges to a slightly different position than the reference position which was derived from the EUREF Permanent GNSS Network (mm level in horizontal components; cm level in vertical component). Although, direct comparison to the results of other authors remains difficult, in general it can be concluded that our performance compares quite favorably to most reported performance measures displayed in table 3.3.

Similar results are presented in fig. 8.42 for the kinematic case. The PPP service of Natural Resources Canada provides smoothed solutions (i.e. after forwards and backwards processing) for kinematic datasets. This cannot fairly be compared to our filtered solutions (i.e. after forwards processing only), and therefore no NRCan solution is included in fig. 8.42. Our code-only solution, which is a single-epoch solution and does not converge, is also not

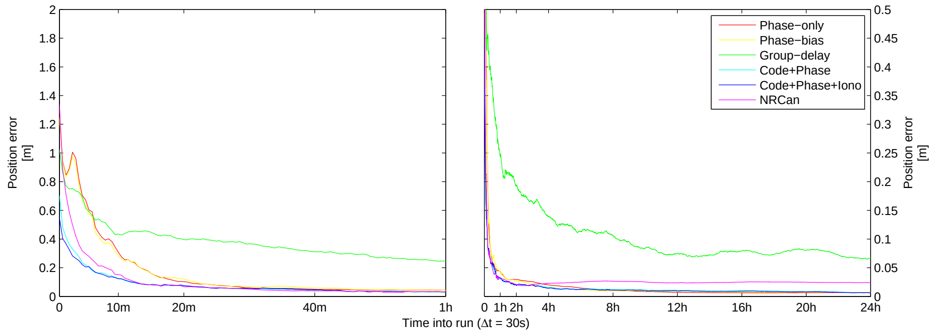

Figure 8.41: Absolute empirical rmse for static positioning models for June, 2012; the models including phase measurements all converge to similar accuracy, but during the initial stages the code measurements and atmosphere constraints play an important role. The NRCan solution converges to a slightly different point.

included. The code+phase models clearly have smaller initial errors and better convergence behavior than the phase-only models, with the atmosphere-constrained model performing best during the first few minutes. After about 2 h all models perform similarly with 2 notable exceptions. The phase-only model with constant phase biases performs worse around 15 h (related to the poor satellite geometry at this time), and the phase-only model with time-varying phase biases around 23 h (related to the IGS orbit and clock products).

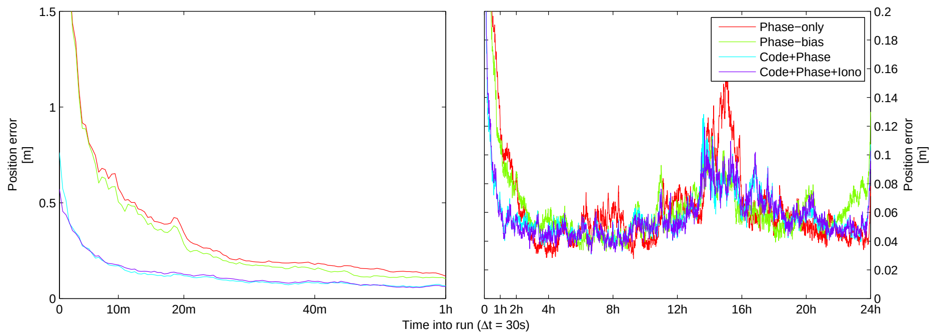

Figure 8.42: Absolute empirical rmse for kinematic positioning models for June, 2012; all models converge to similar accuracy, but during the initial stages, or when disturbances occur, the code measurements and atmosphere constraints play an important role.

Sections 8.2.2 and 8.2.3 showed that the phase-only model with constant phase biases provides a high positioning accuracy, but gives a poor quality description of the estimated position. The formal standard deviation decreases too fast and becomes much smaller than the root-mean-squared empirical position errors. In section 8.2.4 we showed that estimating the phase biases as parameters that are allowed to change slowly over time, significantly improves the quality description while keeping a high position accuracy.

In sections 8.3.2 and 8.3.3 the code-only model, before the receiver-antenna specific group delays were modeled, was shown to provide a good initial position estimate with a reasonable quality description. However, especially the height component shows strong variations in time and is significantly biased with respect to the reference position. These effects are not properly captured by the formal standard deviation of the estimates which is thus ultimately insufficient. This becomes even more apparent if the position is estimated statically. In this case the estimated height remains quite poor, while the formal standard deviation keeps decreasing. Section 8.3.4 demonstrated that improved group delay estimates (in the form of a bias per satellite and a group delay antenna pattern) can effectively solve these problems. In our example, group delays estimated from a single day of data could be used to correct pseudorange observations made up to a month later, and significantly reduce the strong time variations in the position estimates and the bias in the height component.

The problems found with the code-only model before the receiver-antenna specific group delays were modeled, also prevent the pseudorange observations from contributing significantly to the code+phase solution. Either the measurement variance has to be set very high, in which case the code observations get almost no weight in the least squares solution, or if the variance is not set high enough, the bias found in the pseudorange model will also severely degrade the combined solution. In section 8.4 results of the code+phase positioning model with receiver-antenna specific group delays and time varying phase biases were presented. The strength of this model is clear from the excellent convergence performance in both the static and kinematic case, easily outperforming both the code-only and phase-only models. Section 8.5 showed that constraining the atmosphere delays to model values can further improve the initial convergence of the position estimation.

9 Conclusions and Recommendations

This chapter outlines the main conclusions that can be drawn from the work discussed in the previous chapters and provides recommendations for research and practice. The chapter is organized along the main objectives given in section 1.2.

9.1 Functional model

Atmosphere delays From an analysis of conventional PPP models in chapter 2 the treatment of atmosphere delays was identified as a point for improvement. An atmosphere-weighted approach was therefore introduced.

Single and dual-frequency GNSS PPP models differ in their approach to mitigate the atmosphere delays. In the single-frequency approach the atmosphere delays are typically corrected by means of external atmosphere models. In the dual-frequency approach the ionosphere delays are typically eliminated by combining the dual-frequency observations to a single ionosphere-free observation, while the (zenith) troposphere delay is estimated. As a result single-frequency PPP already provides a relatively high accuracy after only a few epochs, but will not improve beyond the accuracy of the used atmosphere models; dual-frequency PPP takes longer to converge but eventually reaches a very high accuracy.

From an estimation point of view these two approaches can be considered as, respectively, an atmosphere-fixed (to the model values) and an atmosphere-free (estimated without any constraints) model. An atmosphere-free approach to single-frequency PPP is possible, but leads to poor convergence performance. Similarly, an atmosphere-fixed approach to dual-frequency PPP is also possible, but the position accuracy would degrade significantly.

To obtain the optimal compromise between these two extremes, the atmosphere-weighted or atmosphere-constrained model was introduced in chapter 4. In this approach the external atmosphere model values are used, but the (residual) atmosphere delays are also estimated from the observations. Or, equivalently, the observations are corrected with the atmosphere models and residual atmosphere delays are estimated in the positioning filter. The estimated values can then be constrained, both in absolute sense (to the model values) as well as their variation in time by means of a dynamic model (NB: neither is possible if the ionosphere is eliminated).

If proper weight is given to the model values, the filter can benefit from the atmosphere models, without being adversely impacted by their limited accuracy. The weight that these models get is determined by the dynamic model used for the estimated parameters including the initial variance. In chapter 6, a method was derived to estimate an autoregressive process from a time series, which can also be used to construct a dynamic model for time-correlated parameters. In chapter 8 this method was applied successfully to the atmosphere delays and indeed improved convergence behavior over the atmosphere-free model.

Rank defects When enough satellites and measurement epochs are available, the estimated receiver coordinates are not effected by any rank efficiencies in the SPP and PPP models because the unit direction vectors from the receiver to the satellites are different for each satellite. This means that if no unmodeled errors occur, the position can be estimated without biases. If a zenith troposphere delay parameter is included in the estimation it will also remain unbiased, and in this respect the zenith troposphere parameter can be viewed as a fourth coordinate for the estimation process.

The GNSS measurement model contains a rank deficiency between the clock offsets and the hardware delays. As a result the estimated clocks are always biased by the hardware delays. The specific combination of hardware delay terms depends on the used observations and positioning model. It is therefore often more appropriate to consider the clock offset that pertains to a certain observable rather than the unbiased clock offset of a satellite or receiver.

From single frequency code-only or phase-only observations the ionosphere cannot be estimated, which means that single frequency users will have to rely on an external ionosphere model to correct the observations for the ionosphere delay. The ionosphere can be estimated from dual frequency observations or single frequency code and phase observations. However, the estimates will be biased by differential hardware delays.

More generally, the analysis in chapter 4 revealed that, if the satellite clock offsets are not provided for each observable some of the estimated parameters will become biased by the satellite differential hardware delays. This does not always negatively impact the user positioning, e.g. when no differential hardware delays are available and the ionosphere delays are estimated without any additional constraints, the ionosphere estimates will be biased and the estimated receiver clock offset will pertain to the ionosphere-free linear combination, but without impacting the receiver position estimate.

However, if unbiased estimates are needed e.g. when we intend to strengthen the positioning model by means of external ionosphere information, the differential hardware delays (in this case the DCBs) are required. Additionally the receiver DCB needs to be estimated as it can no longer be lumped with the ionosphere delay parameters. To strengthen the model in this way the ionosphere information can be added to the model in the form of pseudo observables, or the receiver observables can be corrected with the ionosphere information, both approaches leading to the same model. If the ionosphere model is not considered accurate enough a differential term can be estimated without impacting the redundancy, if the differential term has an expectation of zero.

Another case where unbiased estimates are needed is for ambiguity resolution. Thus for ambiguity resolution to be possible for PPP, it is required that the satellite clock offsets are provided for each observable and more specific the phase observations. These observable specific satellite clock offsets do not all have to be provided in full, if at least one clock offset is provided, the other clock parameters can be expressed in the form of differential delays. An advantage of providing some of the clock offsets as differential delays is that these delays change much slower over time, which means that they can be provided to the user with a lower update rate. The observable specific receiver offsets can also be expressed as one full clock and a number of differential delays as shown in this chapter. The advantage in this case is that due to their slower changes over time, a more strict dynamic model can be used to strengthen the positioning model.

From the phase-only models, only between-satellite single differenced ambiguities can be estimated without being biased by receiver dependent terms, since a rank deficiency exists between the ambiguities and the receiver clock offsets. In the dual frequency code and phase model these rank deficiencies instead exist between the ambiguities and the differential hardware delays, which means that also in this model only single differenced ambiguities can be estimated without being biased by receiver dependent terms.

The phase-only models showed that the presence of the unknown phase ambiguities prevent the estimation of the receiver position from a single epoch of data. For code and phase (Kalman) filter implementation, this means that, if the ambiguities cannot be resolved from a single epoch, the position coordinates and other unknown parameters are first estimated from the code observations with the corresponding uncertainty. Only after the ambiguities have been estimated with enough precision will the phase measurements start to contribute to the estimation of the other parameters.

Ambiguity Resolution

Ambiguity resolution can be considered for the double difference between satellites and between the PPP user and the network of reference stations, but also single differences between epochs (i.e. cycle-slips) can be considered as integer ambiguities. Ambiguity resolution between the PPP user and the reference network receives much attention from several research groups around the world, and is is currently leading to a new type of PPP products that enables ambiguity resolution. In chapter 7 the second type of ambiguity was considered in the time-differenced model. The strong influence of the ionosphere on this problem was found.

From this it was again concluded that the ionosphere variations over time (i.e. the dynamic model) need to be constrained to realistic values for optimal performance. It can be concluded that under moderate ionosphere conditions, errors smaller than the carrier phase wavelength can be detected, enabling cycle-slip detection.

9.2 Stochastic model

Next to the functional PPP model, the stochastic model for PPP was also treated in this dissertation. For PPP the stochastic model consists of two main parts: the GNSS observations and the PPP products. A proper stochastic model is needed for optimal weighting of the observations, to obtain an accurate quality description of the position solution and to perform rigorous integrity monitoring. Additionally, if ambiguity resolution is desired the stochastic model is important to maximize the success-rate.

Satellite Orbit and Clock Products For the above-mentioned reason the quality of the precise satellite orbit and clock products were analyzed in chapter 5.

- The orbit and clock offsets were both studied separately and combined. The results showed that the errors in the orbit and clock products individually are actually larger than the errors in the combined product as they impact the user. This is in part due to correlation resulting from the estimation process, but also due to the use of different phase center offsets. These different PCOs lead to differences in the computed satellite phase center positions (mainly in the radial direction), which are for a large part absorbed by the satellite clock offsets. It can thus be concluded that a PPP user should obtain the satellite orbit and clock products from the same provider and not mix products.

- Another finding was that compared to the IGS satellite orbit prediction the clock prediction is relatively poor, and dominates the combined error. Additionally the clock prediction for older GPS satellites is worse than for the newer satellites. If these products are used for PPP, the stochastic model should reflect both these effects. In recent years the international GNSS community has started to focus on (near) real-time provision of precise satellite orbit and clock products. The RETICLE clock products from DLR/GSOC are one such near real-time product. These satellite clock offsets are estimated while keeping the satellite orbits fixed to the values predicted by the IGS. In this case the products can be mixed since the same PCOs are used by definition and errors in the orbit will (partially) be compensated by the computed satellite clocks. Thanks to the near real-time aspect of these clock offsets the poor predictability of the satellite clocks (and in particular the older GPS satellite clocks) plays a much less significant role. The quality of these products is much higher and approaches the post-processed products. In addition a separate treatment of the older GPS satellites in the stochastic model is not needed (similar to the post-processed products).

Measurement Noise In sections 6.1 and 6.2 the different contributions of the code and phase measurement noise have been investigated with a geometry-free model using measurements from short and zero baselines as well as stand-alone receivers. Using the single, double and time differences of the code-minus-carrier and multipath combinations, the code noise, code multipath delays, and time correlation of the code observations have been quantified.

- From these investigations the undifferenced code noise without multipath could be estimated. The estimated values were in good agreement with the theoretical formulae linking the measurement noise to tracking loop parameters and the C/N_0. Therefore, these theoretical expressions can be used in the stochastic model to account for the pseudo range measurement noise.

- The phase noise and phase multipath have also been studied from the double difference phase observations. The results show that the estimated phase noise is close to the theoretical thermal noise and almost equal for each GNSS as expected. Unlike the code observations the phase observations show very little time correlation at a sampling rate of 1Hz. This means that the theoretical relations again suffice for the part of the stochastic model that accounts for the carrier phase measurement noise.

- The observations made to different satellites turned out to be almost uncorrelated as expected and consequently this correlation can be neglected in the stochastic model.

- The results presented in chapter 6 also showed strong variations of the pseudorange code measurements over longer time periods, with the magnitude of the variations easily reaching up to 20 times the thermal noise standard deviation. These time correlated (multipath) errors were further studied in sections 6.2.3.2 and 6.3.

Multipath The multipath linear combination of GNSS measurements, which is dominated by pseudo range multipath and (time correlated) measurement noise was modeled as an autoregressive process. The estimated AR parameters, the standard deviation of the residuals and their dependence on e.g. satellite elevation differ for each of the GNSS signals and are also different for the two receivers considered in section 6.3. However, the following general conclusion can be reached.

The AR(0), or white noise, model shows a clear dependency of the standard deviation of the residuals on satellite elevation where larger residuals are encountered for smaller elevation angles. This can be translated into a white noise stochastic model with elevation dependent weighting which can be used for positioning. However, the estimated AR(1) parameter is almost always significant to a very high level, which indicates time correlation of the multipath time series. Estimation of an AR(1) model reduces the estimate of σ_ϵ by a significant amount (especially for satellites with low elevation angles), which shows that an AR(1) model fits the data much better than a white noise or AR(0) model does in those cases. The AR(1) parameter itself does not show a strong dependency on satellite elevation, but the standard deviation of the residuals *does* show this dependency. This AR(1) model can be used for the stochastic model by extending the Kalman state vector with an additional entry per signal with multipath. The transition matrix for these entries then takes the (constant) values of the estimated AR(1) parameters and the process noise is taken as a satellite elevation dependent value. With increasing order the estimated AR parameters decrease in magnitude and become less significant. In addition the reduction in σ_ϵ is much less pronounced. Since each increase in the AR order leads to an additional filter state, thereby increasing the computational burden and decreasing the strength of the model, higher order AR models are less attractive for positioning purposes.

This means that for the positioning algorithms the AR(0), or white noise process, and AR(1) models are best suited. A user or application designer can then make a trade-off between using a simple (elevation dependent) white noise model or a more accurate AR(1) model at the cost of additional computational burden.

9.3 Integrity monitoring

In chapter 7 we presented an analytical and numerical study of the integrity of the multi-frequency single-receiver, single-channel GNSS model. The UMPI test statistics for spikes and slips are derived and their detection capabilities are described by means of the concept of minimal detectable biases (MDBs). Analytical closed-form expressions of the phase-slip and code outlier MDBs have been given, thus providing insight into the various factors that contribute to the detection capabilities of the various test statistics. This was also done for the phaseless and codeless cases, as well as for the case of loss-of-lock.

- The MDBs were evaluated numerically for the several GPS and Galileo frequencies. From these analyses it can be concluded that detectability of a single slip in dual- or triple-frequency of observations works well for only 2 epochs of data. Single-frequency phase-slip detectability, however, is problematic, thus requiring more epochs of data.

- From the codeless phase-slip MDBs it follows that detectability is not possible in the single-frequency case, but that it is possible for the dual- and triple-frequency cases. In the dual-frequency case the codeless phase-slip MDBs are less then 10 cm if $\sigma_{d\mathcal{I}} \leq 3$ cm, while for the triple-frequency case this is already true for $\sigma_{d\mathcal{I}} \leq 1$ m. In the triple-frequency case, the phase-slip MDBs get even as small as a few centimeters if $\sigma_{d\mathcal{I}} \leq 3$ cm. These codeless results are important as they show that in the presence of code multipath, one can do away with the code data and then still have integrity for phase slips.

- The code outlier MDBs are, except for the single-frequency case, all relatively insensitive to the smoothness of the ionosphere. The effect of the frequencies is also hardly present in the multi-frequency code-outlier MDBs. Their value is predominantly determined by the precision of the code measurements. From the phaseless code-outlier MDBs it follows that, except for the single-frequency case, code outlier detection is still possible. The multi-frequency phaseless code-outlier MDBs all lie around 1 m for $\sigma_{d\mathcal{I}} \leq 10$ cm. They increase rapidly, however, for larger values of $\sigma_{d\mathcal{I}}$.

- The hypothesis of a simultaneous slip on each phase observable of multi-frequency GNSS data was shown to give a very elongated MDB ellipse or (hyper)ellipsoid with the ionosphere-float model. These very elongated ellipses reveal a weak point of cycleslip detection with an ionosphere-float model because of specific combinations of slips, which can be present in the receiver data after a momentary loss of lock to a satellite and are very difficult to detect. One way to remedy this shortcoming, which is related to the uncertainty in the ionospheric delay, is to use an ionosphere-weighted model. For an ionosphere-weighted approach, the MDB ellipse shrinks when the precision of the ionospheric pseudo observable increases. For optimal performance of a cycleslip detection algorithm, including slip combinations that are difficult to detect, it is advisable to use an ionosphere-weighted model in combination with a short time interval between the measurements.

9.4 Positioning performance

Sections 8.2.2 and 8.2.3 showed that the phase-only model with constant phase biases provides a high positioning accuracy, but gives a poor quality description of the estimated position. The formal standard deviation decreases too fast and becomes much smaller than the root-mean-squared empirical position errors. In section 8.2.4 we showed that estimating the phase biases as parameters that are allowed to change slowly over time, significantly improves the quality description while keeping a high position accuracy.

In sections 8.3.2 and 8.3.3 the code-only model, before the receiver-antenna specific group delays were modeled, was shown to provide a good initial position estimate with a reasonable quality description. However, especially the height component shows strong variations in time and is significantly biased with respect to the reference position. These effects are not properly captured by the formal standard deviation of the estimates which is thus ultimately insufficient. This becomes even more apparent if the position is estimated statically. In this case the estimated height remains quite poor, while the formal standard deviation keeps decreasing. Section 8.3.4 demonstrated that improved group delay estimates (in the form of a bias per satellite and a group delay antenna pattern) can effectively solve these problems. In our example, group delays estimated from a single day of data could be used to correct pseudorange observations made up to a month later, and significantly reduce the strong time variations in the position estimates and the bias in the height component.

The problems found with the code-only model before the receiver-antenna specific group delays were modeled, also prevent the pseudorange observations from contributing significantly to the code+phase solution. Either the measurement variance has to be set very high, in which case the code observations get almost no weight in the least squares solution, or if the variance is not set high enough, the bias found in the pseudorange model will also severely degrade the combined solution. In section 8.4 results of the code+phase positioning model with receiver-antenna specific group delays and time varying phase biases were presented. The strength of this model is clear from the excellent convergence performance in both the static and kinematic case, easily outperforming both the code-only and phase-only models.

Section 8.5 showed that constraining the atmosphere delays to model values can further improve the initial convergence of the position estimation, without degrading the accuracy of the converged solution. The advantage of the atmosphere constraints disappears after several minutes of continuous observations.

9.5 Recommendations

Based on the research in this dissertation, the following recommendations can be made:

- For optimal PPP convergence, atmosphere delay estimation should be constrained by the use of external atmosphere models. The constraint should accurately describe the quality of the models in order to take maximum benefit without being affected by errors in the models.
- Careful application of S-system theory is necessary to achieve a full-rank PPP model without over-constraints, and makes proper interpretation of the estimated parameters possible. This is particularly important for those interested in unbiased estimates of atmosphere parameters and clock offsets.
- Ambiguity resolution should be considered as the next step in global PPP, for which the first steps have been taken by several research groups. Related positioning models

such as PPP-RTK and WA-RTK may lead the way. Resolving cycle-slips can be considered as time-differenced ambiguity resolution, and should form an integral part of PPP. Results show that ionosphere constraints play an integral role in resolving cycle-slips.

- Compared to prediction of satellite clock offsets, (near) real-time estimation greatly reduces the uncertainty of PPP products, and improves performance. However, the correlation resulting from simultaneous orbit and clock estimation should be considered by the user; only consistent combinations of products should be used.

- Theoretical formulae can accurately predict the expected noise on GNSS measurements, but other effects, in particular multipath, are often the dominant error source. The stochastic model should represent these effects including their time-correlation. For high measurement rates, an auto-regressive process can capture the multipath effects much better than a white-noise model can.

- The current lack of integrity information for PPP should be solved by improving the stochastic model for PPP and rigorously applying propagation of uncertainty and hypotheses testing.

- The MDB is a valuable tool to assess the integrity of the PPP system and, when compared to the GNSS carrier wavelengths, gives an indication whether cycle-slips can be detected.

- Very slow changes in the carrier phase biases can be neglected over short time intervals, but should be considered over longer periods.

- Biases in pseudorange observations should be modeled to prevent contamination of the carrier phase results.

Appendix: Autocovariance of Stationary Time Series

A

This derivation shows that, for a *wide sense stationary* time series, the expression $\varrho\sigma_y^2 = \sigma_y^2 - \frac{1}{2}\sigma_{\Delta y}^2$ in fact gives the autocovariance $K_{yy}(\tau) = E\{y(t)\,y(t+\tau)\} - E\{y\}^2$ at time delay τ.

If we have a wide sense stationary time series $y(t)$ with mean value μ, then the expectation value of y at each epoch is equal to the mean value:

$$E\{y(t)\} = E\{y(t+\tau)\} = \mu \tag{A.1}$$

for any time delay τ. For the variance of y we have (which also holds at each epoch):

$$var(y(t)) = var(y(t+\tau)) = E\left\{(y-\mu)^2\right\} = E\left\{y^2\right\} - E\{y\}^2 = \sigma_y^2 \tag{A.2}$$

If we now take the time differences of y as follows:

$$\Delta y = y(t+\tau) - y(t) \tag{A.3}$$

we get the following variance for Δy:

$$var(\Delta y) = E\left\{(y(t+\tau) - y(t))^2\right\} - E\{y(t+\tau) - y(t)\}^2 \tag{A.4}$$

Since the expectation operator is linear, we can rewrite the second term as follows:

$$var(\Delta y) = E\left\{(y(t+\tau) - y(t))^2\right\} - (E\{y(t+\tau)\} - E\{y(t)\})^2 \tag{A.5}$$

Using eq. (A.1), we see that the second term is in fact zero, simplifying the variance for Δy to:

$$var(\Delta y) = E\left\{(y(t+\tau) - y(t))^2\right\} \tag{A.6}$$

which can again be rewritten to:

$$var(\Delta y) = E\left\{y^2(t+\tau) - 2y(t)\,y(t+\tau) + y^2(t)\right\} \tag{A.7}$$

and:

$$var(\Delta y) = E\left\{y^2(t+\tau)\right\} - 2E\{y(t)\,y(t+\tau)\} + E\left\{y^2(t)\right\} \tag{A.8}$$

Given eqs. (A.1) and (A.2), the first and third terms in eq. (A.8) are also equal, which simplifies the expression further to:

$$var(\Delta y) = 2E\left\{y^2(t)\right\} - 2E\{y(t)\,y(t+\tau)\} \tag{A.9}$$

If we now insert eqs. (A.2) and (A.9) into our ad hoc correlation estimator we get:

$$\varrho\sigma_y^2 = \sigma_y^2 - \tfrac{1}{2}\sigma_{\Delta y}^2 = E\left\{y^2\right\} - E\left\{y\right\}^2 - \frac{1}{2}\left[2E\left\{y^2\left(t\right)\right\} - 2E\left\{y\left(t\right)y\left(t+\tau\right)\right\}\right] \quad \text{(A.10)}$$

or:

$$\varrho\sigma_y^2 = \sigma_y^2 - \tfrac{1}{2}\sigma_{\Delta y}^2 = E\left\{y\left(t\right)y\left(t+\tau\right)\right\} - E\left\{y\right\}^2 \quad \text{(A.11)}$$

which is equal to the expression for the autocovariance of a *wide sense stationary* time series at time delay τ.

Appendix: Dynamic Models and Time Correlation B

B.1 Recursive Least-Squares Convergence

The measurement update in our recursive least-squares algorithm can be expressed as follows:

$$E\left\{\begin{bmatrix} \underline{\hat{\boldsymbol{x}}}_{k|K-1} \\ \underline{\boldsymbol{y}}_k \end{bmatrix}\right\} = \begin{bmatrix} \boldsymbol{I} \\ \boldsymbol{A}_k \end{bmatrix} \boldsymbol{x}_k \quad D\left\{\begin{bmatrix} \underline{\hat{\boldsymbol{x}}}_{k|K-1} \\ \underline{\boldsymbol{y}}_k \end{bmatrix}\right\} = \begin{bmatrix} \boldsymbol{Q}_{\hat{\boldsymbol{x}}_{k|K-1}} & \\ & \boldsymbol{Q}_{\boldsymbol{y}_k} \end{bmatrix} \tag{B.1}$$

In which the predicted state vector $\underline{\hat{\boldsymbol{x}}}_{k|K-1}$ for the current epoch k, based on measurements from all previous epochs (denoted as $K-1$), is combined with the measurements of the current epoch $\underline{\boldsymbol{y}}_k$ in a least-squares sense. $\boldsymbol{I}$, $\boldsymbol{A}$ and $\boldsymbol{Q}$ are, respectively, an identity matrix, the design matrix and variance matrix. The predicted state and measurements of the current epoch are assumed to be uncorrelated. The predicted state and its variance matrix follow from the time update step as follows:

$$\begin{cases} \hat{\boldsymbol{x}}_{k|K-1} & = & \boldsymbol{\Phi}_{k-1,k}\hat{\boldsymbol{x}}_{k-1|K-1} \\ \boldsymbol{Q}_{\hat{\boldsymbol{x}}_{k|K-1}} & = & \boldsymbol{\Phi}_{k-1,k}\boldsymbol{Q}_{\hat{\boldsymbol{x}}_{k-1|K-1}}\boldsymbol{\Phi}^*_{k-1,k} + \boldsymbol{Q}_{w_k} \end{cases} \tag{B.2}$$

The solution of eq. (B.1) is given as:

$$\begin{cases} \hat{\boldsymbol{x}}_{k|K} & = & \left(\boldsymbol{Q}^{-1}_{\hat{\boldsymbol{x}}_{k|K-1}} + \boldsymbol{A}^*_k\boldsymbol{Q}^{-1}_{\boldsymbol{y}_k}\boldsymbol{A}_k\right)^{-1}\left(\boldsymbol{Q}^{-1}_{\hat{\boldsymbol{x}}_{k|K-1}}\underline{\hat{\boldsymbol{x}}}_{k|K-1} + \boldsymbol{A}^*_k\boldsymbol{Q}^{-1}_{\boldsymbol{y}_k}\underline{\boldsymbol{y}}_k\right) \\ \boldsymbol{Q}_{\hat{\boldsymbol{x}}_{k|K}} & = & \left(\boldsymbol{Q}^{-1}_{\hat{\boldsymbol{x}}_{k|K-1}} + \boldsymbol{A}^*_k\boldsymbol{Q}^{-1}_{\boldsymbol{y}_k}\boldsymbol{A}_k\right)^{-1} \\ & = & \left(\left(\boldsymbol{\Phi}_{k-1,k}\boldsymbol{Q}_{\hat{\boldsymbol{x}}_{k-1|K-1}}\boldsymbol{\Phi}^*_{k-1,k} + \boldsymbol{Q}_{w_k}\right)^{-1} + \boldsymbol{Q}^{-1}_{\hat{\boldsymbol{x}}_{k|k}}\right)^{-1} \end{cases} \tag{B.3}$$

To study the convergence behavior of this system we will look at the variance matrix of the estimator for $\boldsymbol{x}$ while assuming that $\boldsymbol{\Phi}_{k-1,k}$, $\boldsymbol{Q}_{w_k}$, $\boldsymbol{A}_k$ and $\boldsymbol{Q}_{\boldsymbol{y}_k}$ are all constant and equal to, respectively, $\boldsymbol{\Phi}$, $\boldsymbol{Q}_w$, $\boldsymbol{A}$ and $\boldsymbol{Q}_{\boldsymbol{y}}$ (i.e. we have a static model). If this system fully converges, i.e. if adding new observation $\boldsymbol{y}_{k+1}$ no longer improves the estimate of $\boldsymbol{x}$, than $\lim_{k\to\infty}\boldsymbol{Q}_{\hat{\boldsymbol{x}}_{k+1|K+1}} = \boldsymbol{Q}_{\hat{\boldsymbol{x}}_{k|K}}$, this gives:

$$\boldsymbol{Q}_{\hat{\boldsymbol{x}}_{k|K}} = \left(\left(\boldsymbol{\Phi}\boldsymbol{Q}_{\hat{\boldsymbol{x}}_{k|K}}\boldsymbol{\Phi}^* + \boldsymbol{Q}_w\right)^{-1} + \boldsymbol{A}^*\boldsymbol{Q}^{-1}_{\boldsymbol{y}}\boldsymbol{A}\right)^{-1} \tag{B.4}$$

which works out as:

$$\boldsymbol{Q}_{\hat{\boldsymbol{x}}_{k|K}} = \boldsymbol{\Phi}\boldsymbol{Q}_{\hat{\boldsymbol{x}}_{k|K}}\boldsymbol{\Phi}^* - \boldsymbol{Q}_{\hat{\boldsymbol{x}}_{k|K}}\boldsymbol{A}^*\boldsymbol{Q}^{-1}_{\boldsymbol{y}}\boldsymbol{A}\left(\boldsymbol{\Phi}\boldsymbol{Q}_{\hat{\boldsymbol{x}}_{k|K}}\boldsymbol{\Phi}^* + \boldsymbol{Q}_w\right) + \boldsymbol{Q}_w \tag{B.5}$$

This non-linear matrix equation which describes the steady state of the filter is closely related to the algebraic Riccati equation. This is more easily seen if we consider the variance matrix of the predicted state $\boldsymbol{Q}_{\hat{\boldsymbol{x}}_{k|K-1}}$, and write the measurement update in the equivalent model of condition equations (the so-called B-model, see e.g. Teunissen, 2001):

$$\left\{ \begin{array}{lcl} \hat{\boldsymbol{x}}_{k|K} & = & \underline{\hat{\boldsymbol{x}}}_{k|K-1} + \boldsymbol{Q}_{\hat{\boldsymbol{x}}_{k|K-1}} \boldsymbol{A}_k^* \boldsymbol{Q}_{\boldsymbol{v}_k}^{-1} \left(\underline{\boldsymbol{y}}_k - \boldsymbol{A}_k \underline{\hat{\boldsymbol{x}}}_{k|K-1} \right) \\ \boldsymbol{Q}_{\hat{\boldsymbol{x}}_{k|K}} & = & \boldsymbol{Q}_{\hat{\boldsymbol{x}}_{k|K-1}} - \boldsymbol{Q}_{\hat{\boldsymbol{x}}_{k|K-1}} \boldsymbol{A}_k^* \boldsymbol{Q}_{\boldsymbol{v}_k}^{-1} \boldsymbol{A}_k \boldsymbol{Q}_{\hat{\boldsymbol{x}}_{k|K-1}} \end{array} \right. \tag{B.6}$$

with $\boldsymbol{Q}_{\boldsymbol{v}_k} = \boldsymbol{Q}_{\boldsymbol{y}_k} + \boldsymbol{A}_k \boldsymbol{Q}_{\hat{\boldsymbol{x}}_{k|K-1}} \boldsymbol{A}_k^*$. In this case the fully converged variance ($\lim_{k\to\infty} \boldsymbol{Q}_{\hat{\boldsymbol{x}}_{k+1|K}} = \boldsymbol{Q}_{\hat{\boldsymbol{x}}_{k|K-1}}$) can be found as:

$$\boldsymbol{Q}_{\hat{\boldsymbol{x}}_{k|K-1}} = \boldsymbol{\Phi} \left(\boldsymbol{Q}_{\hat{\boldsymbol{x}}_{k|K-1}} - \boldsymbol{Q}_{\hat{\boldsymbol{x}}_{k|K-1}} \boldsymbol{A}^* \boldsymbol{Q}_{\boldsymbol{v}_k}^{-1} \boldsymbol{A} \boldsymbol{Q}_{\hat{\boldsymbol{x}}_{k|K-1}} \right) \boldsymbol{\Phi}^* + \boldsymbol{Q}_w \tag{B.7}$$

which leads to the classic discrete time algebraic Riccati equation (Lancaster and Rodman, 1995), which can be solved numerically:

$$\boldsymbol{Q}_{\hat{\boldsymbol{x}}_{k|K-1}} = \boldsymbol{\Phi} \boldsymbol{Q}_{\hat{\boldsymbol{x}}_{k|K-1}} \boldsymbol{\Phi}^* - \boldsymbol{\Phi} \boldsymbol{Q}_{\hat{\boldsymbol{x}}_{k|K-1}} \boldsymbol{A}^* \left(\boldsymbol{Q}_{\boldsymbol{y}} + \boldsymbol{A} \boldsymbol{Q}_{\hat{\boldsymbol{x}}_{k|K-1}} \boldsymbol{A}^* \right)^{-1} \boldsymbol{A} \boldsymbol{Q}_{\hat{\boldsymbol{x}}_{k|K-1}} \boldsymbol{\Phi}^* + \boldsymbol{Q}_w \tag{B.8}$$

For more insight and some numerical examples we will also consider a model with only a single unknown parameter x and observable y. Equations (B.1) to (B.3) then reduce to:

$$E\left\{ \left[\begin{array}{c} \underline{\hat{x}}_{k|K-1} \\ \underline{y}_k \end{array} \right] \right\} = \left[\begin{array}{c} 1 \\ a_k \end{array} \right] x_k \quad D\left\{ \left[\begin{array}{c} \underline{\hat{x}}_{k|K-1} \\ \underline{y}_k \end{array} \right] \right\} = \left[\begin{array}{cc} \sigma^2_{\hat{x}_{k|K-1}} & \\ & \sigma^2_{y_k} \end{array} \right] \tag{B.9}$$

$$\left\{ \begin{array}{lcl} \hat{x}_{k|K-1} & = & \phi_{k-1,k} \hat{x}_{k-1|K-1} \\ \sigma^2_{\hat{x}_{k|K-1}} & = & \phi^2_{k-1,k} \sigma^2_{\hat{x}_{k-1|K-1}} + \sigma^2_{w_k} \end{array} \right. \tag{B.10}$$

$$\left\{ \begin{array}{lcl} \hat{x}_{k|K} & = & \left(\sigma^{-2}_{\hat{x}_{k|K-1}} + a_k^2 \sigma^{-2}_{y_k} \right)^{-1} \left(\sigma^{-2}_{\hat{x}_{k|K-1}} \underline{\hat{x}}_{k|K-1} + a_k \sigma^{-2}_{y_k} \underline{y}_k \right) \\ \sigma^2_{\hat{x}_{k|K}} & = & \left(\left(\phi^2_{k-1,k} \sigma^2_{\hat{x}_{k-1|K-1}} + \sigma^2_{w_k} \right)^{-1} + a_k^2 \sigma^{-2}_{y_k} \right)^{-1} \end{array} \right. \tag{B.11}$$

A steady state is reached if $\lim_{k\to\infty} \sigma^2_{\hat{x}_{k+1|K+1}} = \sigma^2_{\hat{x}_{k|K}}$ while further assuming that $\phi_{k-1,k}$, σ_{w_k}, a_k and σ_{y_k} are constant and equal to, respectively, ϕ, σ_w, a and σ_y:

$$\sigma^2_{\hat{x}_{k|K}} = \left(\left(\phi^2 \sigma^2_{\hat{x}_{k|K}} + \sigma^2_w \right)^{-1} + a^2 \sigma_y^{-2} \right)^{-1} \tag{B.12}$$

Solving this equation for $\sigma^2_{\hat{x}_{k|K}}$ gives:

$$\sigma^2_{\hat{x}_{k|K}} = \frac{-\left(\left(1-\phi^2\right) \sigma_y^2 + a^2 \sigma_w^2 \right) \pm \sqrt{\left(\left(1-\phi^2\right) \sigma_y^2 + a^2 \sigma_w^2 \right)^2 + 4a^2 \phi^2 \sigma_y^2 \sigma_w^2}}{2a^2\phi^2} \tag{B.13}$$

Note that the discriminant of these roots is always positive. For the results to be meaningful, the variance itself also needs to be positive. If $0 \leq \phi < 1$, then the first term in eq. (B.13) is always negative, which means that only one of the roots can ever be positive:

$$\sigma^2_{\hat{x}_{k|K}} = \frac{-\left(\left(1-\phi^2\right)\sigma_y^2 + a^2\sigma_w^2\right) + \sqrt{\left(\left(1-\phi^2\right)\sigma_y^2 + a^2\sigma_w^2\right)^2 + 4a^2\phi^2\sigma_y^2\sigma_w^2}}{2a^2\phi^2} \tag{B.14}$$

We will now consider four special cases of these results, and look at the convergence as more observations are accumulated. We will also consider what happens in these cases if no observations are available from a certain epoch on. Simulated results are also provided in fig. B.1.

1. $\sigma_w \to \infty$. If the processing noise goes to infinite the predicted state gets less and less weight, and in the limit the results become equivalent with purely kinematic estimation. Equation (B.11) reduces to $\sigma_{\hat{x}_{k|K}} = \sigma_{\hat{x}_{k|k}} = \sigma_y/a$, with the matrix equivalent $\boldsymbol{Q}_{\hat{\boldsymbol{x}}_{k|K}} = \boldsymbol{Q}_{\hat{\boldsymbol{x}}_{k|k}} = \left(\boldsymbol{A}^*\boldsymbol{Q}_{\boldsymbol{y}}^{-1}\boldsymbol{A}\right)^{-1}$. If no observations are available (or if $\sigma_y \to \infty$) the estimator becomes undefined.

2. $\phi = 1$, $\sigma_w = 0$. If the processing noise is zero and the transition matrix is an identity matrix, a static or constant parameter is estimated. In this case the filter cannot reach a steady state, but rather the estimation keeps improving and the variance of the estimated parameters approaches zero $\sigma_{\hat{x}_{k|K}} \downarrow 0$ and $\boldsymbol{Q}_{\hat{\boldsymbol{x}}_{k|K}} \downarrow \boldsymbol{0}$. When no observations are available the estimated parameters and their variance remain the same.

3. $\phi = 1$, $\sigma_w^2 > 0$. This model, often called random walk, can be used to estimate nonzero-mean parameters whose variation in time is limited but not zero. The variance of the estimated parameter approaches: $\lim_{k\to\infty} \sigma^2_{\hat{x}_{k|K}} = \frac{-\sigma_w^2 + \sqrt{\sigma_w^4 + 4\sigma_y^2\sigma_w^2/a^2}}{2}$ with the matrix equivalent: $\boldsymbol{Q}_{\hat{\boldsymbol{x}}_{k|K}}\boldsymbol{A}^*\boldsymbol{Q}_{\boldsymbol{y}}^{-1}\boldsymbol{A}\left(\boldsymbol{Q}_{\hat{\boldsymbol{x}}_{k|K}} + \boldsymbol{Q}_w\right) = \boldsymbol{Q}_w$. When no observations are available the variance grows to infinity and the parameter slowly becomes undetermined again.

4. $0 < \phi < 1$, $\sigma_w > 0$. This is an observed first order autoregressive process as seen in section 6.3.1. The steady state variances are those provided in eq. (B.14) and eq. (B.5) for matrices. When no observations are available (or $\sigma_y \to \infty$) the variance increases to a new steady state value; eq. (B.11) simplifies to: $\sigma^2_{\hat{x}_{k|K}} = \phi^2_{k-1,k}\sigma^2_{\hat{x}_{k-1|K-1}} + \sigma^2_{w_k}$ with the following limit: $\lim_{k\to\infty} \sigma^2_{\hat{x}_{k|K}} = \frac{\sigma_w^2}{1-\phi^2}$. The matrix equivalent follows from eq. (B.3): $\boldsymbol{Q}_{\hat{\boldsymbol{x}}_{k|K}} = \boldsymbol{\Phi}_{k-1,k}\boldsymbol{Q}_{\hat{\boldsymbol{x}}_{k-1|K-1}}\boldsymbol{\Phi}^*_{k-1,k} + \boldsymbol{Q}_{w_k}$, which is known as the discrete Lyapunov equation. An analytical solution of this equation can be found by applying the following property of the vec-operator and Kronecker product $\mathrm{vec}(\boldsymbol{ABC}) = (\boldsymbol{C}^* \otimes \boldsymbol{A})\,\mathrm{vec}(\boldsymbol{B})$. This leads to: $\mathrm{vec}\left(\boldsymbol{Q}_{\hat{\boldsymbol{x}}_{k|K}}\right) = (\boldsymbol{I} - \boldsymbol{\Phi}_{k-1,k} \otimes \boldsymbol{\Phi}_{k-1,k})^{-1}\,\mathrm{vec}\left(\boldsymbol{Q}_{w_k}\right)$ Note that of the presented models only the AR(1) process has a defined variance at epoch 0 even before the first observations are available.

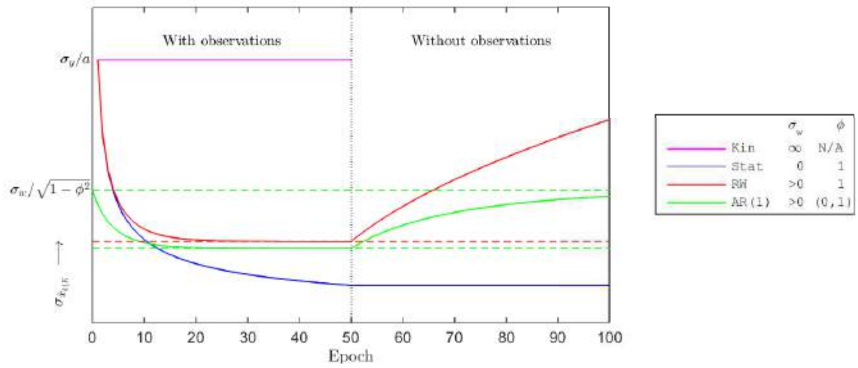

Figure B.1: Convergence of recursive estimation of a single unknown parameter

Another use of the presented equations is to compute the process noise if the steady state variance is known. In this case eq. (B.5) can be solved for $\boldsymbol{Q}_w$ as:

$$\boldsymbol{Q}_w = \left(\boldsymbol{I} - \boldsymbol{Q}_{\hat{\boldsymbol{x}}_{k|K}} \boldsymbol{A}^* \boldsymbol{Q}_{\boldsymbol{y}}^{-1} \boldsymbol{A}\right)^{-1} \boldsymbol{Q}_{\hat{\boldsymbol{x}}_{k|K}} - \boldsymbol{\Phi} \boldsymbol{Q}_{\hat{\boldsymbol{x}}_{k|K}} \boldsymbol{\Phi}^* \tag{B.15}$$

and for the random walk model:

$$\begin{aligned} \boldsymbol{Q}_w &= \left(\boldsymbol{I} - \boldsymbol{Q}_{\hat{\boldsymbol{x}}_{k|K}} \boldsymbol{A}^* \boldsymbol{Q}_{\boldsymbol{y}}^{-1} \boldsymbol{A}\right)^{-1} \boldsymbol{Q}_{\hat{\boldsymbol{x}}_{k|K}} - \boldsymbol{Q}_{\hat{\boldsymbol{x}}_{k|K}} \\ &= \left(\boldsymbol{I} - \boldsymbol{Q}_{\hat{\boldsymbol{x}}_{k|K}} \boldsymbol{A}^* \boldsymbol{Q}_{\boldsymbol{y}}^{-1} \boldsymbol{A}\right)^{-1} \boldsymbol{Q}_{\hat{\boldsymbol{x}}_{k|K}} \boldsymbol{A}^* \boldsymbol{Q}_{\boldsymbol{y}}^{-1} \boldsymbol{A} \boldsymbol{Q}_{\hat{\boldsymbol{x}}_{k|K}} \end{aligned} \tag{B.16}$$

The equivalent single parameter equations are, respectively:

$$\sigma_w^2 = \frac{\sigma_{\hat{x}}^2 \sigma_y^2}{\sigma_y^2 - a^2 \sigma_{\hat{x}}^2} - \phi^2 \sigma_{\hat{x}}^2 \tag{B.17}$$

$$\sigma_w^2 = \frac{a^2 \sigma_{\hat{x}}^4}{\sigma_y^2 - a^2 \sigma_{\hat{x}}^2} \tag{B.18}$$

B.2 Dynamic models and data-rate

In section 6.3 we estimated AR processes from multipath time series. These AR processes can be used to extend the Kalman filter to take care of time correlated errors. The dynamic model for a Kalman filter state is defined by the relevant entry in the transition matrix f (which is the AR(1) parameter) and the variance of the process noise σ_w^2. However, both of these values depend on the data-rate of the Kalman filter. Therefore, the AR(1) processes estimated in section 6.3 from 1Hz observations can only be used directly in a 1 Hz Kalman filter. However, the following equation can be used to recompute these values for other data-rates. Firstly, the time correlation factor τ can be computed from the AR(1) parameter, here f, and the time interval Δt:

$$\tau = -\Delta t / ln\,(f) \tag{B.19}$$

where ln is the natural logarithm. Then the steady-state variance σ_0^2 can be computed from the process noise and f:

$$\sigma_0^2 = \sigma_w^2 / \left(1 - f^2\right) \tag{B.20}$$

Both τ and σ_0 are independent of the data-rate. So now f and σ_w can be computed for a different time interval as follows:

$$f = e^{-\Delta t/\tau} \tag{B.21}$$

and:

$$\sigma_w^2 = \sigma_0^2 \left(1 - f^2\right) \tag{B.22}$$

Appendix: Proofs Integrity Monitoring

C

The proofs in this appendix pertain to chapter 7, they were first published in Teunissen and de Bakker (2012).

Proof of Theorem 1 (UMPI test statistic): First we prove eq. (7.14). Define

$$\begin{array}{lcl} A & = & (A_1, A_2) = (I_{k-1} \otimes G, D_k^* s_l \otimes H) \\ W & = & (D_k^* D_k)^{-1} \otimes Q^{-1} \\ x & = & (dg^*, b^*)^* \end{array} \tag{C.1}$$

Reduction of the system of normal equations $A^* W A \hat{x} = A^* W y$ for $\hat{b}$ gives $\bar{A}_2^* W \bar{A}_2 \hat{b} = \bar{A}_2^* W y$ and thus

$$\hat{b} = (\bar{A}_2^* W \bar{A}_2)^{-1} \bar{A}_2^* W y \quad , \quad Q_{\hat{b}\hat{b}} = (\bar{A}_2^* W \bar{A}_2)^{-1} \tag{C.2}$$

with $\bar{A}_2 = P_{A_1}^{\perp} A_2$ and $P_{A_1}^{\perp} = I - A_1 (A_1^* W A_1)^{-1} A_1^* W$. With the use of eq. (C.1) in eq. (C.2), the result eq. (7.14) follows.

For the UMPI test statistic, we have $T_q = \hat{b}^* Q_{\hat{b}\hat{b}}^{-1} \hat{b} = y^* W \bar{A}_2^* (\bar{A}_2^* W \bar{A}_2)^{-1} \bar{A}_2 W y$. With the use of eq. (C.1), this expression reduces to eq. (7.15). $\triangleleft$

Proof of Theorem 2 (Phase-slip MDB): For an MDB with $k = l = 2$, we have, with $q = 1$ (i.e., $d = \pm 1$), according to eqs. (7.16) and (7.26),

$$\text{MDB} = \sqrt{\frac{2\lambda_0}{H^* Q^{-1} P_G^{\perp} H}} \tag{C.3}$$

For a phase-slip MDB we have $H = (\delta_j^*, 0^*, 0^*)^*$, $Q =$ blockdiag$(\sigma_\phi^2 I_n, \sigma_p^2 I_n, \frac{1}{2}\sigma_{d\mathcal{I}}^2)$ and $P_G^{\perp} = I_n - G(G^* Q^{-1} G)^{-1} G^* Q^{-1}$. Substitution into eq. (C.3) gives the phase-slip MDB as

$$\text{MDB}_{\phi_j} = \sigma_\phi \sqrt{\frac{2\lambda_0}{1 - \frac{1}{n'}}} \tag{C.4}$$

with $\frac{1}{n'} = \delta_j^* G (G^* \sigma_\phi^2 Q^{-1} G)^{-1} G^* \delta_j$. A further simplification of this scalar expression gives eq. (7.30). $\triangleleft$

Proof of Lemma 3 (Phase loss-of-lock MDB upper bounds): We give the proof for the ionosphere-fixed case. For the ionosphere-float case it goes along similar lines.

To determine the eigenvalues of $Q_{\hat{b}\hat{b}}$ (c.f. eq. (7.49)) for $Q_{\phi\phi} = \sigma_\phi^2 I_n$, $Q_{pp} = \sigma_p^2 I_n$ and $\sigma_{d\mathcal{I}}^2 = 0$, we need to determine the root ψ of

$$|2\sigma_\phi^2 I_n + 2\sigma_p^2 e(e^* e)^{-1} e^* - \psi I_n| = 0 \tag{C.5}$$

Let D be an $n \times (n-1)$ basis matrix of the orthogonal complement of e. Then the $n \times n$ matrix $M = [D, e]$ is of full rank. Pre- and post-multiplication of the matrix in eq. (C.5) with M^* and M allows to reduce the determinantal equation into a product,

$$|(2\sigma_\phi^2 - \psi) D^* D| \, |(2\sigma_p^2 - \psi) n + 2\sigma_p^2 n| = 0 \tag{C.6}$$

This shows that there are $(n-1)$ eigenvalues with the value $\psi = 2\sigma_\phi^2$ and one eigenvalue, the largest, with the value $\psi = 2(\sigma_\phi^2 + \sigma_p^2) = 2\sigma_p(1+\epsilon)$. Hence, for the MDB upper bound we get

$$|| \text{MDB}||_\phi \leq \sqrt{\psi_{max} \lambda_0} = \sigma_p \sqrt{2(1+\epsilon)\lambda_0} \tag{C.7}$$

This concludes the proof. $\triangleleft$

Appendix: Redundancy Tables

D

This appendix contains redundancy tables for each of the models discussed in chapter 4. Only temporal parameters, for which we do not have any dynamic model, and global parameters, which are held constant, are considered for these tables. Each table shows the number of observations and unknown parameters, the redundancy and the minimal number of satellites m as a function of the number of epochs k. The number of epochs k is shown up to the value for which the minimal required number of satellites no longer decreases. Both a static user position and a kinematic user position are considered, as well as the models with and without the estimation of a zenith troposphere delay. In the single frequency code-only and phase-only models the slant ionosphere delays are not estimated (but should be corrected by a model), in the dual frequency models the ionosphere delays are estimated and the single frequency code & phase model is shown with and without ionosphere estimation.

static position		without troposphere estimation			with troposphere estimation		
epochs	observations	unknowns	redundancy	min(m)	unknowns	redundancy	min(m)
1	m	4	$m-4$	4	5	$m-5$	5
2	$2m$	5	$2m-5$	3	7	$2m-7$	4
3	$3m$	6	$3m-6$	2	9	$3m-9$	3
k	km	$k+3$	$k(m-1)$ -3	$1+\left\lceil\frac{3}{k}\right\rceil$	$2k+3$	$k(m-2)$ -3	$2+\left\lceil\frac{3}{k}\right\rceil$
kinematic position							
1	m	4	$m-4$	4	5	$m-5$	5
k	km	$4k$	$k(m-4)$	4	$5k$	$k(m-5)$	5

Table D.1: Redundancy of the single frequency code-only model

static position		without troposphere estimation			with troposphere estimation		
epochs	observations	unknowns	redundancy	min(m)	unknowns	redundancy	min(m)
1	$2m$	$m+4$	$m-4$	4	$m+5$	$m-5$	5
2	$4m$	$2m+5$	$2m-5$	3	$2m+7$	$2m-7$	4
3	$6m$	$3m+6$	$3m-6$	2	$3m+9$	$3m-9$	3
k	$2km$	$k(m+1)$ $+3$	$k(m-1)$ -3	$1+\left\lceil\frac{3}{k}\right\rceil$	$k(m+2)$ $+3$	$k(m-2)$ -3	$2+\left\lceil\frac{3}{k}\right\rceil$
kinematic position							
1	$2m$	$m+4$	$m-4$	4	$m+5$	$m-5$	5
k	$2km$	$k(m+4)$	$k(m-4)$	4	$k(m+5)$	$k(m-5)$	5

Table D.2: Redundancy of the dual frequency code-only model

static position		without troposphere estimation			with troposphere estimation		
epochs	observations	unknowns	redundancy	min(m)	unknowns	redundancy	min(m)
1	m	$m+3$	-3	N/A	$m+4$	-4	N/A
2	$2m$	$m+4$	$m-4$	4	$m+6$	$m-6$	6
3	$3m$	$m+5$	$2m-5$	3	$m+8$	$2m-8$	4
4	$4m$	$m+6$	$3m-6$	2	$m+10$	$3m-10$	4
5	$5m$	$m+7$	$4m-7$	2	$m+12$	$4m-12$	3
k	km	$m+k$ $+2$	$m(k-1)$ $-k-2$	$1+\left\lceil\frac{3}{k-1}\right\rceil$	$m+2k$ $+2$	$m(k-1)$ $-2k-2$	$2+\left\lceil\frac{4}{k-1}\right\rceil$
kinematic position							
1	m	$m+3$	-3	N/A	$m+4$	-4	N/A
2	$2m$	$m+7$	$m-7$	7	$m+9$	$m-9$	9
3	$3m$	$m+11$	$2m-11$	6	$m+14$	$2m-14$	7
4	$4m$	$m+15$	$3m-15$	5	$m+19$	$3m-19$	7
5	$5m$	$m+19$	$4m-19$	5	$m+24$	$4m-24$	6
k	km	$m+4k$ -1	$m(k-1)$ $-4k+1$	$4+\left\lceil\frac{3}{k-1}\right\rceil$	$m+5k$ -1	$m(k-1)$ $-5k+1$	$5+\left\lceil\frac{4}{k-1}\right\rceil$

Table D.3: Redundancy of the single frequency phase-only model

static position		without troposphere estimation			with troposphere estimation		
epochs	observations	unknowns	redundancy	min(m)	unknowns	redundancy	min(m)
1	$2m$	$2m+3$	-3	N/A	$2m+4$	-4	N/A
2	$4m$	$3m+4$	$m-4$	4	$3m+6$	$m-6$	6
3	$6m$	$4m+5$	$2m-5$	3	$4m+8$	$2m-8$	4
4	$8m$	$5m+6$	$3m-6$	2	$5m+10$	$3m-10$	4
5	$10m$	$6m+7$	$4m-7$	2	$6m+12$	$4m-12$	3
k	$2km$	$m(k+1)$ $+k+2$	$m(k-1)$ $-k-2$	$1+\left\lceil\frac{3}{k-1}\right\rceil$	$m(k+1)$ $+2k+2$	$m(k-1)$ $-2k-2$	$2+\left\lceil\frac{4}{k-1}\right\rceil$
kinematic position							
1	$2m$	$2m+3$	-3	N/A	$2m+4$	-4	N/A
2	$4m$	$3m+7$	$m-7$	7	$3m+9$	$m-9$	9
3	$6m$	$4m+11$	$2m-11$	6	$4m+14$	$2m-14$	7
4	$8m$	$5m+15$	$3m-15$	5	$5m+19$	$3m-19$	7
5	$10m$	$6m+19$	$4m-19$	5	$6m+24$	$4m-24$	6
k	$2km$	$m(k+1)$ $+4k-1$	$m(k-1)$ $-4k+1$	$4+\left\lceil\frac{3}{k-1}\right\rceil$	$m(k+1)$ $+5k-1$	$m(k-1)$ $-5k+1$	$5+\left\lceil\frac{4}{k-1}\right\rceil$

Table D.4: Redundancy of the dual frequency phase-only model

static position		without troposphere estimation			with troposphere estimation		
epochs	observations	unknowns	redundancy	min(m)	unknowns	redundancy	min(m)
1	$2m$	$2m+3$	-3	N/A	$2m+4$	-4	N/A
2	$4m$	$3m+4$	$m-4$	4	$3m+6$	$m-6$	6
3	$6m$	$4m+5$	$2m-5$	3	$4m+8$	$2m-8$	4
4	$8m$	$5m+6$	$3m-6$	2	$5m+10$	$3m-10$	4
5	$10m$	$6m+7$	$4m-7$	2	$6m+12$	$4m-12$	3
k	$2km$	$m(k+1)$ $+k+2$	$m(k-1)$ $-k-2$	$1+\left\lceil\frac{3}{k-1}\right\rceil$	$m(k+1)$ $+2k+2$	$m(k-1)$ $-2k-2$	$2+\left\lceil\frac{4}{k-1}\right\rceil$
kinematic position							
1	$2m$	$2m+3$	-3	N/A	$2m+4$	-5	N/A
2	$4m$	$3m+7$	$m-7$	7	$3m+9$	$m-9$	9
3	$6m$	$4m+11$	$2m-11$	6	$4m+14$	$2m-14$	7
4	$8m$	$5m+15$	$3m-15$	5	$5m+19$	$3m-19$	7
5	$10m$	$6m+19$	$4m-19$	5	$6m+24$	$4m-24$	6
k	$2km$	$m(k+1)$ $+4k-1$	$m(k-1)$ $-4k+1$	$4+\left\lceil\frac{3}{k-1}\right\rceil$	$m(k+1)$ $+5k-1$	$m(k-1)$ $-5k+1$	$5+\left\lceil\frac{4}{k-1}\right\rceil$

Table D.5: Redundancy of the single frequency code & phase model with ionosphere estimation

static position		without troposphere estimation			with troposphere estimation		
epochs	observations	unknowns	redundancy	min(m)	unknowns	redundancy	min(m)
1	$2m$	$m+4$	$m-4$	4	$m+5$	$m-5$	5
2	$4m$	$m+6$	$3m-6$	2	$m+8$	$3m-8$	3
3	$6m$	$m+8$	$5m-8$	2	$m+11$	$5m-11$	3
4	$8m$	$m+10$	$7m-10$	2	$m+14$	$7m-14$	2
k	$2km$	$m+2k$ $+2$	$m(2k-1)$ $-2k-2$	$1+\left\lceil\frac{3}{2k-1}\right\rceil$	$m+3k$ $+2$	$m(2k-1)$ $-3k-2$	$1+\left\lceil\frac{k+3}{2k-1}\right\rceil$
kinematic position							
1	$2m$	$m+4$	$m-4$	4	$m+5$	$m-5$	5
2	$4m$	$m+9$	$3m-9$	3	$m+11$	$3m-11$	4
k	$2km$	$m+5k$ -1	$m(2k-1)$ $-5k+1$	$2+\left\lceil\frac{k+1}{2k-1}\right\rceil$	$m+6k$ -1	$m(2k-1)$ $-6k+1$	$3+\left\lceil\frac{2}{2k-1}\right\rceil$

Table D.6: Redundancy of the single frequency code & phase model without ionosphere estimation

static position		without troposphere estimation			with troposphere estimation		
epochs	observations	unknowns	redundancy	min(m)	unknowns	redundancy	min(m)
1	$4m$	$3m+4$	$m-4$	4	$3m+5$	$m-5$	5
2	$8m$	$4m+7$	$4m-7$	2	$4m+9$	$4m-9$	3
3	$12m$	$5m+10$	$7m-10$	2	$5m+13$	$7m-13$	2
k	$4km$	$m(k+2)$ $+3k+1$	$m(3k-2)$ $-3k-1$	$1+\left\lceil\frac{3}{3k-2}\right\rceil$	$m(k+2)$ $+4k+1$	$m(3k-2)$ $-4k-1$	$1+\left\lceil\frac{k+3}{3k-2}\right\rceil$
kinematic position							
1	$4m$	$3m+4$	$m-4$	4	$3m+5$	$m-5$	5
2	$8m$	$4m+10$	$4m-10$	3	$4m+12$	$4m-12$	3
k	$4km$	$m(k+2)$ $+6k-2$	$m(3k-2)$ $-6k+2$	$2+\left\lceil\frac{2}{3k-2}\right\rceil$	$m(k+2)$ $+7k-2$	$m(3k-2)$ $-7k+2$	$2+\left\lceil\frac{k+2}{3k-2}\right\rceil$

Table D.7: Redundancy of the dual frequency code & phase model

static position		without troposphere estimation			with troposphere estimation		
epochs	observations	unknowns	redundancy	min(m)	unknowns	redundancy	min(m)
1	$4m$	$2m+5$	$2m-5$	3	$2m+6$	$2m-6$	3
2	$8m$	$2m+9$	$6m-9$	2	$2m+11$	$6m-11$	2
k	$4km$	$2m+4k$ $+1$	$m(4k-2)$ $-4k-1$	$1+\left\lceil\frac{3}{4k-2}\right\rceil$	$2m+5k$ $+1$	$m(4k-2)$ $-5k-1$	$1+\left\lceil\frac{k+3}{4k-2}\right\rceil$
kinematic position							
1	$4m$	$2m+5$	$2m-5$	3	$2m+6$	$2m-6$	3
2	$8m$	$2m+12$	$6m-12$	2	$2m+14$	$6m-14$	3
k	$4km$	$2m+7k$ -2	$m(4k-2)$ $-7k+2$	$1+\left\lceil\frac{3k}{4k-2}\right\rceil$	$2m+8k$ -2	$m(4k-2)$ $-8k+2$	$2+\left\lceil\frac{2}{4k-2}\right\rceil$

Table D.8: Redundancy of the dual frequency code, phase & ionosphere model

Appendix: Group Delay Estimation

E

This appendix treats group delay estimation from a single receiver starting with the code-only PPP model. In section 4.4 it was assumed that the ionosphere-free satellite hardware group delays were provided by the PPP network, and they were consequently removed from the positioning model. This led to the code-only model which can be solved from a single epoch of data, and has good convergence behavior.

However, it is also possible to estimate (corrections to) these delays together with the other unknown parameters. If the ionosphere-free group delays are not removed from the model, the rank defects can be solved as follows:

$$E\left\{\begin{bmatrix}\Delta\boldsymbol{P}^S_{r,L1,k}\\ \Delta\boldsymbol{P}^S_{r,L2,k}\end{bmatrix}\right\} = \begin{bmatrix}-\mathbf{e}^{S*}_{r,k} & \mathbf{m}_m & \mathbf{u}_m & \mathbf{u}_m & \overset{0\cdots0}{\mathbf{I}_{m-1}} & \overset{0\cdots0}{\mathbf{I}_{m-1}}\\ -\mathbf{e}^{S*}_{r,k} & \mathbf{m}_m & \mathbf{u}_m & \gamma\mathbf{u}_m & \overset{0\cdots0}{\mathbf{I}_{m-1}} & \gamma\overset{0\cdots0}{\mathbf{I}_{m-1}}\end{bmatrix}\begin{bmatrix}\Delta\mathbf{r}_r\\ T_{Z,r,k}\\ dt_{r,k}+d_{r,L3,k}-d^1_{L3,k}\\ d_{r,L4,k}+\mathcal{I}^1_{r,k}-d^1_{L4,k}\\ -\boldsymbol{d}^{1S}_{L3,k}\\ \boldsymbol{\mathcal{I}}^{1S}_{r,k}-\boldsymbol{d}^{1S}_{L4,k}\end{bmatrix} \tag{E.1}$$

Note that the delays cannot be estimated as kinematic parameters, but if multiple epoch of data are used they can be estimated as constants or with a dynamic model. Compared to the regular code-only model there are $m-1$ additional unknown bias parameters; estimation of a zenith troposphere delay is optional in both models.

The estimation model can be strengthened further by adding the phase observations. The rank defects in the code+phase model can then be solved as follows.

$$E\left\{\begin{bmatrix}\Delta\boldsymbol{\phi}^S_{r,L1,k}\\ \Delta\boldsymbol{\phi}^S_{r,L2,k}\\ \Delta\boldsymbol{P}^S_{r,L1,k}\\ \Delta\boldsymbol{P}^S_{r,L2,k}\end{bmatrix}\right\} =$$

$$\begin{bmatrix}-\mathbf{e}^{S*}_{r,k} & \mathbf{m}_m & \mathbf{u}_m & -\mathbf{u}_m & & & \overset{0\cdots0}{\mathbf{I}_{m-1}} & -\overset{0\cdots0}{\mathbf{I}_{m-1}} & & \\ -\mathbf{e}^{S*}_{r,k} & \mathbf{m}_m & \mathbf{u}_m & -\gamma\mathbf{u}_m & & & \overset{0\cdots0}{\mathbf{I}_{m-1}} & -\gamma\overset{0\cdots0}{\mathbf{I}_{m-1}} & & \\ -\mathbf{e}^{S*}_{r,k} & \mathbf{m}_m & \mathbf{u}_m & \mathbf{u}_m & \mathbf{u}_m & \mathbf{u}_m & & \overset{0\cdots0}{\mathbf{I}_{m-1}} & \overset{0\cdots0}{\mathbf{I}_{m-1}} & \overset{0\cdots0}{\mathbf{I}_{m-1}}\\ -\mathbf{e}^{S*}_{r,k} & \mathbf{m}_m & \mathbf{u}_m & \gamma\mathbf{u}_m & \mathbf{u}_m & \gamma\mathbf{u}_m & & \gamma\overset{0\cdots0}{\mathbf{I}_{m-1}} & \overset{0\cdots0}{\mathbf{I}_{m-1}} & \gamma\overset{0\cdots0}{\mathbf{I}_{m-1}}\end{bmatrix}\begin{bmatrix}\Delta\mathbf{r}_r\\ T_{Z,r,k}\\ dt_{r,k}+\delta_{r,L3,k}+A^1_{r,L3,k}-\delta^1_{L3,k}\\ -\delta_{r,L4,k}+\mathcal{I}^1_{r,k}-A^1_{r,L4}+\delta^1_{L4,k}\\ d_{r,L3,k}-d^1_{L3,k}-\delta_{r,L3,k}-A^1_{r,L3,k}+\delta^1_{L3,k}\\ d_{r,L4,k}-d^1_{L4,k}+\delta_{r,L4,k}+A^1_{r,L4}-\delta^1_{L4,k}\\ \mathbf{A}^{1S}_{r,L3}-\boldsymbol{\delta}^{1S}_{L3,k}\\ \boldsymbol{\mathcal{I}}^{1S}_{r,k}-\mathbf{A}^{1S}_{r,L4}+\boldsymbol{\delta}^{1S}_{L4,k}\\ -\boldsymbol{d}^{1S}_{L3,k}\\ -\boldsymbol{d}^{1S}_{L4,k}+\mathbf{A}^{1S}_{r,L4}-\boldsymbol{\delta}^{1S}_{L4,k}\end{bmatrix} \tag{E.2}$$

Finally we can simplify the model again if we assume the position to be known, and neglect the phase uncertainty w.r.t. the pseudo range uncertainty, as follows:

$$E\left\{\begin{bmatrix}\Delta\bar{\boldsymbol{P}}^{S}_{r,L1,k}\\ \Delta\bar{\boldsymbol{P}}^{S}_{r,L2,k}\end{bmatrix}\right\} = \begin{bmatrix}\mathbf{u}_m & \mathbf{u}_m & \overset{0\cdots0}{\mathbf{I}_{m-1}} & \overset{0\cdots0}{\mathbf{I}_{m-1}}\\ \mathbf{u}_m & \gamma\mathbf{u}_m & \overset{0\cdots0}{\mathbf{I}_{m-1}} & \gamma\overset{0\cdots0}{\mathbf{I}_{m-1}}\end{bmatrix}\begin{bmatrix}d_{r,L3,k} - d^{1}_{L3,k} - \delta_{r,L3,k} - A^{1}_{r,L3,k} + \delta^{1}_{L3,k}\\ d_{r,L4,k} - d^{1}_{L4,k} + \delta_{r,L4,k} + A^{1}_{r,L4} - \delta^{1}_{L4,k}\\ -\boldsymbol{d}^{1S}_{L3,k}\\ -\boldsymbol{d}^{1S}_{L4,k} + \mathbf{A}^{1S}_{r,L4} - \boldsymbol{\delta}^{1S}_{L4,k}\end{bmatrix} \tag{E.3}$$

Appendix: Partitioned Models

F

This appendix takes a closer look at models that contain a critical partition, i.e. a partition with an equal number of observations and unknown parameters, and without redundancy. The design matrix corresponding to this partition should be square and of full rank, which also makes it invertible.

F.1 Models with critical partition 1

Suppose we have an observation model with the following structure:

$$E\left\{\begin{bmatrix}\underline{\boldsymbol{y}}_1\\ \underline{\boldsymbol{y}}_2\end{bmatrix}\right\}=\begin{bmatrix}\boldsymbol{A}_{1a} & \boldsymbol{A}_{1b}\\ \boldsymbol{A}_{2a} & \boldsymbol{A}_{2b}\end{bmatrix}\begin{bmatrix}\boldsymbol{x}_a\\ \boldsymbol{x}_b\end{bmatrix};\quad D\left\{\begin{bmatrix}\underline{\boldsymbol{y}}_1\\ \underline{\boldsymbol{y}}_2\end{bmatrix}\right\}=\boldsymbol{Q}_{yy} \tag{F.1}$$

with $\boldsymbol{A}_{2b}$ a square matrix of full rank. Since this makes $\boldsymbol{A}_{2b}$ invertible, we can pre-multiply this model with the following invertible transformation matrix $\boldsymbol{Z}$:

$$\boldsymbol{Z}=\begin{bmatrix}\boldsymbol{I}_{m_1} & -\boldsymbol{A}_{1b}\boldsymbol{A}_{2b}^{-1}\\ & \boldsymbol{I}_{m_2}\end{bmatrix} \tag{F.2}$$

This gives the following transformed model:

$$E\left\{\begin{bmatrix}\bar{\underline{\boldsymbol{y}}}_1\\ \underline{\boldsymbol{y}}_2\end{bmatrix}\right\}=\begin{bmatrix}\bar{\boldsymbol{A}}_{1a} & \\ \boldsymbol{A}_{2a} & \boldsymbol{A}_{2b}\end{bmatrix}\begin{bmatrix}\boldsymbol{x}_a\\ \boldsymbol{x}_b\end{bmatrix};\quad D\left\{\begin{bmatrix}\bar{\underline{\boldsymbol{y}}}_1\\ \underline{\boldsymbol{y}}_2\end{bmatrix}\right\}=\bar{\boldsymbol{Q}}_{yy} \tag{F.3}$$

with:

$$\begin{array}{rcl}\bar{\underline{\boldsymbol{y}}}_1 & = & \underline{\boldsymbol{y}}_1-\boldsymbol{A}_{1b}\boldsymbol{A}_{2b}^{-1}\underline{\boldsymbol{y}}_2\\ \bar{\boldsymbol{A}}_{1a} & = & \boldsymbol{A}_{1a}-\boldsymbol{A}_{1b}\boldsymbol{A}_{2b}^{-1}\boldsymbol{A}_{2a}\\ \bar{\boldsymbol{Q}}_{yy} & = & \boldsymbol{Z}\boldsymbol{Q}_{yy}\boldsymbol{Z}^*\end{array} \tag{F.4}$$

Note that the unknown parameters $\boldsymbol{x}_b$ now only occur in the observation equations of $\underline{\boldsymbol{y}}_2$

F.2 Observation decorrelation

Suppose we have an observation model with the following structure:

$$E\left\{\begin{bmatrix}\underline{\boldsymbol{y}}_1\\ \underline{\boldsymbol{y}}_2\end{bmatrix}\right\}=\begin{bmatrix}\boldsymbol{A}_{1a} & \\ \boldsymbol{A}_{2a} & \boldsymbol{A}_{2b}\end{bmatrix}\begin{bmatrix}\boldsymbol{x}_a\\ \boldsymbol{x}_b\end{bmatrix};\quad D\left\{\begin{bmatrix}\underline{\boldsymbol{y}}_1\\ \underline{\boldsymbol{y}}_2\end{bmatrix}\right\}=\begin{bmatrix}\boldsymbol{Q}_{11} & \boldsymbol{Q}_{12}\\ \boldsymbol{Q}_{21} & \boldsymbol{Q}_{22}\end{bmatrix} \tag{F.5}$$

in which unknown parameters $\boldsymbol{x}_b$ only occur in the observation equations of $\underline{\boldsymbol{y}}_2$. The observations can be decorrelated by pre-multiplication with the invertible transformation matrix $\boldsymbol{Z}$:

$$\boldsymbol{Z} = \begin{bmatrix} \boldsymbol{I}_{m_1} & \\ -\boldsymbol{Q}_{21}\boldsymbol{Q}_{11}^{-1} & \boldsymbol{I}_{m_2} \end{bmatrix} \tag{F.6}$$

This gives the following transformed model:

$$E\left\{\begin{bmatrix} \underline{\boldsymbol{y}}_1 \\ \bar{\underline{\boldsymbol{y}}}_2 \end{bmatrix}\right\} = \begin{bmatrix} \boldsymbol{A}_{1a} & \\ \bar{\boldsymbol{A}}_{2a} & \boldsymbol{A}_{2b} \end{bmatrix}\begin{bmatrix} \boldsymbol{x}_a \\ \boldsymbol{x}_b \end{bmatrix}; \quad D\left\{\begin{bmatrix} \underline{\boldsymbol{y}}_1 \\ \bar{\underline{\boldsymbol{y}}}_2 \end{bmatrix}\right\} = \begin{bmatrix} \boldsymbol{Q}_{11} & \\ & \bar{\boldsymbol{Q}}_{22} \end{bmatrix} \tag{F.7}$$

with:

$$\begin{array}{rcl} \bar{\underline{\boldsymbol{y}}}_2 & = & \underline{\boldsymbol{y}}_2 - \boldsymbol{Q}_{21}\boldsymbol{Q}_{11}^{-1}\underline{\boldsymbol{y}}_1 \\ \bar{\boldsymbol{A}}_{2a} & = & \boldsymbol{A}_{2a} - \boldsymbol{Q}_{21}\boldsymbol{Q}_{11}^{-1}\boldsymbol{A}_{1a} \\ \bar{\boldsymbol{Q}}_{22} & = & \boldsymbol{Q}_{22} - \boldsymbol{Q}_{21}\boldsymbol{Q}_{11}^{-1}\boldsymbol{Q}_{12} \end{array} \tag{F.8}$$

Note that the observations $\underline{\boldsymbol{y}}_1$ and $\bar{\underline{\boldsymbol{y}}}_2$ are decorrelated and that the unknown parameters $\boldsymbol{x}_b$ now only occur in the observation equations of $\bar{\underline{\boldsymbol{y}}}_2$

F.3 Models with critical partition 2

Suppose we have an observation model with the following structure:

$$E\left\{\begin{bmatrix} \underline{\boldsymbol{y}}_1 \\ \underline{\boldsymbol{y}}_2 \end{bmatrix}\right\} = \begin{bmatrix} \boldsymbol{A}_{1a} & \\ \boldsymbol{A}_{2a} & \boldsymbol{A}_{2b} \end{bmatrix}\begin{bmatrix} \boldsymbol{x}_a \\ \boldsymbol{x}_b \end{bmatrix}; \quad D\left\{\begin{bmatrix} \underline{\boldsymbol{y}}_1 \\ \underline{\boldsymbol{y}}_2 \end{bmatrix}\right\} = \begin{bmatrix} \boldsymbol{Q}_{11} & \\ & \boldsymbol{Q}_{22} \end{bmatrix} \tag{F.9}$$

in which the observations $\underline{\boldsymbol{y}}_1$ and $\underline{\boldsymbol{y}}_2$ are uncorrelated, the unknown parameters $\boldsymbol{x}_b$ only occur in the observation equations of $\underline{\boldsymbol{y}}_2$, and with $\boldsymbol{A}_{2b}$ a square matrix of full rank. Since this makes $\boldsymbol{A}_{2b}$ invertible, we can pre-multiply this model with the following invertible transformation matrix $\boldsymbol{Z}$:

$$\boldsymbol{Z} = \begin{bmatrix} \boldsymbol{I}_{m_1} & \\ & \boldsymbol{A}_{2b}^{-1} \end{bmatrix} \tag{F.10}$$

This gives the following transformed model:

$$E\left\{\begin{bmatrix} \underline{\boldsymbol{y}}_1 \\ \bar{\underline{\boldsymbol{y}}}_2 \end{bmatrix}\right\} = \begin{bmatrix} \boldsymbol{A}_{1a} & \\ \bar{\boldsymbol{A}}_{2a} & \boldsymbol{I}_{m_2} \end{bmatrix}\begin{bmatrix} \boldsymbol{x}_a \\ \boldsymbol{x}_b \end{bmatrix}; \quad D\left\{\begin{bmatrix} \underline{\boldsymbol{y}}_1 \\ \bar{\underline{\boldsymbol{y}}}_2 \end{bmatrix}\right\} = \begin{bmatrix} \boldsymbol{Q}_{11} & \\ & \bar{\boldsymbol{Q}}_{22} \end{bmatrix} \tag{F.11}$$

with:

$$\begin{array}{rcl} \bar{\underline{\boldsymbol{y}}}_2 & = & \boldsymbol{A}_{2b}^{-1}\underline{\boldsymbol{y}}_2 \\ \bar{\boldsymbol{A}}_{2a} & = & \boldsymbol{A}_{2b}^{-1}\boldsymbol{A}_{2a} \\ \bar{\boldsymbol{Q}}_{22} & = & \boldsymbol{A}_{2b}^{-1}\boldsymbol{Q}_{22}\boldsymbol{A}_{2b}^{-*} \end{array} \tag{F.12}$$

Note that the structure of the model has not changed except that submatrix $\boldsymbol{A}_{2b}$ is now replaced with an identity matrix of equal size. Also note that the $\underline{\boldsymbol{y}}_1$ observations were not transformed.

F.4 Models with critical partition 3

Suppose we have an observation model with the following structure:

$$E\left\{\begin{bmatrix} \underline{\boldsymbol{y}}_1 \\ \underline{\boldsymbol{y}}_2 \end{bmatrix}\right\} = \begin{bmatrix} \boldsymbol{A}_{1a} & \\ \boldsymbol{A}_{2a} & \boldsymbol{I}_{m_2} \end{bmatrix} \begin{bmatrix} \boldsymbol{x}_a \\ \boldsymbol{x}_b \end{bmatrix}; \quad D\left\{\begin{bmatrix} \underline{\boldsymbol{y}}_1 \\ \underline{\boldsymbol{y}}_2 \end{bmatrix}\right\} = \begin{bmatrix} \boldsymbol{Q}_{11} & \\ & \boldsymbol{Q}_{22} \end{bmatrix} \tag{F.13}$$

in which the observations $\underline{\boldsymbol{y}}_1$ and $\underline{\boldsymbol{y}}_2$ are uncorrelated, the unknown parameters $\boldsymbol{x}_b$ only occur in the observation equations of $\underline{\boldsymbol{y}}_2$. The corresponding partitioned system of normal equations is:

$$\begin{bmatrix} \boldsymbol{A}_{1a}^*\boldsymbol{Q}_{11}^{-1}\boldsymbol{A}_{1a} + \boldsymbol{A}_{2a}^*\boldsymbol{Q}_{22}^{-1}\boldsymbol{A}_{2a} & \boldsymbol{A}_{2a}^*\boldsymbol{Q}_{22}^{-1} \\ \boldsymbol{Q}_{22}^{-1}\boldsymbol{A}_{2a} & \boldsymbol{Q}_{22}^{-1} \end{bmatrix} \begin{bmatrix} \underline{\hat{\boldsymbol{x}}}_a \\ \underline{\hat{\boldsymbol{x}}}_b \end{bmatrix} = \begin{bmatrix} \boldsymbol{A}_{1a}^*\boldsymbol{Q}_{11}^{-1} & \boldsymbol{A}_{2a}^*\boldsymbol{Q}_{22}^{-1} \\ & \boldsymbol{Q}_{22}^{-1} \end{bmatrix} \begin{bmatrix} \underline{\boldsymbol{y}}_1 \\ \underline{\boldsymbol{y}}_2 \end{bmatrix} \tag{F.14}$$

The matrix on the left hand side is made block diagonal in two steps. In the first step we pre-multiply the system with transformation matrix $\boldsymbol{Z}_1$:

$$\boldsymbol{Z}_1 = \begin{bmatrix} \boldsymbol{I}_{m_1} & -\boldsymbol{A}_{2a}^* \\ & \boldsymbol{I}_{m_2} \end{bmatrix} \tag{F.15}$$

This gives:

$$\begin{bmatrix} \boldsymbol{A}_{1a}^*\boldsymbol{Q}_{11}^{-1}\boldsymbol{A}_{1a} & \\ \boldsymbol{Q}_{22}^{-1}\boldsymbol{A}_{2a} & \boldsymbol{Q}_{22}^{-1} \end{bmatrix} \begin{bmatrix} \underline{\hat{\boldsymbol{x}}}_a \\ \underline{\hat{\boldsymbol{x}}}_b \end{bmatrix} = \begin{bmatrix} \boldsymbol{A}_{1a}^*\boldsymbol{Q}_{11}^{-1} & \\ & \boldsymbol{Q}_{22}^{-1} \end{bmatrix} \begin{bmatrix} \underline{\boldsymbol{y}}_1 \\ \underline{\boldsymbol{y}}_2 \end{bmatrix} \tag{F.16}$$

The second step is another pre-multiplication with transformation matrix $\boldsymbol{Z}_2$:

$$\boldsymbol{Z}_2 = \begin{bmatrix} \boldsymbol{I}_{m_1} & \\ -\boldsymbol{Q}_{22}^{-1}\boldsymbol{A}_{2a}\left(\boldsymbol{A}_{1a}^*\boldsymbol{Q}_{11}^{-1}\boldsymbol{A}_{1a}\right)^{-1} & \boldsymbol{I}_{m_2} \end{bmatrix} \tag{F.17}$$

which gives:

$$\begin{bmatrix} \boldsymbol{A}_{1a}^*\boldsymbol{Q}_{11}^{-1}\boldsymbol{A}_{1a} & \\ & \boldsymbol{Q}_{22}^{-1} \end{bmatrix} \begin{bmatrix} \underline{\hat{\boldsymbol{x}}}_a \\ \underline{\hat{\boldsymbol{x}}}_b \end{bmatrix} = \begin{bmatrix} \boldsymbol{A}_{1a}^*\boldsymbol{Q}_{11}^{-1} & \\ -\boldsymbol{Q}_{22}^{-1}\boldsymbol{A}_{2a}\left(\boldsymbol{A}_{1a}^*\boldsymbol{Q}_{11}^{-1}\boldsymbol{A}_{1a}\right)^{-1}\boldsymbol{A}_{1a}^*\boldsymbol{Q}_{11}^{-1} & \boldsymbol{Q}_{22}^{-1} \end{bmatrix} \begin{bmatrix} \underline{\boldsymbol{y}}_1 \\ \underline{\boldsymbol{y}}_2 \end{bmatrix} \tag{F.18}$$

The estimators $\underline{\hat{\boldsymbol{x}}}_a$ and $\underline{\hat{\boldsymbol{x}}}_b$ can now be solved by pre-multiplication with the inverse of this diagonal block matrix (the inverse is another diagonal block matrix containing the inverses of the blocks) as follows:

$$\begin{bmatrix} \underline{\hat{\boldsymbol{x}}}_a \\ \underline{\hat{\boldsymbol{x}}}_b \end{bmatrix} = \begin{bmatrix} \left(\boldsymbol{A}_{1a}^*\boldsymbol{Q}_{11}^{-1}\boldsymbol{A}_{1a}\right)^{-1} & \\ & \boldsymbol{Q}_{22} \end{bmatrix} \begin{bmatrix} \boldsymbol{A}_{1a}^*\boldsymbol{Q}_{11}^{-1} & \\ -\boldsymbol{Q}_{22}^{-1}\boldsymbol{A}_{2a}\left(\boldsymbol{A}_{1a}^*\boldsymbol{Q}_{11}^{-1}\boldsymbol{A}_{1a}\right)^{-1}\boldsymbol{A}_{1a}^*\boldsymbol{Q}_{11}^{-1} & \boldsymbol{Q}_{22}^{-1} \end{bmatrix} \begin{bmatrix} \underline{\boldsymbol{y}}_1 \\ \underline{\boldsymbol{y}}_2 \end{bmatrix} \tag{F.19}$$

which gives:

$$\begin{bmatrix} \underline{\hat{\boldsymbol{x}}}_a \\ \underline{\hat{\boldsymbol{x}}}_b \end{bmatrix} = \begin{bmatrix} \left(\boldsymbol{A}_{1a}^*\boldsymbol{Q}_{11}^{-1}\boldsymbol{A}_{1a}\right)^{-1}\boldsymbol{A}_{1a}^*\boldsymbol{Q}_{11}^{-1} & \\ -\boldsymbol{A}_{2a}\left(\boldsymbol{A}_{1a}^*\boldsymbol{Q}_{11}^{-1}\boldsymbol{A}_{1a}\right)^{-1}\boldsymbol{A}_{1a}^*\boldsymbol{Q}_{11}^{-1} & \boldsymbol{I}_{m_2} \end{bmatrix} \begin{bmatrix} \underline{\boldsymbol{y}}_1 \\ \underline{\boldsymbol{y}}_2 \end{bmatrix} \tag{F.20}$$

Variance propagation leads to:

$$D\left\{\begin{bmatrix} \underline{\hat{\boldsymbol{x}}}_a \\ \underline{\hat{\boldsymbol{x}}}_b \end{bmatrix}\right\} = \begin{bmatrix} \left(\boldsymbol{A}_{1a}^*\boldsymbol{Q}_{11}^{-1}\boldsymbol{A}_{1a}\right)^{-1} & -\left(\boldsymbol{A}_{1a}^*\boldsymbol{Q}_{11}^{-1}\boldsymbol{A}_{1a}\right)^{-1}\boldsymbol{A}_{2a}^* \\ -\boldsymbol{A}_{2a}\left(\boldsymbol{A}_{1a}^*\boldsymbol{Q}_{11}^{-1}\boldsymbol{A}_{1a}\right)^{-1} & \boldsymbol{A}_{2a}\left(\boldsymbol{A}_{1a}^*\boldsymbol{Q}_{11}^{-1}\boldsymbol{A}_{1a}\right)^{-1}\boldsymbol{A}_{2a}^* + \boldsymbol{Q}_{22} \end{bmatrix} \tag{F.21}$$

Several remarks can be made based on this result

- The $\underline{\boldsymbol{y}}_2$ observations do not contribute to the estimation of the unknown parameters $\boldsymbol{x}_a$. In fact the estimator $\underline{\hat{\boldsymbol{x}}}_a$ is identical to the estimator of the smaller model where $\underline{\boldsymbol{y}}_1$ are the only observations and $\boldsymbol{x}_a$ the only unknown parameters.

- The variance submatrix $\boldsymbol{Q}_{22}$ does not appear in the estimators $\underline{\hat{\boldsymbol{x}}}_a$ or $\underline{\hat{\boldsymbol{x}}}_b$, and only in the variance of $\underline{\hat{\boldsymbol{x}}}_b$. This means that any changes in this submatrix would not change the solution of the model, except for the variance of the estimated parameters in $\boldsymbol{x}_b$.

The estimated observations are then given as:

$$\begin{bmatrix} \underline{\hat{\boldsymbol{y}}}_1 \\ \underline{\hat{\boldsymbol{y}}}_2 \end{bmatrix} = \begin{bmatrix} \boldsymbol{A}_{1a}\left(\boldsymbol{A}_{1a}^*\boldsymbol{Q}_{11}^{-1}\boldsymbol{A}_{1a}\right)^{-1}\boldsymbol{A}_{1a}^*\boldsymbol{Q}_{11}^{-1} & \\ & \boldsymbol{I}_{m_2} \end{bmatrix} \begin{bmatrix} \underline{\boldsymbol{y}}_1 \\ \underline{\boldsymbol{y}}_2 \end{bmatrix} \tag{F.22}$$

Applying variance propagation once more:

$$D\left\{\begin{bmatrix} \underline{\hat{\boldsymbol{y}}}_1 \\ \underline{\hat{\boldsymbol{y}}}_2 \end{bmatrix}\right\} = \begin{bmatrix} \boldsymbol{A}_{1a}\left(\boldsymbol{A}_{1a}^*\boldsymbol{Q}_{11}^{-1}\boldsymbol{A}_{1a}\right)^{-1}\boldsymbol{A}_{1a}^* & \\ & \boldsymbol{Q}_{22} \end{bmatrix} \tag{F.23}$$

And for the residuals:

$$\begin{bmatrix} \underline{\hat{\boldsymbol{e}}}_1 \\ \underline{\hat{\boldsymbol{e}}}_2 \end{bmatrix} = \begin{bmatrix} \boldsymbol{P}_{\boldsymbol{A}_{1a}}^{\perp} & \\ & \boldsymbol{0}_{m_2} \end{bmatrix} \begin{bmatrix} \underline{\boldsymbol{y}}_1 \\ \underline{\boldsymbol{y}}_2 \end{bmatrix} \tag{F.24}$$

with:

$$D\left\{\begin{bmatrix} \underline{\hat{\boldsymbol{e}}}_1 \\ \underline{\hat{\boldsymbol{e}}}_2 \end{bmatrix}\right\} = \begin{bmatrix} \boldsymbol{P}_{\boldsymbol{A}_{1a}}^{\perp}\boldsymbol{Q}_{11}\boldsymbol{P}_{\boldsymbol{A}_{1a}}^{\perp *} & \\ & \boldsymbol{0}_{m_2} \end{bmatrix} \tag{F.25}$$

in which $\boldsymbol{P}_{\boldsymbol{A}_{1a}}^{\perp}$ is an orthogonal projector given by (see also Teunissen, 2000a)

$$\boldsymbol{P}_{\boldsymbol{A}_{1a}}^{\perp} = \boldsymbol{I}_{m_1} - \boldsymbol{A}_{1a}\left(\boldsymbol{A}_{1a}^*\boldsymbol{Q}_{11}^{-1}\boldsymbol{A}_{1a}\right)^{-1}\boldsymbol{A}_{1a}^*\boldsymbol{Q}_{11}^{-1} \tag{F.26}$$

The $\underline{\hat{\boldsymbol{e}}}_2$ residuals and their variance are zero, which means that these cannot be used to perform quality control of the $\underline{\boldsymbol{y}}_2$ observations, and also that no VCE can be performed for the $\boldsymbol{Q}_{22}$ variance submatrix.

F.5 Block Gauss-Seidel Method for Partitioned Matrix

Suppose we have an observation model with the following structure:

$$E\left\{\left[\ \underline{\boldsymbol{y}}\ \right]\right\} = \left[\ \boldsymbol{A}_a \quad \boldsymbol{A}_b\ \right]\left[\begin{array}{c}\boldsymbol{x}_a\\ \boldsymbol{x}_b\end{array}\right]; \quad D\left\{\left[\ \underline{\boldsymbol{y}}\ \right]\right\} = \boldsymbol{Q}_{yy} \tag{F.27}$$

in which the unknown parameters $\boldsymbol{x}$ are split in two groups. The corresponding partitioned system of normal equations is:

$$\left[\begin{array}{cc}\boldsymbol{A}_a^*\boldsymbol{Q}_{yy}^{-1}\boldsymbol{A}_a & \boldsymbol{A}_a^*\boldsymbol{Q}_{yy}^{-1}\boldsymbol{A}_b\\ \boldsymbol{A}_b^*\boldsymbol{Q}_{yy}^{-1}\boldsymbol{A}_a & \boldsymbol{A}_b^*\boldsymbol{Q}_{yy}^{-1}\boldsymbol{A}_b\end{array}\right]\left[\begin{array}{c}\hat{\underline{\boldsymbol{x}}}_a\\ \hat{\underline{\boldsymbol{x}}}_b\end{array}\right] = \left[\begin{array}{c}\boldsymbol{A}_a^*\boldsymbol{Q}_{yy}^{-1}\underline{\boldsymbol{y}}\\ \boldsymbol{A}_b^*\boldsymbol{Q}_{yy}^{-1}\underline{\boldsymbol{y}}\end{array}\right] \tag{F.28}$$

If both diagonal blocks in the matrix on the left hand side are invertable, eq. (F.28) can be solved with the iterative block Gauss-Seidel method (Ciarlet et al., 1989; Quarteroni et al., 2010). The iterations for this model can be worked out as:

$$\begin{array}{l}\text{for } k = 1, 2, \ldots\\ \hat{\underline{\boldsymbol{x}}}_a^k = \left(\boldsymbol{A}_a^*\boldsymbol{Q}_{yy}^{-1}\boldsymbol{A}_a\right)^{-1}\boldsymbol{A}_a^*\boldsymbol{Q}_{yy}^{-1}\left(\underline{\boldsymbol{y}} - \boldsymbol{A}_b\hat{\underline{\boldsymbol{x}}}_b^{k-1}\right)\\ \hat{\underline{\boldsymbol{x}}}_b^k = \left(\boldsymbol{A}_b^*\boldsymbol{Q}_{yy}^{-1}\boldsymbol{A}_b\right)^{-1}\boldsymbol{A}_b^*\boldsymbol{Q}_{yy}^{-1}\left(\underline{\boldsymbol{y}} - \boldsymbol{A}_a\hat{\underline{\boldsymbol{x}}}_a^k\right)\end{array} \tag{F.29}$$

Only $\hat{\underline{\boldsymbol{x}}}_b^0$ needs to be initialized and iterations can be stopped when the updates of the estimated parameters are below a selected threshold.

In section 8.3.4 the above estimation scheme is used to estimate the positioning parameters and other (time varying) parameters in the first step, while estimating the (constant) group delays in a separate second step. Note that $\underline{\boldsymbol{y}} - \boldsymbol{A}_a\hat{\underline{\boldsymbol{x}}}_a^k$ are the residuals from the first estimation step. $\underline{\boldsymbol{y}} - \boldsymbol{A}_b\hat{\underline{\boldsymbol{x}}}_b^{k-1}$ can then be interpreted as the observations corrected for the group delays estimated in the previous iteration.

G Appendix: Variance Component Estimation

This appendix explains the Variance Component Estimation (VCE) approach used in chapter 8, which applies the iterated almost unbiased estimator (Förstner, 1979) to different groups of GNSS observations. This approach was previously demonstrated in Gündlich and van der Marel (2003) which is in part based on Teunissen (2004). The observations are grouped in satellite elevation bins, which makes it possible to accurately determine the elevation dependent measurement variance. In this section VCE for the phase-only model is considered, but similar derivations hold for the code-only model. In section 4.6 the following dual frequency phase-only functional model for a single epoch was found, see eq. (4.30):

$$E\left\{\begin{bmatrix} \underline{\Delta\boldsymbol{\phi}}^{S}_{r,L1,k} \\ \underline{\Delta\boldsymbol{\phi}}^{S}_{r,L2,k} \end{bmatrix}\right\} = \begin{bmatrix} -\mathbf{e}^{S*}_{r,k} & c\mathbf{u}_m & \mathbf{m}^{S}_{r,k} & -\mathbf{I}_m & \overset{0\cdots0}{\mathbf{I}_{m-1}} \\ -\mathbf{e}^{S*}_{r,k} & c\mathbf{u}_m & \mathbf{m}^{S}_{r,k} & -\gamma\mathbf{I}_m & \overset{0\cdots0}{\mathbf{I}_{m-1}} \end{bmatrix} \begin{bmatrix} \Delta\mathbf{r}_r \\ \overline{\delta t}_{r,L3,k} \\ T_{Z,r,k} \\ \bar{\bar{\boldsymbol{\mathcal{I}}}}^{S}_{r,k} \\ \bar{\mathbf{A}}^{S-1}_{r,L3} \end{bmatrix} \tag{G.1}$$

When combining measurements of multiple epochs of data we can define a dynamic model for each of the unknown parameters. However, here we will only work with kinematic (the ionosphere and clock offset) and static (the ambiguities) parameters.

The kinematic estimation of an ionosphere delay per satellite, leads to a number of unknown parameters equal to the number of observations on a single frequency. This means that we can write the complete observation model (i.e. for all epochs) as:

$$E\left\{\begin{bmatrix} \underline{\Delta\boldsymbol{\phi}}^{S}_{r,L1,K} \\ \underline{\Delta\boldsymbol{\phi}}^{S}_{r,L2,K} \end{bmatrix}\right\} = \begin{bmatrix} \boldsymbol{A}_{1a} & \boldsymbol{A}_{1b} \\ \boldsymbol{A}_{2a} & \boldsymbol{A}_{2b} \end{bmatrix} \begin{bmatrix} \boldsymbol{x} \\ \bar{\bar{\boldsymbol{\mathcal{I}}}}^{S}_{r,K} \end{bmatrix}; \quad D\left\{\begin{bmatrix} \underline{\Delta\boldsymbol{\phi}}^{S}_{r,L1,K} \\ \underline{\Delta\boldsymbol{\phi}}^{S}_{r,L2,K} \end{bmatrix}\right\} = \boldsymbol{Q}_{yy} \tag{G.2}$$

in which $\boldsymbol{A}_{2b}$ is a square matrix of full rank. As a result we can follow the derivations presented in appendix F. First the ionosphere parameters are eliminated from the L1 observation equations as in appendix F.1. In this process the L1 observations are transformed into the L3IF observations. Then the observations are decorrelated as in appendix F.2 by transforming the L2 observations. Note this generally does *not* lead to the ionosphere combination of observations, the actual combination depends on the chosen stochastic model (in fact for a specific choice of the stochastic model the L2 observations even remain unchanged). Appendices F.3 and F.4 then show that the second set of observations get zero residuals which means that their variance components cannot be estimated.

This is an extension of our findings in chapter 4, where we showed that transforming the L1 and L2 observables into the ionosphere-free and ionosphere combination, then the ionosphere observations become free variates if the ionosphere is estimated as a kinematic parameter per satellite. Therefore, for the purpose of VCE, the dual frequency model with unconstrained ionosphere estimation is equivalent with the following ionosphere-free model. (Note that this also implies that the variance components for L1 and L2 cannot be estimated separately.)

$$E\left\{\left[\ \underline{\Delta\boldsymbol{\phi}}^{S}_{r,L3,k}\ \right]\right\} = \left[\begin{array}{cccc} -\mathbf{e}^{S*}_{r,k} & c\mathbf{u}_m & \mathbf{m}^{S}_{r,k} & \overset{0\cdots0}{\mathbf{I}_{m-1}} \end{array}\right]\left[\begin{array}{c} \Delta\mathbf{r}_r \\ \overline{\delta t}_{r,L3,k} \\ T_{Z,r,k} \\ \bar{\mathbf{A}}^{S-1}_{r,L3} \end{array}\right] \tag{G.3}$$

To derive a stochastic model for the phase measurements (as is the goal in section 8.2.1), the position is kept fixed at the accurately known a-priori coordinates. In this case corrections to the position are no longer estimated, which means the model simplifies as follows.

$$E\left\{\left[\Delta\boldsymbol{\phi}^{S}_{r,L3,k} + \mathbf{e}^{S*}_{r,k}\Delta\mathbf{r}_r\right]\right\} = \left[\begin{array}{ccc} c\mathbf{u}_m & \mathbf{m}^{S}_{r,k} & \overset{0\cdots0}{\mathbf{I}_{m-1}} \end{array}\right]\left[\begin{array}{c} \overline{\delta t}_{r,L3,k} \\ T_{Z,r,k} \\ \bar{\mathbf{A}}^{S-1}_{r,L3} \end{array}\right] \quad \text{with } \Delta\mathbf{r}_r = \mathbf{0} \tag{G.4}$$

Note that the fixed coordinates, including the displacement effects, need to be very accurate indeed as their uncertainty is added to the measurement variance.

$$D\left\{\left[\Delta\boldsymbol{\phi}^{S}_{r,L3,k} + \mathbf{e}^{S*}_{r,k}\Delta\mathbf{r}_r\right]\right\} = \boldsymbol{Q}_{\phi^{S}_{r,L3,k}} + \mathbf{e}^{S*}_{r,k}\boldsymbol{Q}_{\mathbf{r}_r}(\mathbf{e}^{S*}_{r,k})^{*} \tag{G.5}$$

However, if the position is accurate enough the added variance may be neglected. In this reduced model the variance matrix of the observations is a diagonal matrix since we assume that the observations to different satellites and from different epochs are not correlated. Therefore, we can use a simplified expression for the Variance Component Estimation given in Gündlich and van der Marel (2003):

$$F_k = \frac{1}{r_k}\sum_{i=1}^{m_k} \hat{e}^2_{ik}/\sigma^2_{y_{ik}} \tag{G.6}$$

with F a multiplication factor that should be applied to update the measurement variance, k corresponds to the observation group, m_k the number of observations of group k, $\hat{e}$ the residuals, σ_y the observation standard deviation, and r the redundancy number given by:

$$r_k = \sum_{i=1}^{m_k} \sigma^2_{e_{ik}}/\sigma^2_{y_{ik}} \tag{G.7}$$

with σ_e the residual standard deviation. With this expression we do not need the entire variance matrix of the residuals, only the diagonal elements. An additional advantage is that we can combine the residuals of different epochs of the recursive least squares without having to take the correlation into account. As mentioned the VCE method is iterative which means that the data should first be processed with an initial stochastic model, which should then be updated with eqs. (G.6) and (G.7) before reprocessing the data and repeating these steps until the stochastic model converges.

To limit the number of additional estimated parameters (the variance components), which is one of the pitfalls of VCE, an intermediate step is added to the procedure. Once the variance component updates are computed for each elevation bin an elevation dependent function is fitted to these values, and the fitted function is used as the updated stochastic model. The exponential function of the form $a(1 + be^{-\theta/\theta_0})$, first introduced by Euler and Goad (1991), where θ is the elevation angle provides a very good fit for the data at hand. This function then limits the number of additional parameters to 3: a which is close to the variance at high elevation angles, b which represents the increase in variance at low elevation angles, and the reference elevation θ_0 which governs the shape of the curve. In this 3 parameter model b and θ_0 can vary significantly due to relatively small changes in the residuals, especially if the elevation cut-off angle is high, which can lead to an unstable (iterative) estimation process. In this case it is advisable to fix the reference elevation to e.g. 10° and only estimate a and b.

Curriculum Vitae

Peter Foeke de Bakker was born in Barendrecht, the Netherlands, on the 4th of January 1980. After completing secondary education at Farel College in 1998, he enrolled at Delft University of Technology. He obtained his MSc in Aerospace engineering in 2007, with a thesis on Detecting radio frequency interference in GNSS receiver output, a study performed at the European Space Agency (ESTEC) in Noordwijk, the Netherlands. Subsequently, he worked as a researcher and PhD student at the faculty of Aerospace engineering (Department of Earth Observation and Space Systems / Mathematical Geodesy and Positioning) of the same university. During this time he was involved in several European projects: Feasibility study of a Wide-Area High-precision Navigation Service for EGNOS & Galileo (FES-WARTK) and the EGNOS Data Collection Network (EDCN). He was seconded to Pildo Labs (Barcelona, Spain) and Septentrio Satellite Navigation (Leuven, Belgium) for his work on the Study of Innovative GNSS Multiconstellation Algorithms (SIGMA). From 2012-2013 he worked as a Research Fellow at the GNSS Research Centre, Curtin University of Technology, Perth, Australia on Array-aided Precise Point Positioning. He is currently working as a Post doctoral researcher at the faculty of Civil Engineering and Geosciences of the Delft University of Technology (Department of Geoscience and Remote Sensing) on various projects related to positioning applications (WEPODS, Taking the fast lane).

Publications

Radio Frequency Interference

Bakker, P.F. de, J. Samson, P. Joosten, M. Spelat, M. Hollreiser, B.A.C. Ambrosius (2006) Effects of Radio Frequency Interference on GNSS Receiver Output. Navitec 2006

Spelat M., M. Crisci, M. Hollreiser, P.F. de Bakker, J. Samson (2006) GIOVE-A Signal In Space and Receiver Test Activity at ESTEC. Navitec 2006

Wide Area RTK

Hernández-Pajares, M., J.M.Juan, J.Sanz, A. Aragon-Angel, P. Ramos-Bosch, D. Odijk, P.F. de Bakker, H. van der Marel, S. Verhagen, I. Fernndez-Hernndez, M. Toledo, J. Samson (2008) Feasibility Study of a European Wide Area Real Time Kinematic System. Navitec 2008

Odijk, D., P.F. de Bakker, S. Verhagen, P.J.G. Teunissen, M. Hernández-Pajares, J. Samson, (2009) Fast LAMBDA-based ambiguity resolution combined with WARTK technique for Galileo data simulated using ESAs Galileo Signal Validation Facility. IGNSS Symposium 2009

Hernández-Pajares, M., J.M. Juan, J. Sanz, A. Aragon-Angel, P. Ramos-Bosch, J. Samson, M. Tossaint, M. Albertazzi, D. Odijk, P.J.G. Teunissen, P.F. de Bakker, S. Verhagen, H. van der Marel (2010) Wide-Area RTK, High Precision Positioning on a Continental Scale. Inside GNSS March-April 2010

Integrity Monitoring

Bakker, P.F. de, H. van der Marel, P.J.G. Teunnisen (2009) The Minimal Detectable Bias for Multi-Frequency GPS and Galileo Observations with a Single Receiver Setup and a Geometry-Free Model. ENC-GNSS 2009

Teunissen, P.J.G., P.F. de Bakker (2009) Next Generation GNSS Single Receiver Cycle Slip Reliability. Hotine Marussi 2009

Teunissen, P.J.G., & de Bakker, P.F. Single-receiver single channel multi-frequency GNSS integrity: Outliers, slips and ionospheric disturbances. Journal of Geodesy 02/2012; 87(2). DOI: 10.1007/s00190-012-0588-x

Teunissen, P. J. G. and P. F. de Bakker (2013, June). Integer cycle-slip resolution for the single receiver single channel multi-frequency GNSS model: An analytical and numerical analysis. In Proceedings of the Hotine Marussi Symposium Rome.

Signal Quality Analysis (GIOVE)

Bakker, P.F. de, C.C.J.M. Tiberius, H. van der Marel (2009) Zero, Single and Double Difference Analysis of GPS, EGNOS and GIOVE-A/B Pseudorange and Carrier Phase Measurements. ENC GNSS 2009

Bakker, P.F. de, H. van der Marel, C.C.J.M. Tiberius (2009). Geometry-Free Undifferenced, Single and Double Differenced Analysis of Single Frequency GPS, EGNOS and GIOVE-A/B Measurements. GPS Solutions 13(4), 305.

Tiberius, C.C.J.M., P.F. de Bakker, H. van der Marel, R.J.P. van Bree (2009) Geometry-free Analysis of GIOVE-A/B E1 - E5a, and GPS L1 - L5 Measurements. ION GNSS 2009. September 22-25, Savannah, GA. pp. 2911-2925.

Bakker, P.F. de, C.C.J.M. Tiberius, H. van der Marel, R.J.P. van Bree (2011) Short and zero baseline analysis of GPS L1 C/A, L5Q, GIOVE E1B, and E5aQ signals. GPS Solutions (4 February 2011), pp. 1-12. doi:10.1007/s10291-011-0202-3

EGNOS Monitoring

Bakker, P.F. de, M. Valk, C.C.J.M. Tiberius, S. Soley, H. van der Marel (2011) EGNOS Performance Evaluated for Static and Kinematic Users. ION GNSS 2011. September

19-23, Portland, OR.

Multipath Modeling

Bakker, P.F. de (2011) Modeling Pseudo Range Multipath as an Autoregressive Process. ION GNSS 2011. September 19-23, Portland, OR.

Single-Frequency Precise Point Positioning

Knoop, V.L., de Bakker, P.F., Tiberius, C.C.J.M., van Arem, B. Single frequency precise point positioning: obtaining a map accurate to lane-level. 16th International IEEE Conference on Intelligent Transportation Systems ITSC2013, At The Hague, The Netherlands

de Bakker, P. F., V. L. Knoop, C. C. J. M. Tiberius, and B. van Arem (2014). Mapping Motorway Lanes and Real-Time Lane Identification with Single-Frequency Precise Point Positioning. In Proceedings of the European Navigation Conference, pp. 12.

van der Marel, H. and P. F. de Bakker (2012). In GNSS Solutions: Single- versus Dual-Frequency Precise Point Positioning. Inside GNSS July August, 3035.

Array-Aided Positioning

Nadarajah, N., Teunissen, P.J.G., de Bakker, P.F., “GNSS Array-Aided Positioning and Attitude Determination: Real Data Analyses,” Proceedings of the 27th International Technical Meeting of The Satellite Division of the Institute of Navigation (ION GNSS+ 2014), Tampa, Florida, September 2014, pp. 2544-2554.

Bibliography

Amiri-Simkooei, A. R. and C. C. J. M. Tiberius (2007). Assessing receiver noise using GPS short baseline time series. *GPS Solutions 11*(1), 21–35.

Arnold, S. (1981). The Theory of Linear Models and Multivariate Analysis. John Wiley & Sons Inc.

Baarda, W. (1967). *Statistical Concepts in Geodesy*, Volume 2 of *Netherlands Geodetic Commission, New Series, Publications on Geodesy*. Delft, the Netherlands: W. D. MEINEMA N.V.

Baarda, W. (1968). A testing procedure for use in geodetic networks. *Netherlands Geodetic Commission, Publications on Geodesy, New Series 2*(5), 97.

Baarda, W. (1973). S-transformations and criterion matrices. Publications on Geodesy, NewSeries , vol 5(1), Netherlands GeodeticCommission, Delft.

Banville, S. (2014). *Improved Convergence For GNSS Precise Point Positioning*. Ph. D. thesis, University of New Brunswick.

Banville, S., R. Santerre, M. Cocard, and R. B. Langley (2008). Satellite and Receiver Phase Bias Calibration for Undifferenced Ambiguity Resolution. In *Proceedings of ION NTM 2008*.

Bar-Sever, Y. (2012, June). personal communication. Jet Propulsion Laboratory, California Institute of Technology.

Bar-Sever, Y. E. and P. M. Kroger (1998, March). Estimating horizontal gradients of tropospheric path delay with a single GPS receiver. *Journal of Geophysical Research 103*(B3), 5019–5035.

Bedford, L., N. Brown, and J. Walford (2009). Leica AR25 – white paper. electronic. Leica Geosystems AG, CityplaceHeerbrugg, Switzerland. 10 pp.

beidou.gov.cn (2015). BeiDou Navigation Satellite System. http://en.beidou.gov.cn/. last accessed on 31-05-2015.

Bertiger, W., S. Desai, B. Haines, N. Harvey, A. Moore, S. Owen, and J. Weiss (2010). Single receiver phase ambiguity resolution with GPS data. *Journal of Geodesy 84*(5), 327–337.

Beutler, G., M. Rothacher, S. Schaer, T. A. Springer, J. Kouba, and R. Neilan (1999). The International GPS Service (IGS): An Interdisciplinary Service in Support of Earth Sciences. *Adv. Space Res. 23(4)*, 631–635.

Bisnath, S. and Y. Gao (2009a). Current State of Precise Point Positioning and Future Prospects and Limitations. *International Association of Geodesy Symposia 133*, 615–623.

Bisnath, S., D. Kim, and R. Langley (2001, May). Carrier Phase Slips: a new approach to an old problem. *GPS World 12*(5), 2–7.

Bisnath, S. and R. Langley (2000). Efficient, automated cycle-slip correction of dual-frequency kinematic GPS data. In *Proceedings ION GPS 2000*, pp. 145–154.

Bisnath, S. B. and Y. Gao (2009b). Innovation: Precise Point Positioning A Powerful Technique with a Promising Future. *GPS World April*, 43–50.

Blewitt, G. (1998). *GPS for Geodesy*, Chapter GPS Data Processing Methodology: from Theory to Applications, pp. 231–270. Springer-Verlag, Berlin.

Boehm, J., P. Mendes Cerveira, H. Schuh, and P. Tregoning (2005, August). The impact of tropospheric mapping functions based on numerical weather models on the determination of geodetic parameters. In *Proceedings of the IAG*, Cairns.

Boehm, J., A. Niell, P. Tregoning, and H. Schuh (2006). The Global Mapping Function (GMF): A new empirical mapping function based on data from numerical weather model data. *Geophysical Research Letters 33*, 4.

Boehm, J. and H. Schuh (2007). Troposphere gradients from the ECMWF in VLBI analysis. *Journal of Geodesy 81*(6), 403–408.

Boehm, J., B. Werl, and H. Schuh (2006). Troposphere mapping functions for GPS and very long baseline interferometry from European Centre for Medium-Range Weather Forecasts operational analysis data. *Journal of Geophysical Research 111*(B2), 9.

Braasch, M. S. and A. J. van Dierendonck (1999, JANUARY). GPS Receiver Architectures and Measurements. In *Proceedings of the IEEE*, Volume 87.

Cai, C. and Y. Gao (2007a). Performance analysis of Precise Point Positioning based on combined GPS GLONASS. In *Proceedings of the ITM ION*, Volume 4, Fort Worth, TX, pp. 858–865.

Cai, C. and Y. Gao (2007b). Precise Point Positioning Using Combined GPS and GLONASS Observations. *Journal of Global Positioning Systems 6*(1), 13–22.

Cai, C., C. He, R. Santerre, L. Pan, X. Cui, and J. Zhu (2015). A comparative analysis of measurement noise and multipath for four constellations: GPS, BeiDou, GLONASS and Galileo. *Survey Review 0*, 9.

Cai, C., Z. Liu, P. Xia, and W. Dai (2013). Cycle slip detection and repair for undifferenced GPS observations under high ionospheric activity. *GPS Solutions 17*(2), 247–260.

Cameron, A. (2010). GLONASS Up to Date and Out of State. *GPS World March*, 1.

Cao, W., A. Hauschild, P. Steigenberger, R. Langley, L. Urquhart, M. Santos, and O. Montenbruck (2010). Performance evaluation of integrated GPS/GIOVE precise point positioning. In *Proceedings of the ITM ION*, Volume 2, San Diego, CA, pp. 710–722.

Chen, G. and T. A. Herring (1997, September). Effects of atmospheric azimuthal asymmetry on the analysis of space geodetic data. *Journal of Geophysical Research 102*(B9), 20489–20502.

Chen, L., W. Jiao, X. Huang, C. Geng, L. Ai, L. Lu, and Z. Hu (2013). Study on Signal-In-Space Errors Calculation Method and Statistical Characterization of BeiDou Navigation Satellite System. In *Proceedings of China satellite navigation conference (CSNC)*, pp. 423–434.

Ciarlet, P., B. Miara, and J. Thomas (1989). *Introduction to Numerical Linear Algebra and Optimisation*. Cambridge Texts in Applied Mathematics. Cambridge University Press.

CNES (2012, July). The PPP-Wizard project. http://www.ppp-wizard.net/index.html. accessed July, 2012.

CODE (2015). Center for Orbit Determination in Europe. http://aiuws.unibe.ch/spec/dcb.php. last accessed on 3-2-2015.

Cohenour, J. C. (2009, August). *Global Positioning System Clock and Orbit Statistics and Precise Point Positioning*. Ph. D. thesis, the Russ College of Engineering and Technology of Ohio University.

Collins, J. and R. Langley (1999). Possible Weighting Schemes for GPS Carrier Phase Observations in the Presence of Multipath. Technical report, University of New Brunswick.

Collins, J. P. (1999). An overview of GPS inter-frequency carrier phase combinations. http://gauss.gge.unb.ca/papers.pdf/L1L2combinations.collins.pdf.

Collins, P., F. Lahaye, P. Héroux, and S. Bisnath (2008). Precise point positioning with ambiguity resolution using the decoupled clock model. In *Proceedings of the 21st international technical meeting of the satellite division of the Institute of Navigation (ION GNSS 2008)*, pp. 1315–1322.

Dai, Z., S. Knedlik, and O. Loffeld (2009). Instantaneous triple-frequency GPS cycle-slip detection and repair. *International Journal of Navigation and Observation 2009*, 15.

de Bakker, P. (2007). Effects of Radio Frequency Interference on GNSS Receiver Output. Master's thesis, Delft University of Technology.

de Bakker, P. (2011). Modeling Pseudo Range Multipath As An Autoregressive Process. In *Proceedings of the GNSS ION 2011*, pp. 1737–1750.

de Bakker, P., C. Tiberius, H. van der Marel, and R. van Bree (2012). Short and zero baseline analysis of GPS L1 C/A, L5Q, GIOVE E1B, and E5aQ signals. *GPS Solutions 16*, 5364.

de Bakker, P., H. van der Marel, and C. Tiberius (2009). Geometry-free undifferenced, single and double differenced analysis of single frequency GPS, EGNOS and GIOVE-A/B measurements. *GPS Solutions 13*(4), 305.

de Bakker, P. F., V. L. Knoop, C. C. J. M. Tiberius, and B. van Arem (2014). Mapping Motorway Lanes and Real-Time Lane Identification with Single-Frequency Precise Point Positioning. In *Proceedings of the European Navigation Conference*, pp. 12.

de Bakker, P. F., H. van der Marel, and P. J. G. Teunissen (2009). The Minimal Detectable Bias for GNSS Observations with a Single Receiver Setup and a Geometry-Free Model. In *GNSS ENC 2009*.

de Haan, S. and H. van der Marel (2004). The influence on GPS estimates of NWP-derived mapping functions. *Physics and Chemistry of the Earth 29*, 159–166.

de Jong, K. (2000). Minimal Detectable Biases of Cross-Correlated GPS Observations. *GPS Solutions 3*, 12–18.

de Jong, K. and P. Teunissen (2000). Minimal Detectable Biases of GPS Observations for a Weighted Ionosphere. *Earth, Planets and Space 52*, 857–862.

de Jonge, P. (1998). *A processin strategy for the application of the GPS in networks*. Ph. D. thesis, Delft University of Technology.

D'Errico, J. (2005, November). Surface Fitting using gridfit. http://www.mathworks.com/matlabcentral/fileexchange/8998-surface-fitting-using-gridfit. last accessed on 4-2-2015.

Doucet, K., M. Herwig, A. Kipka, P. Kreikenbohm, H. Landau, R. Leandro, M. Moessmer, and C. Pagels (2012). Introducing Ambiguity Resolution in Web-hosted Global Multi-GNSS Precise Positioning with Trimble RTX-PP. In *Proceedings of the 25th International Technical Meeting - ION GNSS*, Nashville, Tennessee, pp. 1115–1125. Institute of Navigation.

Dow, J., R. Neilan, and C. Rizos (2009). The International GNSS Service in a changing landscape of Global Navigation Satellite Systems. *Journal of Geodesy 83*, 191–198.

Erker, S., S. Thlert, J. Furthner, M. Meurer, and M. Husler (2009, September 22-25). GPS L5 "Light's on!" - A First Comprehensive Signal Verification and Performance Analysis. In *Proceedings of ION GNSS 2009*, Savannah, GA, pp. 1544–1551.

ESA (2012, January). ESA Galileo Navigation. http://www.esa.int/esaNA/galileo.html.

ESA (2015). ESA Galileo Navigation. http://www.esa.int/Our_Activities/Navigation/The_future_-_Galileo/Launching_Galileo. last accessed on 30-05-2015.

Estey, L. H. and C. M. Meertens (1999). TEQC: The Multi-Purpose Toolkit for GPS/GLONASS Data. *GPS Solutions 3*(1), 42–49.

Euler, H.-J. and C. Goad (1991). On optimal filtering of GPS dual frequency observations without using orbit information. *Bulletin Geodesique 65*, 130–143.

Fan, J., F. Wang, and G. Guo (2006). Automated cycle-slip detection and correction for GPS triple-frequency undifferenced observables. *Journal of science of surveying and mapping 31*(5), 24–36.

Fan, L., G. Zhai, and H. Chai (2011). Study on the processing method of cycle-slips under kinematic mode. In Q. Zhou (Ed.), *ICTMF2011*, pp. 175–183.

Feng, S., A. Jokinen, W. Ochieng, J. Liu, and Q. Zeng (2014). Receiver Autonomous Integrity Monitoring for Fixed Ambiguity Precise Point Positioning. In *Proceedings of China Satellite Navigation Conference (CSNC)*, pp. 159–169.

Feng, S., W. Ochieng, D. Walsh, and R. Ioannides (2006). A measurement domain receiver autonomous integrity monitoring algorithm. *GPS Solutions 10*(2), 85–96.

Förstner, W. (1979). Ein Verfahren zur Schätzung von Varianz- und Kovarianzkomponenten. *Allgemeine Vermessungsnachrichten 86*, 44645.

Förstner, W. (1983). Reliability and discernibility of extended Gauss-Markov models. In *German Geodetic Commission DGK*, Number 98 in A, pp. 79–103. Munich.

Gabor, M. and R. Nerem (1999). GPS Carrier phase Ambiguity Resolution Using Satellite-Satellite Single Differences. In *Proceedings of the ITM of the ION GPS 1999*, pp. 1569–1578.

Galileo OS-SIS-ICD (2008). Galileo Open Service Signal In Space Interface Control Document. Technical report, European Space Agency / European GNSS Supervisory Authority.

Gao, Y. (2008). GNSS Biases, their Effect and Calibration. In *IGS Workshop*.

Gao, Y. and K. Chen (2004). Performance Analysis of Precise Point Positioning Using Real-Time Orbit and Clock Products. *Journal of Global Positioning Systems 3*, 95–100.

Gao, Y. and Z. Li (1999). Cycle slip detection and ambiguity resolution algorithms for dual-frequency GPS data processing. *Marine Geodesy 22*(4), 169–181.

Gao, Y. and X. Shen (2001). Improving Ambiguity Convergence in Carrier Phase-Based Precise Point Positioning. In *Proceedings of ITM ION GPS 2001*, pp. 1532–1539.

Gao, Y., Y. Zhang, and K. Chen (2006). Development of a Real-Time Single-Frequency Precise Point Positioning System and Test Results. In *Proceedings of the ION GNSS ITM*, Fort Worth, TX.

Ge, M., G. Gendt, M. Rothacher, C. Shi, and J. Liu (2008). Resolution of GPS carrier-phase ambiguities in Precise Point Positioning (PPP) with daily observations. *Journal of Geodesy 82*, 389–399.

Geng, J., X. Meng, N. Teferle, A. Dodson, M. Ge, C. Shi, and J. Liu (2008). Performance of hourly precise point positioning with ambiguity resolution. In *Proceedings of ITM ION*, Volume 4, Savannah, GA, pp. 1985–1991.

Geng, J., F. N. Teferle, C. Shi, X. Meng, A. H. Dodson, and J. Liu (2009). Ambiguity resolution in precise point positioning with hourly data. *GPS Solutions 13*, 263–270.

Ghoddousi-Fard, R. (2009). *Modelling Tropospheric Gradients and Parameters from NWP Models: Effects on GPS Estimates*. Ph. D. thesis, University of New Brunswick.

Gibbons, G. (2006). GLONASS: The Once and Future GNSS, GNSS Trilogy: Part II. *Inside GNSS January/February*, 8.

Gibbons, G. (2008). Russia Dwells on Glonass Future. *Inside GNSS March/April*, 1.

Giorgi, G., P. Teunissen, S. Verhagen, and P. Buist (2012). Instantaneous Ambiguity Resolution in GNSS-based Attitude Determination Applications: A Multivariate Constrained Approach. *Journal of Guidance, Control and Dynamics 35*(1), 51–67.

GLONASS (2008). GLOBAL NAVIGATION SATTELITE SYSTEM GLONASS INTERFACE CONTROL DOCUMENT (Edition 5.1). Technical report, Russian Institute of Space Device Engineering.

Gourevitch, S. (1996). Measuring GPS receiver performance: a new approach. *GPS World 7*(10), 56–62.

gps.gov (2015). Official U.S. Government information about the Global Positioning System (GPS) and related topics. website. last accessed on 30-05-2015.

Greene, W. H. (2002). *Econometric Analysis* (fifth ed.). Upper Saddle River, New Jersey 07458: Prentice Hall.

GSA (2014). EGNOS Data Access Service (EDAS) Service Definition Document. Technical Report 2.1, The European GNSS Agency.

Gündlich, B. and H. van der Marel (2003). TOUGH Report - GPS System Research: Robust Quality Indicators. Technical report, Delft University of Technology.

Gurtner, W. and L. Estey (2007). RINEX - the receiver independent exchange format version 3.00. Technical report, Astronomical Institute.

Hartinger, H. and F. Brunner (1999). Variances of GPS Phase Observations: the SIGMA Model. *GPS Solutions 2*(4), 35–43.

Hauschild, A. and O. Montenbruck (2008, September). Real-time Clock Estimation for Precise Orbit Determination of LEO Satellites. In *Proceedings of the ION GNSS Meeting 2008*, Savannah, Georgia, USA, pp. 16–19.

Hein, G. W., J.-A. Avila-Rodriguez, S. Wallner, A. R. Pratt, J. R. Owen, J.-L. Issler, J. W. Betz, C. J. Hegarty, C. S. Lenahan, J. J. Rushanan, A. L. Kraay, and T. A. Stansell (2006). MBOC: The New Optimized Spreading Modulation Recommended for GALILEO L1 OS and GPS L1C. In *Proceedings of IEEE/ION PLANS 2006*, San Diego, California, USA.

Heng, L., G. X. Gao, T. Walter, and P. Enge (2011a). Innovation: Digging into GPS Integrity. *GPS World November*, 5.

Heng, L., G. X. Gao, T. Walter, and P. Enge (2011b). Statistical Characterization of GLONASS Broadcast Ephemeris Errors. In *Proceedings of GNSS ION 2011*.

Heng, L., G. X. Gao, T. Walter, and P. Enge (2011c, January). Statistical characterization of GPS signal-in-space errors. In *Proceedings of the 2011 International Technical Meeting of the Institute of Navigation (ION ITM 2011)*, San Diego, CA.

Hernandez-Pajares, M., J. Juan, J. Sanz, A. Aragon-Angel, P. Ramos-Bosch, D. Odijk, P. de Bakker, H. van der Marel, S. Verhagen, I. Fernádez-Hernández, M. Toledo, and J. Samson (2008). Feasibility Study of a European Wide Area Real Time Kinematic System. In *Proceedings of NAVITEC*.

Héroux, P., Y. Gao, J. Kouba, F. Lahaye, Y. Mireault, P. Collins, K. Macleod, P. Tétreault, and K. Chen (2004). Products and Applications for Precise Point Positioning - Moving Towards Real-Time. In *Proceedings of the ITM of the ION GNSS*.

Herring, T. (1992). Modeling atmospheric delays in the analysis of space geodetic data. In *Refraction of transatmospheric signals in geodesy*, pp. 157164.

Hewitson, S. and J. Wang (2006). GNSS receiver autonomous integrity monitoring (RAIM) performance analysis. *GPS Solutions 10*(3), 155–170.

Hewitson, S. and J. Wang (2010, Feb). Extended Receiver Autonomous Integrity Monitoring (eRAIM) for GNSS/INS Integration. *Journal of Surveying Engineering 136*(1), 13–22.

Hofmann-Wellenhof, B., H. Lichtenegger, and J. Collins (1997). *GPS Theory and Practice.* (4^{th} ed.). Wien: Springer-Verlag.

Hofmann-Wellenhoff, B. and H. Lichtenegger (2001). Global Positioning System: Theory and Practice. (5 ed.). Springer-Verlag, Berlin.

Hopfield, H. (1969). Two-quartic tropospheric refractivity profile for correcting satellite data. *Journal of Geophysical Research 74*, 44874499.

IAC (2015). GLONASS Information-Analytical Centre. www.glonass-ianc.rsa.ru. last accessed on 30-05-2015.

Ifadis, I. (1992). The excess propagation path of radio waves: Study of the influence of the atmospheric parameters on its elevation dependence. *Survey Review 31*, 289298.

IGS (2010, March). Phase Centre Variations. ftp://www.igs.org/pub/station/general/igs05.atx.

IGS (2015a, September). IGS Analysis Center Coordinator (ACC) at NOAA/NGS. http://acc.igs.org/.

IGS (2015b, September). IGS Products. http://igscb.jpl.nasa.gov/components/prods.html.

Irsigler, M., G. W. Hein, and B. Eissfeller (2004). Multipath performance analysis for future GNSS signals. In *Proceedings of ION NTM 2004*.

IS-GPS-200D (2004). NAVSTAR GLOBAL POSITIONING SYSTEM INTERFACE SPECIFICATION. Technical report, GPS Joint Program Office.

isro.org (2015). Indian Space Research Organization (ISRO). http://www.isro.org/. last accessed on 31-05-2015.

Jin, X.-X. (1996). *Theory of Carrier Adjusted DGPS Positioning Approach and Some Experimental Results*. Ph. D. thesis, Delft University of Technology.

Jokinen, A. S. (2014, August). *Enhanced ambiguity resolution and integrity monitoring methods for Precise Point Positioning*. Ph. D. thesis, Imperial College London.

Jonkman, N. and K. de Jong (2000). Integrity monitoring of IGEX-98 data, Part II: Cycle slip and outlier detection. *GPS Solutions 3*(4), 23–34.

JPL (2015, September). GDGPS: Orbit & Clock Corrections. http://www.gdgps.net/products/orbit-clock-corrections.html.

Juan, J. M., M. Hernández-Pajares, J. Sanz, P. Ramos-Bosch, A. Aragón-Àngel, R. Orús, W. Ochieng, S. Feng, M. Jofre, P. Coutinho, J. Samson, and M. Tossaint (2012, October). Enhanced Precise Point Positioning for GNSS Users. *IEEE Transactions on Geoscience and Remote Sensing 50*(10), 4213–4222.

Kaplan, E. and C. Hegarty (2006). *Understanding GPS: principles and applications*. Artech House.

Kechine, M., C. Tiberius, and H. van der Marel (2003). Experimental verification of Internet-based Global Differential GPS. In *Proceedings of the ION GNSS*.

Kersten, T. and S. Schön (2013). Analysis of IfE-Robot based Group Delay Variations for the Positioning and Navigation of Mobile Platforms. In *Proceedings of the European Navigation Conference ENC2013*, pp. 10.

Keshin, M., A. Le, and H. van der Marel (2006). SINGLE AND DUAL-FREQUENCY PRECISE POINT POSTIONING: APPROACHES AND PERFORMANCES. In *Proceedings of the 3rd ESA Workshop on Satellite Navigation User Equipment Technologies, NAVITEC 2006*.

Kleijer, F. (2004). *Troposphere Modeling and Filtering for Precise GPS Leveling*. Ph. D. thesis, Delft University of Technology.

Klobuchar, J. (1987). Ionospheric Time-Delay Algorithm for Single-Frequency GPS Users. *IEEE Transactions on Aerospace and Electronic Systems 23*, 325–331.

Knight, N., J. Wang, and C. Rizos (2010). Generalised measures of reliability for multiple outliers. *Journal of Geodesy 84*(10), 625635.

Koch, K. (1999). *Parameter Estimation and Hypothesis Testing in Linear Models* (2 ed.). Springer-Verlag Berlin Heidelberg.

Kok, J. (1982a). On data snooping and multiple outlier testing. Technical report, National Geodetic Survey, NOAA/NOS.

Kok, J. (1982b). Statistical analysis of deformation problems using Baarda's testing procedures. In *Daar heb ik veertig jaar over nagedacht, Festschrift Willem Baarda, Part 2*, pp. 469–488. Delft: NCG.

Kouba, J. (2009a). A Guide to Using International GNSS Service (IGS) Products. Technical report, IGS. http://igscb.jpl.nasa.gov/components/usage.html.

Kouba, J. (2009b). A simplified yaw-attitude model for eclipsing GPS satellites. *GPS Solutions 13*, 1–12.

Kouba, J. and P. Héroux (2001). Precise Point Positioning Using IGS Orbit and Clock Products. *GPS Solutions 5*, 12–28.

Lacy, M. D., M. Reguzzoni, and F. Sanso (2012). Real-time cycle slip detection in triple-frequency GNSS. *GPS Solutions 16*(3), 353–362.

Lancaster, P. and L. Rodman (1995). *Algebraic Riccati Equations*. Oxford science publications. Clarendon Press.

Landau, H., X. Chen, S. Klose, R. Leandro, and U. Vollath (2008). Trimbles Rtk And Dgps Solutions In Comparison With Precise Point Positioning. In *International Association of Geodesy Symposia*.

Langley, R. (1997). GPS receiver system noise. *GPS World 8*, 40–45.

Langley, R. (1999). Dilution of Precision. *GPS World May*, 52–59.

Langley, R. (2009). The SVN49 pseudorange error. *GPS World August*, 8–14.

Langley, R. B., H. Jannasch, B. Peeters, and S. Bisnath (2000, July). The GPS broadcast orbits: an accuracy analysis. In *33rd COSPAR Scientific Assembly, Warsaw, Poland*.

Lannes, A. and J. Prieur (2013). Calibration of the clock-phase biases of GNSS networks: the closure-ambiguity approach. *Journal of Geodesy 87*(8), 709–731.

Laurichesse, D. and F. Mercier (2007). Integer Ambiguity Resolution on Undifferenced GPS Phase Measurements and its Application to PPP. In *Proceedings of ION GNSS 2007*.

Laurichesse, D., F. Mercier, J. P. Berthias, P. Broca, and L. Cerri (2009). Integer Ambiguity Resolution on Undifferenced GPS Phase Measurements and its Application to PPP and Satellite Precise Orbit Determination. *Journal of the institute of Navigation 56*(2), 135–149.

Le, A. and P. Teunissen (2006, May). Recursive least-squares filtering of pseudorange measurements. In *Proceedings of the European Navigation Conference*, Manchester, pp. 710.

Le, A. Q. (2004). Achieving Decimetre Accuracy with Single Frequency Standalone GPS Positioning. In *Proceedings of the ION GNSS 17th International Technical Meeting of the Satellite Division*.

Le, A. Q. and C. Tiberius (2006a). Single-frequency precise point positioning with optimal filtering. *GPS Solutions 11*, 9.

Le, A. Q. and C. C. J. M. Tiberius (2006b, December). Phase wind-up effects in precise point positioning with kinematic platforms. In *Proceedings of the 3rd ESA Workshop on Satellite Navigation User Equipment Technologies, NAVITEC 2006*, Noordwijk, The Netherlands, pp. 8.

Leandro, R. (2009). *Precise Point Positioning with GPS a new approach for positioning, atmospheric studies, and signal analysis*. Ph. D. thesis, University of New Brunswick.

Leandro, R. F., M. C. Santos, and R. B. Langley (2007). GAPS: The GPS Analysis and Positioning Software A Brief Overview. In *Proceedings ION GNSS 20th International Technical Meeting of the Satellite Division*, Fort Worth, TX, pp. 1807–1811. Institute of Navigation.

Leick, A. (2004). *GPS Satellite Surveying* (3rd ed.). John Wiley and Sons, New York.

Lipp, A. and X. Gu (1994). Cycle slip detection and repair in integrated navigation systems. In *Proceedings IEEE PLANS94*, pp. 681–688.

Liu, X., C. C. J. M. Tiberius, and K. de Jong (2004). Modelling of differential single difference receiver clock bias for precise positioning. *GPS Solutions 7*(4), 209–221.

Liu, Z. (2010). A new automated cycle-slip detection and repair method for a single dual-frequency GPS receiver. *Journal of Geodesy 85*(3), 171–183.

Loyer, S., F. Perosanz, F. Mercier, H. Capdeville, and J. Marty (2012). Zero-difference GPS ambiguity resolution at CNESCLS IGS Analysis Center. *Journal of Geodesy 86*(11), 991–1003.

Maggert, D. (2015, July). [IGSMAIL-7120] MGEX stations added to IGS: AREG, BIK0, CEBR, CHOF, CHPG, CPVG, CUT0, CZTG, DJIG, DLF1, GOP6, GOP7, HRAG, KIR8, KZN2, LLAG, M0SE, MAR7, MAYG, MRO1, NYA2, OBE4, ONS1, PEN2, REDU, RGDG, SCRZ, SGOC, SIN1, STFU, STJ3, THTG, UCAL, UNB3, UNBD, UNBN, UNX2, UNX3, VOIM, WTZ3, WUH2, YEL2, ZIM3. https://igscb.jpl.nasa.gov/pipermail/igsmail/2015/008310.html.

Malys, S., M. Larezos, S. Gottschalk, S. Mobbs, B. Winn, E. Swift, and W. Mathon (1997). The GPS accuracy improvement initiative. In *Proceedings of the ION GPS*, pp. 375384.

Mann, H. and A. Wald (1943). On the Statistical Treatment of Linear Stochastic Difference Equations. *Econometrica 11*(3/4), 173–220.

Marquis, W., M. McFadden, T. Powell, J. Irvine, and B. Erwin (2009, May). L5 Demo Payload - from concept to capability in less than 12 months. *GPS World 20*(5), 27–31.

McCarthy, D. D. (1989). IERS Standards (1989), IERS Technical Note 3. Technical report, IERS.

McCarthy, D. D. and G. Petit (2003). IERS Conventions (2003), IERS Technical Note 32. Technical report, IERS.

McGill, R., J. Tukey, and W. Larsen (1978). Variations of Boxplots. *The American Statistician 32*(1), 1216.

Melgard, T., O. rpen, J. H. Ulstein, and E. Vigen (2010). Pulling in All Signals, PPP with GPS and GLONASS: The New G2. *GPS World March*, 28–35.

Memarzadeh, Y. (2009). *Ionospheric Modeling for Precise GNSS Applications*. Ph. D. thesis, Delft University of Technology.

Mertikas, S. and C. Rizos (1997). On-line detection of abrupt changes in the carrier-phase measurements of GPS. *Journal of Geodesy 71*, 469–482.

Mervart, L., Z. Lukes, C. Rocken, and T. Iwabuchi (2008). Precise Point Positioning With Ambiguity Resolution In Real-Time. In *Proceedings of ION GNSS 2008*.

Miao, Y., Z. Sun, and S. Wu (2011). Error analysis and cycle-slip detection research on satellite-borne GPS observation. *Journal of Aerospace Engineering 24*(1), 95–101.

Mierlo, J. V. (1980). A testing procedure for analytic deformation measurements. In *Proceedings of the Internationales Symposium ueber Deformationsmessungen mit Geodaetischen Methoden*. Verlag Konrad Wittwer, Stuttgart.

Mierlo, J. V. (1981). A review of model checks and reliability. In *Proceedings of the VI-th Int Symp on geodetic Computations*, Munich.

Mireault, Y., P. Tétreault, F. Lahaye, P. Héroux, and J. Kouba (2008, September). Online Precise Point Positioning. *GPS World 19*(9), 5964.

Misra, P. and P. Enge (2001). *Global Positioning System: Signals, Measurements, and Performance* (First ed.). Ganga-Jamuna Press, Lincoln MA.

Misra, P. and P. Enge (2006). *Global Positioning System: Signals, Measurements, and Performance* (Second ed.). Ganga-Jamuna Press.

Monge, B. M., G. Rodríguez-Caderot, and M. C. de Lacy (2014). Multifrequency algorithms for precise point positioning: MAP3. *GPS Solutions 18*(3), 355–364.

Montenbruck, O., A. Hauschild, U. Hessels, P. Steigenberger, and U. Hugentobler (2009). CONGO - First GPS/GIOVE Tracking Network for Science, Research. *GPS World 20*(9), 36–41.

Montenbruck, O., P. Steigenberger, and A. Hauschild (2015). Broadcast versus precise ephemerides: a multi-GNSS perspective. *GPS Solutions 19*(2), 321–333.

Montenbruck, O., P. Steigenberger, R. Khachikyan, G. Weber, R. B. Langley, L. Mervart, and U. Hugentobler (2013, Dec). IGS-MGEX: PREPARING THE GROUND FOR MULTI-CONSTELLATION GNSS SCIENCE. In *Proceedings of the 4th International Colloquium on Scientific and Fundamental Aspects of the Galileo System*, Prague.

Mruthyunjaya, L. (2014). IRNSS SIS ICD for Standard Positioning Service v1.0. Technical report, Indian Space Research Organization - ISRO Satellite Centre.

Muellerschoen, R. J., W. I. Bertiger, M. F. Lough, D. Stowers, and D. Dong (2000a, Jan). An Internet-Based Global Differential GPS System, Initial Results. In *ION National Technical Meeting*, Anaheim, CA USA.

Muellerschoen, R. J., W. I. Bertiger, M. F. Lough, D. Stowers, and D. Dong (2000b, January). An Internet-Based Global Differential GPS System, Initial Results. In *Proceedings of the ION National Technical Meeting*, Anaheim, CA, pp. 6.

NGA (2012, July). NGA GPS Ephemeris/Station/Antenna Offset Documentation. http://earth-info.nga.mil/GandG/sathtml/gpsdoc2012_02a.html.

Niell, A. (1996). Global mapping functions for the atmosphere delay at radio wavelengths. *Journal of Geophysical Research 101*, 32273246.

Niell, A. (2001). Preliminary evaluation of atmospheric mapping functions based on numerical weather models. *Physics and Chemistry of the Earth 26*, 475480.

NIMA (2004). DEPARTMENT OF DEFENSE WORLD GEODETIC SYSTEM 1984 Its Definition and Relationships with Local Geodetic Systems. Technical report, National Imagery and Mapping Agency (NIMA).

Odijk, D. (2002). *Fast Precise GPS Positioning in the Presence of Ionospheric Delays*. Ph. D. thesis, Delft University of Technology.

Odijk, D. (2008, March/April). What does geometry-based and geometry-free mean in the context of GNSS? *Inside GNSS March/April*, 22–24.

Odijk, D., B. S. Arora, and P. J. G. Teunissen (2014). Predicting the Success Rate of Long-baseline GPS+Galileo (Partial) Ambiguity Resolution. *Journal of Navigation 67*(3), 385–401.

Odijk, D. and P. J. G. Teunissen (2013a). Characterization of between-receiver GPS-Galileo inter-system biases and their effect on mixed ambiguity resolution. *GPS Solutions 17*(4), 521–533.

Odijk, D. and P. J. G. Teunissen (2013b, December). Estimation of differential intersystem biases between the overlapping frequencies of GPS, Galileo, BeiDou and QZSS. In *4th International colloquium scientific and fundamental aspects of the Galileo programme*, Prague, Czech Republic, pp. 8.

Odijk, D., B. Zhang, and P. J. G. Teunissen (2015). Multi-GNSS PPP and PPP-RTK: Some GPS+BDS Results in Australia. In *Proceedings of the China Satellite Navigation Conference*, Volume 2, pp. 613–623.

Petit, G. and B. Luzum (2010). IERS Conventions (2010), IERS Technical Note 36. Technical report, International Earth Rotation and Reference Systems Service.

Petrov, L. and J.-P. Boy (2004). Study of the atmospheric pressure loading signal in very long baseline interferometry observations. *J. Geophys. Res. 109*, 14.

Píriz, R., A. Mozo, P. Navarro, and D. Rodríguez (2008, September). magicGNSS: Precise GNSS Products Out of the Box. In *Proceedings of the ION GNSS*, Savannah, GA, pp. 1242–1251.

Priestley, M. (1981). *Spectral Analysis and Time Series*. London: Elsevier Academic Press.

Qu, W.-J., W.-Y. Zhu, S.-L. Song, and J.-S. Ping (2008). Evaluation of the Precision of Three Tropospheric Delay Correction Models. *Chinese Astronomy and Astrophysics 32*, 429 – 438.

Quarteroni, A., R. Sacco, and F. Saleri (2010). *Numerical Mathematics*. Texts in Applied Mathematics. Springer.

qzss.go.jp (2015). Quasi-Zenith Satellite System (QZSS). http://qzss.go.jp/en/index.html. last accessed on 31-05-2015.

Rabbou, M. A. (2015). Multiple Ambiguity Datum Precise Point Positioning Technique Using Multi-Constellation GNSS: GPS, GLONASS, Galileo and BeiDou. *Positioning 6*, 32–43.

Radicella, S. (2009). The NeQuick model genesis, uses and evolution. *Annals of Geophysics 52*, 417–422.

Rao, C. (1973). *Linear statistical inference and its applications*. John Wiley and Sons.

Rothacher, M. and R. Schmid (2010, September). ANTEX: The Antenna Exchange Format, Version 1.4. http://igscb.jpl.nasa.gov/igscb/station/general/antex14.txt.

RTCA (2001). Minimum Operational Performance Standards for Global Positioning System/Wide Area Augmentation System Airborne Equipment. Technical report, RTCA.

Saastamoinen, J. (1972). Atmospheric correction for the troposphere and stratosphere in radio ranging of satellites, The use of artificial satellites for geodesy. *Geophysics Monograph Series 15*, 247251.

Salzmann, M. (1991). MDB: a design tool for integrated navigation systems. *Journal of Geodesy 65*(2), 109–115.

Salzmann, M. and P. Teunissen (1990). Detection and Modelling of Coloured Noise for Kalman Filter Applications. In *Proceedings of the IAG International Symposium 107 on Kinematic Systems in Geodesy, Surveying and Remote Sensing*, New York, pp. 201–217. Springer-Verlag.

Schaer, S., G. Beutler, and M. Rothacher (1998, February). Mapping and predicting the ionosphere. In *Proceedings IGS AC Workshop*, Darmstadt, Germany.

Schmid, R., P. Steigenberger, G. Gendt, M. Ge, and M. Rothacher (2007). Generation of a consistent absolute phase-center correction model for GPS receiver and satellite antennas. *Journal of Geodesy 81*, 781–798.

Seepersad, G. and S. Bisnath (2013, September). Integrity Monitoring in Precise Point Positioning. In *Proceedings of the 26th International Technical Meeting of The Satellite Division of the Institute of Navigation (ION GNSS+ 2013)*, Nashville, TN, pp. 1164–1175.

Shi, C., Q. Zhao, M. Li, W. Tang, Z. Hu, Y. Lou, H. Zhang, X. Niu, and J. Liu (2012). Precise orbit determination of BeiDou Satellites with precise positioning. *Science China Earth Sciences 55*, 10791086.

Simsky, A., D. Mertens, J.-M. Sleewaegen, M. Hollreiser, and M. Crisci (2008). Experimental Results for the Multipath Performance of Galileo Signals Transmitted by GIOVE-A Satellite. *International Journal of Navigation and Observation 2008*, 13.

Simsky, A., D. Mertens, J.-M. Sleewaegen, W. D. Wilde, M. Hollreiser, and M. Crisci (2008). MBOC vs. BOC(1,1) Mulipath Comparison Based on GIOVE-B Data. *Inside GNSS 2008*(September/October), 36–39.

Sleewaegen, J.-M., W. de Wilde, and M. Hollreiser (2004, May). Galileo Alt-BOC receiver. In *Proceedings of ENC-GNSS 2004*, Rotterdam, The Netherlands, pp. 9.

Snyder, J. P. (1987). Map Projections: A Working Manual. Report 1395, Geological Survey (U.S.).

Springer, T. and R. Dach (2010). Innovation: GPS, GLONASS, and More. *GPS World June*, 6.

Springer, T. and U. Hugentobler (2001). IGS ultra rapid products for (near-) real-time applications. *Physics and Chemistry of the Earth, Part A: Solid Earth and Geodesy 26*(68), 623 – 628. Proceedings of the First COST Action 716 Workshop Towards Operational GPS Meteorology and the Second Network Workshop of the International GPS Service (IGS).

Tegedor, J., D. Lapucha, O. Ørpen, E. Vigen, T. Melgard, and R. Strandli (2015). The New G4 Service: Multi-constellation Precise Point Positioning Including GPS, GLONASS, Galileo and BeiDou. In *In Proceedings of ION GNSS+*.

Teunissen, P. J. G. (1985). *Optimization and design of geodetic networks. Springer, Berlin*, Chapter Generalized inverses, adjustment, the datum problem and S-transformations, pp. 11–55. Springer Berlin Heidelberg.

Teunissen, P. J. G. (1986). Adjusting and testing with the models of the affine and similarity transformation. *Manuscripta Geodaetica 11*, 214–225.

Teunissen, P. J. G. (1989). *Developments in Four-Dimensional Geodesy*, Chapter Nonlinear Inversion of Geodetic and Geophysical Data: Diagnosing Nonlinearity, pp. 241–264. Number 29 in Lecture Notes in Earth Sciences. Spinger Verlag.

Teunissen, P. J. G. (1990a). An integrity and quality control procedure for use in multi-sensor integration. In *Proceedings ION GPS-90*, pp. 513–522. Also in: Red Book Series of the Institute of Navigation, 2012, Vol. VII.

Teunissen, P. J. G. (1990b). Quality Control in Integrated Navigation Systems. *IEEE Aerospace and Electronic Systems Magazine 5*(7), 35–41.

Teunissen, P. J. G. (1991). The GPS phase-adjusted pseudorange. In *Proceedings of the 2nd international workshop on high precision navigation*, Stuttgart/Freudenstadt, Germany, pp. 115125.

Teunissen, P. J. G. (1994). The Least-Squares Ambiguity Decorrelation Adjustment: A Method for Fast GPS Integer Ambiguity Estimation. *LGR-report 9*, 18.

Teunissen, P. J. G. (1995). The invertible GPS ambiguity transformations. *manuscripta geodaetica 20*, 489–497.

Teunissen, P. J. G. (1997a). GPS double difference statistics: with and without using satellite geometry. *Journal of Geodesy 71*, 137–148.

Teunissen, P. J. G. (1997b). On the GPS widelane and its decorrelating property. *Journal of Geodesy 71*(9), 577–587.

Teunissen, P. J. G. (1998a). *GPS for Geodesy* (2nd enlarged ed.)., Chapter Quality Control and GPS, pp. 271–318. Springer-Verlag, Berlin.

Teunissen, P. J. G. (1998b). Minimal detectable biases of GPS data. *Journal of Geodesy 72*, 236–244.

Teunissen, P. J. G. (1998c). Success probability of integer GPS ambiguity rounding and bootstrapping. *Journal of Geodesy 72*(10), 606–612.

Teunissen, P. J. G. (2000a). *Adjustment theory; an introduction.* Delft University Press.

Teunissen, P. J. G. (2000b). *Testing theory; An Introduction*. Delft University Press, VSSD.

Teunissen, P. J. G. (2001). *Dynamic Data Processing* (1st ed.). Delft VSSD.

Teunissen, P. J. G. (2004). *Towards a Least-Squares Framework for Adjusting and Testing of both Functional and Stochastic Models*. Number 26 in Mathematical geodesy and positioning. Technische Universiteit Delft. Reprint of original 1988 report.

Teunissen, P. J. G. (2006). *Network quality control*. Delft University Press.

Teunissen, P. J. G. (2014, May). PPP-RTK: Multi-GNSS with Mixed Receivers. In *China Satellite Navigation Conference*.

Teunissen, P. J. G. and P. F. de Bakker (2012). Single-Receiver Single-Channel Multi-Frequency GNSS Integrity: Outliers, Slips and Ionospheric Disturbances. *Journal of Geodesy 87*(2), 161–177.

Teunissen, P. J. G. and P. F. de Bakker (2013, June). Integer cycle-slip resolution for the single receiver single channel multi-frequency GNSS model: An analytical and numerical analysis. In *Proceedings of the Hotine Marussi Symposium Rome*.

Teunissen, P. J. G. and A. Khodabandeh (2015). Review and principles of PPP-RTK methods. *Journal of Geodesy 89*(3), 217–240.

Teunissen, P. J. G. and A. Kleusberg (1998). *GPS for Geodesy*, Chapter GPS Observation Equations and Positioning Concepts, pp. 187–229. Springer-Verlag, Berlin.

Teunissen, P. J. G., D. Odijk, and B. Zhang (2010). PPP-RTK: results of CORS network-based PPP with integer ambiguity resolution. *Journal of Aeronautics, Astronautics and Aviation 42*(4), 223–229.

Teunissen, P. J. G., D. Simons, and C. Tiberius (2007). Probability and Observation Theory. lecture notes.

Tiberius, C. C. J. M. (1998). *Recursive data processing for kinematic GPS surveying*. Ph. D. thesis, Delft University of Technology.

Tiberius, C. C. J. M., P. F. de Bakker, H. van der Marel, and R. J. P. van Bree (2009, September 22-25). Geometry-free Analysis of GIOVE-A/B E1 - E5a, and GPS L1 - L5 Measurements. In *Proceedings of the ION GNSS 2009*, Savannah, GA, pp. 2911–2925.

Tiberius, C. C. J. M., H. van der Marel, J.-M. Sleewaegen, and F. Boon (2008, September/October). Galileo Down to a Millimeter: Analyzing the GIOVE-A/B Double Difference. *Inside GNSS September/October*, 40–44.

Torre, A. D. and A. Caporali (2015). An analysis of intersystem biases for multi-GNSS positioning. *GPS Solutions 19*(2), 297–307.

Trimble Navigation Limited (2008a). *GNSS Geodetic Antennas Brochure*. Sunnyvale, CA, USA: Trimble Navigation Limited.

Trimble Navigation Limited (2008b). *User Guide Trimble NetR8 GNSS Reference Receiver Version 3.80 Revision A*. Sunnyvale, CA, USA.: Trimble Navigation Limited.

u-blox (2015, September). Precise Point Positioning (PPP) High accuracy sub-meter positioning. https://www.u-blox.com/en/precise-point-positioning-ppp. last accessed 25-09-2015.

Urquhart, L. (2009, September). Atmospheric Pressure Loading and its Effects on Precise Point Positioning. In *Proceedings of the 22nd International Technical Meeting of The Satellite Division of the Institute of Navigation (ION GNSS 2009)*, pp. 658–667.

van Bree, R. J. P. and C. C. J. M. Tiberius (2012). Real-time single-frequency precise point positioning: accuracy assessment. *GPS Solutions 16*(2), 259–266.

van der Marel, H. (2009, September). Satellite Navigation (GNSS): GPS Observation Equations. Lecture notes.

van der Marel, H. and P. F. de Bakker (2012). In GNSS Solutions: Single- versus Dual-Frequency Precise Point Positioning. *Inside GNSS July August*, 30–35.

van der Marel, H. and B. Gündlich (2003). TOUGH Report - Development of Models for Use of Slant Delays: Slant Delay Retrieval and Multipath Mapping Software. Technical report, Delft University of Technology.

Vermeer, M. (1997). The Precision of Geodetic GPS and One Way of Improving It. *Journal of Geodesy 71*, 240–245.

Wanninger, L. (2008). GPS + GLONASS + SBAS = GNSS In Innovation: The Future is Now. *GPS World July*, 8.

Ward, P. (1996). *Understanding GPS: Principles and applications*, Chapter Satellite signal acquisition and tracking, pp. 554. Artech House, Boston.

Warren, D. and J. Raquet (2003). Broadcast vs. precise GPS ephemerides: a historical perspective. *GPS Solutions 7*, 151156.

Weber, G., L. Mervart, Z. Lukes, and C. R. J. Dousa (2007). Real-time Clock and Orbit Corrections for Improved Point Positioning via NTRIP. In *Proceedings of the 20th International Technical Meeting of The Institute of Navigation (ION ITM 2007)*.

Wells, D. (1989). *Guide to GPS positioning*. Canadian GPS Associates.

Wieser, A., M. Gaggl, and M. Hartinger (2005). Improved positioning accuracy with high-sensitivity GNSS receivers and SNR aided integrity monitoring of pseudo-range observations. In *Proceedings ION GNSS*, pp. 1545–1554.

Wieser, A., M. Petovello, and G. Lachapelle (2004). Failure scenarios to be considered with kinematic high precision relative GNSS positioning. In *Proceedings ION GNSS*, pp. 6.

Witchayangkoon, B. and P. Segantine (1999). Testing JPL's PPP Service. *GPS Solutions 3*, 73–76.

Wu, Y., S. Jin, Z. Wang, and J. Liu (2010). Cycle-slip detection using multi-frequency GPS carrier phase observations: a simulation study. *Advances in Space Research 46*, 144–149.

Wübbena, G., M. Schmitz, and A. Bagg (2005). PPP-RTK: precise point positioning using state-space representation in RTK networks. In *Proceedings of ION GNSS*, pp. 13–16.

Wübbena, G., M. Schmitz, and M. Propp (2008, June). Antenna Group Delay Calibration with the Geo++ Robot. In *IGS Analysis Workshop*, Miami Beach, Florida.

Xinlong, W., J. Jiaxing, and L. Yafeng (2009). The applicability analysis of troposphere delay error model in GPS positioning. *Aircraft Engineering and Aerospace Technology: An International Journal 81*, 445 – 451.

Xu, D. and Y. Kou (2011). Instantaneous cycle slip detection and repair for a standalone triple-frequency GPS receiver. In *Proceedings 26th ITM-ION*, pp. 3916–3922.

Yunck, T. P. (1996). *Global positioning system: Theory and Applications*, Chapter Orbit determination, pp. 559–592. AIAA Publications Washington DC.

Zhao, Q., J. Guo, M. Li, L. Qu, Z. Hu, C. Shi, and J. Liu (2013). Initial results of precise orbit and clock determination for COMPASS navigation satellite system. *Journal of Geodesy 5*, 475–486.

Zhao, Q., B. Sun, Z. Dai, Z. Hu, C. Shi, and J. Liu (2015). Real-time detection and repair of cycle slips in triple-frequency GNSS measurements. *GPS Solutions 19*(3), 381–391.

Zumberge, J. F., M. B. Heftin, D. C. Jefferson, M. M. Watkins, and F. H. Webb (1997). Precise point positioning for the efficient and robust analysis of GPS data from large networks. *JOURNAL OF GEOPHYSICAL RESEARCH 102*, 5005–5017.